UNIVERSITÄT BAYREUTH

Generating and manipulating non-classical states of light in various quantum dot-cavity setups

Von der Universität Bayreuth

zur Erlangung des Grades eines

Doktors der Naturwissenschaften (Dr. rer. nat.)

genehmigte Abhandlung

von

Tim Seidelmann

aus Bamberg

1. Gutachter: Prof. Dr. V. Martin Axt

2. Gutachter: Prof. Dr. Georg Herink

3. Gutachter: Prof. Dr. Pablo Tamborenea

Tag der Einreichung: 13. Oktober 2022

Tag des Kolloquiums: 25. April 2023

UNIVERSITÄT BAYREUTH

Generating and manipulating non-classical states of light in various quantum dot-cavity setups

Von der Universität Bayreuth

zur Erlangung des Grades eines

Doktors der Naturwissenschaften (Dr. rer. nat.)

genehmigte Abhandlung

von

Tim Seidelmann

aus Bamberg

1. Gutachter: Prof. Dr. V. Martin Axt

2. Gutachter: Prof. Dr. Georg Herink

3. Gutachter: Prof. Dr. Pablo Tamborenea

Tag der Einreichung: 13. Oktober 2022

Tag des Kolloquiums: 25. April 2023

Abstract

In the course of the second quantum revolution, quantum mechanics is put to practice in novel quantum technologies like quantum information technology, quantum cryptography, or quantum computing. Non-classical states of light such as single photons or entangled photon pairs, that are at the heart of many fascinating applications in these fields, can be created in semiconductor quantum dot-cavity systems. This cumulative thesis theoretically investigates the possibility to generate and manipulate highly non-classical states of light in such systems. To this end, the influence of various system parameters, e.g., the energy of involved cavity modes, intrinsic electronic properties, or external optical excitation, is analyzed. Because quantum dots unavoidably interact with their semiconductor environment they are influenced by temperature-dependent lattice vibrations, i.e., phonons, which are known to have a profound impact, even at cryogenic temperatures. In order to assess the impact of longitudinal acoustic phonons on photonic figures of merit without any approximations to the microscopic description, a numerically complete path-integral approach is employed.

This thesis presents a variety of notable results that may pave the way towards more advanced sources of non-classical states of light. Assuming an initially excited quantum dot, the impact of different quantum dot-cavity configurations and phonons on polarization-entangled photon pairs is studied, highlighting the importance of direct two-photon processes. In contrast to previous expectations, parameter areas are found for certain configurations, where a phonon-induced enhancement of photon entanglement takes place.

The possibility to generate different types of entangled Bell states in continuously excited quantum emitter-cavity systems is discussed. Based on an in-depth numerical and analytic investigation of this system, a protocol realizing an active, time-dependent switching between different types of entanglement is proposed. In the case of strongly confined quantum dots, a phase transition-like behavior for photon pair states and the suppression of N-photon bundles due to the strong phonon impact in constantly driven systems is revealed. A profound phonon influence is also encountered during the investigation of shape-changing photon number distributions that emerge after the excitation with chirped laser pulses.

Precisely timed and tailored laser pulses are employed to investigate the quality of single photons and store individual photons in a metastable dark exciton state. Quite remarkably, it is uncovered that the widely used quantum regression theorem systematically overestimates the

phonon impact on the indistinguishability. As highlight of the work, it is demonstrated that the achievable degree of photon entanglement in state-of-the-art experiments is limited due to a Stark-shift introduced by the two-photon resonant excitation scheme.

In total, this thesis gives detailed insights into the generation of non-classical states of light valuable to all working in photonic quantum technologies.

Kurzfassung

Im Zuge der zweite Quantenrevolution wird die Quantenmechanik in neuartigen Quantentechnologien, wie z.B. Quanteninformatik, Quantenkryptographie oder Quantencomputing, in die Praxis umgesetzt. Nichtklassische Lichtzustände, wie einzelnen Photonen oder verschränkte Photonpaare, die das Herzstück vieler faszinierenden Anwendungen in diesen Forschungsfeldern sind, können in Halbleiterquantenpunkt-Resonator-Systemen erzeugt werden. Diese kumulative Dissertation untersucht die Möglichkeit hochgradig nichtklassische Lichtzustände in solchen Systemen zu erzeugen und zu manipulieren auf theoretischer Ebene. Hierfür wird der Einfluss verschiedener Systemparameter, wie z.B. der Energie von Resonatormoden, intrinsischer elektronischer Eigenschaften oder äußerer, optischer Anregungen, analysiert. Da Quantenpunkte zwangsweise mit ihrer Halbleiterumgebung wechselwirken, werden sie von temperaturabhängigen Gitterschwingungen, d.h. Phononen, beeinflusst, von denen man weiß, dass sie bereits bei kryogenen Temperaturen einen tiefgreifenden Einfluss haben. Um die Auswirkungen von longitudinal akustischen Phononen auf photonische Kennzahlen zu beurteilen, ohne dass hierfür Näherungen an der mikroskopischen Beschreibung vorgenommen werden müssen, wird eine numerisch vollständige Pfadintegralmethode angewandt.

In dieser Dissertation wird eine Auswahl von beachtenswerten Ergebnissen präsentiert, welche den Weg hin zu fortgeschrittenen Quellen von nichtklassischen Lichtzuständen bereiten könnten. Ausgehend von einem anfänglich angeregter Quantenpunkt wird der Einfluss von verschiedenen Quantenpunkt-Resonator-Konfigurationen und von Phononen auf polarisationsverschränkte Photonpaare studiert, wodurch die Bedeutung von direkten Zweiphotonprozessen hervorgehoben wird. Im Gegensatz zu der bisherigen Erwartungshaltung, werden für bestimmte Konfigurationen Parameterbereiche gefunden, in denen eine von Phononen induzierte Verbesserung der Photonverschränkung auftritt.

Die Möglichkeit, verschiedene Arten von verschränkten Bellzuständen in konstant getriebenen Quantenemitter-Resonator-Systemen zu erzeugen, wird diskutiert. Basierend auf ausführlichen numerischen und analytischen Untersuchungen dieses Systems, wird ein Protokoll vorgeschlagen, welches ein aktives, zeitabhängiges Hin- und Herschalten zwischen den verschiedenen Verschränkungstypen ermöglicht. Im Fall von stark begrenzten Quantenpunkten wird ein phasenübergangsähnliches Verhalten von Photonpaaren und die Unterdrückung von N-Photonbündeln aufgrund des starken Phononeneinflusses in konstant getriebenen Systemen

aufgezeigt. Ein tiefgreifender Phononeinfluss wird außerdem bei der Untersuchung von formveränderlichen Photonzahlverteilungen gefunden, welche nach der Anregung mit gechirpten Laserpulsen auftreten.

Zeitlich genau abgestimmte und maßgeschneiderte Laserpulse werden benutzt um die Qualität von einzelnen Photonen zu untersuchen und um individuelle Photonen in metastabilen, dunklen Exzitonzuständen zu speichern. Bemerkenswerterweise wird aufgedeckt, dass das häufig benutzte Quantenregressionstheorem den Phononeinfluss auf die Ununterscheidbarkeit systematisch überschätzt. Als Höhepunkt dieser Arbeit wird dargelegt, dass der erreichbare Verschränkungsgrad von Photonen in modernen Experimenten durch eine Starkverschiebung begrenzt wird, welche durch das zweiphotonresonante Anregungsschema hervorgerufen wird.

Insgesamt gibt diese Dissertation detaillierte Einblicke in die Erzeugung nichtklassischer Lichtzustände, die für jeden, der im Bereich photonischer Quantentechnologien arbeitet, nützlich sind.

Contents

1 Motivation

At the beginning of the 20th century, the first quantum revolution brought mankind a deeper understanding of our physical reality and a new set of rules and fundamental laws. This new understanding, most importantly in semiconductor physics, enabled groundbreaking innovations and a first generation of devices based on the features of quantum mechanics like lasers, atomic clocks, or transistors. The latter is the backbone of modern electronics and paved the way for the digital age. At the moment a second quantum revolution takes place where the rules and principles of quantum mechanics, in particular the concepts of superposition and entanglement, are exploited to develop a second generation of devices that actively create, manipulate and read out quantum states. This led to novel and fascinating applications in different fields of quantum technologies such as quantum information technology, quantum cryptography, or quantum computing, that have the potential to drastically change our life once more. Thus, the world is currently at the door step of the quantum age.

Photons, the quanta of light, can be used to exchange quantum information between different parties or systems and to realize quantum bits (qubits), the counterpart to classical bits in information technologies. Among other candidates for these essential tasks, photons stand out, because they move at the speed of light and are hardly influenced by their environment. Therefore, the possibility to generate and manipulate non-classical states of light is integral for various applications in different quantum technologies.

Quantum dots embedded in microcavities are semiconductor nanostructures that have the potential to function as a deterministic, on-demand source of such states. Due to their semiconductor nature, it should be straightforward to combine them with the existing hardware in modern information technology. But unfortunately, this important advantage is also the root of their characteristic drawback. Their semiconductor environment gives rise to electron-phonon interactions, which typically degrade the quality of emitted photonic quantum states.

In this cumulative thesis, the suitability of different quantum dot-cavity setups for the generation and manipulation of highly non-classical states of light is investigated. First, in Chapter 2, a brief introduction into the system, the theoretical model, and the numerical calculation scheme is given. Afterwards, Chapter 3 provides a guide through a selection of relevant publications and highlights their most important results. Finally, Chapter 4 concludes this thesis and discusses two recent developments which might revolutionize theoretical investigations of open

quantum systems like quantum-dot cavity systems and the approach to the optical excitation strategy in these systems.

2 Theoretical background: model and methods

2.1 Semiconductor quantum dot-cavity system

2.1.1 Biexciton-exciton cascade in semiconductor quantum dots

Semiconductor quantum dots (QDs) are structures with typical dimensions on the nanometer scale[1,2]. The strong confinement of charge carriers inside the QD leads to highly localized carrier wave functions and, consequently, to well-separated, discrete energy levels. Therefore, QDs are also referred to as *artificial atoms*[2]. Typically, QDs are realized by embedding a semiconductor material or alloy into another one. There exist several methods to fabricate QDs with different material combinations. In this thesis, typically stongly-confined, self-assembled InGaAs QDs are considered, that are grown on a GaAs bulk material by the Stranski-Krastanow method[3,4]. In this method, one semiconductor material is grown by molecular beam epitaxy on a semiconductor substrate with a slightly different lattice constant. Due to the mismatch in the lattice constants, strain builds up during the growth process. Beyond a critical layer thickness of the deposited material, small islands begin to randomly form on the substrate. Typical spatial dimensions for these QDs are on the order of a few nanometers.

Because of the strong spatial confinement and the corresponding well-separated, discrete energy levels, it is often sufficient to restrict the modeling to the lowest conduction band and the highest valence heavy-hole band. After an excitation, an exciton, i.e., a bound electron-hole pair, consisting of one s-like conduction band electron with spin z-component $S_z^{\mathrm{e}} = \pm\frac{1}{2}$ and one p-like valence band heavy hole with $S_z^{\mathrm{h}} = \pm\frac{3}{2}$ is formed due to the Coulomb interaction. As a consequence of the Pauli principle, only a maximum of two electrons, with opposite spin z-component, can occupy the energetically lowest s-like state. This bound state with a typical binding energy E_{B} on the order of a few meV which comprises two excited electron-hole pairs is referred to as the biexciton state.

Thus, the four possible energetically lowest, charge-neutral excited states are the exciton states denoted by $|S_z^{\mathrm{e}}, S_z^{\mathrm{h}}\rangle$. Due to the optical selection rules, only the two *bright exciton* states $|X_+\rangle = |-\frac{1}{2}, +\frac{3}{2}\rangle$ and $|X_-\rangle = |+\frac{1}{2}, -\frac{3}{2}\rangle$ with a total spin z-component ± 1 can be optically
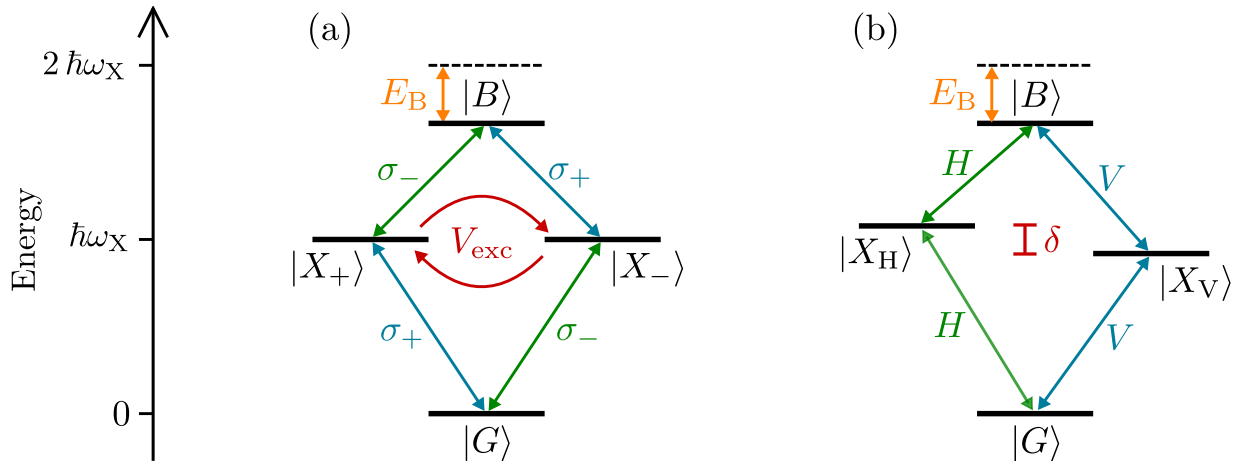
Figure 2.1: Biexciton-exciton cascade consisting of the ground state $|G\rangle$, two bright exciton states, and biexciton state $|B\rangle$. $\hbar\omega_{\mathrm{X}}$ denotes the mean exciton energy and E_{B} is the biexciton binding energy. (a) Electronic transitions between the bright excitons $|X_{\pm}\rangle$ and the remaining states couple to $\sigma_{\pm}$ circularly polarized light. The energetically degenerate bright excitons are coupled by the exchange interaction V_{exc}. (b) Electronic transitions between bright excitons $|X_{\mathrm{H/V}}\rangle$ and the remaining states couple to horizontally (H) or vertically (V) polarized light. The bright excitons are energetically split by the exciton fine-structure splitting δ.

excited by using σ_{+} and σ_{-} circularly polarized light, respectively. The remaining two exciton states with total spin z-component ± 2 are thus referred to as *dark excitons*. The biexciton is also optically bright and can be reached from the bright exciton $|X_{+}\rangle$ ($|X_{-}\rangle$) by absorption of one σ_{-} (σ_{+}) polarized photon. Together with the ground state, i.e., the state without any excitations, the two bright excitons and the biexciton form the optically active *biexciton-exciton cascade*.

In general, the two bright exciton states are coupled by the exchange interaction. Therefore, the energy eigenstates of the electronic system are exciton states $|X_{\mathrm{H}}\rangle = \left(|X_{+}\rangle + |X_{-}\rangle\right)/\sqrt{2}$ and $|X_{\mathrm{V}}\rangle = i\left(|X_{+}\rangle - |X_{-}\rangle\right)/\sqrt{2}$ which are split by the so called *exciton fine-structure splitting* δ and couple to linearly polarized light[5] - here denoted as H (horizontal) and V (vertical) polarization, respectively. Figure 2.1 depicts the biexciton-exciton cascade and the optical selection rules for circularly [panel (a)] and linear [panel (b)] polarized light. After the preparation of the biexciton state, there are two decay paths from the biexciton to an exciton state and subsequently into the ground state. Because of this feature and typically small fine-structure splittings on the order of 10 µeV, the biexciton-exciton cascade in QDs is often discussed as a source for polarization-entangled photon pairs[1,6–10]. Their fundamental advantage is a deterministic on-demand character[11–14]. In contrast to spontaneous parametric down-conversion sources, QDs have the potential to deliver exactly one entangled photon pair per excitation pulse[1].

2.1.2 Optically excited four-level emitter

The biexciton-exciton cascade in semiconductor quantum dots represents one possible realization of a four-level quantum emitter with a diamond-shaped level structure, cf., Figure 2.1. Note that such four-level emitters can also be found in other systems, like F-centers or atoms[15–17]. The diamond-shaped four-level model for the electronic structure of a quantum emitter is predominantly used in this thesis. For some studies, however, slightly different models, e.g., the reduction to a two-level system - in the case of circularly polarized light and insignificant exchange interaction - or the inclusion of dark excitons, are considered (cf., [Pub 3, Pub 6, Pub 7, Pub 8]).

In order to create non-classical states of light, the quantum emitter has to be excited first, from its ground state into an excited state. One possible way to achieve this, are optical excitation schemes employing continuous-wave or pulsed lasers. When an external laser is included into the model using a semi-classical description, the Hamiltonian for the optically driven four-level QD is given by

$$
\begin{aligned}
\hat{H}_{\text{QD-L}} = {} & \left(\Delta_{\text{XL}} + \frac{\delta}{2}\right)|X_{\text{H}}\rangle\langle X_{\text{H}}| + \left(\Delta_{\text{XL}} - \frac{\delta}{2}\right)|X_{\text{V}}\rangle\langle X_{\text{V}}| + (2\Delta_{\text{XL}} - E_{\text{B}})\,|B\rangle\langle B| \\
& + \Omega^*(t)\,\hat{\sigma}_{\text{L}} + \Omega(t)\,\hat{\sigma}_{\text{L}}^{\dagger}
\end{aligned}
\tag{2.1}
$$

where $\Omega(t)$ is proportional to the time-dependent laser amplitude and the star symbol indicates the complex conjugated quantity. Note that the Hamiltonian in Eq. (2.1) is formulated in a frame co-rotating with the laser frequency ω_{L}. Furthermore, the dipole and rotating wave approximations have been applied. E_{B} and δ denote the biexciton binding energy and the fine-structure splitting, respectively, and $\Delta_{\text{XL}} := \hbar(\omega_{\text{X}} - \omega_{\text{L}})$ is the detuning between the energetic position of the laser and the mean exciton energy $\hbar\omega_{\text{X}}$. The polarization of the external laser is encoded in the operator

$$
\hat{\sigma}_{\text{L}} := \alpha_{\text{H}}\,\hat{\sigma}_{\text{H}} + \alpha_{\text{V}}\,\hat{\sigma}_{\text{V}}
\tag{2.2a}
$$

$$
\hat{\sigma}_{\text{H/V}} := |G\rangle\langle X_{\text{H/V}}| + |X_{\text{H/V}}\rangle\langle B|
\tag{2.2b}
$$

where the coefficient $\alpha_{\text{H/V}} \in \mathbb{R}$ represents its component in H/V direction. Finally, the operators $\hat{\sigma}_{\text{H/V}}$ describe electronic transitions that couple to horizontally/vertically polarized light.

2.1.3 Quantum dot-cavity structures

In order to enhance the non-classical light source, the QD is often embedded inside a microcavity. By doing so, the photon emission rate and the light-collection efficiency are increased due to the Purcell effect[18–20]. There exist several different strategies and setups for QD cavity structures[1,6], e.g., one possibility is to place Bragg-reflectors below and on top of the

QD[8,11,21]. In addition to the Purcell effect, embedding the QD inside a cavity structure can also be used to influence the decay mechanism/characteristics. For example, when the energy of the cavity modes is placed at the two-photon resonance between ground and biexciton state, direct two-photon emission processes can be enhanced in comparison to the sequential one-photon emission processes following the biexciton-exciton cascade[22–27]. Thus, the generation of non-classical photon states is affected by the chosen QD-cavity realization, and one might use cavity parameters to manipulate the resulting state.

The surrounding cavity structure modifies the electromagnetic modes in the vicinity of the QD. Due to its resonance conditions, only well-separated electromagnetic field modes exist along the cavity direction. In this thesis, it is always assumed that, for each of the two linear polarizations H and V, only one of these cavity modes is close to resonance with the electronic QD transitions. In this situation, it is sufficient to consider only these two distinct cavity modes and dismiss the rest of them.

In cavity quantum electrodynamics, the interaction of a few-level system, like the biexciton-exciton cascade in QDs, with individual cavity modes can often by described by an extended Jaynes-Cummings model[28,29], exploiting again the dipole and rotating wave approximations. In the frame co-rotating with a frequency ω_L, the interaction of the four-level QD with one horizontally and one vertically polarized cavity mode is given by the Hamiltonian

$$\hat{H}_\mathrm{C} = \sum_{\ell=H,V} \Delta_\mathrm{CL}^{(\ell)} \hat{a}_\ell^\dagger \hat{a}_\ell + \sum_{\ell=H,V} g \left(\hat{a}_\ell^\dagger \hat{\sigma}_\ell + \hat{a}_\ell \hat{\sigma}_\ell^\dagger \right), \tag{2.3}$$

where the QD-cavity coupling strength g is assumed to be equal for all four QD transitions. The bosonic operator $\hat{a}_\mathrm{H/V}^\dagger$ ($\hat{a}_\mathrm{H/V}$) creates (annihilates) one photon in the cavity mode with the respective polarization. The energies of the cavity modes are denoted by $\hbar\omega_\mathrm{H/V}$ and $\Delta_\mathrm{CL}^{(\ell)} = \hbar(\omega_\ell - \omega_\mathrm{L})$ is the energetic detuning between the cavity mode $\ell \in \{H,V\}$ and the frequency of the rotating frame, typically, the external laser frequency. For most studies presented in this thesis, the two orthogonally polarized cavity modes are considered to be energetically degenerate, i.e., the cavity-laser detuning $\Delta_\mathrm{CL}^{(\mathrm{H})} = \Delta_\mathrm{CL}^{(\mathrm{V})} =: \Delta_\mathrm{CL}$ is identical for both modes.

2.1.4 Cavity losses and radiative decay

Especially in an application-oriented description, further processes and mechanisms have to be included in order to reflect realistic quantum emitter-cavity structures and experiments. The first process are cavity losses due to a non-unity reflectance of the cavity mirrors, e.g., Bragg reflectors. Typically, the non-classical photon state created inside a cavity structure has to be delivered to an outside recipient. Thus, these losses are not only unavoidable but also necessary for applications in quantum technologies. The second type of process associated with realistic quantum-emitter cavity structures is the radiative decay of the quantum emitter. This process

captures emission events, where the quantum emitter emits a photon into the continuum of electromagnetic field modes orthogonal to the cavity axis instead of into a cavity mode.

Both processes can be well-described as Markovian processes with phenomenological rates. They are incorporated into the theoretical description using Lindblad operators[30,31]

$$\mathcal{L}_{\hat{O},\Gamma}\hat{\rho} = \frac{\Gamma}{2}\left(2\,\hat{O}\hat{\rho}\hat{O}^{\dagger} - \hat{O}^{\dagger}\hat{O}\hat{\rho} - \hat{\rho}\hat{O}^{\dagger}\hat{O}\right) \tag{2.4}$$

acting on the statistical operator $\hat{\rho}$ of the quantum emitter-cavity system. In this formalism, $\hat{O}$ represents the system operator associated with the respective Markovian process with phenomenological rate Γ. Cavity losses (radiative decay processes) are associated with the operators $\hat{a}_{\ell}$ ($|G\rangle\langle X_{\ell}|$ and $|X_{\ell}\rangle\langle B|$) and, throughout this thesis, the corresponding rate is denoted by κ (γ).

2.1.5 Phonon environment and spectral density

Phonon environment Using semiconductor QDs as source for non-classical states of light has both characteristic advantages and drawbacks. On the one hand, they can be quite easily incorporated into already existing semiconductor devices or setups used in modern (classical) information technology. But on the other hand, they unavoidably interact with their semiconductor environment, which gives rise to charge carrier-phonon interactions.

In the case of strongly-confined, self-assembled QDs, the lattice properties, in particular the lattice constants, of the QD deviate only marginally from the surrounding semiconductor crystal matrix. Thus, in contrast to charge carriers, phonons are not confined to the QD and the consideration of bulk phonons is justified. Furthermore, for GaAs-type QDs at cryogenic temperatures, the deformation potential coupling to longitudinal acoustic (LA) phonons is typically the most important and thus dominant charge carrier-phonon interaction[32–35]. Due to the well-separated energy levels of the QD, acoustic phonons cannot introduce direct transitions between different electronic states. Rather, elastic scattering processes where the QD state remains unchanged lead to a loss of quantum coherence in the QD-cavity system and impact its time-evolution. Consequently, the deformation potential coupling to LA phonons is of the *pure dephasing*-type. Finally, in strongly-confined QDs, the wave function for exciton and biexciton states can in good approximation be factorized into one-particle wave functions for electrons and holes. This directly implies the assumption that the charge carrier-phonon coupling is proportional to the number of electron-hole pairs.

Altogether, the interaction between charge carriers confined inside the QD and the continuum of LA phonons is described by the Hamiltonian

$$\hat{H}_{\text{Ph}} = \hbar\sum_{\mathbf{q}}\omega_{\mathbf{q}}\hat{b}_{\mathbf{q}}^{\dagger}\hat{b}_{\mathbf{q}} + \hbar\sum_{\chi,\mathbf{q}}n_{\chi}\left(\gamma_{\mathbf{q}}^{\text{X}}\hat{b}_{\mathbf{q}}^{\dagger} + \gamma_{\mathbf{q}}^{\text{X}*}\hat{b}_{\mathbf{q}}\right)|\chi\rangle\langle\chi| \tag{2.5}$$

where $\gamma_{\mathbf{q}}^{\mathrm{X}}$ denotes the exciton-phonon coupling strength and $n_\chi \in \{0, 1, 1, 2\}$ is the number of excitons present in the QD state $|\chi\rangle \in \{|G\rangle, |X_{\mathrm{H}}\rangle, |X_{\mathrm{V}}\rangle, |B\rangle\}$. The bosonic operator $\hat{b}_{\mathbf{q}}^\dagger$ ($\hat{b}_{\mathbf{q}}$) creates (annihilates) one bulk phonon with energy $\hbar\omega_{\mathbf{q}}$ in the mode with wave vector $\mathbf{q}$. Although it is obvious, that in this description phonons cannot directly lead to electronic transitions between the bare QD states, they can introduce transitions between (cavity- and laser-)dressed states once the QD is coupled to a cavity or is optically driven[36]. Furthermore, the pure-dephasing coupling to LA phonons is the origin of many, often non-Markovian, effects in solid-state physics, like the renormalization of Rabi frequencies and the damping of Rabi oscillations[37–42], a renormalization of the QD-cavity coupling strength[43–45], the appearance of phonon sidebands in optical spectra[46,47], or a nonexponential partial loss of coherence[32,33] and its non-monotonic temperature dependence[48,49]

Phonon spectral density   The charge carrier-phonon interaction is characterized by the so-called *phonon spectral density* $J(\omega) = \sum_{\mathbf{q}} \left|\gamma_{\mathbf{q}}^{\mathrm{X}}\right|^2 \delta(\omega - \omega_{\mathbf{q}})$, which is determined by the coupling constant. The explicit expression for $J(\omega)$ depends on geometric aspects and material parameters. Typically, the following assumptions are made: (i) a spherically symmetric, harmonic oscillator confinement for electrons and holes, (ii) a linear phonon dispersion $\omega_{\mathbf{q}} = c_{\mathrm{s}} |\mathbf{q}|$ with sound velocity c_{s}, and again (iii) the factorization of the exciton wave function are assumed. After employing these assumptions, the explicit expression for the phonon spectral density reads[50,51]

$$J(\omega) = \frac{\omega^3}{4\pi^2 \hbar \rho_{\mathrm{D}} c_{\mathrm{s}}^5} \left[D_{\mathrm{e}}\, e^{-\omega^2 a_{\mathrm{e}}^2/(4c_{\mathrm{s}}^2)} - D_{\mathrm{h}}\, e^{-\omega^2 a_{\mathrm{h}}^2/(4c_{\mathrm{s}}^2)} \right]^2 \tag{2.6}$$

where a_{e} (a_{h}) is the electron (hole) confinement length. The necessary material parameters - mass density ρ_{D}, electron (hole) deformation potential D_{e} (D_{h}), and the sound velocity - for GaAs-based QDs are taken from the literature and are listed, e.g., in [Pub 1] or [Pub 10]. Note that in the limit of small frequencies, $J(\omega)$ is proportional to ω^3, i.e., the considered coupling is of the super-Ohmic type.

In this thesis, usually, an identical confinement for electrons and holes is assumed. This results in the fixed ratio $a_{\mathrm{e}}/a_{\mathrm{h}} = 1.15$ due to the different effective masses of electrons and holes. In the case of strongly-confined, self-assembled InGaAs QDs, good agreements between theory and experiment were obtained for an electron confinement length around $3...5\,\mathrm{nm}$[52,53]. Note that the assumption of a spherically symmetric QD does not provide a loss of generality, because the theoretical description of any asymmetric QD can be mapped to a symmetric situation with suitable parameters[54]. The resulting phonon spectral density $J(\omega)$ for $a_{\mathrm{e}} = 3$ nm is depicted in Figure 2.2. In this case, the maximum of the phonon spectral density is obtained for a frequency corresponding to roughly 2 meV.
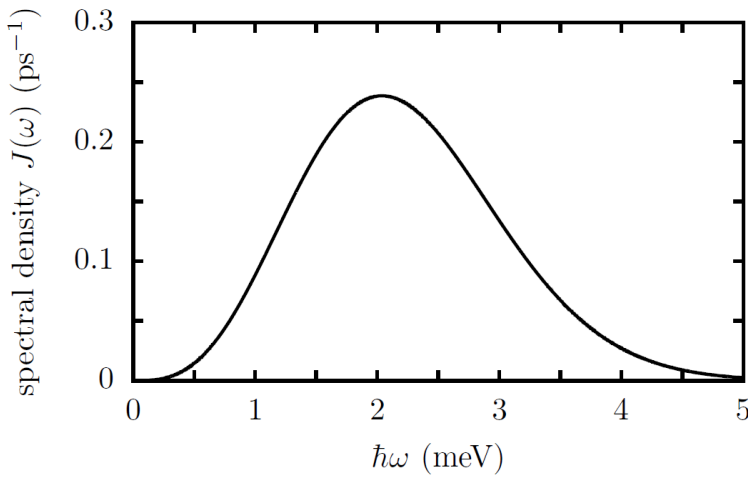
Figure 2.2: [Taken from [Pub 10]] Phonon spectral density $J(\omega)$ for a GaAs-based QD with electron (hole) confinement length $a_{\mathrm{e}} = 3$ nm ($a_{\mathrm{h}} = a_{\mathrm{e}}/1.15$). The remaining material parameters can be found in Table II of [Pub 10].

2.2 The Liouville-von Neumann equation and its solution

The scientific studies presented in this thesis employ some or all building blocks and their corresponding theoretical description as introduced in the previous Section 2.1. A sketch of the system predominantly discussed in this thesis is provided in Figure 2.3. Typical target quantities are the occupation probability for different electronic or photonic states or figures of merit characterizing the non-classical state of light, e.g., common single-photon characteristics or entanglement measures. They are obtained by evaluating time-dependent expectation values or correlation functions containing different operator combinations with one or multiple time arguments.

In the corresponding representation in the Schrödinger picture, these time-dependent quantities can be calculated based on the time-evolution of the system. The dynamical equation governing the time-evolution of the statistical operator $\hat{\rho}$ of the complete system, consisting of electronic, photonic, and phonon degrees of freedom, is the Liouville-von Neumann equation

$$\frac{\mathrm{d}}{\mathrm{d}t}\hat{\rho} = -\frac{i}{\hbar}\left[\hat{H}, \hat{\rho}\right]_{-} + \sum_{\ell=H,V}\left\{\mathcal{L}_{\hat{a}_\ell,\kappa} + \mathcal{L}_{|G\rangle\langle X_\ell|,\gamma} + \mathcal{L}_{|X_\ell\rangle\langle B|,\gamma}\right\}\hat{\rho} =: \mathcal{L}\hat{\rho} \qquad (2.7)$$

Here $\left[\hat{A}, \hat{B}\right]_{-} := \hat{A}\hat{B} - \hat{B}\hat{A}$ is the commutator between two operators $\hat{A}$ and $\hat{B}$, and the complete system Hamiltonian is given by

$$\hat{H} = \hat{H}_{\mathrm{QD\text{-}L}} + \hat{H}_{\mathrm{C}} + \hat{H}_{\mathrm{Ph}} \qquad (2.8)$$

In principle, the formal, exact solution of the Liouville-von Neumann equation is

$$\hat{\rho}(t) = \hat{\mathcal{T}}\exp\left[\int_{t_0}^{t}\mathcal{L}\,\mathrm{d}t'\right]\hat{\rho}(t_0) =: \mathcal{P}_{t_0,t}\left[\hat{\rho}(t_0)\right] \qquad (2.9)$$
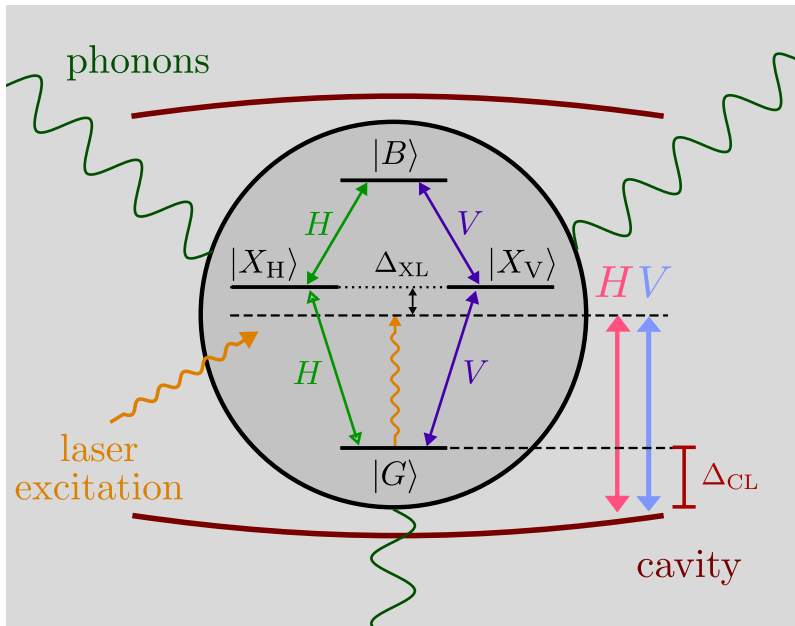
Figure 2.3: Schematic sketch of the considered system. The biexciton-exciton cascade in QDs (cf., Figure 2.1) is embedded inside a lossy cavity and interacts with two orthogonally polarized cavity modes (red and blue double-headed arrows). The QD is excited by an external laser (orange arrow) and can also decay radiatively. Due to its semiconductor environment, the QD is coupled to LA phonons. A possible energetic detuning between exciton (cavity modes) and laser is denoted by Δ_{XL} (Δ_{CL}).

where $\hat{\rho}(t_0)$ denotes the initial statistical operator at the starting time t_0 and $\hat{\mathcal{T}}$ is the time-ordering operator. After introducing a suitable basis of ket states $|j\rangle$ and bra states $\langle k|$ for the Hilbert space, one can change to the density matrix ρ with elements $\rho_{kj} = \langle k|\hat{\rho}|j\rangle$. The time-evolution of these elements can then be numerically calculated by discretizing the formal propagator $\mathcal{P}_{t_0,t}$. However, this brute force approach is only feasible for calculations without phonons, i.e., $\hat{H} = \hat{H}_{\mathrm{QD\text{-}L}} + \hat{H}_{\mathrm{C}}$. Here, the dimension of the Hilbert space is manageable when either a reasonable cut-off is introduced for the maximum number of photons to be considered in each cavity mode (e.g., in [Pub 4] or [Pub 5]), or no surrounding cavity is present (e.g., in [Pub 9]). In contrast, the inclusion of the deformation potential coupling to LA phonons via $\hat{H}_{\mathrm{Ph}}$ results in a genuine many-body problem with infinite degrees of freedom and, consequently, an infinite-dimensional Hilbert space.

In order to tackle this problem, different strategies and methods can be applied. For example, one often used method is a fourth-order correlation expansion, cf., [FPub 6]. In this approach, one starts with the dynamical equations for single-particle expectation values, e.g. $\langle |X_\ell\rangle\langle X_\ell|\rangle$, $\langle |G\rangle\langle X_\ell|\rangle$. Due to the charge carrier-phonon interaction, the equations of motion for these quantities derived from the Heisenberg equation contain expectation values of higher order, e.g., $\left\langle |G\rangle\langle X_\ell|\hat{b}_{\mathbf{q}}^\dagger\right\rangle = \langle |G\rangle\langle X_\ell|\rangle \left\langle \hat{b}_{\mathbf{q}}^\dagger\right\rangle + \delta\left\langle |G\rangle\langle X_\ell|\hat{b}_{\mathbf{q}}^\dagger\right\rangle$ with correlation $\delta\left\langle |G\rangle\langle X_\ell|\hat{b}_{\mathbf{q}}^\dagger\right\rangle$. These correlations are considered as new variables and their equations of motion then contain correlations of an even higher order. By repeating this procedure, one ends up with an infinite hierarchy of equations. They are closed, i.e., cut, by neglecting correlations of fifth order, assuming that the importance of correlations decreases with their order. One advantage of this scheme is that it also provides access to expectation values for phonon variables, e.g., the propagation of phonon wave packets, cf., [FPub 6], or phonon squeezing[55] can be analyzed. But

due to its approximative nature, e.g., phonon processes beyond the second order and higher correlations are neglected. Furthermore, this method is not suitable for simulations on the nanosecond scale, because it becomes unstable after a certain time interval determined by the **q**-discretization[56,57].

Often, one is only interested in electronic or photonic expectation values or correlation functions. In this situation it is sufficient to consider the time-evolution of the QD-cavity subsystem described by the reduced statistical operator $\hat{\bar{\rho}} = \text{Tr}_{\text{Ph}} \{\hat{\rho}\}$ and the corresponding reduced density matrix $\bar{\rho}$, where the phonon degrees of freedom have been traced out. One approximative method that delivers quantities based on the reduced density matrix is the polaron master equation approach[58,59]. The central idea of this method is to perform a transformation into the polaron frame and subsequently derive a time-local master equation in this frame employing a Born-Markov approximation. As a result various non-Markovian features can be observed in this approach, e.g., phonon sidebands in optical spectra, cf., Erratum of [Pub 6]. However, the validity of this approach is not always clear, especially in the case of strong interactions and high temperatures[60].

In order to analyze the impact of phonons without any prejudice, in this thesis, a numerically complete path-integral approach is employed. This method also delivers quantities based on the reduced density matrix and, in contrast to the two previously discussed methods, no further approximations or assumptions are applied to the model. In the following Section 2.3, a brief introduction to the path-integral approach is presented.

2.3 Iterative real-time path-integral method

2.3.1 General and advanced iteration scheme

General iteration scheme   In order to characterize the quantum emitter and the created state of light, electronic and photonic expectation values and correlation functions are of interest. The expectation values of any observable related to the QD-cavity subsystem can be obtained from its reduced density matrix. The iterative real-time path-integral method provides the opportunity to extract the time-evolution of this system of interest without any additional approximations or assumptions to the model as formulated in the Liouville-von Neumann equation (2.7). The principle idea is to discretize the formal time propagator into operators acting on small time intervals Δt, factorize it into contributions that act only on the subsystem of interest, i.e., the QD-cavity system, and the remaining degrees of freedom, i.e., $\hat{H}_{\text{Ph}}$, respectively, and trace out the phonon degrees of freedom. Because of the factorization the standard method is exact in first order of Δt. The general cost of the path-integral approach is a finite memory introduced by the charge carrier-phonon interaction, which renders the subsystem's dynamics non-local in time. However, for a continuum of phonon modes, the induced memory has only a

finite depth. This feature allows for an iterative approach to the solution that makes long-time studies feasible. In the following, a brief description of this path-integral approach is given.

After introducing a basis of ket states $|\mu\rangle$ and corresponding bra states $\langle\nu|$ for the QD-cavity system, the reduced density matrix $\bar{\rho}$ can be expressed in this basis as

$$\bar{\rho} = \sum_{\nu,\mu} \bar{\rho}_{\nu\mu} |\nu\rangle\langle\mu| \tag{2.10a}$$

$$\bar{\rho}_{\nu\mu} = \langle\nu|\mathrm{Tr}_{\mathrm{Ph}}\{\hat{\rho}\}|\mu\rangle \tag{2.10b}$$

Typically, the basis $|\mu\rangle$ is chosen as the combined QD-cavity states $|\chi, n_{\mathrm{H}}, n_{\mathrm{V}}\rangle$ with $\chi \in \{G, X_{\mathrm{H}}, X_{\mathrm{V}}, B\}$, where n_ℓ denotes the number of cavity photons in the mode with polarization $\ell \in \{H, V\}$. In their seminal work in the year 1995[61,62], Makri and Makarov showed that $\bar{\rho}_{\nu\mu}$ can be expressed as a sum over paths which can be performed iteratively, provided that the system dynamics is Hamiltonian. A decade ago, this method was then adopted to QDs by Vagov *et al.*[63]. In recent years, it has been demonstrated that an iterative path-integral approach is still possible when non-Hamiltonian contributions as provided by $\mathcal{L}_{a_\ell,\kappa}$, $\mathcal{L}_{|G\rangle\langle X_\ell|,\gamma}$, and $\mathcal{L}_{|X_\ell\rangle\langle B|,\gamma}$ are included[50].

After introducing an equally spaced time discretization $t_j = j\,\Delta t$ with time step Δt and $j \in \mathbb{N}_0$, the states of the QD-cavity system at time t_j are denoted by ν_j and μ_j, respectively. Due to the finite memory depth, a finite memory length $t_{\mathrm{M}} = n_{\mathrm{M}}\,\Delta t$ can be used and the iteration scheme is based on the so-called *augmented density matrix* (ADM), an object which depends on the current time-step t_n and all prior time-steps that lie within this memory length. The ADM $\bar{\rho}^{\mu_n\ldots\mu_{n-n_{\mathrm{M}}+1}}_{\nu_n\ldots\nu_{n-n_{\mathrm{M}}+1}} := \sum\limits_{\substack{\nu_{n-n_{\mathrm{M}}}\ldots\nu_0 \\ \mu_{n-n_{\mathrm{M}}}\ldots\mu_0}} R^{\mu_n\ldots\mu_0}_{\nu_n\ldots\nu_0}$ obeys the recurrence[50]

$$\bar{\rho}^{\mu_n\ldots\mu_{n-n_{\mathrm{M}}+1}}_{\nu_n\ldots\nu_{n-n_{\mathrm{M}}+1}} = \mathcal{M}^{\nu_{n-1}\mu_{n-1}}_{\nu_n\mu_n} \sum_{\substack{\nu_{n-n_{\mathrm{M}}} \\ \mu_{n-n_{\mathrm{M}}}}} \exp\left(\sum_{j=n-n_{\mathrm{M}}}^{n} S^{\nu_j\mu_j}_{\nu_n\mu_n}\right) \bar{\rho}^{\mu_{n-1}\ldots\mu_{n-n_{\mathrm{M}}}}_{\nu_{n-1}\ldots\nu_{n-n_{\mathrm{M}}}} \tag{2.11}$$

where

$$\mathcal{M}^{\nu_{j-1}\mu_{j-1}}_{\nu_j\mu_j} = \langle\nu_j| \mathcal{M}_{t_{j-1},t_j}\left[|\nu_{j-1}\rangle\langle\mu_{j-1}|\right]|\mu_j\rangle \tag{2.12a}$$

$$\mathcal{M}_{t,t'}[\cdot] = \hat{\mathcal{T}}\exp\left(\int_t^{t'} \mathcal{L}_{\mathrm{QD\text{-}C}}\,dt''\right)[\cdot] \tag{2.12b}$$

$$\mathcal{L}_{\mathrm{QD\text{-}C}}\hat{\rho} = -\frac{i}{\hbar}\left[\hat{H}_{\mathrm{QD\text{-}L}} + \hat{H}_{\mathrm{C}}, \hat{\rho}\right]_- + \sum_{\ell=H,V}\left\{\mathcal{L}_{\hat{a}_\ell,\kappa} + \mathcal{L}_{|G\rangle\langle X_\ell|,\gamma} + \mathcal{L}_{|X_\ell\rangle\langle B|,\gamma}\right\}\hat{\rho} \tag{2.12c}$$

$$R^{\mu_n\ldots\mu_0}_{\nu_n\ldots\nu_0} := \bar{\rho}_{\nu_0\mu_0}\prod_{j=1}^{n}\mathcal{M}^{\nu_{j-1}\mu_{j-1}}_{\nu_j\mu_j}\exp\left(\sum_{j=1}^{n}\sum_{j'=1}^{j} S^{\nu_{j'}\mu_{j'}}_{\nu_j\mu_j}\right). \tag{2.12d}$$

The reduced density matrix at time t_n can then be obtained from the ADM by summation over

the prior time-steps:

$$\bar{\rho}_{\nu_n \mu_n}(t_n) = \sum_{\substack{\nu_{n-1}...\nu_{n-n_{\mathrm{M}}+1} \\ \mu_{n-1}...\mu_{n-n_{\mathrm{M}}+1}}} \bar{\rho}_{\nu_n...\nu_{n-n_{\mathrm{M}}+1}}^{\mu_n...\mu_{n-n_{\mathrm{M}}+1}} \tag{2.13}$$

In this scheme, the formal propagator $\mathcal{M}_{t,t'}$ describes the phonon-free time-evolution of the QD-cavity system and the influence of the phonons is captured completely by the functions $S_{\nu_j \mu_j}^{\nu_{j'} \mu_{j'}}$. Assuming that the initial state of the complete system is the product of a QD-cavity state and a phonon state in thermal equilibrium at temperature T, the explicit expressions for the latter are[63,64]

$$S_{\nu_j \mu_j}^{\nu_{j'} \mu_{j'}} = -K_{\nu_{j'} \nu_j}(t_j - t_{j'}) - K_{\mu_j \mu_{j'}}^*(t_j - t_{j'}) + K_{\nu_j \mu_{j'}}^*(t_j - t_{j'}) + K_{\nu_{j'} \mu_j}(t_j - t_{j'}) \tag{2.14a}$$

$$K_{\nu_j \mu_{j'}}(\tau) = 2 \int\limits_0^\infty d\omega \frac{n_{\nu_j} n_{\mu_{j'}} J(\omega)}{\omega^2} \Big[1 - \cos(\omega \Delta t)\Big] \Big[\coth\Big(\frac{\hbar\omega}{2k_B T}\Big) \cos(\omega\tau) - i \sin(\omega\tau)\Big], \qquad \tau > 0 \tag{2.14b}$$

$$K_{\nu_j \mu_j}(0) = \int\limits_0^\infty d\omega \frac{n_{\nu_j} n_{\mu_{j'}} J(\omega)}{\omega^2} \Big[\coth\Big(\frac{\hbar\omega}{2k_B T}\Big)\Big(1 - \cos(\omega\Delta t)\Big) + i \sin(\omega\Delta t) - i\omega\Delta t\Big] \tag{2.14c}$$

where n_ν is again the number of excitons present in the QD-cavity state $|\nu\rangle$ and $J(\omega)$ is the phonon spectral density as defined in Section 2.1.5.

In this path-integral method, numerical errors can be caused only by two intrinsic parameters: (i) the time step Δt and (ii) the considered memory length t_{M}. Usually, these convergence parameters can be well controlled. In the case of strongly-confined self-assembled GaAs QDs, the memory depth of the memory kernel $K_{\nu_j \mu_{j'}}(t_j - t_{j'})$ is on the order of a few picoseconds. For example, for a confinement length of $a_{\mathrm{e}} = 3\,\mathrm{nm}$, a memory length of $t_{\mathrm{M}} = 3\,\mathrm{ps}$ is usually sufficient. In typical simulations performed in this thesis, the parameter set $n_{\mathrm{M}} = 7$ and $\Delta t = 0.5\,\mathrm{ps}$ leads to *numerically complete* results, i.e., neither a further reduction of Δt nor a further increase of t_{M} causes a noticeable change in the numerical results.

However, the general iteration scheme has its limits. In particular, the study of four-level emitter-cavity systems is impossible. In this scheme, $N_{\mathrm{ADM}} = N_{\mathrm{QD\text{-}C}}^{2n_{\mathrm{M}}}$ elements of the ADM have to be stored, where $N_{\mathrm{QD\text{-}C}}$ is the number of QD-cavity basis states that are considered in the numerical calculations. Even when just basis states $|\chi, n_{\mathrm{H}}, n_{\mathrm{V}}\rangle$ with a total photon number $n_{\mathrm{H}} + n_{\mathrm{V}} \leq 4$ are considered, the number of $N_{\mathrm{ADM}} = 60^{2\times 7} \approx 7.8 \times 10^{24}$ elements clearly exceeds current storage capabilities.

Advanced iteration scheme In order to explore such multi-level QD-cavity systems, an advanced iteration scheme has to be employed, which was first introduced in Ref. [64]. This scheme exploits another important property of the functions $S_{\nu_j \mu_j}^{\nu_{j'} \mu_{j'}}$. According to Equation (2.14), they depend on the indices $\nu_j, \mu_j, \nu_{j'}, \mu_{j'}$ solely via the number of excitons present in the cor-

responding QD-cavity states. Therefore, the QD-cavity states $|\nu\rangle$ can be sorted into three groups $\{|G, n_{\mathrm{H}}, n_{\mathrm{V}}\rangle\}$, $\{|X_{\mathrm{H}}, n_{\mathrm{H}}, n_{\mathrm{V}}\rangle, |X_{\mathrm{V}}, n_{\mathrm{H}}, n_{\mathrm{V}}\rangle\}$, and $\{|B, n_{\mathrm{H}}, n_{\mathrm{V}}\rangle\}$, where each member of one group couples identically to the phonon degrees of freedom. After re-labeling the basis states $|\nu\rangle \to |\lambda, k\rangle$ and $|\mu\rangle \to |\bar{\lambda}, \bar{k}\rangle$, where the group is donated by $\lambda \in \{0, 1, 2\}$ and k distinguishes between different group members, the *partially summed ADM* (PSADM)

$$\bar{\rho}_{(\lambda_n,k_n)\lambda_{n-1}...\lambda_{n-n_{\mathrm{M}}+1}}^{(\bar{\lambda}_n,\bar{k}_n)\bar{\lambda}_{n-1}...\bar{\lambda}_{n-n_{\mathrm{M}}+1}} := \sum_{\substack{k_{n-1}...k_{n-n_{\mathrm{M}}+1} \\ \bar{k}_{n-1}...\bar{k}_{n-n_{\mathrm{M}}+1}}} \bar{\rho}_{(\lambda_n,k_n)(\lambda_{n-1},k_{n-1})...(\lambda_{n-n_{\mathrm{M}}+1},k_{n-n_{\mathrm{M}}+1})}^{(\bar{\lambda}_n,\bar{k}_n)(\bar{\lambda}_{n-1},\bar{k}_{n-1})...(\bar{\lambda}_{n-n_{\mathrm{M}}+1},\bar{k}_{n-n_{\mathrm{M}}+1})}. \tag{2.15}$$

can be defined. This quantity then obeys the recursion relation[64]

$$\bar{\rho}_{(\lambda_n,k_n)\lambda_{n-1}...\lambda_{n-n_{\mathrm{M}}+1}}^{(\bar{\lambda}_n,\bar{k}_n)\bar{\lambda}_{n-1}...\bar{\lambda}_{n-n_{\mathrm{M}}+1}} = \sum_{\substack{k_{n-1} \\ \bar{k}_{n-1}}} \mathcal{M}_{(\lambda_n,k_n)(\bar{\lambda}_n,\bar{k}_n)}^{(\lambda_{n-1},k_{n-1})(\bar{\lambda}_{n-1},\bar{k}_{n-1})} \sum_{\substack{\lambda_{n-n_{\mathrm{M}}} \\ \bar{\lambda}_{n-n_{\mathrm{M}}}}} \exp\left(\sum_{j=n-n_{\mathrm{M}}}^{n} S_{\lambda_n\bar{\lambda}_n}^{\lambda_j\bar{\lambda}_j}\right) \bar{\rho}_{(\lambda_{n-1},k_{n-1})\lambda_{n-2}...\lambda_{n-n_{\mathrm{M}}}}^{(\bar{\lambda}_{n-1},\bar{k}_{n-1})\bar{\lambda}_{n-2}...\bar{\lambda}_{n-n_{\mathrm{M}}}}$$

$$\tag{2.16}$$

and the reduced density matrix at time t_n can be obtained by

$$\bar{\rho}_{\nu_n\mu_n}(t_n) = \sum_{\substack{\lambda_{n-1}...\lambda_{n-n_{\mathrm{M}}+1} \\ \bar{\lambda}_{n-1}...\bar{\lambda}_{n-n_{\mathrm{M}}+1}}} \bar{\rho}_{(\lambda_n,k_n)\lambda_{n-1}...\lambda_{n-n_{\mathrm{M}}+1}}^{(\bar{\lambda}_n,\bar{k}_n)\bar{\lambda}_{n-1}...\bar{\lambda}_{n-n_{\mathrm{M}}+1}} \tag{2.17}$$

Although, Eqs. (2.15)-(2.17) just represent an exact reformulation without any additional assumptions, the numerical demand in the advanced iteration scheme is drastically reduced. The PSADM only contains $N_{\mathrm{PSADM}} = N_{\mathrm{QD\text{-}C}}^2 \times N_{\mathrm{G}}^{2(n_{\mathrm{M}}-1)}$ elements, where N_{G} denotes the number of groups. For the same multi-level system and memory length $n_{\mathrm{M}} = 7$ as before, the number of elements in the central object is reduced by more than 15 orders of magnitude to $N_{\mathrm{PSADM}} = 60^2 \times 3^{12} \approx 1.9 \times 10^9$. Only this immense reduction of the numerical demand due to the advanced iteration scheme enables one to tackle multi-level QD-cavity systems.

2.3.2 Two-time correlation functions

The real-time path-integral approach as discussed so far, can deliver the reduced density matrix of the QD-cavity system $\bar{\rho}$, and, thus, all related expectation values in a numerically complete fashion. However, not all figures of merit and properties of a non-classical state of light and its emitter can be directly obtained from the time-evolution of $\bar{\rho}$. For example, figures of merit related to single-photon states and emitters (cf., [Pub 6], [FPub 5], and [FPub 8]) or the reconstruction of two-photon states via quantum state tomography[65] in entanglement measurements (cf., [Pub 4], [Pub 5], [Pub 9], and [Pub 10]), rely on (polarization-resolved) two-time coincidence measurements, performed in a Hanbury Brown and Twiss[66,67] or Hong-Ou-

Mandel[68] setup. These types of measurements can be theoretically modeled by evaluating two-time correlation functions for the electric field operators[69]. Since the source of the electric field is, depending on the experiment, either a bare QD or a QD-cavity structure, the electric field operators are proportional to the QD transition operators or the cavity operators, respectively. In addition, also other characteristics, e.g., emission spectra, are calculated based on similar correlation functions (cf., Supplement of [Pub 6]).

A numerically complete calculation scheme for general two-time correlations functions

$$G^{(2)}(t, \tau) = \left\langle \hat{O}_1(t) \hat{O}_2(t + \tau) \hat{O}_3(t + \tau) \hat{O}_4(t) \right\rangle \tag{2.18}$$

within the path-integral framework was introduced in Ref. [70]. Here, the four operators $\hat{O}$ denote any set of operators that act only on the system of interest, i.e., the QD-cavity subsystem, like the electronic transition operators, $|G\rangle\langle X_\ell|$ and $|X_\ell\rangle\langle B|$, or the cavity mode operators $\hat{a}_\ell$. The first time argument, t, represents the (real) time of the first detection event and τ is the delay time until a subsequent second one. After reformulating Equation (2.18) in the Schrödinger picture, the resulting expression

$$G^{(2)}(t, \tau) = \mathrm{Tr} \left\{ \hat{O}_2 \hat{O}_3 \mathcal{P}_{t,t+\tau} \left[\hat{O}_4 \mathcal{P}_{t_0,t} \left[\hat{\rho}(t_0) \right] \hat{O}_1 \right] \right\} \tag{2.19}$$

can be evaluated by the following procedure: (i) First, until the time $t = n\,\Delta t$ is reached, one can use the advanced algorithm and iterate the PSADM according to Equation (2.16). (ii) Then, at this step, the operators $\hat{O}_1$ and $\hat{O}_4$, which act at this point in time, are multiplied to the PSADM from the right and the left, respectively. The resulting, new object is a *modified PSADM* (MPSADM)

$$
\begin{aligned}
\bar{\rho}_{\hat{O}_4 \hat{O}_1 (\lambda_n, k_n) \lambda_{n-1} \dots \lambda_{n-n_{\mathrm{M}}+1}}^{(\bar{\lambda}_n, \bar{k}_n) \bar{\lambda}_{n-1} \dots \bar{\lambda}_{n-n_{\mathrm{M}}+1}} = {} & \sum_{\substack{\lambda'_n, k'_n \; k_{n-1} \\ \bar{\lambda}'_n, \bar{k}'_n \; \bar{k}_{n-1}}} (O_4)_{(\lambda_n, k_n)(\lambda'_n, k'_n)} \mathcal{M}_{(\lambda'_n, k'_n)(\bar{\lambda}'_n, \bar{k}'_n)}^{(\lambda_{n-1}, k_{n-1})(\bar{\lambda}_{n-1}, \bar{k}_{n-1})} (O_1)_{(\bar{\lambda}'_n, \bar{k}'_n)(\bar{\lambda}_n, \bar{k}_n)} \\
& \times \sum_{\substack{\lambda_{n-n_{\mathrm{M}}} \\ \bar{\lambda}_{n-n_{\mathrm{M}}}}} \exp\left(\sum_{j=n-n_m}^{n} S_{\lambda_n \bar{\lambda}_n}^{\lambda_j \bar{\lambda}_j} \right) \bar{\rho}_{(\lambda_{n-1}, k_{n-1})\lambda_{n-2} \dots \lambda_{n-n_{\mathrm{M}}}}^{(\bar{\lambda}_{n-1}, \bar{k}_{n-1})\bar{\lambda}_{n-2} \dots \bar{\lambda}_{n-n_{\mathrm{M}}}}
\end{aligned}
\tag{2.20}
$$

where $(O)_{(\lambda_j, k_j)(\lambda'_j, k'_j)} := \langle \lambda_j, k_j | \hat{O} | \lambda'_j, k'_j \rangle$ for any operator $\hat{O}$ acting on the QD-cavity subsystem. (iii) For subsequent time steps, the MPSADM is iterated instead of the PSADM, obeying the same recursion relation as the latter. (iv) Assuming that the time $t + \tau$ is reached after m further time steps, i.e., $\tau = m\,\Delta t$, the correlation function $G^{(2)}(t, \tau)$ is finally obtained by multiplying the remaining pair of operators to the MPSADM and performing the trace over

the phonon-induced memory:

$$G^{(2)}(t,\tau) = \sum_{\substack{\lambda_{n+m}...\lambda_{n+m-n_{\mathrm{M}}+1},k_{n+m} \\ \bar{\lambda}_{n+m}...\bar{\lambda}_{n+m-n_{\mathrm{M}}+1},\bar{k}_{n+m}}} (O_2O_3)_{(\bar{\lambda}_{n+m},\bar{k}_{n+m})(\lambda_{n+m},k_{n+m})} \, \bar{\rho}_{\hat{O}_4\hat{O}_1(\lambda_{n+m},k_{n+m})\lambda_{n+m-1}...\lambda_{n+m-n_{\mathrm{M}}+1}}^{(\bar{\lambda}_{n+m},\bar{k}_{n+m})\bar{\lambda}_{n+m-1}...\bar{\lambda}_{n+m-n_{\mathrm{M}}+1}}$$

(2.21)

Note that, in this calculation scheme, the phonon-induced memory accumulated during the first propagation in the real time t is completely kept for the second propagation related to the delay time τ. Thus, the presented iteration scheme is still numerically complete and provides the unique opportunity to evaluate the validity of approximate strategies like the *quantum regression theorem* (QRT)[31]. This approximate tool is often employed for the calculation of two-time correlation functions, even when the system dynamcis is non-Markovian.

2.4 Entangled photon pairs

2.4.1 Bell states and different realizations

Although this thesis also discusses single-photon states ([Pub 6] and [Pub 8]) and non-classical multi-photon statistics ([Pub 3] and [Pub 7]), its major focus is the generation and manipulation of entangled photon pairs in quantum emitter-cavity systems as well as the influence of phonons or other system parameters on the latter.

Entanglement is a genuine quantum effect, sometimes contrary to man's physical intuition. In quantum mechanics, two particles or systems are entangled when their combined state cannot be factorized into states that describe just one of the two constituents. As a consequence, a measurement performed on one particle or system directly impacts the state of the other, even when they do not interact with each other or are far apart. Historically, this counter-intuitive *spooky action on a distance*, e.g., in the EPR-gedankenexperiment[71], was one major criticism of quantum mechanics in its earlier years. Nowadays, after quantum mechanics and its predictions have been proven time and time again, entanglement is key to novel quantum science and technologies, like, quantum cryptography[72–75], quantum communication[6,76], or quantum information and quantum computation[77–80].

Many fascinating applications in these fields rely on entangled quantum bits (qubits). A qubit is a quantum mechanical two-state system, that in contrast to its classical analogue, can be in any superposition of its two states. For two entangled qubits, there exist four maximally entangled states

$$|\Phi_\pm\rangle = \frac{1}{\sqrt{2}}\left(|0\rangle_A|0\rangle_B \pm |1\rangle_A|1\rangle_B\right) \tag{2.22a}$$

$$|\Psi_\pm\rangle = \frac{1}{\sqrt{2}}\left(|0\rangle_A|1\rangle_B \pm |1\rangle_A|0\rangle_B\right) \tag{2.22b}$$

which became known as the four *Bell states* (BSs). Here, $|0\rangle$ and $|1\rangle$ denote the two possible states that each of the two qubits, labeled by A and B, can assume. The four BSs form a basis of the two-qubit Hilbert space and violate Bell's inequalities[81,82], a fundamental test for entanglement, with the highest possible value.

Among other possible realization of qubits, like superconducting qubits[83] or trapped ions[84], that satisfy DiVincenzo's criteria for quantum computation[85], photons stand out, because they travel at the speed of light and are only weakly influenced by their environment[1,6]. In the case of photonic qubits, several degrees of freedom can be used to encode the two general one-qubit states $|0\rangle$ and $|1\rangle$: For example, the frequency or orbital angular momentum (OAM), as well as different temporal or spatial modes. Consequently, in the recent years, photons entangled in their frequency[86], OAM[87], or spatial mode[88] and time-bin entangled photon pairs[89–92] have been reported. However, the most common and, arguably, most straightforward realization are polarization-entangled photon pairs, where the two different states are encoded in two orthogonal polarizations, e.g., H and V. They are especially attractive, because they can be quite easily created, manipulated, and measured using polarizers and waveplates. As mentioned in Section 2.1.1, the biexciton-exciton cascade in QDs provides a natural platform for the generation of polarization-entangled photon pairs.

2.4.2 Reconstructing the two-photon state

After a two-photon state has been generated, e.g., by the subsequent decay of an excited biexciton in QDs, it has to be characterized. To this end, in standard experiments, the resulting photon pair state is usually reconstructed in the basis $\{|HH\rangle, |HV\rangle, |VH\rangle, |VV\rangle\}$, where H and V denote the two orthogonal linear polarizations and the order corresponds to the first and second detected photon. Typically, quantum state tomography[65] is employed, a reconstruction technique based on polarization-resolved two-time coincidence measurements. From a theoretical point of view, these measurements can be modeled with second-order correlation functions.

In the case of QDs interacting with only one cavity mode per polarization as introduced in Section 2.1.3, the detected signals in such coincidence measurements are proportional to the two-time correlation functions

$$G^{(2)}_{jk,\ell m}(t,\tau) = \left\langle \hat{a}^{\dagger}_j(t)\hat{a}^{\dagger}_k(t+\tau)\hat{a}_m(t+\tau)\hat{a}_\ell(t) \right\rangle \tag{2.23}$$

where $j, k, \ell, m \in \{H, V\}$, cf., e.g., [FPub 1] or [Pub 10]. Here, t is the (real) time when the first photon is detected, and τ denotes the delay-time until the detection of the subsequent second one occurs. Note that $G^{(2)}_{jk,\ell m}(t,\tau)$ describes photons within the cavity structure, while in standard experiments the measurements are performed on photons that have already left the

cavity. However, if the outcoupling of light from the cavity into free space is assumed to be a Markovian process, Equation (2.23) can also be used to model the latter[93].

In an actual experiment, the coincidence measurements are always performed over finite real time and delay time intervals, i.e., the experimental result represents a statistical average over these intervals. Therefore, the reconstructed two-photon density matrix $\rho^{2\mathrm{p}}$ is theoretically calculated as

$$\rho^{2\mathrm{p}}_{jk,\ell m} = \frac{\overline{G}^{(2)}_{jk,\ell m}}{\mathrm{Tr}\left\{\overline{G}^{(2)}\right\}} \tag{2.24a}$$

$$\overline{G}^{(2)}_{jk,\ell m} = \int\limits_{t_0}^{t_0+T_{\mathrm{ave}}} \mathrm{d}t \int\limits_0^{\tau_{\mathrm{ave}}} \mathrm{d}\tau\, G^{(2)}_{jk,\ell m}(t,\tau) \tag{2.24b}$$

where T_{ave} (τ_{ave}) is the real (delay) time interval used in experiment. The trace $\mathrm{Tr}\left\{\overline{G}^{(2)}\right\}$ in Equation (2.24) assures that $\rho^{2\mathrm{p}}$ is normalized. While one typically considers all detection events until the emitter has returned into its ground state, different delay time windows can be applied to select different photonic subsets, cf., [FPub 1]. Once the two-photon density matrix $\rho^{2\mathrm{p}}$ has been obtained, the created type of BS can be identified based on its elements.

2.4.3 Entanglement measures and concurrence

In order to quantify the degree of entanglement associated with a given two-photon state, a suitable measure has to be selected. If the two-photon density matrix $\rho^{2\mathrm{p}}$ describes a pure two-photon state $|\psi^{2\mathrm{p}}\rangle$ with subsystems, i.e., photons, A and B, it is common to use the von-Neumann entropy of any of the two subsystems to define the degree of entanglement $E(|\psi^{2\mathrm{p}}\rangle)$ as[94]

$$E(|\psi^{2\mathrm{p}}\rangle) = -\mathrm{Tr}_A\left\{\rho_A \log_2 \rho_A\right\} = -\mathrm{Tr}_B\left\{\rho_B \log_2 \rho_B\right\} \tag{2.25}$$

where $\rho_A = \mathrm{Tr}_B\{\rho^{2\mathrm{p}}\}$ and $\rho_B = \mathrm{Tr}_A\{\rho^{2\mathrm{p}}\}$ are the reduced density matrices of each subsystem, respectively. From a physical point of view, E represents the missing information about one photon due to its entanglement with the other one. It is straightforward to show that all four BSs introduced in Equation (2.22) display the maximum possible value $E = 1$.

However, in the case of a mixed state, this quantity cannot be used, because the missing information about one subsystem can also be caused by ensemble averaging instead of entanglement. In this situation, several ways to identify the contribution due to entanglement have been proposed[94,95] and different entanglement measures, e.g, *fidelity*[96] - the overlap with a desired maximally entangled state - or *negativity*[97] based on the Peres-Horodecki criterium[98,99], are used. In this thesis, *concurrence*[95,100] is employed to quantify the degree of entanglement, a well-established measure that is directly linked to the entanglement of formation.

The entanglement of formation itself is closely related to the von-Neumann entropy. The

basic idea is to determine the minimal amount of pure-state entanglement that is at least present in a given mixed two-photon state ρ^{2p}. To this end, one considers possible decompositions of ρ^{2p} into a set of pure two-photon states $|\psi_j\rangle$ with corresponding probabilities p_j. Following Equation (2.25), any such decomposition $\rho^{2p} = \sum\limits_j p_j |\psi_j\rangle\langle\psi_j|$ is assigned the degree of entanglement

$$E(\{p_j, |\psi_j\rangle\}) = \sum_j p_j E(|\psi_j\rangle) \tag{2.26}$$

The entanglement of formation is then defined as[95]

$$E_{\mathrm{F}} = \inf_{\{p_j, |\psi_j\rangle\}} E(\{p_j, |\psi_j\rangle\}) \tag{2.27}$$

where one takes the infimum over all possible decompositions. Although this quantity has a clear physical meaning and interpretation, it is hardly practical due to the infimum operation.

The concurrence C has a one-to-one correspondence to the entanglement of formation, i.e., it is related to the latter according to

$$E_{\mathrm{F}} = \mathcal{E}(C) \tag{2.28}$$

where $\mathcal{E}$ is a monotonically increasing function for $0 \leq C \leq 1$[95]. Furthermore, the concurrence assumes its minimal (0) and maximal (1) value in accordance with the entanglement of formation. Thus, the concurrence can be used as a measure for the degree of entanglement in its own right. Although its physical interpretation is not as intuitive and its meaning is only derived from the entanglement of formation, the concurrence is arguably the most widely-used entanglement measure. In contrast to E_{F}, the concurrence can be directly calculated from the elements of the two-photon density matrix ρ^{2p}, a property which makes it especially attractive for practical applications. In the (computational) basis $\{|HH\rangle, |HV\rangle, |VH\rangle, |VV\rangle\}$, the concurrence is given by[65,100]

$$C = \max\left\{0, \sqrt{\lambda_1} - \sqrt{\lambda_2} - \sqrt{\lambda_3} - \sqrt{\lambda_4}\right\} \tag{2.29}$$

where $\lambda_1 \geq \lambda_2 \geq \lambda_3 \geq \lambda_4$ are the real and positive eigenvalues of the 4×4-matrix

$$M = \rho^{2p} \, \Sigma \, (\rho^{2p})^* \, \Sigma \quad \text{with} \quad \Sigma = \begin{pmatrix} 0 & 0 & 0 & -1 \\ 0 & 0 & 1 & 0 \\ 0 & 1 & 0 & 0 \\ -1 & 0 & 0 & 0 \end{pmatrix} \tag{2.30}$$

Depending on the actual form of ρ^{2p}, this abstract formula can be approximated or exactly written using just a few of its elements. For example, when the two-photon density matrix

takes the form

$$\rho^{2\mathrm{P}} = \begin{pmatrix} a & 0 & 0 & c \\ 0 & b & d & 0 \\ 0 & d^* & b & 0 \\ c^* & 0 & 0 & a \end{pmatrix} \tag{2.31}$$

where the parameters $a, b \in \mathbb{R}$ and $c, d \in \mathbb{C}$ fulfill the requirements for a general density matrix, i.e., $2(a + b) = 1$ as well as $|c| \leq a$ and $|d| \leq b$, it is straightforward to show that the definition of the concurrence reduces to

$$C = \begin{cases} 2\left(|c| - b\right), & |c| > b \\ 2\left(|d| - a\right), & |d| > a \\ 0, & \text{else} \end{cases} \tag{2.32}$$

Note that due to the above-mentioned requirements, the first two cases are mutually exclusive.

3 Guide through the publications

The thesis at hand deals with the generation and manipulation of highly non-classical states of light in different QD-cavity setups. In particular, the impact of system parameters, like external laser fields, surrounding cavity structures, or the exciton fine-structure splitting, as well as of LA phonons is studied. In this chapter, a guide through the publications is given, highlighting the most important results of every article and connecting them to each other. The overall storyline follows loosely the chronological order, reflected in the increasing complexity of the external excitation.

Starting with an initially prepared biexciton state in Section 3.1, entangled photon pairs can be created exploiting the biexciton-exciton cascade. Four QD-cavity configurations are discussed, revealing the importance of two-photon processes and regions of phonon-induced enhancement of photon entanglement. Next, in Section 3.2, the creation of different types of entangled Bell states in constantly driven quantum emitter-cavity systems is investigated. As a result, a protocol for entanglement switching is developed and a phase transition-like behavior in strongly confined QDs is predicted. A profound phonon impact is also found when N-photon bundles and time-dependent photon number distributions are studied in Section 3.3. Afterwards, in Section 3.4, short, time-dependent laser pulses are employed to generate and control single photon states. It is uncovered that the QRT systematically overestimates the phonon impact on the indistinguishability, and a QD-based photon storage devise is proposed. Finally, in Section 3.5, numerical and analytical considerations reveal that the laser pulse in the two-photon resonant excitation scheme introduces an AC-Stark splitting between exciton states which degrades the degree of entanglement.

3.1 Entangled photons from an initially prepared biexciton

After a QD has been prepared in its biexciton state $|B\rangle$, the two different decay paths in the biexciton-exciton cascade can be exploited to create polarization-entangled photon pairs, cf., Figure 2.1. If both decay paths are indistinguishable, i.e., when the fine-structure splitting δ is zero and both exciton states are energetically degenerate, a maximally entangled ΦBS

$$|\Phi_+\rangle = \frac{1}{\sqrt{2}} \left(|HH\rangle + |VV\rangle \right) \tag{3.1}$$

is created. In this section, a QD without external laser excitation and an initially prepared biexciton state is assumed and the generated two-photon state is analyzed for different QD-cavity configurations. The preparation of the biexciton state can be achieved employing different excitation schemes, e.g., two-photon resonant excitation with short laser pulses[10,12,14,74,101–104], phonon-assisted off-resonant excitation[51,52,105–107], adiabatic rapid passage protocols[108–110], or far off-resonant excitation schemes, where charge carriers subsequently relax into the biexciton state[9,20,21,111,112].

3.1.1 Different cavity configurations and their temperature-dependent entanglement

One obstacle that inhibits the generation of the maximally entangled two-photon state $|\Phi_+\rangle$ in QDs is the fine-structure splitting δ. If δ is finite, the system is asymmetric and the two possible decay paths in the biexciton-exciton cascade become distinguishable. Thus, a finite fine-structure splitting introduces a *which-path information* that results in a reduced degree of entanglement. For this reason several methods and strategies were developed to reduce the fine-structure splitting in QDs[6,9,101,111–116].

However, because such strategies are quite restrictive and cannot always be applied, different, less demanding solutions were proposed. One prominent proposal is to exploit a QD with sizable biexciton binding energy in combination with a favorable cavity mode placement[23,25,27]. By adjusting the energy of the two cavity modes - one for each polarization - to the two-photon resonance between ground and biexciton state, direct, simultaneous two-photon processes become likely to occur. Since these processes do not involve the intermediate exciton states, the fine-structure splitting is effectively not probed, leading to a strongly reduced which-path information. In addition, due to the large biexciton binding energy the sequential single-photon processes following the biexciton-exciton cascade are strongly detuned from the cavity modes. Altogether, the weak impact of the fine-structure splitting in the case of two-photon processes and the suppression of one-photon processes should result in a high degree of entanglement, even in the presence of a large fine-structure splitting.

In order to analyze the influence of phonons as well as the impact of direct two-photon and sequential one-photon processes on the created two-photon state and its degree of entanglement, four different QD-cavity configurations are compared in [Pub 1]: the two-photon resonant (2PR) and the one-photon resonant (1PR) configuration with a vanishing as well as a finite biexciton binding energy E_B, cf., Figure 3 in [Pub 1]. As expected, in the absence of a fine-structure splitting, there is no which-path information in the system and, consequently, all four configurations result in a maximally entangled ΦBS with unity concurrence, independent of the temperature.

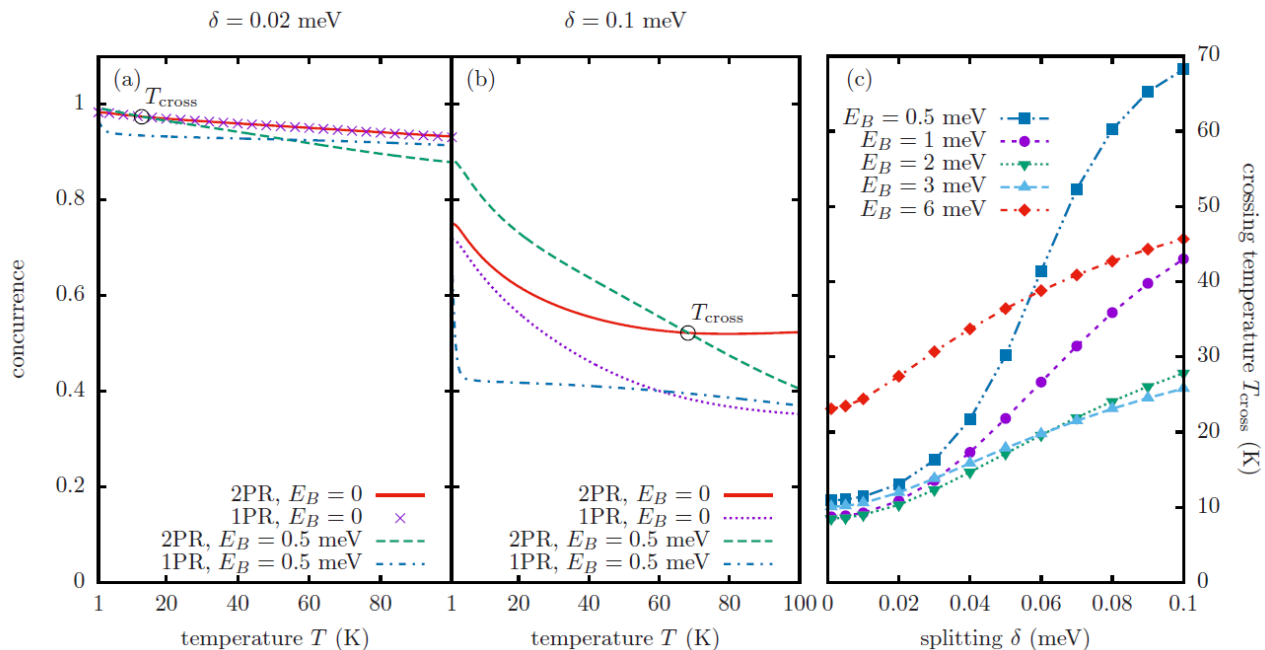However, if the fine-structure splitting is finite, strikingly different dependences on the fine-

Figure 3.1: [Taken from [Pub 1]] Concurrence as a function of temperature for all four QD-cavity configurations. Results are shown for two different fine-structure splittings: (a) $\delta = 0.02$ meV and (b) $\delta = 0.1$ meV. Circles mark the crossing temperature T_{cross} of the concurrence in the 2PR configuration with $E_{\text{B}} = 0$ and the concurrence in the 2PR configuration with $E_{\text{B}} = 0.5$ meV. (c) Crossing temperature T_{cross} as a function of δ for different biexciton binding energies E_{B}.

structure splitting and the temperature are observed, cf., Figure 5 in [Pub 1]. The origin of these different dependences is traced back to the competition between direct two-photon and sequential one-photon processes, in particular, the relative importance of the latter. The results show that the higher the contribution of direct two-photon processes, the higher the degree of entanglement.

The main result that follows from the newly gained insights is visualized in Figure 3.1. The expectation that the 2PR configuration combined with a sizable biexciton binding energy E_{B} is the best choice to protect the degree of entanglement against the destructive influence of a finite fine-structure splitting is only valid for low temperatures. Only in this limit, the 2PR configuration with a finite E_{B} results in the highest degree of entanglement, as measured by the concurrence. But with rising temperature, this configuration exhibits the strongest decrease in concurrence, leading to subsequent crossing points with all other considered configurations. This steep decrease can be explained with an enhanced phonon impact due to the frequency dependence of the phonon spectral density, cf., Figure 2.2. For typical biexciton binding energies of a few meV, this results in a stronger and more effective phonon coupling compared to the 2PR configuration with vanishing E_{B}.

In addition to a phonon-related loss of coherence that reduces the degree of entanglement,

phonon emission and absorption processes also assist the off-resonant sequential one-photon processes, shifting the competition between two- and one-photon processes towards the latter. Because of the enhanced phonon impact, this effect is more prominent in the 2PR configuration with a sizable biexciton binding energy. Consequently, the initial advantage of the 2PR configuration with $E_B > 0$ at low temperatures is more and more diminished with rising temperature until the resulting concurrence drops below the respective concurrence for the 2PR configuration with vanishing E_B at a certain crossing temperature T_{cross}, cf., Figure 3.1(a) and (b).

This crossing temperature depends on the biexciton binding energy E_B and the fine-structure splitting, cf., Figure 3.1(c). However, for typical values of the exciton fine-structure splitting on the order of several 10 μeV the crossing temperature is around 10 K. Thus, in realistic QD-cavity systems, the expected advantage of the 2PR configuration with a sizable E_B is lost already at rather low temperatures due to the interaction with LA phonons. Instead, at elevated temperatures, the 2PR configuration with a vanishing biexciton binding energy is more favorable for the creation of entangled photon pairs in the case of a finite fine-structure splitting.

3.1.2 Phonon-induced enhancement of photon entanglement

The results of the previous section demonstrate that the interaction with LA phonons typically leads to a reduced degree of entanglement compared with phonon-free calculations, and a monotonic decrease of concurrence with rising temperature, cf., Figure 3.1. A high degree of entanglement requires stable phases between the involved states. But, phonons are known as a major source of decoherence in QDs[42,49,117–124]. Therefore, one could expect that phonons always degrade the degree of entanglement, an observation that was also reported in further theoretical simulations, e.g., in References [27], [125] or [FPub 1].

In contrast to this expectation, it is discovered in [Pub 2] that the phonon impact on the degree of photon entanglement is not necessarily destructive in nature. Rather, the destructive loss of coherence due to LA phonons can be overcompensated by a phonon-related non-Markovian effect: the renormalization of the QD-cavity coupling strength. This renormalization effect can cause a non-monotonic temperature dependence and even lead to a phonon-induced enhancement of photon entanglement.

One prerequisite for this unexpected phonon-induced enhancement is a decreasing degree of photon entanglement with rising QD-cavity coupling strength g in the phonon-free case. Such a behavior is found in the 2PR configuration with vanishing biexciton binding energy in the case of a finite fine-structure splitting δ [consult Figure 3.2(a) for a sketch of this QD-cavity configuration]. Here, the degree of entanglement, as measured by the concurrence, exhibits a non-monotonic behavior with a pronounced minimum for $g \simeq \delta/2$ in the phonon-free case, cf.,
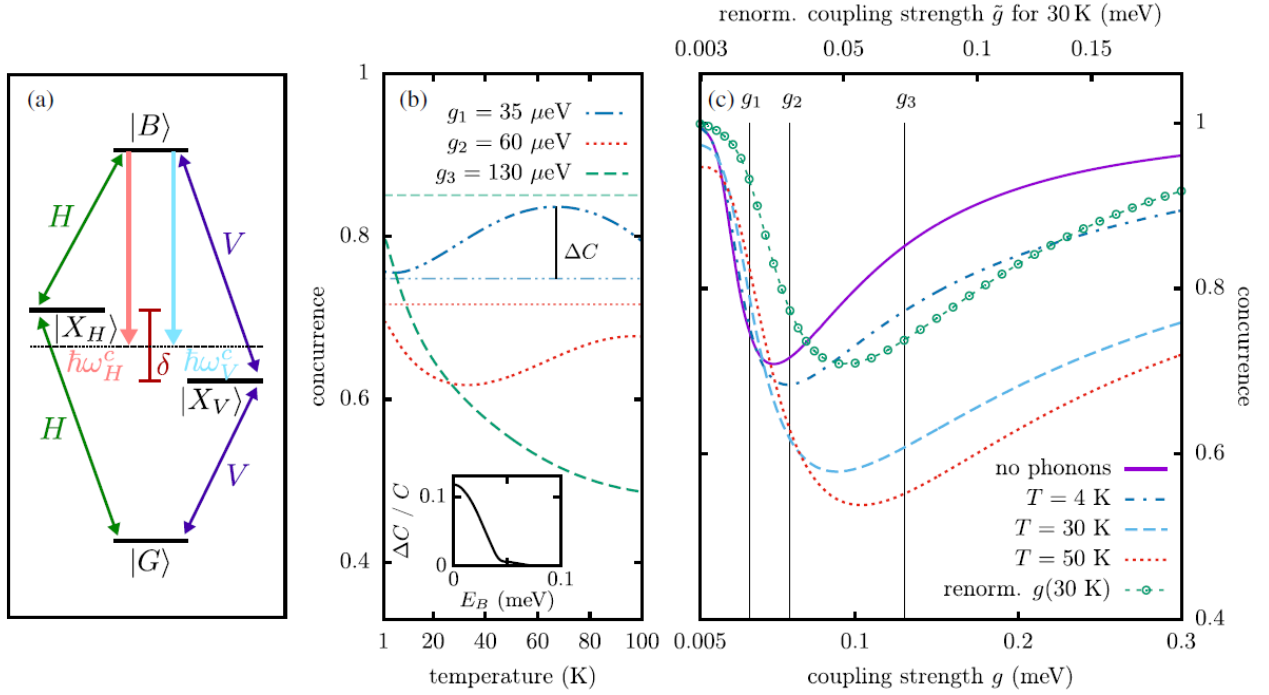
Figure 3.2: [Taken from [Pub 2]] (a) The considered QD-cavity configuration with finite fine-structure splitting δ, vanishing biexciton binding energy E_B, and two-photon resonant cavity modes. (b) Concurrence in dependence of temperature for three selected QD-cavity coupling strengths. The corresponding phonon-free result is indicated by straight (faded) lines. Inset: (normalized) difference ΔC between the maximum concurrence value at finite temperature and the corresponding phonon-free value in dependence of E_B for $g_1 = 35$ µeV. (c) Concurrence as a function of the QD-cavity coupling for three temperatures. Also shown are phonon-free results (solid purple line) and phonon-free calculation using the phonon-renormalized coupling $\tilde{g}(g)$ for $T = 30$ K (green curve with circles). Vertical lines mark the coupling values used in (b). Parameters: $\delta = 0.1$ meV, $\kappa = 0.025$ ps^{-1}.

purple curve in Figure 3.2(c).

When the interaction with LA phonons is accounted for in the numerical calculations, the temperature dependence of the concurrence can display qualitatively different behaviors, depending on the QD-cavity coupling g. This observation is demonstrated for three selected values in Figure 3.2(b). Only in the case of $g_3 = 130$ µeV, the expected monotonic decrease of the concurrence is obtained. For the two remaining coupling values, a non-monotonic temperature dependence is uncovered. Most strikingly, in the case of $g_1 = 35$ µeV, the concurrence can even exceed the corresponding phonon-free value by more than 10% (cf., blue dash-dotted line).

The origin of this remarkable phonon-induced enhancement of the photon entanglement is visualized in Figure 3.2(c). With rising temperature, the minimum of the concurrence is lowered and shifted to higher coupling strength values. While the lowering is indeed caused by phonon-induced dephasing, the shift occurs due to the renormalization of the QD-cavity coupling. This interpretation is supported by phonon-free calculations where the corresponding phonon-

renormalized coupling $\tilde{g}(g)$ at $T = 30$ K is used (green curve with circles). The position of the minimum agrees well with the full path-integral calculations at the same temperature (red dotted line). Because the shift increases with temperature, displacing the phonon-free curve results in a higher degree of entanglement in regions where the concurrence decreases monotonically in the phonon-free case. Thus, phonon-induced enhancement of the concurrence can appear in a finite range of coupling strength values, as long as the renormalization effect overcompensates the phonon-induced decoherence.

Although this is no longer the case for binding energies on the order of a few meV due to a stronger dephasing action caused by an enhanced phonon impact (cf., Figure 2 in [Pub 2]), there exists a finite range of binding energies $E_{\mathrm{B}} \lesssim \delta/2$ where the phonon-induced enhancement can be observed. This is highlighted in the inset of Figure 3.2(b). Note that one can tune the biexciton binding energy into this region by employing different strategies [126–129]. Furthermore, the phonon-induced enhancement can also be found in the case of degenerate excitons but a finite cavity mode splitting, cf., Supplemental Material of [Pub 2].

3.2 Different types of entanglement from constantly driven quantum emitters

After investigating the generation of entangled photon pair states from the biexciton-exciton cascade without external excitation, and in particular, the impact of different QD-cavity configurations and LA phonons, the discussion now turns to constantly driven systems. Due to the optical selection rules, the former systems only support the creation of an entangled ΦBS

$$|\Phi_\pm\rangle = \frac{1}{\sqrt{2}} \left(|HH\rangle \pm |VV\rangle \right) \tag{3.2}$$

where the order reflects the order of photon detection. Indeed, various theoretical [23,25,27,130,131] and experimental [8–12,20,21,74,75,102–104,111–113,132–134] studies reported the possibility to create entangled photon pairs of this type, where the first and second detected photon always display the same polarization.

However, this can change if the system is continuously driven by an external laser. In Ref. [26], it was demonstrated that under specific conditions also a ΨBS

$$|\Psi_\pm\rangle = \frac{1}{\sqrt{2}} \left(|HV\rangle \pm |VH\rangle \right) \tag{3.3}$$

can be generated in the same polarization basis. In this type of BS, the first and second detected photon display always the opposite polarization and the two-photon states $|HV\rangle$ and $|VH\rangle$ differ in the temporal order of the H and V polarized photon.

3.2.1 Creating different types of photon entanglement

In [Pub 4], the possibility to create both types of BSs is investigated, in particular, the conditions that lead to a high degree of entanglement are determined. To this end, an excited general four-level emitter with a diamond-type level structure, as introduced in Section 2.1.2, is considered. The general four-level emitter can be realized, e.g., by QDs, F-centers or atoms. Because a general quantum emitter is analyzed, the QD-specific coupling to LA phonons is omitted here. The quantum emitter is continuously driven by a constant external laser with driving strength Ω tuned to the two-photon transition between ground state $|G\rangle$ and the double-excited state $|XX\rangle$ (i.e., the biexciton state in case of a QD). A corresponding schematics of the system can be found in Figure 1 of [Pub 5]. The polarization of the laser is chosen to be diagonal in the basis spanned by H and V, in accordance with Ref. [26]. Thus, this system has two remaining free parameters: the driving strength and the energetic position of the cavity modes.

Due to the continuous laser excitation, four (time-independent) laser-dressed states emerge (cf., Equations (10)-(12) in [Pub 4]), which are denoted as the "Uppermost" (U), "Middle" (M), "Null" (N), and "Lowest" (L) dressed state, according to their respective energies. The dependence of these energies on the driving strength (in units of the cavity coupling strength g) is depicted in the inset of Figure 3.3(a). In addition to the energy of the laser-dressed states, also their composition in terms of the bare states can vary with the driving strength. This feature enables changing optical selection rules and the opportunity to manipulate the emitted two-photon state by varying both free parameters. Due to the constant excitation on one hand, and loss mechanisms, i.e., cavity losses and radiative decay, on the other, a steady state is reached in the system dynamics. For this steady state, the emitted two-photon state is reconstructed based on two-time correlation functions, where only photon pairs with a delay time $\tau \leq 50$ ps are accepted.

It turns out that, indeed, both types of BSs can be created for various parameter combinations, but the cavity placement is even more crucial than in the undriven situation, cf., Figure 6 in [Pub 4]. Only if the energy of the cavity modes is close to a multi-photon resonance between two laser-dressed states an entangled state of any kind is obtained. In particular, a high degree of entanglement is always related to matching a two-photon resonance between the laser-dressed states. Furthermore, employing a perturbative approach, the so-called Schrieffer-Wolff transformation[135–137], the resulting type of photon entanglement at any given two-photon resonance can be predicted.

The created type of photon entanglement changes with the driving strength and/or cavity-laser detuning. A particularly interesting behavior is found when the cavity modes are always kept in resonance with the two-photon transition between the laser-dressed states $|U\rangle$ and $|L\rangle$, cf., Figure 3.3. Here, a sharp transition between regions of high ΦBS and ΨBS entanglement takes place. While for small driving strength values, a ΦBS (blue segment) is obtained [cf.,
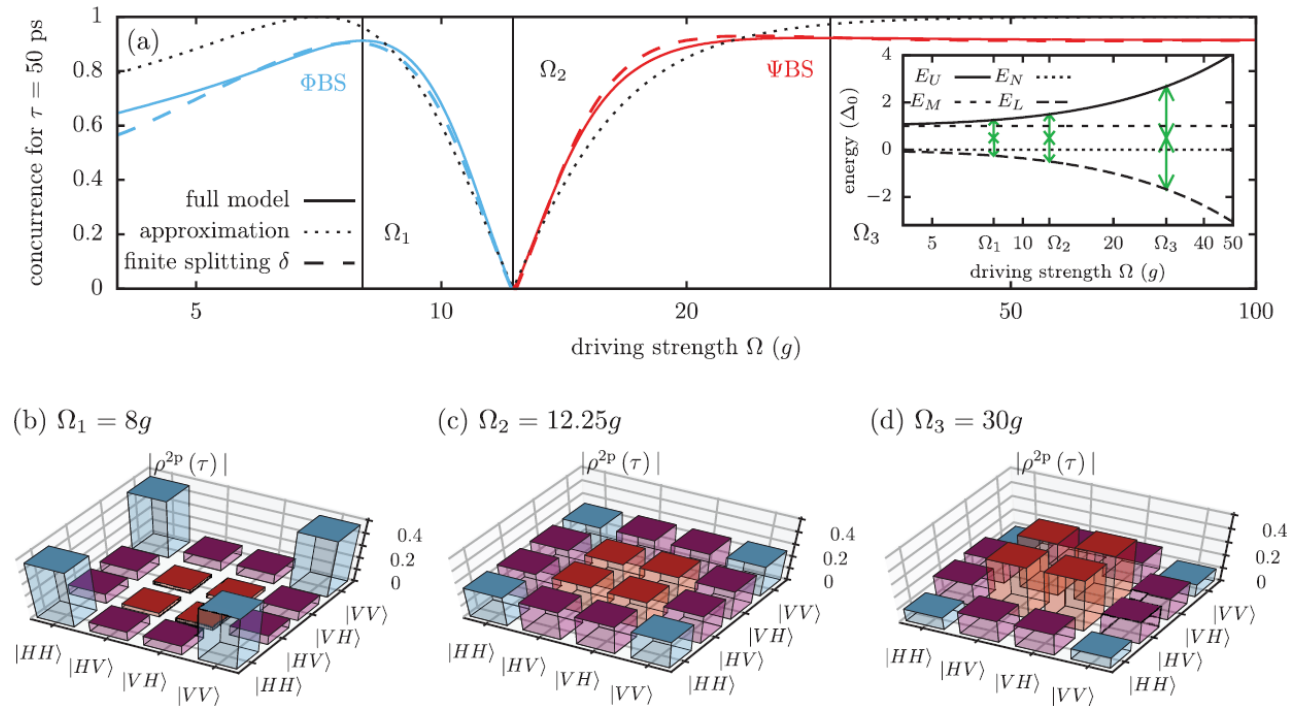
27

Figure 3.3: [Taken from [Pub 4]] (a) Concurrence as function of the laser driving strength Ω. Results are shown for the full model (solid line), the analytic approximation $C(r)$ according to Equation (3.4) (dotted line), and with a finite fine-structure splitting $\delta = 0.1\,E_\mathrm{B}/2$ (dashed line). Inset: Dressed state energies as a function of the driving strength. Green arrows indicate the two-photon resonant cavity modes for three selected Ω values. (b)–(d) Two-photon density matrix $\rho^{2\mathrm{p}}$ (absolute values) for three different driving strengths Ω_j [indicated by vertical lines in panel (a)].

panel (b)], a ΨBS (red segment) is created for high driving strength values [cf., panel (d)]. In between the two regions of high entanglement, a special point occurs, where the degree of entanglement vanishes and a factorizable two-photon state is emitted.

The regions of different photon entanglement as well as the occurrence of the special point can be understood by constructing an approximate, effective Hamiltonian for the chosen two-photon resonance according to the Schrieffer-Wolff transformation. This analysis reveals that the emitted two-photon state depends on the ratio $r = \gamma_1^\mathrm{UL}/\gamma_2^\mathrm{UL} = 16\,(\Omega/E_\mathrm{B})^2 - 1/2$, where γ_1^UL (γ_2^UL) is the effective coupling associated with a two-photon process that leads to the creation of a ΨBS (ΦBS). The good agreement between the full calculation and the analytic approximation for the concurrence

$$C(r) = \frac{|1 - r^2|}{1 + r^2} \tag{3.4}$$

[dotted line in Figure 3.3(a)] supports this interpretation. Furthermore, the observed features are only weakly influenced by typical fine-structure splittings much smaller than the binding energy E_B (dashed line).

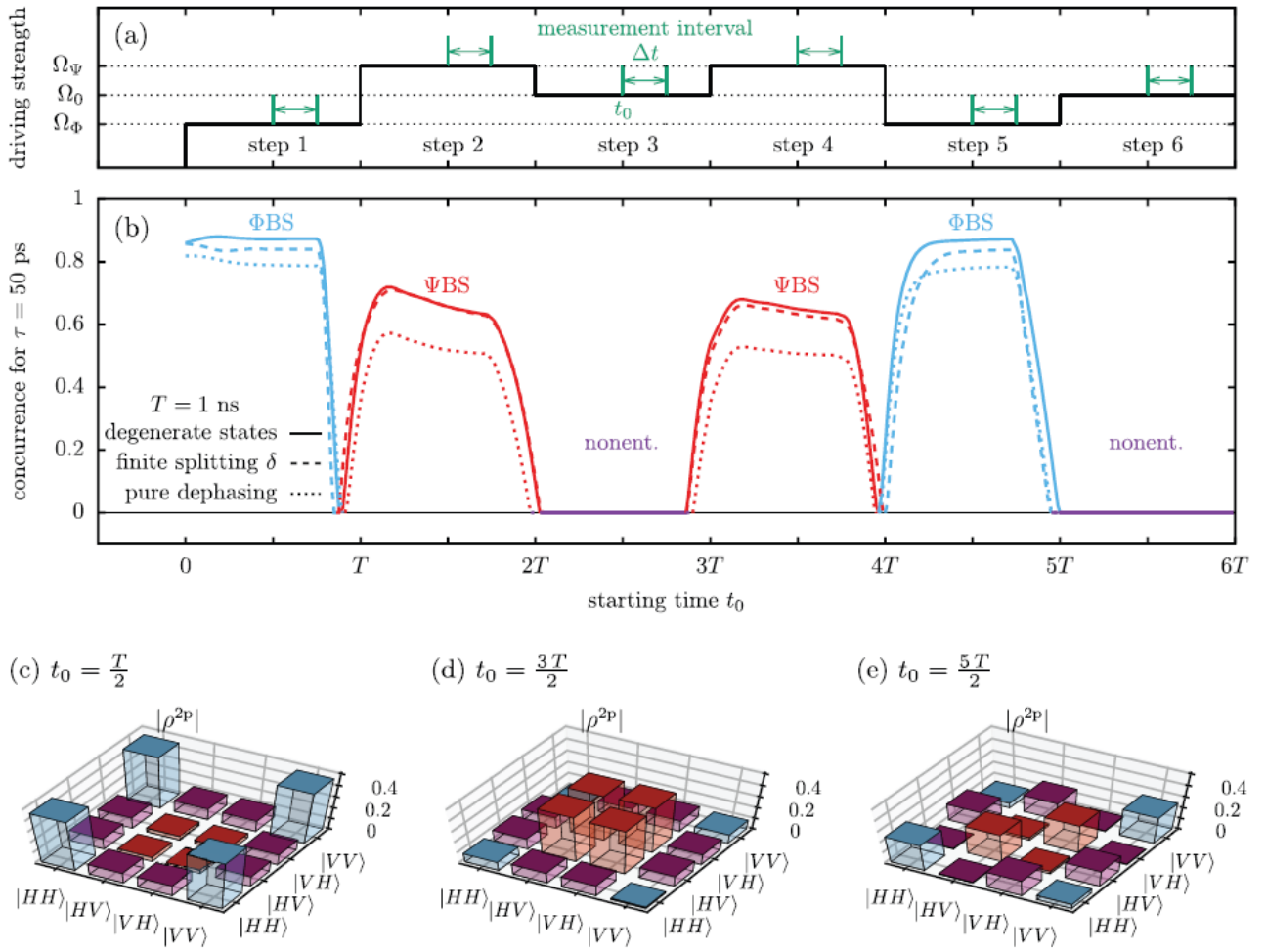Similar considerations at the remaining two-photon resonances enable one to predict the

Figure 3.4: [Taken from [Pub 5]] (a) In the proposed protocol, the driving strength is changed in a step-like fashion with step length T. (b) Concurrence calculated for respective measurements with starting time t_0 and (real-time) interval Δt as a function of t_0. Results are shown for degenerate states $|X_{\mathrm{H/V}}\rangle$ (solid line), for a finite fine-structure splitting (dashed line), and including pure dephasing (dotted line). (c)–(e) Two-photon density matrices $\rho^{2\mathrm{p}}$ (absolute values) for degenerate states and measurements performed at three different starting times t_0.

generated two-photon state and its type of entanglement, cf., Table 2 in [Pub 4]. In conclusion, the generation of the desired BS can be achieved by tailoring the driving strength and the cavity mode placement.

3.2.2 Time-dependent entanglement switching

The new physical insights gained in [Pub 4] are employed in [Pub 5] to manipulate the created two-photon state in a time-dependent fashion. A protocol for an active, time-dependent entanglement switching is proposed that can be operated by just changing the external driving strength.

A sketch of the proposed protocol is depicted in Figure 3.4(a). The central idea is to fix

29

the cavity mode energy such that for a small driving strength Ω_Φ the cavity modes are in resonance with the two-photon transition between the laser-dressed states $|U\rangle$ and $|L\rangle$. Thus, in accordance with [Pub 4], a ΦBS is created as long as the quantum emitter is excited with this driving strength. Consequently, when a measurement is performed during the first step a ΦBS with a high degree of entanglement [cf., panels (b) and (c)] is obtained. After a certain time period T the external driving strength is abruptly changed to a higher value Ω_Ψ, which brings the two-photon transition between the dressed states $|N\rangle$ and $|L\rangle$ in resonance with the fixed cavity modes. Because this two-photon resonance is associate with the second type of photon entanglement, a ΨBS is created and measured during the second step [cf., panels (b) and (d)]. Furthermore, steps 4 and 5 show that the switching does not depend on the order and is possible in both directions. Thus, one can actively switch back and forth between the generation of different types of photon entanglement.

In addition, it is also possible, to turn off the creation of entangled photon pairs for a given time period by choosing an intermediate driving strength Ω_0 that is not associated with a two-photon resonance. Note that Ω_0 can be chosen such, that the same photon yield is obtained as for the former driving strength values. Thus, the amount of emitted photons stays the same, but a measurement performed on photon pairs emitted during this step (step 3 and 6) will result in a mixed state with vanishing degree of entanglement [cf., panels (b) and (e)].

The proposed protocol is also robust against typical fine-structure splittings much smaller than the binding energy E_B (dashed line). Altogether, the proposed protocol enables one to perform a time-dependent switching between the generation of either different entangled two-photon states or entangled and nonentangled states from the same source without the need of post processing, e.g., with waveplates.

3.2.3 Phase transition-like behavior in quantum dots

When the four-level emitter is realized by a strongly-confined self-assembled InGaAs QD, the surrounding semiconductor environment has to be accounted for. In [Pub 10], the impact of LA phonons on photon pairs created in continuously driven QD-cavity systems is studied. It is found that the phonon impact is much more severe and qualitatively different than in the case without constant laser excitation.

Figure 3.5(a) depicts the resulting concurrence as a function of the driving strength for calculations without phonons (solid line) and including LA phonons at 4 K (green dots). Similar to the results presented in Figure 3.3, the cavity modes are always adjusted to the two-photon resonance between the laser-dressed states $|U\rangle$ and $|L\rangle$, i.e., their energy changes alongside the driving strength. As discussed in Section 3.2.1, a sharp transition between regions of high ΦBS and ΨBS entanglement is obtained in the phonon-free situation.

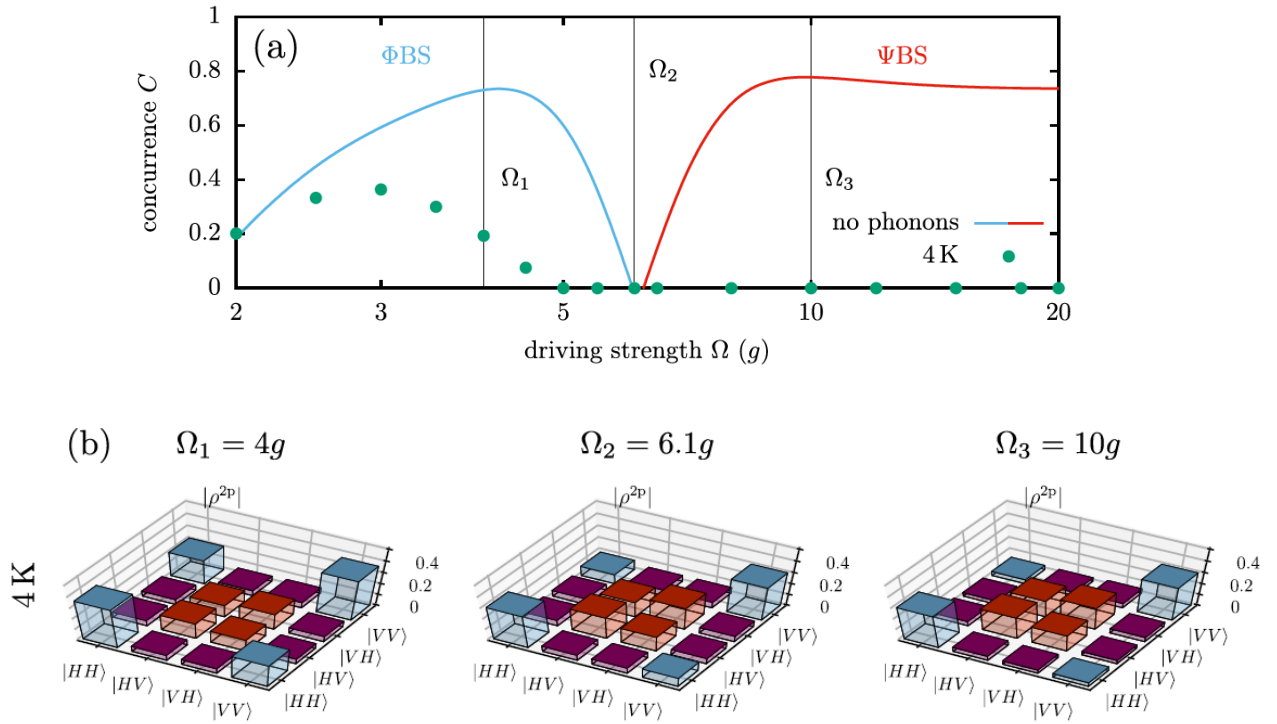But already at cryogenic temperatures of 4 K, the results including the interaction with LA

Figure 3.5: [Adopted from [Pub 10]] (a) Concurrence as a function of the driving strength. Results are shown for calculations without phonons (solid line) and with phonons at a temperature of 4 K (green dots). Straight vertical lines mark three driving strength values associated with either a high concurrence or a vanishing degree of entanglement in the phonon-free situation. (b) Two-photon density matrices (absolute values) at $T = 4$ K for the three driving strength values Ω_j indicated in panel (a).

phonons only follow the phonon-free results for small driving strength values. With increasing driving strength, phonons lead to a strong decrease in the degree of entanglement and the concurrence vanishes already before the special point at Ω_2 and the subsequent region of ΨBS entanglement cannot be reached. When the driving strength is increased further, the concurrence remains zero. Thus, a behavior similar to a phase transition is encountered, where the concurrence takes on the role of the order parameter. Only below a certain driving strength an entangled two-photon state is created. Above this critical parameter, the emitted photon pair state is not entangled.

The physical origin behind the severe phonon impact and the phase transition-like behavior are phonon-induced transitions between the dressed states of the driven QD-cavity system. These processes compete with the remaining relaxation processes, i.e., cavity losses and radiative decay, and have a severe impact on the resulting steady state. With rising driving strength the phonon-related relaxation processes become more and more dominant, cf., Figure 4 in

[Pub 10], pulling the resulting two-photon density matrix towards

$$\rho_{\text{th}}^{2\text{p}} = \frac{1}{6} \left[2 \left(|HH\rangle\langle HH| + |VV\rangle\langle VV| \right) + \left(|HV\rangle + |VH\rangle \right) \left(\langle HV| + \langle VH| \right) \right] \tag{3.5}$$

This effect can be well observed in the sequence of density matrices presented in Figure 3.5(b). The characteristic form of $\rho_{\text{th}}^{2\text{p}}$ can be explained by a phonon-related thermalization of the dressed states. The increasing phonon impact with rising driving strength is traced back to a more effective phonon coupling due to the frequency dependence of the phonon spectral density and the changing character of the laser-dressed states.

A similar behavior is also found for fixed driving strength values. Here the degree of entanglement decreases with rising temperature until it vanishes for a certain critical value. Above this temperature the concurrence, again, remains zero. Although many similarities with a phase transition can be found, the observed behavior is not an actual phase transition. For example, no critical slowing down or discontinuity in any quantity can be observed.

3.3 Photon statistics in driven quantum emitter-cavity systems

In general, driven quantum emitter-cavity systems offer interesting physics, as the transitions that lead to photon emission take place between laser-dressed states instead of the bare emitter states. By enhancing specific multi-photon processes due to clever cavity mode placement, also other fascinating non-classical states of light can be generated in constantly driven systems, e.g., the recently proposed N-photon bundles[138]. A characteristic fingerprint of these multi-photon structures is their specific stationary photon number distribution.

Additionally, transiently changing photon number distributions arise due to the excitation with chirped laser pulses. Chirped laser pulses fall into the middle ground between continuous excitation and short femto- or picosecond pulses, since their effective pulse length increases drastically when chirps are introduced by a Gaussian chirp filter, cf., [Pub 3]. Furthermore, they can also be used to excite spatio-spectrally distinct QDs, exploiting the adiabatic rapid passage mechanism, cf., [FPub 10].

3.3.1 N-photon bundles

Another highly non-classical state of light that can be created in constantly driven quantum emitter-cavity structures are N-photon bundles[138,139]. In these recently proposed multi-photon structures, photons are released from the cavity only in groups of N subsequent photons with a specific temporal spacing between them. In theory, they can be generated in (off-resonantly)
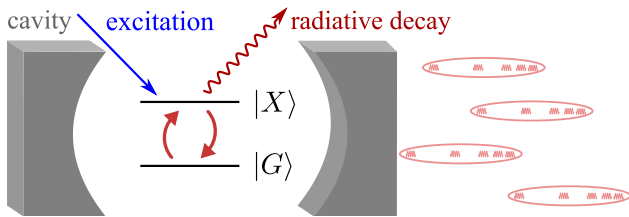
Figure 3.6: [Taken from [Pub 7]] Sketch of a two-level emitter embedded in a lossy cavity. The emitter is driven by a continuous excitation and interacts with one cavity mode. In addition, it can decay radiatively. For specific parameters, N-photon bundles leave the cavity.

driven two-level emitter-resonator systems when the cavity mode energy is in resonance with a specific N-photon transition between the emerging pair of laser-dressed states. A schematic sketch of the considered system is depicted in Figure 3.6.

In the ideal situation, an N-photon Fock state $|N\rangle$ is created inside the cavity by a simultaneous emission of N photons due to the chosen resonance condition. Because of the cavity losses these N photons are then released from the cavity as $|N\rangle$ decays following a cascade over Fock states $|n\rangle$ ($N \geq n \geq 0$). Since the cavity loss rate for an n-photon Fock state is proportional to the number of photons, a specific temporal spacing between the subsequently emitted N photons emerges that is also reflected in the characteristic stationary photon statistics

$$
P_N(n) = \begin{cases} 1 - \frac{\langle n \rangle}{N} \sum\limits_{j=1}^{N} \frac{1}{j}, & n = 0 \\ \frac{\langle n \rangle}{N} \frac{1}{n}, & 1 \leq n \leq N \\ 0, & n > N \end{cases} \tag{3.6}
$$

of an N-photon bundle. Here, $\langle n \rangle$ is the average number of photons in the cavity mode.

Besides other characteristics, like its emission properties[140,141] or internal correlations[142], $P_N(n)$ is established as a major fingerprint of an N-photon bundle. Due to the sharp cut-off for $n > N$ and the relatively high N-photon component, N-photon bundles are especially attractive for quantum cryptography, cf., [FPub 8], or medical applications[138,143–147]. In [Pub 7] the possibility to generate N-photon bundles in two different solid state realizations for the integral two-level emitter is discussed. In particular, the case $N = 2$ is analyzed.

Strongly-confined QD-cavity system Employing realistic, state-of-the-art values for cavity parameters and radiative decay in phonon-free calculations suggests that QD-cavity systems might be suitable platforms for the generation of 2-photon bundles, cf., Figure 3.7(a), as argued in Ref. [138]. For these parameters, indeed, a stationary photon distribution very close to the characteristic fingerprint $P_{N=2}(n)$ is obtained (black column). But, when the coupling to LA phonons is taken into account, the relative contribution of the two-photon Fock state is strongly reduced (colored columns). Thus, already at temperatures of 4 K the characteristic fingerprint is essentially lost.

Similar to the discussion presented in Section 3.1.1, phonons assist off-resonant single-photon
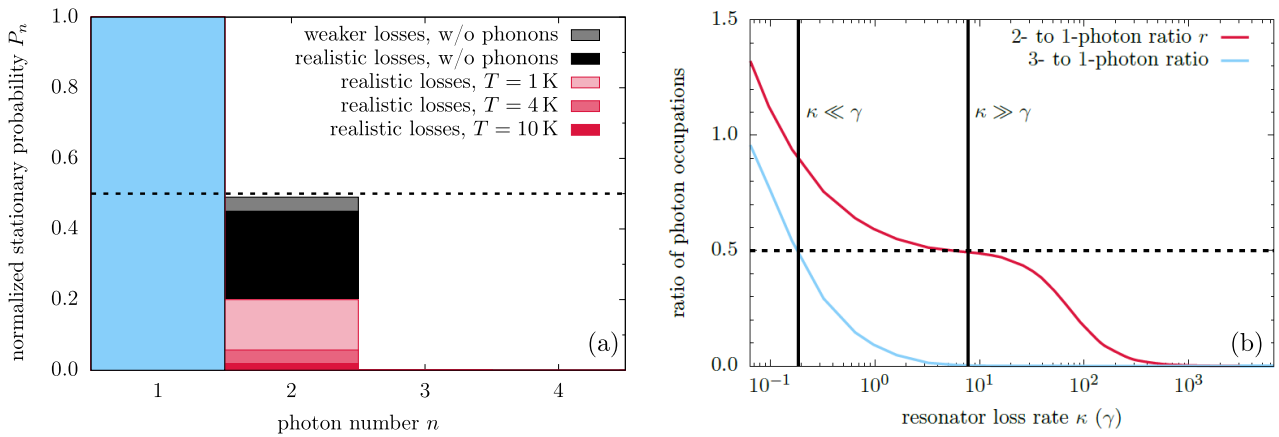
Figure 3.7: [Adopted from [Pub 7]] (a) QD–cavity system: The stationary probability P_n of occupying the photon number states $|n\rangle$ normalized to its value at $n = 1$. Results are shown for calculations without phonons and including the coupling to LA phonons. (b) Superconducting qubit–microwave resonator system: The stationary ratios of the 2- to 1-photon occupation probabilities and of the 3- to 1-photon occupation probabilities as functions of the resonator loss rate. The dotted black line indicates the target value of $r = 0.5$.

processes. These one-photon processes are in competition with the simultaneous two-photon process that is crucial for the creation of the 2-photon bundle. Since phonons shift this competition strongly towards the single-photon processes, the generation mechanism of the bundle is overshadowed. Therefore, the unavoidable phonon environment in strongly-confined QDs suppresses already the creation of 2-photon bundles, and, consequently, also the generation of higher N-photon bundles.

Superconducting qubit–microwave resonator system In contrast to QD-based systems, superconducting qubits are not prone to pure-dephasing caused by interactions with phonons. Thus, it is found in [Pub 7] that superconducting qubit–microwave resonator system are a suitable platform for the generation of N-photon bundles, in agreement with Ref. [148]. However, it is revealed that the bundle generation is only possible for a certain range of resonator loss rates κ. This is highlighted in Figure 3.7(b). According to the characteristic fingerprint $P_{N=2}(n)$, an ideal 2-photon bundle is only created if the stationary 2- to 1-photon ratio $r := P_2/P_1$ takes the value 0.5 and, simultaneously, all n- to 1-photon ratios with $n > N$ vanish. On the one hand, this is only possible if the cavity loss rate is much larger than the radiative decay rate γ [cf., Figure 3.7(b)] as the latter can introduce transitions between the laser-dressed states that interfere with the cascade over subsequent Fock states in the generation process of the bundle. On the other hand, if the cavity loss rate is too large, the linewidth of the cavity mode overlaps with off-resonant one-photon processes between the laser-dressed states. This results in an increase of one-photon emission processes that also destroy the characteristic fingerprint.

3.3.2 Time-dependent photon number distributions

Although photon number distributions do not contain the full information about the emitted light since, e.g., coherences are not captured, they can indicate non-classical states of light, cf., Section 3.3.1. Furthermore, they are directly accessible in experiments[149–151]. Often, photon number distributions are described by extracting a few characteristic numbers, like the mean photon number $\langle n \rangle$ and/or the Mandel parameter[152]

$$Q = \frac{\left\langle \Delta n^2 \right\rangle - \langle n \rangle}{\langle n \rangle} \tag{3.7}$$

The latter is a measure for the derivation of the mean-square fluctuation Δn^2 from $\langle n \rangle$ and vanishes for a Poissonian distribution. Because a negative Mandel parameter $Q < 0$ has no classical analog[153], it is also an indicator for highly non-classical states of light.

The main focus of [Pub 3] is the transient behavior of photon number distributions in QD-cavity systems excited by chirped laser pulses. A two-level system comprising the ground state and one exciton state is considered that couples to one cavity mode. The chirped laser pulses used to excite the QD display a central frequency that changes linearly over time. Whether the frequency of the laser increases or decreases over time is determined by the sign of the chirp parameter α.

Quite interestingly, it is discovered that the shape of resulting photon number distributions can change drastically over the course of time, cf., Figure 3.8. In calculations without phonons [panel (a) and (b)] - which also corresponds to the limit of atomic cavity systems - the photon number distribution displays several different and interesting shapes after the time of the pulse maximum. For example, while two smooth peaks can be observed at $t - t_0 = 20$ ps, jagged shapes with multiple maxima emerge at later points in time. An analysis performed in the basis of cavity-dressed states reveals that this transient behavior of the photon number distribution originates from subsequent crossings of resonance by the instantaneous laser frequency. Note that, in the phonon-free situation, the system dynamics is symmetric with respect to the sign of the chirp parameter α.

The interaction with LA phonons at a temperature of 4 K has a strong and qualitative impact on the time evolution of the photon number distribution, cf., panels (c) and (d). Most strikingly, the symmetry with respect to the sign of α disappears. Only in the case of a positive chirp parameter, shapes with multiple maxima can be observed [cf., panel (d)]. Although the distributions are quite similar to the phonon-free situation shortly after the pulse maximum, they approach a thermal distribution already after 80 ps due to the phonon influence. In stark contrast, the resulting photon number distribution is always close to a thermal distribution when the chirp parameter is negative.
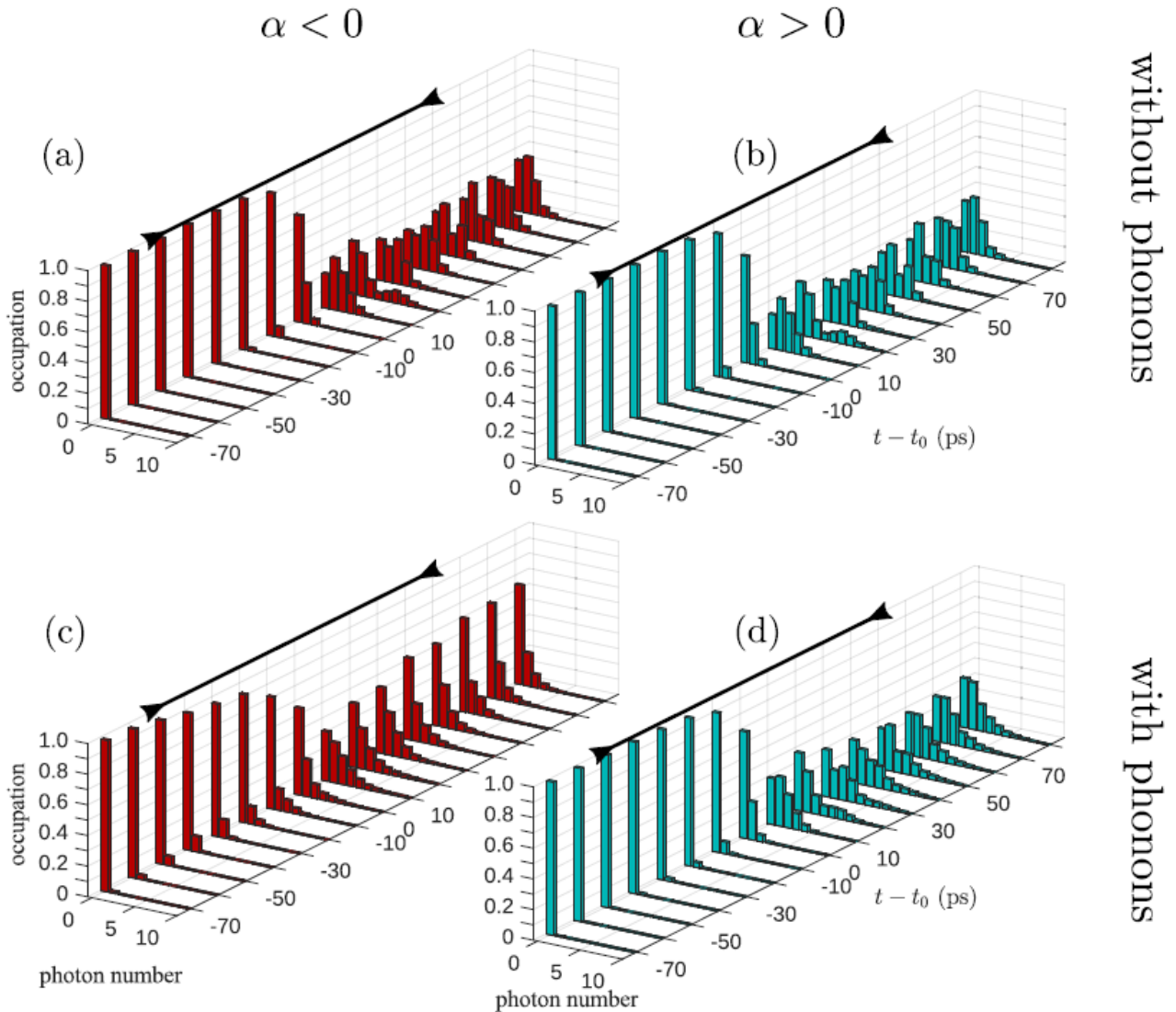
Figure 3.8: [Taken from [Pub 3]] Transient photon number distributions for laser excitations with chirped pulses. The pulse has its maximum at t_0 and black markers indicate its full-width-at-half-maximum. (a) and (c) Calculated with a negative chirp parameter $\alpha < 0$, (b) and (d) $\alpha > 0$. (c) and (d) Results accounting for phonons at a temperature of 4 K. The corresponding phonon-free results are shown in (a) and (b).

The observed asymmetry can be understood by an analysis in the basis of laser-dressed states in combination with the well-known asymmetry between phonon emission and absorption processes, cf., Figure 4 in [Pub 3]. At low temperatures the latter are essentially suppressed and only phonon emission processes are likely to occur. As a consequence, the impact of LA phonons is more pronounced in the case of a negative chirp parameter, where an interplay between photon and phonon emission processes already results in a thermalization before the pulse maximum hits the system. For a positive chirp, phonons affect the system dynamics only after the pulse maximum due to the strong suppression of phonon absorption processes at low temperatures.

Nevertheless, the Mandel parameter Q changes its sign over the course of time in all considered situations. This indicates that in each situation a genuine quantum state of light is reached at some point in time. A closer investigation of $Q(t)$ leads to another important conclusion: A vanishing Mandel parameter is not necessarily related to a Poissonian statistics. For example, $Q = 0$ is obtained for $t - t_0 \approx 40$ ps in Figure 3.8(b), although the respective photon number distribution is far away from a Poissonian distribution.

3.4 Generation and storage of single photons employing short laser pulses

Precisely timed and tailored laser pulses can be used to deterministically excite a QD into an exciton or biexciton state or to manipulate and control the dynamics in QD-cavity systems. For example, short resonant laser pulses and/or off-resonant AC-Stark pulses can be employed to prepare non-classical states of light, such as higher-order Fock states ([FPub 2]) or Schrödinger cat states ([FPub 3]), as well as to control the dark exciton occupation ([FPub 4]).

In this thesis, the validity of the QRT for the calculation of different single-photon characteristics in the presence of phonons is investigated by studying QDs under short resonant laser excitation of an exciton state. Afterwards, off-resonant AC-Stark pulses in combination with a magnetic dopant are employed to store one photon in an optically dark state.

3.4.1 Single photons and the quantum regression theorem

In addition to entangled photon pairs, indistinguishable single photons represent another key ingredient for applications in quantum technologies[154]. QDs are often discussed as a practical source for these non-classical states of light, because single photons can be created on-demand after the preparation of an exciton state with a short, resonant π-pulse excitation.

It is common to characterize single-photon sources with three figures of merit that capture properties relevant for typical applications: (i) the source brightness $\mathcal{B}$, (ii) the single-photon purity $\mathcal{P}$, and (iii) the indistinguishability $\mathcal{I}$. Definitions and models to calculate these quantities can be found in Equations (1)-(5) of [Pub 6]. While the brightness is related to a time-integrated expectation value, the two latter quantities involve the evaluation of two-time correlation functions. The QRT is probably the most widely used tool to calculate such correlation functions in open quantum systems[155]. It states that the same dynamical map that is used to propagate the system in the real time t, can also be used for the subsequent propagation in the delay time τ. The QRT is typically also employed for studies in QD systems[156–158], despite the fact that its central assumption - a factorization of system and environment at all times - should be quite problematic in systems with strong non-Markovian effects. For example, it was found in
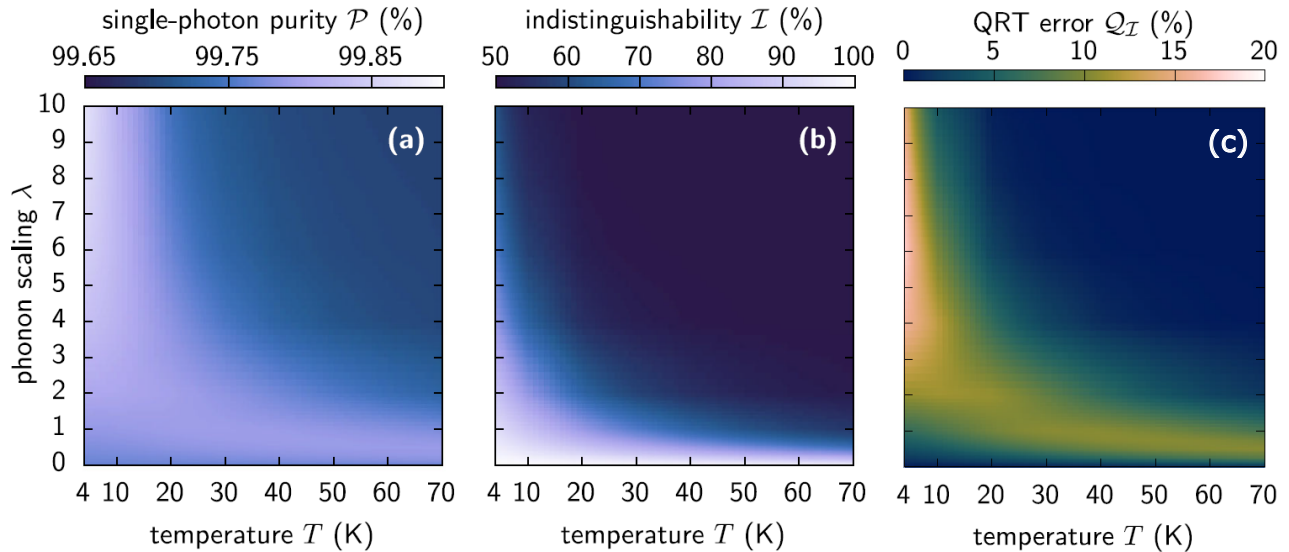
Figure 3.9: [Adopted from [Pub 6]] The single-photon purity $\mathcal{P}$ (a), the indistinguishability $\mathcal{I}$ of two successively emitted photons (b), and the relative error $\mathcal{Q}_{\mathcal{I}}$ for the indistinguishability (c) in a two-level QD for a temperature range between 4 K and 70 K and phonon scalings from 0 to 10.

Ref. [47] that a naive application of the QRT predicts the phonon sideband in photon emission spectra on the energetically wrong side.

The phonon impact on the major characteristics of single-photon sources is studied in [Pub 6], in particular, the validity of the QRT in QDs is investigated. As discussed in Section 2.3.2, the path-integral formalism provides a numerically complete approach for the calculation of multi-time correlation functions, and can thus be used to benchmark approximate QRT results.

In [Pub 6], the three figures of merit are investigated as a function of temperature and the phonon coupling strength, employing the numerically complete path-integral formalism. In order to vary the coupling strength, the phonon spectral density is scaled by a factor λ. Thus, $\lambda = 0$ represents the phonon-free situation, while $\lambda = 1$ corresponds to GaAs-based QDs and larger coupling values $1 < \lambda \leq 10$ to piezoelectric materials like GaN[34]. In general, all three figures of merit decrease with rising temperature or coupling strength. However, the purity is hardly influenced by the presence of phonons, cf., Figure 3.9(a). In contrast, indistinguishability [panel (b)] and brightness (not shown) strongly decrease with rising temperature and/or coupling strength. For standard GaAs parameters, i.e., $\lambda = 1$, the indistinguishability drops below 70% already at 30 K. Nevertheless, for a temperature of 4 K, an almost perfect single-photon source is realized.

Quite remarkably, it is uncovered that the validity of the QRT depends on the considered quantity. While the relative error in the single-photon purity is on the order of 10^{-4}, the relative error of the indistinguishability $\mathcal{Q}_{\mathcal{I}}$ can reach values up to 18%, cf., Figure 3.9(c). In

the latter situation, the QRT calculations always suggest a worse indistinguishability. Thus the QRT systematically overestimates the phonon impact on this figure of merit. This is an important new insight, given the widespread use of the QRT and the current race for an ideal single-photon source[159]. The QRT-related error can, indeed, be traced back to a strong non-Markovianity of the system dynamics. Comparing the relative error of the indistinguishabilty with a measure for non-Markovianity demonstrates that the regions of large deviations between QRT and numerically complete path-integral results coincide with strong non-Markovian effects in the system dynamics, cf., Figure 2 in [Pub 6].

3.4.2 Photon storage exploiting AC-Stark pulses and dark states

After discussing QDs as single-photon sources, this Section explores the potential of QD-cavity systems as storage devices for individual photons. Such storage devices are necessary in actual realizations of quantum technologies, e.g., to achieve the synchronization of different signals.

In [Pub 8], a protocol for photon buffering, i.e, the temporary storage of a single photon, based on a QD-cavity system is proposed. The central idea is to absorb the photon and temporarily convert it into an excitation of the QD in order to release it at a later point in time. Unfortunately, the optically active bright exciton state $|X\rangle$ in typical QDs has rather short lifetimes in the range of a few 100 ps up to 1 ns. On the other hand, dark excitons $|D\rangle$ are metastable and display lifetimes that are at least one order of magnitude larger, but cannot be addressed optically. Nevertheless a coupling to the bright exciton state can be facilitated by introducing a single magnetic dopant inside the QD. The exchange interaction between the electron spin and the spin of the dopant introduces an effective coupling J between the bright and dark exciton state under a simultaneous spin flip of the dopant. However, the induced coupling strength J is typically much smaller than the dark-bright splitting δ_{eff} between the two exciton states. Thus, the interaction between $|X\rangle$ and $|D\rangle$ is effectively suppressed.

To overcome this hurdle, a strongly off-resonant AC-Stark pulse can be applied to the optically active ground state-to-bright exciton transition. Due to the AC-Stark effect[160] the energy of the bright exciton can be shifted in resonance with its dark counterpart by exactly compensating the dark-bright splitting, enabling a controllable transfer of occupations between them, cf., [FPub 4].

In order to demonstrate the potential of QD-cavity systems as photon storage devices, a Manganese (Mn) doped CaTe/ZnTe QD inside a microcavity is considered[161]. The corresponding theoretical model takes the form of a Λ-type three-level system, cf., inset of Figure 3.10(b). It comprises the ground state $|G\rangle$ and the bright exciton in resonance with one cavity mode (coupling strength g), as well as one dark exciton coupled to the latter due to the Mn-induced interaction J. The proposed protocol is visualized in Figure 3.10(a). One photon that is initially in the cavity mode interacts with the QD and Rabi-oscillations between the 1-photon Fock
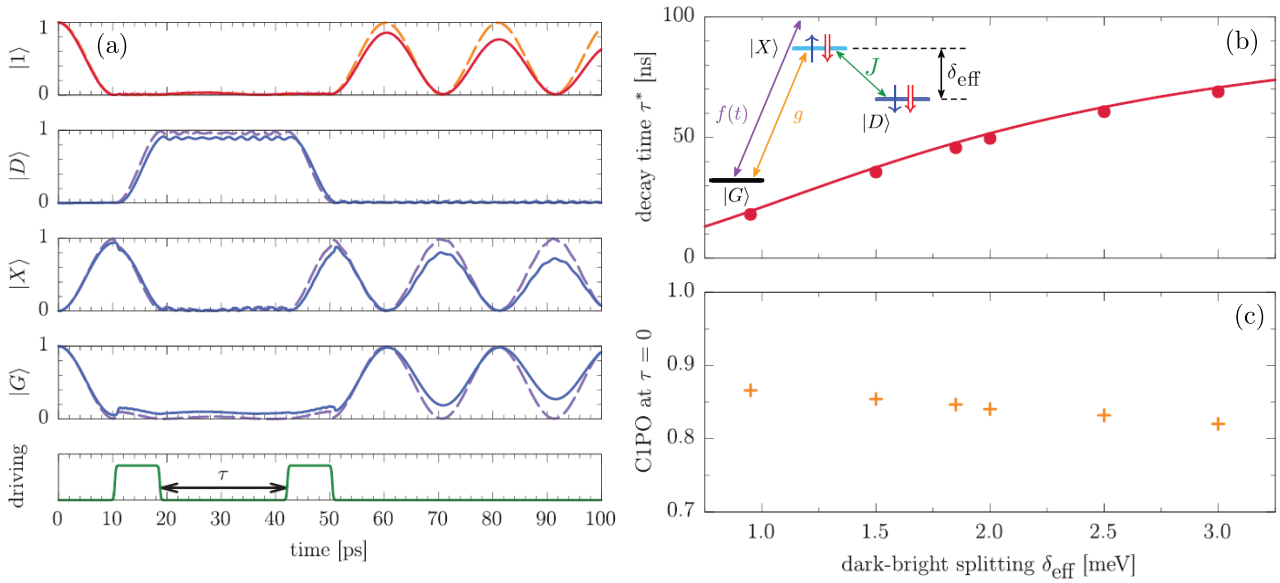
Figure 3.10: [Adopted from [Pub 8]] (a) A first writing AC-Stark pulse is used to store a single cavity photon in the dark exciton state. The occupations of the ground state, the bright exciton, the dark exciton, and the 1-photon Fock state are depicted. Results are shown for the ideal case without phonons and losses (dashed lines) and including radiative and cavity loss effects (solid lines). Afterwards, the single photon is retrieved by a second readout AC-Stark pulse. (b) and (c) Decay time τ^* and the C1PO at $\tau = 0$ in dependence of the effective splitting δ_{eff} between the dark and bright exciton state without taking phonons into account. The red line represents an analytic estimate. Inset: The Λ-type three-level model of the QD. The spin configuration of the two exciton states is symbolized by arrows (blue: electron; red: hole).

state and the bright exciton take place. After half the Rabi period, an off-resonant AC-Stark pulse is applied. This pulse shifts the energy of the bright exciton. The Rabi-oscillation stops as the bright exciton is now in resonance with its dark counterpart. Instead, the occupation of the bright exciton is converted into the dark exciton. After the conversion, the pulse is turned off and the photon is stored in $|D\rangle$. A specific storage time τ later, a second AC-Stark pulse is applied, reversing the storage process and releasing the captured photon.

The performance of the storage device is characterized by the captured 1-photon occupation C1PO. This quantity measures the maximal single-photon occupation after the second pulse. In the ideal situation, without losses and phonons, the protocol works perfectly. When loss processes, i.e., cavity losses and radiative decay, with realistic parameters are considered, the C1PO exhibits a dependence on the coupling J and the dark-bright splitting. Furthermore, it decreases exponentially with rising storage time τ. The corresponding characteristic decay time τ^* of the C1PO can be interpreted as the time interval during which the photon can be stored successfully. τ^* is indeed up to two orders of magnitude larger than the lifetime of the bright exciton and increases with the dark-bright splitting, cf., Figure 3.10(b). This dependency is caused by a residual coupling between the two exciton states during the storage time and can

be quantified analytically (solid red line). In addition, C1PO at $\tau = 0$ measures the photon occupation that is lost during the write and read pulse. It is found, that well above 80% of the photon occupation can be successfully stored and released again, cf., Figure 3.10(c).

Although the interaction with LA phonons has a strong impact on the performance of the proposed scheme at higher temperatures, only slightly reduced characteristics are obtained at low temperatures around 4 K, cf., Figures 3(c) and (d) in [Pub 8]. Thus, [Pub 8] demonstrates a feasible QD-based device for the storage of individual photons.

3.5 Limited entanglement due to pulsed optical excitation

In the final Section, arguably the most important result and new physical insight is presented. State-of-the-art experiments, that demonstrate polarization-entangled photon pairs with degrees of entanglement close to unity, employ a coherent two-photon resonant excitation (TPE) scheme, cf., Figure 3.11(a), with linearly polarized laser light and typical pulse durations on the order of 10 ps[10,12,14,74,101–104]. Because of the practically suppressed re-excitation probability in the TPE scheme[13,162], one expects the creation of a perfectly entangled photon pair, provided that the exciton fine-structure splitting is zero. However, even in the absence of an exciton fine-structure splitting, no polarization-entangled photon pairs with a unity degree of entanglement have been reported to this day, the current record concurrence being 0.97(1)[102].

In [Pub 9], the impact of the TPE scheme on polarization-entangled photon pairs and their degree of entanglement is analyzed. To this end, a short Gaussian laser pulse with a finite full-width-at-half-maximum (FWHM) is employed to prepare the biexciton state. It is discovered that the degree of entanglement decreases monotonically with a rising FWHM of the laser pulse, cf., Figure 3.11(b). Based on analytical considerations and calculations an intuitive picture for the physical origin as well as an analytic expression for the resulting concurrence is presented.

These considerations reveal that the TPE excitation scheme itself introduces a which-path information. If a laser polarization is considered that coincides with the optical selection rules of the QD, e.g., the horizontal polarization H, only the corresponding exciton state $|X_\mathrm{H}\rangle$ interacts with the laser pulse. Due to the AC-Stark effect, the energy of this exciton state is shifted, resulting in a sizable energetic splitting $E_\mathrm{S} \sim \hbar\pi/\mathrm{FWHM}$ between the two exciton states during the laser pulse, cf., Figure 3.11(c) left column. Since a finite probability exists that the first photon is emitted while the laser pulse still interacts with the QD, this laser-induced splitting impacts the obtained two-photon state similar to an exciton fine-structure splitting. During the laser pulse, the two decay paths become distinguishable and, consequently a which-path information is introduced by the TPE scheme itself. As a result the coherence in the two-photon density matrix ρ^2p is reduced, leading to a deviation from the ideal state $|\Phi_+\rangle$ and a degraded concurrence. With rising pulse duration, the laser-induced splitting persists for a longer time
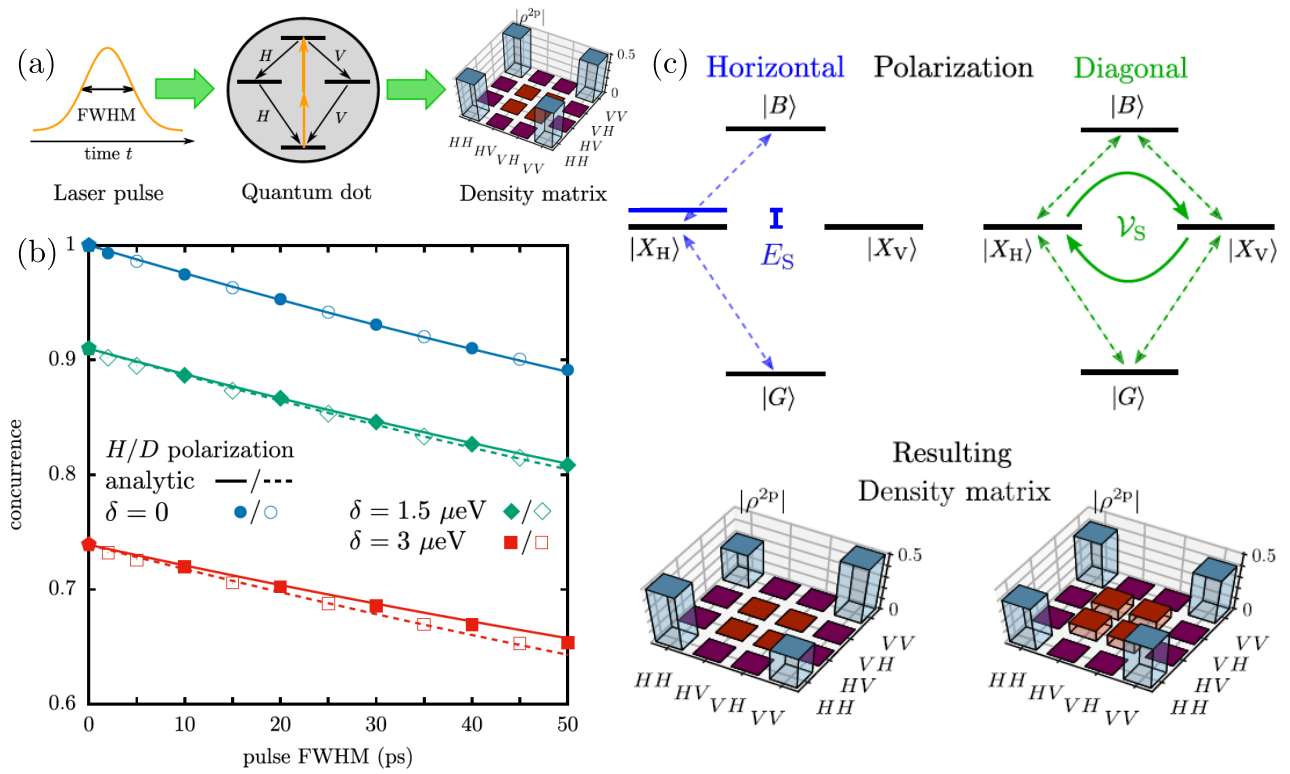
Figure 3.11: [Adopted from [Pub 9]] (a) A Gaussian pulse with finite full-width-at-half-maximum (FWHM) excites a quantum dot in the two-photon resonant excitation scheme. Expectation: The excited quantum dot decays radiatively, resulting in a maximally entangled state $|\Phi_+\rangle$. (b) Concurrence in dependence of the pulse FWHM for two laser polarizations [horizontal (H) and diagonal (D)] and three fine-structure splittings δ. Symbols: numerical results; Lines: analytic expression according to Eq. (8) in [Pub 9]; Pentagons at FWHM = 0: initially prepared biexciton without optical excitation. (c) Laser-induced effects. Horizontal polarization (left column): A laser-induced splitting E_S introduces a which-path information that reduces the coherence. Diagonal polarization (right column): A laser-induced coupling $\mathcal{V}_S$ leads to the creation of unwanted two-photon states $|HV\rangle$ and $|VH\rangle$.

period and the probability that the first photon is emitted during the pulse increases. Therefore, the concurrence drops with rising FWHM.

Because the loss in concurrence is related to an asymmetry during the pulse, one could naively assume that the detrimental impact of the TPE scheme can be avoided by using a laser polarization that is symmetric in H and V polarization, i.e., diagonal in this polarization basis. However, in this situation, the same laser-induced splitting is still present, just in a rotated basis. In the computational basis H and V, a diagonal laser polarization results in an effective coupling $\mathcal{V}_S$ between the two exciton states $|X_H\rangle$ and $|X_H\rangle$, cf., Figure 3.11(c) right column. As a consequence unwanted two-photon states $|HV\rangle$ and $|VH\rangle$ can be created, resulting again in a reduced degree of entanglement. Note that the effective coupling is equivalent to the induced splitting E_S, similar to the fine-structure splitting, which can also be interpreted as an energetic

splitting or an exchange interaction, depending on the chosen basis, cf., Figure 2.1.

When the exciton fine-structure splitting is zero, the resulting concurrence is independent of the chosen (linear) laser polarization, cf., Figure 3.11(b), because all situations are physically equivalent. However, when δ is finite, using a horizontal laser polarization results in a slightly higher degree of entanglement. Although the concurrence approaches the value associated with the respective initial value calculation, the limit FWHM $\rightarrow 0$ is not desirable for practical realizations. Because the spectrum of the laser pulse starts to overlap with the exciton transitions for short laser pulses, the TPE scheme breaks down below a FWHM of 2...3 ps. Thus, the laser-induced which-path information cannot be avoided in the TPE scheme, resulting in a fundamental limit for the achievable degree of entanglement.

All essential features and dependencies are well described by the analytic expression presented in Equation (8) of [Pub 9], cf., Figure 3.11(b). Furthermore, the theoretical upper bound for the concurrence $C \approx 0.975$ predicted for realistic parameters and a typical pulse FWHM of 10 ps agrees well with the current record concurrence. Thus, the laser-induced which-path information explains the observed deviation from unity even quantitatively.

4 Summary and outlook

Semiconductor quantum dots (QDs) are one of the most promising and versatile platforms for the creation of highly non-classical states of light that should be straightforward to incorporate in modern information technologies. But in contrast to other candidates, they are prone to a typically detrimental interaction with longitudinal acoustic (LA) phonons due to their semiconductor environment. In this thesis, the possibility to generate and manipulate highly non-classical states of light in different QD-cavity setups was investigated theoretically. The impact of various system parameters, like external laser fields or the energetic position of cavity modes as well as the fine-structure splitting and the biexciton binding energy was discussed. In particular, the influence of LA phonons was in the focus of the conducted studies.

It was discovered, that almost all tuning nobs available in QD-cavity systems have a profound impact on the generated state. The energetic placement of the cavity modes plays a decisive role in the generation of N-photon bundles or entangled photon pairs, in particular, in the presence of a continuous laser excitation. Furthermore, sophisticated protocols for the storage of single-photon states or a time-dependent switching of the photonic entanglement type are proposed that rely on precisely timed and/or tailored optical laser pulses.

The impact of LA phonons on the resulting photonic quantum state of light can be qualitatively different. Although LA phonons often result in a tolerable gradual degradation of the target state or quantity with rising temperature, a strong phonon impact in some situations can lead to a qualitatively different system behavior that essentially suppresses the generation of the desired state of light. For example, highly non-classical single-photon states can be successfully created and manipulated at low temperatures. On the other hand, the creation of more complex states, like entangled Ψ Bell states or N-photon bundles, that rely on a strong, continuous laser excitation and direct multi-photon transitions between dressed states, seem to be out of reach in strongly-confined self-assembled QDs. Nevertheless, their generation might be achievable in alternative solid-state realizations of quantum emitters or larger QDs with a less effective phonon coupling. Most strikingly, the impact of phonons can even be beneficial and boost the degree of photon entanglement when other phonon-related effects overcompensate the phonon-induced dephasing.

Arguably the most important result of this thesis is the realization that the two-photon excitation scheme itself prohibits the creation of perfectly entangled photon pairs due to a

laser-induced which path information. This newly discovered feature fits well to the current record concurrence and recent experiments performed in the group of Armando Rastelli at the University of Linz, cf., [FPub 11]. With state-of-the-art setups employed by current collaborators working in experimental groups in Innsbruck, Linz, or Vienna other predictions and mechanisms discussed in this thesis might be verified in the future.

Furthermore, a recent methodological break through by one of the author's prime collaborators enables one to push for new physical frontiers regarding numerical studies of open quantum systems[163]. Although the path-integral method allows for an accurate description of the LA phonon environment, it is restricted to a diagonal pure-dephasing type coupling. In contrast, the newly developed calculation scheme based on the *automated compression of environments* (ACE) has the potential to be a multi-purpose tool for a numerically complete investigation of almost arbitrary environments. Multiple environments can be taken into account on the same microscopic level, provided that no direct interaction between their degrees of freedom exists. One of the first important results of the ACE algorithm was the justification of a central assumption used in this thesis: the flat electromagnetic environment responsible for cavity losses and radiative decay and the LA phonon environment couple indeed additively[163]. Thus, Equation (2.7) is an accurate description for lossy QD-cavity systems. At the moment, the applicability of ACE seems limitless: for the first time a large variety of open quantum systems with multiple bosonic, fermionic, or spin environments can be investigated, that range from infinite to negligible memory depths and from strong to weak system-environment correlations.

Finally, a recently proposed and already experimentally demonstrated coherent, but strongly off-resonant excitation scheme, cf., [FPub 5] and [FPub 7], respectively, has the potential of powering high-purity photon sources with superior photon count rates. In this so-called *Swing-UP of quantum EmitteR population* (SUPER) scheme, two red-detuned laser pulses are employed to excite the exciton state in QDs. This excitation scheme also relies on transitions between dressed states, cf., [FPub 9]. Because of its genuine off-resonant character with detunings of several milli-electronvolts, no post-processing is needed to separate emitted photons from the laser light. Thus, future studies might find that the SUPER scheme is superior in comparison to resonant or incoherent excitation schemes, in particular for single-photon sources. Because current investigations indicate that also a preparation of the biexciton state is possible, cf., [FPub 9], its use in preparation schemes for entangled photon pairs is also an interesting topic for future studies.

In summary, highly non-classical states of light in general, and entangled photon pairs in particular, are key to many novel quantum technologies and thus remain a fascinating and important research topic. This is also reflected in the Nobel Prize in Physics 2022 awarded to Alain Aspect, John F. Clauser, and Anton Zeilinger "for experiments with entangled photons, establishing the violation of Bell inequalities and pioneering quantum information science"[164].

Bibliography

[1] A. Orieux, M. A. M. Versteegh, K. D. Jöns, and S. Ducci, "Semiconductor devices for entangled photon pair generation: a review," *Rep. Prog. Phys.* **80**, 076001 (2017).

[2] L. Jacak, P. Hawrylak, and A. Wójs, *Quantum Dots* (Springer-Verlag, Berlin, 1998).

[3] I. N. Stranski and L. Krastanow, "Zur Theorie der orientierten Ausscheidung von Ionenkristallen aufeinander," *Monatsh. Chem.* **71**, 351 (1937).

[4] E. Bauer, "Phänomenologische Theorie der Kristallabscheidung an Oberflächen. I," *Z. Kristallogr. - Cryst. Mater.* **110**, 372 (1958).

[5] D. Gammon, E. S. Snow, B. V. Shanabrook, D. S. Katzer, and D. Park, "Fine Structure Splitting in the Optical Spectra of Single GaAs Quantum Dots," *Phys. Rev. Lett.* **76**, 3005 (1996).

[6] D. Huber, M. Reindl, J. Aberl, A. Rastelli, and R. Trotta, "Semiconductor quantum dots as an ideal source of polarization-entangled photon pairs on-demand: a review," *J. Opt.* **20**, 073002 (2018).

[7] O. Benson, C. Santori, M. Pelton, and Y. Yamamoto, "Regulated and Entangled Photons from a Single Quantum Dot," *Phys. Rev. Lett.* **84**, 2513 (2000).

[8] N. Akopian, N. H. Lindner, E. Poem, Y. Berlatzky, J. Avron, D. Gershoni, B. D. Gerardot, and P. M. Petroff, "Entangled Photon Pairs from Semiconductor Quantum Dots," *Phys. Rev. Lett.* **96**, 130501 (2006).

[9] R. J. Young, R. M. Stevenson, P. Atkinson, K. Cooper, D. A. Ritchie, and A. J. Shields, "Improved fidelity of triggered entangled photons from single quantum dots," *New J. Phys.* **8**, 29 (2006).

[10] C. Schimpf, M. Reindl, F. Basso Basset, K. D. Jöns, R. Trotta, and A. Rastelli, "Quantum dots as potential sources of strongly entangled photons: Perspectives and challenges for applications in quantum networks," *Appl. Phys. Lett.* **118**, 100502 (2021).

[11] M. Müller, S. Bounouar, K. D. Jöns, M. Glässl, and P. Michler, "On-demand generation of indistinguishable polarization-entangled photon pairs," *Nat. Photonics* **8**, 224 (2014).

[12] R. Winik, D. Cogan, Y. Don, I. Schwartz, L. Gantz, E. R. Schmidgall, N. Livneh, R. Rapaport, E. Buks, and D. Gershoni, "On-demand source of maximally entangled photon pairs using the biexciton-exciton radiative cascade," *Phys. Rev. B* **95**, 235435 (2017).

[13] L. Schweickert, K. D. Jöns, K. D. Zeuner, S. F. Covre da Silva, H. Huang, T. Lettner, M. Reindl, J. Zichi, R. Trotta, A. Rastelli, and V. Zwiller, "On-demand generation of background-free single photons from a solid-state source," *Appl. Phys. Lett.* **112**, 093106 (2018).

[14] C. Hopfmann, W. Nie, N. L. Sharma, C. Weigelt, F. Ding, and O. G. Schmidt, "Maximally entangled and gigahertz-clocked on-demand photon pair source," *Phys. Rev. B* **103**, 075413 (2021).

[15] K. Edamatsu, "Entangled photons: generation, observation, and characterization," *Jpn. J. Appl. Phys.* **46**, 7175 (2007).

[16] S. J. Freedman and J. F. Clauser, "Experimental Test of Local Hidden-Variable Theories," *Phys. Rev. Lett.* **28**, 938 (1972).

[17] J. Park, T. Jeong, H. Kim, and H. S. Moon, "Time-Energy Entangled Photon Pairs from Doppler-Broadened Atomic Ensemble via Collective Two-Photon Coherence," *Phys. Rev. Lett.* **121**, 263601 (2018).

[18] E. M. Purcell, "Spontaneous Emission Probabilities at Radio Frequencies," *Phys. Rev.* **69**, 681 (1946).

[19] A. Badolato, K. Hennessy, M. Atatüre, J. Dreiser, E. Hu, P. M. Petroff, and A. Imamoğlu, "Deterministic Coupling of Single Quantum Dots to Single Nanocavity Modes," *Science* **308**, 1158 (2005).

[20] A. Dousse, J. Suffczyński, A. Beveratos, O. Krebs, A. Lemaître, I. Sagnes, J. Bloch, P. Voisin, and P. Senellart, "Ultrabright source of entangled photon pairs," *Nature* **466**, 217 (2010).

[21] R. Hafenbrak, S. M. Ulrich, P. Michler, L. Wang, A. Rastelli, and O. G. Schmidt, "Triggered polarization-entangled photon pairs from a single quantum dot up to 30 K," *New J. Phys.* **9**, 315 (2007).

[22] Y. Ota, S. Iwamoto, N. Kumagai, and Y. Arakawa, "Spontaneous Two-Photon Emission from a Single Quantum Dot," *Phys. Rev. Lett.* **107**, 233602 (2011).

[23] S. Schumacher, J. Förstner, A. Zrenner, M. Florian, C. Gies, P. Gartner, and F. Jahnke, "Cavity-assisted emission of polarization-entangled photons from biexcitons in quantum dots with fine-structure splitting," *Opt. Express* **20**, 5335 (2012).

[24] E. del Valle, A. Gonzalez-Tudela, E. Cancellieri, F. P. Laussy, and C. Tejedor, "Generation of a two-photon state from a quantum dot in a microcavity," *New J. Phys.* **13**, 113014 (2011).

[25] E. del Valle, "Distilling one, two and entangled pairs of photons from a quantum dot with cavity QED effects and spectral filtering," *New J. Phys.* **15**, 025019 (2013).

[26] C. Sánchez Muñoz, F. P. Laussy, C. Tejedor, and E. del Valle, "Enhanced two-photon emission from a dressed biexciton," *New J. Phys.* **17**, 123021 (2015).

[27] D. Heinze, A. Zrenner, and S. Schumacher, "Polarization-entangled twin photons from two-photon quantum-dot emission," *Phys. Rev. B* **95**, 245306 (2017).

[28] E. Jaynes and F. Cummings, "Comparison of quantum and semiclassical radiation theories with application to the beam maser," *Proc. IEEE* **51**, 89 (1963).

[29] J. Larson and T. Mavrogordatos, *The Jaynes–Cummings Model and Its Descendants* (IOP Publishing, Bristol, 2021).

[30] G. Lindblad, "On the generators of quantum dynamical semigroups," *Commun. Math. Phys.* **48**, 119 (1976).

[31] H. Carmichael, *An Open Systems Approach to Quantum Optics* (Springer-Verlag, Berlin, 1993).

[32] L. Besombes, K. Kheng, L. Marsal, and H. Mariette, "Acoustic phonon broadening mechanism in single quantum dot emission," *Phys. Rev. B* **63**, 155307 (2001).

[33] B. Krummheuer, V. M. Axt, and T. Kuhn, "Theory of pure dephasing and the resulting absorption line shape in semiconductor quantum dots," *Phys. Rev. B* **65**, 195313 (2002).

[34] B. Krummheuer, V. M. Axt, T. Kuhn, I. D'Amico, and F. Rossi, "Pure dephasing and phonon dynamics in GaAs- and GaN-based quantum dot structures: Interplay between material parameters and geometry," *Phys. Rev. B* **71**, 235329 (2005).

[35] D. E. Reiter, T. Kuhn, and V. M. Axt, "Distinctive characteristics of carrier-phonon interactions in optically driven semiconductor quantum dots," *Adv. Phys.: X* **4**, 1655478 (2019).

[36] M. R. Klaßen and D. E. Reiter, "Optical Signals to Monitor the Dynamics of Phonon-Modified Rabi Oscillations in a Quantum Dot," *Ann. Phys. (Berlin)* **533**, 2100086 (2021).

[37] I. Wilson-Rae and A. Imamoğlu, "Quantum dot cavity-QED in the presence of strong electron-phonon interactions," *Phys. Rev. B* **65**, 235311 (2002).

[38] J. Förstner, C. Weber, J. Danckwerts, and A. Knorr, "Phonon-Assisted Damping of Rabi Oscillations in Semiconductor Quantum Dots," *Phys. Rev. Lett.* **91**, 127401 (2003).

[39] P. Machnikowski and L. Jacak, "Resonant nature of phonon-induced damping of Rabi oscillations in quantum dots," *Phys. Rev. B* **69**, 193302 (2004).

[40] A. Krügel, V. M. Axt, T. Kuhn, P. Machnikowski, and A. Vagov, "The role of acoustic phonons for Rabi oscillations in semiconductor quantum dots," *Appl. Phys. B* **81**, 897 (2005).

[41] A. Vagov, M. D. Croitoru, V. M. Axt, T. Kuhn, and F. M. Peeters, "Nonmonotonic Field Dependence of Damping and Reappearance of Rabi Oscillations in Quantum Dots," *Phys. Rev. Lett.* **98**, 227403 (2007).

[42] A. J. Ramsay, A. V. Gopal, E. M. Gauger, A. Nazir, B. W. Lovett, A. M. Fox, and M. S. Skolnick, "Damping of exciton Rabi rotations by acoustic phonons in optically excited InGaAs/GaAs quantum dots," *Phys. Rev. Lett.* **104**, 017402 (2010).

[43] P. Kaer, T. R. Nielsen, P. Lodahl, A.-P. Jauho, and J. Mørk, "Non-Markovian Model of Photon-Assisted Dephasing by Electron-Phonon Interactions in a Coupled Quantum-Dot-Cavity System," *Phys. Rev. Lett.* **104**, 157401 (2010).

[44] C. Roy and S. Hughes, "Polaron master equation theory of the quantum-dot Mollow triplet in a semiconductor cavity-QED system," *Phys. Rev. B* **85**, 115309 (2012).

[45] A. Vagov, M. Glässl, M. D. Croitoru, V. M. Axt, and T. Kuhn, "Competition between pure dephasing and photon losses in the dynamics of a dot-cavity system," *Phys. Rev. B* **90**, 075309 (2014).

[46] T. Jakubczyk, V. Delmonte, S. Fischbach, D. Wigger, D. E. Reiter, Q. Mermillod, P. Schnauber, A. Kaganskiy, J.-H. Schulze, A. Strittmatter, S. Rodt, W. Langbein, T. Kuhn, S. Reitzenstein, and J. Kasprzak, "Impact of Phonons on Dephasing of Individual Excitons in Deterministic Quantum Dot Microlenses," *ACS Photonics* **3**, 2461 (2016).

[47] D. P. S. McCutcheon, "Optical signatures of non-Markovian behavior in open quantum systems," *Phys. Rev. A* **93**, 022119 (2016).

[48] A. Vagov, V. M. Axt, and T. Kuhn, "Impact of pure dephasing on the nonlinear optical response of single quantum dots and dot ensembles," *Phys. Rev. B* **67**, 115338 (2003).

[49] A. Vagov, V. M. Axt, T. Kuhn, W. Langbein, P. Borri, and U. Woggon, "Nonmonotonous temperature dependence of the initial decoherence in quantum dots," *Phys. Rev. B* **70**, 201305(R) (2004).

[50] A. M. Barth, A. Vagov, and V. M. Axt, "Path-integral description of combined Hamiltonian and non-Hamiltonian dynamics in quantum dissipative systems," *Phys. Rev. B* **94**, 125439 (2016).

[51] A. M. Barth, S. Lüker, A. Vagov, D. E. Reiter, T. Kuhn, and V. M. Axt, "Fast and selective phonon-assisted state preparation of a quantum dot by adiabatic undressing," *Phys. Rev. B* **94**, 045306 (2016).

[52] S. Bounouar, M. Müller, A. M. Barth, M. Glässl, V. M. Axt, and P. Michler, "Phonon-assisted robust and deterministic two-photon biexciton preparation in a quantum dot," *Phys. Rev. B* **91**, 161302(R) (2015).

[53] T. Kaldewey, S. Lüker, A. V. Kuhlmann, S. R. Valentin, J.-M. Chauveau, A. Ludwig, A. D. Wieck, D. E. Reiter, T. Kuhn, and R. J. Warburton, "Demonstrating the decoupling regime of the electron-phonon interaction in a quantum dot using chirped optical excitation," *Phys. Rev. B* **95**, 241306(R) (2017).

[54] S. Lüker, T. Kuhn, and D. E. Reiter, "Phonon impact on optical control schemes of quantum dots: Role of quantum dot geometry and symmetry," *Phys. Rev. B* **96**, 245306 (2017).

[55] D. Wigger, S. Lüker, V. M. Axt, D. E. Reiter, and T. Kuhn, "Squeezed Phonon Wave Packet Generation by Optical Manipulation of a Quantum Dot," *Photonics* **2**, 214 (2015).

[56] S. Lüker, *Einfluss akustischer Phononen auf die optische Kontrolle von Halbleiter-Quantenpunkten*, Diploma thesis, University of Münster (2012).

[57] M. Cosacchi, *Semiconductor quantum-dot–cavity systems as sources of highly nonclassical states of light*, Dissertation, University of Bayreuth (2022).

[58] D. P. S. McCutcheon, N. S. Dattani, E. M. Gauger, B. W. Lovett, and A. Nazir, "A general approach to quantum dynamics using a variational master equation: Application to phonon-damped Rabi rotations in quantum dots," *Phys. Rev. B* **84**, 081305 (2011).

[59] C. Roy and S. Hughes, "Influence of Electron–Acoustic-Phonon Scattering on Intensity Power Broadening in a Coherently Driven Quantum-Dot–Cavity System," *Phys. Rev. X* **1**, 021009 (2011).

[60] D. P. S. McCutcheon and A. Nazir, "Quantum dot Rabi rotations beyond the weak exciton-phonon coupling regime," *New J. Phys.* **12**, 113042 (2010).

[61] N. Makri and D. E. Makarov, "Tensor propagator for iterative quantum time evolution of reduced density matrices. I. Theory," *J. Chem. Phys.* **102**, 4600 (1995).

[62] N. Makri and D. E. Makarov, "Tensor propagator for iterative quantum time evolution of reduced density matrices. II. Numerical methodology," *J. Chem. Phys.* **102**, 4611 (1995).

[63] A. Vagov, M. D. Croitoru, M. Glässl, V. M. Axt, and T. Kuhn, "Real-time path integrals for quantum dots: Quantum dissipative dynamics with superohmic environment coupling," *Phys. Rev. B* **83**, 094303 (2011).

[64] M. Cygorek, A. M. Barth, F. Ungar, A. Vagov, and V. M. Axt, "Nonlinear cavity feeding and unconventional photon statistics in solid-state cavity qed revealed by many-level real-time path-integral calculations," *Phys. Rev. B* **96**, 201201(R) (2017).

[65] D. F. V. James, P. G. Kwiat, W. J. Munro, and A. G. White, "Measurement of qubits," *Phys. Rev. A* **64**, 052312 (2001).

[66] R. Hanbury Brown and R. Q. Twiss, "LXXIV. A new type of interferometer for use in radio astronomy," *London, Edinburgh, Dublin Philos. Mag. J. Sci.* **45**, 663 (1954).

[67] R. Hanbury Brown and R. Q. Twiss, "Correlation between Photons in two Coherent Beams of Light," *Nature* **177**, 27 (1956).

[68] C. K. Hong, Z. Y. Ou, and L. Mandel, "Measurement of Subpicosecond Time Intervals between Two Photons by Interference," *Phys. Rev. Lett.* **59**, 2044 (1987).

[69] R. J. Glauber, *Quantum Theory of Optical Coherence* (Wiley-VCH, Weinheim, 2007).

[70] M. Cosacchi, M. Cygorek, F. Ungar, A. M. Barth, A. Vagov, and V. M. Axt, "Path-integral approach for nonequilibrium multitime correlation functions of open quantum systems coupled to Markovian and non-Markovian environments," *Phys. Rev. B* **98**, 125302 (2018).

[71] A. Einstein, B. Podolsky, and N. Rosen, "Can Quantum-Mechanical Description of Physical Reality Be Considered Complete?" *Phys. Rev.* **47**, 777 (1935).

[72] N. Gisin, G. Ribordy, W. Tittel, and H. Zbinden, "Quantum cryptography," *Rev. Mod. Phys.* **74**, 145 (2002).

[73] H.-K. Lo, M. Curty, and K. Tamaki, "Secure quantum key distribution," *Nat. Photonics* **8**, 595 (2014).

[74] C. Schimpf, M. Reindl, D. Huber, B. Lehner, S. F. Covre Da Silva, S. Manna, M. Vyvlecka, P. Walther, and A. Rastelli, "Quantum cryptography with highly entangled photons from semiconductor quantum dots," *Sci. Adv.* **7**, eabe8905 (2021).

[75] F. Basso Basset, M. Valeri, E. Roccia, V. Muredda, D. Poderini, J. Neuwirth, N. Spagnolo, M. B. Rota, G. Carvacho, F. Sciarrino, and R. Trotta, "Quantum key distribution with entangled photons generated on demand by a quantum dot," *Sci. Adv.* **7**, eabe6379 (2021).

[76] L.-M. Duan, M. D. Lukin, J. I. Cirac, and P. Zoller, "Long-distance quantum communication with atomic ensembles and linear optics," *Nature* **414**, 413 (2001).

[77] C. H. Bennett and D. P. DiVincenzo, "Quantum information and computation," *Nature* **404**, 247 (2000).

[78] J. Audretsch, ed., *Entangled World: The Fascination of Quantum Information and Computation* (Whiley-VCH, Weinheim, 2006).

[79] J.-W. Pan, Z.-B. Chen, C.-Y. Lu, H. Weinfurter, A. Zeilinger, and M. Żukowski, "Multiphoton entanglement and interferometry," *Rev. Mod. Phys.* **84**, 777 (2012).

[80] A. Zeilinger, "Light for the quantum. Entangled photons and their applications: a very personal perspective," *Phys. Scr.* **92**, 072501 (2017).

[81] J. S. Bell, "On the Einstein Podolsky Rosen paradox," *Physics* **1**, 195 (1964).

[82] J. F. Clauser, M. A. Horne, A. Shimony, and R. A. Holt, "Proposed Experiment to Test Local Hidden-Variable Theories," *Phys. Rev. Lett.* **23**, 880 (1969).

[83] C. Song, K. Xu, W. Liu, C.-p. Yang, S.-B. Zheng, H. Deng, Q. Xie, K. Huang, Q. Guo, L. Zhang, P. Zhang, D. Xu, D. Zheng, X. Zhu, H. Wang, Y.-A. Chen, C.-Y. Lu, S. Han, and J.-W. Pan, "10-Qubit Entanglement and Parallel Logic Operations with a Superconducting Circuit," *Phys. Rev. Lett.* **119**, 180511 (2017).

[84] N. Friis, O. Marty, C. Maier, C. Hempel, M. Holzäpfel, P. Jurcevic, M. B. Plenio, M. Huber, C. Roos, R. Blatt, and B. Lanyon, "Observation of Entangled States of a Fully Controlled 20-Qubit System," *Phys. Rev. X* **8**, 021012 (2018).

[85] D. P. DiVincenzo, "The Physical Implementation of Quantum Computation," *Fortschr. Phys.* **48**, 771 (2000).

[86] L. Olislager, E. Woodhead, K. Phan Huy, J.-M. Merolla, P. Emplit, and S. Massar, "Creating and manipulating entangled optical qubits in the frequency domain," *Phys. Rev. A* **89**, 052323 (2014).

[87] A. Mair, A. Vaziri, G. Weihs, and A. Zeilinger, "Entanglement of the orbital angular momentum states of photons," *Nature* **412**, 313 (2001).

[88] M. Barbieri, C. Cinelli, P. Mataloni, and F. De Martini, "Polarization-momentum hyper-entangled states: Realization and characterization," *Phys. Rev. A* **72**, 052110 (2005).

[89] J. Brendel, N. Gisin, W. Tittel, and H. Zbinden, "Pulsed Energy-Time Entangled Twin-Photon Source for Quantum Communication," *Phys. Rev. Lett.* **82**, 2594 (1999).

[90] H. Jayakumar, A. Predojević, T. Kauten, T. Huber, G. S. Solomon, and G. Weihs, "Time-bin entangled photons from a quantum dot," *Nat. Commun.* **5**, 4251 (2014).

[91] T. Huber, L. Ostermann, M. Prilmüller, G. S. Solomon, H. Ritsch, G. Weihs, and A. Predojević, "Coherence and degree of time-bin entanglement from quantum dots," *Phys. Rev. B* **93**, 201301(R) (2016).

[92] L. Ginés, C. Pepe, J. Gonzales, N. Gregersen, S. Höfling, C. Schneider, and A. Predojević, "Time-bin entangled photon pairs from quantum dots embedded in a self-aligned cavity," *Opt. Express* **29**, 4174 (2021).

[93] S. C. Kuhn, A. Knorr, S. Reitzenstein, and M. Richter, "Cavity assisted emission of single, paired and heralded photons from a single quantum dot device," *Opt. Express* **24**, 25446 (2016).

[94] C. H. Bennett, D. P. DiVincenzo, J. A. Smolin, and W. K. Wootters, "Mixed-state entanglement and quantum error correction," *Phys. Rev. A* **54**, 3824 (1996).

[95] W. K. Wootters, "Entanglement of Formation and Concurrence," *Quantum Inf. Comput.* **1**, 27 (2001).

[96] R. Jozsa, "Fidelity for Mixed Quantum States," *J. Mod. Opt.* **41**, 2315 (1994).

[97] G. Vidal and R. F. Werner, "Computable measure of entanglement," *Phys. Rev. A* **65**, 032314 (2002).

[98] A. Peres, "Separability Criterion for Density Matrices," *Phys. Rev. Lett.* **77**, 1413 (1996).

[99] M. Horodecki, P. Horodecki, and R. Horodecki, "Separability of mixed states: necessary and sufficient conditions," *Phys. Lett. A* **223**, 1 (1996).

[100] W. K. Wootters, "Entanglement of Formation of an Arbitrary State of Two Qubits," *Phys. Rev. Lett.* **80**, 2245 (1998).

[101] D. Huber, M. Reindl, Y. Huo, H. Huang, J. S. Wildmann, O. G. Schmidt, A. Rastelli, and R. Trotta, "Highly indistinguishable and strongly entangled photons from symmetric GaAs quantum dots," *Nat. Commun.* **8**, 15506 (2017).

[102] D. Huber, M. Reindl, S. F. Covre da Silva, C. Schimpf, J. Martín-Sánchez, H. Huang, G. Piredda, J. Edlinger, A. Rastelli, and R. Trotta, "Strain-Tunable GaAs Quantum Dot: A Nearly Dephasing-Free Source of Entangled Photon Pairs on Demand," *Phys. Rev. Lett.* **121**, 033902 (2018).

[103] H. Wang, H. Hu, T.-H. Chung, J. Qin, X. Yang, J.-P. Li, R.-Z. Liu, H.-S. Zhong, Y.-M. He, X. Ding, Y.-H. Deng, Q. Dai, Y.-H. Huo, S. Höfling, C.-Y. Lu, and J.-W. Pan, "On-Demand Semiconductor Source of Entangled Photons Which Simultaneously Has High Fidelity, Efficiency, and Indistinguishability," *Phys. Rev. Lett.* **122**, 113602 (2019).

[104] J. Liu, R. Su, Y. Wei, B. Yao, S. F. Covre da Silva, Y. Yu, J. Iles-Smith, K. Srinivasan, A. Rastelli, J. Li, and X. Wang, "A solid-state source of strongly entangled photon pairs with high brightness and indistinguishability," *Nat. Nanotechnol.* **14**, 586 (2019).

[105] M. Glässl, A. M. Barth, and V. M. Axt, "Proposed Robust and High-Fidelity Preparation of Excitons and Biexcitons in Semiconductor Quantum Dots Making Active Use of Phonons," *Phys. Rev. Lett.* **110**, 147401 (2013).

[106] P.-L. Ardelt, L. Hanschke, K. A. Fischer, K. Müller, A. Kleinkauf, M. Koller, A. Bechtold, T. Simmet, J. Wierzbowski, H. Riedl, G. Abstreiter, and J. J. Finley, "Dissipative preparation of the exciton and biexciton in self-assembled quantum dots on picosecond time scales," *Phys. Rev. B* **90**, 241404(R) (2014).

[107] M. Reindl, K. D. Jöns, D. Huber, C. Schimpf, Y. Huo, V. Zwiller, A. Rastelli, and R. Trotta, "Phonon-assisted two-photon interference from remote quantum emitters," *Nano Lett.* **17**, 4090 (2017).

[108] M. Glässl, A. M. Barth, K. Gawarecki, P. Machnikowski, M. D. Croitoru, S. Lüker, D. E. Reiter, T. Kuhn, and V. M. Axt, "Biexciton state preparation in a quantum dot via adiabatic rapid passage: Comparison between two control protocols and impact of phonon-induced dephasing," *Phys. Rev. B* **87**, 085303 (2013).

[109] A. Debnath, C. Meier, B. Chatel, and T. Amand, "High-fidelity biexciton generation in quantum dots by chirped laser pulses," *Phys. Rev. B* **88**, 201305(R) (2013).

[110] T. Kaldewey, S. Lüker, A. V. Kuhlmann, S. R. Valentin, A. Ludwig, A. D. Wieck, D. E. Reiter, T. Kuhn, and R. J. Warburton, "Coherent and robust high-fidelity generation of a biexciton in a quantum dot by rapid adiabatic passage," *Phys. Rev. B* **95**, 161302(R) (2017).

[111] A. Muller, W. Fang, J. Lawall, and G. S. Solomon, "Creating Polarization-Entangled Photon Pairs from a Semiconductor Quantum Dot Using the Optical Stark Effect," *Phys. Rev. Lett.* **103**, 217402 (2009).

[112] A. J. Bennett, M. A. Pooley, R. M. Stevenson, M. B. Ward, R. B. Patel, A. Boyer de la Giroday, N. Sköld, I. Farrer, C. A. Nicoll, D. A. Ritchie, and A. J. Shields, "Electric-field-induced coherent coupling of the exciton states in a single quantum dot," *Nat. Phys.* **6**, 947 (2010).

[113] R. M. Stevenson, R. J. Young, P. Atkinson, K. Cooper, D. A. Ritchie, and A. J. Shields, "A semiconductor source of triggered entangled photon pairs," *Nature* **439**, 179 (2006).

[114] S. Seidl, M. Kroner, A. Högele, K. Karrai, R. J. Warburton, A. Badolato, and P. M. Petroff, "Effect of uniaxial stress on excitons in a self-assembled quantum dot," *Appl. Phys. Lett.* **88**, 203113 (2006).

[115] R. M. Stevenson, R. J. Young, P. See, D. G. Gevaux, K. Cooper, P. Atkinson, I. Farrer, D. A. Ritchie, and A. J. Shields, "Magnetic-field-induced reduction of the exciton polarization splitting in InAs quantum dots," *Phys. Rev. B* **73**, 033306 (2006).

[116] J. Zhang, J. S. Wildmann, F. Ding, R. Trotta, Y. Huo, E. Zallo, D. Huber, A. Rastelli, and O. G. Schmidt, "High yield and ultrafast sources of electrically triggered entangled-photon pairs based on strain-tunable quantum dots," *Nat. Commun.* **6**, 10067 (2015).

[117] J. Förstner, C. Weber, J. Danckwerts, and A. Knorr, "Phonon-Assisted Damping of Rabi Oscillations in Semiconductor Quantum Dots," *Phys. Rev. Lett.* **91**, 127401 (2003).

[118] V. M. Axt, T. Kuhn, A. Vagov, and F. M. Peeters, "Phonon induced pure dephasing in exciton-biexciton quantum dot systems driven by ultrafast laser pulse sequences," *Phys. Rev. B* **72**, 125309 (2005).

[119] P. Machnikowski, "Theory of two-photon processes in quantum dots: Coherent evolution and phonon-induced dephasing," *Phys. Rev. B* **78**, 195320 (2008).

[120] C. Roy and S. Hughes, "Phonon-Dressed Mollow Triplet in the Regime of Cavity Quantum Electrodynamics: Excitation-Induced Dephasing and Nonperturbative Cavity Feeding Effects," *Phys. Rev. Lett.* **106**, 247403 (2011).

[121] T. Close, E. M. Gauger, and B. W. Lovett, "Overcoming phonon-induced dephasing for indistinguishable photon sources," *New J. Phys.* **14**, 113004 (2012).

[122] P. Kaer and J. Mørk, "Decoherence in semiconductor cavity QED systems due to phonon couplings," *Phys. Rev. B* **90**, 035312 (2014).

[123] D. E. Reiter, "Time-resolved pump-probe signals of a continuously driven quantum dot affected by phonons," *Phys. Rev. B* **95**, 125308 (2017).

[124] A. Reigue, J. Iles-Smith, F. Lux, L. Monniello, M. Bernard, F. Margaillan, A. Lemaitre, A. Martinez, D. P. S. McCutcheon, J. Mørk, R. Hostein, and V. Voliotis, "Probing Electron-Phonon Interaction through Two-Photon Interference in Resonantly Driven Semiconductor Quantum Dots," *Phys. Rev. Lett.* **118**, 233602 (2017).

[125] M. B. Harouni, "Phonon impacts on entangled photon pair generation from the biexciton cascade in a quantum dot: phonon coherent state representation," *Laser Phys.* **24**, 115202 (2014).

[126] M. E. Reimer, M. P. van Kouwen, A. W. Hidma, M. H. M. van Weert, E. P. A. M. Bakkers, L. P. Kouwenhoven, and V. Zwiller, "Electric Field Induced Removal of the Biexciton Binding Energy in a Single Quantum Dot," *Nano Lett.* **11**, 645 (2011).

[127] F. Ding, R. Singh, J. D. Plumhof, T. Zander, V. Křápek, Y. H. Chen, M. Benyoucef, V. Zwiller, K. Dörr, G. Bester, A. Rastelli, and O. G. Schmidt, "Tuning the Exciton Binding Energies in Single Self-Assembled InGaAs/GaAs Quantum Dots by Piezoelectric-Induced Biaxial Stress," *Phys. Rev. Lett.* **104**, 067405 (2010).

[128] R. Trotta, P. Atkinson, J. D. Plumhof, E. Zallo, R. O. Rezaev, S. Kumar, S. Baunack, J. R. Schröter, A. Rastelli, and O. G. Schmidt, "Nanomembrane Quantum-Light-Emitting Diodes Integrated onto Piezoelectric Actuators," *Adv. Mater.* **24**, 2668 (2012).

[129] R. Trotta, E. Zallo, E. Magerl, O. G. Schmidt, and A. Rastelli, "Independent control of exciton and biexciton energies in single quantum dots via electroelastic fields," *Phys. Rev. B* **88**, 155312 (2013).

[130] A. Carmele and A. Knorr, "Analytical solution of the quantum-state tomography of the biexciton cascade in semiconductor quantum dots: Pure dephasing does not affect entanglement," *Phys. Rev. B* **84**, 075328 (2011).

[131] F. Troiani, J. I. Perea, and C. Tejedor, "Cavity-assisted generation of entangled photon pairs by a quantum-dot cascade decay," *Phys. Rev. B* **74**, 235310 (2006).

[132] R. M. Stevenson, C. L. Salter, J. Nilsson, A. J. Bennett, M. B. Ward, I. Farrer, D. A. Ritchie, and A. J. Shields, "Indistinguishable Entangled Photons Generated by a Light-Emitting Diode," *Phys. Rev. Lett.* **108**, 040503 (2012).

[133] S. Bounouar, C. de la Haye, M. Strauß, P. Schnauber, A. Thoma, M. Gschrey, J.-H. Schulze, A. Strittmatter, S. Rodt, and S. Reitzenstein, "Generation of maximally entangled states and coherent control in quantum dot microlenses," *Appl. Phys. Lett.* **112**, 153107 (2018).

[134] A. Fognini, A. Ahmadi, M. Zeeshan, J. T. Fokkens, S. J. Gibson, N. Sherlekar, S. J. Daley, D. Dalacu, P. J. Poole, K. D. Jöns, V. Zwiller, and M. E. Reimer, "Dephasing Free Photon Entanglement with a Quantum Dot," *ACS Photonics* **6**, 1656 (2019).

[135] J. R. Schrieffer and P. A. Wolff, "Relation between the Anderson and Kondo Hamiltonians," *Phys. Rev.* **149**, 491 (1966).

[136] R. Winkler, *Spin-Orbit Coupling Effects in Two-Dimensional Electron and Hole Systems*, Springer Tracts in Modern Physics, Vol. 191 (Springer, Berlin, 2003).

[137] S. Bravyi, D. P. DiVincenzo, and D. Loss, "Schrieffer–Wolff transformation for quantum many-body systems," *Ann. Phys. (N. Y.)* **326**, 2793 (2011).

[138] C. Sánchez Muñoz, E. del Valle, A. González Tudela, K. Müller, S. Lichtmannecker, M. Kaniber, C. Tejedor, J. J. Finley, and F. P. Laussy, "Emitters of N-photon bundles," *Nat. Photonics* **8**, 550 (2014).

[139] Q. Bin, Y. Wu, and X.-Y. Lü, "Parity-Symmetry-Protected Multiphoton Bundle Emission," *Phys. Rev. Lett.* **127**, 073602 (2021).

[140] C. Sánchez Muñoz, F. P. Laussy, E. del Valle, C. Tejedor, and A. González-Tudela, "Filtering multiphoton emission from state-of-the-art cavity quantum electrodynamics," *Optica* **5**, 14 (2018).

[141] G. Diaz-Camacho, E. Zubizarreta Casalengua, J. C. López Carreño, S. Khalid, C. Tejedor, E. del Valle, and F. P. Laussy, "Multiphoton Emission," arXiv:2109.12049 [quant-ph] (2021).

[142] J. C. López Carreño, E. del Valle, and F. P. Laussy, "Frequency-resolved Monte Carlo," *Sci. Rep.* **8**, 6975 (2018).

[143] W. Denk, J. H. Strickler, and W. W. Webb, "Two-Photon Laser Scanning Fluorescence Microscopy," *Science* **248**, 73 (1990).

[144] N. G. Horton, K. Wang, D. Kobat, C. G. Clark, F. W. Wise, C. B. Schaffer, and C. Xu, "In vivo three-photon microscopy of subcortical structures within an intact mouse brain," *Nat. Photonics* **7**, 205 (2013).

[145] C. J. Rowlands, D. Park, O. T. Bruns, K. D. Piatkevich, D. Fukumura, R. K. Jain, M. G. Bawendi, E. S. Boyden, and P. T. So, "Wide-field three-photon excitation in biological samples," *Light Sci. Appl.* **6**, e16255 (2017).

[146] D. G. Ouzounov, T. Wang, M. Wang, D. D. Feng, N. G. Horton, J. C. Cruz-Hernández, Y.-T. Cheng, J. Reimer, A. S. Tolias, N. Nishimura, and C. Xu, "In vivo three-photon imaging of activity of GCaMP6-labeled neurons deep in intact mouse brain," *Nat. Methods* **14**, 388 (2017).

[147] A. Escobet-Montalbán, F. M. Gasparoli, J. Nylk, P. Liu, Z. Yang, and K. Dholakia, "Three-photon light-sheet fluorescence microscopy," *Opt. Lett.* **43**, 5484 (2018).

[148] S.-l. Ma, X.-k. Li, Y.-l. Ren, J.-k. Xie, and F.-l. Li, "Antibunched N-photon bundles emitted by a Josephson photonic device," *Phys. Rev. Res.* **3**, 043020 (2021).

[149] M. Schmidt, M. von Helversen, M. López, F. Gericke, E. Schlottmann, T. Heindel, S. Kück, S. Reitzenstein, and J. Beyer, "Photon-Number-Resolving Transition-Edge Sensors for the Metrology of Quantum Light Sources," *J. Low Temp. Phys.* **193**, 1243 (2018).

[150] E. Schlottmann, M. von Helversen, H. A. Leymann, T. Lettau, F. Krüger, M. Schmidt, C. Schneider, M. Kamp, S. Höfling, J. Beyer, J. Wiersig, and S. Reitzenstein, "Exploring the Photon-Number Distribution of Bimodal Microlasers with a Transition Edge Sensor," *Phys. Rev. Appl.* **9**, 064030 (2018).

[151] M. Schmidt, I. H. Grothe, S. Neumeier, L. Bremer, M. von Helversen, W. Zent, B. Melcher, J. Beyer, C. Schneider, S. Höfling, J. Wiersig, and S. Reitzenstein, "Bimodal behavior of microlasers investigated with a two-channel photon-number-resolving transition-edge sensor system," *Phys. Rev. Res.* **3**, 013263 (2021).

[152] L. Mandel, "Sub-Poissonian photon statistics in resonance fluorescence," *Opt. Lett.* **4**, 205 (1979).

[153] W. Vogel and D.-G. Welsch, *Quantum Optics* (Wiley-VCH, Weinheim, 2006).

[154] P. Senellart, G. Solomon, and A. White, "High-performance semiconductor quantum-dot single-photon sources," *Nat. Nanotechnol.* **12**, 1026 (2017).

[155] H. P. Breuer and F. Petruccione, *The Theory of Open Quantum Systems*, 1st ed. (Oxford University Press, Oxford, 2002).

[156] R. Manson, K. Roy-Choudhury, and S. Hughes, "Polaron master equation theory of pulse-driven phonon-assisted population inversion and single-photon emission from quantum-dot excitons," *Phys. Rev. B* **93**, 155423 (2016).

[157] J. Iles-Smith, D. P. S. McCutcheon, A. Nazir, and J. Mørk, "Phonon scattering inhibits simultaneous near-unity efficiency and indistinguishability in semiconductor single-photon sources," *Nat. Photonics* **11**, 521 (2017).

[158] C. Gustin and S. Hughes, "Pulsed excitation dynamics in quantum-dot–cavity systems: Limits to optimizing the fidelity of on-demand single-photon sources," *Phys. Rev. B* **98**, 045309 (2018).

[159] S. Thomas and P. Senellart, "The race for the ideal single-photon source is on," *Nat. Nanotechnol.* **16**, 367 (2021).

[160] S. H. Autler and C. H. Townes, "Stark Effect in Rapidly Varying Fields," *Phys. Rev.* **100**, 703 (1955).

[161] W. Pacuski, T. Jakubczyk, C. Kruse, J. Kobak, T. Kazimierczuk, M. Goryca, A. Golnik, P. Kossacki, M. Wiater, P. Wojnar, G. Karczewski, T. Wojtowicz, and D. Hommel, "Micropillar Cavity Containing a CdTe Quantum Dot with a Single Manganese Ion," *Cryst. Growth Des.* **14**, 988 (2014).

[162] L. Hanschke, K. A. Fischer, S. Appel, D. Lukin, J. Wierzbowski, S. Sun, R. Trivedi, J. Vucković, J. J. Finley, and K. Müller, "Quantum dot single-photon sources with ultra-low multi-photon probability," *npj Quantum Inf.* **4**, 43 (2018).

[163] M. Cygorek, M. Cosacchi, A. Vagov, V. M. Axt, B. W. Lovett, J. Keeling, and E. M. Gauger, "Simulation of open quantum systems by automated compression of arbitrary environments," *Nat. Phys.* **18**, 662 (2022).

[164] "The Nobel Prize in Physics 2022," NobelPrize.org. Nobel Prize Outreach AB 2022. (2022), URL: https://www.nobelprize.org/prizes/physics/2022/summary/. Accessed: Sat 8 Oct 2022.

Acknowledgments

First of all, I thank my doctoral adviser, Vollrath Martin Axt, for his guidance, patience, and support during all these years that I had the privilege to be part of his group, starting with my Bachelor's thesis all the way to my dissertation. The way he taught and lived physics was always inspiring, and I learned a lot from him about conducting physical research and the scientific background of any topic that came up during our discussions in the weekly group meetings. I am going to miss these refreshing meetings and the fantastic, supportive, and cooperative atmosphere that he managed to establish in his group. By granting me independence and the time I needed to conduct thorough research, he strengthened my trust in my own skills and fostered my growth as a scientist.

Next, I would like to thank Georg Herink and Pablo Tamborenea for their time and effort to review this thesis, as well as Stephan Kümmel and Markus Lippitz for agreeing to serve on my examination commission.

A warm thank-you goes to Monika Birkelbach, Christina Wunderlich, and Susanne Süss for their valuable support in all administrative matters. Furthermore, I thank Markus Hilt for his always prompt and professional help with any larger or smaller problem concerning our IT infrastructure or machines, especially during the home-office period due to the pandemic.

A scientific network is an important building block for fruitful and enjoyable scientific work. Therefore, I thank all my collaborators in general, and Moritz Cygorek, Thomas Bracht, Armando Rastelli, and Barbara Lehner in particular, for our fun and interesting discussions on physics and other topics. A very special thanks in this regard goes to Doris Reiter, who also co-supervised most of my scientific work, and taught me how to highlight the import aspects of my publications and to improve their presentation. Her distinct fingerprints can be found in all of our joined publications.

During my time in the group of Martin Axt, I really enjoyed the wonderful and supportive atmosphere. Thus, I thank all past and present members of the chair for Theoretical Physics III - Quantum Theory of Condensed Matter, especially Alexei Vagov, Andreas Barth, and Moritz Cygorek for their seminal work on the path-integral method and implementation that my studies were built upon.

An especially heartfelt thank-you goes to my esteemed colleague and doctoral brother Michael Cosacchi. By combining our skills and talents, we filled the DFG project with live and led it to

Publications

List of publications as referred to in this thesis

[Pub 1] **T. Seidelmann**, F. Ungar, M. Cygorek, A. Vagov, A. M. Barth, T. Kuhn, and V. M. Axt.
"From strong to weak temperature dependence of the two-photon entanglement resulting from the biexciton cascade inside a cavity"
Phys. Rev. B **99**, 245301 (2019).

[Pub 2] **T. Seidelmann**, F. Ungar, A. M. Barth, A. Vagov, V. M. Axt, M. Cygorek, and T. Kuhn.
"Phonon-Induced Enhancement of Photon Entanglement in Quantum Dot-Cavity Systems"
Phys. Rev. Lett. **123**, 137401 (2019).

[Pub 3] M. Cosacchi, **T. Seidelmann**, F. Ungar, M. Cygorek, A. Vagov, and V. M. Axt.
"Transiently changing shape of the photon number distribution in a quantum-dot–cavity system driven by chirped laser pulses"
Phys. Rev. B **101**, 205304 (2020).

[Pub 4] **T. Seidelmann**, M. Cosacchi, M. Cygorek, D. E. Reiter, A. Vagov, and V. M. Axt.
"Different Types of Photon Entanglement from a Constantly Driven Quantum Emitter Inside a Cavity"
Adv. Quantum Technol. **4**, 2000108 (2021).
& Correction: *Adv. Quantum Technol.* **5**, 2200058 (2022).

[Pub 5] **T. Seidelmann**, D. E. Reiter, M. Cosacchi, M. Cygorek, A. Vagov, and V. M. Axt.
"Time-dependent switching of the photon entanglement type using a driven quantum emitter-cavity system"
Appl. Phys. Lett. **118**, 164001 (2021).

[Pub 6] M. Cosacchi, **T. Seidelmann**, M. Cygorek, A. Vagov, D. E. Reiter, and V. M. Axt.
"Accuracy of the Quantum Regression Theorem for Photon Emission from a Quantum Dot"
Phys. Rev. Lett. **127**, 100402 (2021).
& Erratum: *Phys. Rev. Lett.* **128**, 079901(E) (2022).

[Pub 7] M. Cosacchi, A. Mielnik-Pyszczorski, **T. Seidelmann**, M. Cygorek, A. Vagov, D. E. Reiter, and V. M. Axt.
"*N*-photon bundle statistics on different solid-state platforms"
Phys. Rev. B **106**, 115304 (2022).

[Pub 8] M. Cosacchi, **T. Seidelmann**, A. Mielnik-Pyszczorski, M. Neumann, T. K. Bracht, M. Cygorek, A. Vagov, D. E. Reiter, and V. M. Axt.
"Deterministic Photon Storage and Readout in a Semimagnetic Quantum Dot-Cavity System Doped with a Single Mn Ion"
Adv. Quantum Technol. **5**, 2100131 (2022).

[Pub 9] **T. Seidelmann**, C. Schimpf, T. K. Bracht, M. Cosacchi, A. Vagov, A. Rastelli, D. E. Reiter, and V. M. Axt.
"Two-Photon Excitation Sets Fundamental Limit to Entangled Photon Pair Generation from Quantum Emitters"
arXiv:2205.03390v1 [quant-ph] (2022), accepted at *Phys. Rev. Lett.*
Note: As of the publication of this thesis, a revised version of this article, entitled "Two-Photon Excitation Sets Limit to Entangled Photon Pair Generation from Quantum Emitters", is published as
Phys. Rev. Lett. **129**, 193604 (2022).

[Pub 10] **T. Seidelmann**, M. Cosacchi, M. Cygorek, D. E. Reiter, A. Vagov, and V. M. Axt.
"Phonon-induced transition between entangled and nonentangled phases in constantly driven quantum dot-cavity systems"
arXiv:2205.04389v1 [cond-mat.mes-hall] (2022), under consideration at *Phys. Rev. B.*
Note: As of the publication of this thesis, a revised version of this article, entitled "Phonon-induced transition between entangled and nonentangled photon emission in constantly driven quantum-dot–cavity systems", is published as
Phys. Rev. B **107**, 075301 (2023).

Further publications contributed to by the author

[FPub 1] M. Cygorek, F. Ungar, **T. Seidelmann**, A. M. Barth, A. Vagov, V. M. Axt, and T. Kuhn.
"Comparison of different concurrences characterizing photon pairs generated in the biexciton cascade in quantum dots coupled to microcavities"
Phys. Rev. B **98**, 045303 (2018).

[FPub 2] M. Cosacchi, J. Wiercinski, **T. Seidelmann**, M. Cygorek, A. Vagov, D. E. Reiter, and V. M. Axt
"On-demand generation of higher-order Fock states in quantum-dot–cavity systems"
Phys. Rev. Res. **2**, 033489 (2020).

[FPub 3] M. Cosacchi, **T. Seidelmann**, J. Wiercinski, M. Cygorek, A. Vagov, D. E. Reiter, and V. M. Axt
"Schrödinger cat states in quantum-dot-cavity systems"
Phys. Rev. Res. **3**, 023088 (2021).

[FPub 4] M. Neumann, F. Kappe, T. K. Bracht, M. Cosacchi, **T. Seidelmann**, V. M. Axt, G. Weihs, and D. E. Reiter
"Optical Stark shift to control the dark exciton occupation of a quantum dot in a tilted magnetic field"
Phys. Rev. B **104**, 075428 (2021).

[FPub 5] T. K. Bracht, M. Cosacchi, **T. Seidelmann**, M. Cygorek, A. Vagov, V. M. Axt, T. Heindel, and D. E. Reiter
"Swing-Up of Quantum Emitter Population Using Detuned Pulses"
PRX Quantum **2**, 040354 (2021). *Editors' Suggestion*

[FPub 6] T. K. Bracht, **T. Seidelmann**, T. Kuhn, V. M. Axt, and D. E. Reiter
"Phonon Wave Packet Emission during State Preparation of a Semiconductor Quantum Dot using Different Schemes"
Phys. Status Solidi B **259**, 2100649 (2022).

[FPub 7] Y. Karli, F. Kappe, V. Remesh, T. K. Bracht, J. Münzberg, S. Covre da Silva, **T. Seidelmann**, V. M. Axt, A. Rastelli, D. E. Reiter, and G. Weihs
"SUPER Scheme in Action: Experimental Demonstration of Red-Detuned Excitation of a Quantum Emitter"
Nano Lett. **22**, 6567 (2022).

[FPub 8] M. Bozzio, M. Vyvlecka, M. Cosacchi, C. Nawrath, **T. Seidelmann**, J. C. Loredo, S. L. Portalupi, V. M. Axt, P. Michler, and P. Walther

"Enhancing quantum cryptography with quantum dot single-photon sources"
npj Quantum Inf. **8**, 104 (2022).

[FPub 9] T. K. Bracht, **T. Seidelmann**, Y. Karli, F. Kappe, V. Remesh, G. Weihs, V. M. Axt, and D. E. Reiter
"Dressed-state analysis of the Swing-UP of quantum EmitteR population (SUPER) excitation"
No preprint available, under review at *Phys. Rev. B*.
Note: As of the publication of this thesis, a revised version of this article, entitled "Dressed-state analysis of two-color excitation schemes", is published as
Phys. Rev. B **107**, 035425 (2023).

[FPub 10] F. Kappe, Y. Karli, T. K. Bracht, S. Covre da Silva, **T. Seidelmann**, V. M. Axt, A. Rastelli, G. Weihs, D. E. Reiter, and V. Remesh
"Collective Excitation of Spatio-Spectrally Distinct Quantum Dots Enabled by Chirped Pulses"
arXiv:2209.08972 [quant-ph] (2022), under review at *Optica*.
Note: As of the publication of this thesis, a revised version of this article is accepted at *Mater. Quantum Technol.*

Note: As of the publication of this thesis, two further publications are submitted or published:

[FPub 11] B. U. Lehner, **T. Seidelmann**, G. Undeutsch, C. Schimpf, S. Manna, M. Gawełczyk, S. F. Covre da Silva, X. Yuan, S. Stroj, D. E. Reiter, V. M. Axt, and A. Rastelli
"Beyond the Four-Level Model: Dark and Hot States in Quantum Dots Degrade Photonic Entanglement"
Nano Lett. **23**, 1409 (2023).

[FPub 12] **T. Seidelmann**, T. K. Bracht, B. U. Lehner, C. Schimpf, M. Cosacchi, M. Cygorek, A. Vagov, A. Rastelli, D. E. Reiter, and V. M. Axt
"Two-photon excitation with finite pulses unlocks pure dephasing-induced degradation of entangled photons emitted by quantum dots"
arXiv:2301.10820 [cond-mat.mes-hall] (2023), under review at *Phys. Rev. B*.

Conference and seminar contributions

Parts of this work and/or other research were presented by the author during his time as a doctoral candidate at the following conferences:

- OPON 2020, Warsaw, Poland (2020) - Poster presentation

- NOEKS 15, Münster, Germany (2020) - Poster presentation
  [online format due to the COVID-19 pandemic]

- PLMCN 2020, Clermont-Ferrand, France (2020) - Poster presentation
  [online format due to the COVID-19 pandemic]

- CQIQC-IX, Toronto, Canada (2022) - Poster presentation

In addition, the author has given several oral presentations in regularly scheduled meetings of the D-A-CH Joint Project "Advanced Entanglement from Quantum Dots (AEQuDot)" organized by Gregor Weihs [University of Innsbruck, Austria], Doris E. Reiter [first University of Münster, later TU Dortmund, Germany], and Armando Rastelli [University of Linz, Austria]. Due to the COVID-19 pandemic all meetings and discussions were held in an online format, the only exception being one presence meeting in St. Johann (Tirol) on July 20th and 21st 2022. Furthermore, in May 2022, the author was invited by Armando Rastelli to visit Linz and take part in discussions regarding joint work.

Publication 1

"From strong to weak temperature dependence of the two-photon
entanglement resulting from the biexciton cascade inside a cavity"

T. Seidelmann, F. Ungar, M. Cygorek, A. Vagov, A. M. Barth, T. Kuhn,
and V. M. Axt.

Phys. Rev. B **99**, 245301 (2019).

Author contributions

The author has designed the concept of this study, has performed the numerical data generation and analysis, and has implemented the problem-specific C++ code. He has provided interpretations of the results and has written the first draft of the publication. During the publication process, he has organized the submission and revision of the manuscript and has written the answer to the referees.

F. Ungar has participated in the discussion of the results and their interpretations. He has also contributed to the optimization of the presentation, revisions of the draft, and the answers to the referees. In particular, he has rewritten and shortened parts of the first draft provided by the author.

M. Cygorek, A. Vagov, and T. Kuhn have co-supervised this work. In particular, they have participated in the discussion of the results and their interpretations. They have also contributed to the optimization of the presentation, revisions of the draft, and the answers to the referees. Furthermore, M. Cygorek suggested the ratio r to quantify the competition between one-photon and two-photon processes.

A. M. Barth has written the original C++ implementations of the path-integral method, which the numerical studies are based on.

V. M. Axt has advised the author throughout his work as the main supervisor, has obtained the funding for this work, and has provided the practical means. He has participated in the discussion of the results and their interpretations. He has also contributed to the optimization of the presentation, revisions of the draft, and the answers to the referees.

From strong to weak temperature dependence of the two-photon entanglement resulting from the biexciton cascade inside a cavity

T. Seidelmann,[1] F. Ungar,[1] M. Cygorek,[2] A. Vagov,[1,3] A. M. Barth,[1] T. Kuhn,[4] and V. M. Axt[1]

[1]*Lehrstuhl für Theoretische Physik III, Universität Bayreuth, 95440 Bayreuth, Germany*
[2]*Department of Physics, University of Ottawa, Ottawa, Ontario, Canada K1N 6N5*
[3]*ITMO University, St. Petersburg, 197101, Russia*
[4]*Institut für Festkörpertheorie, Universität Münster, 48149 Münster, Germany*

We investigate the degree of entanglement quantified by the concurrence of photon pairs that are simultaneously emitted in the biexciton-exciton cascade from a quantum dot in a cavity. Four dot-cavity configurations are compared that differ with respect to the detuning between the cavity modes and the quantum dot transitions, corresponding to different relative weights of direct two-photon and sequential single-photon processes. The dependence of the entanglement on the exciton fine-structure splitting δ is found to be significantly different for each of the four configurations. For a finite splitting and low temperatures, the highest entanglement is found when the cavity modes are in resonance with the two-photon transition between the biexciton and the ground state and, in addition, the biexciton has a finite binding energy of a few meV. However, this widely used configuration is rather strongly affected by phonons such that other dot-cavity configurations, that are commonly regarded as less suited for obtaining high degrees of entanglement, become more favorable already at temperatures on the order of 10 K and above. If the cavity modes are kept in resonance with one of the exciton-to-ground-state transitions and the biexciton binding energy is finite, the entanglement drastically drops for positive δ with rising temperatures when T is below $\simeq 4$ K, but is virtually independent of the temperature for higher T.

I. INTRODUCTION

Entangled photon pairs can be used as the fundamental building blocks for a wide range of applications in quantum communications, quantum cryptography, or quantum computation [1–3]. Furthermore, entanglement can be used to test fundamentals of quantum mechanics, e.g., by revealing violations of Bell's inequality [1,4]. Different devices and protocols for the generation of entangled photon pairs have been proposed. A well-established and especially attractive way of producing (polarization) entangled photon pairs is the emission of photon pairs via the biexciton cascade in semiconductor quantum dots (QDs) inside a microcavity which enhances the light collection efficiency [5–12]. One special advantage of using semiconductor quantum dots is the possibility to generate triggered [5–7] or even on-demand [10,11,13] entangled photon pairs which is of utmost importance for applications.

Entanglement generation from the biexciton cascade is possible since the biexciton can decay via two paths, first into one of the two exciton states and a photon which can be either polarized horizontally (H) or vertically (V). Subsequently, the exciton generated in the first step can further decay to the QD ground state by emitting a second photon with the same polarization as the photon generated in the biexciton decay. Ideally, the two paths are fully symmetric and the corresponding quantum state is a coherent superposition of the respective amplitudes, resulting in a maximally entangled two-photon state. However, when which-path information is introduced by disturbing the symmetry, e.g., by a finite

fine-structure splitting between the intermediate exciton states, the superposition becomes asymmetric and the entanglement decreases. In principle, it is possible to come close to maximal entanglement in current experiments, either by selecting QDs which naturally have a sufficiently small fine-structure splitting [7,10], by tuning the splitting with external fields [5,6,14], or by applying strain [15]. However, these requirements are rather restrictive. Therefore, it has been proposed to look for less demanding conditions which still allow for a high degree of entanglement. A prominent proposal of this type considers QDs with a sizable biexciton binding energy which are embedded in a microcavity. Besides the possibility of an increased light extraction efficiency, a microcavity offers the advantage that the resonance between the cavity modes and electronic transitions in the dot can be used to enhance, e.g., direct two-photon transitions between the biexciton and the ground state compared to sequential transitions from the biexciton to the exciton or from the exciton to the ground state. Since the direct two-photon transitions do not involve the occupation of exciton states, the fine-structure splitting is effectively not probed, leading to drastically reduced which-path information and therefore increased entanglement [16,17]. When the cavity mode is tuned to the two-photon resonance, a finite biexciton binding energy is typically favorable for entanglement since it shifts the sequential single-photon transitions further away from resonance.

In order to systematically compare different configurations of cavity and QD transition frequencies, a measure for the entanglement is required. A widely accepted measure is the

concurrence, which has a one-to-one correspondence to the entanglement of formation [18]. The latter represents the amount of pure-state entanglement that is at least present in a mixed state described by a given density matrix. The concurrence has the advantage that it can be directly calculated from the values of the reduced density matrix of the bipartite system for which the entanglement is to be measured [19]. Here, we focus on the concurrence of simultaneously emitted photon pairs which, albeit yielding lower signals due to filtering only photons with equal emission times from the cavity, typically show the highest degree of entanglement in experiments [20,21], as well as theoretical calculations [17,22].

Phonons are known to have a tremendous impact on the dynamics of QDs in general [23–33] and on QD-cavity systems in particular [34–43]. Since the pure dephasing induced by acoustic phonons is a major source of decoherence in QDs [24–26], phonons might also limit the entanglement of the two-photon states generated in the biexciton cascade. However, in many studies of the entanglement phonons have either been completely disregarded [13,17] or accounted for by a phenomenological pure dephasing rate [16,44,45]. The description based on rates ignores that phonon-induced pure dephasing leads only to a partial loss of coherence which is nonexponential [46,47] and is the origin of many other non-Markovian effects [37,48,49]. Furthermore, with phenomenological rates the temperature dependence of the degree of entanglement cannot be predicted. An explicit treatment of the phonon impact on the concurrence in the biexciton cascade has been presented in Ref. [50]. However, that paper concentrates on the contributions from the sequential decay of the biexciton via intermediate excitons and misses the competition with the direct two-photon decay to the ground state, which is at the heart of the protocol based on resonant two-photon transitions in systems with finite biexciton binding energies proposed in Ref. [16]. The effect of phonons on the concurrence in the case where two-photon transitions dominate the biexciton decay has been analyzed in Ref. [51] where, however, no selection of simultaneously emitted photon pairs has been considered. As mentioned above, the latter is more favorable for obtaining a high degree of photon entanglement.

In this paper, we investigate the phonon impact on the degree of two-photon polarization entanglement obtained after the decay of a biexciton in a cavity as measured by the concurrence of simultaneously emitted photon pairs. We present a comprehensive comparison of representative configurations of cavity and QD transition frequencies referring to physical situations with different relative importance of two-photon and sequential single-photon pathways, respectively. We find that the phonon influence in combination with the competition between two-photon and one-photon processes leads to strikingly different dependences on the exciton splitting as well as strongly different temperature dependences.

Tuning the cavity to the two-photon resonance and considering a quantum dot with a biexciton binding energy of a few meV is likely to be the most widely studied configuration in the literature because it is commonly expected to yield the highest two-photon entanglement at finite fine-structure splitting. Indeed at low temperatures we confirm this expectation. The main result of the present paper is, however, that the

distinction of the two-photon resonant configuration with finite biexciton binding energy to yield the highest concurrence is lost typically already at temperatures as low as ~ 10 K.

The article is structured as follows. In Sec. II we specify the model and the method used. We discuss the concurrence of simultaneously emitted photon pairs as the measure of choice when high degrees of entanglement are targeted and explain how this quantity is extracted from the numerical calculations. In Sec. III four configurations with different resonance settings and biexciton binding energies are introduced which enable us to analyze most clearly the competition between direct two-photon and sequential single-photon processes and its impact on the degree of entanglement. In Sec. IV we demonstrate that the phonon impact strongly depends on the considered configuration, resulting in substantially different dependences on the fine-structure splitting and the temperature. Deviations from the standard bell shape dependence on the splitting or asymmetries reflect the competition between single- and two-photon processes. Finally, in the Conclusion, Sec. V, we present a brief summary of the main results of this article.

II. THEORETICAL APPROACH

A. Model

We consider a semiconductor QD embedded in a microcavity which is initially prepared in the biexciton state. The dynamics of the statistical operator of the system $\hat{\rho}$ is determined by the Liouville–von Neumann equation

$$\frac{d}{dt}\hat{\rho} = -\frac{i}{\hbar}[\hat{H}, \hat{\rho}] + \mathcal{L}[\hat{\rho}], \tag{1}$$

where [,] denotes the commutator. The Hamiltonian

$$\hat{H} = \hat{H}_{\text{QD-cav}} + \hat{H}_{\text{QD-phon}} \tag{2}$$

takes into account the interaction between the QD and two linearly polarized cavity modes ($\hat{H}_{\text{QD-cav}}$) as well as a pure dephasing type coupling to a continuum of longitudinal acoustic (LA) phonons ($\hat{H}_{\text{QD-phon}}$). The Lindblad operator $\mathcal{L}[\hat{\rho}]$ allows the inclusion of non-Hamiltonian dynamics, i.e., cavity losses due to for example imperfect mirrors. Thus the model contains three parts, which are discussed separately in the following.

The first part describes the coupling between the QD and two linearly polarized cavity modes and is modeled by the Hamiltonian [51]

$$\hat{H}_{\text{QD-cav}} = \hbar\omega_H |X_H\rangle\langle X_H| + \hbar\omega_V |X_V\rangle\langle X_V|$$
$$+ \hbar(2\bar{\omega}_X - \omega_B)|B\rangle\langle B| + \sum_{\ell=H,V} \hbar\omega_\ell^c \hat{a}_\ell^\dagger \hat{a}_\ell + \hat{\mathcal{X}}, \tag{3}$$

where the interaction part is given by

$$\hat{\mathcal{X}} = -g(|G\rangle\langle X_H|\hat{a}_H^\dagger + |X_H\rangle\langle B|\hat{a}_H^\dagger$$
$$+ |G\rangle\langle X_V|\hat{a}_V^\dagger - |X_V\rangle\langle B|\hat{a}_V^\dagger) + \text{H.c.} \tag{4}$$

Here, the four states of the QD are represented by the biexciton state $|B\rangle$, the two possible exciton states $|X_H\rangle$ and $|X_V\rangle$, and the ground state $|G\rangle$. The exciton states as well as the two photon modes are labeled with H (horizontal

polarization) and V (vertical polarization). The bosonic operator $\hat{a}_{H/V}^{\dagger}$ creates one photon with frequency $\omega_{H/V}^c$ and corresponding polarization H or V and H.c. denotes the Hermitian conjugate. The light-matter coupling strength g is assumed to be equal for all couplings and the dipole approximation as well as the rotating-wave approximation are used. The energies $\hbar\omega_{H/V}$ denote the exciton energies, while the energy of the biexciton is $\hbar(2\bar{\omega}_X - \omega_B)$, where $E_B = \hbar\omega_B$ represents the biexciton binding energy and $\hbar\bar{\omega}_X = \hbar(\omega_H + \omega_V)/2$ is the mean exciton energy. The energy of the ground state is set to zero. When the QD is initially prepared in the biexciton state without any photons present in the two orthogonal cavity modes, the total number of excitations (number of excitons plus number of photons) is initially two. Since without losses the excitation number is conserved, the number of states that are accessible by the coherent QD-cavity coupling is restricted to five states of the form $|\chi, n_H, n_V\rangle$ with χ denoting the QD state and $n_{H/V}$ the number of photons present in the corresponding cavity mode. To be specific, these five states are given by $|B, 0, 0\rangle$, $|X_H, 1, 0\rangle$, $|X_V, 0, 1\rangle$, $|G, 2, 0\rangle$, and $|G, 0, 2\rangle$. States with lower excitation numbers become accessible via cavity losses by removing photons from the system. However, we do not need to consider these states explicitly in our calculations, first, because the corresponding dynamical variables do not couple back to the dynamics of the above five states and, second, only states with at least two photons contribute to the concurrence [19,22], which is the target quantity of our analysis.

In Fig. 1 a schematic sketch of the biexciton cascade with the two cavity modes is shown. Because of the exchange interaction the two exciton states X_H and X_V are split by the fine-structure splitting δ symmetric to the mean exciton energy $\hbar\bar{\omega}_X$. Thus the energy of the horizontally polarized exciton state is $\hbar\omega_H = \hbar\bar{\omega}_X + \delta/2$ and the energy of the vertically polarized exciton state is $\hbar\omega_V = \hbar\bar{\omega}_X - \delta/2$. Furthermore, a possible biexciton binding energy E_B can lower the energy of the biexciton state with respect to $2\hbar\bar{\omega}_X$. In general, the energies of the two orthogonally polarized cavity modes do not match any of the electronic transition energies of the QD.

In addition to the light-matter interaction also a pure dephasing type coupling to a continuum of LA phonons is
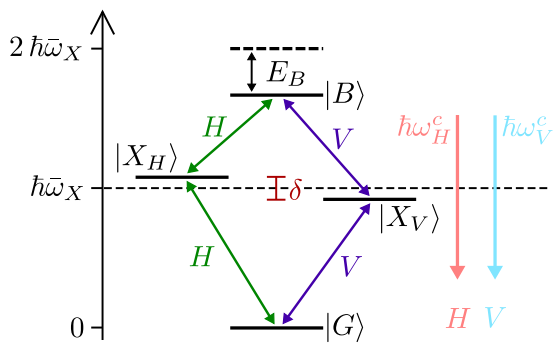

FIG. 1. Schematic sketch of the biexciton cascade with a fine-structure splitting δ between the two exciton states, a mean exciton energy $\hbar\bar{\omega}_X = \hbar(\omega_H + \omega_V)/2$, and a possible biexciton binding energy E_B. In general, both cavity modes can be detuned from the electronic transitions of the QD.

included in the model via

$$\hat{H}_{\text{QD-phon}} = \sum_{\mathbf{q}} \hbar\omega_{\mathbf{q}}\hat{b}_{\mathbf{q}}^{\dagger}\hat{b}_{\mathbf{q}} + \sum_{\mathbf{q},\chi} n_{\chi}(\gamma_{\mathbf{q}}\hat{b}_{\mathbf{q}}^{\dagger} + \gamma_{\mathbf{q}}^*\hat{b}_{\mathbf{q}})|\chi\rangle\langle\chi|.$$
(5)

Here, n_{χ} denotes the number of excitons in the different QD states $|\chi\rangle$ and $\gamma_{\mathbf{q}}$ is the coupling constant. We account for deformation potential coupling which is known to dominate for GaAs-type QDs [46] and $\hat{b}_{\mathbf{q}}^{\dagger}$ are bosonic creation operators for phonons with energy $\hbar\omega_{\mathbf{q}}$ in the mode with wave vector $\mathbf{q}$.

Finally, possible cavity losses of photons are taken into account using the Lindblad operator

$$\mathcal{L}_{\text{cav}}[\hat{\rho}] = \sum_{\ell=H,V} \frac{\kappa_{\ell}}{2}(2\hat{a}_{\ell}\hat{\rho}\hat{a}_{\ell}^{\dagger} - \hat{\rho}\hat{a}_{\ell}^{\dagger}\hat{a}_{\ell} - \hat{a}_{\ell}^{\dagger}\hat{a}_{\ell}\hat{\rho}),$$
(6)

which allows the inclusion of non-Hamiltonian dynamics while preserving the physically important properties of the statistical operator [52]. In the following we assume the loss rates for the two differently polarized cavity modes to be equal ($\kappa_H = \kappa_V = \kappa$).

Longitudinal optic (LO) phonons have been shown to affect the two-photon entanglement by multiphonon transitions to the continuum of wetting layer states [53]. This mechanism is, however, negligible for temperatures below ~80 K. Since all major findings of the present paper occur at much lower temperatures, effects of LO phonons can safely be disregarded. Nevertheless, we show in the present paper a few results for temperatures above 80 K in order to illustrate how the contribution of LA phonons behaves at elevated temperatures.

B. Method

Equation (1) is numerically solved by using a real-time path-integral (PI) approach. As almost all modern implementations of the real-time PI concept, also our simulations are based on an iteration scheme for the so called *augmented density matrix* which was introduced in the pioneering work of Makri and Makarov [54,55]. This scheme exploits the finiteness of the environment memory to obtain an efficient algorithm for performing efficiently a numerically complete summation over the paths. A specialization of these general ideas to QDs with a super-Ohmic pure-dephasing coupling to a continuum of phonons has been worked out, e.g., in Ref. [56]. Important for the present investigations are two recent extensions of the standard PI treatment. The first is a translation of the PI method from the usual Hilbert space formulation to Liouville space [57]. In this way, the non-Hamiltonian contributions to the dynamics, like, e.g., Lindblad-type loss rates, can be accounted for in a natural way while still treating the phonons without approximation to the model. The second is a reformulation of the PI algorithm such that now a partially summed augmented density matrix is iterated. This reformulation is described in detail in the supplement of Ref. [58], which in principle contains all information about the actually used PI method. For systems like QDs coupled to cavities the reformulation reduces the numerical demands by many orders of magnitude and thus numerically complete simulations for such systems would not be feasible without it. The numerical efficiency might be
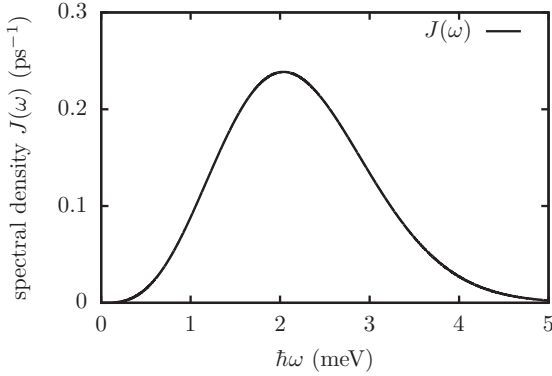
FIG. 2. Phonon spectral density $J(\omega)$ for a spherical GaAs QD with an electron (hole) geometrical confinement length $a_e = 3$ nm ($a_h = a_e/1.15$). The deformation potential constants and the mass density, as well as the sound velocity for a GaAs QD are taken from Ref. [60] and are listed in Table I. An explicit formula for $J(\omega)$ can be found in Ref. [56] or Ref. [57].

further boosted by using recently developed tensor-network techniques [59] which could further extend the applicability of PI methods in future work.

We consider a spherically symmetric GaAs QD with a harmonic oscillator confinement resulting in an electron (hole) confinement length $a_e = 3$ nm ($a_h = a_e/1.15$). The deformation potential constants and the mass density as well as the sound velocity are taken from the literature [60] and enter the phonon spectral density

$$J_{\chi\chi'}(\omega) = n_\chi n_{\chi'} J(\omega), \qquad (7)$$

with

$$J(\omega) = \sum_{\mathbf{q}} \gamma_{\mathbf{q}} \gamma_{\mathbf{q}}^* \delta(\omega - \omega_{\mathbf{q}}) \qquad (8)$$

appearing in the memory kernels of the PI approach [57]. It is worthwhile to note that all phonon related influences on the dynamics of the QD-photon system enter only via $J(\omega)$. Thus the assumption of a symmetric QD does not entail a loss of generality as long as only the dynamics of QD and photons are concerned, since as shown in Ref. [61] for any QD (not necessarily assuming a symmetric confinement) it is always possible to find a symmetric QD with the same $J(\omega)$.

In Fig. 2 $J(\omega)$ is depicted for the chosen parameters of the QD. For low frequencies $J(\omega)$ approaches zero $\sim \omega^3$ as can be seen from the explicit expression for the deformation potential coupling [46]. We are therefore dealing with a coupling of super-Ohmic type which is responsible for striking non-Markovian effects such as the nonexponential partial loss of coherence [46,47]. Furthermore, we note a pronounced maximum at about 2 meV that is the origin of the resonant structure of the phononic response [24,62].

Assuming that initially the phonons are in thermal equilibrium and the electronic system is prepared in the biexciton state without photons, our PI approach delivers the time dependence of the reduced density matrix $\hat{\bar{\rho}}$ in the subspace spanned by the five states $|B, 0, 0\rangle$, $|X_H, 1, 0\rangle$, $|X_V, 0, 1\rangle$, $|G, 2, 0\rangle$, and $|G, 0, 2\rangle$, where the phonon degrees of freedom have been traced out.

C. Concurrence

As a measure for the degree of entanglement we use the concurrence of simultaneously emitted photons that for brevity will be referred to in the following simply as the *concurrence*. This quantity can be directly calculated from the time-averaged values of the reduced density matrix $\hat{\bar{\rho}}$ of the system [22,45,53]. The time-dependent populations of the two states where two photons are present and the coherences between these states are given by

$$\rho_{mn}(t) = \langle mm | \hat{\bar{\rho}}(t) | nn \rangle, \qquad (9)$$

with $m, n \in \{H, V\}$. Here $|HH\rangle := |G, 2, 0\rangle$ is the state with two horizontally polarized photons and $|VV\rangle := |G, 0, 2\rangle$ denotes the state with two vertically polarized photons. The corresponding time-averaged quantities $\bar{\rho}_{mn}$ are calculated according to

$$\bar{\rho}_{mn} = \frac{1}{T_{\mathrm{av}}} \int_0^{T_{\mathrm{av}}} \rho_{mn}(t) dt. \qquad (10)$$

From these quantities, the concurrence C is derived as [19,22]

$$C = 2 \left| \bar{\rho}_{HV}^N \right|, \qquad (11)$$

where all quantities entering the normalized two-photon coherence

$$\bar{\rho}_{HV}^N = \frac{\bar{\rho}_{HV}}{\bar{\rho}_{HH} + \bar{\rho}_{VV}} \qquad (12)$$

are evaluated in the limit $T_{\mathrm{av}} \to \infty$. We average the time-dependent quantities $\rho_{mn}(t)$ until all excitations have left the cavity and the system has reached its ground state $|G, 0, 0\rangle$. Experimentally, the concurrence C is accessible [20,21] by measuring the two-photon correlation function $G_{ij,kl}^{(2)}(t, \tau)$ and extrapolating towards zero delay time $\tau = 0$.

Before presenting the results of our calculations, let us briefly comment on different measures to quantify the entanglement in the biexciton cascade and the impact of the cavity loss rate (a more extended discussion of these issues can be found, e.g., in Ref. [22]). Indeed, for an analysis of polarization entanglement there is a variety of choices for selecting photon pairs for which to calculate the concurrence. Probably the most widely used choice is to inspect the concurrence of all photon pairs that are detected in coincidence measurements without discriminating between the detection times of the two photons. The obvious advantage of this scheme is the high signal yield. For the corresponding theoretical description, the calculation of the two-time two-photon correlation function $G^{(2)}(t, \tau)$ is required [16,22,51,63,64]. Another approach is to consider the concurrence of frequency filtered coincidence measurements [17,63] or for a subsystem of the detected photons, e.g., by only selecting photon pairs with equal emission times from the cavity [17,45]. As stated previously, we follow the latter scheme and focus on the concurrence of simultaneously emitted photon pairs. The reasons behind this choice are presented in the following.

The concurrence calculated for a selected subset of photons is in general quantitatively as well as qualitatively different from the concurrence obtained for another photon subset. For example, it has been found [22] that the concurrence of simultaneously emitted photons shows qualitatively different
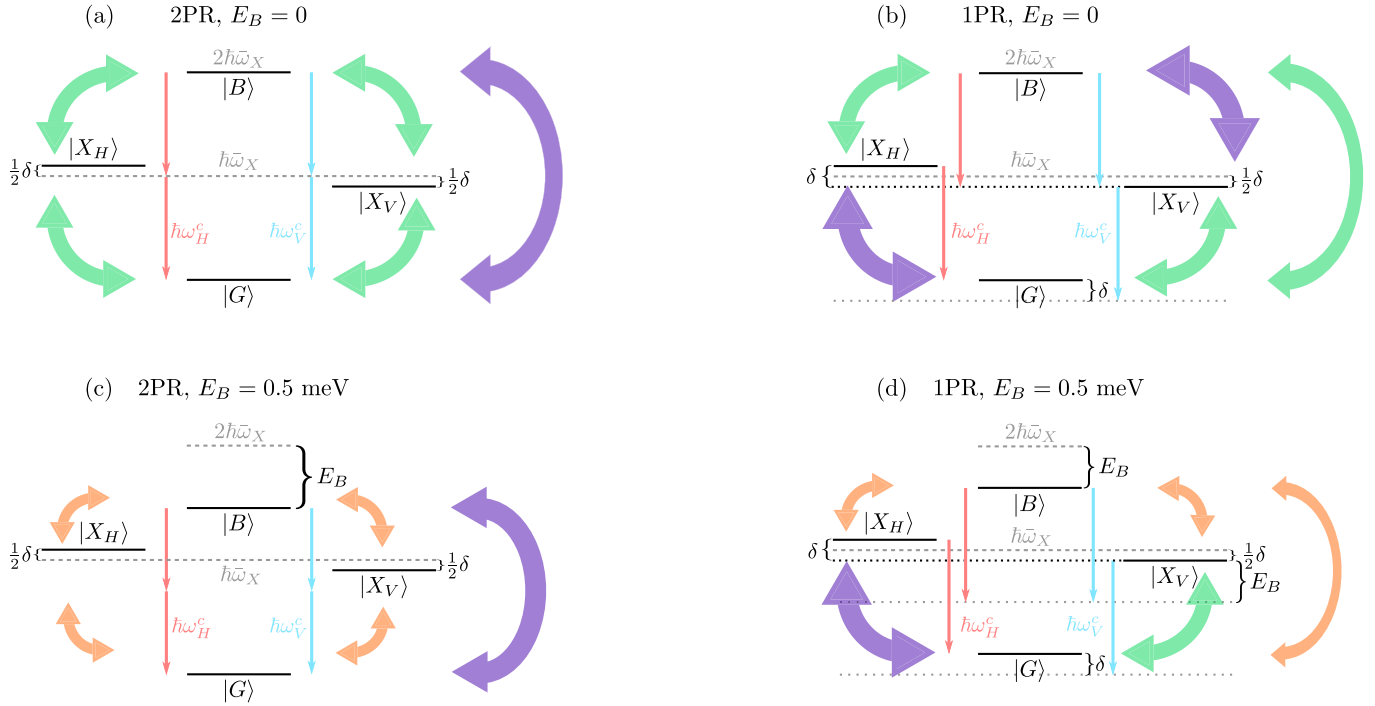
FIG. 3. Schematic sketches of the four different configurations of the QD-cavity system studied in this paper. Big curved purple arrows indicate transitions that are resonant with the corresponding cavity mode. Transitions which are detuned on the order of the fine-structure splitting δ are represented by medium-sized curved green arrows and small curved orange arrows indicate transitions where the detuning is on the order of the biexciton binding energy E_B.

trends with varying cavity losses than observed for photon pairs without selection of the emission time (an increase of the concurrence with rising loss rate is turned into a decrease). Thus these two concurrences calculated for different photon subsets cannot be equivalent measures for the same physical quantity. Nevertheless, in both cases, the phonon impact is reduced with rising loss rate and the concurrence approaches its phonon-free value in the limit of infinite losses [22]. This can be explained by noting that the phonon impact requires a finite time to develop. The loss rate limits the available time window and when the latter becomes too small the phonons cannot efficiently act on the QD degrees of freedom. Besides the different trends regarding the cavity loss rate, experiments [20,21] as well as theory [17,22] indicate that simultaneously emitted photons exhibit a significantly higher degree of entanglement and are much less affected by the which-path information introduced by a finite fine-structure splitting than photon pairs detected without emission time selection. In particular, the concurrence of simultaneously emitted photons represents an upper limit for the achievable degree of entanglement in the latter situation. Since we are interested in the highest possible degree of entanglement for a given QD-cavity configuration we solely concentrate on the concurrence of simultaneously emitted photons. Detecting photon pairs without emission time filtering, on the other hand, would maximize the emission efficiency.

III. DIFFERENT CAVITY CONFIGURATIONS

In this section, four configurations of the QD-cavity system are considered which differ in the value of the biexciton

binding energy E_B as well as in the way the cavity modes are energetically positioned. Throughout this paper, the two orthogonal linearly polarized cavity modes are assumed to have the same frequency ($\omega_H^c = \omega_V^c$). The main difference between the configurations is the position of the cavity modes with respect to the QD transitions. When the cavity modes are kept in resonance with the direct two-photon transition to the biexciton, such that $\omega_{H/V}^c = \bar{\omega}_X - \omega_B/2$, we refer to the configuration as *two-photon resonant* (2PR). In contrast, if the cavity mode frequencies are chosen to match the transition frequency of one of the excitons (without loss of generality we choose the H exciton), such that $\omega_{H/V}^c = \omega_H$, we refer to the configuration as *one-photon resonant* (1PR). In both configurations, we further distinguish between the case of a vanishing biexciton binding energy and a finite value of the latter (in this paper, we consider finite values 0.5 meV $\leqslant E_B \leqslant 6$ meV). Note that if a finite biexciton binding energy is introduced, the energy of the biexciton state is no longer the sum of the energies of the two exciton states.

In Fig. 3 schematic sketches of the 2PR and 1PR configuration with and without a biexciton binding energy are shown. In order to highlight the difference concerning the respective resonance situations, QD transitions are marked by three types of curved arrows in the figure that correspond to different detunings of these transitions from the cavity mode frequency (red or blue straight arrow). Resonant transitions are represented by big curved purple arrows. The medium-sized curved green arrows denote transitions which are detuned on the order of the fine-structure splitting δ and strongly off-resonant transitions with a detuning on the order of the biexciton binding energy E_B (typically

much larger than δ) are indicated by small curved orange arrows.

The special characteristic of the 2PR configurations [Figs. 3(a) and 3(c)] is that the $|G\rangle \leftrightarrow |B\rangle$ transition is resonant with a direct two-photon emission or absorption process, respectively. Therefore, there are two competing channels for the biexciton decay. The biexciton state can decay either via two sequential single-photon emission processes via the exciton states or via a coherent two-photon process from the biexciton state directly to the ground state. For vanishing E_B [Fig. 3(a)] the energies of the exciton states $\hbar\omega_{H/V} = \hbar\bar{\omega}_X \pm \delta/2$ are detuned by $\pm\delta/2$ from the cavity modes which are fixed at $\omega^c_{H/V} = \bar{\omega}_X$. Thus all four electronic transitions involved in the sequential emission paths are weakly detuned by half the value of the fine-structure splitting δ. The direct two-photon processes stay resonant in the 2PR configuration when a finite binding energy E_B is introduced as the cavity modes are changed accordingly. But the four electronic transitions involving an exciton state become strongly detuned on the order of half the biexciton binding energy $E_B/2$ [Fig. 3(c)] when E_B is finite.

In the 1PR configurations [Figs. 3(b) and 3(d)], the $|X_H\rangle \leftrightarrow |G\rangle$ transition is chosen to be resonant with the corresponding cavity mode. Therefore, in the case of a vanishing biexciton binding energy [Fig. 3(b)], the $|X_V\rangle \leftrightarrow |B\rangle$ transition is also resonant, whereas the two remaining cascade transitions as well as the direct two-photon processes are detuned by the value of the splitting δ. Introducing a finite biexciton binding energy does not change the situation for the exciton-to-ground-state transitions but the two transitions between the biexciton state and one of the exciton states as well as the direct two-photon processes are now strongly off resonant and detuned on the order of E_B [cf. Fig. 3(d)].

IV. RESULTS

In this section we analyze how the degree of entanglement between the two states with two photons ($|HH\rangle$ and $|VV\rangle$) is affected by various system parameters. As mentioned before, the system is initially prepared in the biexciton state without any photons and the phonons are assumed to be initially in thermal equilibrium. If not stated otherwise, a light-matter coupling strength $g = 0.1$ meV, a finite exciton splitting $\delta = 0.1$ meV, a biexciton binding energy $E_B = 0.5$ meV, and a cavity loss rate $\kappa = 0.025$ ps^{-1} corresponding to a cavity quality factor $Q \approx 45\,000$ are used. Table I displays these default values and all other material parameters used for the numerical calculations. The given value for the biexciton binding energy E_B is the difference between twice the polaron shifted mean exciton energy and the polaron shifted biexciton energy. In the corresponding phonon-free situation the value for E_B is kept the same in order to compare QD-cavity systems with identical energetic detunings between the cavity modes and the QD transition energies. After quantifying the competition between direct two-photon and sequential single-photon processes in Sec. IV A, the dependence of the concurrence on the exciton fine-structure splitting is investigated in Sec. IV B. Finally, we discuss the temperature dependence of the concurrence for fixed splittings in Sec. IV C.

A. Competition between direct two-photon and sequential single-photon transitions

As pointed out before, e.g., by Schumacher *et al.* [16] or del Valle [17], the competition between the direct two-photon processes from the biexciton state to the ground state and the sequential single-photon processes via the exciton states is of utmost importance for the concurrence. Obviously, by considering configurations with different resonance situations, in particular when switching between 2PR and 1PR configurations, we are comparing situations with different relative importance of two-photon and sequential single-photon processes. To quantify the relative impact of these processes, we introduce the quantity

$$r_{2P/1P} = \frac{|\bar{\rho}_{B,HH}| + |\bar{\rho}_{B,VV}|}{\bar{\rho}_{X_H} + \bar{\rho}_{X_V}}, \tag{13}$$

i.e., $r_{2P/1P}$ is a ratio where the numerator is derived from the coherences $\rho_{B,HH} = \langle B, 0, 0|\hat{\bar{\rho}}|G, 2, 0\rangle$ and $\rho_{B,VV} = \langle B, 0, 0|\hat{\bar{\rho}}|G, 0, 2\rangle$ between the biexciton and the ground state with either two horizontally or vertically polarized photons. The denominator represents the total exciton occupation $\rho_{X_H} + \rho_{X_V}$, where ρ_{X_H} and ρ_{X_V} denote the occupations of the states $|X_H, 1, 0\rangle$ and $|X_V, 0, 1\rangle$, respectively. The bar over these quantities indicates a time averaging as introduced in Eq. (10).

The coherences between the biexciton state and the two states containing the ground state represent a measure for the direct two-photon processes. Note that by inspecting the equations of motion for all elements of the reduced density matrix it becomes apparent that only the equations for these coherences introduce a resonance when the biexciton-to-ground-state transition frequency matches twice the photon frequency. This is the distinctive property of a two-photon process. In contrast, the characteristic feature of sequential single-photon emission processes is the occupation of the intermediate electronic states, in our case the excitons. Thus the total exciton occupation reflects the importance of sequential processes. Altogether, this justifies that the ratio $r_{2P/1P}$ is a possible measure for the relative importance of the direct

TABLE I. Material parameters for the GaAs quantum dot and the default values for the system parameters: light-matter coupling strength g, exciton splitting δ, biexciton binding energy E_B, and cavity loss rate κ. If not stated otherwise these default values are used for the calculations.

| Parameter		Value
Electron geometrical confinement length (nm)	a_e	3.0
Hole geometrical confinement length (nm)	a_h	$a_e/1.15$
Mass density (kg/m^3)	ρ	5370 [65]
Longitudinal sound velocity (m/s)	c_s	5110 [65]
Electron deformation potential constant (eV)	D_e	7.0 [66]
Hole deformation potential constant (eV)	D_h	-3.5 [66]
Light-matter coupling strength (meV)	g	0.1
Exciton fine-structure splitting (meV)	δ	0.1
Biexciton binding energy (meV)	E_B	0.5
Cavity loss rate (ps^{-1})	κ	0.025
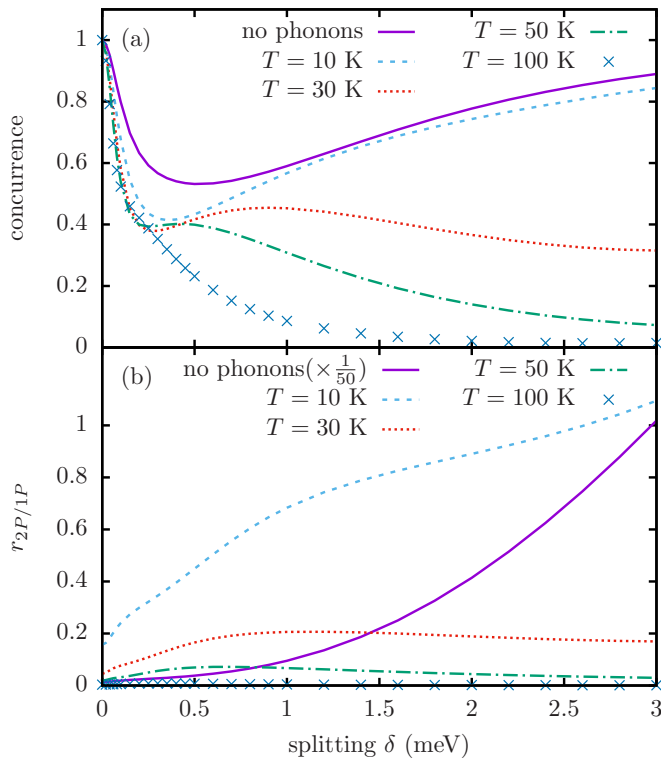
FIG. 4. Comparison of the concurrence [panel (a)] and a measure for the relative importance of two-photon and sequential single-photon processes $r_{2P/1P}$ [panel (b)] as a function of the exciton splitting δ. Different temperatures as well as the limit without phonons are considered. Note that $r_{2P/1P}$ is scaled by the factor $1/50$ in the phonon-free case. The cavity modes are arranged in the 2PR configuration and a vanishing biexciton binding energy is assumed.

two-photon processes compared with the sequential single-photon processes.

Figure 4 displays the concurrence [panel (a)] along with $r_{2P/1P}$ [panel (b)] as a function of δ. The analysis is carried out exemplarily for the 2PR configuration with $E_B = 0$ for four temperatures as well as for the phonon-free case. The plotted range for the fine-structure splitting is chosen larger than usually covered by typical QDs as the role of the two-photon processes can be better highlighted on this extended scale.

As can be seen in Fig. 4(a), the concurrence exhibits a nonmonotonic dependence on the exciton splitting for low temperatures and the phonon-free situation. This behavior can be traced back to the competition between two-photon and sequential single-photon processes. Recalling that in the 2PR configuration the two-photon processes are chosen to be always resonant independent of δ, it follows that any which-path information introduced by the fine-structure splitting affects only the sequential single-photon processes. Figure 4(b) reveals a dominance of sequential emission processes for small exciton splittings. Therefore, the concurrence decreases with rising $|\delta|$ in the small splitting limit since (i) the which-path information is larger for larger $|\delta|$ and (ii) it efficiently affects the concurrence due to the dominance of sequential single-photon processes.

As the splitting increases further, $r_{2P/1P}$ rises because the single-photon processes become more off-resonant and

thus the relative importance of two-photon processes grows, since the latter are always resonant. When either the interaction with the phonons is switched off or the temperature is low enough, $r_{2P/1P}$ increases strongly for larger exciton splittings, indicating a dominance of two-photon processes [cf. Fig. 4(b) for $T = 10\,\mathrm{K}$]. As a result, the concurrence rises and eventually approaches unity because the which-path information introduced by the exciton splitting is no longer tested. The local maximum of the concurrence seen at higher temperatures of 30 K and 50 K can also be understood with the help of $r_{2P/1P}$ since it shows a similar behavior. Hence the nonmonotonic behavior of the concurrence is a result of the competition between the coherent direct two-photon and sequential single-photon emission processes.

At higher temperatures the relative importance of the sequential emission processes is raised, as can be seen in Fig. 4(b). As the electronic transitions become detuned from the corresponding cavity modes the sequential single-photon processes are assisted by phonon absorption and emission processes to compensate the energy differences, an effect which is enhanced with increasing temperature. In addition, for larger exciton splittings the phonon spectral density is effectively probed at higher values of ω (on the order of δ), resulting in a stronger phonon influence on the system (cf. Fig. 2). Furthermore, coherences, such as the ones relevant for the two-photon processes, are more strongly affected by phonon-induced decoherence than occupations. The combination of these effects explains why $r_{2P/1P}$ decreases for larger splittings at higher temperatures and the concurrence approaches zero.

B. Dependence of the concurrence on the exciton splitting for different configurations

For all four QD-cavity configurations illustrated in Fig. 3, the dependence of the concurrence on the exciton splitting is shown in Fig. 5. First of all, for a vanishing fine-structure splitting, the concurrence is strictly one regardless of the phonon influence since the system is completely symmetric with respect to $H \leftrightarrow V$ so that no which-path information is introduced. This result was also found on the basis of a phenomenological rate equation approach for the phonon-induced pure dephasing [45].

With increasing $|\delta|$ the concurrence decreases, reflecting the increase of which-path information. Furthermore, phonons generally reduce the concurrence for a given splitting, an effect which typically becomes more pronounced at higher temperatures. This can be understood by noting that phonons typically enhance the differences between different pathways and thus increase the which-path information. To see this, we first recall that, when the electronic transitions of the QD are detuned from the corresponding cavity modes, the photon emission processes are assisted by phonon emission and absorption processes to compensate the energy differences. For a finite splitting, depending on the configuration, the two sequential emission paths differ either in the values or the order of the detunings and are therefore influenced differently by the phonons. For example, in the 2PR configuration with $\delta > 0$ and $E_B = 0$, the sequential emission process of two horizontally polarized photons is at first assisted by phonon
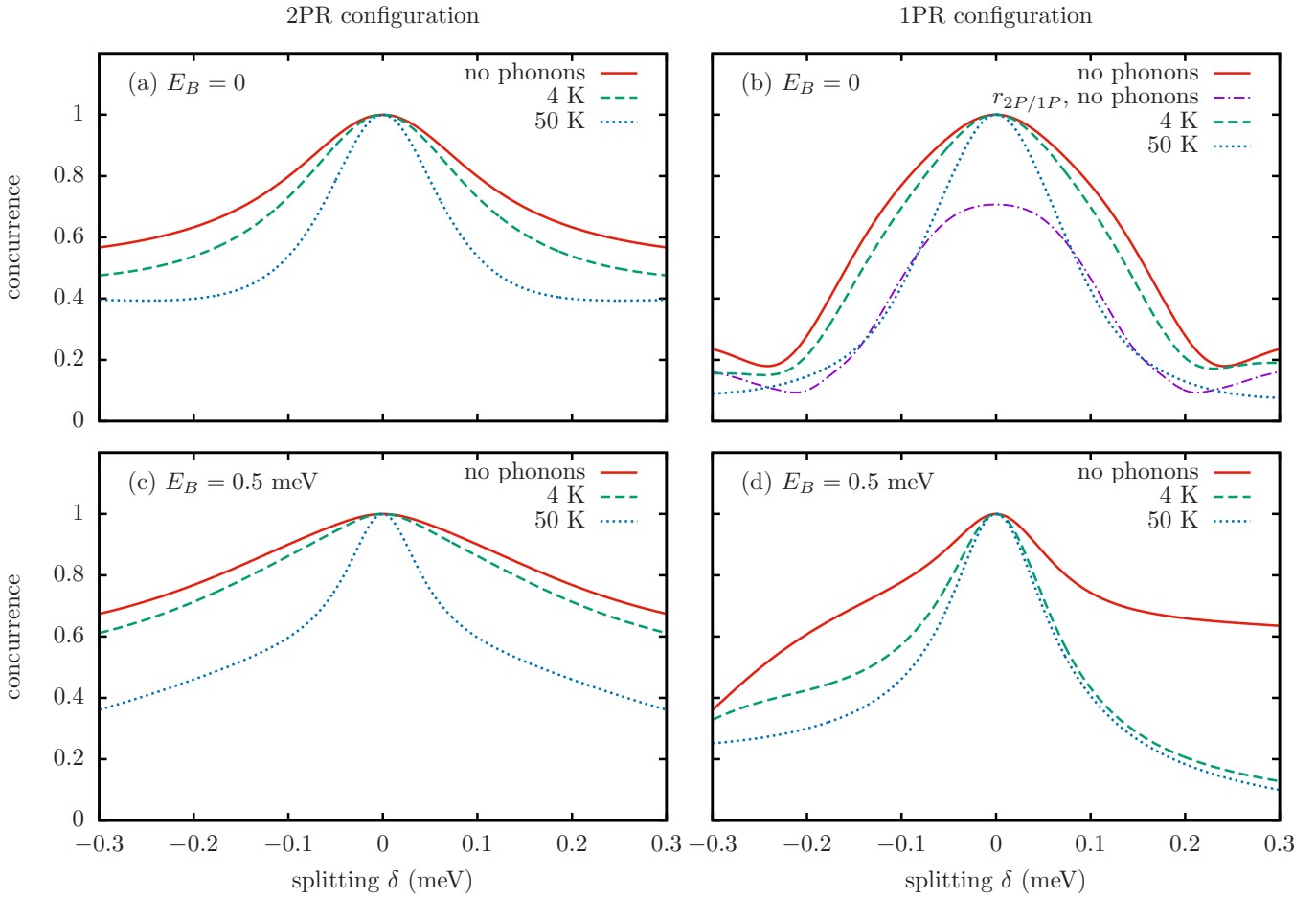
FIG. 5. Impact of the exciton splitting δ on the concurrence for all four cavity configurations introduced in Sec. III and depicted in Fig. 3. Results are shown for two different temperatures and without phonons. Panel (b) additionally displays the ratio $r_{2P/1P}$ for the phonon-free case.

absorption and in the second step phonon emission occurs for the exciton-to-ground-state transition. This order is reversed for the sequential emission path for two vertically polarized photons. Obviously, this enhances the difference between both pathways compared with the phonon-free case at least at low temperatures where emission and absorption are noticeably different. In general, as discussed in Sec. IV A, with increasing temperature more phonons are thermally excited and sequential one-photon transitions can be more efficiently bridged by phonon-assisted processes. In combination with the increased phonon-induced decoherence, this leads to a smaller impact of two-photon transitions and therefore a lower concurrence at higher temperatures.

Despite these common tendencies, the detailed dependences of the concurrence on the exciton splitting differ significantly in the respective configurations. For $E_B = 0$, the results for the 2PR configuration [Fig. 5(a)] and the 1PR configuration [Fig. 5(b)] are qualitatively similar for small $|\delta|$ but differ strongly for larger detunings. This can be understood by consulting Fig. 3(a) and Fig. 3(b) which reveals that these configurations become identical in the limit of vanishing splitting. The corresponding concurrences are thus very close to each other for small exciton splittings.

The deviation for larger splittings between the two configurations can be explained by the competition between the

coherent direct two-photon and the sequential single-photon processes. In the 2PR configuration, the relative importance of two-photon processes rises with increasing $|\delta|$ as already discussed in Sec. IV A. However, compared with the 2PR case, the influence of two-photon processes is reduced in the 1PR configuration since they are detuned by the exciton splitting [cf. Fig. 3(b)]. Thus the concurrence in the 2PR configuration is significantly higher for larger $|\delta|$ than in the 1PR configuration.

Nevertheless, the competition between two-photon and single-photon processes also influences the 1PR configuration where the concurrence exhibits a local minimum for low temperatures as well as without phonons, which means that this is not a phonon-induced effect. In fact, phonons cause this minimum to eventually disappear, as can be seen in Fig. 5(b) at 50 K. Figure 5(b) reveals that the nonmonotonic behavior of the concurrence reflects the behavior of $r_{2P/1P}$. Compared with the 2PR configuration [cf. Fig. 4(a)], here the local minima are found already at smaller $|\delta|$ because the electronic transitions of the QD are now detuned by the value of δ, whereas the detuning is only $\delta/2$ in the 2PR configuration. Furthermore, although the value of $r_{2P/1P}$ at vanishing splitting without phonons in Fig. 5(b) is the same as in Fig. 4(b) (note the different scaling in the latter figure), the ratio between two- and one-photon processes is a decreasing function of δ in

the 1PR configuration since a finite splitting also causes a detuning of the direct two-photon transitions in this case. This is in contrast to the 2PR case in Fig. 4, where $r_{2P/1P}$ rises with increasing δ in the phonon-free case.

Next, we consider the results for the 2PR configuration with a finite biexciton binding energy $E_B = 0.5$ meV plotted in Fig. 5(c). In the phonon-free situation and for a temperature of 4 K the concurrence decreases only weakly with increasing $|\delta|$, but at $T = 50$ K it is drastically reduced at finite $|\delta|$. Therefore, a finite biexciton binding energy in the 2PR configuration significantly affects the concurrence [cf. Fig. 5(a)] since it leads to strongly detuned biexciton-to-exciton and exciton-to-ground-state transitions, while the direct two-photon processes remain resonant. Thus, without phonons, the direct two-photon processes are strongly enhanced compared with the sequential single-photon processes, resulting in a significantly higher concurrence that is much less influenced by the splitting.

On the other hand, in the 2PR configuration with finite E_B, phonons with energies $\hbar\omega_\mathbf{q} \simeq E_B/2$ are required to bridge the detunings of the sequential transitions. In contrast, for vanishing E_B, the required phonon energies are given by the much smaller value of $|\delta|/2$. At the same time, the relative weight of the phonon influence is proportional to $J(\omega)$. Figure 2 shows that $J(\frac{E_B}{2\hbar}) > J(\frac{\delta}{2\hbar})$ for $E_B = 0.5$ meV and $|\delta| < 0.3$ meV, i.e., the phonon influence and thus the temperature dependence of the concurrence is stronger for a finite biexciton binding energy. This results in the significantly larger difference of the concurrence for 4 K and 50 K in Fig. 5(c) compared with curves for the same parameters but vanishing binding energy in Fig. 5(a). We note in passing that, keeping the splitting in the typical range $|\delta| < 0.3$ meV, for rather high values of the biexciton binding energy the relation $J(\frac{E_B}{2\hbar}) > J(\frac{\delta}{2\hbar})$ is reversed (cf. Fig. 2). However, this limit is usually not reached since typical biexciton binding energies stay below ~6 meV.

In contrast to the configurations discussed up to now, the interaction with phonons in the 1PR configuration with a finite biexciton binding energy, depicted in Fig. 5(d), drastically reduces the concurrence already at low temperatures. In this situation, both biexciton-to-exciton-transitions are strongly detuned from the corresponding cavity modes. The horizontally polarized exciton-to-ground-state transition is resonant by definition, while the vertically polarized one is detuned by δ. In addition, also the direct two-photon processes are highly off resonant. As all possible electronic transitions starting from the biexciton state are strongly detuned, the initially prepared occupation of the biexciton state decreases only very slowly when phonons are not accounted for. Hence the occupations of the exciton states and the QD ground state with two photons are always very small. In both the H and V pathway the exciton can be reached by emission of a photon only when a phonon with an energy on the order of $\simeq E_B$ is absorbed. At this energy $J(\omega)$ is even larger than in the 2PR configuration with finite E_B where phonons with energies $\simeq E_B/2$ are required, which explains the dramatic drop of the concurrence from the phonon-free case to the values obtained for 4 K. Furthermore, the concurrence is clearly asymmetric with respect to the exciton splitting in this configuration. Especially in the phonon-free case the concurrence decays much stronger with rising $|\delta|$ for negative than for positive δ.

This is due to the fact that for negative δ one comes closer to the condition that the transition from the biexciton to the H exciton is getting in resonance. Since the decay from the H exciton to the ground state is held in resonance in this configuration, the pathway $|B\rangle \rightarrow |X_H, 1, 0\rangle \rightarrow |G, 2, 0\rangle$ is strongly favored compared with $|B\rangle \rightarrow |X_V, 0, 1\rangle \rightarrow |G, 0, 2\rangle$, resulting in low values of the concurrence. Interestingly, for $\delta > 0$ the concurrence decreases only very little when the temperature is raised further from 4 K to 50 K.

In general, the symmetry with respect to δ is found to be another distinguishing feature between the 2PR and the 1PR configuration. In the 2PR configuration, independent of the biexciton binding energy, the concurrence is a symmetric function of the splitting no matter whether phonons are included or not. In contrast, in the 1PR configuration with a finite binding energy, the concurrence always shows an asymmetric dependence on δ. In this situation, changing the sign of δ changes the absolute value of the detuning between the horizontally polarized cavity mode and the corresponding biexciton-to-exciton transition $\Delta_{B,X_H}(\delta) = E_B + \delta$, while the absolute values of the detunings of the remaining sequential transitions are unaffected. The direct two-photon processes are also detuned by the same value $\Delta E_{2P}(\delta) = E_B + \delta$. Since without phonons the dynamics depends only on the absolute values of the detunings between the electronic transitions and their corresponding cavity modes, an asymmetric concurrence is expected, which is also visible when phonons are accounted for. This asymmetry is stronger at low temperatures since there phonon absorption and emission processes are not equally likely. Turning finally to the 1PR configuration with $E_B = 0$, changing the sign of the exciton splitting no longer changes the absolute values of the detunings. Thus, without phonons, the concurrence is once more symmetric and only a slight asymmetry is observed when phonons are included.

We conclude that the competition between single-photon and two-photon processes plays a decisive role for the concurrence. Furthermore, the arrangement of the cavity modes strongly affects the concurrence as one of the competing processes can be either favored or suppressed. Finally, the values of the various detunings depend on the chosen configuration, resulting in different effective phonon influences and very different dependences of the concurrence on the exciton splitting for each of the considered QD-cavity configurations.

C. Temperature dependence of the concurrence at a finite exciton splitting

After the discussion in the last section it is clear that the temperature dependence of the concurrence also differs for each of the four configurations. In this section we investigate in more detail the concurrence as a function of temperature for different fixed values of the exciton splitting.

Figure 6(a) displays the concurrence as a function of the temperature for a typical value of the exciton splitting $\delta = 0.02$ meV, while a larger value $\delta = 0.1$ meV is used in Fig. 6(b). As expected after the discussion of the 1PR configuration with a finite biexciton binding energy in Sec. IV B, the concurrence drops in this setting steeply for low temperatures followed by a very weak T dependence compared with the other configurations for $T > 4$ K and both splittings. Note that
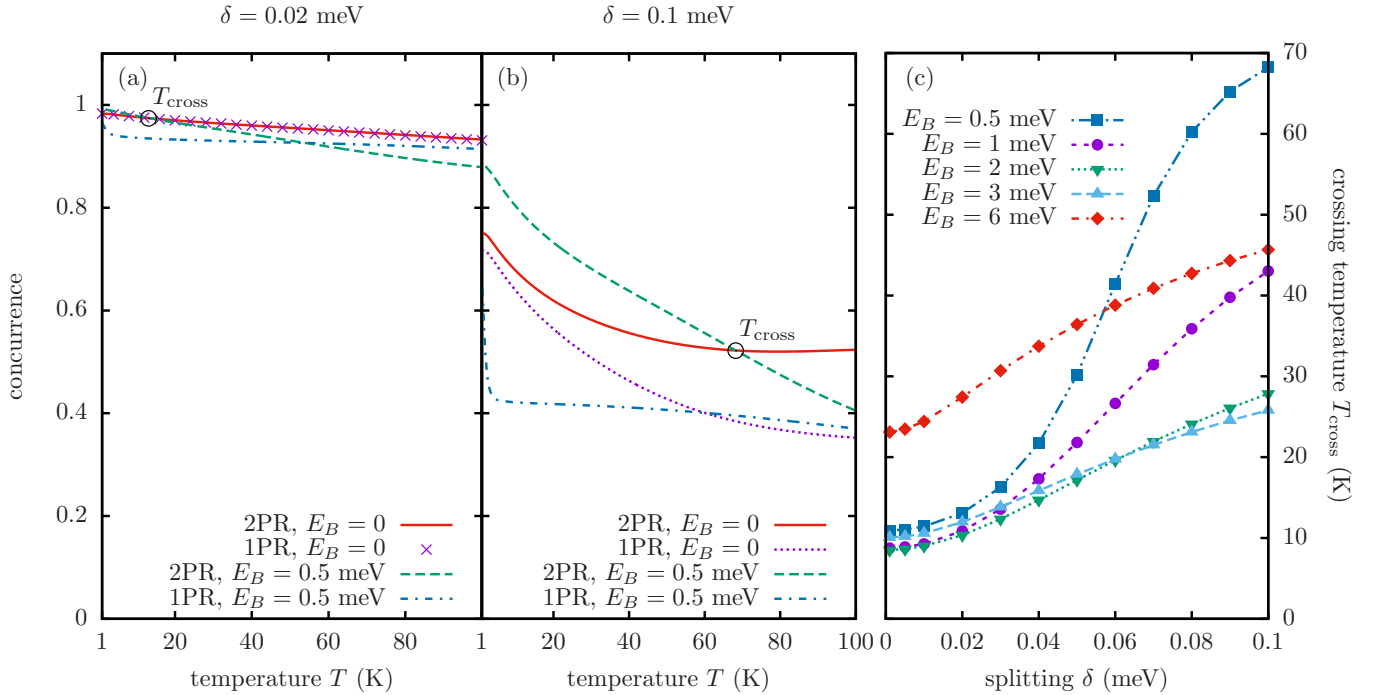
FIG. 6. Concurrence as a function of temperature for a fine-structure splitting $\delta = 0.02$ meV [panel (a)] and $\delta = 0.1$ meV [panel (b)] for all four QD-cavity configurations introduced in Sec. III. Also shown is the crossing temperature T_{cross} of the concurrence in the 2PR configuration with $E_B = 0$ and the concurrence in the 2PR configuration with $E_B > 0$ as a function of δ for several values of the binding energy E_B [panel (c)]. T_{cross} is marked in panels (a) and (b) by a circle.

for $\delta > 0$ in this configuration all sequential processes require the absorption of phonons to bridge the energy mismatches and thus for $T \to 0$ the phonon-free result should be reached. Indeed, as seen in Fig. 6(b), changing the temperature from 1 to 4 K entails a very steep drop of the concurrence before it becomes almost independent of T for $T > 4$ K.

The 2PR configuration with a finite binding energy exhibits a rather strong temperature dependence for both selected values of δ. Because of the weak influence of the exciton splitting in this configuration the concurrence reaches almost one for temperatures close to zero.

The 2PR and 1PR configuration with a vanishing binding energy are, as discussed earlier, almost the same for small δ. Therefore, for $\delta = 0.02$ meV, the concurrence as a function of temperature is nearly identical for both configurations, with the 1PR result being marginally lower. For the larger splitting $\delta = 0.1$ meV these two configurations show a similar temperature dependence at very low temperatures but at higher temperatures the concurrence decreases noticeably stronger in the 1PR configuration.

In the 2PR as well as in the 1PR configuration the sequential single-photon processes are detuned on the order of δ when the biexciton binding energy is zero. Since two-photon processes are more important in the 2PR configuration the corresponding concurrence is higher for all temperatures than in the 1PR configuration when $E_B = 0$. However, this trend reverses for finite E_B at high temperatures.

Let us now compare 2PR results with and without a finite biexciton binding energy. As can be seen in Fig. 6(a) and Fig. 6(b), introducing a finite value for E_B in the 2PR configuration leads to a higher concurrence only below a crossing temperature which depends on δ. In fact, there is a crossing

point of the 2PR concurrence evaluated at finite E_B with each of the three other concurrences considered here. It turns out that the setting with the lowest crossing temperature is the 2PR configuration with vanishing biexciton binding energy. We will denote the corresponding crossing temperature by T_{cross} in the following.

For large splittings, a finite biexciton binding energy can raise the concurrence significantly at low temperatures since the sequential single-photon emission processes become largely detuned and the importance of the two-photon processes is raised. Therefore, in the absence of phonons, a finite binding energy in general results in an increased concurrence, a finding which was already proposed and discussed by Schumacher *et al.* [16].

Above the crossing temperature, however, the pure dephasing coupling to the phonons alters this effect and a finite binding energy in the 2PR configuration reduces the concurrence. As the temperature increases, phonons raise the importance of the detuned single-photon processes because they become assisted by phonon absorption and emission. In the case of a finite binding energy, the cavity modes are more detuned from the electronic transitions involving exciton states. Therefore, the phonon spectral density $J(\omega)$ is probed at larger values so that the effective phonon coupling is stronger compared with the situation without biexciton binding energy. These two effects combined lead to a stronger decrease of the concurrence with increasing temperature for a finite E_B. Thus, above T_{cross}, a finite biexciton binding energy reduces the concurrence and the protection of entanglement in the 2PR configuration is lost.

By comparing Fig. 6(a) and Fig. 6(b), one notices that the crossing point of the concurrence in the 2PR configuration

with and without a finite binding energy moves to lower temperatures for smaller values of the exciton splitting. For the concurrence, this means that the advantage provided by a finite E_B is lost for small δ already at low temperatures $T \sim 10$ K. In Fig. 6(c) this crossing temperature is plotted against δ for several values of E_B. For a given binding energy, T_{cross} exhibits a monotonic increase with increasing exciton splitting and converges to a finite value of about 10 K in the limit $\delta \rightarrow 0$ and typical binding energies. Therefore, for typical splittings on the order of several $10 \, \mu$eV, the protection of the entanglement due to a finite binding energy is already lost at quite low temperatures. As can be seen by comparing the results in Fig. 5(a) and Fig. 5(c), the protection of the concurrence due to a finite E_B in the 2PR configuration at temperatures close to zero improves for larger δ. Thus, for larger δ, higher temperatures are needed to destroy this protection and T_{cross} increases with increasing splitting for a given E_B.

Comparing the crossing temperature for different values of the binding energy, a nonmonotonic behavior is found at a given exciton splitting. On the one hand, a higher value of the binding energy results in a better protection of the entanglement at temperatures close to zero. But, on the other hand, the phonon influence and thus the influence of the temperature depends on the energy of the phonons needed to assist the detuned single-photon processes as the phonon spectral density $J(\omega)$ depends (nonmonotonically) on this energy. In the case of the 2PR configuration with finite E_B, this roughly corresponds to half the binding energy. The nonmonotonic behavior of T_{cross} as a function of E_B at a given exciton splitting thus originates from the trade-off between a better protection of the concurrence for higher binding energies at temperatures close to zero and the varying influence of the phonons due to the nonmonotonic behavior of the phonon spectral density. For example, the crossing point temperature in Fig. 6(c) for $E_B = 1$ meV is always higher than for $E_B = 2$ meV. The reason is the much stronger temperature dependence in the latter situation as the phonon spectral density is much higher for a phonon energy of 1 meV than for a value of 0.5 meV (cf. Fig. 2). However, at $\hbar\omega = 1$ meV and $\hbar\omega = 3$ meV the values of $J(\omega)$ are similar, which means that the phonon influence is similar for $E_B = 2$ meV and $E_B = 6$ meV and T_{cross} is always higher in the latter case because of the stronger protection due to the higher binding energy.

V. CONCLUSION

We have analyzed how the competition between two-photon and single-photon emission processes as well as the coupling to LA phonons influences the degree of two-photon entanglement created in a QD-cavity system. To this end we have calculated the concurrence of photon pairs simultaneously emitted in a biexciton-exciton cascade of a QD in a cavity for four different configurations. We account for four electronic states (biexciton, two excitons, and the ground state), two degenerate orthogonally polarized cavity modes that are coupled to the electronic transitions, and cavity losses, as well as for a continuum of LA phonons coupled by the deformation potential interaction to the QD. The numerical simulations are based on a path-integral scheme that allows

the evaluation of quantities of interest without approximation to the model.

The four configurations considered in this paper comprise the two-photon resonant (2PR) and the one-photon resonant (1PR) configuration with a vanishing as well as a finite biexciton binding energy. We find a wealth of interesting results and insights in the physics of the system at hand which we would like to briefly summarize below before we outline our main result at the end.

(a) The competition between two-photon and one-photon processes plays a decisive role for the concurrence and leads to strikingly different dependences on the exciton splitting δ. Among other things, we find, e.g., nonmonotonic dependences and deviations from the standard bell shape in the 2PR as well as in the 1PR configuration. While the 2PR and 1PR configuration without a biexciton binding energy lead to almost the same degree of entanglement for small splittings the 2PR configuration is favorable for larger splittings. These results and the different dependences on the splitting δ can be very well explained by the different relative importance of direct two-photon and sequential single-photon contributions as well as the changing phonon impact when the resonance settings are varied.

(b) The concurrence is in general only symmetric regarding the exciton splitting δ in the 2PR configurations. Additionally, LA phonons affect or even introduce the asymmetry in the 1PR configurations. Because of the characteristics of the phonon coupling this asymmetry is stronger at low temperatures as phonon absorption and emission processes are not equally likely to occur.

(c) The chosen configuration defines the detunings in the quantum dot-cavity system and results in different effective phonon influences and therefore also strongly different temperature dependences of the concurrence. The 2PR and 1PR configuration with a vanishing binding energy have almost the same concurrence value and temperature dependence for the usual exciton splittings of several $10 \, \mu$eV. The concurrence can be virtually independent of the temperature over a wide temperature range, as it is the case in the 1PR configuration with a finite binding energy and positive δ after the concurrence has fallen drastically with rising temperature for T below 4 K.

In order to appreciate our main result, it should be noted that the 2PR configuration with finite biexciton binding energy has attracted a lot of attention [16,17,51] since this configuration has been proposed in order to reach high degrees of entanglement at finite fine-structure splittings. The idea is that two-photon transitions are favored which are much less affected by the which-path information introduced by the fine-structure splitting than sequential single-photon processes. Thus a finite biexciton binding energy protects the entanglement from the destructive impact of the fine-structure splitting by making single-photon processes off-resonant. Indeed, at low temperatures we find the highest degree of entanglement for this configuration which depends only little on the fine-structure splitting. However, the concurrence in the 2PR configuration with finite biexciton binding energy exhibits a steep decrease with rising temperature, which can be explained by an enhanced interaction with phonons resulting from the frequency dependence of the phonon-spectral density combined with

an increase of the importance of sequential single-photon processes at higher temperatures.

This strong temperature dependence is the origin of our most important result that for each of the other three considered configurations there is a finite temperature above which the corresponding concurrence is higher than in the 2PR case with finite biexciton binding energy. Out of the configurations that we compare, the 2PR configuration with vanishing biexciton binding energy has the lowest such crossing temperature T_{cross}, which is found to depend on the fine-structure splitting as well as on the biexciton binding energy. For splittings that are typically found in experiments on the order of several $10\,\mu\mathrm{eV}$ or below and typical biexciton binding energies of few meV, T_{cross} is around or even below 10 K. Thus the special distinction of the 2PR configuration with finite biexciton binding energy in terms of yielding the highest degree of entanglement for finite fine-structure splittings is lost already at rather low temperatures due to the phonon impact and the 2PR configuration with vanishing biexciton binding energy becomes more favorable for achieving the highest value of the concurrence.

[1] N. Akopian, N. H. Lindner, E. Poem, Y. Berlatzky, J. Avron, D. Gershoni, B. D. Gerardot, and P. M. Petroff, Phys. Rev. Lett. **96**, 130501 (2006).

[2] J.-W. Pan, Z.-B. Chen, C.-Y. Lu, H. Weinfurter, A. Zeilinger, and M. Żukowski, Rev. Mod. Phys. **84**, 777 (2012).

[3] A. Orieux, M. A. M. Versteegh, K. D. Jöns, and S. Ducci, Rep. Prog. Phys. **80**, 076001 (2017).

[4] K. D. Jöns, L. Schweickert, M. A. M. Versteegh, D. Dalacu, P. J. Poole, A. Gulinatti, A. Giudice, V. Zwiller, and M. E. Reimer, Sci. Rep. **7**, 1700 (2017).

[5] R. M. Stevenson, R. J. Young, P. Atkinson, K. Cooper, D. A. Ritchie, and A. J. Shields, Nature (London) **439**, 179 (2006).

[6] R. J. Young, R. M. Stevenson, P. Atkinson, K. Cooper, D. A. Ritchie, and A. J. Shields, New J. Phys. **8**, 29 (2006).

[7] R. Hafenbrak, S. M. Ulrich, P. Michler, L. Wang, A. Rastelli, and O. G. Schmidt, New J. Phys. **9**, 315 (2007).

[8] A. Dousse, J. Suffczyński, A. Beveratos, O. Krebs, A. Lemaître, I. Sagnes, J. Bloch, P. Voisin, and P. Senellart, Nature (London) **466**, 217 (2010).

[9] E. del Valle, A. Gonzalez-Tudela, E. Cancellieri, F. P. Laussy, and C. Tejedor, New J. Phys. **13**, 113014 (2011).

[10] M. Müller, S. Bounouar, K. D. Jöns, M. Glässl, and P. Michler, Nat. Photon. **8**, 224 (2014).

[11] R. Winik, D. Cogan, Y. Don, I. Schwartz, L. Gantz, E. R. Schmidgall, N. Livneh, R. Rapaport, E. Buks, and D. Gershoni, Phys. Rev. B **95**, 235435 (2017).

[12] O. Benson, C. Santori, M. Pelton, and Y. Yamamoto, Phys. Rev. Lett. **84**, 2513 (2000).

[13] R. Johne, N. A. Gippius, G. Pavlovic, D. D. Solnyshkov, I. A. Shelykh, and G. Malpuech, Phys. Rev. Lett. **100**, 240404 (2008).

[14] R. M. Stevenson, R. J. Young, P. See, D. G. Gevaux, K. Cooper, P. Atkinson, I. Farrer, D. A. Ritchie, and A. J. Shields, Phys. Rev. B **73**, 033306 (2006).

[15] J. Zhang, J. S. Wildmann, F. Ding, R. Trotta, Y. Huo, E. Zallo, D. Huber, A. Rastelli, and O. G. Schmidt, Nat. Commun. **6**, 10067 (2015).

[16] S. Schumacher, J. Förstner, A. Zrenner, M. Florian, C. Gies, P. Gartner, and F. Jahnke, Opt. Express **20**, 5335 (2012).

[17] E. del Valle, New J. Phys. **15**, 025019 (2013).

[18] W. K. Wootters, Quantum Inf. Comput. **1**, 27 (2001).

[19] W. K. Wootters, Phys. Rev. Lett. **80**, 2245 (1998).

[20] R. M. Stevenson, A. J. Hudson, A. J. Bennett, R. J. Young, C. A. Nicoll, D. A. Ritchie, and A. J. Shields, Phys. Rev. Lett. **101**, 170501 (2008).

[21] S. Bounouar, C. de la Haye, M. Strauß, P. Schnauber, A. Thoma, M. Gschrey, J.-H. Schulze, A. Strittmatter, S. Rodt, and S. Reitzenstein, Appl. Phys. Lett. **112**, 153107 (2018).

[22] M. Cygorek, F. Ungar, T. Seidelmann, A. M. Barth, A. Vagov, V. M. Axt, and T. Kuhn, Phys. Rev. B **98**, 045303 (2018).

[23] J. Förstner, C. Weber, J. Danckwerts, and A. Knorr, Phys. Rev. Lett. **91**, 127401 (2003).

[24] A. Vagov, M. D. Croitoru, V. M. Axt, T. Kuhn, and F. M. Peeters, Phys. Rev. Lett. **98**, 227403 (2007).

[25] A. J. Ramsay, A. V. Gopal, E. M. Gauger, A. Nazir, B. W. Lovett, A. M. Fox, and M. S. Skolnick, Phys. Rev. Lett. **104**, 017402 (2010).

[26] A. J. Ramsay, T. M. Godden, S. J. Boyle, E. M. Gauger, A. Nazir, B. W. Lovett, A. M. Fox, and M. S. Skolnick, Phys. Rev. Lett. **105**, 177402 (2010).

[27] M. Glässl, A. M. Barth, and V. M. Axt, Phys. Rev. Lett. **110**, 147401 (2013).

[28] P.-L. Ardelt, L. Hanschke, K. A. Fischer, K. Müller, A. Kleinkauf, M. Koller, A. Bechtold, T. Simmet, J. Wierzbowski, H. Riedl, G. Abstreiter, and J. J. Finley, Phys. Rev. B **90**, 241404(R) (2014).

[29] V. M. Axt, T. Kuhn, A. Vagov, and F. M. Peeters, Phys. Rev. B **72**, 125309 (2005).

[30] T. Jakubczyk, V. Delmonte, S. Fischbach, D. Wigger, D. E. Reiter, Q. Mermillod, P. Schnauber, A. Kaganskiy, J.-H. Schulze, A. Strittmatter, S. Rodt, W. Langbein, T. Kuhn, S. Reitzenstein, and J. Kasprzak, ACS Photon. **3**, 2461 (2016).

[31] S. Bounouar, M. Müller, A. M. Barth, M. Glässl, V. M. Axt, and P. Michler, Phys. Rev. B **91**, 161302(R) (2015).

[32] D. E. Reiter, Phys. Rev. B **95**, 125308 (2017).

[33] D. P. S. McCutcheon and A. Nazir, New J. Phys. **12**, 113042 (2010).

[34] I. Wilson-Rae and A. Imamoğlu, Phys. Rev. B **65**, 235311 (2002).

[35] U. Hohenester, A. Laucht, M. Kaniber, N. Hauke, A. Neumann, A. Mohtashami, M. Seliger, M. Bichler, and J. J. Finley, Phys. Rev. B **80**, 201311(R) (2009).

[36] K. Müller, K. A. Fischer, A. Rundquist, C. Dory, K. G. Lagoudakis, T. Sarmiento, Y. A. Kelaita, V. Borish, and J. Vučković, Phys. Rev. X **5**, 031006 (2015).

[37] P. Kaer, T. R. Nielsen, P. Lodahl, A.-P. Jauho, and J. Mørk, Phys. Rev. Lett. **104**, 157401 (2010).

[38] P. Kaer, T. R. Nielsen, P. Lodahl, A.-P. Jauho, and J. Mørk, Phys. Rev. B **86**, 085302 (2012).

[39] C. Roy and S. Hughes, Phys. Rev. X **1**, 021009 (2011).

[40] M. Glässl, L. Sörgel, A. Vagov, M. D. Croitoru, T. Kuhn, and V. M. Axt, Phys. Rev. B **86**, 035319 (2012).

[41] C. Roy and S. Hughes, Phys. Rev. B **85**, 115309 (2012).

[42] S. Hughes and H. J. Carmichael, New J. Phys. **15**, 053039 (2013).

[43] J. Iles-Smith, D. P. S. McCutcheon, A. Nazir, and J. Mørk, Nat. Photon. **11**, 521 (2017).

[44] F. Troiani, J. I. Perea, and C. Tejedor, Phys. Rev. B **74**, 235310 (2006).

[45] A. Carmele and A. Knorr, Phys. Rev. B **84**, 075328 (2011).

[46] B. Krummheuer, V. M. Axt, and T. Kuhn, Phys. Rev. B **65**, 195313 (2002).

[47] L. Besombes, K. Kheng, L. Marsal, and H. Mariette, Phys. Rev. B **63**, 155307 (2001).

[48] A. Vagov, V. M. Axt, T. Kuhn, W. Langbein, P. Borri, and U. Woggon, Phys. Rev. B **70**, 201305(R) (2004).

[49] M. Thorwart, J. Eckel, and E. R. Mucciolo, Phys. Rev. B **72**, 235320 (2005).

[50] M. B. Harouni, Laser Phys. **24**, 115202 (2014).

[51] D. Heinze, A. Zrenner, and S. Schumacher, Phys. Rev. B **95**, 245306 (2017).

[52] G. Lindblad, Commun. Math. Phys. **48**, 119 (1976).

[53] A. Carmele, F. Milde, M.-R. Dachner, M. B. Harouni, R. Roknizadeh, M. Richter, and A. Knorr, Phys. Rev. B **81**, 195319 (2010).

[54] N. Makri and D. E. Makarov, J. Chem. Phys. **102**, 4600 (1995).

[55] N. Makri and D. E. Makarov, J. Chem. Phys. **102**, 4611 (1995).

[56] A. Vagov, M. D. Croitoru, M. Glässl, V. M. Axt, and T. Kuhn, Phys. Rev. B **83**, 094303 (2011).

[57] A. M. Barth, A. Vagov, and V. M. Axt, Phys. Rev. B **94**, 125439 (2016).

[58] M. Cygorek, A. M. Barth, F. Ungar, A. Vagov, and V. M. Axt, Phys. Rev. B **96**, 201201(R) (2017).

[59] A. Strathearn, P. Kirton, D. Kilda, J. Keeling, and B. W. Lovett, Nat. Commun. **9**, 3322 (2018).

[60] B. Krummheuer, V. M. Axt, T. Kuhn, I. D'Amico, and F. Rossi, Phys. Rev. B **71**, 235329 (2005).

[61] S. Lüker, T. Kuhn, and D. E. Reiter, Phys. Rev. B **96**, 245306 (2017).

[62] P. Machnikowski and L. Jacak, Phys. Rev. B **69**, 193302 (2004).

[63] G. Pfanner, M. Seliger, and U. Hohenester, Phys. Rev. B **78**, 195410 (2008).

[64] M. Cosacchi, M. Cygorek, F. Ungar, A. M. Barth, A. Vagov, and V. M. Axt, Phys. Rev. B **98**, 125302 (2018).

[65] *Physics of Group IV Elements and III-V Compounds*, edited by O. Madelung, Landolt-Börnstein, New Series, Group III Vol. 17, Pt. a (Springer, Berlin, 1982).

[66] P. E. Selbmann, M. Gulia, F. Rossi, E. Molinari, and P. Lugli, Phys. Rev. B **54**, 4660 (1996).

Publication 2

"Phonon-Induced Enhancement of Photon Entanglement in Quantum Dot-Cavity Systems"

T. Seidelmann, F. Ungar, A. M. Barth, A. Vagov, V. M. Axt, M. Cygorek, and T. Kuhn.

Author contributions

The author has designed the concept of this study, has performed the numerical data generation and analysis, and has implemented the problem-specific C++ code. He has provided interpretations of the results and has designed the figures in the publication. In particular, he has pinpointed the phonon-induced renormalization as the origin of the unexpected phonon-enhancement. During the publication process, he has organized the submission and revision of the manuscript and has written the answer to the referees.

F. Ungar has participated in the discussion of the results and their interpretations. He has also contributed to the optimization of the presentation, revisions of the draft, and the answers to the referees. In particular, he has suggested the inset in Fig. 1 during the revision process.

A. M. Barth has written the original C++ implementations of the path-integral method, which the numerical studies are based on.

A. Vagov, M. Cygorek, and T. Kuhn have co-supervised this work. In particular, they have participated in the discussion of the results and their interpretations. They have also contributed to the optimization of the presentation, revisions of the draft, and the answers to the referees.

V. M. Axt has advised the author throughout his work as the main supervisor, has obtained the funding for this work, and has provided the practical means. He has written the first draft of the publication and has participated in the discussion of the results and their interpretations. He has also contributed to the optimization of the presentation, revisions of the draft, and the answers to the referees.

Phonon-Induced Enhancement of Photon Entanglement in Quantum Dot-Cavity Systems

T. Seidelmann,[1] F. Ungar,[1] A. M. Barth,[1] A. Vagov,[1,2] V. M. Axt,[1] M. Cygorek,[3] and T. Kuhn[4]

[1]*Universität Bayreuth, Lehrstuhl für Theoretische Physik III, Universitätsstraße 30, 95447 Bayreuth, Germany*
[2]*ITMO University, St. Petersburg 197101, Russia*
[3]*Department of Physics, University of Ottawa, Ottawa, Ontario, Canada K1N 6N5*
[4]*Institut für Festkörpertheorie, Universität Münster, 48149 Münster, Germany*

We report on simulations of the degree of polarization entanglement of photon pairs simultaneously emitted from a quantum dot-cavity system that demand revisiting the role of phonons. Since coherence is a fundamental precondition for entanglement and phonons are known to be a major source of decoherence, it seems unavoidable that phonons can only degrade entanglement. In contrast, we demonstrate that phonons can cause a degree of entanglement that even surpasses the corresponding value for the phonon-free case. In particular, we consider the situation of comparatively small biexciton binding energies and either finite exciton or cavity mode splitting. In both cases, combinations of the splitting and the dot-cavity coupling strength are found where the entanglement exhibits a nonmonotonic temperature dependence which enables entanglement above the phonon-free level in a finite parameter range. This unusual behavior can be explained by phonon-induced renormalizations of the dot-cavity coupling g in combination with a nonmonotonic dependence of the entanglement on g that is present already without phonons.

The appearance of entangled states is one of the showcase effects that highlights most impressively the dramatic conceptual changes brought forth by going over from classical to quantum physics [1,2]. Moreover, realizations of entangled states, mostly with photons, have paved the way toward many innovative applications [3], e.g., in quantum cryptography [4,5], quantum teleportation [6], quantum information processing [7–10], and photonics [11]. In particular, quantum dot (QD) cavity systems have attracted a lot of attention as sources for triggered entangled photon pairs [12–19], not only because these systems hold the promise of a natural integration in solid-state devices. Embedding a QD in a microcavity enables the manipulation of few-electron and few-photon states in a system with high optical nonlinearities, which can be used for realizing a few-photon logic in quantum optical networks [20]. Furthermore, the cavity boosts the quantum yield due to the Purcell effect [14,21] and, for high cavity quality factors Q, it reduces the detrimental effects of phonons on the photon indistinguishability [22].

The essence of entanglement in a bipartite system is the creation of a state that cannot be factorized into parts referring to the constituent subsystems, which requires the buildup of a superposition state. Polarization entanglement between horizontally (H) or vertically (V) polarized photon pairs is established, e.g., by creating superpositions of the states $|HH\rangle$ and $|VV\rangle$ with two photons with either H or V polarizations exploiting the biexciton cascade [12–18]. Starting from the biexciton, the system can decay first into one of the two excitons and a photon with the corresponding

polarization (H or V). The excitons then decay further to the QD ground state emitting a second photon with the same polarization as in the biexciton decay. Ideally, the resulting quantum state is a coherent superposition and maximally entangled. Which-path information introduced, e.g., by the fine-structure splitting of the excitons, leads to an asymmetric superposition and decreased entanglement. The system can also decay from the biexciton directly to the ground state by simultaneous two-photon emission, a process which is much less affected by which-path information than the sequential single-photon decay [23–25].

Obviously, maintaining a coherent superposition requires stable relative phases between the involved states. However, in a solid-state system, the interaction with the environment unavoidably leads to a loss of phase coherence. In particular, phonons are known to provide a major source of decoherence [26–35], which led to the expectation that phonons should always degrade the entanglement. Indeed, recent simulations [24,36,37] are in line with this expectation.

In this Letter, we demonstrate that the phonon influence is not necessarily destructive. On the contrary, phonons can increase the degree of photon entanglement when the destructive effect resulting from phonon-induced decoherence is overcompensated by phonon-related renormalizations of the QD-cavity coupling that shift the system into a regime of higher photon entanglement. A precondition of this mechanism is a decrease of the degree of entanglement with rising QD-cavity coupling g in the phonon-free case in a finite g range. This is realized,

e.g., in the limit of weak biexciton binding and finite exciton or cavity mode splitting. In both cases, the phonon-induced enhancement is found in a finite range of binding energies and couplings g.

Our studies are based on the Hamiltonian [24,37]:

$$
\begin{aligned}
\hat{H} &= \hbar\omega_H |X_H\rangle\langle X_H| + \hbar\omega_V |X_V\rangle\langle X_V| \\
&+ \hbar(\omega_H + \omega_V - \omega_B)|B\rangle\langle B| + \sum_{\ell=H,V} \hbar\omega_\ell^c \hat{a}_\ell^\dagger \hat{a}_\ell \\
&+ \sum_{\mathbf{q}} \hbar\omega_{\mathbf{q}} \hat{b}_{\mathbf{q}}^\dagger \hat{b}_{\mathbf{q}} + \sum_{\mathbf{q},\chi} n_\chi (\gamma_{\mathbf{q}} \hat{b}_{\mathbf{q}}^\dagger + \gamma_{\mathbf{q}}^* \hat{b}_{\mathbf{q}})|\chi\rangle\langle\chi| + \hat{\mathcal{X}}, \quad (1)
\end{aligned}
$$

where $|B\rangle$ is the biexciton state with energy $\hbar(\omega_H + \omega_V - \omega_B)$ and a biexciton binding energy $E_B = \hbar\omega_B$, while $|X_{H/V}\rangle$ denote the two exciton states with energies $\hbar\omega_{H/V}$ that couple to H or V polarized cavity modes with destruction (creation) operators $\hat{a}_{H/V}(\hat{a}_{H/V}^\dagger)$ and mode energies $\hbar\omega_{H/V}^c$. $\hat{b}_{\mathbf{q}}(\hat{b}_{\mathbf{q}}^\dagger)$ are operators that destroy (create) longitudinal acoustic phonons with wave vector $\mathbf{q}$ and energy $\hbar\omega_{\mathbf{q}}$. We consider bulk phonons with a linear dispersion and account for the deformation potential coupling $\gamma_{\mathbf{q}}$. n_χ is the number of electron-hole pairs contained in the states $|\chi\rangle \in \{|B\rangle, |X_{H/V}\rangle\}$. Finally, the Jaynes-Cummings type coupling of the cavity modes to the QD with coupling constant g is given by:

$$
\begin{aligned}
\hat{\mathcal{X}} = -g(&|G\rangle\langle X_H|\hat{a}_H^\dagger + |X_H\rangle\langle B|\hat{a}_H^\dagger \\
&+ |G\rangle\langle X_V|\hat{a}_V^\dagger - |X_V\rangle\langle B|\hat{a}_V^\dagger) + \text{H.c.}, \quad (2)
\end{aligned}
$$

where H.c. stands for the Hermitian conjugate and $|G\rangle$ is the QD ground state, the energy of which is taken as the zero of energy. In addition, we account for cavity losses with a rate κ by the Lindblad operator:

$$
\mathcal{L}_{\text{cav}}[\hat{\rho}] = \sum_{\ell=H,V} \frac{\kappa}{2}(2\hat{a}_\ell\hat{\rho}\hat{a}_\ell^\dagger - \hat{\rho}\hat{a}_\ell^\dagger\hat{a}_\ell - \hat{a}_\ell^\dagger\hat{a}_\ell\hat{\rho}). \quad (3)
$$

We assume that the system is initially prepared in the biexciton state, without photons and that the phonons are initially in equilibrium at a temperature T. This can be achieved, e.g., by using two-photon resonant or near-resonant excitation with short coherent pulses [16, 38–41], which introduces much less decoherence and time jitter than, e.g., pumping the wetting layer and subsequent relaxation to the biexciton. The dynamics of the reduced density matrix $\hat{\rho}$ is determined by the equation:

$$
\frac{d}{dt}\hat{\rho} = -\frac{i}{\hbar}[\hat{H}, \hat{\rho}]_- + \mathcal{L}_{\text{cav}}[\hat{\rho}], \quad (4)
$$

where $[,]_-$ denotes the commutator. As in Ref. [37], we evaluate $\hat{\rho}$ numerically in the subspace spanned by the five states $|B, 0, 0\rangle$, $|X_H, 1, 0\rangle$, $|X_V, 0, 1\rangle$, $|G, 2, 0\rangle$, and

$|G, 0, 2\rangle$, where the numbers $n_{H/V}$ in $|\chi, n_H, n_V\rangle$ denote the number of H/V photons. We use a path-integral approach that does not introduce approximations to the model. This is made possible by recent methodological advances that allow for a natural inclusion of non-Hamiltonian parts of the dynamics (e.g., represented by Lindblad operators) in the path-integral formalism [42] as well as huge improvements of the performance by iterating instead of the augmented density matrix, introduced in the pioneering work of Makri and Makarov [43,44], a partially summed augmented density matrix [45]. We quantify the degree of entanglement by the concurrence, a quantity which has a one-to-one correspondence to the entanglement of formation [46]. To be precise, we use the concurrence of simultaneously emitted photon pairs

$$
C = 2\frac{|\bar{\rho}_{HV}|}{\bar{\rho}_{HH} + \bar{\rho}_{VV}} \quad (5)
$$

(see the Supplemental Material [47] for further details) that can be calculated directly from the time-averaged occupations $\bar{\rho}_{HH}$, $\bar{\rho}_{VV}$ and coherence $\bar{\rho}_{HV}$ of the states $|HH\rangle$ and $|VV\rangle$ [25,37,57]. We focus on simultaneously emitted photon pairs since experiments [58,59] agree with theory [15,37] that this case is favorable for the entanglement.

First, we present results for the situation sketched in Fig. 1(a) where the excitons have a finite fine-structure splitting $\delta = \hbar(\omega_H - \omega_V)$, the biexciton binding energy is zero and both cavity modes are tuned to the two-photon resonance $2\omega_H^c = 2\omega_V^c = \omega_H + \omega_V - \omega_B$. In the situation with phonons, these QD energies denote the polaron-shifted ones. To compare QD-cavity systems with identical energy relations, the energy values are kept the same in the corresponding phonon-free calculations thus keeping the polaron shifts.

Figure 1(b) displays the temperature dependence of the concurrence for three values of the QD-cavity coupling. Only the result for $g = 130 \ \mu$eV agrees with the common expectation that the entanglement should monotonically decrease with temperature. In contrast, for $g = 60 \ \mu$eV and $g = 35 \ \mu$eV, unusual nonmonotonic T dependences are found. Most interestingly, for $g = 35 \ \mu$eV, the concurrence is noticeably higher than the corresponding value obtained without phonons in the entire T range that we consider ($T \in [1 \text{ K}, 100 \text{ K}]$); i.e., for certain values of g we find indeed a phonon-induced enhancement of entanglement while in other cases the expectation that phonons reduce the entanglement is confirmed.

The reason for this remarkable behavior becomes apparent when looking at the g dependence of the concurrence in Fig. 1(c). Already without phonons, the concurrence is a nonmonotonic function of g (purple curve) with a pronounced minimum reached roughly for $g \simeq \delta/2$. Dividing Eq. (4) by the coupling strength g and leaving out the coupling to phonons, the system dynamics is described by the rescaled quantities $t' = gt$,
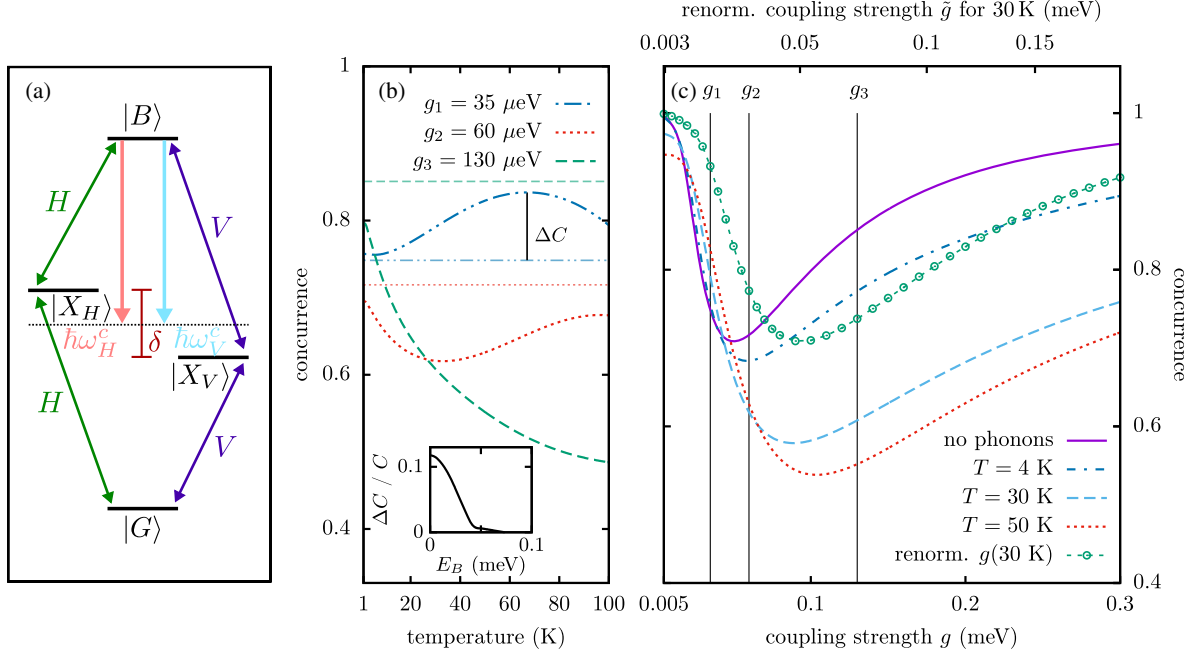
FIG. 1.   (a) Sketch of the level scheme of a QD-cavity system with finite fine-structure splitting, zero biexciton binding energy and two-photon resonant cavity modes. (b) Concurrence as a function of the temperature for three selected values of the QD-cavity coupling. The corresponding values obtained without phonons are drawn as straight (faded) lines with the same linetype. Inset: difference ΔC between the maximum concurrence value at finite temperature and the corresponding phonon-free value normalized by the latter as a function of the biexciton binding energy E_B for $g_1 = 35$ μeV. (c) Concurrence as a function of the QD-cavity coupling for three temperatures together with the phonon-free result. In addition $C[\tilde{g}(g)]$ is plotted using the phonon-renormalized coupling $\tilde{g}(g)$ for $T = 30$ K (indicated on the upper axis), where $C(g)$ is the phonon-free concurrence. The values of the QD-cavity coupling used in (b) are marked in (c) by vertical lines. Parameters: $\delta = 0.1$ meV, $\kappa = 0.025$ ps^{-1}, electron (hole) confinement length $a_e = 3$ nm, $a_h = a_e/1.15$ where we assume a spherical GaAs-type QD with harmonic confinement. All other parameters, e.g., concerning the phonon coupling, are taken from Ref. [60].

$g' = g/g = 1$, $\delta' = \delta/g$, and $\kappa' = \kappa/g$. Since the concurrence is the asymptotic value of the normalized coherence at long averaging times [37], the rescaling of the time is irrelevant. For large values of g, both parameters δ' and κ' tend to zero. This implies that the concurrence approaches unity for large coupling strengths because the which-path information disappears for a vanishing splitting and thus the concurrence is one [37,57]. For very small QD-cavity couplings, κ' and δ' become arbitrarily large. Therefore, the sequential single photon decay via the intermediate exciton states becomes strongly off-resonant and is thus negligible compared with contributions from a direct two-photon transition, which is always resonant in the present case [25]. Since the which-path information is contained only in the sequential decay, the concurrence approaches unity again. But for finite splittings, the concurrence is smaller than one and thus a minimum must appear at a certain coupling strength g.

When phonons are accounted for, the minimum is lowered and shifted to a higher coupling strength depending on the temperature. We attribute the shift to the well known effect of phonon-induced renormalization of the

light-matter coupling [61]. To support this assignment we have estimated the renormalized coupling $\tilde{g}(g)$ as in Ref. [62] by fitting equations with phenomenological renormalizations of a resonantly driven two-level system to path-integral calculations. The results are shown in the Supplemental Material [47]. If the only effect introduced by phonons was the g renormalization, then the value of the concurrence found without phonons at a particular value of g should be shifted by phonons to $\tilde{g}(g)$. Indeed, in Fig. 1(c) we have plotted $C[\tilde{g}(g)]$ using the phonon-renormalized coupling $\tilde{g}(g)$ for $T = 30$ K, where $C(g)$ is the concurrence in the phonon-free case (green curve with circles). We find that, despite the crudeness of the estimation for $\tilde{g}(g)$, the minimum of the shifted curve agrees even quantitatively well with the minimum found in the full path-integral simulation for this temperature (red dotted curve). Since the shift is larger for higher temperatures, displacing the phonon-free curve necessarily leads to higher values of the shifted curves in regions where the phonon-free concurrence is monotonically decreasing with g. Consequently, in this region, phonon-induced enhancement appears for a finite g range.
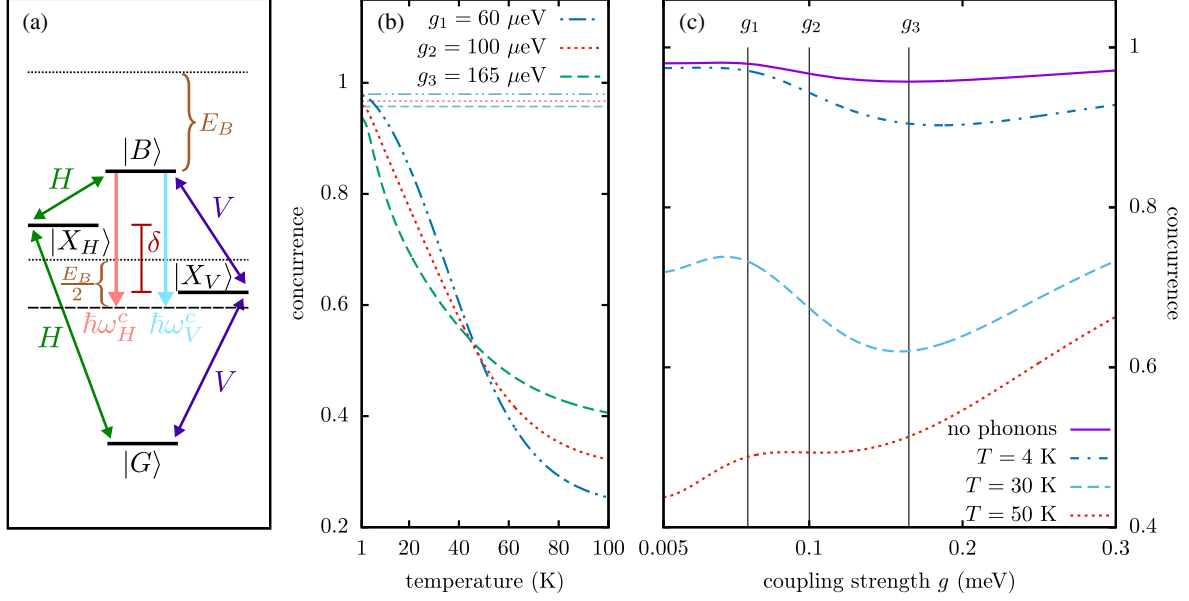
FIG. 2. (a) Sketch of the level scheme of a QD-cavity system with finite fine-structure splitting, biexciton binding energy $E_B = 1$ meV and two-photon resonant cavity modes. (b) Concurrence as a function of the temperature for three selected values of the QD-cavity coupling. The corresponding values obtained without phonons are drawn as straight (faded) lines with the same linetype. (c) Concurrence as a function of the QD-cavity coupling for three temperatures together with the phonon-free result. The values of the QD-cavity coupling used in (b) are marked in (c) by vertical lines. Apart from E_B, the same parameters are used as in Fig. 1.

The total effect of phonons is, however, not merely a shift but also a lowering of the curves with rising temperature, which is indeed due to the dephasing action of phonons. It is important for obtaining a phonon-induced entanglement that the gain in entanglement resulting from the shift of the phonon-free curve due the phonon-induced g renormalization is not destroyed by the overall lowering of the concurrence caused by the decoherence. Figure 1(c) demonstrates that it is indeed possible that the renormalization-induced shift overcompensates the dephasing action. Additionally, when accounting for pure dephasing by introducing a phenomenological rate [23], the phonon-induced enhancement disappears (see the Supplemental Material [47]). This result reaffirms the g renormalization as the main origin of the effect, since it is absent in the phenomenological model.

It is instructive to contrast the above findings with simulations for the more commonly considered situation sketched in Fig. 2(a), where the biexciton binding energy has the finite value $E_B = 1$ meV and the cavity modes are in resonance with the two-photon transition to the biexciton. Again, the phonon-free curve exhibits a minimum which is, however, rather flat [purple line in Fig. 2(c)]. In the limit $g \to \infty$ the concurrence approaches unity since the argument given for the case of vanishing biexciton binding energy applies here as well. For the case that both $g/(\frac{1}{2}E_B)$ and δ/E_B are small parameters, it has been shown analytically in Ref. [37] that the phonon-free concurrence approaches $[(E_B^2 - \delta^2)/(E_B^2 + \delta^2)]$, which is smaller than

one for a finite δ. Including phonons, the reduction of the concurrence for small g values is strongly magnified as seen in Fig. 2(c). Overall, the dephasing action induced by phonons is so strong that the line shape of the concurrence as a function of g is significantly deformed, and the effects related to a renormalization of g cannot be identified. As a consequence, the concurrence monotonically decreases with rising temperature and always stays below the phonon-free calculation for all values of g as exemplarily shown in Fig. 2(b). This demonstrates that the phonon-induced enhancement of entanglement described above can only occur when the g-renormalization effects dominate over the phonon-induced dephasing. The stronger phonon-induced dephasing for E_B on the order of a few meV compared with vanishing E_B has been explained recently [25] by noting that the energies bridged by phonon-assisted processes are closer to the maximum of the phonon spectral density in the former case.

It is worthwhile to note that phonon-induced enhancement of photon entanglement is not restricted to the singular case of vanishing E_B but rather appears for a finite range of binding energies as demonstrated in the inset of Fig. 1(b). The difference ΔC between the maximum concurrence value at finite temperatures and the corresponding phonon-free value is positive clearly for an extended range. Further analysis (shown in the Supplemental Material [47]) reveals that the effect can be observed as long as $E_B \lesssim \delta/2$ holds for our realistic parameters.

We note in passing that the situation considered in Fig. 1 is not the only one where the conditions for phonon-induced entanglement are realized. This phenomenon can also be observed in a system with weak biexciton binding and degenerate excitons where which-path information is introduced by a finite splitting of the cavity modes (see the Supplemental Material [47]). There the concurrence calculated without phonons is again a nonmonotonic function of g, which exhibits even more than one extremum. Also in this case, the phonon-induced renormalization is strong enough to evoke a phonon-induced entanglement for finite parameter ranges.

In conclusion, we demonstrate that phonon-induced renormalizations of the dot-cavity coupling can overcompensate decoherence effects and shift the system to a region of higher entanglement. In combination with a nonmonotonic dependence of the phonon-free concurrence, this can result in a nonmonotonic temperature dependence of the concurrence. Most interestingly, the concurrence can even reach values above the phonon-free level, thus causing phonon-induced photon entanglement.

[1] R. Horodecki, P. Horodecki, M. Horodecki, and K. Horodecki, Rev. Mod. Phys. **81**, 865 (2009).

[2] J. Audretsch, *Entangled Systems: New Directions in Quantum Physics* (Whiley-VCH, Weinheim, 2007).

[3] A. Zeilinger, Phys. Scr. **92**, 072501 (2017).

[4] R. M. Stevenson, R. M. Thompson, A. J. Shields, I. Farrer, B. E. Kardynal, D. A. Ritchie, and M. Pepper, Phys. Rev. B **66**, 081302(R) (2002).

[5] N. Gisin, G. Ribordy, W. Tittel, and H. Zbinden, Rev. Mod. Phys. **74**, 145 (2002).

[6] D. Bouwmeester, J.-W. Pan, K. Mattle, M. Eibl, H. Weinfurter, and A. Zeilinger, Nature (London) **390**, 575 (1997).

[7] J.-W. Pan, Z.-B. Chen, C.-Y. Lu, H. Weinfurter, A. Zeilinger, and M. Żukowski, Rev. Mod. Phys. **84**, 777 (2012).

[8] C. H. Bennett and D. P. DiVincenzo, Nature (London) **404**, 247 (2000).

[9] *Entangled World: The Fascination of Quantum Information and Computation*, edited by J. Audretsch (Whiley-VCH, Weinheim, 2006).

[10] S. C. Kuhn, A. Knorr, S. Reitzenstein, and M. Richter, Opt. Express **24**, 25446 (2016).

[11] J. L. O'Brian, A. Furusawa, and J. Vućković, Nat. Photonics **3**, 687 (2009).

[12] R. M. Stevenson, R. J. Young, P. Atkinson, K. Cooper, D. A. Ritchie, and A. J. Shields, Nature (London) **439**, 179 (2006).

[13] R. Hafenbrak, S. M. Ulrich, P. Michler, L. Wang, A. Rastelli, and O. G. Schmidt, New J. Phys. **9**, 315 (2007).

[14] A. Dousse, J. Suffczyński, A. Beveratos, O. Krebs, A. Lemaître, I. Sagnes, J. Bloch, P. Voisin, and P. Senellart, Nature (London) **466**, 217 (2010).

[15] E. del Valle, New J. Phys. **15**, 025019 (2013).

[16] M. Müller, S. Bounouar, K. D. Jöns, M. Glässl, and P. Michler, Nat. Photonics **8**, 224 (2014).

[17] N. Akopian, N. H. Lindner, E. Poem, Y. Berlatzky, J. Avron, D. Gershoni, B. D. Gerardot, and P. M. Petroff, Phys. Rev. Lett. **96**, 130501 (2006).

[18] A. Orieux, M. A. M. Versteegh, K. D. Jöns, and S. Ducci, Rep. Prog. Phys. **80**, 076001 (2017).

[19] C. Sánchez Muñoz, F. P. Laussy, C. Tejedor, and E. del Valle, New J. Phys. **17**, 123021 (2015).

[20] A. Faraon, A. Majumdar, D. Englund, E. Kim, M. Bajcsy, and J. Vukovi, New J. Phys. **13**, 055025 (2011).

[21] A. Badolato, K. Hennessy, M. Atatüre, J. Dreiser, E. Hu, P. M. Petroff, and A. Imamoğlu, Science **308**, 1158 (2005).

[22] T. Grange, N. Somaschi, C. Antón, L. De Santis, G. Coppola, V. Giesz, A. Lemaître, I. Sagnes, A. Auffèves, and P. Senellart, Phys. Rev. Lett. **118**, 253602 (2017).

[23] S. Schumacher, J. Förstner, A. Zrenner, M. Florian, C. Gies, P. Gartner, and F. Jahnke, Opt. Express **20**, 5335 (2012).

[24] D. Heinze, A. Zrenner, and S. Schumacher, Phys. Rev. B **95**, 245306 (2017).

[25] T. Seidelmann, F. Ungar, M. Cygorek, A. Vagov, A. M. Barth, T. Kuhn, and V. M. Axt, Phys. Rev. B **99**, 245301 (2019).

[26] J. Förstner, C. Weber, J. Danckwerts, and A. Knorr, Phys. Rev. Lett. **91**, 127401 (2003).

[27] A. Vagov, V. M. Axt, T. Kuhn, W. Langbein, P. Borri, and U. Woggon, Phys. Rev. B **70**, 201305(R) (2004).

[28] V. M. Axt, T. Kuhn, A. Vagov, and F. M. Peeters, Phys. Rev. B **72**, 125309 (2005).

[29] P. Machnikowski, Phys. Rev. B **78**, 195320 (2008).

[30] A. J. Ramsay, A. V. Gopal, E. M. Gauger, A. Nazir, B. W. Lovett, A. M. Fox, and M. S. Skolnick, Phys. Rev. Lett. **104**, 017402 (2010).

[31] C. Roy and S. Hughes, Phys. Rev. Lett. **106**, 247403 (2011).

[32] T. Close, E. M. Gauger, and B. W. Lovett, New J. Phys. **14**, 113004 (2012).

[33] P. Kaer and J. Mørk, Phys. Rev. B **90**, 035312 (2014).

[34] D. E. Reiter, Phys. Rev. B **95**, 125308 (2017).

[35] A. Reigue, J. Iles-Smith, F. Lux, L. Monniello, M. Bernard, F. Margaillan, A. Lemaitre, A. Martinez, D. P. S. McCutcheon, J. Mørk, R. Hostein, and V. Voliotis, Phys. Rev. Lett. **118**, 233602 (2017).

[36] M. B. Harouni, Laser Phys. **24**, 115202 (2014).

[37] M. Cygorek, F. Ungar, T. Seidelmann, A. M. Barth, A. Vagov, V. M. Axt, and T. Kuhn, Phys. Rev. B **98**, 045303 (2018).

[38] L. Hanschke, K. A. Fischer, S. Appel, D. Lukin, J. Wierzbowski, S. Sun, R. Trivedi, J. Vucković, J. J. Finley, and K. Müller, npj Quantum Inf. **4**, 43 (2018).

[39] S. Bounouar, M. Müller, A. M. Barth, M. Glässl, V. M. Axt, and P. Michler, Phys. Rev. B **91**, 161302(R) (2015).

[40] D. Huber, M. Reindl, Y. Huo, H. Huang, J. S. Wildmann, O. G. Schmidt, A. Rastelli, and R. Trotta, Nat. Commun. **8,** 15506 (2017).

[41] M. Reindl, K. D. Jöns, D. Huber, C. Schimpf, Y. Huo, V. Zwiller, A. Rastelli, and R. Trotta, Nano Lett. **17,** 4090 (2017).

[42] A. M. Barth, A. Vagov, and V. M. Axt, Phys. Rev. B **94,** 125439 (2016).

[43] N. Makri and D. E. Makarov, J. Chem. Phys. **102,** 4600 (1995).

[44] N. Makri and D. E. Makarov, J. Chem. Phys. **102,** 4611 (1995).

[45] M. Cygorek, A. M. Barth, F. Ungar, A. Vagov, and V. M. Axt, Phys. Rev. B **96,** 201201(R) (2017).

[46] W. K. Wootters, Quantum Inf. Comput. **1,** 27 (2001).

[47] See Supplemental Material at http://link.aps.org/supplemental/10.1103/PhysRevLett.123.137401 for a precise definition of the concurrence of simultaneously emitted photon pairs, details how the renormalization of the coupling g is estimated, some numerical remarks, and for an additional configuration exhibiting phonon-induced entanglement. It also includes Refs. [48–56] in addition to references already cited in the main text. Results obtained using an approximate phenomenological rate model are shown as well as results regarding the dependence on the binding energy.

[48] W. K. Wootters, Phys. Rev. Lett. **80,** 2245 (1998).

[49] G. Pfanner, M. Seliger, and U. Hohenester, Phys. Rev. B **78,** 195410 (2008).

[50] M. Cosacchi, M. Cygorek, F. Ungar, A. M. Barth, A. Vagov, and V. M. Axt, Phys. Rev. B **98,** 125302 (2018).

[51] D. F. V. James, P. G. Kwiat, W. J. Munro, and A. G. White, Phys. Rev. A **64,** 052312 (2001).

[52] M. E. Reimer, M. P. van Kouwen, A. W. Hidma, M. H. M. van Weert, E. P. A. M. Bakkers, L. P. Kouwenhoven, and V. Zwiller, Nano Lett. **11,** 645 (2011).

[53] F. Ding, R. Singh, J. D. Plumhof, T. Zander, V. K řápek, Y. H. Chen, M. Benyoucef, V. Zwiller, K. Dörr, G. Bester, A. Rastelli, and O. G. Schmidt, Phys. Rev. Lett. **104,** 067405 (2010).

[54] R. Trotta, P. Atkinson, J. D. Plumhof, E. Zallo, R. O. Rezaev, S. Kumar, S. Baunack, J. R. Schrter, A. Rastelli, and O. G. Schmidt, Adv. Mater. **24,** 2668 (2012).

[55] R. Trotta, E. Zallo, E. Magerl, O. G. Schmidt, and A. Rastelli, Phys. Rev. B **88,** 155312 (2013).

[56] F. Troiani, J. I. Perea, and C. Tejedor, Phys. Rev. B **74,** 235310 (2006).

[57] A. Carmele and A. Knorr, Phys. Rev. B **84,** 075328 (2011).

[58] R. M. Stevenson, A. J. Hudson, A. J. Bennett, R. J. Young, C. A. Nicoll, D. A. Ritchie, and A. J. Shields, Phys. Rev. Lett. **101,** 170501 (2008).

[59] S. Bounouar, C. de la Haye, M. Strau, P. Schnauber, A. Thoma, M. Gschrey, J.-H. Schulze, A. Strittmatter, S. Rodt, and S. Reitzenstein, Appl. Phys. Lett. **112,** 153107 (2018).

[60] B. Krummheuer, V. M. Axt, T. Kuhn, I. D'Amico, and F. Rossi, Phys. Rev. B **71,** 235329 (2005).

[61] A. J. Ramsay, T. M. Godden, S. J. Boyle, E. M. Gauger, A. Nazir, B. W. Lovett, A. M. Fox, and M. S. Skolnick, Phys. Rev. Lett. **105,** 177402 (2010).

[62] A. Vagov, M. Glässl, M. D. Croitoru, V. M. Axt, and T. Kuhn, Phys. Rev. B **90,** 075309 (2014).

Supplement: Phonon-Induced Enhancement of Photon Entanglement in Quantum Dot-Cavity Systems

T. Seidelmann,[1] F. Ungar,[1] A. M. Barth,[1] A. Vagov,[1, 2] V. M. Axt,[1] M. Cygorek,[3] and T. Kuhn[4]

[1] *Universität Bayreuth, Lehrstuhl für Theoretische Physik III,*
Universitätsstraße 30, 95447 Bayreuth, Germany
[2] *ITMO University, St. Petersburg, 197101, Russia*
[3] *Department of Physics, University of Ottawa, Ottawa, Ontario, Canada K1N 6N5*
[4] *Institut für Festkörpertheorie, Universität Münster, 48149 Münster, Germany*

CONCURRENCE OF SIMULTANEOUSLY EMITTED PHOTONS

The concurrence is a widely used measure for the entanglement of a bipartite system. It has a one-to-one correspondence to the entanglement of formation [1] which represents the amount of pure-state entanglement that is at least present in a mixed state described by a given density matrix. Even though the entanglement of formation is more intuitive, the concurrence is usually preferred since it can be extracted directly from the values of the reduced density matrix of the bipartite system for which the entanglement is to be measured [2].

It is worthwhile to note that the photons emitted from the biexciton-exciton cascade can be subdivided in different ways into bipartite subsystems [3]. The associated concurrences are not necessarily equivalent since they may exhibit opposite trends when varying parameters such as, e.g., the cavity losses [3]. Widely used is the concurrence of all photon pairs that are detected in coincidence measurements without discriminating between the detection times of the two photons [3–7]. This choice results in a high signal yield but measurements [8, 9] as well as theoretical considerations [3, 10] indicate that significantly higher degrees of entanglement can be reached by selecting simultaneously emitted photon pairs. For this reason the concurrence of simultaneously emitted pairs is preferred in the present study. The more general expression given in Ref. [2] reduces in our case to

$$C = 2\,|\bar{\rho}^N_{HV}|, \tag{S1}$$

where the normalized two-photon coherence

$$\bar{\rho}^N_{HV} = \frac{\bar{\rho}_{HV}}{\bar{\rho}_{HH} + \bar{\rho}_{VV}} \tag{S2}$$

is calculated from the time-averaged elements of the reduced density matrix

$$\bar{\rho}_{mn} = \frac{1}{T_{\mathrm{av}}} \int\limits_0^{T_{\mathrm{av}}} \langle mm|\hat{\rho}(t)|nn\rangle \, \mathrm{d}t. \tag{S3}$$

Here, $|HH\rangle := |G, 2, 0\rangle$ ($|VV\rangle := |G, 0, 2\rangle$) denotes the state with two horizontally (vertically) polarized photons. The averaging is performed until the time T_{av} is reached where the initially prepared biexciton has fully decayed and the system has reached its ground state without any photons inside the cavity.

In experiments, the two-photon density matrix, from which the concurrence can be derived, is usually reconstructed using quantum state tomography, a technique based on polarization-dependent photon coincidence measurements [11]. This technique gives access to information about the polarization degree of freedom and the delay time between the two detection events. The concurrence of simultaneously emitted photon pairs can be obtained from the reconstructed density matrix elements in the limit where the delay time approaches zero. Typically, in the corresponding experiments, data points are recorded over extended delay time intervals. Here, the limit of zero delay time can be approached by using time-windowing techniques where signals over different delay time windows are recorded and then the data is extrapolated towards zero delay time [8, 9].

RENORMALIZATION OF THE QUANTUM DOT-CAVITY COUPLING

In the main text we argue that the shift of the minimum in the concurrence plotted versus the dot-cavity coupling g is caused by the phonon-induced renormalization of g. This renormalization occurs already in a two-level system

where it is much simpler to analyze than in the five-level system considered in the present manuscript. For vanishing biexciton binding energy and the usually not very large fine-structure splitting, the transitions from the biexciton to the exciton states and from the exciton states to the ground state are similar and their phonon-induced renormalization can be expected to be close to the case of resonant coupling. Therefore, we followed Ref. [12] in order to obtain a simple estimate for the renormalization, i.e., we have performed path-integral calculations for a resonantly driven two-level system with the same dot and phonon parameters as used in the main text but for $\kappa = 0$. For driving with constant amplitude the exciton occupation is well fitted by the expression:

$$\rho_X = \frac{1}{2}\big[1 - e^{-\Gamma t}\cos(\omega t)\big], \tag{S4}$$

where $\Gamma = \Gamma(g, T)$ and $\omega = \omega(g, T)$ are used as fitting parameters. As explained in detail in Ref. [12], the renormalized dot-cavity coupling is related to Γ and ω by:

$$\tilde{g}(g, T) = [\Gamma^2(g, T) + \omega^2(g, T)]/(4g) \tag{S5}$$
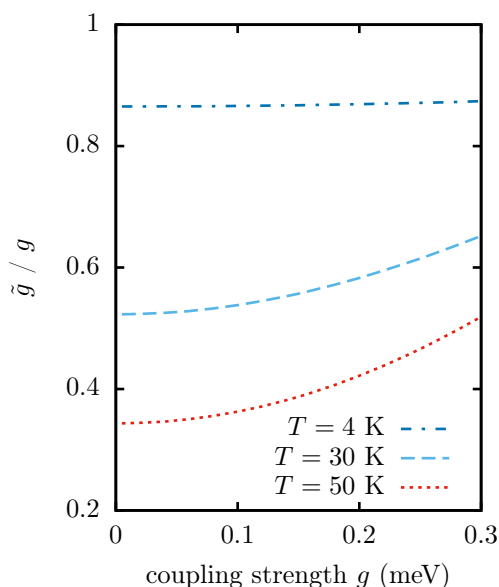
FIG. S1. Renormalized dot-cavity coupling $\tilde{g}(g, T)/g$ as a function of the original coupling g for different temperatures.

Figure S1 displays the resulting renormalized dot-cavity coupling as a function of the original coupling for different temperatures. Clearly, for not too high values of g (which constitutes the typical situation) the phonon renormalization leads to a reduction of the effective coupling. Thus, in order to achieve the same effect with the renormalized g as without renormalization one needs to increase the bare value of g, which explains why the minimum in Fig. 1(c) in the main text is shifted to higher g values.

PHONON-INDUCED ENTANGLEMENT FOR DEGENERATE EXCITONS AND FINITE CAVITY MODE SPLITTING

In this section we present numerical simulations of the concurrence for the situation sketched in Fig. S2(a), i.e., a system with vanishing biexciton binding energy, degenerate excitons and cavity modes with a finite splitting given by $\delta^c = \hbar(\omega_H^c - \omega_V^c)$. Since the excitons are degenerate, which-path information is introduced in this configuration only by the cavity mode splitting.

The concurrence is again a non-monotonic function of g already in the phonon-free case [purple curve in Fig. S2(c)]. However, the situation here is more involved than in Fig. 1(c) in the main text, since instead of a single minimum we now have two well pronounced minima. Accounting for phonons, we observe also in this configuration a clear shift of the curves toward higher g values with rising temperature accompanied by an overall lowering of the curves. As in

FIG. S2. (a) Sketch of the level scheme of a QD-cavity system with finite cavity mode splitting, zero biexciton binding energy, and degenerate excitons. (b) Concurrence as a function of the temperature for three selected values of the QD-cavity coupling. The corresponding values obtained without phonons are drawn as straight (faded) lines with the same linetype. The inset shows the difference ΔC between the maximum concurrence value at a finite temperature and the corresponding phonon-free value (only positive values are shown) normalized 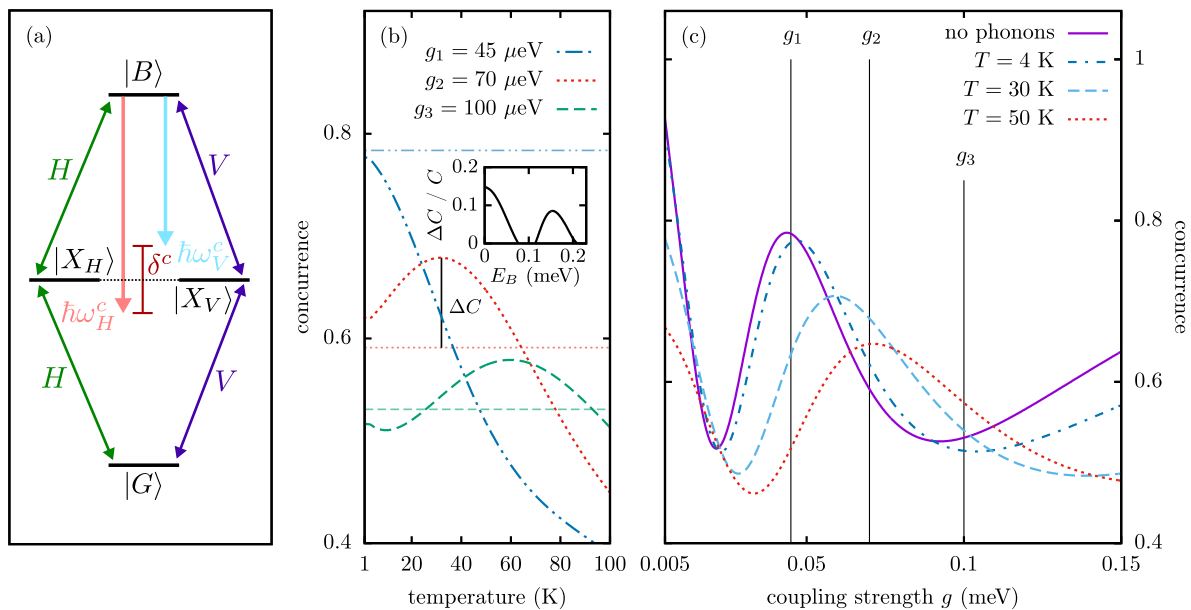by the latter as a function of the biexciton binding energy E_B for $g_2 = 70$ µeV. In the case of a finite E_B, the cavity modes are adjusted such that their mean energy coincides with the degenerate exciton energy $\hbar\omega_X$: $\hbar\omega^c_{H/V} = \hbar\omega_X \pm \delta^c/2$. (c) Concurrence as a function of the QD-cavity coupling for three temperatures together with the phonon-free result. The values of the QD-cavity coupling used in (b) are marked in (c) by vertical lines. Parameters: $\delta^c = 0.07$ meV, $\kappa = 0.05\,\mathrm{ps}^{-1}$. All other parameters are the same as in Fig. 1 in the main text.

Fig. 1(c) in the main text also here the shift caused by the renormalization is the dominant phonon-induced effect and consequently the temperature dependence of the concurrence depends crucially on the chosen value of g [cf. Fig. S2(b)]. For example, for $g = 45\,\mu\mathrm{eV}$ we find the usually encountered monotonic decrease with rising temperature. In contrast, for $g = 70\,\mu\mathrm{eV}$ and $g = 100\,\mu\mathrm{eV}$ the concurrence exhibits different non-monotonic temperature dependences. In both cases extended ranges for g are found where the concurrence reaches values above the corresponding phonon-free level. This demonstrates that the phenomenon of phonon-induced entanglement as described in the main text can also be observed in a configuration where the cavity modes are split while the excitons are degenerate and the biexciton binding is weak. Again, similar to the configuration discussed in the main text, this effect occurs for a finite range of biexciton binding energies [cf. inset panel (b)]. Here, the effect can be observed even when the binding energy is a few times the value of the splitting δ^c.

DEPENDENCE ON THE BIEXCITON BINDING ENERGY

The effect of phonon-induced enhancement of photon entanglement does not only occur in the singular case of a vanishing biexciton binding energy but rather for a finite range of binding energies depending on the respective splitting. It is worthwhile to note that apart from the natural occurrence of QDs with small biexciton binding energies, the biexciton binding energy can also be tuned into this regime, e.g., by the application of an electrical field [13] or a biaxial strain [14, 15], or both combined [16]. In the main text, the case of a vanishing and a finite (large) E_B value are discussed in detail and presented in Figs. 1 and 2 for a quantum dot-cavity system with finite fine-structure splitting and two photon resonant cavity modes. While in the first case phonon-induced enhancement can be observed this effect does not occur in the latter one. A continuous transition between these two types of behavior is expected.

Figure S3 shows the dependence on the biexciton binding energy E_B of the difference ΔC between the maximum concurrence value at a finite temperature and the corresponding phonon-free value normalized by the latter one. Figure S3(a) displays results for the situation considered in the main text where the cavity modes are degenerate
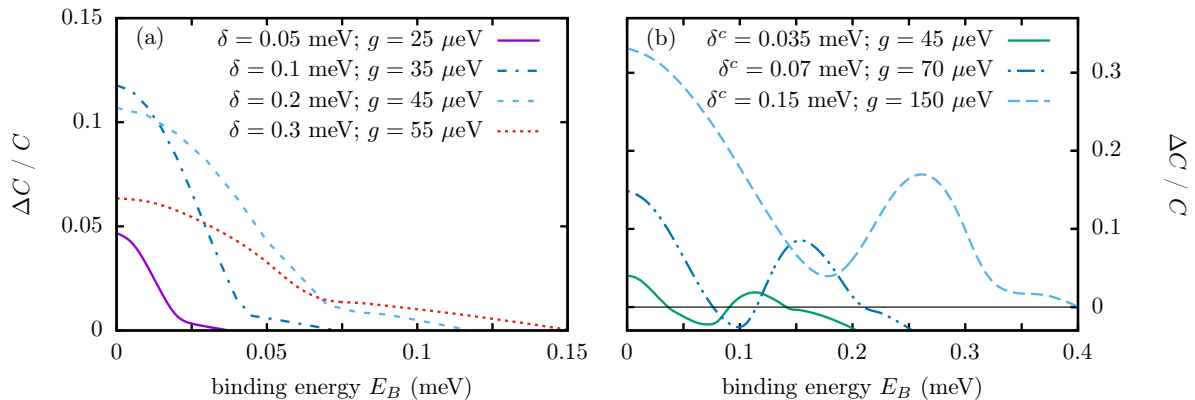
FIG. S3. Difference ΔC between the maximum concurrence value at a finite temperature and the corresponding phonon-free value normalized by the latter as a function of the biexciton binding energy E_B. (a) Results for a QD-cavity system with two-photon resonant cavity modes and cavity loss rate $\kappa = 0.025$ ps^{-1} for four different combinations of finite fine-structure splittings δ and light-matter coupling strengths g. Corresponding level schemes can be found in the main text in Figs. 1 and 2. (b) Results for a QD-cavity system with degenerate excitons and cavity loss rate $\kappa = 0.05$ ps^{-1} for three different combinations of finite cavity mode splittings δ^c and light-matter coupling strengths g. The corresponding level scheme for a vanishing E_B can be found in Fig. S2. In the case of a finite binding energy, the cavity modes are adjusted such that their mean energy coincides with the degenerate exciton energy $\hbar\omega_X$: $\hbar\omega_{H/V}^c = \hbar\omega_X \pm \delta^c/2$.

and the excitons exhibit a finite fine-structure splitting δ, while the curves in Figure S3(b) are obtained for the case described in the previous section where the excitons are degenerate and the cavity modes are split. Different combinations of exciton (cavity mode) splittings δ (δ^c) and coupling strengths g are considered. Indeed, in both QD-cavity configurations discussed in the main text and the supplement, which exhibit phonon-induced enhancement of photon entanglement, this effect occurs for a finite range of binding energies. For both configurations this range is roughly proportional to the respective splitting δ or δ^c. In the case of a QD-system with a finite fine-structure splitting δ and two-photon resonant cavity modes, the effect can be seen until the binding energy reaches approximately half the value of the splitting δ [cf. Fig. S3(a)].

For the second QD-cavity configuration [Fig. S3(b), degenerate exciton energies, finite cavity mode splitting δ^c] the situation is more involved since ΔC turns out to depend non-monotonically on E_B. Nevertheless, also here a finite range of binding energies exists where phonon-induced enhancement of photon entanglement can be found. Again this range is roughly proportional to the splitting δ^c. For some combinations of g and δ^c, the value of ΔC first drops below zero and then phonon-induced entanglement enhancement is recovered at higher values of E_B, while for other combinations the minimum of ΔC as a function of E_B has a positive value. In all cases, phonon-induced enhancement is observed in the E_B range from zero to at least δ^c. After ΔC recovers from its minimum, positive values, indicating the entanglement enhancement compared with the phonon-free case, are found for binding energies approximately up to 2.5 - 4 times the value of the splitting δ^c.

PHENOMENOLOGICAL DEPHASING RATE MODEL

A simple standard approximate method used to model pure dephasing is the introduction of phenomenological pure dephasing rates [5, 17]. Instead of the exact treatment of the continuum of longitudinal acoustic phonons, a Lindblad-type operator is introduced. Here, we follow the methodology of Ref. [5] and use the operator

$$\mathcal{L}_{PD}[\hat{\rho}] = -\frac{1}{2} \sum_{\substack{\chi,\chi' \\ \chi \neq \chi'}} \gamma_{PD} |\chi\rangle\langle\chi|\hat{\rho}|\chi'\rangle\langle\chi'|, \tag{S6}$$

with $\chi, \chi' \in \{G, X_H, X_V, B\}$ and a pure dephasing rate γ_{PD}. Typical values for γ_{PD} correspond to several µeV. In Fig. S4, results are shown for the two configurations discussed in Fig. 1 of the main text and Fig. S2, where phonon-induced enhancement of photon entanglement has been found in simulations fully accounting for phonons on a microscopic level.
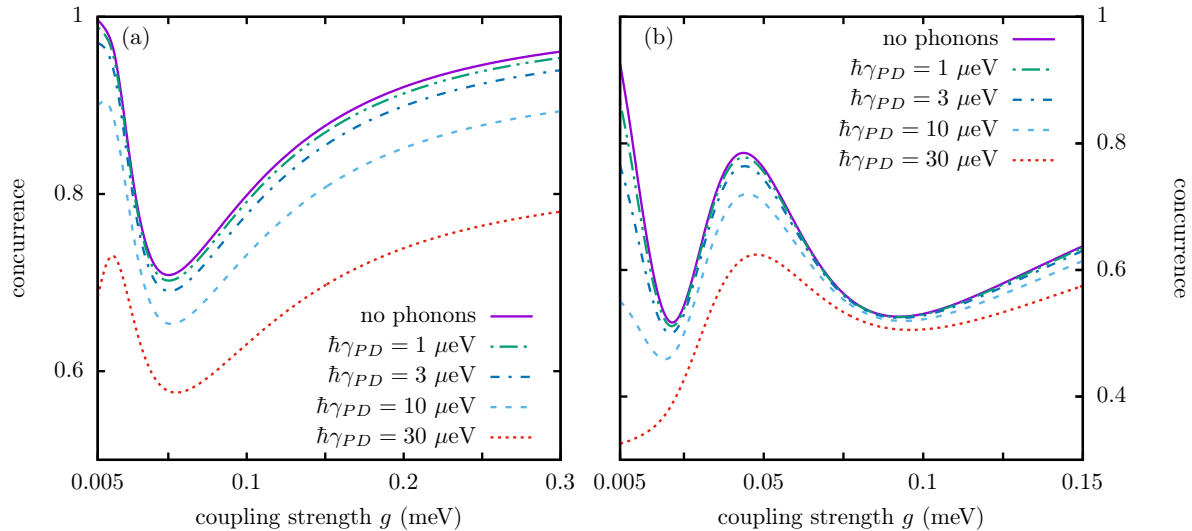
FIG. S4. Results obtained using a phenomenological pure dephasing rate model with different rates γ_{PD} instead of the exact path-integral method. (a) Results for the configuration discussed in Fig. 1 in the main text with parameters $\delta = 0.1$ meV, $\kappa = 0.025$ ps^{-1}. (b) Results for the configuration discussed in Fig. S2 with parameters $\delta^c = 0.07$ meV, $\kappa = 0.05$ ps^{-1}.

Clearly, the effect of phonon-enhanced entanglement does not occur, as the introduction of a pure dephasing rate just leads to a reduction of the concurrence. Furthermore, when one models a higher temperature with a higher loss rate γ_{PD}, an increasing temperature results always in a decreasing degree of entanglement. Thus, the simple phenomenological rate approximation is not sufficient to model the system dynamics in this situation. This finding further strengthens the explanation of the effect given in the main text where we concluded that the phonon-induced enhancement appears because of a renormalization of the light-matter coupling g. This renormalization is, however, absent in the simple rate model and, consequently, the phonon-induced enhancement of photon entanglement does not appear.

NUMERICAL REMARKS

We use for our simulations a recently developed real-time path-integral algorithm to determine the temporal evolution of the reduced density matrix. Two major achievements enable us to obtain numerically complete results for the dynamics of the biexciton cascade coupled to a continuum of longitudinal acoustic phonons. The first is a translation of concepts originally developed in Hilbert space [18, 19] to Liouville space [20], which allows us to account for non-Hamiltonian contributions, like the Lindblad-type losses, to the dynamics. The second is a reformulation of the algorithm to perform the sum over paths. Instead of the widely used iteration scheme worked out by Makri and Makarov [18, 19] for the so called *augmented density matrix*, only a partially summed augmented density matrix is iterated. A detailed derivation and description of this improved iteration scheme can be found in the supplement of Ref. [21]. For systems like quantum dots coupled to cavities and longitudinal acoustic phonons, the numerical demand is reduced by many orders of magnitude in this way. Two parameters, the step size of the time discretization Δt and the number of time steps N_{mem} used to scan the finite memory, determine the quality of the numerical results. These parameters can be well controlled and we speak of *numerically complete results* when no visible change of the results occurs when further decreasing Δt or increasing N_{mem}. For the QD-cavity systems considered in the present paper, numerically converged results are obtained for $\Delta t = 0.5$ ps and $N_{\mathrm{mem}} = 7$.

[1] W. K. Wootters, Quantum Inf. Comput. **1**, 27 (2001).
[2] W. K. Wootters, Phys. Rev. Lett. **80**, 2245 (1998).
[3] M. Cygorek, F. Ungar, T. Seidelmann, A. M. Barth, A. Vagov, V. M. Axt, and T. Kuhn, Phys. Rev. B **98**, 045303 (2018).
[4] G. Pfanner, M. Seliger, and U. Hohenester, Phys. Rev. B **78**, 195410 (2008).

[5] S. Schumacher, J. Förstner, A. Zrenner, M. Florian, C. Gies, P. Gartner, and F. Jahnke, Opt. Express **20**, 5335 (2012).

[6] D. Heinze, A. Zrenner, and S. Schumacher, Phys. Rev. B **95**, 245306 (2017).

[7] M. Cosacchi, M. Cygorek, F. Ungar, A. M. Barth, A. Vagov, and V. M. Axt, Phys. Rev. B **98**, 125302 (2018).

[8] R. M. Stevenson, A. J. Hudson, A. J. Bennett, R. J. Young, C. A. Nicoll, D. A. Ritchie, and A. J. Shields, Phys. Rev. Lett. **101**, 170501 (2008).

[9] S. Bounouar, C. de la Haye, M. Strau, P. Schnauber, A. Thoma, M. Gschrey, J.-H. Schulze, A. Strittmatter, S. Rodt, and S. Reitzenstein, Appl. Phys. Lett. **112**, 153107 (2018).

[10] E. del Valle, New J. Phys. **15**, 025019 (2013).

[11] D. F. V. James, P. G. Kwiat, W. J. Munro, and A. G. White, Phys. Rev. A **64**, 052312 (2001).

[12] A. Vagov, M. Glässl, M. D. Croitoru, V. M. Axt, and T. Kuhn, Phys. Rev. B **90**, 075309 (2014).

[13] M. E. Reimer, M. P. van Kouwen, A. W. Hidma, M. H. M. van Weert, E. P. A. M. Bakkers, L. P. Kouwenhoven, and V. Zwiller, Nano Letters **11**, 645 (2011).

[14] F. Ding, R. Singh, J. D. Plumhof, T. Zander, V. Křápek, Y. H. Chen, M. Benyoucef, V. Zwiller, K. Dörr, G. Bester, A. Rastelli, and O. G. Schmidt, Phys. Rev. Lett. **104**, 067405 (2010).

[15] R. Trotta, P. Atkinson, J. D. Plumhof, E. Zallo, R. O. Rezaev, S. Kumar, S. Baunack, J. R. Schrter, A. Rastelli, and O. G. Schmidt, Advanced Materials **24**, 2668 (2012).

[16] R. Trotta, E. Zallo, E. Magerl, O. G. Schmidt, and A. Rastelli, Phys. Rev. B **88**, 155312 (2013).

[17] F. Troiani, J. I. Perea, and C. Tejedor, Phys. Rev. B **74**, 235310 (2006).

[18] N. Makri and D. E. Makarov, J. Chem. Phys. **102**, 4600 (1995).

[19] N. Makri and D. E. Makarov, J. Chem. Phys. **102**, 4611 (1995).

[20] A. M. Barth, A. Vagov, and V. M. Axt, Phys. Rev. B **94**, 125439 (2016).

[21] M. Cygorek, A. M. Barth, F. Ungar, A. Vagov, and V. M. Axt, Phys. Rev. B **96**, 201201(R) (2017).

Publication 3

"Transiently changing shape of the photon number distribution in a quantum-dot–cavity system driven by chirped laser pulses"

M. Cosacchi, **T. Seidelmann**, F. Ungar, M. Cygorek, A. Vagov, and V. M. Axt.

Phys. Rev. B **101**, 205304 (2020).

Author contributions

M. Cosacchi has designed the concept of this study, has performed the numerical data generation and analysis, and has implemented the problem-specific C++ code. He has provided interpretations of the results and has written the first draft of the publication. During the publication process, he has moderated all discussions, has organized the submission and revision of the manuscript, and has written the answer to the referees.

The author has participated in the general discussion of the results and their interpretations. Furthermore, he has discussed the results in detail with M. Cosacchi and has contributed the interpretation in terms of the laser-dressed states. He has also contributed to revisions of the draft and the answers to the referees.

F. Ungar has participated in the general discussion of the results and their interpretations. Furthermore, he has discussed the results in detail with M. Cosacchi and has also contributed to revisions of the draft and the answers to the referees.

M. Cygorek and A. Vagov have co-supervised this work. In particular, they have participated in the discussion of the results and their interpretations. They have also contributed to the optimization of the presentation, revisions of the draft, and the answers to the referees.

V. M. Axt has advised M. Cosacchi throughout his work as the main supervisor, has obtained the funding for this work, and has provided the practical means. He has participated in the discussion of the results and their interpretations. He has also contributed to the optimization of the presentation, revisions of the draft, and the answers to the referees.

Transiently changing shape of the photon number distribution in a quantum-dot–cavity system driven by chirped laser pulses

M. Cosacchi,[1] T. Seidelmann,[1] F. Ungar,[1] M. Cygorek,[2] A. Vagov,[1,3] and V. M. Axt[1]

[1]*Theoretische Physik III, Universität Bayreuth, D-95440 Bayreuth, Germany*
[2]*Department of Physics, University of Ottawa, Ottawa, Ontario, Canada K1N 6N5*
[3]*ITMO University, St. Petersburg, 197101, Russia*

We have simulated the time evolution of the photon number distribution in a semiconductor quantum-dot–microcavity system driven by chirped laser pulses and compare with unchirped results. When phonon interactions with the dot are disregarded—thus corresponding to the limit of atomic cavity systems—chirped pulses generate photon number distributions that change their shape drastically in the course of time. Phonons have a strong and qualitative impact on the photon statistics. The asymmetry between phonon absorption and emission destroys the symmetry of the photon distributions obtained for positive and negative chirps. While for negative chirps transient distributions resembling thermal ones are observed, for positive chirps the photon number distribution still resembles its phonon-free counterpart but with overall smoother shapes. In sharp contrast, using unchirped pulses of the same pulse area and duration wave packets are found that move up and down the Jaynes-Cummings ladder with a bell shape that changes little in time. For shorter pulses and lower driving strength Rabi-like oscillations occur between low photon number states. For all considered excitation conditions transitions between sub- and super-Poissonian statistics are found at certain times. For resonant driving with low intensity the Mandel parameter oscillates and is mostly negative, which indicates a nonclassical state in the cavity field. Finally, we show that it is possible that the Mandel parameter dynamically approaches zero and still the photon distribution exhibits two maxima and thus is far from being a Poissonian.

I. INTRODUCTION

Semiconductor quantum-dot–cavity (QDC) systems continue to raise attention as highly integrable on-demand emitters of nonclassical states of light. In particular, QDCs have proven to be rather successful providing, e.g., reliable on-demand high quality single photon sources [1–10] as well as sources for entangled photon pairs [11–18]. Clearly, QDCs support a much larger class of excitations when higher mean photon numbers are reached. The additional degrees of freedom provided by higher number photon states obviously allow for a rich variety of dynamical scenarios and may open the way to new kinds of applications such as, e.g., the encoding of quantum information in the photon number state distribution. These possibilities are, however, far from being explored.

Often, the first step to characterize systems with photon distributions ranging up to higher photon numbers is to record a few characteristic numbers such as the mean photon number [19] and/or the Mandel parameter [20]. In simple cases, the mean photon number is indeed enough to capture the whole information about the photon distribution even when the latter is time dependent. This applies in particular when photons are generated by classically driving an empty cavity without a quantum dot (QD) where the photonic system is at all times in a coherent state and thus the distribution is a Poissonian [21,22], i.e., in this case the photonic excitation is always as close as possible to a classical light field and thus nonclassical

states cannot be reached. Moreover, although the mean photon number varies in time, the photon distribution keeps its shape at all times.

The situation is different when a system with few discrete levels near resonance to a cavity mode such as an atom or a quantum dot is placed inside the cavity. When driving transitions between these discrete levels deviations from the coherent state may occur as is evident, e.g., by monitoring the Mandel parameter,

$$Q(t) = (\langle \Delta n^2 \rangle - \langle n \rangle)/\langle n \rangle. \tag{1}$$

$Q(t)$ measures the deviation of the mean-square fluctuation from the mean photon number normalized to the latter. Therefore, Q vanishes for a Poisson distribution. A positive Q indicates a super-Poissonian distribution with larger fluctuations than in a coherent state with the same mean photon number while negative Q values correspond to the sub-Poissonian regime which is known to have no classical analog [23]. Indeed, deviations from the coherent state have been reported for the stationary distribution obtained in an atomic cavity with constant driving where different signs of Q have been found for different ratios between cavity loss and radiative decay rates [24]. In Ref. [25] it has been shown that the statistics of photons emitted from the exciton-biexciton system of a QD can be steered from sub- to the super-Poissonian by varying the biexciton binding energy, the pump strength or the temperature [26]. Although the experiments in

Ref. [25] have been performed on QDs without cavity, the number of modes in the theoretical modeling was restricted to two which corresponds to the situation in a QDC. Therefore, the results should also apply to QDCs. Simulations for a pulsed excitation of a QDC indicate that Q can exhibit oscillations and change its sign repeatedly in time [27].

It is clear, however, that in general the photon number distribution contains much more detailed information than captured by the mean photon number or the Mandel parameter. Recently, calculations of the stationary photon number distribution in a constantly driven QDC revealed a strong qualitative influence of phonons on the shape of the distribution [28,29]. While without phonons distributions with many different shapes were found for different detunings, the stationary distribution with phonons turned out to be close to a thermal state with a high effective temperature. Note that the case without phonons describes, e.g., a cavity with a trapped atom.

Advances in measuring techniques have demonstrated possibilities for observing directly the photon number resolved distributions in various systems without the necessity to perform quantum tomography to reconstruct the entire state [30], ranging from bimodal microlasers [31] over QDs [32,33] to exciton-polariton condensates [34]. Furthermore, a novel algorithm for data evaluation free of systematic errors to obtain number distributions has been successfully employed [35]. These achievements could pave the way to novel applications where easy access to information encoded in the photon number distribution is needed.

The focus of the present paper is on the transient behavior of the photon number distribution in a QDC system driven by chirped pulses in comparison to the unchirped case. Our most striking result is the finding that the shape of the number distribution changes dynamically when driving the QDC with chirped pulses. In sharp contrast, for sufficiently strong unchriped excitations a wave packet which keeps a bell shape for all times moves up and down the Jaynes-Cummings ladder. Phonons have noticeable effects on the photon statistics for all excitation conditions that we compare. Notably, for chirped excitation the phonon impact induces qualitative changes of the shape of the distribution in particular for negative chirps.

II. THEORY

A. Model and methods

We study a self-assembled QD, e.g., GaAs/In(Ga)As, with strong electronic confinement, such that only the lowest conduction and the highest valence band states need to be taken into account. Furthermore, we consider only situations where the system is well represented by a two-level model. The latter applies, e.g., for resonant driving of the exciton by circularly polarized light when the fine-structure splitting is negligible or when all other states such as the biexciton are sufficiently far from resonance. Then the Hamiltonian for the laser driven dot reads

$$H_{\text{DL}} = -\hbar\Delta\omega_{\text{LX}}|X\rangle\langle X| - \frac{\hbar}{2}f(t)$$
$$\times \left(e^{-i\varphi(t)}|X\rangle\langle G| + e^{i\varphi(t)}|G\rangle\langle X|\right), \quad (2)$$

where the detuning between the exciton and central laser frequency $\Delta\omega_{\text{LX}} := \omega_{\text{L}} - \omega_{\text{X}}$ is introduced. Here, the ground state $|G\rangle$ is chosen as the zero of the energy scale. Note that the usual dipole and rotating wave approximations are employed and the Hamiltonian is written down in a frame co-rotating with the laser frequency ω_{L}. The real amplitude $f(t)$ and the phase $\varphi(t)$ are related to the instantaneous Rabi frequency $\Omega(t)$ by

$$\Omega(t) := 2\mathbf{M_0} \cdot \mathbf{E}(t) = f(t) e^{-i(\omega_{\text{L}}t + \varphi(t))}, \quad (3)$$

where $\mathbf{M_0}$ is the dipole matrix element of the transition between the QD ground $|G\rangle$ and exciton state $|X\rangle$ and $\mathbf{E}$ is the positive frequency part of the laser field.

To enhance the coupling between the QD and the electromagnetic field, the dot can be placed into a microcavity. We account for a single cavity mode with frequency ω_{C} far from the electromagnetic continuum and a QD coupled to that mode close to resonance via

$$H_{\text{C}} = \hbar\Delta\omega_{\text{CL}}a^{\dagger}a + \hbar g\left(a^{\dagger}|G\rangle\langle X| + a|X\rangle\langle G|\right), \quad (4)$$

where the cavity photons are created (annihilated) by the bosonic operator $a^{\dagger}$ (a) and are detuned by $\Delta\omega_{\text{CL}} := \omega_{\text{C}} - \omega_{\text{L}}$ from the laser frequency. The QD is coupled to the cavity with a strength of $\hbar g$.

The subsystem of interest comprising the dot laser and the cavity Hamiltonian H_{DL} and H_{C}, respectively, is not an ideal few-level system, since it is embedded into the surrounding solid-state matrix. Even at cryogenic temperatures of a few Kelvin, the QD exciton is prone to the coupling to phonons. In strongly confined excitonic systems, the most important phononic contribution usually results from the deformation potential coupling to longitudinal acoustic (LA) phonons and is of the elastic pure dephasing type [36–39],

$$H_{\text{Ph}} = \hbar\sum_{\mathbf{q}}\omega_{\mathbf{q}}b_{\mathbf{q}}^{\dagger}b_{\mathbf{q}} + \hbar\sum_{\mathbf{q}}\left(\gamma_{\mathbf{q}}^{\text{X}}b_{\mathbf{q}}^{\dagger} + \gamma_{\mathbf{q}}^{\text{X}*}b_{\mathbf{q}}\right)|X\rangle\langle X|, \quad (5)$$

where the bosonic operator $b_{\mathbf{q}}^{\dagger}$ ($b_{\mathbf{q}}$) creates (destroys) phonons with frequency $\omega_{\mathbf{q}}$. $\gamma_{\mathbf{q}}^{\text{X}}$ denotes the coupling constant between the exciton state and the bosonic mode labeled by its wave vector $\mathbf{q}$ which is adequate for bulk phonons. Here, we use the fact that in GaAs/In(Ga)As the lattice properties of the dot and its surroundings are similar, such that phonon confinement is negligible. Other QD-phonon interaction mechanisms like, e.g., the piezoelectric coupling to LA and transverse acoustic (TA) phonons can become important in strongly polar crystals such as, e.g., GaN-based QDs [40,41], but are of minor importance for GaAs-type structures.

Finally, we account for Markovian loss processes by phenomenological decay rates for the radiative decay and cavity losses, respectively, that are incorporated into the model as Lindblad-type superoperators $\mathcal{L}_{|G\rangle\langle X|,\gamma}\bullet + \mathcal{L}_{a,\kappa}\bullet$ with

$$\mathcal{L}_{O,\Gamma}\bullet = \Gamma\left(O\bullet O^{\dagger} - \frac{1}{2}\{\bullet, O^{\dagger}O\}_{+}\right), \quad (6)$$

where $\{\cdot, \cdot\}_{+}$ denotes the anticommutator. O is a system operator and Γ the decay rate of the associated loss process, i.e., in our case γ stands for the radiative decay rate while κ is the cavity loss rate.

The dynamical equation to be solved is the Liouville-von Neumann equation for the density matrix,

$$\frac{\partial}{\partial t}\rho = -\frac{i}{\hbar}\{H,\rho\}_- + \mathcal{L}_{|G\rangle\langle X|,\gamma}\rho + \mathcal{L}_{a,\kappa}\rho, \qquad (7)$$

with the total Hamiltonian $H = H_{DL} + H_C + H_{Ph}$ and $\{\cdot,\cdot\}_-$ denotes the commutator.

We employ a path-integral formalism for simulating the dynamics in the above-defined model in a numerically complete fashion. By tracing out the phonon degrees of freedom analytically, a non-Markovian memory kernel decaying on a time scale of a few picoseconds is obtained that manifests in experiments as, e.g., non-Lorentzian line shapes in linear and nonlinear spectra [37,38,42,43] or in characteristic dependencies of the phonon-induced damping of Rabi rotations [44–47]. Therefore, this memory cannot be neglected in calculating the QD dynamics which takes place on a similar time scale. We call a numerical solution complete if a finer time discretization or a longer cutoff of the phonon-induced memory kernel does not change the results noticeably.

Most current implementations of the real-time path-integral approach are based on the pioneering work of Makri and Makarov [48,49], who introduced an iterative scheme for the augmented density matrix of the subsystem of interest. We are using an extension of this scheme that allows the inclusion of non-Hamiltonian Lindblad-type contributions into the path-integral algorithm without the loss of precision with respect to the phonon-induced part of the dynamics by formulating the iterative scheme not in a Hilbert, but a Liouville space [50]. In the present study, the system that couples to the phonons is represented by a large number of basis states of the form $|G,n\rangle$ and $|X,n\rangle$ where n denotes the photon number and G or X indicates whether the dot is in its ground or excited state. A numerically complete study of such systems is currently impossible with the Makri-Makarov algorithm due to the extreme growth of the numerical demand with rising number of system states. Nevertheless, we are able to present numerically complete results because we are using a recently developed reformulation of the algorithm that iterates a partially summed augmented density matrix [28]. Note that this reformulation of the path-integral algorithm does not introduce any additional approximations. For details on the methods, consider the supplement of Ref. [28]. The photon number distribution is obtained by taking the corresponding matrix element of the subsystem's reduced density operator $\bar{\rho} = \text{Tr}_{Ph}[\rho]$, with Tr_{Ph} denoting the trace over the phonon degrees of freedom,

$$P_n(t) = \sum_{\nu=G,X}\langle\nu,n|\bar{\rho}(t)|\nu,n\rangle. \qquad (8)$$

B. Chirped pulses and laser-dressed states

In order to generate a chirped pulse one usually starts with a Gaussian pulse with an envelope and phase:

$$f_0(t) = \frac{\Theta}{\sqrt{2\pi}\sigma}e^{-\frac{(t-t_0)^2}{2\sigma^2}}, \qquad (9)$$

$$\varphi(t) = \text{const.}, \qquad (10)$$

where Θ denotes the pulse area and σ determines the duration corresponding to a full width at half maximum (FWHM) of FWHM $= 2\sqrt{2\ln(2)}\sigma$ and t_0 marks the time of the pulse maximum. We shall assume in the following a resonant excitation where $\varphi(t) = 0$ in Eq. (3) for an unchirped pulse. We note in passing that also other pulse shapes are possible as a starting point for the generation of chirped pulses. In particular, secant hyperbolic pulses may have advantages in certain circumstances [51].

Passing the initial pulse in Eq. (9) through a Gaussian chirp filter [52] yields a chirped pulse with envelope and phase:

$$f_{chirp}(t) = \frac{\Theta_{chirp}}{\sqrt{2\pi}\sigma_{chirp}}e^{-\frac{(t-t_0)^2}{2\sigma_{chirp}^2}}, \qquad (11)$$

$$\varphi(t) = a(t-t_0)^2/2, \qquad (12)$$

pulse area $\Theta_{chirp} = \Theta\sqrt{\sigma_{chirp}/\sigma}$ and duration $\sigma_{chirp} = \sqrt{(\alpha^2/\sigma^2) + \sigma^2}$. The phase in Eq. (3) has acquired a quadratic time dependence, which corresponds to an instantaneous laser frequency $\omega_L + \dot{\varphi} = \omega_L + a(t-t_0)$ that changes linearly in time and for $\omega_L = \omega_X$ crosses the exciton resonance at the pulse maximum $t = t_0$. The strength of the chirp is commonly expressed in terms of the chirp parameter α which is related to the coefficient a in Eq. (12) by $a = \alpha/(\alpha^2 + \sigma^4)$. Note that the pulse area and in particular the pulse length increases drastically when chirps are introduced (cf. the definition of σ_{chirp}).

III. NUMERICAL RESULTS ON TRANSIENT PHOTON STATISTICS

For the numerical calculations, we assume a QD with 6-nm diameter and standard GaAs parameters [28,41]. The cavity is coupled to the QD exciton with a strength of $\hbar g = 0.1$ meV while it is on resonance, i.e., $\Delta\omega_{CX} := \omega_C - \omega_X = 0$. The cavity losses are taken to be $\hbar\kappa = 6.6\,\mu$eV, which corresponds to a quality factor $\approx 10^5$ assuming a mode frequency of $\hbar\omega_C = 1.5$ eV. The radiative decay rate of the QD exciton is set to $\hbar\gamma = 2\,\mu$eV.

A. The chirp-free situation

Let us first concentrate on the chirp-free case. Figures 1(a) and 1(c) display photon number distributions at different times for a QDC driven by an unchirped Gaussian pulse with a pulse area of 5π and a duration of 2.4 ps FWHM. Figure 1(a) shows results without phonons while in Fig. 1(c) the corresponding simulations with phonons are depicted assuming the phonons before the pulse to be in thermal equilibrium at a temperature of T = 4 K. The initial state for the cavity photons is taken to be the vacuum, i.e., the $n = 0$ Fock state and the QD is initially in the ground state.

As expected the photons stay in the vacuum state until the arrival of the pulse. At the end of the 5π pulse (cf. black markers in Fig. 1) the QD is in the exciton state and the resonant coupling to the cavity initiates vacuum Rabi oscillations [53–57], i.e., oscillations between the $|X,n=0\rangle$ and the $|G,n=1\rangle$ states. This is reflected in the photon distribution as oscillations between the $n = 0$ and $n = 1$ Fock states and results in damped oscillations of the mean photon number
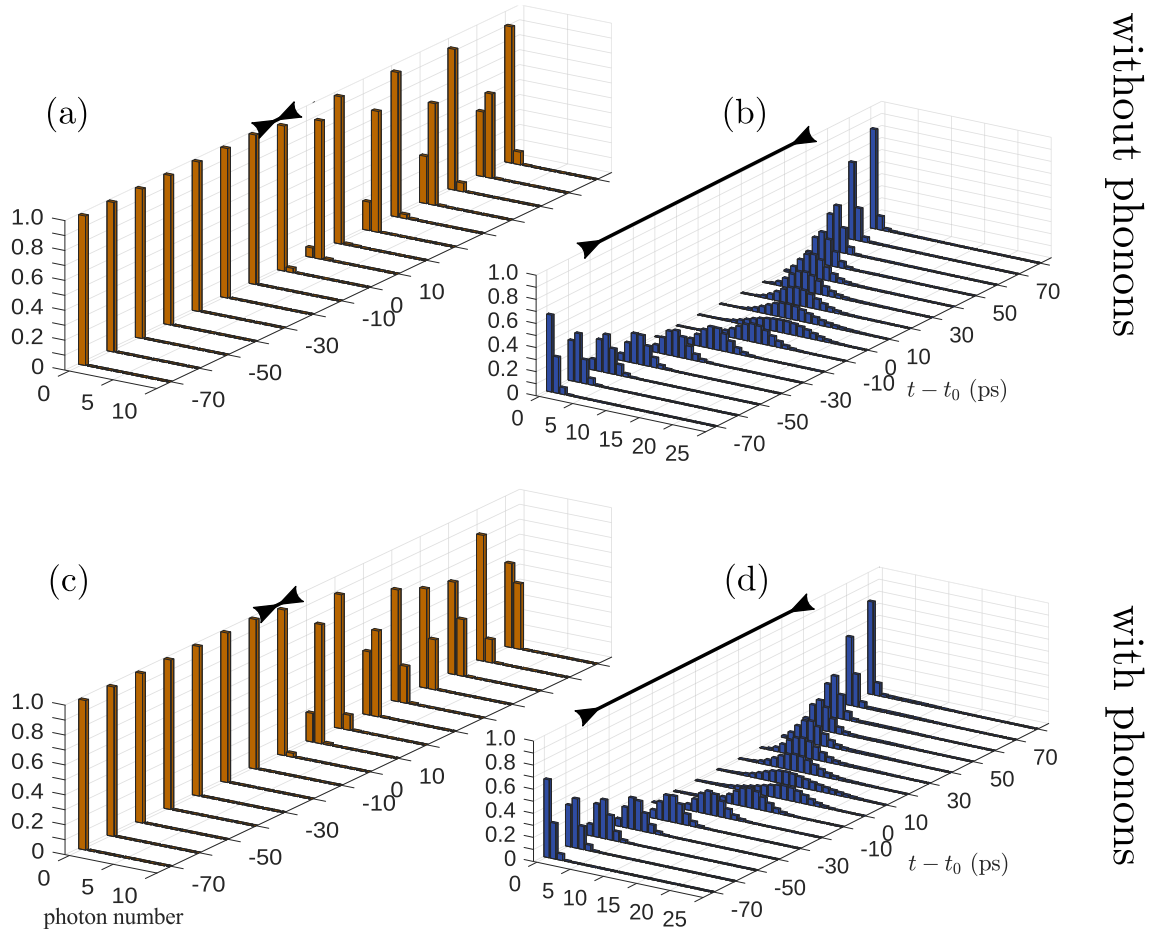
FIG. 1. Transient photon number distributions for laser excitations with unchirped pulses with (a) and (c) pulse area $\Theta = 5\pi$ and duration FWHM=2.4 ps, (b) and (d) pulse area $\Theta = 31.63\pi$ and duration FWHM = 94.22 ps. Panels (c) and (d) display results accounting for phonons that are initially at equilibrium at a temperature of $T = 4$ K while the corresponding phonon-free results are shown in (a) and (b). The pulse has its maximum at $t = t_0$. Black markers indicate the FWHM of the pulse.

between zero and and a maximal amplitude that due to losses and phonon effects is below one [cf. orange curve in Fig. 3(a)]. Quantitatively, a small occupation of the two-photon state $|2\rangle$ is observed, seen, e.g., for $t - t_0 = 10$ ps in Figs. 1(a) and 1(c). The reason lies in the re-excitation of the QD during the same pulse, whereby effectively two photons can be put into the single cavity mode.

The phonon impact on Rabi-type oscillations in a two-level system has been extensively studied [29,44–47,58–64] and shall therefore not be analyzed here in detail. We just note that the main effects are a phonon-induced damping, which depends on the driving strength, and a renormalization of the Rabi frequency. The renormalization of g is reflected in Figs. 1(a) and 1(c) by slightly different oscillation frequencies. The damping seen in the orange curve in Fig. 3(a) is the result of the combined effects of phonons, cavity losses, and radiative decay.

For a fair comparison between unchirped and chirped pulses, recall that the application of a Gaussian chirp filter involves besides the time-dependent variation of the phase $\varphi(t)$ in Eq. (12) also a considerable increase of the pulse duration and of the pulse area. Therefore, we show in Figs. 1(b) and 1(d) the photon distribution with and without the influence of phonons for a pulse with pulse area $\Theta = 31.63\pi$ and duration

FWHM = 94.22 ps, which corresponds to the application of a filter with an effective value of $|\alpha| = 40$ ps^2 in Eq. (11) but keeping the phase $\varphi(t) = 0$ constant. Most strikingly, with this driving there are no traces of vacuum Rabi oscillations visible. Instead, a wave-packet-type dynamics sets in, where a bell-shaped distribution is found for all times. The mean photon number rises monotonically in time to values $n \approx 12$ [note that the blue curve in Fig. 3(a) is scaled down by a factor of 5 for better visibility] and subsequently falls back to zero after the pulse has vanished.

B. Finite chirps

Figure 2 displays transient photon number distributions obtained for chirped pulses that are generated by passing the Gaussian pulse used in Figs. 1(a) and 1(c) through a chirp filter with $\alpha = \pm 40$ ps^2 [(a) and (c) $\alpha = -40$ ps^2, (b) and (d) $\alpha = +40$ ps^2]. The upper panels correspond to simulations without phonons while for the lower panels the interaction with phonons has been included. Note that the pulses used in Fig. 2 have the same pulse area and duration as the unchirped pulses used in Figs. 1(b) and 1(d) which allows us to compare excitation conditions where the only difference is the frequency modulation.
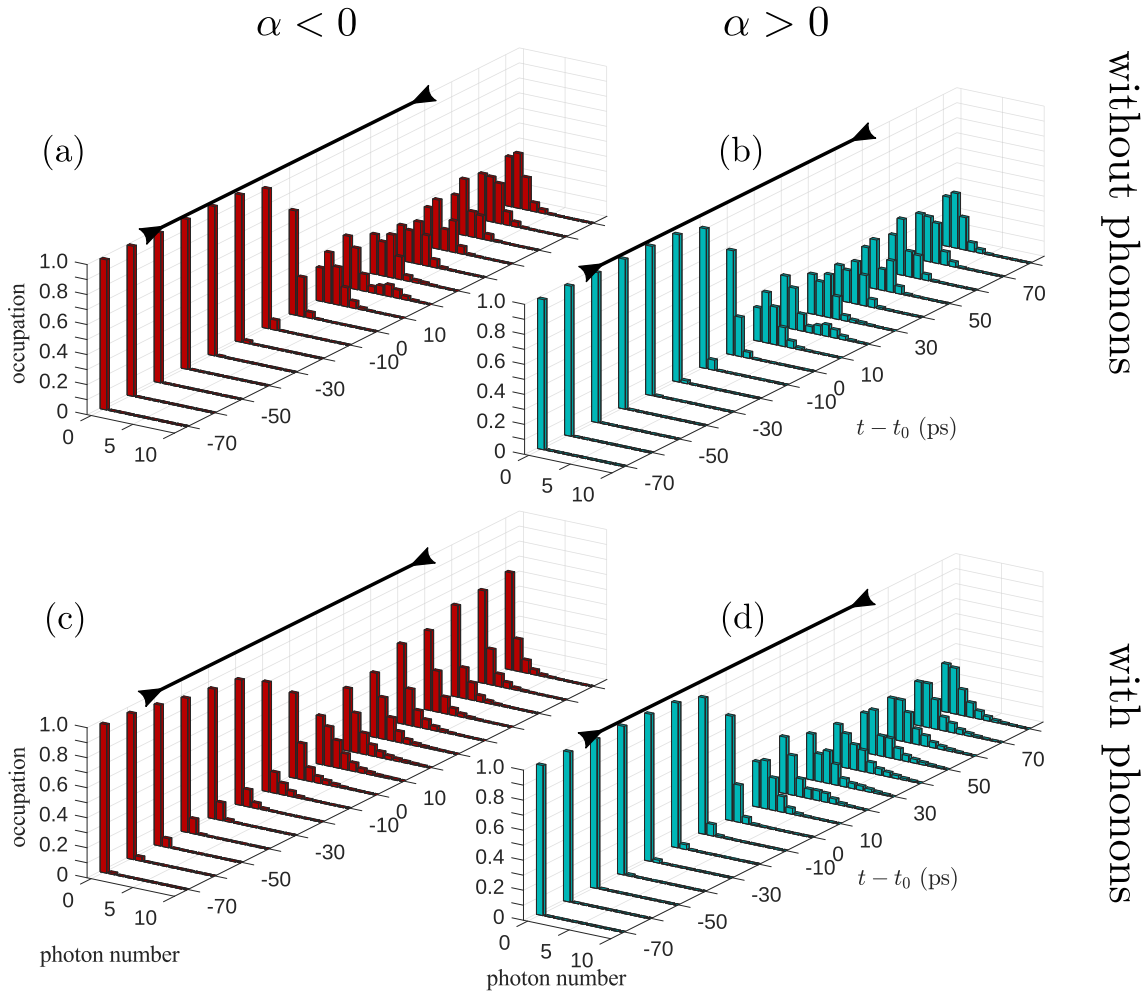
FIG. 2. Transient photon number distributions for laser excitations with chirped pulses with pulse area and FWHM before the chirp filter of $\Theta = 5\pi$ and FWHM=2.4 ps, i.e., $\Theta_{\text{chirp}} = 31.63\pi$ and duration $\text{FWHM}_{\text{chirp}} = 94.22$ ps for $|\alpha| = 40$ ps^2. (a) and (c) Calculated with chirp parameter $\alpha = -40$ ps^2, (b) and (d) $\alpha = +40$ ps^2. (c) and (d) Displayed are results accounting for phonons that are initially at equilibrium at a temperature of $T = 4$ K while the corresponding phonon-free results are shown in (a) and (b). The pulse has its maximum at $t = t_0$. Black markers indicate the FWHM of the pulse after the chirp filter.
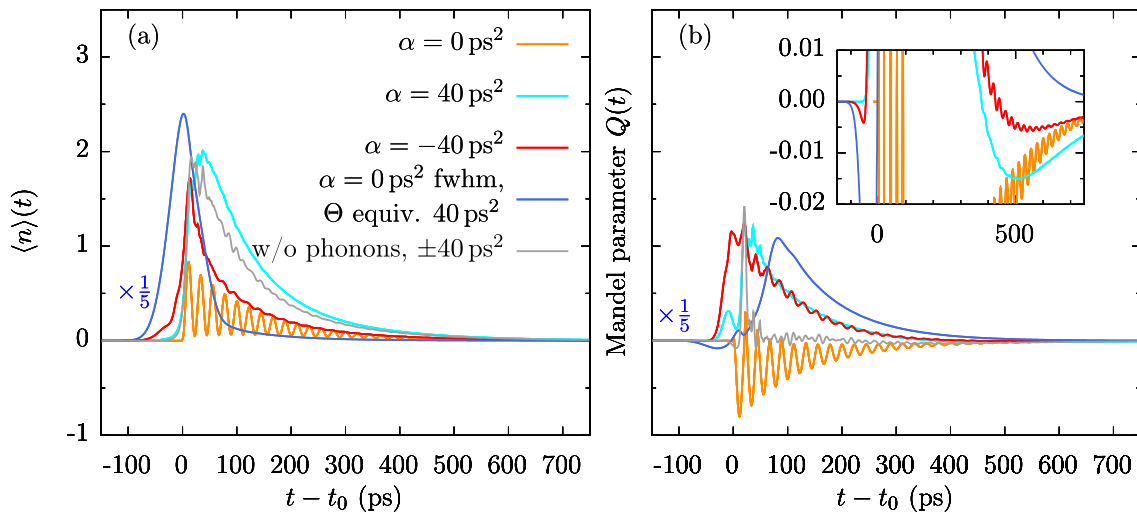
FIG. 3. The time-dependent (a) mean photon number and (b) Mandel parameter $Q(t) = (\langle \Delta n^2 \rangle - \langle n \rangle)/\langle n \rangle$ for the cases indicated by the labels. All curves are calculated with phonons initially at $T = 4$ K, except for the gray curves which correspond to the phonon-free case. The blue curve is scaled down by a factor of 5 for better visibility. The inset in (b) corresponds to a zoomed-in scale.

In the phonon-free case identical distributions are obtained for positive and negative chirp [cf. Figs. 2(a) and 2(b)]. This symmetry is removed when phonons are taken into account [cf. Figs. 2(c) and 2(d)]. In contrast to the unchirped case with the same pulse area and duration in Figs. 1(b) and 1(d), the photon number is close to zero until the pulse maximum is reached, which can be explained by noting that for chirped pulses the instantaneous laser frequency is strongly detuned from the QD resonance for times away from the pulse maximum. The most striking difference compared with Figs. 1(b) and 1(d) is, however, that the photon distributions in Fig. 2 significantly change their shape in time. The distributions found in the phonon free case have at early times after the pulse maximum a bell shape with a single maximum and transform into a bimodal distribution with two well-separated bell-shaped contributions at later times [cf. $t - t_0 = 20$ ps in Fig. 2(a)]. Subsequently, at times $t - t_0 \approx 30-50$ ps the distribution still has two peaks but looks rather jagged having little resemblance with bell-shaped distributions. Eventually, at later times only a single maximum is found which appears at a finite photon number or at zero, depending on time.

Phonons change the situation qualitatively for negative chirp [cf. Fig. 2(c)], where now the photon number distribution has a single maximum at $n = 0$ for all times. The shape of the transient distribution resembles thermal photon occupations, which due to mean photon numbers around $n = 2$ [cf. Fig. 3(a)] corresponds to an effective temperature above $T_{\mathrm{eff}} \approx 40\,000$ K for photon energies $\hbar\omega_{\mathrm{C}} \approx 1.5$ eV. A similar impact of phonons on the photon number distribution has been reported previously for the stationary distribution found at long times for permanent driving [28]. The phonon impact for positive chirp is less dramatic [cf. Fig. 2(d)]. As in the phonon-free case, there are still times where the distribution is bi-modal while at other times only a single maximum is found. Overall, the irregular looking shape appearing at certain times in Figs. 2(a) and 2(b) is smoothened. Moreover, there is a tendency to build up a maximum near $n = 0$.

Further differences between the number distributions in Figs. 1 and 2 are revealed by looking at the time evolution of the corresponding Mandel parameters $Q(t)$ in Fig. 3(b). For a Fock state the number fluctuation disappears, leading to a negative Mandel parameter, except for the $n = 0$ Fock state, where the Mandel parameter approaches an expression of the form zero divided by zero. We see from the orange curves in Fig. 3 that for weakly driven unchirped pulses the damped oscillation of the mean photon number between 0 and at most 1 is accompanied by damped oscillations of the Mandel parameter ranging down to almost -1 and up to essentially 0. The negative values of the minima correspond to times where the system is close to the $n = 1$ Fock state. If the dynamics would exclusively involve states with photon numbers 0 or 1 such that only P_0 and P_1 are different from zero, it is easy to show that for all times, where $P_1 \neq 0$, the Mandel parameter is $Q(t) = -\langle n \rangle$. Therefore, Q should approach 0 when the $n = 0$ Fock state is approached. We see, however, from the orange curve in Fig. 3(b) that the first maxima of the Mandel parameter Q are a bit above 0, indicating small admixtures of higher number states.

For higher pulse areas Q is positive for most of the time for chirped as well as for unchirped pulses. Interestingly, although the bell-shaped distributions in Figs. 1(b) and 1(d) at first glance resemble much more Poissonian distributions than the somehow irregular ones found for chirped pulses in Figs. 2(b) and 2(d) their deviation from a Poissonian as measured by the Mandel parameter is much larger than for chirped pulses [note that the blue curve in Fig. 3(b) is scaled down by a factor of 5]. But most remarkably, in the calculation with finite chirp without phonons [cf. the gray line in Fig. 3(b)] the Mandel parameter decays extremely fast after its initial rise to positive values compared with the other situations considered. Most notably, already at around ~ 40 ps after the pulse maximum it has dropped close to zero. In sharp contrast to the common interpretation that a Mandel parameter near zero implies a distribution with a shape close to a Poissonian, Fig. 2(b) shows a jagged distribution with two maxima at ~ 40 ps after the pulse maximum. Therefore, using the Mandel parameter as a measure for the deviation from a Poisonian is not valid in all physically relevant situations.

We further note that the Mandel parameter calculated for all excitation conditions studied in this paper changes its sign during the course of time. Without chirp and low intensities (orange curve) this happens near the first maxima of the Q oscillations, as discussed above, but also for higher driving strength (blue curve) a sign change occurs indicating that before the pulse maximum is reached the photon distribution is sub-Poissonian and switches at the pulse maximum to super-Poissonian. Also for the chirped excitations Q exhibits sign changes as revealed by the inset in Fig. 3(b). Actually, the Mandel parameter calculated for high pulse areas falls below zero before approaching its asymptotic value of zero from below for chirped as well as for unchirped excitations. Indeed, also the blue curve in Fig. 3(b) falls below zero at $t - t_0 = 1090$ ps (not seen in the plotted range). This sign change of Q shortly before cavity losses have relaxed the photon distribution to the empty cavity, can be understood as follows. The maximal photon numbers that are transiently reached for high pulse areas are well above one. The cavity losses remove photons from the cavity such that eventually the limit of $n = 0$ with zero fluctuations is reached. However, since the cavity losses for a state with n photons scale like $\sim n$, the relaxation from states with $n > 1$ to lower states is faster than the final relaxation from the $n = 1$ to the $n = 0$ states. Therefore, before the final relaxation is completed the photons preferably occupy the $n = 1$ state which results in a negative Mandel parameter before the asymptotic value of zero is reached. Note that this effect presumes only $\kappa \neq 0$ and thus should be robust with respect to variations of this parameter.

Finally, we note that Q exhibits small amplitude oscillations for chirped pulses which are absent in the unchirped case. A similar but less pronounced tendency is seen in the mean photon number.

C. Interpretation in terms of laser-dressed states

A popular application of driving QDs with chirped laser pulses is the robust preparation of exciton or biexciton states by invoking an adiabatic rapid passage (ARP) process [65–75]. ARP exploits the adiabatic theorem of quantum mechanics which predicts a time evolution through instantaneous
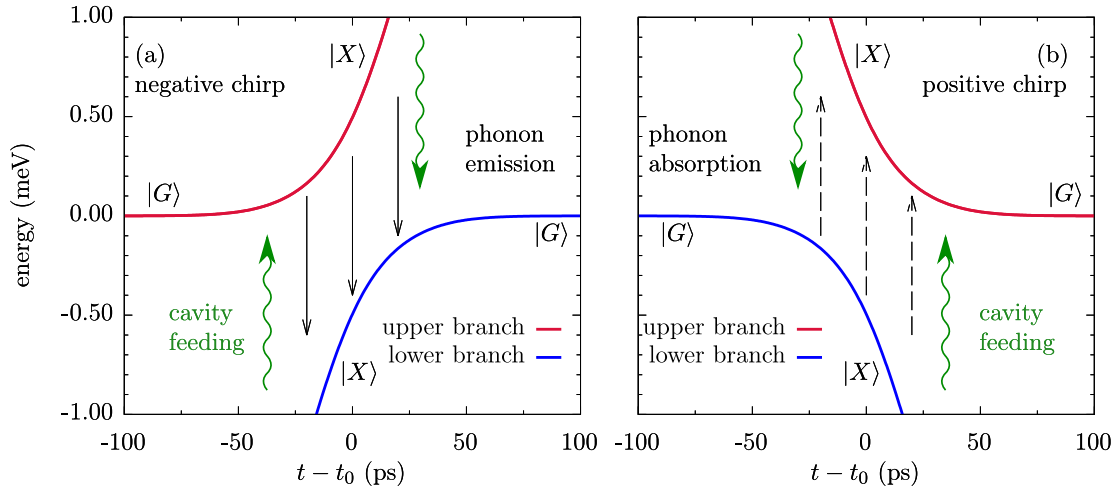
FIG. 4. Time evolution of the upper and lower laser-dressed state energies with respect to the excitation pulse maximum at $t = t_0$. While for negative chirps (a) phonon emission is probable (represented by black arrows), for positive chirps (b) phonon absorption is suppressed at low temperatures, which is indicated by the dashed arrows. Green curly arrows indicate transitions between laser-dressed states due to the QD cavity feeding.

eigenstates (dressed states) of the system provided the external driving fulfills the restrictions of the adiabatic regime [76]. In order to comply with these restrictions for a two-level system driven by Gaussian chirped pulses with a frequency modulation given by Eq. (12), it is advisable to transform the QD-laser Hamiltonian H_{DL} in Eq. (13) to a frame co-rotating with the phase φ to get rid of a possibly rapidly changing coupling. The transformed Hamiltonian reads

$$\widetilde{H}_{DL} = -\hbar(\Delta\omega_{LX} + a\,(t - t_0))|X\rangle\langle X|$$
$$- \frac{\hbar}{2}f(t)(|X\rangle\langle G| + |G\rangle\langle X|). \quad (13)$$

The laser-dressed states can now be defined as the instantaneous eigenstates of $\widetilde{H}_{DL}$. The corresponding eigenenergies are plotted in Fig. 4, where the left panel corresponds to a negative chirp while the result for positive chirp is shown in the right panel. The distinctive feature of ARP is that when the system is in the ground state $|G\rangle$ long before the pulse (i.e., for $t \to -\infty$) it will evolve adiabatically towards the exciton state $|X\rangle$ after the pulse (i.e., for $t \to +\infty$) independent of the sign of the chirp. However, it is important to note that the evolution proceeds along the lower (upper) branch for positive (negative) chirp. This affects in particular the impact of phonons. In general phonons can efficiently induce transitions between the two branches. However, at low temperatures phonon absorption is strongly suppressed and phonon emission can invoke only transitions from the upper to the lower branch (cf. the black arrows in Fig. 4). That is why phonons have little effects on the ARP dynamics for positive chirp while for negative chirp the ARP-based exciton preparation is strongly disturbed [68,70,73,74]. In order to preserve an efficient exciton preparation also at negative chirps, it has been recently demonstrated that high pulse areas can be used since this effectively decouples the phonons from the electronic system [29,75].

When also a cavity is coupled to the QD, then the coupling leads to Rabi-type rotations between states $|X, n\rangle$ and

$|G, n + 1\rangle$ with different numbers n of cavity photons. In particular for times when the laser is far off-resonant and the laser-dressed states are close to the undressed states, the effect of coupling the QD to a cavity can be understood as inducing a transition between the dressed states similar to the coupling to phonons. To be a bit more specific, when the system is in the exciton state the QD-cavity coupling leads to a feeding of the cavity by an additional photon accompanied by a transition from the $|X\rangle$-like branch to the $|G\rangle$-like branch (cf. the green curly arrows in Fig. 4). At early times, the reverse process, where one photon disappears from the cavity while transferring the system from the ground to the exciton state is suppressed since there are initially no photons in the cavity.

We shall now try to interpret the pertinent features of the photon dynamics in some more detail using the simplified picture where the system evolves adiabatically through the laser-dressed states in Fig. 4 while phonons and cavity feeding induce transitions between these states.

In the case of a negative chirp [cf. Fig. 4(a)] transitions form the upper branch to the lower branch of the laser-dressed states accompanied by phonon emission are possible before and after the pulse maximum at $t = t_0$. Thus, phonons should have a profound impact on the resulting photon statistics during the entire pulse. In fact, this explains why the distribution is close to a thermal one at all times [cf. Fig. 2(c)]. For times before the pulse reaches its maximum, cavity feeding can occur form the excitonlike lower branch to the upper branch, which has a large ground-state contribution. Subsequently, the system can again decay to the lower branch by phonon emission followed by another cavity feeding process back into the upper branch and so on. Because of this constructive interplay between phonon and cavity feeding processes, higher photon states can be reached compared with the phonon-free situation for $t \leqslant t_0$ [cf. Figs. 2(a) and 2(c)]. In the time interval shortly after the pulse maximum the upper branch becomes the state with the excitonlike characteristics and cavity feeding now takes place from the upper branch into the ground-state-like lower branch of the laser-dressed states. Thus, after the pulse
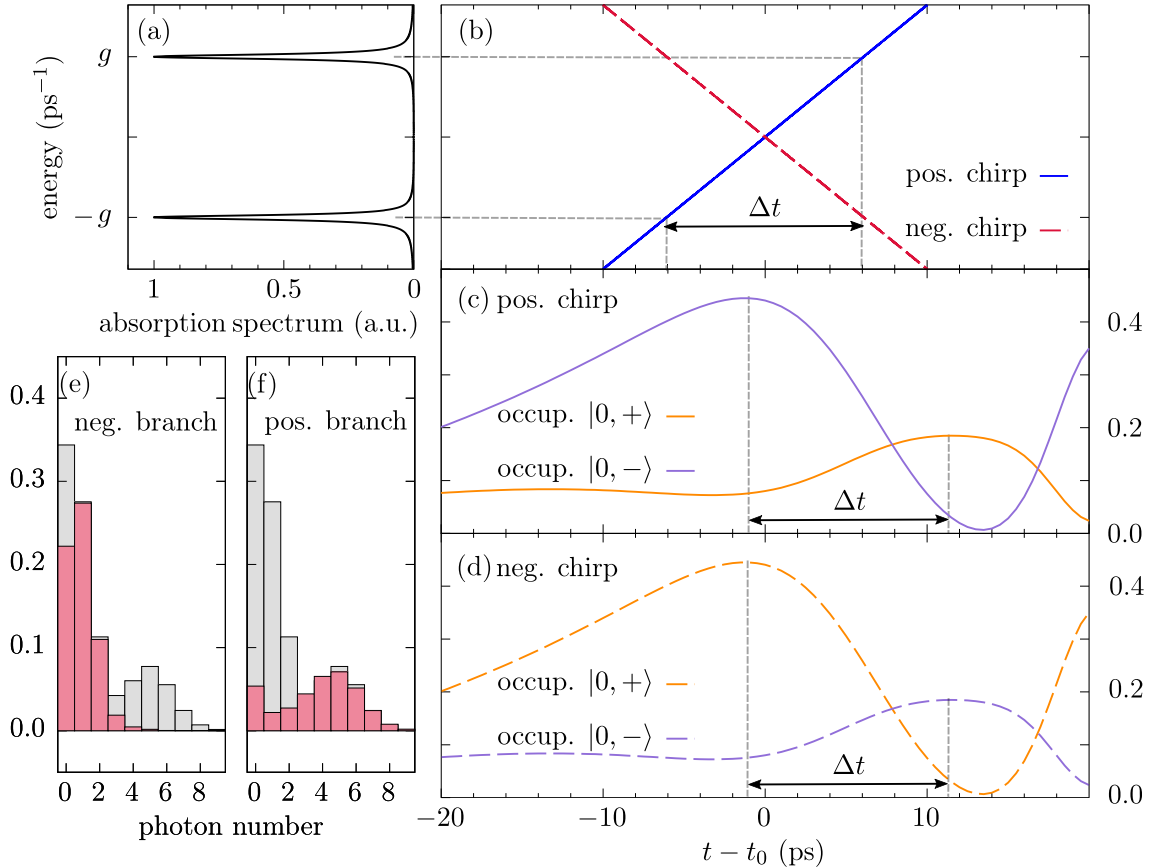
FIG. 5. (a) Linear absorption spectrum of the QDC system. (b) Time-dependent instantaneous frequency, blue (red) for positive (negative) chirp. Δt marks the time elapsed between the crossing of the two resonances. (c) and (d) Time evolution of the occupations of the lowest excited eigenstates of the QDC system [(c) for positive and (d) for negative chirp]. (e) and (f) Photon number distribution at $t - t_0 = 20 \, \text{ps}$ (gray); red, accounting only for $|n, +\rangle$ (e) or $|n, -\rangle$ (f) states. Here, only phonon-free results are shown.

maximum has appeared phonon and cavity feeding processes are now in direct competition with each other. Therefore, compared with the phonon-free situation, the mean photon number should be reduced. Altogether, for negative chirp, the phonon impact on the photon distributions is visible at all times leading to nearly thermal distributions. At times before the pulse maximum the interaction with phonons increases the mean photon number because of a constructive interplay between phonon and cavity feeding processes. This effect is reversed after the pulse maximum and the mean photon number is reduced compared with the phonon-free situation due to the phonon interaction, as can be seen comparing the red with the gray curve in Fig. 3(a).

The situation is different when the chirp is positive as seen in Figs. 2(b) and 2(d). Here, a phonon influence on the photon statistics can be hardly seen before the pulse maximum. This can again be explained by inspection of the branches of the laser-dressed states. Starting in the ground state the system evolves adiabatically alongside the lower branch. Since phonon absorption processes are suppressed at low temperatures, transitions to the excitonlike upper state are unlikely to occur. Also cavity feeding is hardly possible [cf. Fig. 4(b)] and, like in the phonon-free situation, the system remains essentially in the ground state without photons and phonons have almost no visible effect. This observation changes after the pulse maximum. Now, cavity feeding pro-

cesses accompanied by transitions from the excitonlike lower branch to the upper branch appear. Subsequently, phonon emission processes take place, resulting in a transition back to the lower branch. Thus, now, a constructive interplay between phonon emission and cavity feeding is possible, leading to a thermalization of the photon distribution. Therefore, after a transition time of a few 10 ps the distribution resembles a thermal distribution. Because of the constructive interplay the mean photon number is increased compared with the phonon-free situation, as can be seen comparing the cyan with the gray curve in Fig. 3(a). Consequently, only for a finite time interval after the pulse maximum photon distributions can be detected which are similar to the distributions in the phonon-free situation and display irregular behavior or several maxima.

D. Interpretation in terms of cavity-dressed states

Finally, we would like to explain why chirped pulse excitation leads to photon number distributions where the number of maxima changes dynamically from one to two and back to one. To this end we have to go beyond the laser-dressed state picture and recall that the linear absorption of a QDC comprises two lines split by $\Delta \omega = 2g$ [cf. Fig. 5(a)]. Thus, the instantaneous frequency of a pulse with positive chirp first crosses the energetically lower resonance and then, delayed

by a time $\Delta t = 2g/a$, the higher one [cf. Fig. 5(b)]. Each crossing of these resonances initiates a wave packet climbing up the Jaynes-Cummings ladder. This behavior is efficiently described in the picture of the cavity-dressed states, i.e., the eigenstates of the dot-cavity Hamiltonian, which relate to the bare QD states by

$$|n, +\rangle = \frac{1}{\sqrt{2}}(+|X, n\rangle + |G, n+1\rangle),$$

$$|n, -\rangle = \frac{1}{\sqrt{2}}(-|X, n\rangle + |G, n+1\rangle), \qquad (14)$$

in the case of a resonant cavity mode $\omega_X - \omega_C = 0$.

Starting from the state $|G, 0\rangle$ only the two states $|0, \pm\rangle$ can be reached directly by the laser coupling and thus climbing up the Jaynes cummings ladder one has to pass these states. Since the corresponding eigenenergies are separated by $2g$, the transitions to these states are in resonance with the instantaneous frequency of a chirped pulse at different times. Indeed, Fig. 5(c) reveals that the occupation of the lowest excited eigenstate of the QDC system $|0, -\rangle$ rises before the upper state $|0, +\rangle$ acquires a noticeable occupation. The maximum occupation of $|0, -\rangle$ is reached ≈ 5 ps after the instantaneous frequency has crossed the lower resonance, revealing the reaction time of the system. $|0, +\rangle$ is maximally occupied delayed exactly by Δt from the maximal occupation of $|0, -\rangle$. The time ordering of the excitation of the $|0, \pm\rangle$ states is reversed when reversing the sign of the chirp [cf. Fig. 5(d)] since now the upper resonance is crossed first.

The laser driving couples $|n, +\rangle$ to $|n, -\rangle$ states. However, when the instantaneous frequency is in resonance with transitions between $|n, +\rangle$ states with adjacent n then the transitions to $|n, -\rangle$ states are off-resonant and vice versa. Thus, it can be expected that the packets running up the Jaynes-Cummings ladder are essentially composed either of $|n, +\rangle$ or $|n, -\rangle$ states. Indeed, this is confirmed by Figs. 5(e) and 5(f) which displays in gray the photon number distribution at time $t - t_0 = 20$ ps, i.e., the time where according to Fig. 2(b) the two maxima are most pronounced. Also shown in red are photon number distributions calculated according to

$$P_n^{(\pm)} = \begin{cases} \frac{1}{2} \left(\langle n, \pm|\rho|n, \pm\rangle + \langle n-1, \pm|\rho|n-1, \pm\rangle \right) \\ \quad \text{for } n > 0, \\ \frac{1}{2} \left(\langle 0, \pm|\rho|0, \pm\rangle + \langle G, 0|\rho|G, 0\rangle \right) \\ \quad \text{for } n = 0 \end{cases}.$$

$$(15)$$

Recalling that for a cavity in resonance with the QD transition the $|n, \pm\rangle$ states have a probability of $1/2$ for finding n or $n+1$ photons, Eq. (15) yields, for $n > 0$, the probability for having n photons when accounting only for either the $|n, +\rangle$ or the $|n, -\rangle$ states. For $n = 0$ the contribution from $|G, 0\rangle$ is counted by $1/2$ for the plus and minus branch, since this state can be counted as lower or upper state. We note in passing that $P_n^{(-)}$ [red bars in Fig. 5(e)] does not add up with $P_n^{(+)}$ [red bars in Fig. 5(f)] to the total photon number P_n (gray bars in Fig. 5), because P_n comprises coherences between the $|n, +\rangle$ and the $|n, -\rangle$ states in addition to their occupations. Nevertheless, Fig. 5 reveals that the two peaks in the photon number distribution can be attributed unambiguously either to the upper or lower branch of the QDC states.

Altogether this explains the time evolution of the peaks in the photon number distribution. After crossing the first resonance the distribution has a single peak since at first only a single packet is climbing up the Jaynes-Cumming ladder. When the second resonance is crossed a second packet is initiated such that at $t - t_0 \approx 20$ ps two well-resolved packets are observed. Both packets move up and down the Jaynes-Cummings ladder similar to the single wave packet observed for the unchirped excitation in Figs. 1(b) and 1(d). Since the decline of the first packet starts while the second is still rising, at some time both packets overlap. Although the packets are no longer well resolved, two maxima are still found over an extended time period [30 ps $\lesssim t - t_0 \lesssim 50$ ps in Fig. 2(b)]. At later times the relaxation drives both packets to low photon numbers such that the maxima merge and a single-peaked distribution is recovered.

Finally, we note that for a cavity in resonance with the QD transition the energies of the QDC eigenstates $|n, \pm\rangle$ are found in the rotating frame at $\hbar\omega_{n,\pm} = \pm g\sqrt{n+1}$ such that the transition energies between states with adjacent n are all different and decrease with rising n. Therefore, the instantaneous frequency of a chirped pulse crosses all of these resonances at different times which is likely to contribute to the somewhat irregular looking time evolution of the photon number distribution found in particular in the intermediate time interval 30 ps $\lesssim t - t_0 \lesssim 50$ ps in Fig. 2(b).

IV. CONCLUSION

We have studied transient photon number distributions generated in a microcavity by a pulsed excitation of an embedded quantum dot. We find qualitatively different photon distributions for chirped and unchirped pulses. Phonons have a noticeable influence on the photon distributions in particular for negative chirps, where the phonon coupling introduces qualitative changes of the shape of the distribution already at a temperature of $T = 4$ K. To be more specific, phonons lead in this case to almost thermalized photon distributions at high effective temperatures for all times. For positive chirp, the transient distributions are far away from a thermal one for times after the pulse maximum until about 80 ps afterwards.

For all investigated cases, we find that the Mandel parameter changes its sign during the time evolution of the system, indicating the ability to enter and leave a regime of genuine nonclassical photon statistics in the course of time. Moreover, cases were encountered where the Mandel parameter is zero, but the photon number distribution has two peaks and is definitely not a Poissonian. Therefore, one has to be careful when using the Mandel parameter as a measure for the deviation from a Poissonian distribution, as it is often done [24,77–80]. This finding underlines the necessity to carefully consider the definition of the Mandel parameter, which indeed yields zero for a Poissonian distribution. But the reverse implication is obviously not true for all cases.

Our most striking result is, however, that the shape of the photon number distribution changes significantly during the time evolution when the system is excited by chirped pulses. In fact, when the excitation starts to populate states with higher photon numbers, one observes at first bell-shaped distributions with a single maximum that increases in time.

Subsequently, two well-separated bell-shaped contributions develop which at later times first evolve into a single broad feature with two peaks and eventually merge into a distribution with a single peak. This is in sharp contrast to the unchirped case, where for the same high driving strengths the photon number distributions keep a bell shape with a single maximum for all times. Our analysis reveals that the transient changes of the shape of the photon distribution in the chirped case can be attributed to subsequent crossings of resonances of the quantum-dot–cavity system by the instantaneous frequency.

We believe that our findings deepen the understanding of the transient behavior of photon distributions in a driven quantum-dot–cavity system and its dependence on the driving conditions. This might pave the way to targeted manipulations of photon distributions which could result in new types of photonic applications in the future.

[1] P. Michler, A. Kiraz, C. Becher, W. V. Schoenfeld, P. M. Petroff, L. Zhang, E. Hu, and A. Imamoglu, Science **290**, 2282 (2000).

[2] C. Santori, M. Pelton, G. Solomon, Y. Dale, and Y. Yamamoto, Phys. Rev. Lett. **86**, 1502 (2001).

[3] C. Santori, D. Fattal, J. Vuckovic, G. S. Solomon, and Y. Yamamoto, Nature (London) **419**, 594 (2002).

[4] Y.-M. He, Y. He, Y.-J. Wei, D. Wu, M. Atatüre, C. Schneider, S. Höfling, M. Kamp, C.-Y. Lu, and J.-W. Pan, Nat. Nanotechnol. **8**, 213 (2013).

[5] Y.-J. Wei, Y.-M. He, M.-C. Chen, Y.-N. Hu, Y. He, D. Wu, C. Schneider, M. Kamp, S. Höfling, C.-Y. Lu, and J.-W. Pan, Nano Lett. **14**, 6515 (2014).

[6] X. Ding, Y. He, Z.-C. Duan, N. Gregersen, M.-C. Chen, S. Unsleber, S. Maier, C. Schneider, M. Kamp, S. Höfling, C.-Y. Lu, and J.-W. Pan, Phys. Rev. Lett. **116**, 020401 (2016).

[7] N. Somaschi, V. Giesz, L. De Santis, J. C. Loredo, M. P. Almeida, G. Hornecker, S. L. Portalupi, T. Grange, C. Antón, J. Demory, C. Gómez, I. Sagnes, N. D. Lanzillotti-Kimura, A. Lemaítre, A. Auffeves, A. G. White, L. Lanco, and P. Senellart, Nat. Photonics **10**, 340 (2016).

[8] L. Schweickert, K. D. Jöns, K. D. Zeuner, S. F. Covre da Silva, H. Huang, T. Lettner, M. Reindl, J. Zichi, R. Trotta, A. Rastelli, and V. Zwiller, Appl. Phys. Lett. **112**, 093106 (2018).

[9] L. Hanschke, K. A. Fischer, S. Appel, D. Lukin, J. Wierzbowski, S. Sun, R. Trivedi, J. Vučković, J. J. Finley, and K. Müller, npj Quantum Inf. **4** (2018).

[10] M. Cosacchi, F. Ungar, M. Cygorek, A. Vagov, and V. M. Axt, Phys. Rev. Lett. **123**, 017403 (2019).

[11] N. Akopian, N. H. Lindner, E. Poem, Y. Berlatzky, J. Avron, D. Gershoni, B. D. Gerardot, and P. M. Petroff, Phys. Rev. Lett. **96**, 130501 (2006).

[12] R. M. Stevenson, R. J. Young, P. Atkinson, K. Cooper, D. A. Ritchie, and A. J. Shields, Nature (London) **439**, 179 (2006).

[13] R. Hafenbrak, S. M. Ulrich, P. Michler, L. Wang, A. Rastelli, and O. G. Schmidt, New J. Phys. **9**, 315 (2007).

[14] A. Dousse, J. Suffczynski, A. Beveratos, O. Krebs, A. Lemaître, I. Sagnes, J. Bloch, P. Voisin, and P. Senellart, Nature (London) **466**, 217 (2010).

[15] E. del Valle, New J. Phys. **15**, 025019 (2013).

[16] M. Müller, S. Bounouar, K. D. Jöns, M. Glässl, and P. Michler, Nat. Photonics **8**, 224 (2014).

[17] A. Orieux, M. A. M. Versteegh, K. D. Jöns, and S. Ducci, Rep. Prog. Phys. **80**, 076001 (2017).

[18] T. Seidelmann, F. Ungar, A. M. Barth, A. Vagov, V. M. Axt, M. Cygorek, and T. Kuhn, Phys. Rev. Lett. **123**, 137401 (2019).

[19] Y. T. Chough and H. J. Carmichael, Phys. Rev. A **54**, 1709 (1996).

[20] L. Mandel, Opt. Lett. **4**, 205 (1979).

[21] C. Gerry and P. L. Knight, *Introductory Quantum Optics* (Cambridge University Press, Cambridge, 2004).

[22] Note that fields produced by lasers in real experiments usually have some degree of amplitude noise. Therefore, the photon number distribution is always a bit wider than the Poissonian one.

[23] W. Vogel and D.-G. Welsch, *Quantum Optics* (Wiley-VCH, Weinheim, 2006).

[24] T. Quang and H. Freedhoff, Phys. Rev. A **47**, 2285 (1993).

[25] G. Callsen, A. Carmele, G. Hönig, C. Kindel, J. Brunnmeier, M. R. Wagner, E. Stock, J. S. Reparaz, A. Schliwa, S. Reitzenstein, A. Knorr, A. Hoffmann, S. Kako, and Y. Arakawa, Phys. Rev. B **87**, 245314 (2013).

[26] Although the experiments in Ref. [25] have been performed on QDs without cavity, the number of modes in the theoretical modeling was restricted to two which corresponds to the situation in a QDC. Therefore, the results should also apply to QDCs.

[27] M. Bagheri Harouni, R. Roknizadeh, and M. H. Naderi, Phys. Rev. B **79**, 165304 (2009).

[28] M. Cygorek, A. M. Barth, F. Ungar, A. Vagov, and V. M. Axt, Phys. Rev. B **96**, 201201(R) (2017).

[29] D. E. Reiter, T. Kuhn, and V. M. Axt, Adv. Phys.: X **4**, 1655478 (2019).

[30] A. I. Lvovsky and M. G. Raymer, Rev. Mod. Phys. **81**, 299 (2009).

[31] E. Schlottmann, M. von Helversen, H. A. M. Leymann, T. Lettau, F. Krüger, M. Schmidt, C. Schneider, M. Kamp, S. Höfling, J. Beyer, J. Wiersig, and S. Reitzenstein, Phys. Rev. Appl. **9**, 064030 (2018).

[32] M. Schmidt, M. von Helversen, M. López, F. Gericke, E. Schlottmann, T. Heindel, S. Kück, S. Reitzenstein, and J. Beyer, J. Low Temp. Phys. **193**, 1243 (2018).

[33] M. v. Helversen, J. Böhm, M. Schmidt, M. Gschrey, J.-H. Schulze, A. Strittmatter, S. Rodt, J. Beyer, T. Heindel, and S. Reitzenstein, New J. Phys. **21**, 035007 (2019).

[34] M. Klaas, E. Schlottmann, H. Flayac, F. Laussy, F. Gericke, M. Schmidt, M. Helversen, J. Beyer, S. Brodbeck, H. Suchomel,

S. Höfling, S. Reitzenstein, and C. Schneider, Phys. Rev. Lett. **121**, 047401 (2018).

[35] J. Hloušek, M. Dudka, I. Straka, and M. Ježek, Phys. Rev. Lett. **123**, 153604 (2019).

[36] L. Besombes, K. Kheng, L. Marsal, and H. Mariette, Phys. Rev. B **63**, 155307 (2001).

[37] P. Borri, W. Langbein, S. Schneider, U. Woggon, R. L. Sellin, D. Ouyang, and D. Bimberg, Phys. Rev. Lett. **87**, 157401 (2001).

[38] B. Krummheuer, V. M. Axt, and T. Kuhn, Phys. Rev. B **65**, 195313 (2002).

[39] V. M. Axt, T. Kuhn, A. Vagov, and F. M. Peeters, Phys. Rev. B **72**, 125309 (2005).

[40] I. A. Ostapenko, G. Hönig, S. Rodt, A. Schliwa, A. Hoffmann, D. Bimberg, M. R. Dachner, M. Richter, A. Knorr, S. Kako, Y. Arakawa, Phys. Rev. B **85**, 081303(R) (2012).

[41] B. Krummheuer, V. M. Axt, T. Kuhn, I. D'Amico, and F. Rossi, Phys. Rev. B **71**, 235329 (2005).

[42] A. Vagov, V. M. Axt, T. Kuhn, W. Langbein, P. Borri, and U. Woggon, Phys. Rev. B **70**, 201305(R) (2004).

[43] D. E. Reiter, Phys. Rev. B **95**, 125308 (2017).

[44] J. Förstner, C. Weber, J. Danckwerts, and A. Knorr, Phys. Rev. Lett. **91**, 127401 (2003).

[45] A. Krügel, V. M. Axt, T. Kuhn, P. Machnikowski, and A. Vagov, Appl. Phys. B **81**, 897 (2005).

[46] A. Vagov, M. D. Croitoru, V. M. Axt, T. Kuhn, and F. M. Peeters, Phys. Rev. Lett. **98**, 227403 (2007).

[47] A. J. Ramsay, A. V. Gopal, E. M. Gauger, A. Nazir, B. W. Lovett, A. M. Fox, and M. S. Skolnick, Phys. Rev. Lett. **104**, 017402 (2010).

[48] N. Makri and D. E. Makarov, J. Chem. Phys. **102**, 4600 (1995).

[49] N. Makri and D. E. Makarov, J. Chem. Phys. **102**, 4611 (1995).

[50] A. M. Barth, A. Vagov, and V. M. Axt, Phys. Rev. B **94**, 125439 (2016).

[51] J. S. Melinger, D. McMorrow, C. Hillegas, and W. S. Warren, Phys. Rev. A **51**, 3366 (1995).

[52] B. Saleh and M. Teich, *Fundamentals of Photonics, 2 Volume Set*, Wiley Series in Pure and Applied Optics (Wiley Interscience, New York, 2019).

[53] J. P. Reithmaier, G. Sęk, A. Löffler, C. Hofmann, S. Kuhn, S. Reitzenstein, L. V. Keldysh, V. D. Kulakovskii, T. L. Reinecke, and A. Forchel, Nature (London) **432**, 197 (2004).

[54] T. Yoshie, A. Scherer, J. Hendrickson, G. Khitrova, H. M. Gibbs, G. Rupper, C. Ell, O. B. Shchekin, and D. G. Deppe, Nature (London) **432**, 200 (2004).

[55] G. Khitrova, H. M. Gibbs, M. Kira, S. W. Koch, and A. Scherer, Nat. Phys. **2**, 81 (2006).

[56] D. G. Nahri, F. H. A. Mathkoor, and C. H. R. Ooi, J. Phys.: Condens. Matter **29**, 055701 (2017).

[57] K. Kuruma, Y. Ota, M. Kakuda, S. Iwamoto, and Y. Arakawa, Phys. Rev. B **97**, 235448 (2018).

[58] P. Machnikowski and L. Jacak, Phys. Rev. B **69**, 193302 (2004).

[59] A. Krügel, V. M. Axt, and T. Kuhn, Phys. Rev. B **73**, 035302 (2006).

[60] D. Mogilevtsev, A. P. Nisovtsev, S. Kilin, S. B. Cavalcanti, H. S. Brandi, and L. E. Oliveira, Phys. Rev. Lett. **100**, 017401 (2008).

[61] D. Mogilevtsev, A. P. Nisovtsev, S. Kilin, S. B. Cavalcanti, H. S. Brandi, and L. E. Oliveira, J. Phys.: Condens. Matter **21**, 055801 (2009).

[62] A. J. Ramsay, T. M. Godden, S. J. Boyle, E. M. Gauger, A. Nazir, B. W. Lovett, A. M. Fox, and M. S. Skolnick, Phys. Rev. Lett. **105**, 177402 (2010).

[63] D. P. S. McCutcheon and A. Nazir, New J. Phys. **12**, 113042 (2010).

[64] D. P. S. McCutcheon, N. S. Dattani, E. M. Gauger, B. W. Lovett, and A. Nazir, Phys. Rev. B **84**, 081305(R) (2011).

[65] E. R. Schmidgall, P. R. Eastham, and R. T. Phillips, Phys. Rev. B **81**, 195306 (2010).

[66] C.-M. Simon, T. Belhadj, B. Chatel, T. Amand, P. Renucci, A. Lemaitre, O. Krebs, P. A. Dalgarno, R. J. Warburton, X. Marie, and B. Urbaszek, Phys. Rev. Lett. **106**, 166801 (2011).

[67] Y. Wu, I. M. Piper, M. Ediger, P. Brereton, E. R. Schmidgall, P. R. Eastham, M. Hugues, M. Hopkinson, and R. T. Phillips, Phys. Rev. Lett. **106**, 067401 (2011).

[68] S. Lüker, K. Gawarecki, D. E. Reiter, A. Grodecka-Grad, V. M. Axt, P. Machnikowski, and T. Kuhn, Phys. Rev. B **85**, 121302(R) (2012).

[69] K. Gawarecki, S. Lüker, D. E. Reiter, T. Kuhn, M. Glässl, V. M. Axt, A. Grodecka-Grad, and P. Machnikowski, Phys. Rev. B **86**, 235301 (2012).

[70] A. Debnath, C. Meier, B. Chatel, and T. Amand, Phys. Rev. B **86**, 161304(R) (2012).

[71] A. Debnath, C. Meier, B. Chatel, and T. Amand, Phys. Rev. B **88**, 201305(R) (2013).

[72] M. Glässl, A. M. Barth, K. Gawarecki, P. Machnikowski, M. D. Croitoru, S. Lüker, D. E. Reiter, T. Kuhn, and V. M. Axt, Phys. Rev. B **87**, 085303 (2013).

[73] R. Mathew, E. Dilcher, A. Gamouras, A. Ramachandran, Hong Yi Shi Yang, S. Freisem, D. Deppe, and K. C. Hall, Phys. Rev. B **90**, 035316 (2014).

[74] D. E. Reiter, T. Kuhn, M. Glässl, and V. M. Axt, J. Phys.: Condens. Matter **26**, 423203 (2014).

[75] T. Kaldewey, S. Lüker, A. V. Kuhlmann, S. R. Valentin, A. Ludwig, A. D. Wieck, D. E. Reiter, T. Kuhn, and R. J. Warburton, Phys. Rev. B **95**, 161302(R) (2017).

[76] M. Born and V. Fock, Z. Phys. **51**, 165 (1928).

[77] W. M. Itano, J. C. Bergquist, and D. J. Wineland, Phys. Rev. A **38**, 559 (1988).

[78] I. S. Osad'ko, J. Exp. Theor. Phys. **101**, 64 (2005).

[79] X.-Z. Zhang, Z.-H. Wang, H. Li, Q. Wu, B.-Q. Tang, F. Gao, and J.-J. Xu, Chin. Phys. Lett. **25**, 3976 (2008).

[80] J. Sanders, M. Jonckheere, and S. Kokkelmans, Phys. Rev. Lett. **115**, 043002 (2015).

Publication 4

"Different Types of Photon Entanglement from a Constantly Driven Quantum Emitter Inside a Cavity"

T. Seidelmann, M. Cosacchi, M. Cygorek, D. E. Reiter, A. Vagov, and V. M. Axt.

Adv. Quantum Technol. **4**, 2000108 (2021).

&

Correction: "Different Types of Photon Entanglement from a Constantly Driven Quantum Emitter Inside a Cavity"

T. Seidelmann, M. Cosacchi, M. Cygorek, D. E. Reiter, A. Vagov, and V. M. Axt.

Adv. Quantum Technol. **5**, 2200058 (2022).

Author contributions

The author has designed the concept of this study, has performed the numerical data generation and analysis, and has implemented the problem-specific C++ code. He has provided interpretations of the results and has written the first draft of the publication and the correction. In particular, he performed the analytic calculations that enabled the detailed analysis and explanations of the system. During the publication process, he has organized the submission and revision of the manuscript and has written the answer to the referees.

M. Cosacchi has participated in the general discussion of the results and their interpretations. Furthermore, he has discussed the results in detail with the author and has assisted with the numerical implementation. He has also contributed to revisions of the draft, the answers to the referees, and the correction.

M. Cygorek, D. E. Reiter, and A. Vagov have co-supervised this work. In particular, they have participated in the discussion of the results and their interpretations. They have also contributed to the optimization of the presentation, revisions of the draft, the answers to the referees, and the correction.

V. M. Axt has advised the author throughout his work as the main supervisor, has obtained the funding for this work, and has provided the practical means. He has participated in the discussion of the results and their interpretations. He has also contributed to the optimization of the presentation, revisions of the draft, the answers to the referees, and the correction.

Different Types of Photon Entanglement from a Constantly Driven Quantum Emitter Inside a Cavity

Tim Seidelmann,* Michael Cosacchi, Moritz Cygorek, Doris E. Reiter, Alexei Vagov, and Vollrath M. Axt

Bell states are the most prominent maximally entangled photon states. In a typical four-level emitter, like a semiconductor quantum dot, the photon states exhibit only one type of Bell state entanglement. By adding an external driving to the emitter system, also other types of Bell state entanglement are reachable without changing the polarization basis. In this work, it is shown under which conditions the different types of entanglement occur and analytical equations are given to explain these findings. Furthermore, special points are identified, where the concurrence, being a measure for the degree of entanglement, drops to zero, while the coherences between the two-photon states stay strong. Results of this work pave the way to achieve a controlled manipulation of the entanglement type in practical devices.

1. Introduction

Entanglement of quantum states is one of the most remarkable and interesting physical effects that separate the quantum mechanical from the classical world.[1,2] Entanglement can be used to test quantum mechanical principles on a fundamental level, for example, by revealing violations of Bell inequalities.[2,3] Furthermore, many fascinating and innovative applications, for example, in quantum cryptography,[4,5] quantum communication,[6,7] or quantum information processing and computing,[8–11] rely on entangled photon pairs.

T. Seidelmann, M. Cosacchi, Dr. A. Vagov, Prof. V. M. Axt
Lehrstuhl für Theoretische Physik III
Universität Bayreuth
Universitätsstraße 30, 95447 Bayreuth, Germany
E-mail: tim1.seidelmann@uni-bayreuth.de
Dr. M. Cygorek
Institute of Photonics and Quantum Sciences
Heriot-Watt University
Edinburgh EH14 4AS, UK
Dr. D. E. Reiter
Institut für Festkörpertheorie
Universität Münster
Wilhelm-Klemm-Straße 10, 48149 Münster, Germany
Dr. A. Vagov
ITMO University
Kronverksky Pr. 49, St. Petersburg 197101, Russia

The defining property of an entangled bipartite system is that its quantum mechanical state cannot be factorized into parts corresponding to the constituent subsystems. There are four prominent states, which are maximally entangled and known as the Bell states, established for two entangled photons with horizontal H polarization and vertical V polarization

$$|\Phi_\pm\rangle = \frac{1}{\sqrt{2}}(|HH\rangle \pm |VV\rangle), \tag{1}$$

$$|\Psi_\pm\rangle = \frac{1}{\sqrt{2}}(|HV\rangle \pm |VH\rangle). \tag{2}$$

In the following we will refer to these states as Φ Bell state (ΦBS) and ΨBS. To create maximally entangled states, one of the best established routes is via the cascaded relaxation in few-level systems like atoms, semiconductor quantum dots or F-centers.[12–15]

In this paper, we study under which driving conditions, a four-level emitter (FLE) placed in a microcavity produces entangled photons being either in a ΦBS or ΨBS. We demonstrate that a constantly driven FLE undergoes a sharp transition between regions of high ΦBS and ΨBS entanglement for a certain two-photon resonance. At the transition the degree of entanglement drops to zero at a special point, because the quantum state of the system becomes factorizable. We will further study all two-photon resonances revealing a rich variety of different scenarios with or without switching the type of entanglement and with or without special points of zero concurrence.

2. Generation of Entangled States

The generation procedure of entangled photons in a typical (non-driven) four-level system is as follows [see also **Figure 1** (left)]: In a first step the uppermost state is prepared, for example, by using two-photon resonant or near-resonant excitation with short coherent pulses[16–24] or adiabatic rapid passage protocols.[25–28] The excited emitter then decays into a superposition of the two intermediate states which can be reached from the uppermost state by emission of either a horizontally or vertically polarized photon. In the subsequent decay to the ground state a second photon is emitted. Since a component in the superposition that was created by emitting a photon with a given polarization gives rise to a second photon having the same polarization a ΦBS two-photon state is generated. Experiments and theoretical studies in semiconductor quantum dots demonstrated the possibility to generate ΦBS entanglement.[3,16,29–50]

ADVANCED
SCIENCE NEWS

www.advancedsciencenews.com

ADVANCED
QUANTUM
TECHNOLOGIES

www.advquantumtech.com

The situation changes profoundly when the few-level system is continuously driven by an external laser. Then additionally, it becomes possible to create ΨBS entanglement. A possible mechanism could be that the uppermost state emits a horizontally polarized photon via one path way, is then re-excited by the laser and then emits a vertically polarized photon via the other path. Since the sequence of emission of a pair of *H, V* or *V, H* polarized photons is identical, this process results in an entangled ΨBS. Note that the states $|HV\rangle$ and $|VH\rangle$ are distinguished by the temporal order of the *H* or *V* polarized photon emissions. Indeed, Sánchez Muñoz et al. found that under specific conditions the resulting two-photon state is close to the ΨBS.[51] Here we will show that ΨBS entanglement occurs under various conditions, but also ΦBS entanglement is supported by a driven FLE system. The key is adjusting the cavity modes to two-photon transitions between the emerging laser-dressed states of the FLE. The situation of constant driving was also studied experimentally,[52,53] where the emission spectra clearly demonstrated the transition from the bare states toward the laser-dressed states.

To create entangled photon states in an optimal way, the FLE is embedded inside a microcavity. By this, the coupling to the cavity enhances the light-collection efficiency and the photon emission rate due to the Purcell effect.[42,54] Additionally, the energetic placement of the cavity modes can have a profound impact on the resulting degree of entanglement. By placing the cavity modes in resonance with a two-photon transition of the emitter[29,32,33,47,51,55] direct two-photon emission processes dominate over sequential single-photon ones. Since the direct two-photon emission is much less affected by a possible which-path information this configuration results in a high degree of entanglement of the emitted photon pairs,[32,33] at least at low temperature.[29]

3. Driven Four-Level Emitter

3.1. Bare State Picture

We consider an externally driven FLE embedded inside a microcavity, adopting the model from ref. [51]. The FLE comprises the energetic ground state $|G\rangle$ at energy 0, two degenerate intermediate states $|X_{H/V}\rangle$ with energy $\hbar\omega_X$, and the upper state $|XX\rangle$ at energy $2\hbar\omega_X - E_B$. Note that it is quite common to find the state $|XX\rangle$ not exactly at twice the energy of the single excited states, which in quantum dots is known as the biexciton binding energy.[2,55,56] Optical transitions which involve the state $|X_H\rangle$ ($|X_V\rangle$) are evoked by horizontally (vertically) polarized light. Following ref. [51], we assume the fine-structure splitting between these two intermediate states to be zero. A sketch of the FLE is shown in Figure 1 (left). The Hamiltonian of the FLE reads

$$\hat{H}_{\text{FLE}} = \hbar\omega_X\big(|X_H\rangle\langle X_H| + |X_V\rangle\langle X_V|\big) + \big(2\hbar\omega_X - E_B\big)|XX\rangle\langle XX|. \tag{3}$$

The FLE is continuously driven by an external laser with frequency ω_L and driving strength Ω. The laser driving is assumed to be linearly polarized, such that the *H* and *V* polarized transitions are driven with equal strength ensuring that there is no preferred polarization and, consequently, no which-path
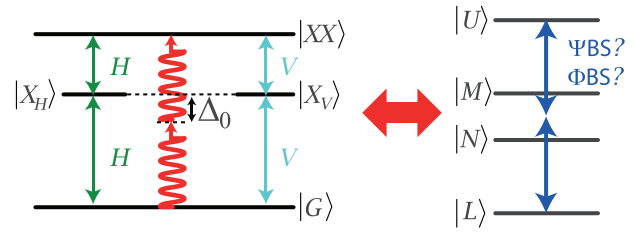
Figure 1. Left: Sketch of the FLE including optical selection rules for transitions with either horizontally (*H*) or vertically (*V*) polarized light. In addition, an external laser field excites the system. Right: Sketch of the laser-dressed states.

information is introduced by the external laser. In the frame co-rotating with the laser frequency ω_L the corresponding Hamiltonian reads

$$\hat{H}_L = \Omega\big(\hat{\sigma}_D + \hat{\sigma}_D^\dagger\big); \qquad \hat{\sigma}_D = \big(\hat{\sigma}_H + \hat{\sigma}_V\big)/\sqrt{2} \tag{4}$$

with the transition operators

$$\hat{\sigma}_H = |G\rangle\langle X_H| + |X_H\rangle\langle XX|, \tag{5a}$$

$$\hat{\sigma}_V = |G\rangle\langle X_V| + |X_V\rangle\langle XX|. \tag{5b}$$

We fix the laser frequency to $\hbar\omega_L = (2\hbar\omega_X - E_B)/2$, such that the energetic detuning between emitter transitions and laser is set to

$$\Delta_0 := \hbar\big(\omega_X - \omega_L\big) = \frac{E_B}{2}. \tag{6}$$

By this, we resonantly drive the two-photon transition between ground state $|G\rangle$ and upper state $|XX\rangle$.

The FLE is embedded inside a microcavity and coupled to two orthogonal linearly polarized cavity modes with energies $\hbar\omega_H^c$ and $\hbar\omega_V^c$, which we assume to be energetically degenerate, that is, $\omega_c := \omega_H^c = \omega_V^c$. The cavity mode is best defined with respect to the driving laser frequency (or the two-photon resonance to $|XX\rangle$) via the cavity laser detuning

$$\Delta := \hbar\big(\omega_c - \omega_L\big) = \hbar\omega_c - \big(\hbar\omega_X - \Delta_0\big). \tag{7}$$

The Hamiltonian describing the cavity modes and their interaction with the FLE reads

$$\hat{H}_c = \sum_{\ell=H,V} \Delta\hat{a}_\ell^\dagger\hat{a}_\ell + \hat{H}_{\text{FLE-c}}. \tag{8}$$

In matrix form, using the basis $|XX\rangle$, $|X_H\rangle$, $|X_V\rangle$, and $|G\rangle$, the interaction Hamiltonian is given as

$$\hat{H}_{\text{FLE-c}} = \begin{pmatrix} 0 & g\hat{a}_H & g\hat{a}_V & 0 \\ g\hat{a}_H^\dagger & 0 & 0 & g\hat{a}_H \\ g\hat{a}_V^\dagger & 0 & 0 & g\hat{a}_V \\ 0 & g\hat{a}_H^\dagger & g\hat{a}_V^\dagger & 0 \end{pmatrix}, \tag{9}$$

where the emitter-cavity coupling constant *g* is assumed equal for all transitions. The bosonic operators $\hat{a}_{H/V}^\dagger$ ($\hat{a}_{H/V}$) create (annihilate) one cavity photon with frequency ω_c and *H/V* polarization.

**ADVANCED
SCIENCE NEWS**

www.advancedsciencenews.com

**ADVANCED
QUANTUM
TECHNOLOGIES**

www.advquantumtech.com

Note that $\hat{H}_c$ is again written in the rotating frame. From the interaction Hamiltonian we can already see that in the un-driven situation the cascade from the state $|XX\rangle$ into the state $|G\rangle$ can only go via the emission of two H or two V polarized photons and therefore can result exclusively in the generation of ΦBS entanglement.

3.2. Laser-Dressed States

The creation of entangled two-photon states is facilitated by resonant transitions between quantum states of the FLE with the emission of two photons. Further analysis of the system dynamics reveals that such transitions take place not between the original FLE basis states but between the dressed states of the laser driven FLE, obtained by diagonalizing $\hat{H}_{FLE} + \hat{H}_L$. For the diagonalization we go into a frame rotating with the laser frequency ω_L. The eigenenergies of the dressed states read

$$E_U = \frac{1}{2}\left(\Delta_0 + \sqrt{\Delta_0^2 + 8\Omega^2}\right) \tag{10a}$$

$$E_M = \Delta_0 \tag{10b}$$

$$E_N = 0 \tag{10c}$$

$$E_L = \frac{1}{2}\left(\Delta_0 - \sqrt{\Delta_0^2 + 8\Omega^2}\right) \tag{10d}$$

and the corresponding laser-dressed states are

$$|U\rangle = c(|G\rangle + |XX\rangle) + \tilde{c}(|X_H\rangle + |X_V\rangle) \tag{11a}$$

$$|M\rangle = \frac{1}{\sqrt{2}}(|X_H\rangle - |X_V\rangle) \tag{11b}$$

$$|N\rangle = \frac{1}{\sqrt{2}}(|G\rangle - |XX\rangle) \tag{11c}$$

$$|L\rangle = \tilde{c}(|G\rangle + |XX\rangle) - c(|X_H\rangle + |X_V\rangle) \tag{11d}$$

with the coefficients

$$c = \frac{2\Omega}{\sqrt{8\Omega^2 + \left(\Delta_0 + \sqrt{\Delta_0^2 + 8\Omega^2}\right)^2}}, \quad \tilde{c} = \sqrt{\frac{1}{2} - c^2}. \tag{12}$$

A sketch of the four laser-dressed states is given in Figure 1 (right panel). The dependence of the dressed state energies on the driving strength Ω is illustrated in **Figure 2**. The uppermost $|U\rangle$ and the lowest $|L\rangle$ states have contributions of all four original (bare) FLE states. In the limiting case of strong driving the contribution coefficients c and $\tilde{c}$ approach $1/2$. On the other hand, the composition and energies of the intermediate dressed states $|M\rangle$ ("middle") and $|N\rangle$ ("null") are independent of Ω. In general, the laser-dressed states and the transition energies between them are functions of Ω. Therefore, also the cavity frequency associated with a two-photon resonance between two given dressed states depends on the driving strength, the only exception being the resonance between the states $|M\rangle$ and $|N\rangle$.
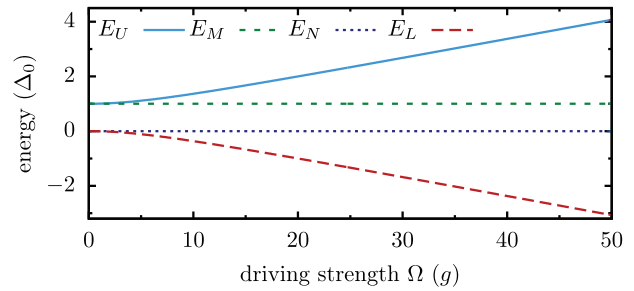
Figure 2. Energies of the laser dressed states (in the units of the emitter-laser detuning Δ_0) as a function of the driving strength Ω (in the units of the emitter-cavity coupling strength g).

The Hamiltonian describing the coupling to the cavity also changes profoundly by using the dressed state basis and now reads in the basis $|U\rangle, |M\rangle, |N\rangle, |L\rangle$

$$\hat{H}_{DS-c} = g\begin{pmatrix} 2\sqrt{2}c\tilde{c}\,\hat{a}_D^\dagger & c\,\hat{a}_A^\dagger & -\tilde{c}\,\hat{a}_D^\dagger & \sqrt{2}(\tilde{c}^2 - c^2)\hat{a}_D^\dagger \\ c\,\hat{a}_A^\dagger & 0 & \frac{-1}{\sqrt{2}}\hat{a}_A^\dagger & \tilde{c}\,\hat{a}_A^\dagger \\ \tilde{c}\,\hat{a}_D^\dagger & \frac{1}{\sqrt{2}}\hat{a}_A^\dagger & 0 & -c\,\hat{a}_D^\dagger \\ \sqrt{2}(\tilde{c}^2 - c^2)\hat{a}_D^\dagger & \tilde{c}\,\hat{a}_A^\dagger & c\,\hat{a}_D^\dagger & -2\sqrt{2}c\tilde{c}\,\hat{a}_D^\dagger \end{pmatrix} + c.c. \tag{13}$$

with $\hat{a}_D^\dagger = (\hat{a}_H^\dagger + \hat{a}_V^\dagger)/\sqrt{2}$ and $\hat{a}_A^\dagger = (\hat{a}_H^\dagger - \hat{a}_V^\dagger)/\sqrt{2}$ being the creation operators in the diagonal and anti-diagonal polarization, respectively.

One notes that the two-photon transitions between the dressed states can follow different pathways that connect those states. Considering as an example the transition from $|U\rangle$ to $|L\rangle$, one path is to emit two photons with anti-diagonal polarization A via the intermediate state $|M\rangle$, while another path is a self interaction within $|U\rangle$ and then a direct transition to $|L\rangle$ via emission of two diagonally D-polarized photons. This already indicates that due to the constant optical driving it is not clear a priori, which entanglement type occurs. We will show below that new types of entanglement become possible and analyze their respective strength.

3.3. Cavity Losses and Radiative Decay

To account for cavity losses and radiative decay, present in every FLE-cavity system, we introduce Lindblad-type operators

$$\mathcal{L}_{\hat{O},\Gamma}\hat{\rho} = \frac{\Gamma}{2}\left(2\hat{O}\hat{\rho}\hat{O}^\dagger - \hat{\rho}\hat{O}^\dagger\hat{O} - \hat{O}^\dagger\hat{O}\hat{\rho}\right), \tag{14}$$

where $\hat{O}$ is the system operator associated with a loss process with corresponding loss rate Γ in the bare state system. The dynamics of the statistical operator of the system $\hat{\rho}$ is then determined by the Liouville-von Neumann equation

$$\frac{d}{dt}\hat{\rho} = \mathcal{L}\hat{\rho} := -\frac{i}{\hbar}[\hat{H}, \hat{\rho}] + \sum_{\ell=H,V}\left\{\mathcal{L}_{\hat{a}_\ell,\kappa} + \mathcal{L}_{|G\rangle\langle X_\ell|,\gamma} + \mathcal{L}_{|X_\ell\rangle\langle XX|,\gamma}\right\}\hat{\rho}, \tag{15}$$

ADVANCED
SCIENCE NEWS
www.advancedsciencenews.com

ADVANCED
QUANTUM
TECHNOLOGIES
www.advquantumtech.com

Table 1. Fixed system parameters used in the calculations.

Parameter		Value
Emitter-cavity coupling strength	g	0.051 meV
Detuning	Δ_0	$20 \times g = 1.02$ meV
Cavity loss rate	κ	$0.1 \times g/\hbar \approx 7.8$ ns^{-1}
Radiative decay rate	γ	$0.01 \times g/\hbar \approx 0.78$ ns^{-1}

where $[\cdot, \cdot]$ denotes the commutator, κ is the cavity loss rate, and γ the radiative decay rate. The complete system Hamiltonian $\hat{H}$ includes all contributions discussed in Section 3.1. The system is assumed initially in the ground state $|G\rangle$ without any cavity photons. Note that we performed all numerical calculations in the rotating frame with the laser frequency ω_L and use the bare state system, while for the interpretation the dressed state picture is advantageous.

The parameter values used in our simulations are listed in **Table 1**, where we followed ref. [51]. The frequency of the cavity mode is taken to be $\hbar\omega_c = 1.5$ eV. The adopted parameter values correspond to a high quality cavity resonator with $Q = 1.5 \times 10^5$.

4. Photon Entanglement

4.1. Two-Photon Density Matrix

The basis for quantifying the degree of entanglement is the determination of the two-photon density matrix ρ^{2p}. Experimentally, ρ^{2p} can be reconstructed using methods of quantum state tomography,[57] a technique based on polarization-resolved two-time coincidence measurements. The detected signals are proportional to the two-time correlation functions

$$G^{(2)}_{jk,lm}(t, \tau) = \left\langle \hat{a}_j^\dagger(t)\hat{a}_k^\dagger(t+\tau)\hat{a}_m(t+\tau)\hat{a}_l(t) \right\rangle, \tag{16}$$

where $\{j, k, l, m\} \in \{H, V\}$, t is the real time when the first photon is detected, and τ the delay time between the detection of the first and the second photon. Note that in experiments one typically measures photons that have already left the cavity. However, considering the out-coupling of light out of the cavity to be a Markovian process, Equation (16) can also describe $G^{(2)}_{jk,lm}(t, \tau)$ measured outside the cavity.[10,30]

In experiments data is typically averaged over finite real time and delay time windows. Thus, the experimentally reconstructed two-photon density matrix is calculated as [30,51]

$$\rho^{2p}_{jk,lm}(\tau) = \frac{\overline{G}^{(2)}_{jk,lm}(\tau)}{\text{Tr}\left\{\overline{G}^{(2)}(\tau)\right\}}, \tag{17}$$

where $\overline{G}^{(2)}$ is the time-averaged correlation with

$$\overline{G}^{(2)}_{jk,lm}(\tau) = \frac{1}{\Delta t \, \tau} \int_{t_0}^{t_0+\Delta t} dt \int_0^\tau d\tau' \, G^{(2)}_{jk,lm}(t, \tau'). \tag{18}$$

Here, τ (Δt) is the delay time (real time) window used in the co-incidence measurement and t_0 is its starting time. The trace $\text{Tr}\{\cdot\}$ is introduced for normalization. For simplicity we refer to ρ^{2p} as the two-photon density matrix in the following.

Throughout this work we calculate the two-photon density matrix for the system that reached its steady state so that the t-average is independent of t_0 and Δt. The steady state of the system $\hat{\rho}_s$ is defined by $\frac{d}{dt}\hat{\rho}_s = \mathcal{L}\hat{\rho}_s = 0$. This state is obtained numerically by letting the system evolve in time until its density matrix becomes stationary. We will further set $\tau = 50$ ps, which is a realistic value for the delay time window used in experiment.[58] More details on the calculation of the two-time correlation functions for systems including Markovian loss processes can be found in ref. [60].

4.2. Concurrence

Using the two-photon density matrix we determine the corresponding concurrence C,[59] which is a widely accepted measure for the degree of entanglement of a bipartite system. The concurrence is calculated from a given two-photon density matrix ρ^{2p} according to [47,57,59]

$$C = \max\left\{0, \sqrt{\lambda_1} - \sqrt{\lambda_2} - \sqrt{\lambda_3} - \sqrt{\lambda_4}\right\} \tag{19}$$

where λ_j are the (real and positive) eigenvalues in decreasing order, $\lambda_1 \geq \lambda_2 \geq \lambda_3 \geq \lambda_4$, of the matrix

$$M = \rho^{2p} \, T \, (\rho^{2p})^* \, T, \tag{20}$$

where T is an anti-diagonal matrix of rank 4 with elements $\{-1, 1, 1, -1\}$ and $(\rho^{2p})^*$ is the complex conjugated two-photon density matrix. In the standard situation without driving, where only a ΦBS $|\Phi_\pm\rangle$ can be generated, the full expression for the concurrence reduces to $C = 2|\rho^{2p}_{HH,VV}|$. Thus, the degree of entanglement is closely related to the corresponding coherences in the two-photon density matrix. Note that like the two-photon density matrix $\rho^{2p}(\tau)$ also the concurrence $C(\tau)$ depends on the measurement window τ. A finite delay time window τ is necessary for the detection of ΨBS entanglement since the two contributions that build up $|\Psi_+\rangle$ in Equation (2) can only be distinguished if the two photons are detected at different times.[51]

For the numerical calculation of the concurrence we use the following procedure: First, following ref. [60], the averaged two-time photon correlation $\overline{G}^{(2)}$ is calculated. This quantity is then used to obtain the time-averaged two-photon density matrix in Equation (17). Finally from the two-photon density matrix the concurrence is determined according to Equation (19). Note that we do not use any further approximations in the calculation of $\overline{G}^{(2)}$.

5. Two-Photon Transition Between Upper and Lower Dressed State

The emission of entangled two-photon states is associated with two photon transitions between the dressed FLE states. The dressed FLE states feature two-photon emissions, which are
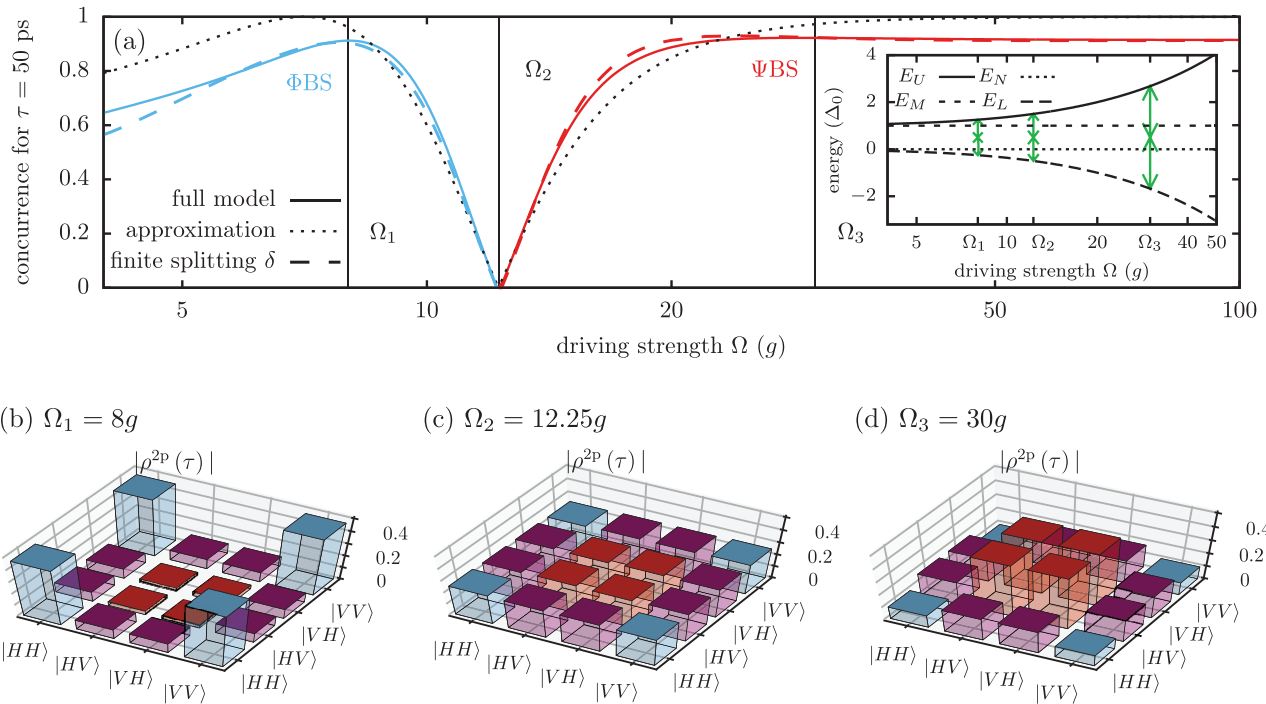
**ADVANCED
SCIENCE NEWS**
www.advancedsciencenews.com

**ADVANCED
QUANTUM
TECHNOLOGIES**
www.advquantumtech.com

Figure 3. a) Concurrence as function of the laser driving strength Ω for the full model (solid line), the analytic approximation $C(r)$ presented in Equation (29) (dotted line), and with a finite fine-structure splitting $\delta = 0.1\Delta_0$ (dashed line). Inset: Dressed state energies as a function of the driving strength and the two-photon resonant cavity modes (green arrows) for three selected Ω values. b–d) Absolute value of the two-photon density matrix $|\rho^{2\mathrm{p}}(\tau)|$ for driving strength (b) $\Omega_1 = 8 \times g$, (c) $\Omega_2 = 12.25 \times g$, and (d) $\Omega_3 = 30 \times g$ (indicated by vertical lines in (a)).

largest every time the cavity frequency is tuned in resonance with a possible two-photon transition, that is, when twice the photon energy (here Δ) is equal to the transition energy between the dressed state pairs. Therefore, the analysis is focused on these resonant situations.

We start our analysis with the case where the cavity photons are in resonance with the transition between the states $|U\rangle$ and $|L\rangle$, that is, the cavity frequency is always tuned such that

$$\Delta = \frac{E_U - E_L}{2} = \frac{1}{2}\sqrt{\Delta_0^2 + 8\Omega^2}. \tag{21}$$

Notice, that keeping this condition requires the cavity frequency ω_c to change with the driving strength Ω. This resonance for a driven FLE was considered in earlier works,[51] where a possibility to achieve a high degree of ΨBS entanglement was demonstrated. Here we demonstrate that ΨBS entanglement is not the only type of two-photon entanglement that can be obtained. It will be shown that by varying the driving strength (while keeping the system at the considered resonance) the FLE can reach the domain of ΦBS entanglement, separated from that of the ΨBS by a special critical point of zero concurrence.

5.1. Transition Between ΦBS and ΨBS Entanglement

The concurrence as a function of the driving strength Ω is shown in **Figure 3**a, where the inset illustrates the resonance in question. In full agreement with earlier calculations[51] one observes ΨBS entanglement when the driving is strong. However, when

the driving strength is lowered the entanglement changes its type to ΦBS entanglement. A sharp transition between the two types occurs at a special critical point $\Omega \approx 12.25 \times g$ where the concurrence is exactly zero. The ΦBS entanglement obtained for weak driving reflects the fact that for small Ω the system approaches the undriven case. Recalling that ΨBS entanglement has been found in ref. [51] for higher Ω, it is clear that a transition has to take place in between.

More insight into the entanglement change is obtained by calculating the corresponding two-photon density matrices as presented in Figure 3b for the driving strength $\Omega_1 = 8 \times g$ and Figure 3d $\Omega_3 = 30 \times g$. At Ω_1 the occupations of the states $|HH\rangle$ and $|VV\rangle$ and their coherence clearly dominate over the remaining elements representing ΦBS entanglement. A very different behavior is found at $\Omega_3 = 30 \times g$, where the occupations of the states $|HV\rangle$ and $|VH\rangle$ and the corresponding coherences exhibit the highest values and, consequently, are associated with ΨBS entanglement.

Let us now focus on the special point at $\Omega_2 = 12.25 \times g$. The two-photon density matrix at the special point, shown in Figure 3c, reveals that the concurrence does not vanish because of the absence of coherences. On the contrary, all coherences are close to their maximal possible value of about 0.25. Further analysis reveals that the corresponding two-photon state is

$$
\begin{aligned}
|\psi_{\mathrm{sp}}\rangle &= \frac{1}{2}\left(|HH\rangle - |HV\rangle - |VH\rangle + |VV\rangle\right) \\
&= \frac{1}{\sqrt{2}}\left(|H_1\rangle - |V_1\rangle\right)\frac{1}{\sqrt{2}}\left(|H_2\rangle - |V_2\rangle\right).
\end{aligned}
\tag{22}
$$

2000108 (5 of 14)

ADVANCED
SCIENCE NEWS
www.advancedsciencenews.com

ADVANCED
QUANTUM
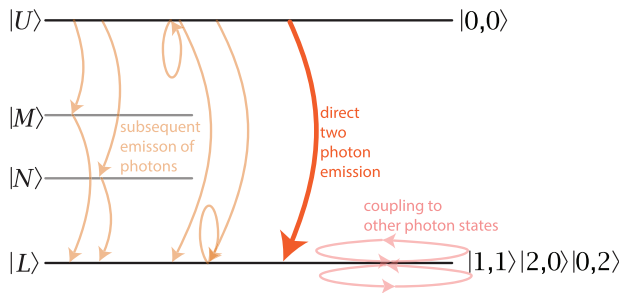TECHNOLOGIES
www.advquantumtech.com

Figure 4. Schematic depiction of the possible transitions connecting $|U, 0, 0\rangle$ to the two-photon states $|L, 1, 1\rangle$, $|L, 2, 0\rangle$, and $|L, 0, 2\rangle$. All but the direct two-photon emission process (bold orange arrow) are eliminated in the Schrieffer–Wolff transformation.

Remarkably, this is a pure state and $|\psi_{sp}\rangle$ can be factorized into a product of two one-photon states describing the first and second detected photon, respectively (indicated by 1 and 2). Since $|\psi_{sp}\rangle$ can be factorized, it is not entangled and, thus, the concurrence vanishes at this point. Therefore, instead of a direct transition from high ΦBS to high ΨBS entanglement the system passes through this special point with vanishing degree of entanglement.

We note that the special point occurs at a distinct resonance condition. Beside the two-photon transition between the two outermost dressed states, also the one-photon process between the intermediate states $|M\rangle$ and $|N\rangle$ becomes resonant.

5.2. Effective Hamiltonian of the System at the Resonance

In order to understand the underlying physics of the crossover between the entanglement types we derive an effective Hamiltonian that describes the most relevant transition processes involving the $|U\rangle$ and $|L\rangle$ states. To be more specific, we account only for the uppermost state without photons $|U, 0, 0\rangle$ and the lowest states with two photons $|L, 1, 1\rangle$, $|L, 2, 0\rangle$, and $|L, 0, 2\rangle$. Here, $|\chi, n_H, n_V\rangle$ is the product state of $|\chi\rangle \in \{|U\rangle, |M\rangle, |N\rangle, |L\rangle\}$ and the photon number state for H and V polarization.

Besides the direct two-photon transitions, there are several other possibilities to go from the initial to the final states. One example are subsequent one photon transitions, either going via one of the intermediate states or by a self-interaction and then a one-photon process. Also, from the final states, a sequential photon emission and absorption (or the other way around) can take place. These processes are depicted in **Figure 4**. Therefore, the states mentioned above are coupled to a bunch of other states, namely the one-photon states $|\chi, 1, 0\rangle$, $|\chi, 0, 1\rangle$ and the three-photon states $|\chi, 3, 0\rangle$, $|\chi, 2, 1\rangle$, $|\chi, 1, 2\rangle$, and $|\chi, 0, 3\rangle$ (with $\chi \in \{U, M, N, L\}$), while the latter can be reached in sequential emission/absorption processes.

Using a Schrieffer–Wolff transformation, it is now possible to encode these transitions into a single matrix, acting only within the basis spanned by the direct two-photon transitions, that is, $|U, 0, 0\rangle$, $|L, 1, 1\rangle$, $|L, 2, 0\rangle$, and $|L, 0, 2\rangle$.[61,62] A Schrieffer–Wolff transformation thereby performs a block-diagonalization, which decouples the desired states from the rest. This is reasonable, because the removed states are strongly off-resonant in this situ-

ation and, thus, represent a small perturbation. More details on the Schrieffer–Wolff transformation can be found in Appendix A.

After the Schrieffer–Wolff transformation, which is treated within the photon number states, we afterward perform additionally a basis transformation to rotate the system partially into the Bell basis with $\{|U, 0, 0\rangle, |L, 1, 1\rangle, |L, \Phi_+\rangle, |L, \Phi_-\rangle\}$. In this representation $|L, 1, 1\rangle$ corresponds to the possibility of ΨBS entanglement, where two photons are generated such that one is H- and the other V-polarized. However, without further analysis, we cannot distinguish between $\Psi_\pm$BS entanglement. The effective Schrieffer–Wolff Hamiltonian is then given by

$$\hat{H}_{UL}^{(2)} = g^2 \begin{pmatrix} \delta^{UL} & \gamma_1^{UL} & -\gamma_2^{UL} & 0 \\ \gamma_1^{UL} & -\delta^{UL} & \alpha^{UL} & 0 \\ -\gamma_2^{UL} & \alpha^{UL} & -\delta^{UL} & 0 \\ 0 & 0 & 0 & -\delta^{UL} \end{pmatrix} \tag{23}$$

with

$$\delta^{UL} = \left(\tilde{c}^2 - c^2\right)\left(\frac{2}{\Delta_0} + \frac{4}{\Delta_{UL}}\right)$$

$$\gamma_1^{UL} = 4c\tilde{c}\frac{1}{\Delta_0} - 16c\tilde{c}\left(\tilde{c}^2 - c^2\right)\frac{1}{\Delta_{UL}}$$

$$\gamma_2^{UL} = 16c\tilde{c}\left(\tilde{c}^2 - c^2\right)\frac{1}{\Delta_{UL}}$$

$$\alpha^{UL} = \frac{1}{\Delta_0} - \left(1 - 16c^2\tilde{c}^2\right)\frac{1}{\Delta_{UL}}, \tag{24}$$

where $\Delta_{UL} = E_U - E_L$. The given expressions contain only the most important contributions. The full expressions can be found in Appendix A.1. It is interesting to note that the coefficients $\gamma_{1/2}^{UL}$ stem from the subsequent emission of two single photons (faded orange arrows in Figure 4) and simultaneous two-photon emission, while α^{UL} accounts for the fact that from the two photon states, coupling to higher (lower) photon states can take place and therefore couple different types of two-photon states (faded red arrows in Figure 4). An example for the latter case is the coupling of $|L, 2, 0\rangle \rightarrow |L, 2, 1\rangle$, followed by a photon number reduction via $|L, 2, 1\rangle \rightarrow |L, 1, 1\rangle$ illustrating why different two-photon states are coupled.

From this Hamiltonian, we can now deduce which type of entanglement is created: First of all we find that the state $|L, \Phi_-\rangle$ is decoupled, such that we see that photons with this type of entanglement are not created. In contrast, the initial state $|U, 0, 0\rangle$ is coupled to the $|L, \Phi_+\rangle$ state via γ_2^{UL} and to the state $|L, 1, 1\rangle$ via γ_1^{UL}. Therefore in principle both ΦBS and ΨBS entanglement can be created. The different types of entangled states are coupled via the coefficient α^{UL}, however, we will for now neglect this coupling (see discussion at the end of the next section). Which type of entanglement dominates depends on the ratio

$$r = \frac{\gamma_1^{UL}}{\gamma_2^{UL}} = 4\left(\frac{\Omega}{\Delta_0}\right)^2 - \frac{1}{2}. \tag{25}$$

This means, we obtain preferably ΦBS entanglement, when $\gamma_2^{UL} > \gamma_1^{UL}$ (or $|r| < 1$), and preferably ΨBS entanglement if
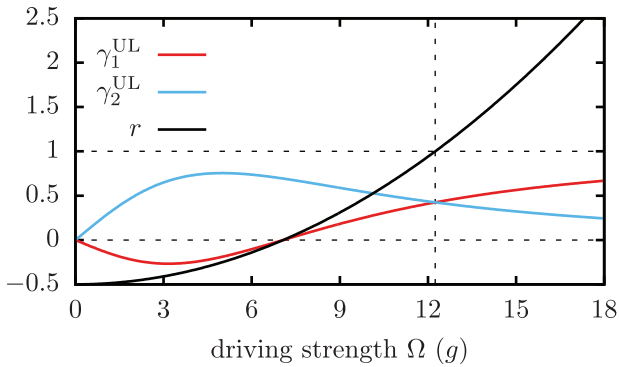
**ADVANCED
SCIENCE NEWS**

www.advancedsciencenews.com

**ADVANCED
QUANTUM
TECHNOLOGIES**

www.advquantumtech.com

Figure 5. Effective coupling constants γ_1^{UL} and γ_2^{UL} and the ratio $r = \gamma_1^{\mathrm{UL}}/\gamma_2^{\mathrm{UL}}$ as function of the driving strength Ω.

$\gamma_2^{\mathrm{UL}} < \gamma_1^{\mathrm{UL}}$ (or $|r| > 1$). **Figure 5** displays the ratio r as well as the couplings γ_1^{UL} and γ_2^{UL} as a function of the driving strength Ω. Indeed, $r = 1$ corresponds to $\Omega_{\mathrm{sp}} = \sqrt{3/8}\Delta_0$ and we obtain our special point, when both types of entanglement are occurring with equal weight and we have zero concurrence since their superposition results in a factorizable state.

5.3. Approximate Two-Photon Density Matrix

Further insight is obtained by calculating the two-photon density matrix assuming the delay window τ is small and can be neglected so that

$$\rho_{jk,lm}^{2\mathrm{p}}(\tau) \approx \mathcal{N} \mathrm{Tr}\left\{ \hat{a}_m \hat{a}_l \hat{\rho}_s \hat{a}_j^\dagger \hat{a}_k^\dagger \right\} \tag{26}$$

where $\mathcal{N}$ is a normalization constant and $\hat{\rho}_s$ describes the steady state of the system. Note that only states with at least two photons inside the cavity contribute to the two-photon density matrix. Neglecting the coupling α^{UL} in the effective Hamiltonian (23) and performing another basis transformation, one finds that the only two-photon state coupled to $|U, 0, 0\rangle$ is

$$|\psi_s\rangle = \frac{1}{\sqrt{\left(\gamma_1^{\mathrm{UL}}\right)^2 + \left(\gamma_2^{\mathrm{UL}}\right)^2}} \left(\gamma_1^{\mathrm{UL}}|L, 1, 1\rangle - \gamma_2^{\mathrm{UL}}|L, \Phi_+\rangle\right). \tag{27}$$

Therefore, in this approximation, also the contribution to the steady state which contains two photons inside the cavity should be proportional to $|\psi_s\rangle$. Consequently, the approximate normalized two-photon density matrix can be calculated by inserting $\rho_s = |\psi_s\rangle\langle\psi_s|$ into Equation (26) which results in

$$\rho_{\mathrm{approx}}^{2\mathrm{p}} = \frac{1}{2(1+r^2)} \begin{pmatrix} 1 & -r & -r & 1 \\ -r & r^2 & r^2 & -r \\ -r & r^2 & r^2 & -r \\ 1 & -r & -r & 1 \end{pmatrix}, \tag{28}$$

For this simplified density matrix, we can analytically calculate the concurrence C [Equation (19)] to

$$C(r) = \frac{|1 - r^2|}{1 + r^2}. \tag{29}$$

In Figure 3a the approximate result $C(r)$ is included as a dotted line. The approximate solution agrees quite well with the numerical results. This underlines the idea that the concurrence depends essentially on the ratio r. Also for the approximate solution we have the special point at $r = 1$ and the regions of high entanglement and the corresponding type of entanglement can be directly extracted from the analytical result. Below the special point we have $|r| < 1$, therefore, $r^2 < |r|$, resulting in a density matrix of $\Phi\mathrm{BS}$ entanglement. The maximum concurrence value appears around $\Omega = \frac{1}{2\sqrt{2}}\Delta_0 \approx 7.1 \times g$ where the ratio r passes through zero. Above Ω_{sp}, we have $r \geq 1$ and $r^2 > r$. Thus, in this regime one obtains $\Psi\mathrm{BS}$ entanglement in the two-photon density matrix.

We now discuss the deviations between the numerical and the approximate result for the concurrence. One obvious reason for the difference is the obmission of the coupling between the two-photon states (via one- or three-photon states), as indicated by α^{UL} in Equation (23). This coupling mixes $\Phi\mathrm{BS}$ and $\Psi\mathrm{BS}$, such that in the full model, the total obtained concurrence is reduced. Nonetheless, neglecting α^{UL} for the analysis is reasonable, when taking the cavity losses into account. By analyzing the values of α^{UL} and γ^{UL}, we find that these are always smaller than the cavity loss rate κ. This means that the losses relax the system before the coupling between the different photon states becomes efficient. Another reason for the deviations is that for low driving strength values, other transitions between the laser-dressed states besides the discussed direct two-photon one become important as they get closer to resonance.

5.4. Influence of a Finite Fine-Structure Splitting

So far only the situation of degenerate intermediate bare states $|X_{\mathrm{H}}\rangle$ and $|X_{\mathrm{V}}\rangle$ has been analyzed. However, an often discussed asymmetry in the system is a possible finite fine-structure splitting δ between these two intermediate states.[29,32,41,45,46] A finite fine-structure splitting introduces which-path information into the system and can, therefore, result in a reduced degree of entanglement.[3,29,32]

In Figure 3a the influence of a finite splitting δ on the concurrence is shown, where $\delta = \hbar\omega_{X_{\mathrm{H}}} - \hbar\omega_{X_{\mathrm{V}}}$ is the difference between the energies of the horizontally and vertically polarized intermediate state $\hbar\omega_{X_{\mathrm{H/V}}} = \hbar\omega_X \pm \delta/2$. Even in the case of a rather large splitting $\delta = 0.1\Delta_0$, the resulting degree of entanglement as measured by the concurrence is only weakly influenced by the fine-structure splitting. Furthermore, all main features discussed before remain unchanged: A sharp transition between regions of high $\Phi\mathrm{BS}$ and $\Psi\mathrm{BS}$ entanglement takes place at a special point of vanishing concurrence. Note that the chosen parameters reflect the often realized situation where the fine-structure splitting is one order of magnitude smaller than the binding energy.[3,16,41,45] Thus, the energies of the laser-dressed states and their character do not change significantly. Therefore, also the resonance conditions and optical selection rules stay roughly the same leading to very similar results. Consequently, the resulting two-photon state and its degree of entanglement are robust against a possible fine-structure splitting.

**ADVANCED
SCIENCE NEWS**
www.advancedsciencenews.com

**ADVANCED
QUANTUM
TECHNOLOGIES**
www.advquantumtech.com
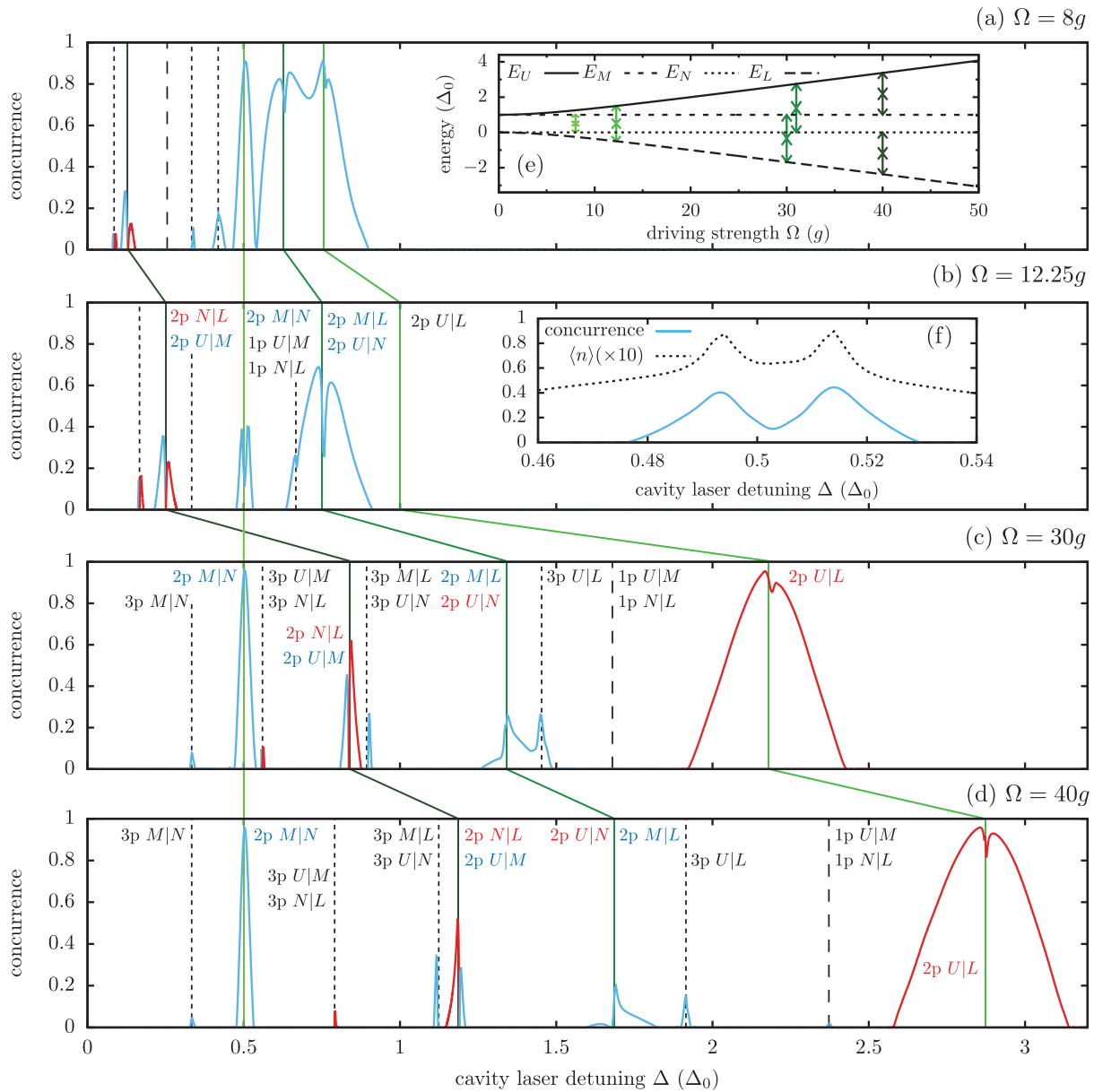
Figure 6. Concurrence as function of the cavity laser detuning Δ for fixed values of the external laser driving a) $\Omega = 8 \times g$, b) $\Omega = 12.25 \times g$, c) $\Omega = 30 \times g$, and d) $\Omega = 40 \times g$. The color code indicates the type of entanglement: blue curves symbolize ΦBS and red curves are ΨBS entanglement. The vertical lines mark the position of photon resonances labeled by $np\ \chi_1|\chi_2$. e) Energy of the laser-dressed states as a function of the driving strength Ω marking the four selected two-photon resonance conditions which correspond to the two-photon resonances of the same color in panels (a)–(d). f) Concurrence and mean photon number $\langle n \rangle$ for $\Omega = 12.25 \times g$ in the vicinity of $\Delta = \Delta_{MN}/2$.

6. Entanglement at the Other Two-Photon Transitions

Having discussed the transition between $|U\rangle$ and $|L\rangle$, we now want to examine the behavior of the other two-photon resonances. In particular, there are three other two-photon resonances matching the transitions between the corresponding dressed states (given by $\Delta_{\chi_1\chi_2} = E_{\chi_1} - E_{\chi_2}$) in the system at

$$\frac{\Delta_{UM}}{2} = \frac{\Delta_{NL}}{2} = \frac{1}{4}\left(\sqrt{\Delta_0^2 + 8\Omega^2} - \Delta_0\right)$$

$$\frac{\Delta_{UN}}{2} = \frac{\Delta_{ML}}{2} = \frac{1}{4}\left(\sqrt{\Delta_0^2 + 8\Omega^2} + \Delta_0\right)$$

$$\frac{\Delta_{MN}}{2} = \frac{\Delta_0}{2}. \tag{30}$$

Therefore, to sweep through the respective resonances, we now fix the driving strength and vary the cavity laser detuning Δ. The corresponding concurrence is calculated and the results are shown in **Figure 6** for four different driving strength values $\Omega = 8 \times g$, $12.25 \times g$, $30 \times g$, and $40 \times g$.

**ADVANCED
SCIENCE NEWS**

www.advancedsciencenews.com

**ADVANCED
QUANTUM
TECHNOLOGIES**

www.advquantumtech.com

The type of entanglement is encoded in the color: Blue lines are for ΦBS and red lines for ΨBS entanglement. On first sight, we find that both types of entanglement occur when we vary Δ. In addition to a strong concurrence at the four two-photon resonances, we find several other cavity detuning values with non-vanishing concurrence. We can attribute these to the one-photon resonances $U|M$ and $N|L$ and several three-photon resonances, which occur between the respective states. Accordingly, we have labeled all resonances by $np\ \chi_1|\chi_2$, which denotes the n-photon resonances between the laser-dressed states $|\chi_1\rangle$ and $|\chi_2\rangle$.

Figure 6e shows the dressed states as a function of the driving strength and we used colored arrows to mark the different two-photon resonances. The same colors are used to indicate the position of the two-photon resonances in Figure 6a–d. Before we will go through the two-photon resonances one-by-one (note that we already discussed the 2p $U|L$ resonance), let us briefly remark some general findings:

While some n-photon transitions are always associated with the same type of entanglement, others can change from one to the other. This change may happen as a result of changing the cavity laser detuning or the driving strength. Furthermore, in between some of the resonance conditions the concurrence value stays at a finite level, whereas it passes through zero in other situations. A striking feature is the appearance of a second special point with vanishing concurrence between regions of high entanglement when the cavity laser detuning is approximately $\Delta \approx \Delta_{\mathrm{UM}}/2 = \Delta_{\mathrm{NL}}/2$, which we will discuss in detail in Section 6.2.

Next, we will go through the two-photon resonances one-by-one. For each two-photon resonance we perform a Schrieffer–Wolff transformation, followed by a rotation of the states, such that each Hamiltonian in the following is given in the basis

$$\{|\chi_1, 0, 0\rangle, |\chi_2, 1, 1\rangle, |\chi_2, \Phi_+\rangle, |\chi_2, \Phi_-\rangle\} \tag{31}$$

with χ_1 being the higher energy state and χ_2 being the lower energy state of the 2p $\chi_1|\chi_2$ resonance. More details on the Schrieffer–Wolff transformation are given in Appendix A.

6.1. Two-Photon $M|N$ Resonance

We start by looking at 2p $M|N$, which is the only two-photon transition for which the resonance condition does not depend on the driving strength. The corresponding transitions are marked by a light green line in Figure 6. At this resonance the concurrence always displays ΦBS entanglement. While the concurrence is mostly maximal at the resonance, we find a decrease in strength at the maximum at $\Omega = 12.25 \times g$.

We use the Schrieffer–Wolff transformation to obtain the effective Hamiltonian

$$\hat{H}_{\mathrm{MN}}^{(2)} = g^2 \begin{pmatrix} \delta^{\mathrm{MN}} & 0 & 0 & \gamma_2^{\mathrm{MN}} \\ 0 & -\delta^{\mathrm{MN}} & -\delta^{\mathrm{MN}} & 0 \\ 0 & -\delta^{\mathrm{MN}} & -\delta^{\mathrm{MN}} & 0 \\ \gamma_2^{\mathrm{MN}} & 0 & 0 & -\delta^{\mathrm{MN}} \end{pmatrix} \tag{32}$$

with

$$\delta^{\mathrm{MN}} = 2\left(\tilde{c}^2 - c^2\right)\frac{1}{\Delta_{\mathrm{UL}}}$$

$$\gamma_2^{\mathrm{MN}} = -4\,c\,\tilde{c}\frac{1}{\Delta_{\mathrm{UL}}}. \tag{33}$$

Note that these are shortened expressions and the full expressions can be found in Appendix A.2. From the Hamiltonian, it is obvious that the initial state is only coupled to the final state $|N, \Phi_-\rangle$, while the other two-photon states become uncoupled. This is in agreement with Figure 6, where we only find ΦBS entanglement at the 2p $M|N$ resonance.

The smaller height in concurrence at $\Omega = 12.25 \times g$ (see also Figure 6f), can be traced back to the occurrence of several resonance conditions at the same driving strength, in particular the one-photon transitions 1p $U|M$ and 1p $N|L$. This is confirmed by looking at the mean photon number $\langle n \rangle = \langle \hat{a}_H^\dagger \hat{a}_H + \hat{a}_V^\dagger \hat{a}_V \rangle$ as displayed in Figure 6f. The alignment of several resonance conditions causes the peak to split into two separate resonances, as indicated by the mean photon number. Due to the additional one-photon resonances three-photon states with all four possible combinations of polarized photons gain a noticeable population and the extracted (two-photon) coherence $\rho_{\mathrm{HH,VV}}^{2\mathrm{p}}$ reaches only about half the value of the occupations $\rho_{\mathrm{HH,HH}}^{2\mathrm{p}}$ and $\rho_{\mathrm{VV,VV}}^{2\mathrm{p}}$. As a result, the degree of entanglement is strongly reduced.

6.2. Two-Photon $U|M$ and Two-Photon $N|L$ Resonance

Next we consider the two-photon resonances between the laser-dressed states $|U\rangle$ and $|M\rangle$, and between $|N\rangle$ and $|L\rangle$, which have the same energy. In Figure 6, these resonances are indicated by a dark green line. From Figure 6, we see that here always a sharp transition between ΦBS and ΨBS entanglement takes place. This is highlighted in **Figure 7**a, which presents a closer look at this resonance condition for $\Omega = 30 \times g$. Figure 7b–d display the corresponding two-photon density matrices for three selected detuning values. With rising cavity laser detuning the entangled state created inside the cavity changes from ΦBS to ΨBS entanglement, passing through a special point at $\Delta \approx 0.836\Delta_0$ where the concurrence drops to zero.

Here, we have two transitions, for which the corresponding Schrieffer–Wolff analysis yields the Hamiltonians

$$\hat{H}_{\mathrm{UM}}^{(2)} = g^2 \begin{pmatrix} \delta_1^{\mathrm{UM}} - \delta_2^{\mathrm{UM}} & 0 & 0 & \gamma_2^{\mathrm{UM}} \\ 0 & \delta_3^{\mathrm{UM}} & \alpha^{\mathrm{UM}} & 0 \\ 0 & \alpha^{\mathrm{UM}} & \delta_3^{\mathrm{UM}} & 0 \\ \gamma_2^{\mathrm{UM}} & 0 & 0 & \delta_3^{\mathrm{UM}} \end{pmatrix} \tag{34}$$

and

$$\hat{H}_{\mathrm{NL}}^{(2)} = g^2 \begin{pmatrix} \delta_1^{\mathrm{UM}} - \delta_2^{\mathrm{UM}} & \gamma_1^{\mathrm{NL}} & \gamma_2^{\mathrm{NL}} & 0 \\ \gamma_1^{\mathrm{NL}} & \delta_3^{\mathrm{NL}} & \alpha^{\mathrm{NL}} & 0 \\ \gamma_2^{\mathrm{NL}} & \alpha^{\mathrm{NL}} & \delta_3^{\mathrm{NL}} & 0 \\ 0 & 0 & 0 & \delta_3^{\mathrm{NL}} \end{pmatrix} \tag{35}$$

**ADVANCED
SCIENCE NEWS**

www.advancedsciencenews.com

**ADVANCED
QUANTUM
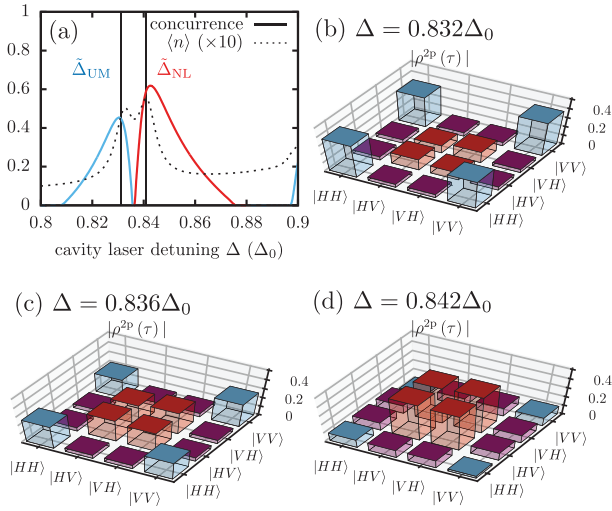TECHNOLOGIES**

www.advquantumtech.com

Figure 7. a) Concurrence and mean photon number $\langle n \rangle$ for $\Omega = 30 \times g$. Vertical lines indicate the position of $\tilde{\Delta}_{\mathrm{UM}}$ (Equation (37)) and $\tilde{\Delta}_{\mathrm{NL}}$ (Equation (38)). b–d) Absolute values of the two-photon density matrices $|\rho^{2\mathrm{p}}(\tau)|$ for Δ as indicated.

with the coefficients given in Appendix A.3. While the Hamiltonian $\hat{H}_{\mathrm{UM}}^{(2)}$ has the same form as $\hat{H}_{\mathrm{MN}}^{(2)}$ in Equation (32), the Hamiltonian $\hat{H}_{\mathrm{NL}}^{(2)}$ has a form similar to $\hat{H}_{\mathrm{UL}}^{(2)}$ in Equation (23).

From the effective Hamiltonian, it is evident that the isolated 2p $U|M$ resonance supports only ΦBS entanglement, while the isolated 2p $N|L$ resonance has competing channels for both ΦBS and ΨBS entanglement. From the coefficients, we can deduce the strengths of the competing channels, finding that

$$|\gamma_1^{\mathrm{NL}}| = |\gamma_2^{\mathrm{NL}}| + \frac{2\sqrt{2}\tilde{c}}{2\Delta_0 + \Delta_{\mathrm{UM}}}. \tag{36}$$

Therefore the ratio $\gamma_1^{\mathrm{NL}}/\gamma_2^{\mathrm{NL}}$ is always larger than 1 and the preferred type of entanglement for the 2p $N|L$ resonance is always ΨBS entanglement.

A zoom in around the two-photon transition at $\Delta = \Delta_{\mathrm{UM}}/2$, presented in Figure 7a for $\Omega = 30 \times g$, shows clearly that two peaks appear, a ΦBS one and a ΨBS one. The approximate position of these peaks can be determined by the diagonal elements of the Schrieffer–Wolff Hamiltonians in Equation (34) and Equation (35). Due to the transformation, diagonal elements appear encoded by $\delta_j^{\chi_1\chi_2}$, which slightly shift the resulting resonance, such that now we have the resonances for the 2p $U|M$ transition with ΦBS entanglement at

$$\tilde{\Delta}_{\mathrm{UM}} = \frac{1}{2}\left(\Delta_{\mathrm{UM}} + (\delta_1^{\mathrm{UM}} - \delta_2^{\mathrm{UM}}) - \delta_3^{\mathrm{UM}}\right) \tag{37}$$

and the 2p $N|L$ transition with ΨBS entanglement at

$$\tilde{\Delta}_{\mathrm{NL}} = \frac{1}{2}\left(\Delta_{\mathrm{UM}} + (\delta_1^{\mathrm{UM}} - \delta_2^{\mathrm{UM}}) - \delta_3^{\mathrm{NL}}\right). \tag{38}$$

The values of the different $\delta_j^{\chi_1\chi_2}$ are given in Appendix A.3. Indeed, the position of the peak maxima visible in Figure 7 agree well with these shifted resonances (indicated by vertical lines).

This interpretation is confirmed by the mean photon number $\langle n \rangle$ (dotted line in Figure 7) which also displays two separate maxima, indicating two close-by resonances (confer Figure 7a).

Also, the $\delta_j^{\chi_1\chi_2}$ depend sensibly on the driving strength Ω. For a driving strength being smaller than $\Omega_{\mathrm{m}} = \sqrt{3}\Delta_0 \approx 34.6 \times g$ we find that $\tilde{\Delta}_{\mathrm{UM}} < \tilde{\Delta}_{\mathrm{NL}}$, while for $\Omega > \Omega_{\mathrm{m}}$ this order is reversed. Therefore, in Figure 6d for a driving strength $\Omega = 40 \times g$ the arrangement of ΨBS and ΦBS entanglement is swapped.

In between the regions of ΦBS and ΨBS entanglement we have the special point at $(\tilde{\Delta}_{\mathrm{UM}} + \tilde{\Delta}_{\mathrm{NL}})/2$. From the density matrix at this special point (confer Figure 7c), we see that the concurrence does not vanish due to the lack of coherences. We find that at the special point the generated two-photon state is essentially the superposition of the two density matrices created by each transition individually with

$$\rho_{\mathrm{sp2}}^{2\mathrm{p}} = \frac{1}{2}\left[\frac{1}{2}\begin{pmatrix} 0 & 0 & 0 & 0 \\ 0 & 1 & 1 & 0 \\ 0 & 1 & 1 & 0 \\ 0 & 0 & 0 & 0 \end{pmatrix} + \frac{1}{2}\begin{pmatrix} 1 & 0 & 0 & -1 \\ 0 & 0 & 0 & 0 \\ 0 & 0 & 0 & 0 \\ -1 & 0 & 0 & 1 \end{pmatrix}\right] \tag{39}$$

This can be rewritten into

$$\rho_{\mathrm{sp2}}^{2\mathrm{p}} = \frac{1}{2}|\psi_{\mathrm{sp2}}^{(+)}\rangle\langle\psi_{\mathrm{sp2}}^{(+)}| + \frac{1}{2}|\psi_{\mathrm{sp2}}^{(-)}\rangle\langle\psi_{\mathrm{sp2}}^{(-)}|, \tag{40}$$

with

$$|\psi_{\mathrm{sp2}}^{(\pm)}\rangle = \frac{1}{\sqrt{2}}\left(|H_1\rangle \pm i|V_1\rangle\right)\frac{1}{\sqrt{2}}\left(|H_2\rangle \pm i|V_2\rangle\right). \tag{41}$$

Thus, the density matrix can be written as a mixed state, where both contributing states are products of two one-photon states, that is, the states are factorizable states, and, accordingly, the corresponding concurrence vanishes.

We emphasize that this is a different type of special point than the one discussed in Section 5.1 where the system approaches a pure factorizable state. Another difference in comparison to the 2p $U|L$ resonance can be found in the limit $\Omega \to \infty$. While the concurrence obtained at the 2p $U|L$ resonance approaches a high finite value and becomes independent of the driving strength, the concurrence for the 2p $U|M$ and 2p $N|L$ resonances approach zero. In the limiting case the difference $\tilde{\Delta}_{\mathrm{UM}} - \tilde{\Delta}_{\mathrm{NL}}$ vanishes and, therefore, the two resonances merge together and the different types of entanglement cancel each other.

6.3. Two-Photon $U|N$ and Two-Photon $M|L$ Resonance

Finally, we analyze the remaining two resonances 2p $U|N$ and 2p $M|L$. In Figure 6 we see that always ΦBS occurs at this transition.

The analysis with the Schrieffer–Wolff transformation results in a similar situation as discussed in the previous subsection 6.2: The Hamiltonian of the 2p $M|L$ transition has the same form as the 2p $U|M$ transition [Equation (34) or also Equation (32)] and therefore promotes exclusively ΦBS entanglement. On the other hand, the Hamiltonian of the 2p $U|N$ transition has the same form as the 2p $N|L$ transition [Equation (35) or also Equation (23)] and therefore promotes both ΦBS and ΨBS entanglement. The

**ADVANCED
SCIENCE NEWS**

www.advancedsciencenews.com

**ADVANCED
QUANTUM
TECHNOLOGIES**

www.advquantumtech.com

Table 2. Various scenarios: Similarities and differences at the different two-photon resonances.

Resonance	Small driving Ω	Large driving Ω	Special point	Limit $\Omega \to \infty$
2p $U\|L$	$\Omega < 12.25 \times g$: ΦBS	$\Omega > 12.25 \times g$: ΨBS	for $\Omega \approx 12.25 \times g$	high ΨBS ent.
2p $M\|N$	always ΦBS		none	high ΦBS ent.
2p $U\|M$	always ΦBS		in between the two close-by resonances	resonances coincide and ent. vanishes
2p $N\|L$	always ΨBS		in between the two close-by resonances	resonances coincide and ent. vanishes
2p $U\|N$	$\Omega < 20 \times g$: ΦBS	$\Omega > 20 \times g$: ΨBS	not observed for $\Omega \leq 40 \times g$	resonances coincide and ent. vanishes
2p $M\|L$	ΦBS (irrelevant)	ΦBS (dominant)	not observed for $\Omega \leq 40 \times g$	resonances coincide and ent. vanishes

dominating type of entanglement depends on the ratio of γ_1^{UN} to γ_2^{UN}, but also on the splitting from the other resonances given by the diagonal elements $\delta_j^{\chi_1\chi_2}$. For small driving strength values $\Omega < 20 \times g$ the 2p $U|N$ transition dominates the dynamics and the resulting entanglement is ΦBS entanglement. For larger Ω both two-photon resonances become of equal importance and a transition between ΦBS and ΨBS entanglement is expected, similar to the results presented in Section 6.2. But, in contrast to the previous section, here, the splitting of the two peaks is too small for the given driving strength values, therefore, we only observe ΦBS entanglement in Figure 6. The corresponding Hamiltonians and constants are given in Appendix A.4.

By investigating the various two-photon resonances we are able to understand the origins of all regions of high entanglement observable in Figure 3 and 6. We stress that, we find a rich variety of different scenarios depending on the considered resonance condition, which are all equally fascinating. For example, at the 2p $M|N$ resonance one always obtains a high ΦBS entanglement. In contrast to this, in case of the 2p $U|L$ transition, the type of entanglement undergoes a sharp transition at a special point of vanishing concurrence when the driving strength is varied. Additionally, a second type of special point can occur between two close-by resonances, as demonstrated by the 2p $U|M$ and 2p $N|L$ resonances. Table 2 provides a short overview over the similarities and differences between the various scenarios at the different two-photon resonances. Using the same analytic formalism based on a Schrieffer–Wolff transformation, we are able to successfully predict the resulting type of entanglement at all two-photon resonances, and even more important, we can also explain these various features.

7. Conclusion

In conclusion, we have investigated the possible types of entanglement generated by a driven four-level emitter-cavity system. We found that two different types of entanglement can occur, which we classified as ΦBS and ΨBS entanglement.

By adjusting the driving strength as well as the cavity detuning, we found a rich picture showing a finite concurrence at various transitions. Using a Schrieffer–Wolff transformation, we were able to give analytical insight into the occurrence of the different types of entanglement showing that either ΦBS or a mixture of ΦBS and ΨBS is promoted at the two-photon transitions. Most excitingly, we found special points, where the concurrence, a measure for the entanglement, drops to zero, though the corresponding coherences in the two-photon density matrix are not

absent. Instead, factorizable (and therefore not entangled states) are reached.

In principle, the resulting type of Bell state could also be changed afterward, for example, by the use of waveplates or polarization filters. But these additional components often lead to a significant loss of photon yield. These kinds of losses can be avoided when the target photonic state is generated directly. Furthermore, although ΦBS and ΨBS entanglement can be converted into each other by postprocessing, they are clearly distinguishable in a fixed basis and reflect the systems ability to get entangled in more than one fashion. Seeing that entanglement, being one of the most remarkable and interesting physical effects that separates the quantum mechanical from the classical world, can change its character by just adding an external driving to a few-level emitter is exciting from a fundamental point of view and can also lead to new possibilities for using few-level emitters in quantum information technology.

Appendix A: Schrieffer–Wolff Transformation

For the Schrieffer–Wolff transformation we consider the FLE-cavity system without losses and use the states $|\chi, n_{\text{H}}, n_{\text{V}}\rangle$ where $|\chi\rangle \in \{|U\rangle, |M\rangle, |N\rangle, |L\rangle\}$ is one of the four laser-dressed states defined in Section 3.2 and n_{H} (n_{V}) denotes the number of photons present in the horizontally (vertically) polarized cavity mode. The direct two-photon transition from $|\chi_1\rangle$ to $|\chi_2\rangle$ involves only the states

$$A: |\chi_1, 0, 0\rangle, |\chi_2, 1, 1\rangle, |\chi_2, 2, 0\rangle, |\chi_2, 0, 2\rangle. \tag{A.1}$$

As discussed in Section 5.2, there are also several other paths to create the two-photon states, thereby coupling the aforementioned states. These processes are depicted in Figure 4 and include the states

$$B: |\chi, 1, 0\rangle, |\chi, 0, 1\rangle,$$
$$|\chi, 3, 0\rangle, |\chi, 2, 1\rangle, |\chi, 1, 2\rangle, |\chi, 0, 3\rangle, \tag{A.2}$$

where the one- and three-photon states include all four bare states, that is, $|\chi\rangle = |U\rangle, |M\rangle, |N\rangle, |L\rangle$. This results in a 28×28 matrix. To reduce this to a 4×4 matrix for the relevant states in subset A [see Equation (A.1)], we use a Schrieffer–Wolff transformation.[61,62] In the transformation, we perform a

block-diagonalization of the system Hamiltonian via the unitary transformation

$$e^{-\hat{S}}\hat{H}e^{\hat{S}}, \tag{A.3}$$

where $\hat{S}$ is an anti-Hermitian operator.[61] After the decoupling procedure, the states in set B [see Equation (A.2)] can be disregarded as they are insignificant for the system dynamics. This formalism can be applied here since, for a given two-photon resonance, where the cavity laser detuning matches half the transition energy between the states $|\chi_1\rangle$ and $|\chi_2\rangle$, one-photon transition processes between the laser-dressed states are typically strongly off-resonant.

In second order the effective Hamiltonian for the states in set A is then given by $\hat{H}^{(2)}_{\chi_1\chi_2} = \{H^{(2)}_{a,a'}\}_{\chi_1\chi_2}$ with the matrix elements[61]

$$H^{(2)}_{a,a'} = H_{a,a'} + \frac{1}{2}\left\{ \sum_b H_{a,b}H_{b,a'}\left[\frac{1}{E_a - E_b} + \frac{1}{E_{a'} - E_b} \right] \right\}, \tag{A.4}$$

where a runs over the states in subset A, the index b runs over the states in B, and

$$E_j = \langle j|\hat{H}|j\rangle = E_\chi + (n_{\mathrm{H}} + n_{\mathrm{V}})\Delta \tag{A.5}$$

is the energy of the state $|j\rangle = |\chi, n_{\mathrm{H}}, n_{\mathrm{V}}\rangle \in A, B$. The matrix elements are calculated from the system Hamiltonian with

$$H_{a,a'} = E_a \delta_{a,a'}, \tag{A.6}$$

This term can be dropped since it represents a constant energy shift as the four states in set A are energetically degenerate. The remaining matrix elements for $a \neq b$ are given by the coupling Hamiltonian in the dressed state basis [Equation (13)] with

$$H_{a,b} = \langle a|\hat{H}_{\mathrm{DS\text{-}c}}|b\rangle \tag{A.7}$$

After the Schrieffer–Wolff transformation we perform a rotation to the basis

$$|\chi_1, 0, 0\rangle, |\chi_2, 1, 1\rangle, |\chi_2, \Phi_+\rangle, |\chi_2, \Phi_-\rangle \tag{A.8}$$

using

$$\hat{H}^{(2)}_{\chi_1\chi_2} = T^\dagger \hat{H}^{(2)}_{\chi_1\chi_2} T \text{ with } T = \begin{pmatrix} 1 & 0 & 0 & 0 \\ 0 & 1 & 0 & 0 \\ 0 & 0 & \frac{1}{\sqrt{2}} & \frac{1}{\sqrt{2}} \\ 0 & 0 & \frac{1}{\sqrt{2}} & -\frac{1}{\sqrt{2}} \end{pmatrix} \tag{A.9}$$

We performed this procedure for all two-photon resonances.

A.1. Effective Hamiltonian for the 2p U|L Resonance

The effective Hamiltonian is

$$\hat{H}^{(2)}_{\mathrm{UL}} = g^2 \times \begin{pmatrix} \delta^{\mathrm{UL}} & \gamma_1^{\mathrm{UL}} & -\gamma_2^{\mathrm{UL}} & 0 \\ \gamma_1^{\mathrm{UL}} & -\delta^{\mathrm{UL}} - \delta_3^{\mathrm{UL}} & \alpha^{\mathrm{UL}} & 0 \\ -\gamma_2^{\mathrm{UL}} & \alpha^{\mathrm{UL}} & -\delta^{\mathrm{UL}} - \delta_3^{\mathrm{UL}} & 0 \\ 0 & 0 & 0 & -\delta^{\mathrm{UL}} - \delta_3^{\mathrm{UL}} \end{pmatrix} \tag{A.10}$$

in the basis $|U, 0, 0\rangle$, $|L, 1, 1\rangle$, $|L, \Phi_+\rangle$ and $|L, \Phi_-\rangle$ with

$$\delta^{\mathrm{UL}} = (\tilde{c}^2 - c^2)\left(\frac{2}{\Delta_0} + \frac{4}{\Delta_{\mathrm{UL}}} \right)$$

$$\delta_3^{\mathrm{UL}} = \frac{8(\tilde{c}^2 - c^2)^2}{3\Delta_{\mathrm{UL}}} + \frac{2\tilde{c}^2}{\Delta_{\mathrm{UL}} + \Delta_0/2} + \frac{2c^2}{\Delta_{\mathrm{UL}} - \Delta_0/2}$$

$$\gamma_1^{\mathrm{UL}} = 4c\tilde{c}\frac{1}{\Delta_0} - 16c\tilde{c}(\tilde{c}^2 - c^2)\frac{1}{\Delta_{\mathrm{UL}}}$$

$$\gamma_2^{\mathrm{UL}} = 16c\tilde{c}(\tilde{c}^2 - c^2)\frac{1}{\Delta_{\mathrm{UL}}}$$

$$\alpha^{\mathrm{UL}} = \frac{1}{\Delta_0} - (1 - 16c^2\tilde{c}^2)\frac{1}{\Delta_{\mathrm{UL}}} - \frac{1}{2}\delta_3^{\mathrm{UL}} + \frac{2\tilde{c}^2}{\Delta_{\mathrm{UL}} + \Delta_0/2}. \tag{A.11}$$

A.2. Effective Hamiltonian for the 2p M|N Resonance

The effective Hamiltonian is

$$\hat{H}^{(2)}_{\mathrm{MN}} = g^2 \times \begin{pmatrix} \delta^{\mathrm{MN}} & 0 & 0 & \gamma_2^{\mathrm{MN}} \\ 0 & -\delta^{\mathrm{MN}} + \delta_3^{\mathrm{MN}} & \alpha^{\mathrm{MN}} & 0 \\ 0 & \alpha^{\mathrm{MN}} & -\delta^{\mathrm{MN}} + \delta_3^{\mathrm{MN}} & 0 \\ \gamma_2^{\mathrm{MN}} & 0 & 0 & -\delta^{\mathrm{MN}} + \delta_3^{\mathrm{MN}} \end{pmatrix} \tag{A.12}$$

in the basis $|M, 0, 0\rangle$, $|N, 1, 1\rangle$, $|N, \Phi_+\rangle$ and $|N, \Phi_-\rangle$ with

$$\delta^{\mathrm{MN}} = 2(\tilde{c}^2 - c^2)\frac{1}{\Delta_{\mathrm{UL}}}$$

$$\delta_3^{\mathrm{MN}} = -\frac{4\tilde{c}^2}{2\Delta_0 + \Delta_{\mathrm{UL}}} - \frac{2}{3\Delta_0} - \frac{4c^2}{2\Delta_0 - \Delta_{\mathrm{UL}}}$$

$$\gamma_2^{\mathrm{MN}} = -4c\,\tilde{c}\frac{1}{\Delta_{\mathrm{UL}}}$$

$$\alpha^{\mathrm{MN}} = -\delta^{\mathrm{MN}} + \frac{1}{2}\delta_3^{\mathrm{MN}} + \frac{1}{3\Delta_0}. \tag{A.13}$$

**ADVANCED
SCIENCE NEWS**

www.advancedsciencenews.com

**ADVANCED
QUANTUM
TECHNOLOGIES**

www.advquantumtech.com

A.3. Effective Hamiltonians for the 2p U|M and 2p N|L Resonance

The effective Hamiltonian for the 2p $U|M$ resonance is

$$
\hat{H}_{\mathrm{UM}}^{(2)} = g^2 \times \begin{pmatrix} \delta_1^{\mathrm{UM}} - \delta_2^{\mathrm{UM}} & 0 & 0 & \gamma_2^{\mathrm{UM}} \\ 0 & \delta_3^{\mathrm{UM}} & \alpha^{\mathrm{UM}} & 0 \\ 0 & \alpha^{\mathrm{UM}} & \delta_3^{\mathrm{UM}} & 0 \\ \gamma_2^{\mathrm{UM}} & 0 & 0 & \delta_3^{\mathrm{UM}} \end{pmatrix} \text{ for } \begin{matrix} |U,0,0\rangle \\ |M,1,1\rangle \\ |M,\Phi_+\rangle \\ |M,\Phi_-\rangle \end{matrix}
$$

(A.14)

where

$$
\delta_1^{\mathrm{UM}} = -\frac{16c^2\tilde{c}^2}{\Delta_{\mathrm{UM}}} + \frac{2\tilde{c}^2}{2\Delta_0 + \Delta_{\mathrm{UM}}} + \frac{4(\tilde{c}^2 - c^2)^2}{2\Delta_0 + 3\Delta_{\mathrm{UM}}}
$$

$$
\delta_2^{\mathrm{UM}} = -\frac{2c^2}{\Delta_{\mathrm{UM}}} + \frac{1}{2\Delta_0 + \Delta_{\mathrm{UM}}} + \frac{2\tilde{c}^2}{2\Delta_0 + 3\Delta_{\mathrm{UM}}}
$$

$$
\delta_3^{\mathrm{UM}} = -\frac{4c^2}{3\Delta_{\mathrm{UM}}} + \frac{2}{2\Delta_0 - \Delta_{\mathrm{UM}}} + \frac{4\tilde{c}^2}{2\Delta_0 + \Delta_{\mathrm{UM}}}
$$

$$
\gamma_2^{\mathrm{UM}} = -\frac{4\sqrt{2}c^2\tilde{c}}{\Delta_{\mathrm{UM}}} - \frac{\sqrt{2}\tilde{c}}{2\Delta_0 + \Delta_{\mathrm{UM}}} + \frac{2\sqrt{2}(\tilde{c}^2 - c^2)\tilde{c}}{2\Delta_0 + 3\Delta_{\mathrm{UM}}}
$$

$$
\alpha^{\mathrm{UM}} = -\delta_2^{\mathrm{UM}} - \frac{1}{2}\delta_3^{\mathrm{UM}}
$$

(A.15)

The effective Hamiltonian for the two-photon transition between the states $|N\rangle$ and $|L\rangle$ is given by

$$
\hat{H}_{\mathrm{NL}}^{(2)} = g^2 \times \begin{pmatrix} \delta_1^{\mathrm{UM}} - \delta_2^{\mathrm{UM}} & \gamma_1^{\mathrm{NL}} & \gamma_2^{\mathrm{NL}} & 0 \\ \gamma_1^{\mathrm{NL}} & \delta_3^{\mathrm{NL}} & \alpha^{\mathrm{NL}} & 0 \\ \gamma_2^{\mathrm{NL}} & \alpha^{\mathrm{NL}} & \delta_3^{\mathrm{NL}} & 0 \\ 0 & 0 & 0 & \delta_3^{\mathrm{NL}} \end{pmatrix} \text{ for } \begin{matrix} |N,0,0\rangle \\ |L,1,1\rangle \\ |L,\Phi_+\rangle \\ |L,\Phi_-\rangle \end{matrix}
$$

(A.16)

with

$$
\delta_3^{\mathrm{NL}} = -\frac{32c^2\tilde{c}^2}{\Delta_{\mathrm{UM}}} - \frac{4c^2}{3\Delta_{\mathrm{UM}}} - \frac{8(\tilde{c}^2 - c^2)}{2\Delta_0 + 5\Delta_{\mathrm{UM}}} - \frac{4\tilde{c}^2}{2\Delta_0 + 3\Delta_{\mathrm{UM}}}
$$

$$
\gamma_1^{\mathrm{NL}} = \gamma_2^{\mathrm{UM}}
$$

$$
\gamma_2^{\mathrm{NL}} = \gamma_2^{\mathrm{UM}} + \frac{2\sqrt{2}\tilde{c}}{2\Delta_0 + \Delta_{\mathrm{UM}}}
$$

$$
\alpha^{\mathrm{NL}} = -\delta_1^{\mathrm{UM}} + \frac{1}{2}\delta_3^{\mathrm{NL}} + \frac{4\tilde{c}^2}{2\Delta_0 + \Delta_{\mathrm{UM}}} + \frac{4\tilde{c}^2}{2\Delta_0 + 3\Delta_{\mathrm{UM}}}
$$

(A.17)

A.4. Effective Hamiltonians for the 2p U|N and 2p M|L Resonance

For the 2p $U|N$ transition we obtain

$$
\hat{H}_{\mathrm{UN}}^{(2)} = g^2 \times \begin{pmatrix} \delta_1^{\mathrm{UN}} - \delta_2^{\mathrm{UN}} & \gamma_1^{\mathrm{UN}} & \gamma_2^{\mathrm{UN}} & 0 \\ \gamma_1^{\mathrm{UN}} & \delta_3^{\mathrm{UN}} & \alpha^{\mathrm{UN}} & 0 \\ \gamma_2^{\mathrm{UN}} & \alpha^{\mathrm{UN}} & \delta_3^{\mathrm{UN}} & 0 \\ 0 & 0 & 0 & \delta_3^{\mathrm{UN}} \end{pmatrix} \text{ for } \begin{matrix} |U,0,0\rangle \\ |N,1,1\rangle \\ |N,\Phi_+\rangle \\ |N,\Phi_-\rangle \end{matrix}
$$

(A.18)

The energies and coupling strengths are

$$
\delta_1^{\mathrm{UN}} = -\frac{16c^2\tilde{c}^2}{\Delta_{\mathrm{UN}}} + \frac{2c^2}{\Delta_{\mathrm{UN}} - 2\Delta_0} + \frac{4(\tilde{c}^2 - c^2)^2}{3\Delta_{\mathrm{UN}} - 2\Delta_0}
$$

$$
\delta_2^{\mathrm{UN}} = -\frac{2\tilde{c}^2}{\Delta_{\mathrm{UN}}} + \frac{1}{\Delta_{\mathrm{UN}} - 2\Delta_0} + \frac{2c^2}{3\Delta_{\mathrm{UN}} - 2\Delta_0}
$$

$$
\delta_3^{\mathrm{UN}} = -\frac{4\tilde{c}^2}{3\Delta_{\mathrm{UN}}} - \frac{2}{2\Delta_0 + \Delta_{\mathrm{UN}}} - \frac{4c^2}{2\Delta_0 - \Delta_{\mathrm{UN}}}
$$

$$
\gamma_1^{\mathrm{UN}} = -\frac{4\sqrt{2}c\tilde{c}^2}{\Delta_{\mathrm{UN}}} - \frac{\sqrt{2}c}{\Delta_{\mathrm{UN}} - 2\Delta_0} - \frac{2\sqrt{2}(\tilde{c}^2 - c^2)c}{3\Delta_{\mathrm{UN}} - 2\Delta_0}
$$

$$
\gamma_2^{\mathrm{UN}} = \gamma_1^{\mathrm{UN}} + \frac{2\sqrt{2}c}{\Delta_{\mathrm{UN}} - \Delta_0}
$$

$$
\alpha^{\mathrm{UN}} = \delta_2^{\mathrm{UN}} + \frac{1}{2}\delta_3^{\mathrm{UN}} - \frac{2}{\Delta_{\mathrm{UN}} - 2\Delta_0} + \frac{2}{2\Delta_0 + \Delta_{\mathrm{UN}}}.
$$

(A.19)

For the 2p $M|L$ transition we have

$$
\hat{H}_{\mathrm{ML}}^{(2)} = g^2 \times \begin{pmatrix} \delta_1^{\mathrm{UN}} - \delta_2^{\mathrm{UN}} & 0 & 0 & \gamma_1^{\mathrm{UN}} \\ 0 & \delta_3^{\mathrm{ML}} & \alpha^{\mathrm{ML}} & 0 \\ 0 & \alpha^{\mathrm{ML}} & \delta_3^{\mathrm{ML}} & 0 \\ \gamma_1^{\mathrm{UN}} & 0 & 0 & \delta_3^{\mathrm{ML}} \end{pmatrix} \text{ for } \begin{matrix} |M,0,0\rangle \\ |L,1,1\rangle \\ |L,\Phi_+\rangle \\ |L,\Phi_-\rangle \end{matrix}
$$

(A.20)

with

$$
\delta_3^{\mathrm{ML}} = \frac{8(\tilde{c}^2 - c^2)^2}{2\Delta_0 - 5\Delta_{\mathrm{UN}}} - \frac{4\tilde{c}^2}{3\Delta_{\mathrm{UN}}} + \frac{4c^2}{2\Delta_0 - 3\Delta_{\mathrm{UN}}} - \frac{32c^2\tilde{c}^2}{\Delta_{\mathrm{UN}}}
$$

$$
\alpha^{\mathrm{ML}} = -\delta_1^{\mathrm{UN}} + \frac{1}{2}\delta_3^{\mathrm{ML}} + \frac{4\tilde{c}^2}{3\Delta_{\mathrm{UN}}}.
$$

(A.21)

Conflict of Interest

The authors declare no conflict of interest.

**ADVANCED
SCIENCE NEWS**

www.advancedsciencenews.com

**ADVANCED
QUANTUM
TECHNOLOGIES**

www.advquantumtech.com

[1] R. Horodecki, P. Horodecki, M. Horodecki, K. Horodecki, *Rev. Mod. Phys.* **2009**, *81*, 865.

[2] A. Orieux, M. A. M. Versteegh, K. D. Jöns, S. Ducci, *Rep. Prog. Phys.* **2017**, *80*, 076001.

[3] N. Akopian, N. H. Lindner, E. Poem, Y. Berlatzky, J. Avron, D. Gershoni, B. D. Gerardot, P. M. Petroff, *Phys. Rev. Lett.* **2006**, *96*, 130501.

[4] N. Gisin, G. Ribordy, W. Tittel, H. Zbinden, *Rev. Mod. Phys.* **2002**, *74*, 145.

[5] H.-K. Lo, M. Curty, K. Tamaki, *Nat. Photonics* **2014**, *8*, 595.

[6] L.-M. Duan, M. D. Lukin, J. I. Cirac, P. Zoller, *Nature* **2001**, *414*, 413.

[7] D. Huber, M. Reindl, J. Aberl, A. Rastelli, R. Trotta, *J. Opt.* **2018**, *20*, 073002.

[8] J.-W. Pan, Z.-B. Chen, C.-Y. Lu, H. Weinfurter, A. Zeilinger, M. Żukowski, *Rev. Mod. Phys.* **2012**, *84*, 777.

[9] C. H. Bennett, D. P. DiVincenzo, *Nature* **2000**, *404*, 247.

[10] S. C. Kuhn, A. Knorr, S. Reitzenstein, M. Richter, *Opt. Express* **2016**, *24*, 25446.

[11] A. Zeilinger, *Phys. Scr.* **2017**, *92*, 072501.

[12] K. Edamatsu, *Jpn. J. Appl. Phys.* **2007**, *46*, 7175.

[13] S. J. Freedman, J. F. Clauser, *Phys. Rev. Lett.* **1972**, *28*, 938.

[14] J. Wen, S. Du, Y. Zhang, M. Xiao, M. H. Rubin, *Phys. Rev. A* **2008**, *77*, 033816.

[15] J. Park, T. Jeong, H. Kim, H. S. Moon, *Phys. Rev. Lett.* **2018**, *121*, 263601.

[16] M. Müller, S. Bounouar, K. D. Jöns, M. Glässl, P. Michler, *Nat. Photonics* **2014**, *8*, 224.

[17] L. Hanschke, K. A. Fischer, S. Appel, D. Lukin, J. Wierzbowski, S. Sun, R. Trivedi, J. Vucković, J. J. Finley, K. Müller, *npj Quantum Inf.* **2018**, *4*, 43.

[18] D. Huber, M. Reindl, Y. Huo, H. Huang, J. S. Wildmann, O. G. Schmidt, A. Rastelli, R. Trotta, *Nat. Commun.* **2017**, *8*, 15506.

[19] M. Reindl, K. D. Jöns, D. Huber, C. Schimpf, Y. Huo, V. Zwiller, A. Rastelli, R. Trotta, *Nano Lett.* **2017**, *17*, 4090.

[20] P.-L. Ardelt, L. Hanschke, K. A. Fischer, K. Müller, A. Kleinkauf, M. Koller, A. Bechtold, T. Simmet, J. Wierzbowski, H. Riedl, G. Abstreiter, J. J. Finley, *Phys. Rev. B* **2014**, *90*, 241404(R).

[21] S. Bounouar, M. Müller, A. M. Barth, M. Glässl, V. M. Axt, P. Michler, *Phys. Rev. B* **2015**, *91*, 161302(R).

[22] M. Glässl, A. M. Barth, V. M. Axt, *Phys. Rev. Lett.* **2013**, *110*, 147401.

[23] A. M. Barth, S. Lüker, A. Vagov, D. E. Reiter, T. Kuhn, V. M. Axt, *Phys. Rev. B* **2016**, *94*, 045306.

[24] D. E. Reiter, T. Kuhn, M. Glässl, V. M. Axt, *J. Phys.: Condens. Matter* **2014**, *26*, 423203.

[25] A. Debnath, C. Meier, B. Chatel, T. Amand, *Phys. Rev. B* **2013**, *88*, 201305(R).

[26] M. Glässl, A. M. Barth, K. Gawarecki, P. Machnikowski, M. D. Croitoru, S. Lüker, D. E. Reiter, T. Kuhn, V. M. Axt, *Phys. Rev. B* **2013**, *87*, 085303.

[27] T. Kaldewey, S. Lüker, A. V. Kuhlmann, S. R. Valentin, A. Ludwig, A. D. Wieck, D. E. Reiter, T. Kuhn, R. J. Warburton, *Phys. Rev. B* **2017**, *95*, 161302(R).

[28] D. E. Reiter, T. Kuhn, V. M. Axt, *Adv. Phys.: X* **2019**, *4*, 1655478.

[29] T. Seidelmann, F. Ungar, M. Cygorek, A. Vagov, A. M. Barth, T. Kuhn, V. M. Axt, *Phys. Rev. B* **2019**, *99*, 245301.

[30] M. Cygorek, F. Ungar, T. Seidelmann, A. M. Barth, A. Vagov, V. M. Axt, T. Kuhn, *Phys. Rev. B* **2018**, *98*, 045303.

[31] T. Seidelmann, F. Ungar, A. M. Barth, A. Vagov, V. M. Axt, M. Cygorek, T. Kuhn, *Phys. Rev. Lett.* **2019**, *123*, 137401.

[32] S. Schumacher, J. Förstner, A. Zrenner, M. Florian, C. Gies, P. Gartner, F. Jahnke, *Opt. Express* **2012**, *20*, 5335.

[33] D. Heinze, A. Zrenner, S. Schumacher, *Phys. Rev. B* **2017**, *95*, 245306.

[34] A. Carmele, A. Knorr, *Phys. Rev. B* **2011**, *84*, 075328.

[35] R. M. Stevenson, R. J. Young, P. Atkinson, K. Cooper, D. A. Ritchie, A. J. Shields, *Nature* **2006**, *439*, 179.

[36] R. J. Young, R. M. Stevenson, P. Atkinson, K. Cooper, D. A. Ritchie, A. J. Shields, *New J. Phys.* **2006**, *8*, 29.

[37] A. Muller, W. Fang, J. Lawall, G. S. Solomon, *Phys. Rev. Lett.* **2009**, *103*, 217402.

[38] D. Huber, M. Reindl, S. F. Covre da Silva, C. Schimpf, J. Martín-Sánchez, H. Huang, G. Piredda, J. Edlinger, A. Rastelli, R. Trotta, *Phys. Rev. Lett.* **2018**, *121*, 033902.

[39] H. Wang, H. Hu, T.-H. Chung, J. Qin, X. Yang, J.-P. Li, R.-Z. Liu, H.-S. Zhong, Y.-M. He, X. Ding, Y.-H. Deng, Q. Dai, Y.-H. Huo, S. Höfling, C.-Y. Lu, J.-W. Pan, *Phys. Rev. Lett.* **2019**, *122*, 113602.

[40] J. Liu, R. Su, Y. Wei, B. Yao, S. F. C. d. Silva, Y. Yu, J. Iles-Smith, K. Srinivasan, A. Rastelli, J. Li, X. Wang, *Nat. Nanotechnol.* **2019**, *14*, 586.

[41] S. Bounouar, C. de la Haye, M. Strauß, P. Schnauber, A. Thoma, M. Gschrey, J.-H. Schulze, A. Strittmatter, S. Rodt, S. Reitzenstein, *Appl. Phys. Lett.* **2018**, *112*, 153107.

[42] A. Dousse, J. Suffczyński, A. Beveratos, O. Krebs, A. Lemaître, I. Sagnes, J. Bloch, P. Voisin, P. Senellart, *Nature* **2010**, *466*, 217.

[43] R. Winik, D. Cogan, Y. Don, I. Schwartz, L. Gantz, E. R. Schmidgall, N. Livneh, R. Rapaport, E. Buks, D. Gershoni, *Phys. Rev. B* **2017**, *95*, 235435.

[44] A. Fognini, A. Ahmadi, M. Zeeshan, J. T. Fokkens, S. J. Gibson, N. Sherlekar, S. J. Daley, D. Dalacu, P. J. Poole, K. D. Jöns, V. Zwiller, M. E. Reimer, *ACS Photonics* **2019**, *6*, 1656.

[45] R. Hafenbrak, S. M. Ulrich, P. Michler, L. Wang, A. Rastelli, O. G. Schmidt, *New J. Phys.* **2007**, *9*, 315.

[46] A. J. Bennett, M. A. Pooley, R. M. Stevenson, M. B. Ward, R. B. Patel, A. Boyer de la Giroday, N. Sköld, I. Farrer, C. A. Nicoll, D. A. Ritchie, A. J. Shields, *Nat. Phys.* **2010**, *6*, 947.

[47] E. del Valle, *New J. Phys.* **2013**, *15*, 025019.

[48] F. Troiani, J. I. Perea, C. Tejedor, *Phys. Rev. B* **2006**, *74*, 235310.

[49] R. M. Stevenson, C. L. Salter, J. Nilsson, A. J. Bennett, M. B. Ward, I. Farrer, D. A. Ritchie, A. J. Shields, *Phys. Rev. Lett.* **2012**, *108*, 040503.

[50] O. Benson, C. Santori, M. Pelton, Y. Yamamoto, *Phys. Rev. Lett.* **2000**, *84*, 2513.

[51] C. Sánchez Muñoz, F. P. Laussy, C. Tejedor, E. del Valle, *New J. Phys.* **2015**, *17*, 123021.

[52] P.-L. Ardelt, M. Koller, T. Simmet, L. Hanschke, A. Bechtold, A. Regler, J. Wierzbowski, H. Riedl, J. J. Finley, K. Müller, *Phys. Rev. B* **2016**, *93*, 165305.

[53] F. Hargart, M. Müller, K. Roy-Choudhury, S. L. Portalupi, C. Schneider, S. Höfling, M. Kamp, S. Hughes, P. Michler, *Phys. Rev. B* **2016**, *93*, 115308.

[54] A. Badolato, K. Hennessy, M. Atatüre, J. Dreiser, E. Hu, P. M. Petroff, A. Imamoğlu, *Science* **2005**, *308*, 1158.

[55] Y. Ota, S. Iwamoto, N. Kumagai, Y. Arakawa, *Phys. Rev. Lett.* **2011**, *107*, 233602.

[56] Q. Mermillod, D. Wigger, V. Delmonte, D. E. Reiter, C. Schneider, M. Kamp, S. Höfling, W. Langbein, T. Kuhn, G. Nogues, J. Kasprzak, *Optica* **2016**, *3*, 377.

[57] D. F. V. James, P. G. Kwiat, W. J. Munro, A. G. White, *Phys. Rev. A* **2001**, *64*, 052312.

[58] R. M. Stevenson, A. J. Hudson, A. J. Bennett, R. J. Young, C. A. Nicoll, D. A. Ritchie, A. J. Shields, *Phys. Rev. Lett.* **2008**, *101*, 170501.

[59] W. K. Wootters, *Phys. Rev. Lett.* **1998**, *80*, 2245.

[60] M. Cosacchi, M. Cygorek, F. Ungar, A. M. Barth, A. Vagov, V. M. Axt, *Phys. Rev. B* **2018**, *98*, 125302.

[61] R. Winkler, *Spin-Orbit Coupling Effects in Two-Dimensional Electron and Hole Systems*, Springer Tracts in Modern Physics, Vol. *191*, Springer, Berlin **2003**.

[62] S. Bravyi, D. P. DiVincenzo, D. Loss, *Ann. Phys.* **2011**, *326*, 2793.

2000108 (14 of 14)

Different Types of Photon Entanglement from a Constantly Driven Quantum Emitter Inside a Cavity

Tim Seidelmann, Michael Cosacchi, Moritz Cygorek, Doris E. Reiter, Alexei Vagov, and Vollrath M. Axt

In the original article, a factor $(\tilde{c}^2 - c^2)$ is missing in the explicit expression for the quantity δ^{UL} shortly after Eqs. (23) and (A.10). In both occasions, the correct expression should read

$$\delta^{\mathrm{UL}} = \left(\tilde{c}^2 - c^2\right)\left(\frac{2}{\Delta_0} + \frac{4\left(\tilde{c}^2 - c^2\right)}{\Delta_{\mathrm{UL}}}\right)$$

The authors state that this correction has no impact on any subsequent formula or conclusion presented in the original article and apologize for any confusion this may have caused.

Publication 5

"Time-dependent switching of the photon entanglement type using a driven quantum emitter-cavity system"

T. Seidelmann, D. E. Reiter, M. Cosacchi, M. Cygorek, A. Vagov, and V. M. Axt.

Appl. Phys. Lett. **118**, 164001 (2021).

Author contributions

The author has designed the concept of this study, has performed the numerical data generation and analysis, and has implemented the problem-specific C++ code. He has provided interpretations of the results and has written the first draft of the publication. In particular, he has proposed a feasible protocol to realize time-dependent entanglement switching. During the publication process, he has organized the submission and revision of the manuscript and has written the answer to the referees.

D. E. Reiter was invited to contribute an article in this journal. She has participated in detailed discussion of the results and their interpretations and has helped optimizing the presentation of the results. She has also contributed to revisions of the draft and the answers to the referees.

M. Cosacchi has participated in the general discussion of the results and their interpretations. Furthermore, he has discussed the results in detail with the author. He has also contributed to revisions of the draft and the answers to the referees.

M. Cygorek and A. Vagov have co-supervised this work. In particular, they have participated in the discussion of the results and their interpretations. They have also contributed to the optimization of the presentation, revisions of the draft, and the answers to the referees.

V. M. Axt has advised the author throughout his work as the main supervisor, has obtained the funding for this work, and has provided the practical means. He has participated in the discussion of the results and their interpretations. He has also contributed to the optimization of the presentation, revisions of the draft, and the answers to the referees.

T. Seidelmann, D. E. Reiter, M. Cosacchi, et al.

COLLECTIONS

Paper published as part of the special topic on Non-Classical Light Emitters and Single-Photon Detectors

View Online   Export Citation   CrossMark

ARTICLES YOU MAY BE INTERESTED IN

Quantum dots as potential sources of strongly entangled photons: Perspectives and challenges for applications in quantum networks
Applied Physics Letters **118**, 100502 (2021); https://doi.org/10.1063/5.0038729

A bright source of telecom single photons based on quantum frequency conversion
Applied Physics Letters **118**, 174003 (2021); https://doi.org/10.1063/5.0045413

A broad-band planar-microcavity quantum-dot single-photon source with a solid immersion lens
Applied Physics Letters **118**, 174001 (2021); https://doi.org/10.1063/5.0046065

Time-dependent switching of the photon entanglement type using a driven quantum emitter–cavity system

T. Seidelmann,[1,a)] (iD) D. E. Reiter,[2,b)] (iD) M. Cosacchi,[1] (iD) M. Cygorek,[3] A. Vagov,[1,4] and V. M. Axt[1]

AFFILIATIONS

[1]Lehrstuhl für Theoretische Physik III, Universität Bayreuth, 95440 Bayreuth, Germany
[2]Institut für Festkörpertheorie, Universität Münster, 48149 Münster, Germany
[3]Heriot-Watt University, Edinburgh EH14 4AS, United Kingdom
[4]ITMO University, St. Petersburg 197101, Russia

Note: This paper is part of the APL Special Collection on Non-Classical Light Emitters and Single-Photon Detectors.
[a)]Author to whom correspondence should be addressed: tim.seidelmann@uni-bayreuth.de
[b)]Electronic mail: doris.reiter@uni-muenster.de

ABSTRACT

The cascaded decay in a four-level quantum emitter is a well-established mechanism to generate polarization-entangled photon pairs, the building blocks of many applications in quantum technologies. The four most prominent maximally entangled photon pair states are the Bell states. In a typical experiment based on an undriven emitter, only one type of Bell state entanglement can be observed in a given polarization basis. Other types of Bell state entanglement in the same basis can be created by continuously driving the system by an external laser. In this work, we propose a protocol for time-dependent entanglement switching in a four-level quantum emitter–cavity system that can be operated by changing the external driving strength. By selecting different two-photon resonances between the laser-dressed states, we can actively switch back and forth between the different types of Bell state entanglement in the same basis as well as between entangled and nonentangled photon pairs. This remarkable feature demonstrates the possibility to achieve a controlled, time-dependent manipulation of the entanglement type that could be used in many innovative applications.

Published under license by AIP Publishing. https://doi.org/10.1063/5.0045377

Entangled qubits are the building blocks for fascinating applications in many innovative research fields, like quantum cryptography,[1,2] quantum communication,[3,4] or quantum information processing and computing.[5–8] Besides possible applications, the phenomenon of entanglement is also important from a fundamental point of view, being a genuine quantum effect. Especially, attractive realizations of two entangled qubits are polarization-entangled photon pairs, because they travel at the speed of light and are hardly influenced by the environment.[9]

The most prominent maximally entangled states, established for polarization-entangled photons pairs, are the four Bell states (BS)

$$|\Phi_\pm\rangle = \frac{1}{\sqrt{2}}(|HH\rangle \pm |VV\rangle), \tag{1a}$$

$$|\Psi_\pm\rangle = \frac{1}{\sqrt{2}}(|HV\rangle \pm |VH\rangle), \tag{1b}$$

where H and V denote horizontally and vertically polarized photons, respectively. The order corresponds to the order of photon detection: in a Φ Bell state (ΦBS), the first and second detected photon exhibit the same polarization, whereas in a Ψ Bell state (ΨBS), the two detected photons have exactly the opposite polarization.

A well-established mechanism for the creation of these maximally entangled Bell states is the cascaded decay that takes place in a four-level quantum emitter (FLE) after an initial excitation. Such an FLE can be realized by a variety of systems, including F-centers, semiconductor quantum dots, or atoms.[10–13] Employing a FLE, ΦBS entanglement in the chosen basis of linearly polarized photons was demonstrated for various conditions in both theoretical and experimental studies.[14–37] In contrast, ΨBS entanglement in the same linearly polarized basis has only been predicted in the case of continuous laser driving.[38,39] For the driven FLE, laser-dressed states emerge, which have been observed experimentally.[40,41] By embedding the FLE

inside a microcavity with cavity modes tuned in resonance with the desired emission process, certain two-photon emission processes between the laser-dressed states can be favored.[38,39] The emerging type and degree of entanglement depend strongly on the dominant two-photon emission path between the laser-dressed states, which, in turn, can be tuned by the external driving strength.[39]

Based on these findings, we propose a protocol for time-dependent entanglement switching using a driven FLE-cavity system. Simply changing the external driving strength in a step-like manner enables one to actively switch between the generation of ΦBS and ΨBS entanglement as well as between entangled and nonentangled photon pairs. Therefore, different entangled states can be generated from the same source without further processing the photons to change the entanglement, e.g., by wave plates.

We consider an externally driven FLE-cavity system, which has been presented in detail in Refs. 38 and 39. Figure 1 depicts a sketch of this system. A generic FLE comprises the ground state $|G\rangle$, two degenerate intermediate single-excited states $|X_{H/V}\rangle$, and the upper state $|XX\rangle$. Typically, $|XX\rangle$ is not found at twice the energy of the single-excited states but is shifted by the value E_B, e.g., in quantum dots, E_B is referred to as the biexciton binding energy.[9,42] Transitions between the FLE states that involve the state $|X_{H/V}\rangle$ are coupled to horizontally/ vertically polarized light. If the $|XX\rangle$ state has been prepared,[29,43–45] cascaded photon emission takes place when the FLE relaxes to its ground state resulting in the typical ΦBS.

An external laser with driving strength Ω is used to excite the FLE. The laser frequency is adjusted such that the two-photon transition between the ground state $|G\rangle$ and $|XX\rangle$ is driven resonantly, resulting in a fixed energetic detuning $\Delta_0 = E_B/2$ between the single-excitation transitions and the laser (cf. Fig. 1). The laser polarization is chosen to be linear with equal components of the H and V polarization. The FLE is placed inside a microcavity and coupled to its two energetically degenerate linearly polarized modes, H and V. The energetic placement of the cavity modes is described by the cavity laser detuning Δ, i.e., the difference between the cavity mode and laser energy. In typical setups, the fabrication process determines Δ, and it cannot be changed afterward. Accordingly, we fix the cavity laser
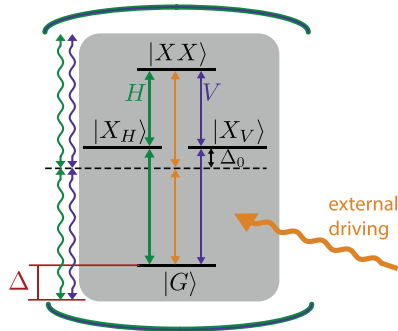

FIG. 1. Sketch of the driven FLE-cavity system. The FLE consists of the states $|G\rangle$, $|X_{H/V}\rangle$, and $|XX\rangle$, which are coupled via optical transitions by horizontally/vertically polarized light (green/purple straight arrows). The FLE is driven by an external laser at the two-photon resonance, which results in a detuning of Δ_0 to the intermediate states (orange arrows). The FLE is embedded into a cavity with two energetically degenerate but orthogonal horizontally/vertically polarized cavity modes (green/purple wavy arrows) detuned by Δ to the laser energy.

detuning to $\Delta = 0.8\Delta_0$. The coupling strength g between cavity and FLE is assumed to be equal for all FLE transitions.

Furthermore, important loss processes, i.e., radiative decay with rate γ and cavity losses with rate κ, are included using Lindblad-type operators.[39,46] The time evolution of the statistical operator of the system and two-time correlation functions are calculated by numerically solving the resulting Liouville–von Neumann equation.[47] The system parameters for the calculations are displayed in Table I.[38,39] Initially, the system is in the FLE ground state $|G\rangle$ without any cavity photons. For the Hamiltonian and details on the calculations, we refer to Ref. 39.

The entanglement characterization relies on the standard two-time correlation functions

$$G^{(2)}_{jk,lm}(t, \tau') = \langle \hat{a}_j^\dagger(t)\hat{a}_k^\dagger(t+\tau')\hat{a}_m(t+\tau')\hat{a}_l(t)\rangle, \quad (2)$$

with $\{j, k, l, m\} \in \{H, V\}$.[15] Here, t is the real time of the first photon detection and τ' is the delay time between this detection event and the detection of the second photon. The operator $\hat{a}_{H/V}^\dagger$ creates one horizontally/vertically polarized cavity photon.[48] In realistic two-time coincidence experiments, the data are always obtained by averaging the signal over finite real time and delay time intervals. Consequently, we use averaged correlation functions that depend on the starting time of the coincidence measurement t_0, the used real time measurement interval Δt, and the delay time window τ (see also Ref. 39).

A measure to classify the entanglement is the two-photon density matrix ρ^{2p}, from which the resulting type of entanglement can be extracted directly from its form. In standard experiments, ρ^{2p} is reconstructed employing quantum state tomography,[49] and, consequently, it is obtained from the averaged correlation functions as detailed in Ref. 39.

To quantify the degree of entanglement, we use the concurrence C, which can be calculated directly from the two-photon density matrix.[34,39,49–51] Note that both, the two-photon density matrix and the concurrence, depend on the parameters of the coincidence measurements: t_0, Δt, and τ. Throughout this article, a delay time window $\tau = 50$ ps is assumed.[52]

Before presenting the switching protocol, we study the behavior of the constantly driven FLE-cavity system as a function of the driving strength for a fixed selected cavity laser detuning. The resulting type of entanglement and its degree depend on the cavity laser detuning Δ and the driving strength Ω, as demonstrated in Ref. 39. In particular, a high degree of ΦBS or ΨBS entanglement is only possible, when the cavity modes are close to or in resonance with a direct two-photon transition between the laser-dressed states of the FLE. In the present setup, we have fixed all frequencies and detunings, such that the only free tuning parameter is the driving strength Ω.

TABLE I. Fixed system parameters used in the calculations.

Parameter		Value
Coupling strength	g	0.051 meV
Detuning	Δ_0	$20g = 1.02$ meV
Cavity laser detuning	Δ	$0.8\Delta_0 = 0.816$ meV
Cavity loss rate	κ	$0.1g/\hbar \approx 7.8$ ns^{-1}
Radiative decay rate	γ	$0.01g/\hbar \approx 0.78$ ns^{-1}

The constant driving of the FLE results in a mixing of the bare states $|G\rangle$, $|X_{H/V}\rangle$, and $|XX\rangle$, such that the new eigenstates are the laser-dressed states, which we label by $|U\rangle$, $|M\rangle$, $|N\rangle$, and $|L\rangle$. Their respective energies are given by[39]

$$E_U = \frac{1}{2}\left(\Delta_0 + \sqrt{\Delta_0^2 + 8\Omega^2}\right), \quad (3a)$$

$$E_M = \Delta_0, \quad (3b)$$

$$E_N = 0, \quad (3c)$$

$$E_L = \frac{1}{2}\left(\Delta_0 - \sqrt{\Delta_0^2 + 8\Omega^2}\right). \quad (3d)$$

Both the state mixing and the energies depend on the driving strength Ω, which we will now use to tune certain two-photon transitions in resonance with the cavity modes.

Figure 2 depicts the dressed state energies [panel (a)], the mean photon number $\langle n \rangle = \langle \hat{a}_H^\dagger \hat{a}_H + \hat{a}_V^\dagger \hat{a}_V \rangle$ [panel (b)], and the concurrence [panel (c)] as functions of the driving strength Ω. All quantities are calculated at times where the system has reached its steady state, i.e., it is assumed that the coincidence measurements necessary to determine ρ^{2p} and C are performed after the steady state in the system
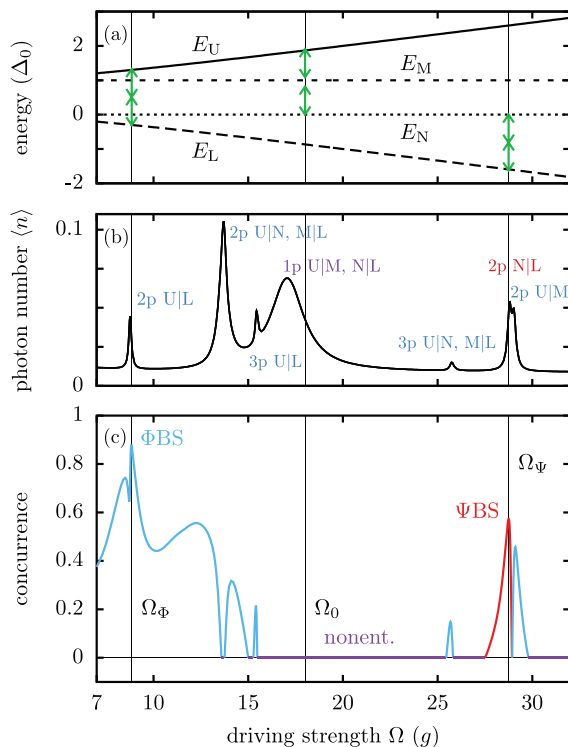

FIG. 2. (a) Energies of the four laser-dressed states as function of Ω (in units of g). Green double-headed arrows symbolize the cavity mode energy. (b) Mean photon number $\langle n \rangle$ and (c) concurrence as functions of the driving strength Ω for a cavity laser detuning $\Delta = 0.8\Delta_0$. n-photon resonances between the dressed states $|\chi_1\rangle$ and $|\chi_2\rangle$ are labeled by np $\chi_1|\chi_2$. The type of entanglement is color-coded: blue = ΦBS entanglement, red = ΨBS entanglement, purple = no entanglement. Straight lines mark the driving strengths used for switching in Fig. 3.

dynamics has been achieved.[53] A color code is used to distinguish among ΦBS (blue) entanglement, ΨBS (red) entanglement, and non-entangled photon pairs (purple).

The mean photon number exhibits a series of differently shaped peaks related to n-photon transitions between the four laser-dressed states. An n-photon transition between a pair of dressed states $|\chi_1\rangle$ and $|\chi_2\rangle$, labeled as np $\chi_1|\chi_2$ in Fig. 2(b), is in resonance with the cavity modes when n-times the cavity laser detuning Δ matches the transition energy $E_{\chi_1} - E_{\chi_2}$. Based on this condition, all peaks of enhanced photon production can be linked to one-, two-, or three-photon resonances between the dressed states. In particular, two-photon resonances manifest themselves as high and narrow peaks, e.g., for $\Omega \approx 9g$, $14g$, or $29g$.

Turning to the concurrence, presented in Fig. 2(c), one obtains again a peak-like structure and both types of Bell state entanglement occur. By comparing the concurrence and $\langle n \rangle$, one notes that the regions of high entanglement are associated with two-photon resonances. A more detailed analysis reveals that the features observable for $\Omega \approx 14g$ ($29g$) are actually caused by two closely spaced resonances, 2p U|N and 2p M|L (2p U|M and 2p N|L), which result in a double peak in the concurrence. A particularly high degree of ΦBS entanglement is obtained for $\Omega_\Phi = 8.85g$ when the cavity mode is almost at resonance with the two-photon transition between the dressed states $|U\rangle$ and $|L\rangle$, while at $\Omega_\Psi = 28.75g$, a high ΨBS entanglement occurs at the two-photon transition between $|N\rangle$ and $|L\rangle$. This behavior can be well understood using an analysis based on a Schrieffer–Wolff transformation.[39] Additionally, three-photon resonances lead to small peaks in the concurrence and in the mean photon number.

Besides the regions of high ΦBS and ΨBS entanglement, also a wide regime of vanishing concurrence is found, between $\Omega = 16g, ..., 25g$, where the cavity modes do not match any multi-photon transition process, cf. Fig. 2. Note that the vanishing degree of entanglement in this parameter regime is not due to a lack of emitted photons. On the contrary, the photon generation can be comparatively high due to the proximity to one-photon resonances, cf. Fig. 2(b). Therefore, in this parameter regime, the measurement detects two subsequent photons that are not entangled.

According to our findings, we choose three driving strengths Ω_j with similar photon number, but different types of entanglement for the switching protocol: at $\Omega_\Phi = 8.85g$, we have a strong ΦBS entanglement, at $\Omega_0 = 18.00g$, we have no entanglement, and at $\Omega_\Psi = 28.75g$, we have a strong ΨBS entanglement.

We propose a step-like excitation protocol to demonstrate time-dependent entanglement switching. The results are presented in Fig. 3. A schematic sketch of the protocol is depicted in Fig. 3(a). The basic idea is to change between three different driving strengths Ω_j that, in the stationary case, are associated with different types of entangled photon pairs. During the protocol, the FLE is continuously driven with a constant driving strength Ω_j for a fixed time period T, and then Ω changes step-like to one of the other two values. Accordingly, the resulting time-dependent laser driving has a step-like structure with step length T. In order to allow for a time resolved detection of the entanglement type, measurements with measurement interval $\Delta t = T/4$, delay time window $\tau = 50$ ps, and varying starting times t_0 are performed.

Figure 3(b) displays the calculated concurrence for each measurement as a function of its respective starting time t_0, where a step length
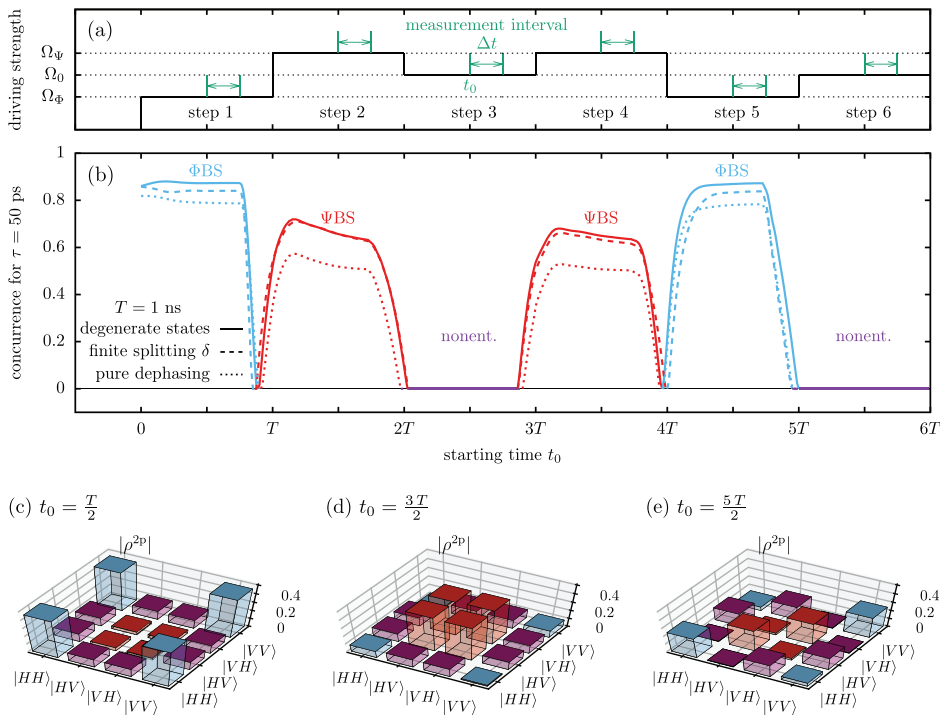
FIG. 3. (a) The proposed protocol that enables time-dependent entanglement switching. The driving strength is changed instantaneously between the three values Ω_Φ, Ω_Ψ, and Ω_0 after a time interval T, resulting in a step-like time-dependent laser driving with step length T. During each step j, coincidence measurements with starting time t_0, measurement interval $\Delta t = T/4$, and delay time window $\tau = 50$ ps can be performed. (b) Concurrence calculated for the respective measurements as a function of the starting time t_0 for a step length $T = 1$ ns. Results are calculated for degenerate intermediate states $|X_{H/V}\rangle$ (solid line), for the finite fine-structure splitting $\delta = 0.1\Delta_0$ between them (dashed line), and including pure dephasing with $\hbar\gamma_{PD} = 3$ μeV (dotted line). The cavity laser detuning is set to $\Delta = 0.8\Delta_0$, and the driving strength values $\Omega_\Phi = 8.85\,g$, $\Omega_\Psi = 28.75\,g$, and $\Omega_0 = 18\,g$ are used. A color code indicates ΦBS (blue) and ΨBS (red) entanglement as well as nonentangled photon pairs (purple). (c)–(e) Corresponding two-photon density matrices ρ^{2p} obtained for the measurements performed at $t_0 = T/2$, $3T/2$, and $5T/2$ for the case of degenerate intermediate states.

of $T = 1$ ns is assumed. As before, the entanglement type is color coded: blue (red) indicates ΦBS (ΨBS) entanglement and purple symbolizes nonentangled photon pairs. The corresponding two-photon density matrices for the measurements performed at $t_0 = T/2$, $3T/2$, and $5T/2$ are depicted in Figs. 3(c)–3(e).

The protocol starts with the driving strength Ω_Φ, and indeed, ΦBS entanglement with a high concurrence is obtained. The corresponding two-photon density matrix shown in Fig. 3(c) represents a two-photon state close to a maximally entangled ΦBS. We find that the occupations of the states with two equally polarized photons, $|HH\rangle$ and $|VV\rangle$, and the coherence between them dominate ρ^{2p} such that their absolute values are close to 1/2. In the second step, we switch to Ω_Ψ and obtain a high concurrence related to ΨBS entanglement. In the two-photon density matrix, presented in Fig. 3(d), the states $|HV\rangle$ and $|VH\rangle$ display the highest occupations and coherence values. In the third step with Ω_0, the entanglement is switched off with zero concurrence. The corresponding, reconstructed density matrix is similar to a statistical mixture, where the coherences needed for an entangled Bell state are practically absent, resulting in a vanishing degree of entanglement.

Having demonstrated that all types of entanglement can be created, we continue the protocol demonstrating that the order of switching does not play a role. Accordingly, in step 4, we switch into ΨBS entanglement; in step 5, we switch into ΦBS entanglement; and in step 6, back to no entanglement. The obtained concurrence is similar to that in steps 1–3. We also checked that density matrices ρ^{2p} obtained in the middle of steps 4, 5, and 6 are almost identical to those presented in Figs. 3(c)–3(e) for the respective driving strength (not shown).

It is also interesting to look at the case when the measurements start in the vicinity of switching times jT, where $j \in \{1, 2, \ldots, 5\}$.

Here, one observes a continuous transition between the different entanglement types. This transition begins when the measurement starting at t_0 extends into the next step, i.e., when $t_0 \geq jT - \Delta t$. During this transition process, the degree of entanglement, as measured by the concurrence, passes through zero when one switches between ΦBS and ΨBS entanglement, or vice versa. After a short transition interval, the measured concurrence enters either a plateau of high entanglement associated with the used driving strength or remains zero, when the driving strength is Ω_0.

An important question is how sensitive the proposed protocol is to parameter variations. The main requirement is that different types of entanglement can be obtained at different driving strength values. While regions of high ΦBS entanglement can be found rather easily, ΨBS entanglement occurs not so often. Only the two-photon transition 2p N|L always features ΨBS entanglement, while for high driving strengths, it can be found also at the 2p U|L resonance.[39] Furthermore, the necessary precondition to obtain ΨBS entanglement at these resonances is a finite detuning Δ_0. In principle, in these situations, one can then switch between the different entanglement types using any finite cavity laser detuning Δ. Hence, we expect that the protocol also works for different values of Δ_0 and Δ. However, a more elaborate analysis suggests that high concurrence values for both entanglement types are only obtained if Δ and Δ_0 are of the same order.

Another possible perturbation is an energy difference between the single-excited states $|X_{H/V}\rangle$, which, in quantum dots, is known as the fine-structure splitting (FSS). A finite FSS, defined as $\delta = \hbar\omega_{X_H} - \hbar\omega_{X_V}$, between the energies of the intermediate bare states $|X_{H/V}\rangle$, is regarded as a main obstacle for entanglement generation,[14,17,26,32,33] because it introduces which-path information and, thus, reduces the degree of entanglement.[14,17,31]

To consider the effect of a FSS on the switching protocol and entangled photon pair generation, we included an FSS of $\delta = 0.1\Delta_0$ in our calculations [dashed line in Fig. 3(b)], which is a typical value being one order of magnitude smaller than the binding energy.[26,29,31,32] We find that this rather large FSS only marginally reduces the concurrence compared with the previous results. The reason is that the transitions in the driven system take place between the laser-dressed states. The FSS affects the energies of the laser-dressed states and their composition only weakly such that the resonance conditions and optical selection rules hold. This implies that the generated photonic states are practically the same, and the proposed protocol is robust with respect to a nonzero FSS.

By adding a phenomenological rate model[17,35]

$$\mathcal{L}_{\mathrm{PD}}\hat{\rho} = -\frac{1}{2} \sum_{\substack{\chi,\chi' \\ \chi \neq \chi'}} \gamma_{\mathrm{PD}} |\chi\rangle\langle\chi|\hat{\rho}|\chi'\rangle\langle\chi'|, \qquad (4)$$

with rate γ_{PD} and $\chi, \chi' \in \{G, X_{\mathrm{H}}, X_{\mathrm{V}}, XX\}$ acting on the statistical operator $\hat{\rho}$, we, furthermore, consider the influence of pure dephasing. Using a realistic value for quantum dots at low temperatures,[17] $\hbar\gamma_{\mathrm{PD}} = 3\ \mu\mathrm{eV}$, we find that, although the concurrence is reduced, all essential features are unaffected. In particular, one can still switch between different entanglement types with corresponding concurrence $C \geq 0.5$ [dotted line in Fig. 3(b)].

In conclusion, this work presents a protocol for time-dependent entanglement switching based on a driven four-level emitter–cavity system. The protocol is operated by simply switching between different driving strengths in a step-like manner. Depending on the driving strength, one obtains either ΦBS entanglement, ΨBS entanglement, or nonentangled photon pairs in the respective measurements. Thus, this work demonstrates a possibility to actively switch between different types of entanglement using a time-dependent external laser excitation. The protocol is also robust against a possible FSS. It is stressed that the protocol enables one to achieve different types of entanglement within the same basis and without further post-processing of the generated photons.

The proposed protocol is, therefore, a suitable candidate for the realization of time-dependent entanglement switching, which is an important step toward future applications.

DATA AVAILABILITY

The data that support the findings of this study are available from the corresponding author upon reasonable request.

REFERENCES

[1]N. Gisin, G. Ribordy, W. Tittel, and H. Zbinden, Rev. Mod. Phys. **74**, 145 (2002).
[2]H.-K. Lo, M. Curty, and K. Tamaki, Nat. Photonics **8**, 595 (2014).
[3]L.-M. Duan, M. D. Lukin, J. I. Cirac, and P. Zoller, Nature **414**, 413 (2001).
[4]D. Huber, M. Reindl, J. Aberl, A. Rastelli, and R. Trotta, J. Opt. **20**, 073002 (2018).

[5]J.-W. Pan, Z.-B. Chen, C.-Y. Lu, H. Weinfurter, A. Zeilinger, and M. Żukowski, Rev. Mod. Phys. **84**, 777 (2012).
[6]C. H. Bennett and D. P. DiVincenzo, Nature **404**, 247 (2000).
[7]S. C. Kuhn, A. Knorr, S. Reitzenstein, and M. Richter, Opt. Express **24**, 25446 (2016).
[8]A. Zeilinger, Phys. Scr. **92**, 072501 (2017).
[9]A. Orieux, M. A. M. Versteegh, K. D. Jöns, and S. Ducci, Rep. Prog. Phys. **80**, 076001 (2017).
[10]K. Edamatsu, Jpn. J. Appl. Phys., Part 1 **46**, 7175 (2007).
[11]S. J. Freedman and J. F. Clauser, Phys. Rev. Lett. **28**, 938 (1972).
[12]J. Wen, S. Du, Y. Zhang, M. Xiao, and M. H. Rubin, Phys. Rev. A **77**, 033816 (2008).
[13]J. Park, T. Jeong, H. Kim, and H. S. Moon, Phys. Rev. Lett. **121**, 263601 (2018).
[14]T. Seidelmann, F. Ungar, M. Cygorek, A. Vagov, A. M. Barth, T. Kuhn, and V. M. Axt, Phys. Rev. B **99**, 245301 (2019).
[15]M. Cygorek, F. Ungar, T. Seidelmann, A. M. Barth, A. Vagov, V. M. Axt, and T. Kuhn, Phys. Rev. B **98**, 045303 (2018).
[16]T. Seidelmann, F. Ungar, A. M. Barth, A. Vagov, V. M. Axt, M. Cygorek, and T. Kuhn, Phys. Rev. Lett. **123**, 137401 (2019).
[17]S. Schumacher, J. Förstner, A. Zrenner, M. Florian, C. Gies, P. Gartner, and F. Jahnke, Opt. Express **20**, 5335 (2012).
[18]D. Heinze, A. Zrenner, and S. Schumacher, Phys. Rev. B **95**, 245306 (2017).
[19]A. Carmele and A. Knorr, Phys. Rev. B **84**, 075328 (2011).
[20]R. M. Stevenson, R. J. Young, P. Atkinson, K. Cooper, D. A. Ritchie, and A. J. Shields, Nature **439**, 179 (2006).
[21]R. J. Young, R. M. Stevenson, P. Atkinson, K. Cooper, D. A. Ritchie, and A. J. Shields, New J. Phys. **8**, 29 (2006).
[22]A. Muller, W. Fang, J. Lawall, and G. S. Solomon, Phys. Rev. Lett. **103**, 217402 (2009).
[23]D. Huber, M. Reindl, S. F. Covre da Silva, C. Schimpf, J. Martín-Sánchez, H. Huang, G. Piredda, J. Edlinger, A. Rastelli, and R. Trotta, Phys. Rev. Lett. **121**, 033902 (2018).
[24]H. Wang, H. Hu, T.-H. Chung, J. Qin, X. Yang, J.-P. Li, R.-Z. Liu, H.-S. Zhong, Y.-M. He, X. Ding, Y.-H. Deng, Q. Dai, Y.-H. Huo, S. Höfling, C.-Y. Lu, and J.-W. Pan, Phys. Rev. Lett. **122**, 113602 (2019).
[25]J. Liu, R. Su, Y. Wei, B. Yao, S. F. C. d Silva, Y. Yu, J. Iles-Smith, K. Srinivasan, A. Rastelli, J. Li, and X. Wang, Nat. Nanotechnol. **14**, 586 (2019).
[26]S. Bounouar, C. de la Haye, M. Strauß, P. Schnauber, A. Thoma, M. Gschrey, J.-H. Schulze, A. Strittmatter, S. Rodt, and S. Reitzenstein, Appl. Phys. Lett. **112**, 153107 (2018).
[27]A. Dousse, J. Suffczyński, A. Beveratos, O. Krebs, A. Lemaître, I. Sagnes, J. Bloch, P. Voisin, and P. Senellart, Nature **466**, 217 (2010).
[28]R. Winik, D. Cogan, Y. Don, I. Schwartz, L. Gantz, E. R. Schmidgall, N. Livneh, R. Rapaport, E. Buks, and D. Gershoni, Phys. Rev. B **95**, 235435 (2017).
[29]M. Müller, S. Bounouar, K. D. Jöns, M. Glässl, and P. Michler, Nat. Photonics **8**, 224 (2014).
[30]A. Fognini, A. Ahmadi, M. Zeeshan, J. T. Fokkens, S. J. Gibson, N. Sherlekar, S. J. Daley, D. Dalacu, P. J. Poole, K. D. Jöns, V. Zwiller, and M. E. Reimer, ACS Photonics **6**, 1656 (2019).
[31]N. Akopian, N. H. Lindner, E. Poem, Y. Berlatzky, J. Avron, D. Gershoni, B. D. Gerardot, and P. M. Petroff, Phys. Rev. Lett. **96**, 130501 (2006).
[32]R. Hafenbrak, S. M. Ulrich, P. Michler, L. Wang, A. Rastelli, and O. G. Schmidt, New J. Phys. **9**, 315 (2007).
[33]A. J. Bennett, M. A. Pooley, R. M. Stevenson, M. B. Ward, R. B. Patel, A. B. de la Giroday, N. Sköld, I. Farrer, C. A. Nicoll, D. A. Ritchie, and A. J. Shields, Nat. Phys. **6**, 947 (2010).
[34]E. del Valle, New J. Phys. **15**, 025019 (2013).
[35]F. Troiani, J. I. Perea, and C. Tejedor, Phys. Rev. B **74**, 235310 (2006).
[36]R. M. Stevenson, C. L. Salter, J. Nilsson, A. J. Bennett, M. B. Ward, I. Farrer, D. A. Ritchie, and A. J. Shields, Phys. Rev. Lett. **108**, 040503 (2012).
[37]O. Benson, C. Santori, M. Pelton, and Y. Yamamoto, Phys. Rev. Lett. **84**, 2513 (2000).
[38]F. Sánchez Muñoz, F. P. Laussy, C. Tejedor, and E. del Valle, New J. Phys. **17**, 123021 (2015).
[39]T. Seidelmann, M. Cosacchi, M. Cygorek, D. E. Reiter, A. Vagov, and V. M. Axt, Adv. Quantum Technol. **4**, 2000108 (2021).
[40]P.-L. Ardelt, M. Koller, T. Simmet, L. Hanschke, A. Bechtold, A. Regler, J. Wierzbowski, H. Riedl, J. J. Finley, and K. Müller, Phys. Rev. B **93**, 165305 (2016).

[41]F. Hargart, M. Müller, K. Roy-Choudhury, S. L. Portalupi, C. Schneider, S. Höfling, M. Kamp, S. Hughes, and P. Michler, Phys. Rev. B **93**, 115308 (2016).

[42]Q. Mermillod, D. Wigger, V. Delmonte, D. E. Reiter, C. Schneider, M. Kamp, S. Höfling, W. Langbein, T. Kuhn, G. Nogues, and J. Kasprzak, Optica **3**, 377 (2016).

[43]D. E. Reiter, T. Kuhn, M. Glässl, and V. M. Axt, J. Phys. **26**, 423203 (2014).

[44]M. Reindl, K. D. Jöns, D. Huber, C. Schimpf, Y. Huo, V. Zwiller, A. Rastelli, and R. Trotta, Nano Lett. **17**, 4090 (2017).

[45]L. Hanschke, K. A. Fischer, S. Appel, D. Lukin, J. Wierzbowski, S. Sun, R. Trivedi, J. Vucković, J. J. Finley, and K. Müller, npj Quantum Inf. **4**, 43 (2018).

[46]G. Lindblad, Commun. Math. Phys. **48**, 119 (1976).

[47]M. Cosacchi, M. Cygorek, F. Ungar, A. M. Barth, A. Vagov, and V. M. Axt, Phys. Rev. B **98**, 125302 (2018).

[48]Note that in typical experiments the measurements are performed on photons which have already left the cavity. Nevertheless, when the out-coupling of light out of the cavity is considered to be a Markovian process, Eq. (2) can be used to describe $G^{(2)}(t, \tau')$ as measured outside of the cavity (cf. Refs. 7 and 15).

[49]D. F. V. James, P. G. Kwiat, W. J. Munro, and A. G. White, Phys. Rev. A **64**, 052312 (2001).

[50]W. K. Wootters, Phys. Rev. Lett. **80**, 2245 (1998).

[51]$C = \max\{\sqrt{\lambda_1} - \sqrt{\lambda_2} - \sqrt{\lambda_3} - \sqrt{\lambda_4}, 0\}$ where $\lambda_j \geq \lambda_{j+1}$ are the eigenvalues of $\rho^{2p} T \rho^{2p*} T$ in decreasing order and T is the antidiagonal matrix with elements $\{-1, 1, 1, -1\}$.

[52]R. M. Stevenson, A. J. Hudson, A. J. Bennett, R. J. Young, C. A. Nicoll, D. A. Ritchie, and A. J. Shields, Phys. Rev. Lett. **101**, 170501 (2008).

[53]Note that in the steady state situation with constant continuous driving, ρ^{2p} and C do not depend on Δt since the statistical operator and the Hamiltonian $\hat{H}$ are constant during the measurement process.

Publication 6

"Accuracy of the Quantum Regression Theorem for Photon Emission from a Quantum Dot"

M. Cosacchi, **T. Seidelmann**, M. Cygorek, A. Vagov, D. E. Reiter, and V. M. Axt.

Phys. Rev. Lett. **127**, 100402 (2021).

&

"Erratum: Accuracy of the Quantum Regression Theorem for Photon Emission from a Quantum Dot"

M. Cosacchi, **T. Seidelmann**, M. Cygorek, A. Vagov, D. E. Reiter, and V. M. Axt.

Phys. Rev. Lett. **128**, 079901(E) (2022).

Author contributions

M. Cosacchi has designed the concept of this study, has performed the numerical data generation and analysis, and has implemented the problem-specific C++ code. He has provided interpretations of the results and has written the first drafts of the publication and the erratum. In particular, he had the original idea to use photonic characteristics of a two-level system to compare numerically exact calculations with results employing the quantum regression theorem. During the publication process, he has moderated all discussions, has organized the submission and revision of the manuscript, and has written the answer to the referees.

The author has participated in the general discussion of the results and their interpretations. Furthermore, he has discussed the results in detail with M. Cosacchi and has assisted in the numerical implementation of the quantum regression theorem and convergence tests. He has also contributed to revisions of the draft, the answers to the referees, and the erratum.

M. Cygorek, A. Vagov, and D. E. Reiter have co-supervised this work. In particular, they have participated in the discussion of the results and their interpretations. They have also contributed to the optimization of the presentation, revisions of the draft, the answers to the referees, and the erratum.

V. M. Axt has advised M. Cosacchi throughout his work as the main supervisor, has obtained the funding for this work, and has provided the practical means. He has participated in the discussion of the results and their interpretations. He has also contributed to the optimization of the presentation, revisions of the draft, the answers to the referees, and the erratum.

Accuracy of the Quantum Regression Theorem for Photon Emission from a Quantum Dot

M. Cosacchi[●],[1] T. Seidelmann[●],[1] M. Cygorek[●],[2] A. Vagov[●],[1,3] D. E. Reiter[●],[4] and V. M. Axt[1]

[1]*Theoretische Physik III, Universität Bayreuth, 95440 Bayreuth, Germany*
[2]*Heriot-Watt University, Edinburgh EH14 4AS, United Kingdom*
[3]*ITMO University, St. Petersburg 197101, Russia*
[4]*Institut für Festkörpertheorie, Universität Münster, 48149 Münster, Germany*

The quantum regression theorem (QRT) is the most widely used tool for calculating multitime correlation functions for the assessment of quantum emitters. It is an approximate method based on a Markov assumption for environmental coupling. In this Letter we quantify properties of photons emitted from a single quantum dot coupled to phonons. For the single-photon purity and the indistinguishability, we compare numerically exact path-integral results with those obtained from the QRT. It is demonstrated that the QRT systematically overestimates the influence of the environment for typical quantum dots used in quantum information technology.

To be used as photon sources for quantum information technology [1,2], semiconductor quantum dots (QDs) must deliver photons with high-quality characteristics such as a high brightness, a perfect single-photon purity, and indistinguishability. However, due to the electron-phonon interaction in QDs these quantities can be degraded [3,4]. In the current race for the perfect single-photon source [5,6] with achieved purities and indistinguishabilities close to unity [4,7–12], it is crucial to understand the influence of the phonon-induced dephasing on the properties of emitted photons. The coupling to environmental phonons has been shown to lead to several important phenomena like the phonon sidebands [13,14], damping of Rabi oscillations [15–19], and the possibility for a dynamic decoupling of electronic and phononic subsystems [20,21], or degradation of photon properties [22].

The quantum regression theorem (QRT) known from quantum optics is probably the most widely used standard tool to investigate the above photon properties [23]. In essence, the QRT prescribes to calculate the two- (or multi-) time correlation functions using the same dynamical equation for both the (real-) time and the delay-time arguments, which is used to determine the time evolution of the single-time correlations. Solving an initial value problem for the delay-time propagation as done in the QRT disregards the memory that has build up until the start of the propagation, and thus, the use of the QRT may become critical when used for non-Markovian dynamics. With the help of the QRT, multitime correlation functions yielding, e.g., the purity and indistinguishability can be deduced. The QRT can be extended such that it also accounts for the electron-phonon interaction [24–28]. For our current study it is most important that phonons are known to induce non-Markovian dynamics [24,26,29–32] which provides a

situation where the QRT may come to its limits [33–37]. Because the QRT is an approximation it is not always clear, whether the assumptions made in the derivation are fulfilled.

Testing the limits of the QRT has recently become possible by a path-integral approach to calculate multitime photon correlation functions [38]. This approach is numerically exact meaning that the time-dependent solution to the many-body Hamiltionian model is obtained without any further approximations, and thus the phonon influence including its non-Markovian part is fully taken into account [39–41]. The accuracy of the result is controlled by choosing an appropriate time discretization and memory length.

In this Letter, we explore the limits of the QRT approximation for calculating multitime correlation functions using a QD coupled to phonons as an example. To compare numerically exact results with the QRT approximation in the most transparent way, we implement the QRT directly within the path-integral method. Since apart from the QRT no further approximations are involved, this approach offers a direct way to evaluate the influence of the QRT on the multitime correlations. Details of the implementations are found in the Supplemental Material [42].

We demonstrate that the QRT systematically overestimates the phonon impact on the indistinguishability, in particular for standard GaAs QDs relevant for technological applications [51–58]. We show that this is connected to the non-Markovian part of the dynamics. In contrast, the QRT yields quantitatively correct results for the purity.

We consider a model where a two-level QD can emit photons and interacts with environmental longitudinal acoustic (LA) phonons [14,32,59]. For the calculations we consider GaAs QDs of radius 3 nm and standard material parameters for the phonon coupling with the

exception that we introduce a scaling factor λ modifying the overall coupling amplitude. Details of the model are found in the Supplemental Material [42]. We assume that this scaling is a variable in the interval $\lambda \in [0, 10]$, where 0 means the absence of phonons, 1 corresponds to the GaAs QDs, and larger values allow us to explore strongly coupled QD-phonon systems [39,60]. Larger couplings $1 < \lambda \leq 10$ can be found in piezoelectric materials like GaN [61]. We further account for the radiative decay of the QD exciton by introducing a Lindblad superoperator, setting the radiative decay rate to $\gamma = 1 \text{ ns}^{-1}$. The QD is excited by an external laser pulse with a Gaussian envelope. We consider a resonant [62] excitation scheme with a π pulse of 3 ps length (full width at half maximum) [63] to prepare the excited state in the QD [7,28]. Using this model, we can then calculate the photonic properties.

The single-photon purity $\mathcal{P}$ is defined as

$$\mathcal{P} = 1 - p \quad \text{with} \quad p = \frac{\int_{-T_{\text{Pulse}}/2}^{T_{\text{Pulse}}/2} d\tau G^{(2)}(\tau)}{\int_{T_{\text{Pulse}}/2}^{3T_{\text{Pulse}}/2} d\tau G^{(2)}(\tau)}. \quad (1)$$

T_{Pulse} is the separation of the pulses in the excitation pulse train, and

$$G^{(2)}(\tau) \coloneqq \lim_{T \to \infty} \frac{1}{T} \int_{-T}^{T} dt G^{(2)}(t, \tau), \quad (2a)$$

$$G^{(2)}(t, \tau) \coloneqq \langle \sigma_X^\dagger(t) \sigma_X^\dagger(t+\tau) \sigma_X(t+\tau) \sigma_X(t) \rangle \quad (2b)$$

with σ_X describing the QD transition from the excited to the ground state. $\mathcal{P}$ is a measure for the single-photon component of the photonic state [1,7,8,64–68]. It is measured using a Hanbury Brown-Twiss setup [69], which is a coincidence measurement and can thus be modeled with a second-order two-time correlation function $G^{(2)}(\tau)$. $\mathcal{P} = 1$ implies a perfect single-photon purity. The quantity has no lower bound, $-\infty < \mathcal{P} \leq 1$, since p can be larger than 1 in the case of bunching instead of antibunching behavior.

The indistinguishability $\mathcal{I}$ of two successively emitted photons is obtained as

$$\mathcal{I} = 1 - p_{\text{HOM}} \quad \text{with} \quad p_{\text{HOM}} = \frac{\int_{-T_{\text{Pulse}}/2}^{T_{\text{Pulse}}/2} d\tau \, G_{\text{HOM}}^{(2)}(\tau)}{\int_{T_{\text{Pulse}}/2}^{3T_{\text{Pulse}}/2} d\tau \, G_{\text{HOM}}^{(2)}(\tau)} \quad (3)$$

with the correlation functions [28,70,71]

$$G_{\text{HOM}}^{(2)}(\tau) \coloneqq \lim_{T \to \infty} \frac{1}{T} \int_{-T}^{T} dt \, G_{\text{HOM}}^{(2)}(t, \tau) \quad (4a)$$

$$G_{\text{HOM}}^{(2)}(t, \tau) \coloneqq \frac{1}{2} [\langle \sigma_X^\dagger(t) \sigma_X(t) \rangle \langle \sigma_X^\dagger(t+\tau) \sigma_X(t+\tau) \rangle \\ - |\langle \sigma_X^\dagger(t+\tau) \sigma_X(t) \rangle|^2 + G^{(2)}(t, \tau)], \quad (4b)$$

where the last term in Eq. (4b) accounts for nonunity single-photon purities. This quantity is measured in a Hong-Ou-Mandel setup [72]. Perfect indistinguishability corresponds to $\mathcal{I} = 1$, and using the definition Eq. (4b) it is bounded by $0.5 \leq \mathcal{I} \leq 1$ [71]. We note that other definitions of $\mathcal{I}$ are often used which are not applicable when the single-photon purity deviates from unity and where the lower bound is 0 rather than 0.5 [22,73].

The brightness $\mathcal{B}$ of a photon source is defined as the number of photons emitted per excitation laser pulse [8]. It is given as [28,74]

$$\mathcal{B} \coloneqq \gamma \int_{t_0 - T_{\text{Pulse}}/2}^{t_0 + T_{\text{Pulse}}/2} dt \, \langle \sigma_X^\dagger(t) \sigma_X(t) \rangle, \quad (5)$$

where t_0 is the center time of the pulse and $0 \leq \mathcal{B} \leq \gamma T_{\text{Pulse}}$. A value of $\mathcal{B}$ of 100% corresponds to the ideal case of a delta-pulse excitation.

To calculate these quantities we use the path-integral method both without and with the QRT. The path-integral method propagates the augmented density matrix that contains the information about the memory induced by the environment to the QD dynamics. Since the phonon-induced memory depth is finite, a memory window is formed in each time step. To implement the QRT, the augmented density matrix is traced over all memory-related variables at the end of the t propagation to yield a new initial reduced density matrix before the subsequent τ propagation. Thus, the accumulated phonon memory is discarded for the τ propagation. Therefore, the τ propagation becomes independent from the past evolution in t, which is the central assumption of the QRT. We have checked the validity of this approach by comparing our results with a standard implementation of the QRT as discussed in Ref. [26] and verify the finding therein that the QRT yields the phonon sidebands in emission spectra on the energetically wrong side, cf., Fig. 2 in the Supplemental Material [42].

Using the path-integral method, we calculate the photon properties $\mathcal{P}$, $\mathcal{I}$, and $\mathcal{B}$ for a wide parameter range as shown in Fig. 1, which displays the results using the path-integral approach without the QRT approximation. In the phonon-free case, $\lambda = 0$, the excitation of the QD leads to a near-optimal single-photon source with $\mathcal{P} = 99.76\%$, $\mathcal{I} = 99.76\%$, and $\mathcal{B} = 99.82\%$. Slight deviations ($< 0.3\%$) from the perfect source can be traced back to the finite pulse length.

While the single-photon purity is close to unity for the entire parameter range under consideration, for a finite phonon scaling λ, the indistinguishability rapidly deteriorates with rising temperature T, such that for $\lambda = 1$ it falls below 70% when $T > 30$ K. For large phonon scalings, the indistinguishability cannot exceed 60% even at $T = 4$ K. At higher temperatures and for large phonon scaling, the indistinguishability decreases to its lowest possible value of
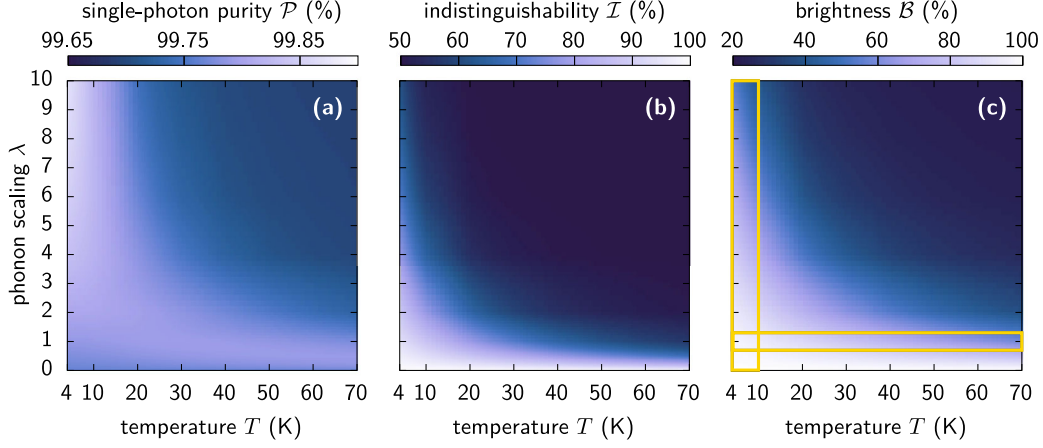
FIG. 1. The single-photon purity (a), the indistinguishability of two successively emitted photons (b), and their brightness (c) in a two-level QD for a temperature range between 4 and 70K and phonon scalings from 0 to 10. Yellow rectangles in panel (c) mark the physically important parameter regime of GaAs around $\lambda = 1$ for different temperatures and different phonon scalings for temperatures below 10K.

50%. Nonetheless, the corresponding brightness is non-vanishing, such that the QD becomes a source of distinguishable single photons in this regime of higher temperatures and stronger QD-phonon coupling.

We have marked the most physically relevant regions with yellow boxes in Fig. 1(c). They correspond to the low-temperature regime in which experiments are typically conducted for different QD materials from GaAs to GaN modeled here by different scalings λ (vertical box) as well as over a temperature range between liquid helium and nitrogen temperatures (horizontal box) for GaAs ($\lambda = 1$). In the parameter range of highest interest, i.e., where the boxes overlap at $\lambda = 1$ and $T = 4$ K, we find $\mathcal{P} = 99.79\%$, $\mathcal{I} = 93.16\%$, and $\mathcal{B} = 96.75\%$.

We now evaluate how the QRT approximation changes these results. It is usually conjectured that the QRT might fail when the dynamics is non-Markovian, i.e., when memory effects are nonnegligible [34,35]. Furthermore, there is a class of environmental couplings for which the QRT cannot be accurately applied, even when the single-time dynamics is Markovian [36]. In order to describe the contribution of the memory effects quantitatively, we consider a non-Markovianity measure for our system.

In contrast to classical Markovian stochastic processes, in open quantum systems there is no single definition of Markovianity (or non-Markovianity) that is agreed upon. Rather, there are different measures that capture different aspects of Markovian quantum dynamics [75–81], one of
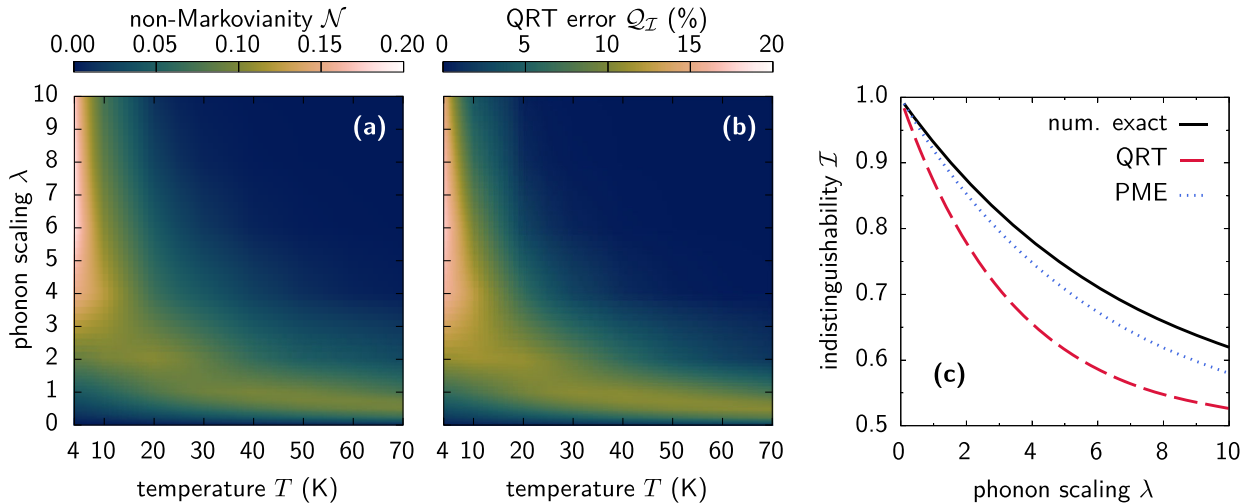
FIG. 2. The non-Markovianity measure $\mathcal{N}$ (a) and the relative error $\mathcal{Q}_\mathcal{I}$ for the indistinguishability (b) as a function of temperature T and phonon scaling λ. (c) The indistinguishability as a function of the phonon scaling parameter l at 4K, calculated with the numerically exact path-integral method (num. exact), by using the QRT in the lab frame (QRT), and by applying the QRT in the polaron transformed frame within the PME approach (PME).

which is the trace distance measure. The trace distance between two states described by the reduced density matrices ρ_1 and ρ_2 is defined as

$$D[\rho_1(t),\rho_2(t)] := \frac{1}{2}\|\rho_1(t) - \rho_2(t)\|_1 = \frac{1}{2}\sum_k |x_k(t)|, \quad (6)$$

where $x_k(t)$ are the eigenvalues of the difference matrix $\rho_1(t) - \rho_2(t)$. In our case, ρ_1 and ρ_2 correspond to arbitrary states chosen on the Bloch sphere of the two-level QD.

For Markovian dynamics, this quantity is a contraction:

$$\frac{d}{dt}D[\rho_1(t),\rho_2(t)] \leq 0. \quad (7)$$

The intuitive explanation for this behavior lies in the loss of information in a Markovian system: two originally distinct states monotonically lose their distinguishability over time. Only in a non-Markovian system, information can flow back from the environment to the system, making the trace distance a nonmonotonic function of time. Therefore, the non-Markovianity of a system can be quantified as [26,36,75]

$$\mathcal{N} := \max_{\rho_1,\rho_2} \int_{\Omega_+} \frac{d}{dt}D[\rho_1(t),\rho_2(t)]dt. \quad (8)$$

Ω_+ is the union of the intervals on which $(d/dt)D[\rho_1(t),\rho_2(t)] > 0$. The maximum is taken over all pairs of possible initial states. Fortunately, only the subset of those states, which are orthogonal to each other, needs to be considered [82]. For our two-level system, this means that the corresponding Bloch sphere needs to be sampled only for pairs of opposing points on its surface.

While $\mathcal{N} = 0$ implies Markovianity, it is important to realize that $\mathcal{N} \neq 0$ implies that the underlying dynamical map is *indivisible* [36]. Therefore, the measure $\mathcal{N}$ captures the appearance of memory effects in the dynamics of the system, which is a fundamental aspect of non-Markovianity both in classical stochastic processes and open quantum systems.

To quantify the deviations introduced by the QRT, we define the relative error of evaluating a target quantity M using the QRT as a measure for the validity of the QRT with respect to M:

$$\mathcal{Q}_M = \left|\frac{M - M_{\mathrm{QRT}}}{M}\right|, \quad (9)$$

where M is calculated numerically exact and M_{QRT} using the QRT.

The QRT states that the same dynamical map that is used to evolve the density matrix and, in extension, expectation values of any subsystem operator, can be used for the time evolution of multitime correlation functions used in

Eqs. (2b) and (4b). In particular, the differential equation propagating the density matrix in the real time t is reused for the propagation in the delay time τ [83,84]. This assumption presumes that the initial factorization of subsystem and environment common in the description of open quantum systems is also used at the beginning of the τ dynamics. In other words, this factorization is assumed for every t.

Now, we examine the impact of the QRT approximation on the photon source characteristics considered above. The non-Markovianity measure $\mathcal{N}$ and the relative error $\mathcal{Q}_{\mathcal{I}}$ for the indistinguishability are depicted in Figs. 2(a) and 2(b) as a function of T and λ. We see large values of $\mathcal{N}$ and $\mathcal{Q}_{\mathcal{I}}$, in particular, in the physically relevant parameter regimes, i.e., at $\lambda = 1$ and low temperatures. The largest $\mathcal{N}$ is found for $\lambda > 1$ and $T < 10$ K [cf., Fig. 2(a)], where the error introduced by using the QRT also rises up to roughly 18%. This behavior can be related to the connection between Markovianity and the QRT. Interestingly, there are also parameter ranges with a nonzero $\mathcal{N}$, where the QRT error is insignificant, e.g., at $\lambda = 10$ and $T = 20$ K, where $\mathcal{N} = 0.0125$, while $\mathcal{Q}_{\mathcal{I}} = 0.3\%$. This means that there are parameter sets where the QRT approximation is valid to a better degree than a Markovian description. This is unexpected since the former imposes more restrictive conditions on the system dynamics: for the QRT to hold, the subsystem and environment have to factorize for all times t, not only at the initial time. In the entire parameter regime considered here, the QRT overestimates the phonon influence on $\mathcal{I}$, that is $\mathcal{I} > \mathcal{I}_{\mathrm{QRT}}$, cf., Fig. 2(c) for a slice at 4K.

In contrast, the error $\mathcal{Q}_{\mathcal{P}}$ introduced by the QRT to the single-photon purity is negligible, and the brightness is unaffected by the QRT, since its definition in Eq. (5) contains only expectation values at a single time. Surprisingly, $\mathcal{Q}_{\mathcal{P}}$ is also extraordinarily small, being on the order of 10^{-4} for all considered parameter values (not shown), in contrast to $\mathcal{Q}_{\mathcal{I}}$.

In order to understand this, we examine the multitime correlation functions. While the purity contains only the second-order correlation $G^{(2)}(t,\tau)$, the indistinguishability also includes the correlation $G^{(1)}(t,\tau) := \langle\sigma_X^\dagger(t+\tau)\sigma_X(t)\rangle$. In $G^{(2)}(t,\tau)$ the operators $\sigma_X^\dagger$ and σ_X appear in pairs at each time t and $t+\tau$, respectively, hence modeling intensity-intensity correlation measurements, i.e., the correlation between occupations. In $G^{(1)}(t,\tau)$ on the other hand, $\sigma_X^\dagger$ and σ_X appear as stand-alone operators for each time argument in $G^{(1)}(t,\tau)$. Therefore, this function correlates coherences rather than occupations. Because the coupling to the LA phonon environment has a stronger impact on coherences than on occupations, it becomes clear why the approximations introduced by the QRT have a significantly stronger impact on $\mathcal{I}$ than on $\mathcal{P}$.

This finding implies two consequences: first, the single-photon purity can be calculated using the QRT with

negligible error, even for those parameters, where the dynamics is clearly non-Markovian according to the measure $\mathcal{N}$ [cf., Fig. 2(a)]. Second, one cannot use $\mathcal{Q}_\mathcal{P}$ as a *general* measure for the validity of the QRT. Using it in such a way would imply the validity of the QRT, which is misleading since in the same parameter regimes considered, the indistinguishability is off by up to 18% when evaluating with the QRT.

Finally, we analyze the frame dependence of the QRT by applying it in a polaron transformed frame. This technique is widely used in the polaron master equation approach (PME) [85–87] (see also Supplemental Material [42]). In Fig. 2(c), the indistinguishability is shown for a varying phonon scaling parameter λ at $T = 4$ K. The numerically exact result (black solid line) is compared with the calculation using the QRT in the lab frame (red dashed line) and the PME approach applying the QRT in the polaron frame (blue dotted line). While all methods yield qualitatively the same dependency, the PME produces results closer to the numerically exact calculation. While the largest relative error encountered in the slice shown in Fig. 2(c) is 18% for the QRT in the lab frame (red dashed line), it is only 6% when the QRT is applied in the polaron frame within the PME. The better performance of the PME is expected because due to the transformation to the polaron frame a variety of, but not all, non-Markovian effects are captured. Therefore, changing the frame improves the usage of the QRT, but still a significant systematic overestimation of phonon effects on the photon indistinguishability is obtained.

In summary, assessing the validity of the commonly used QRT is dependent on the target quantity that is calculated. In particular, there is no single measure by which the validity of the QRT could be estimated for all possible figures of merit derived from multitime correlation functions. Using a numerically exact path-integral method to calculate the properties of photons emitted from a QD coupled to LA phonons enabled us to explore the boundaries of the QRT, showing that the phonon effect on photon indistinguishability is systematically overestimated by the QRT, while the purity can be safely calculated using the QRT. Unlike what is found for other systems [36], the QRT induces errors in the photon emission from QDs typically only when the dynamics is non-Markovian. Though we show that due to the phonons the photon properties are limited close to but below unity in typical cases, there is still room for improvement, e.g., by placing the QD in a cavity. Furthermore, our results should be applicable to a broad range of physical two-level systems, such as defects in diamonds [88–93], silicon [94,95], hexagonal boron nitride [96,97], or other solid-state emitters [98] coupled to a continuum of environmental oscillators.

[1] P. Michler, A. Kiraz, C. Becher, W. V. Schoenfeld, P. M. Petroff, L. Zhang, E. Hu, and A. Imamoglu, A quantum dot single-photon turnstile device, Science **290**, 2282 (2000).

[2] P. Senellart, G. Solomon, and A. White, High-performance semiconductor quantum-dot single-photon sources, Nat. Nanotechnol. **12**, 1026 (2017).

[3] S. Gerhardt, J. Iles-Smith, D. P. S. McCutcheon, Y.-M. He, S. Unsleber, S. Betzold, N. Gregersen, J. Mørk, S. Höfling, and C. Schneider, Intrinsic and environmental effects on the interference properties of a high-performance quantum dot single-photon source, Phys. Rev. B **97**, 195432 (2018).

[4] B.-Y. Wang, E. V. Denning, U. M. Gür, C.-Y. Lu, and N. Gregersen, Micropillar single-photon source design for simultaneous near-unity efficiency and indistinguishability, Phys. Rev. B **102**, 125301 (2020).

[5] H. Vural, S. L. Portalupi, and P. Michler, Perspective of self-assembled ingaas quantum-dots for multi-source quantum implementations, Appl. Phys. Lett. **117**, 030501 (2020).

[6] S. Thomas and P. Senellart, The race for the ideal single-photon source is on, Nat. Nanotechnol. **16**, 367 (2021).

[7] X. Ding, Y. He, Z.-C. Duan, N. Gregersen, M.-C. Chen, S. Unsleber, S. Maier, C. Schneider, M. Kamp, S. Höfling, C.-Y. Lu, and J.-W. Pan, On-Demand Single Photons with High Extraction Efficiency and Near-Unity Indistinguishability from a Resonantly Driven Quantum Dot in a Micropillar, Phys. Rev. Lett. **116**, 020401 (2016).

[8] N. Somaschi *et al.*, Near-optimal single-photon sources in the solid state, Nat. Photonics **10**, 340 (2016).

[9] Y. Arakawa and M. J. Holmes, Progress in quantum-dot single photon sources for quantum information technologies: A broad spectrum overview, Appl. Phys. Rev. **7**, 021309 (2020).

[10] N. Tomm, A. Javadi, N. O. Antoniadis, D. Najer, M. C. Löbl, A. R. Korsch, R. Schott, S. R. Valentin, A. D. Wieck, A. Ludwig, and R. J. Warburton, A bright and fast source of coherent single photons, Nat. Nanotechnol. **16**, 399 (2021).

[11] S. E. Thomas, M. Billard, N. Coste, S. C. Wein, Priya, H. Ollivier, O. Krebs, L. Tazaïrt, A. Harouri, A. Lemaitre, I. Sagnes, C. Anton, L. Lanco, N. Somaschi, J. C. Loredo, and P. Senellart, Bright Polarized Single-Photon Source Based on a Linear Dipole, Phys. Rev. Lett. **126**, 233601 (2021).

[12] L. Zhai, G. N. Nguyen, C. Spinnler, J. Ritzmann, M. C. Lbl, A. D. Wieck, A. Ludwig, A. Javadi, and R. J. Warburton, Quantum interference of identical photons from remote quantum dots, arXiv:2106.03871.

[13] L. Besombes, K. Kheng, L. Marsal, and H. Mariette, Acoustic phonon broadening mechanism in single quantum dot emission, Phys. Rev. B **63**, 155307 (2001).

[14] B. Krummheuer, V. M. Axt, and T. Kuhn, Theory of pure dephasing and the resulting absorption line shape in semiconductor quantum dots, Phys. Rev. B **65**, 195313 (2002).

[15] J. Förstner, C. Weber, J. Danckwerts, and A. Knorr, Phonon-Assisted Damping of Rabi Oscillations in Semiconductor Quantum Dots, Phys. Rev. Lett. **91**, 127401 (2003).

[16] P. Machnikowski and L. Jacak, Resonant nature of phonon-induced damping of Rabi oscillations in quantum dots, Phys. Rev. B **69**, 193302 (2004).

[17] A. Vagov, V. M. Axt, T. Kuhn, W. Langbein, P. Borri, and U. Woggon, Nonmonotonous temperature dependence of the

initial decoherence in quantum dots, Phys. Rev. B **70**, 201305(R) (2004).

[18] A. Vagov, M. D. Croitoru, V. M. Axt, T. Kuhn, and F. M. Peeters, Nonmonotonic Field Dependence of Damping and Reappearance of Rabi Oscillations in Quantum Dots, Phys. Rev. Lett. **98**, 227403 (2007).

[19] A. J. Ramsay, A. V. Gopal, E. M. Gauger, A. Nazir, B. W. Lovett, A. M. Fox, and M. S. Skolnick, Damping of Exciton Rabi Rotations by Acoustic Phonons in Optically Excited InGaAs/GaAs Quantum Dots, Phys. Rev. Lett. **104**, 017402 (2010).

[20] T. Kaldewey, S. Lüker, A. V. Kuhlmann, S. R. Valentin, J.-M. Chauveau, A. Ludwig, A. D. Wieck, D. E. Reiter, T. Kuhn, and R. J. Warburton, Demonstrating the decoupling regime of the electron-phonon interaction in a quantum dot using chirped optical excitation, Phys. Rev. B **95**, 241306 (R) (2017).

[21] S. Lüker and D. E. Reiter, A review on optical excitation of semiconductor quantum dots under the influence of phonons, Semicond. Sci. Technol. **34**, 063002 (2019).

[22] J. Iles-Smith, D. P. S. McCutcheon, A. Nazir, and J. Mørk, Phonon scattering inhibits simultaneous near-unity efficiency and indistinguishability in semiconductor single-photon sources, Nat. Photonics **11**, 521 (2017).

[23] H. Breuer and F. Petruccione, *The Theory of Open Quantum Systems* (Oxford University Press, New York, 2002).

[24] P. Kaer, P. Lodahl, A.-P. Jauho, and J. Mork, Microscopic theory of indistinguishable single-photon emission from a quantum dot coupled to a cavity: The role of non-Markovian phonon-induced decoherence, Phys. Rev. B **87**, 081308(R) (2013).

[25] K. Roy-Choudhury and S. Hughes, Quantum theory of the emission spectrum from quantum dots coupled to structured photonic reservoirs and acoustic phonons, Phys. Rev. B **92**, 205406 (2015).

[26] D. P. S. McCutcheon, Optical signatures of non-Markovian behavior in open quantum systems, Phys. Rev. A **93**, 022119 (2016).

[27] J. Iles-Smith, D. P. S. McCutcheon, J. Mørk, and A. Nazir, Limits to coherent scattering and photon coalescence from solid-state quantum emitters, Phys. Rev. B **95**, 201305(R) (2017).

[28] C. Gustin and S. Hughes, Pulsed excitation dynamics in quantum-dot–cavity systems: Limits to optimizing the fidelity of on-demand single-photon sources, Phys. Rev. B **98**, 045309 (2018).

[29] P. Kaer, T. R. Nielsen, P. Lodahl, A.-P. Jauho, and J. Mørk, Non-Markovian Model of Photon-Assisted Dephasing by Electron-Phonon Interactions in a Coupled Quantum-Dot-Cavity System, Phys. Rev. Lett. **104**, 157401 (2010).

[30] D. P. S. McCutcheon and A. Nazir, Quantum dot Rabi rotations beyond the weak exciton–phonon coupling regime, New J. Phys. **12**, 113042 (2010).

[31] A. Carmele and S. Reitzenstein, Non-Markovian features in semiconductor quantum optics: Quantifying the role of phonons in experiment and theory, Nanophotonics **8**, 655 (2019).

[32] D. E. Reiter, T. Kuhn, and V. M. Axt, Distinctive characteristics of carrier-phonon interactions in optically driven semiconductor quantum dots, Adv. Phys. **4**, 1655478 (2019).

[33] T. Renger and R. A. Marcus, On the relation of protein dynamics and exciton relaxation in pigmentprotein complexes: An estimation of the spectral density and a theory for the calculation of optical spectra, J. Chem. Phys. **116**, 9997 (2002).

[34] H.-P. Breuer, E.-M. Laine, J. Piilo, and B. Vacchini, Colloquium: Non-Markovian dynamics in open quantum systems, Rev. Mod. Phys. **88**, 021002 (2016).

[35] I. de Vega and D. Alonso, Dynamics of non-Markovian open quantum systems, Rev. Mod. Phys. **89**, 015001 (2017).

[36] G. Guarnieri, A. Smirne, and B. Vacchini, Quantum regression theorem and non-Markovianity of quantum dynamics, Phys. Rev. A **90**, 022110 (2014).

[37] A. Kurt, Two-time correlation functions beyond quantum regression theorem: Effect of external noise, Quantum Inf. Process. **20**, 238 (2021).

[38] M. Cosacchi, M. Cygorek, F. Ungar, A. M. Barth, A. Vagov, and V. M. Axt, Path-integral approach for nonequilibrium multitime correlation functions of open quantum systems coupled to Markovian and non-Markovian environments, Phys. Rev. B **98**, 125302 (2018).

[39] A. Vagov, M. D. Croitoru, M. Glässl, V. M. Axt, and T. Kuhn, Real-time path integrals for quantum dots: Quantum dissipative dynamics with superohmic environment coupling, Phys. Rev. B **83**, 094303 (2011).

[40] A. M. Barth, A. Vagov, and V. M. Axt, Path-integral description of combined Hamiltonian and non-Hamiltonian dynamics in quantum dissipative systems, Phys. Rev. B **94**, 125439 (2016).

[41] M. Cygorek, A. M. Barth, F. Ungar, A. Vagov, and V. M. Axt, Nonlinear cavity feeding and unconventional photon statistics in solid-state cavity QED revealed by many-level real-time path-integral calculations, Phys. Rev. B **96**, 201201(R) (2017).

[42] See Supplemental Material at http://link.aps.org/supplemental/10.1103/PhysRevLett.127.100402 for a complete definition of our model, in particular the phonon coupling, and a detailed explanation of the numerical procedure. Additionally, further details on the QRT in a polaron transformed frame are presented. It includes Refs. [43–50] in addition to other references already cited in the main text.

[43] P. Borri, W. Langbein, S. Schneider, U. Woggon, R. L. Sellin, D. Ouyang, and D. Bimberg, Ultralong Dephasing Time in InGaAs Quantum Dots, Phys. Rev. Lett. **87**, 157401 (2001).

[44] P. Machnikowski, V. M. Axt, and T. Kuhn, Quantum-information encoding in dressed qubits, Phys. Rev. A **75**, 052330 (2007).

[45] M. Florian, P. Gartner, C. Gies, and F. Jahnke, Phonon-mediated off-resonant coupling effects in semiconductor quantum-dot lasers, New J. Phys. **15**, 035019 (2013).

[46] A. Nysteen, P. Kaer, and J. Mork, Proposed Quenching of Phonon-Induced Processes in Photoexcited Quantum Dots due to Electron-Hole Asymmetries, Phys. Rev. Lett. **110**, 087401 (2013).

[47] D. P. S. McCutcheon and A. Nazir, Model of the Optical Emission of a Driven Semiconductor Quantum Dot:

Phonon-Enhanced Coherent Scattering and Off-Resonant Sideband Narrowing, Phys. Rev. Lett. **110**, 217401 (2013).

[48] D. E. Reiter, T. Kuhn, M. Glssl, and V. M. Axt, The role of phonons for exciton and biexciton generation in an optically driven quantum dot, J. Phys. Condens. Matter **26**, 423203 (2014).

[49] M. Reindl, K. D. Jöns, D. Huber, C. Schimpf, Y. Huo, V. Zwiller, A. Rastelli, and R. Trotta, Phonon-assisted two-photon interference from remote quantum emitters, Nano Lett. **17**, 4090 (2017).

[50] A. Strathearn, P. Kirton, D. Kilda, J. Keeling, and B. W. Lovett, Efficient non-Markovian quantum dynamics using time-evolving matrix product operators, Nat. Commun. **9**, 3322 (2018).

[51] S. Hepp, F. Hornung, S. Bauer, E. Hesselmeier, X. Yuan, M. Jetter, S. L. Portalupi, A. Rastelli, and P. Michler, Purcell-enhanced single-photon emission from a strain-tunable quantum dot in a cavity-waveguide device, Appl. Phys. Lett. **117**, 254002 (2020).

[52] L. Bremer, K. Weber, S. Fischbach, S. Thiele, M. Schmidt, A. Kaganskiy, S. Rodt, A. Herkommer, M. Sartison, S. L. Portalupi, P. Michler, H. Giessen, and S. Reitzenstein, Quantum dot single-photon emission coupled into single-mode fibers with 3D printed micro-objectives, APL Photonics **5**, 106101 (2020).

[53] P. Holewa, M. Burakowski, A. Musiał, N. Srocka, D. Quandt, A. Strittmatter, S. Rodt, S. Reitzenstein, and G. Sęk, Thermal stability of emission from single InGaAs/GaAs quantum dots at the telecom O-band, Sci. Rep. **10**, 21816 (2020).

[54] N. Srocka, P. Mrowiski, J. Groe, M. Schmidt, S. Rodt, and S. Reitzenstein, Deterministically fabricated strain-tunable quantum dot single-photon sources emitting in the telecom O-band, Appl. Phys. Lett. **117**, 224001 (2020).

[55] C. L. Phillips, A. J. Brash, D. P. S. McCutcheon, J. Iles-Smith, E. Clarke, B. Royall, M. S. Skolnick, A. M. Fox, and A. Nazir, Photon Statistics of Filtered Resonance Fluorescence, Phys. Rev. Lett. **125**, 043603 (2020).

[56] A. J. Brash, J. Iles-Smith, C. L. Phillips, D. P. S. McCutcheon, J. O'Hara, E. Clarke, B. Royall, L. R. Wilson, J. Mørk, M. S. Skolnick, A. M. Fox, and A. Nazir, Light Scattering from Solid-State Quantum Emitters: Beyond the Atomic Picture, Phys. Rev. Lett. **123**, 167403 (2019).

[57] E. Schöll, L. Schweickert, L. Hanschke, K. D. Zeuner, F. Sbresny, T. Lettner, R. Trivedi, M. Reindl, S. F. Covre da Silva, R. Trotta, J. J. Finley, J. Vučković, K. Müller, A. Rastelli, V. Zwiller, and K. D. Jöns, Crux of Using the Cascaded Emission of a Three-Level Quantum Ladder System to Generate Indistinguishable Photons, Phys. Rev. Lett. **125**, 233605 (2020).

[58] S. Manna, H. Huang, S. F. C. da Silva, C. Schimpf, M. B. Rota, B. Lehner, M. Reindl, R. Trotta, and A. Rastelli, Surface passivation and oxide encapsulation to improve optical properties of a single GaAs quantum dot close to the surface, Appl. Surf. Sci. **532**, 147360 (2020).

[59] V. M. Axt, T. Kuhn, A. Vagov, and F. M. Peeters, Phonon-induced pure dephasing in exciton-biexciton quantum dot systems driven by ultrafast laser pulse sequences, Phys. Rev. B **72**, 125309 (2005).

[60] S. Lüker, T. Kuhn, and D. E. Reiter, Phonon impact on optical control schemes of quantum dots: Role of quantum dot geometry and symmetry, Phys. Rev. B **96**, 245306 (2017).

[61] B. Krummheuer, V. M. Axt, T. Kuhn, I. D'Amico, and F. Rossi, Pure dephasing and phonon dynamics in GaAs- and GaN-based quantum dot structures: Interplay between material parameters and geometry, Phys. Rev. B **71**, 235329 (2005).

[62] Note that the excitation has to be resonant to the polaron shifted exciton energy, when phonons are taken into account.

[63] For resonant excitation, this value has been shown both experimentally Ding2016 and theoretically [28] to be a favorable value concerning the photonic figures of merit.

[64] C. Santori, M. Pelton, G. Solomon, Y. Dale, and Y. Yamamoto, Triggered Single Photons from a Quantum Dot, Phys. Rev. Lett. **86**, 1502 (2001).

[65] C. Santori, D. Fattal, J. Vuckovic, G. S. Solomon, and Y. Yamamoto, Indistinguishable photons from a single-photon device, Nature (London) **419**, 594 (2002).

[66] Y.-M. He, Y. He, Y.-J. Wei, D. Wu, M. Atatüre, C. Schneider, S. Höfling, M. Kamp, C.-Y. Lu, and J.-W. Pan, On-demand semiconductor single-photon source with near-unity indistinguishability, Nat. Nanotechnol. **8**, 213 (2013).

[67] Y.-J. Wei, Y.-M. He, M.-C. Chen, Y.-N. Hu, Y. He, D. Wu, C. Schneider, M. Kamp, S. Höfling, C.-Y. Lu, and J.-W. Pan, Deterministic and robust generation of single photons from a single quantum dot with 99.5% indistinguishability using adiabatic rapid passage, Nano Lett. **14**, 6515 (2014).

[68] L. Schweickert, K. D. Jöns, K. D. Zeuner, S. F. Covre da Silva, H. Huang, T. Lettner, M. Reindl, J. Zichi, R. Trotta, A. Rastelli, and V. Zwiller, On-demand generation of background-free single photons from a solid-state source, Appl. Phys. Lett. **112**, 093106 (2018).

[69] R. Hanbury Brown and R. Q. Twiss, A test of a new type of stellar interferometer on sirius, Nature (London) **178**, 1046 (1956).

[70] A. Kiraz, M. Atatüre, and A. Imamoğlu, Quantum-dot single-photon sources: Prospects for applications in linear optics quantum-information processing, Phys. Rev. A **69**, 032305 (2004).

[71] K. A. Fischer, K. Müller, K. G. Lagoudakis, and J. Vučković, Dynamical modeling of pulsed two-photon interference, New J. Phys. **18**, 113053 (2016).

[72] C. K. Hong, Z. Y. Ou, and L. Mandel, Measurement of Subpicosecond Time Intervals between Two Photons by Interference, Phys. Rev. Lett. **59**, 2044 (1987).

[73] R. Manson, K. Roy-Choudhury, and S. Hughes, Polaron master equation theory of pulse-driven phonon-assisted population inversion and single-photon emission from quantum-dot excitons, Phys. Rev. B **93**, 155423 (2016).

[74] M. Cosacchi, F. Ungar, M. Cygorek, A. Vagov, and V. M. Axt, Emission-Frequency Separated High Quality Single-Photon Sources Enabled by Phonons, Phys. Rev. Lett. **123**, 017403 (2019).

[75] H.-P. Breuer, E.-M. Laine, and J. Piilo, Measure for the Degree of Non-Markovian Behavior of Quantum Processes in Open Systems, Phys. Rev. Lett. **103**, 210401 (2009).

[76] A. Rivas, S. F. Huelga, and M. B. Plenio, Entanglement and Non-Markovianity of Quantum Evolutions, Phys. Rev. Lett. **105,** 050403 (2010).

[77] X.-M. Lu, X. Wang, and C. P. Sun, Quantum Fisher information flow and non-Markovian processes of open systems, Phys. Rev. A **82,** 042103 (2010).

[78] S. Lorenzo, F. Plastina, and M. Paternostro, Geometrical characterization of non-Markovianity, Phys. Rev. A **88,** 020102(R) (2013).

[79] Á. Rivas, S. F. Huelga, and M. B. Plenio, Quantum non-Markovianity: Characterization, quantification and detection, Rep. Prog. Phys. **77,** 094001 (2014).

[80] D. Chruścinńskiand S. Maniscalco, Degree of Non-Markovianity of Quantum Evolution, Phys. Rev. Lett. **112,** 120404 (2014).

[81] L. Li, M. J. Hall, and H. M. Wiseman, Concepts of quantum non-Markovianity: A hierarchy, Phys. Rep. **759,** 1 (2018).

[82] S. Wißmann, A. Karlsson, E.-M. Laine, J. Piilo, and H.-P. Breuer, Optimal state pairs for non-Markovian quantum dynamics, Phys. Rev. A **86,** 062108 (2012).

[83] W. H. Louisell, *Quantum Statistical Properties of Radiation* (Wiley, New York, 1973).

[84] H. Carmichael, *An Open Systems Approach to Quantum Optics* (Springer, Berlin, 1993).

[85] C. Roy and S. Hughes, Influence of Electron—Acoustic-Phonon Scattering on Intensity Power Broadening in a Coherently Driven Quantum-Dot—Cavity System, Phys. Rev. X **1,** 021009 (2011).

[86] A. Nazir and D. P. S. McCutcheon, Modelling exciton-phonon interactions in optically driven quantum dots, J. Phys. Condens. Matter **28,** 103002 (2016).

[87] J. Iles-Smith and A. Nazir, Quantum correlations of light and matter through environmental transitions, Optica **3,** 207 (2016).

[88] D. Englund, B. Shields, K. Rivoire, F. Hatami, J. Vučković, H. Park, and M. D. Lukin, Deterministic coupling of a single nitrogen vacancy center to a photonic crystal cavity, Nano Lett. **10,** 3922 (2010).

[89] K. Beha *et al.*, Diamond nanophotonics, Beilstein J. Nanotechnol. **3,** 895 (2012).

[90] I. Aharonovich, D. Englund, and M. Toth, Solid-state single-photon emitters, Nat. Photonics **10,** 631 (2016).

[91] K. G. Fehler, A. P. Ovvyan, N. Gruhler, W. H. P. Pernice, and A. Kubanek, Efficient coupling of an ensemble of nitrogen vacancy center to the mode of a high-Q, Si_3N_4 photonic crystal cavity, ACS Nano **13,** 6891 (2019).

[92] E. Janitz, M. K. Bhaskar, and L. Childress, Cavity quantum electrodynamics with color centers in diamond, Optica **7,** 1232 (2020).

[93] P. P. J. Schrinner, J. Olthaus, D. E. Reiter, and C. Schuck, Integration of diamond-based quantum emitters with nanophotonic circuits, Nano Lett. **20,** 8170 (2020).

[94] J. C. Lee, I. Aharonovich, A. P. Magyar, F. Rol, and E. L. Hu, Coupling of silicon-vacancy centers to a single crystal diamond cavity, Opt. Express **20,** 8891 (2012).

[95] K. G. Fehler, A. P. Ovvyan, L. Antoniuk, N. Lettner, N. Gruhler, V. A. Davydov, V. N. Agafonov, W. H. Pernice, and A. Kubanek, Purcell-enhanced emission from individual SiV- center in nanodiamonds coupled to a Si_3N_4-based, photonic crystal cavity, Nanophotonics **9,** 3655 (2020).

[96] N. V. Proscia, H. Jayakumar, X. Ge, G. Lopez-Morales, Z. Shotan, W. Zhou, C. A. Meriles, and V. M. Menon, Microcavity-coupled emitters in hexagonal boron nitride, Nanophotonics **9,** 2937 (2020).

[97] J. E. Fröch, S. Kim, N. Mendelson, M. Kianinia, M. Toth, and I. Aharonovich, Coupling hexagonal boron nitride quantum emitters to photonic crystal cavities, ACS Nano **14,** 7085 (2020).

[98] S. Rodt, S. Reitzenstein, and T. Heindel, Deterministically fabricated solid-state quantum-light sources, J. Phys. Condens. Matter **32,** 153003 (2020).

Supplement: Accuracy of the quantum regression theorem for photon emission from a quantum dot

M. Cosacchi,[1] T. Seidelmann,[1] M. Cygorek,[2] A. Vagov,[1,3] D. E. Reiter,[4] and V. M. Axt[1]

[1]*Theoretische Physik III, Universität Bayreuth, 95440 Bayreuth, Germany*
[2]*Heriot-Watt University, Edinburgh EH14 4AS, United Kingdom*
[3]*ITMO University, St. Petersburg, 197101, Russia*
[4]*Institut für Festkörpertheorie, Universität Münster, 48149 Münster, Germany*

I. HAMILTONIAN AND MODEL EQUATION

Our model Hamiltonian reads as:

$$H = H_{\text{QD}} + H_{\text{Ph}} + H_{\text{driving}}. \tag{1}$$

The two-level quantum dot (QD) has an excited state $|X\rangle$ at energy $\hbar\omega_X$ and the energy of the ground state $|G\rangle$ is set to zero. In a frame co-rotating with the laser frequency ω_L the corresponding Hamiltonian is

$$H_{\text{QD}} = \hbar\Delta\omega_{XL}|X\rangle\langle X| \tag{2}$$

with the exciton-laser detuning $\Delta\omega_{XL} = \omega_X - \omega_L$. The QD interacts with an environment of longitudinal acoustic (LA) phonons via a pure-dephasing coupling Hamiltonian [1–5]

$$H_{\text{Ph}} = \hbar\sum_{\mathbf{q}}\omega_{\mathbf{q}}b_{\mathbf{q}}^{\dagger}b_{\mathbf{q}} + \hbar\sqrt{\lambda}\sum_{\mathbf{q}}\left(\gamma_{\mathbf{q}}^{\text{X}}b_{\mathbf{q}}^{\dagger} + \gamma_{\mathbf{q}}^{\text{X}*}b_{\mathbf{q}}\right)|X\rangle\langle X|, \tag{3}$$

where $b_{\mathbf{q}}$ ($b_{\mathbf{q}}^{\dagger}$) annihilates (creates) a phonon in the mode $\mathbf{q}$ with energy $\hbar\omega_{\mathbf{q}}$. The coupling strength to the QD is denoted by $\gamma_{\mathbf{q}}^{\text{X}}$. In order to analyze the impact of the phonon coupling, we introduce a scaling parameter λ, with $0 \leq \lambda \leq 10$. $\lambda = 0$ describes the phonon-free case, $\lambda = 1$ the coupling in a GaAs QD. $1 < \lambda \leq 10$ roughly estimates the stronger phonon coupling in piezoelectric materials like GaN [6]. λ is referred to as the phonon scaling in the main text. Note that we followed the standard way to write the phonon coupling in Eq. (3) to the exciton state $|X\rangle$ only. But in fact, it can be written to the ground state $|G\rangle$ without any influence on the stationary emission spectrum, which we checked numerically by calculating the QRT spectrum in Fig. 1 (red dashed line) both ways.

The QD is driven by an external laser pulse described by

$$H_{\text{driving}} = -\frac{\hbar}{2}f_{\text{p}}(t)\left(\sigma_X + \sigma_X^{\dagger}\right). \tag{4}$$

$\sigma_X := |G\rangle\langle X|$ is the operator for the transition between $|X\rangle$ and the ground state $|G\rangle$. $f_{\text{p}}(t)$ is the real envelope function of the external laser pulse. Throughout the main text, we consider a Gaussian pulse with an area of π and pulse duration as measured by the full width at half maximum $\tau_{\text{FWHM}} = 3\,\text{ps}$ resonant to the polaron shifted QD transition energy. We further account for the radiative decay of the QD exciton by introducing a Lindblad superoperator acting on the density matrix ρ to our model

$$\mathcal{L}_{\sigma_X,\gamma}\rho = \gamma\left(\sigma_X\rho\sigma_X^{\dagger} - \frac{1}{2}\left\{\rho,\sigma_X^{\dagger}\sigma_X\right\}_{+}\right), \tag{5}$$

where $\{A,B\}_{+}$ denotes the anti-commutator of operators A and B and γ the radiative decay rate set to a typical value of $1\,\text{ns}^{-1}$ unless noted otherwise.

In this model the QD environment consists of two parts: the coupling to photon modes which is responsible for the radiative decay and the coupling to phonons. Since the radiative decay is modeled by a Markovian rate, it is not expected to limit the validity of the QRT. Phonons are known to influence the QD dynamics profoundly [1, 7–18] and to be the origin of non-Markovian behavior [5, 19–23], which might entail errors of the QRT.

While the Hamiltonian in Eq. (1) defines the model, the corresponding Liouville-von Neumann equation for the density matrix ρ reads

$$\frac{\partial}{\partial t}\rho = -\frac{i}{\hbar}\{H,\rho\}_{-} + \mathcal{L}_{\sigma_X,\gamma}\rho \tag{6}$$

TABLE I. Parameters typical for GaAs QDs [6].

Electron deformation potential	D_e (eV)	7.0
Hole deformation potential	D_h (eV)	-3.5
Density	ρ_D (kg/m^3)	5370
Sound velocity	c_s (m/s)	5110
Electron-to-hole confinement ratio	a_e/a_h	1.15
Electron confinement radius	a_e (nm)	3.0

with the commutator $\{A, B\}_-$ of operators A and B. This equation is solved in a numerically exact way for the time evolution of the QD subsystem's reduced density matrix $\bar{\rho} = \mathrm{Tr_{Ph}}[\rho]$, where the trace is taken over the phonon subspace, by employing an iterative real-time path-integral formalism (details are explained in Refs. 24–26).

The deformation potential coupling of the QD to LA phonons influences the reduced electronic density matrix via the phonon spectral density $J(\omega) = \sum_{\mathbf{q}} |\gamma_{\mathbf{q}}^X|^2 \delta(\omega - \omega_{\mathbf{q}})$. Note that the sign or even the phase of the coupling has no influence on the electronic dynamics, since only the absolute square enters the spectral density. Assuming a linear dispersion $\omega_{\mathbf{q}} = c_s|\mathbf{q}|$ with sound velocity c_s and Gaussian wave functions for both electrons and holes with radii a_e and a_h, the spectral density becomes [24, 26, 27]

$$J(\omega) = \frac{\omega^3}{4\pi^2 \rho_D \hbar c_s^5} \left(D_e e^{-\omega^2 a_e^2/(4c_s^2)} - D_h e^{-\omega^2 a_h^2/(4c_s^2)} \right)^2 . \tag{7}$$

We use typical GaAs parameters for a QD with radius $a_e = 3.0\,\mathrm{nm}$ listed in Tab. I. Note that scaling the phonon coupling $\gamma_{\mathbf{q}}^X$ with $\sqrt{\lambda}$ as in Eq. (3) implies that the spectral density $J(\omega)$ is scaled with λ.

The low-frequency behavior of this spectral density is given by $J(\omega) \propto \omega^s$ with $s = 3$. Spectral densities with such a power law dependence are classified as super-Ohmic, in contrast to the Ohmic case, for which $s = 1$, and the sub-Ohmic case with $0 \leq s < 1$. The super-Ohmic case is known to result in a nonexponential and only partial polarization decay [3] which is a clear signature of non-Markovian dynamics. Rather generally, the low-frequency behavior has been shown to potentially play a decisive role for the relation between Markovianity and QRT errors [28].

II.   EVALUATION OF $G^{(2)}(t, \tau)$

Numerically Exact Evaluation To evaluate the two-time correlation function introduced in the main text $G^{(2)}(t, \tau) = \langle \sigma_X^\dagger(t) \sigma_X^\dagger(t+\tau) \sigma_X(t+\tau) \sigma_X(t) \rangle$ within the path-integral formalism, first, we assume a time discretization of n equidistant time steps with length Δt for the interval $[0, t]$ and of another m time steps of the same length to cover $[t, t+\tau]$, i.e., $t = n\Delta t$ and $\tau = m\Delta t$. The object propagated in time is the augmented density matrix (ADM), a $2n_c$-rank tensor that contains all the information induced by the $n_c\Delta t$ long memory. The iterative propagation of the ADM is summarized as [25]:

$$\bar{\rho}_{\nu_n \ldots \nu_{n-n_c+1}}^{\mu_n \ldots \mu_{n-n_c+1}} = \mathcal{M}_{\nu_n \mu_n}^{\nu_{n-1} \mu_{n-1}} \sum_{\substack{\nu_{n-n_c} \\ \mu_{n-n_c}}} \exp \left(\sum_{l=n-n_c}^n S_{\nu_n \nu_l \mu_n \mu_l} \right) \bar{\rho}_{\nu_{n-1} \ldots \nu_{n-n_c}}^{\mu_{n-1} \ldots \mu_{n-n_c}} , \tag{8}$$

where $\mathcal{M}_{\nu_n \mu_n}^{\nu_{n-1} \mu_{n-1}}$ is the subsystem propagator and $S_{\nu_n \nu_l \mu_n \mu_l}$ the phonon influence functional. The indices μ_j and ν_j describe the subsystem state μ and ν, respectively, at the time step j. The subsystem's reduced density matrix at time $n\Delta t$, which is the quantity necessary to calculate any expectation value of observables within the subsystem, is obtained by tracing out the memory contained in the ADM, i.e.,

$$\bar{\rho}_{\nu_n \mu_n} = \sum_{\substack{\nu_{n-1} \ldots \nu_{n-n_c+1} \\ \mu_{n-1} \ldots \mu_{n-n_c+1}}} \bar{\rho}_{\nu_n \ldots \nu_{n-n_c+1}}^{\mu_n \ldots \mu_{n-n_c+1}} . \tag{9}$$

In order to calculate the two-time correlation function $G^{(2)}(t, \tau)$, the ADM is propagated for the first n steps, after

which the operators evaluated at time t are multiplied to produce a modified ADM (MADM):

$$\bar{\rho}_{\sigma_X \sigma_X^\dagger \nu_n \dots \nu_{n-n_c+1}}^{\mu_n \dots \mu_{n-n_c+1}} = \sum_{\nu_n' \mu_n'} (\sigma_X)_{\nu_n \nu_n'} \mathcal{M}_{\nu_n' \mu_n'}^{\nu_{n-1} \mu_{n-1}} (\sigma_X^\dagger)_{\mu_n' \mu_n} \sum_{\substack{\nu_{n-n_c} \\ \mu_{n-n_c}}} \exp\left(\sum_{l=n-n_c}^{n} S_{\nu_n \nu_l \mu_n \mu_l} \right) \bar{\rho}_{\nu_{n-1} \dots \nu_{n-n_c}}^{\mu_{n-1} \dots \mu_{n-n_c}} , \tag{10}$$

The MADM follows the same recursion as the ADM, such that for the subsequent m steps until $t + \tau$, the MADM is iterated instead of the ADM. Finally, the two-time correlation function is obtained by multiplying the operators evaluated at time $t + \tau$ and the trace is performed to yield

$$G^{(2)}(t, \tau) = \sum_{\substack{\nu_{n+m} \dots \nu_{n+m-n_c+1} \\ \mu_{n+m} \dots \mu_{n+m-n_c+1}}} \left[\sigma_X^\dagger \sigma_X \right]_{\mu_{n+m} \nu_{n+m}} \bar{\rho}_{\sigma_X \sigma_X^\dagger \nu_{n+m} \dots \nu_{n+m-n_c+1}}^{\mu_{n+m} \dots \mu_{n+m-n_c+1}} . \tag{11}$$

A derivation of this scheme with detailed explanations can be found in Ref. [29]. Note that the first-order correlation function $\langle \sigma_X^\dagger(t + \tau) \sigma_X(t) \rangle$ appearing in the main text can be obtained using the same method by simply exchanging $\sigma_X^\dagger(t)$ and $\sigma_X(t + \tau)$ with identity operators in $G^{(2)}(t, \tau)$.

QRT Evaluation To implement the QRT within this framework, one traces out the memory of the ADM after reaching the time $n\Delta t$ as in Eq. (9) to obtain the reduced density matrix (RDM) $\bar{\rho}_{\nu_n \mu_n}$. Then, a modified RDM (MRDM) which is defined as

$$\bar{\rho}_{\sigma_X \sigma_X^\dagger \nu_n}^{\mu_n} = \sum_{\nu_n' \mu_n'} (\sigma_X)_{\nu_n \nu_n'} \bar{\rho}_{\nu_n' \mu_n'} (\sigma_X^\dagger)_{\mu_n' \mu_n} \tag{12}$$

is used as the new initial RDM for the next m time steps, which now describe the propagation in τ. The essential difference to the exact propagation scheme is that here the memory acquired until the time t is discarded for the subsequent τ-propagation. As for the initial (real) time $t = 0$, the phonon subspace is assumed to be in equilibrium at a temperature of T at the time $n\Delta t$, when the propagation of the MRDM begins. The statistical operator of the total system is approximated by the QRT at the beginning of the τ-propagation by a product of the statistical operators for the two-level system and the environment, thus ignoring the entanglement between these subsystems that has been built up during the t-propagation due to their mutual interaction [30].

III. EMISSION SPECTRA AND QRT IMPLEMENTATION

The emission spectrum $S(\omega)$ is obtained in a stationary nonequilibrium state of the system. To this end, the first-order two-time correlation function $G^{(1)}(t, \tau) = \langle \sigma_X^\dagger(t + \tau) \sigma_X(t) \rangle$ is considered in the limit $t \to \infty$. After subtraction of the coherent part of the emission [29, 31] $\lim_{t, \tau \to \infty} G^{(1)}(t, \tau)$ the Fourier transform is taken:

$$S(\omega) = \text{Re}\left[\int_{-\infty}^{\infty} d\tau \lim_{t \to \infty} \left(G^{(1)}(t, \tau) - \lim_{\tau \to \infty} G^{(1)}(t, \tau) \right) e^{-i\omega\tau} \right] . \tag{13}$$

In Fig. 1 QD emission spectra calculated for a constantly driven QD with a field strength of $\hbar f_p(t) = 0.079\,\text{meV}$ and a radiative decay rate of $\gamma = 0.01\,\text{ps}^{-1}$ at $T = 10\,\text{K}$ are shown. As a reference, the phonon-free result, i.e., for $\lambda = 0$, is depicted (orange dashed-dotted line), where no sidebands appear. The inset in Fig. 1 shows the same data zoomed in on the energy scale and zoomed out on the intensity axis. On this scale, the Mollow triplet becomes visible with the peaks at $\pm \hbar f_p$, which corresponds to the Rabi splitting. For finite temperature, the peaks shift to smaller energies and broaden slightly, which corresponds to the phonon-induced renormalization of the Rabi frequency and its damping, respectively. Note that the numerically exact result at $10\,\text{K}$ has been obtained by employing a matrix-product-state representation of the iterative path-integral method [32] to enable calculations with very fine time discretization.

We stress that there is a clear physical picture that the phonon sideband has to be on the left side of the zero phonon line (ZPL). At low temperatures, phonon emission is strongly favored over phonon absorption. Therefore, the energies of the emitted photon and of the emitted phonon have to add up to the QD transition energy due to energy conservation. Accordingly, in an emission spectrum, the energy of the emitted photon after phonon emission has to be smaller than the QD transition energy. This results in the phonon emission sideband being on the energetically lower side of the ZPL.

The numerically exact approach (black solid line) gives the physically correct results showing the phonon sideband on the energetically lower side of the ZPL. In contrast, when the QRT is applied, the phonon sideband appears on
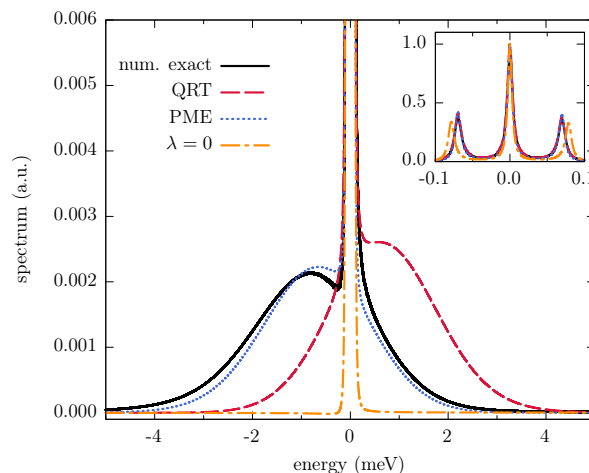
FIG. 1. The QD emission spectrum [29] calculated for a constantly driven QD with $\hbar f_{\mathrm{p}}(t) = 0.079\,\mathrm{meV}$ and a radiative decay rate of $\gamma = 0.01\,\mathrm{ps}^{-1}$ at $T = 10\,\mathrm{K}$. The numerically exact result (num. exact) is compared with results obtained using the QRT in the lab frame (QRT) and in the polaron frame (PME). As a reference, the phonon-free case $\lambda = 0$ is also shown. The inset depicts the same data on a different scale, where the Mollow triplet becomes visible.

the energetically higher side (red dashed line). This wrong outcome of the QRT was already discussed in Ref. 22, where it was explicitly shown that by neglecting correlations resulting in memory effects, physically wrong results are obtained. We consider our implementation of the QRT as verified, since it reproduces this result of Ref. 22, which was obtained within a completely different methodological framework. When including said correlations and memory effects on the other hand, as they are in our numerically exact path-integral approach, the physically correct picture of a phonon sideband at the lower energy side of the emission spectrum is found.

IV. THE QRT IN THE POLARON TRANSFORMED FRAME

An approximate method to account for the coupling to the LA phonon environment is the polaron master equation approach (PME) [33–35]. The core idea of this method is to transform the system into the polaron frame by

$$H' = e^S H e^{-S} \tag{14a}$$

$$S = \sigma_X^\dagger \sigma_X \sum_{\mathbf{q}} \frac{\sqrt{\lambda}}{\omega_{\mathbf{q}}} \left(\gamma_{\mathbf{q}}^X b_{\mathbf{q}}^\dagger - \gamma_{\mathbf{q}}^{X*} b_{\mathbf{q}} \right) . \tag{14b}$$

Only then the Markov approximation is employed to obtain a time-local master equation for the reduced subsystem dynamics. This method becomes exact in the weak-driving limit. Since we consider strong pulsed excitation, it is not a priori clear if this condition is fulfilled. The PME approach captures a variety of non-Markovian features that would be lost if the Markov approximation had been used in the original laboratory frame.

Therefore, the question arises whether the QRT is also frame dependent. Indeed, QD emission spectra calculated within the PME approach by employing the QRT in the polaron frame show the correct phonon sidebands [36], cf., blue dotted line in Fig. 1.

In the following, we describe the procedure to compare the effect of using the QRT in the lab and the polaron frame on the indistinguishability, cf., Fig. 2(c) in the main text. To obtain the indistinguishability in the lab frame within the PME approach, one has to transform it back after using the QRT in the polaron frame. In this transformation, all $\sigma_X^\dagger$ (σ_X) operators acquire a B_+ (B_-) operator with $B_\pm = \exp\left[\pm \sum_{\mathbf{q}} (\sqrt{\lambda}/\omega_{\mathbf{q}})(\gamma_{\mathbf{q}}^{X*} b_{\mathbf{q}} - \gamma_{\mathbf{q}}^X b_{\mathbf{q}}^\dagger) \right]$. Hence, whenever the two transition operators appear in pairs at equal times as in the second-order correlation function $G^{(2)}(t, \tau)$ the back transform is the identity operation. In contrast, the function $G^{(1)}(t, \tau)$ is influenced by the back transform. In particular, a term $\langle B_+(\tau) B_-(0) \rangle$ appears, which is simplified to $\langle B \rangle^2 e^{\phi(\tau)}$ [37]. The so-called Franck-Condon factor

[16] $\langle B \rangle$ is defined as

$$\langle B \rangle = \langle B_\pm \rangle = \exp \left[-\frac{1}{2} \int_0^\infty d\omega \frac{J(\omega)}{\omega^2} \coth \left(\hbar\omega/(2k_B T) \right) \right],$$ (15)

where k_B denotes the Boltzmann constant. The phonon correlation function is

$$\phi(\tau) = \int_0^\infty d\omega \frac{J(\omega)}{\omega^2} [\coth \left(\hbar\omega/(2k_B T) \right) \cos \left(\omega\tau \right) - i \sin \left(\omega\tau \right)].$$ (16)

[1] L. Besombes, K. Kheng, L. Marsal, H. Mariette. 'Acoustic phonon broadening mechanism in single quantum dot emission'. *Phys. Rev. B* **63**, 155307 (2001). doi:10.1103/PhysRevB.63.155307.

[2] P. Borri, W. Langbein, S. Schneider, U. Woggon, R. L. Sellin, D. Ouyang, D. Bimberg. 'Ultralong dephasing time in InGaAs quantum dots'. *Phys. Rev. Lett.* **87**, 157401 (2001). doi:10.1103/PhysRevLett.87.157401.

[3] B. Krummheuer, V. M. Axt, T. Kuhn. 'Theory of pure dephasing and the resulting absorption line shape in semiconductor quantum dots'. *Phys. Rev. B* **65**, 195313 (2002). doi:10.1103/PhysRevB.65.195313.

[4] V. M. Axt, T. Kuhn, A. Vagov, F. M. Peeters. 'Phonon-induced pure dephasing in exciton-biexciton quantum dot systems driven by ultrafast laser pulse sequences'. *Phys. Rev. B* **72**, 125309 (2005). doi:10.1103/PhysRevB.72.125309.

[5] D. E. Reiter, T. Kuhn, V. M. Axt. 'Distinctive characteristics of carrier-phonon interactions in optically driven semiconductor quantum dots'. *Adv. Phys.: X* **4**, 1655478 (2019). doi:10.1080/23746149.2019.1655478.

[6] B. Krummheuer, V. M. Axt, T. Kuhn, I. D'Amico, F. Rossi. 'Pure dephasing and phonon dynamics in GaAs- and GaN-based quantum dot structures: Interplay between material parameters and geometry'. *Phys. Rev. B* **71**, 235329 (2005). doi:10.1103/PhysRevB.71.235329.

[7] J. Förstner, C. Weber, J. Danckwerts, A. Knorr. 'Phonon-assisted damping of rabi oscillations in semiconductor quantum dots'. *Phys. Rev. Lett.* **91**, 127401 (2003). doi:10.1103/PhysRevLett.91.127401.

[8] P. Machnikowski, L. Jacak. 'Resonant nature of phonon-induced damping of Rabi oscillations in quantum dots'. *Phys. Rev. B* **69**, 193302 (2004). doi:10.1103/PhysRevB.69.193302.

[9] A. Vagov, V. M. Axt, T. Kuhn, W. Langbein, P. Borri, U. Woggon. 'Nonmonotonous temperature dependence of the initial decoherence in quantum dots'. *Phys. Rev. B* **70**, 201305(R) (2004). doi:10.1103/PhysRevB.70.201305.

[10] A. Vagov, M. D. Croitoru, V. M. Axt, T. Kuhn, F. M. Peeters. 'Nonmonotonic field dependence of damping and reappearance of Rabi oscillations in quantum dots'. *Phys. Rev. Lett.* **98**, 227403 (2007). doi:10.1103/PhysRevLett.98.227403.

[11] A. J. Ramsay, A. V. Gopal, E. M. Gauger, A. Nazir, B. W. Lovett, A. M. Fox, M. S. Skolnick. 'Damping of exciton Rabi rotations by acoustic phonons in optically excited InGaAs/GaAs quantum dots'. *Phys. Rev. Lett.* **104**, 017402 (2010). doi:10.1103/PhysRevLett.104.017402.

[12] M. Florian, P. Gartner, C. Gies, F. Jahnke. 'Phonon-mediated off-resonant coupling effects in semiconductor quantum-dot lasers'. *New J. Phys.* **15**, 035019 (2013). doi:10.1088/1367-2630/15/3/035019.

[13] A. Nysteen, P. Kaer, J. Mork. 'Proposed quenching of phonon-induced processes in photoexcited quantum dots due to electron-hole asymmetries'. *Phys. Rev. Lett.* **110**, 087401 (2013). doi:10.1103/PhysRevLett.110.087401.

[14] D. P. S. McCutcheon, A. Nazir. 'Model of the optical emission of a driven semiconductor quantum dot: Phonon-enhanced coherent scattering and off-resonant sideband narrowing'. *Phys. Rev. Lett.* **110**, 217401 (2013). doi:10.1103/PhysRevLett.110.217401.

[15] D. E. Reiter, T. Kuhn, M. Glässl, V. M. Axt. 'The role of phonons for exciton and biexciton generation in an optically driven quantum dot'. *Journal of Physics: Condensed Matter* **26**, 423203 (2014). doi:10.1088/0953-8984/26/42/423203.

[16] J. Iles-Smith, D. P. S. McCutcheon, A. Nazir, J. Mørk. 'Phonon scattering inhibits simultaneous near-unity efficiency and indistinguishability in semiconductor single-photon sources'. *Nature Photonics* **11**, 521 (2017). doi:10.1038/nphoton.2017.101.

[17] T. Kaldewey, S. Lüker, A. V. Kuhlmann, S. R. Valentin, J.-M. Chauveau, A. Ludwig, A. D. Wieck, D. E. Reiter, T. Kuhn, R. J. Warburton. 'Demonstrating the decoupling regime of the electron-phonon interaction in a quantum dot using chirped optical excitation'. *Phys. Rev. B* **95**, 241306 (2017). doi:10.1103/PhysRevB.95.241306.

[18] M. Reindl, K. D. Jöns, D. Huber, C. Schimpf, Y. Huo, V. Zwiller, A. Rastelli, R. Trotta. 'Phonon-assisted two-photon interference from remote quantum emitters'. *Nano Lett.* **17**, 4090 (2017). doi:10.1021/acs.nanolett.7b00777.

[19] P. Kaer, T. R. Nielsen, P. Lodahl, A.-P. Jauho, J. Mørk. 'Non-Markovian Model of Photon-Assisted Dephasing by Electron-Phonon Interactions in a Coupled Quantum-Dot-Cavity System'. *Phys. Rev. Lett.* **104**, 157401 (2010). doi:10.1103/PhysRevLett.104.157401.

[20] D. P. S. McCutcheon, A. Nazir. 'Quantum dot Rabi rotations beyond the weak exciton–phonon coupling regime'. *New Journal of Physics* **12**, 113042 (2010). doi:10.1088/1367-2630/12/11/113042.

[21] P. Kaer, P. Lodahl, A.-P. Jauho, J. Mork. 'Microscopic theory of indistinguishable single-photon emission from a quantum dot coupled to a cavity: The role of non-Markovian phonon-induced decoherence'. *Phys. Rev. B* **87**, 081308 (2013). doi:10.1103/PhysRevB.87.081308.

[22] D. P. S. McCutcheon. 'Optical signatures of non-Markovian behavior in open quantum systems'. *Phys. Rev. A* **93**, 022119 (2016). doi:10.1103/PhysRevA.93.022119.

[23] A. Carmele, S. Reitzenstein. 'Non-Markovian features in semiconductor quantum optics: quantifying the role of phonons in experiment and theory'. *Nanophotonics* **8**, 655 (2019). doi:doi:10.1515/nanoph-2018-0222.

[24] A. Vagov, M. D. Croitoru, M. Glässl, V. M. Axt, T. Kuhn. 'Real-time path integrals for quantum dots: Quantum dissipative dynamics with superohmic environment coupling'. *Phys. Rev. B* **83**, 094303 (2011). doi:10.1103/PhysRevB.83.094303.

[25] A. M. Barth, A. Vagov, V. M. Axt. 'Path-integral description of combined Hamiltonian and non-Hamiltonian dynamics in quantum dissipative systems'. *Phys. Rev. B* **94**, 125439 (2016). doi:10.1103/PhysRevB.94.125439.

[26] M. Cygorek, A. M. Barth, F. Ungar, A. Vagov, V. M. Axt. 'Nonlinear cavity feeding and unconventional photon statistics in solid-state cavity QED revealed by many-level real-time path-integral calculations'. *Phys. Rev. B* **96**, 201201(R) (2017). doi:10.1103/PhysRevB.96.201201.

[27] S. Lüker, T. Kuhn, D. E. Reiter. 'Phonon impact on optical control schemes of quantum dots: Role of quantum dot geometry and symmetry'. *Phys. Rev. B* **96**, 245306 (2017). doi:10.1103/PhysRevB.96.245306.

[28] G. Guarnieri, A. Smirne, B. Vacchini. 'Quantum regression theorem and non-Markovianity of quantum dynamics'. *Phys. Rev. A* **90**, 022110 (2014). doi:10.1103/PhysRevA.90.022110.

[29] M. Cosacchi, M. Cygorek, F. Ungar, A. M. Barth, A. Vagov, V. M. Axt. 'Path-integral approach for nonequilibrium multitime correlation functions of open quantum systems coupled to Markovian and non-Markovian environments'. *Phys. Rev. B* **98**, 125302 (2018). doi:10.1103/PhysRevB.98.125302.

[30] P. Machnikowski, V. M. Axt, T. Kuhn. 'Quantum-information encoding in dressed qubits'. *Phys. Rev. A* **75**, 052330 (2007). doi:10.1103/PhysRevA.75.052330.

[31] H. Carmichael. *An open systems approach to Quantum Opt.* Springer, Berlin (1993).

[32] A. Strathearn, P. Kirton, D. Kilda, J. Keeling, B. W. Lovett. 'Efficient non-Markovian quantum dynamics using time-evolving matrix product operators'. *Nat. Commun.* **9**, 3322 (2018). doi:10.1038/s41467-018-05617-3.

[33] C. Roy, S. Hughes. 'Influence of electron–acoustic-phonon scattering on intensity power broadening in a coherently driven quantum-dot–cavity system'. *Phys. Rev. X* **1**, 021009 (2011). doi:10.1103/PhysRevX.1.021009.

[34] A. Nazir, D. P. S. McCutcheon. 'Modelling exciton-phonon interactions in optically driven quantum dots'. *J. Phys.: Condens. Matter* **28**, 103002 (2016). doi:10.1088/0953-8984/28/10/103002.

[35] J. Iles-Smith, A. Nazir. 'Quantum correlations of light and matter through environmental transitions'. *Optica* **3**, 207 (2016). doi:10.1364/OPTICA.3.000207.

[36] K. Roy-Choudhury, S. Hughes. 'Quantum theory of the emission spectrum from quantum dots coupled to structured photonic reservoirs and acoustic phonons'. *Phys. Rev. B* **92**, 205406 (2015). doi:10.1103/PhysRevB.92.205406.

[37] C. Gustin, S. Hughes. 'Pulsed excitation dynamics in quantum-dot–cavity systems: Limits to optimizing the fidelity of on-demand single-photon sources'. *Phys. Rev. B* **98**, 045309 (2018). doi:10.1103/PhysRevB.98.045309.

Erratum: Accuracy of the Quantum Regression Theorem for Photon Emission from a Quantum Dot
[Phys. Rev. Lett. 127, 100402 (2021)]

M. Cosacchi, T. Seidelmann, M. Cygorek, A. Vagov, D. E. Reiter, and V. M. Axt

In our Letter, the main investigation was a comparison between a numerically exact path-integral (PI) method and the quantum regression theorem (QRT) to model photonic figures of merit in quantum-dot–cavity systems obtained from two-time correlation functions. As a side aspect, we discussed the dependence of applying the quantum regression theorem in different frames, in particular, the lab frame and the polaron frame. The latter was achieved by considering the polaron master equation (PME) approach. Upon closer inspection of our numerical analysis, we have found a parameter discrepancy as explained below that affects the results obtained within the PME approach. We stress that this correction does not affect the majority of the results and the main message of the Letter, namely that the QRT overestimates the phonon influence on the indistinguishability.

Concerning Fig. 2(c) of our original Letter, the numerically exact PI results and the ones obtained by using the QRT in the lab frame were calculated for a quantum dot (QD) with an electron confinement radius of $a_e = 3$ nm (as defined in Table 1 in Supplemental Material of our Letter [1]). In contrast, the PME results were calculated for $a_e = 4.175$ nm by mistake, which prohibits a meaningful comparison of the different methods. In Fig. 2(c), the corresponding PME results for a 3 nm QD are shown (blue dotted line).

Furthermore, in the PME community, two different ways to account for the radiative decay by a phenomenological Lindblad term are being used: either the corresponding rate is scaled by a factor $\langle B \rangle^2$ (as done in, e.g., Ref. [85] of our Letter) or not (as done in, e.g., Ref. [87] of our Letter), where $\langle B \rangle$ is the phonon Franck-Condon factor as given in Eq. (15) in Supplemental Material of our Letter. In the calculations shown in our Letter, we had scaled the radiative decay rate by the factor $\langle B \rangle^2$. The assumption, though, that the radiative decay of the QD into a spectrally flat electromagnetic field environment is not affected by the phonon environment has recently been confirmed by taking into account both environments microscopically within the numerically exact algorithm ACE [2]. Therefore, we continue here without using the factor $\langle B \rangle^2$. This different scaling, though, has only a marginal influence on the corresponding results for our parameters. The different QD size a_e is responsible for the larger contribution to the change of the PME results.

As was stated in the original Letter, the QRT applied both in the lab frame and in the polaron frame systematically overestimate the phonon influence on the indistinguishability. But in contrast to the previous comparison, the correct PME results now basically coincide with the QRT results [cf. Fig. 2(c)]. Therefore, applying the QRT in the polaron frame does not improve the accuracy of the indistinguishability.
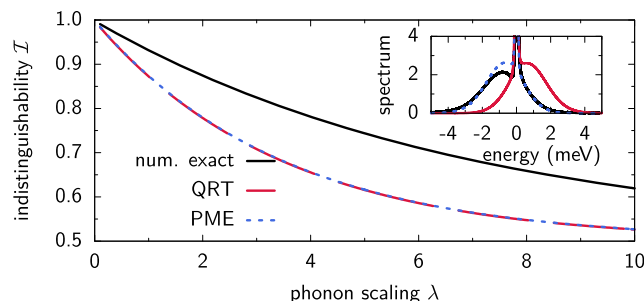

FIG. 2.   (c) The indistinguishability as a function of the phonon scaling parameter λ at 4 K, calculated with the numerically exact PI method (num. exact), by using the QRT in the lab frame (QRT) and in the polaron frame (PME). Phonon sidebands of the QD emission spectra at 10 K are shown in the inset.

To explain this finding, we look at each term of Eq. (4b) of our Letter and compare their derivation within the different methods. The factors in the first term are both (single-time) expectation values of the exciton occupation. We have checked that the PME approach without using the scaling $\langle B \rangle^2$ agrees well with the path-integral method regarding the exciton occupation for all parameters concerned. The last term is the second-order two-time correlation function $G^{(2)}(t, \tau)$, upon which the single-photon purity $\mathcal{P}$ is based. In our Letter, we found that the QRT introduces basically no error to this quantity compared with the numerically exact evaluation of the two-time function.

The second term $|\langle \sigma_X^\dagger(t + \tau) \sigma_X(t) \rangle|^2$ is the absolute square of the first-order correlation function $G^{(1)}(t, \tau)$. Without the factor $\langle B \rangle^2$ the PME spectrum is almost a mirror image of the spectrum obtained by applying the QRT in the lab frame [cf. inset of Fig. 2(c)] similar to what was found earlier by a perturbative approach (cf. Ref. [26] of our Letter). This implies that the QRT and PME results differ basically only by the sign of the imaginary part of $G^{(1)}(t, \tau)$, which does not affect the absolute square.

In summary, we find that the QRT and PME agree in most parts and both exhibit deviations by up to 18% from the numerically exact PI results.

[1] M. Cosacchi, T. Seidelmann, M. Cygorek, A. Vagov, D. E. Reiter, and V. M. Axt, Phys. Rev. Lett. **127**, 100402 (2021).
[2] M. Cygorek, M. Cosacchi, A. Vagov, V. M. Axt, B. W. Lovett, J. Keeling, and E. M. Gauger, arXiv:2101.01653.

Publication 7

"*N*-photon bundle statistics on different solid-state platforms"

M. Cosacchi, A. Mielnik-Pyszczorski, **T. Seidelmann**, M. Cygorek,
A. Vagov, D. E. Reiter, and V. M. Axt.

Author contributions

M. Cosacchi has designed the concept of this study, has performed the numerical data generation and analysis, and has implemented the problem-specific C++ code. He has provided interpretations of the results and has written the first draft of the publication. In particular, he has proposed superconducting qubits as an alternative solid-state system. During the publication process, he has moderated all discussions, has organized the submission and revision of the manuscript, and has contributed to the answer to the referees.

A. Mielnik-Pyszczorski has participated in the general discussion of the results and their interpretations. Furthermore, he has discussed the results in detail with M. Cosacchi and has optimized all figures. He has also contributed to revisions of the draft and the answers to the referees.

The author has participated in the general discussion of the results and their interpretations. Furthermore, he has discussed the results in detail with M. Cosacchi and has proposed the interpretation in terms of the laser-dressed states as well as Figures 2, 3(c), and 7. He has also contributed to revisions of the draft and has written the answers to the referees.

M. Cygorek, A. Vagov, and D. E. Reiter have co-supervised this work. In particular, they have participated in the discussion of the results and their interpretations. They have also contributed to the optimization of the presentation, revisions of the draft, and the answers to the referees.

V. M. Axt has advised M. Cosacchi throughout his work as the main supervisor, has obtained the funding for this work, and has provided the practical means. He has participated in the discussion of the results and their interpretations. He has also contributed to the optimization of the presentation, revisions of the draft, and the answers to the referees.

N-photon bundle statistics on different solid-state platforms

M. Cosacchi ●,[1] A. Mielnik-Pyszczorski ●,[1,2] T. Seidelmann ●,[1] M. Cygorek,[3] A. Vagov ●,[1] D. E. Reiter,[4] and V. M. Axt[1]

[1]*Theoretische Physik III, Universität Bayreuth, 95440 Bayreuth, Germany*
[2]*Department of Theoretical Physics, Wrocław University of Science and Technology, 50-370 Wrocław, Poland*
[3]*Heriot-Watt University, Edinburgh EH14 4AS, United Kingdom*
[4]*Institut für Festkörpertheorie, Universität Münster, 48149 Münster, Germany*

The term *N*-photon bundles has been coined for a specific type of photon emission, where light quanta are released from a cavity only in groups of *N* particles. This emission leaves a characteristic number distribution of the cavity photons that may be taken as one of their fingerprints. We study this characteristic *N*-photon bundle statistics considering two solid-state cavity quantum electrodynamics (cQED) systems. As one example, we consider a semiconductor quantum-dot–microcavity system coupled to longitudinal acoustic phonons. There, we find the environmental influence to be detrimental to the bundle statistics. The other example is a superconducting qubit inside a microwave resonator. In these systems, pure dephasing is not important and an experimentally feasible parameter regime is found, where the bundle statistics prevails.

I. INTRODUCTION

Many innovative applications of the quantum realm rely on the on-demand preparation of specific, highly nonclassical target states. Cavity quantum electrodynamics (cQED) is a well established tool for this purpose. On numerous different platforms, e.g., atoms in resonators [1–3], superconducting qubits in microwave resonators [4,5], or semiconductor quantum dots in microcavities [6–26], preparation of single photons, entangled photon pairs, Fock states, and Schrödinger or Voodoo cat states has been proposed or achieved. Recently, a new class of emitters has been proposed [27,28], where the photon emission takes place only in groups of an integer number *N*. The term *N*-photon bundle has been coined to describe these multiphoton structures. There are numerous ways to characterize these structures, e.g., in terms of their emission properties [29,30] or their internal correlations between the constituent photons [31], which can be interpreted as a consequence of their specific temporal spacing, see sketch in Fig. 1. In contrast to the ordinary Fock state $|N\rangle$, a bundle is emitted as a cascade over successive Fock states $|n\rangle$, where $0 \leqslant n \leqslant N$, after the preparation of the state $|N\rangle$. The cascade is a direct result of the outcoupling via resonator losses. In a resonator with loss rate κ, the Fock state $|n\rangle$ effectively decays with the rate $n\kappa$, explaining the temporal spacing between the photons constituting the bundle. A feature that has been established in Ref. [27] as a major fingerprint of an *N*-photon bundle, resulting from its cascaded generation, is its characteristic stationary photon statistics:

$$P_N(n) = \begin{cases} 1 - \frac{\langle n \rangle}{N} \sum_{j=1}^{N} \frac{1}{j} & n = 0 \\ \frac{\langle n \rangle}{N} \frac{1}{n} & 1 \leqslant n \leqslant N \\ 0 & n > N \end{cases} \tag{1}$$

with $\langle n \rangle$ being the average photon number in the resonator. Note that the stationary distribution of photon number states

is directly accessible to experiments [32–34], and thus the statistics given by Eq. (1) is a measurable quantity.

The *N*-photon bundle is highly nonclassical and exhibits two attractive properties: (i) a sharp cutoff for photon number occupation probabilities $P_N(n)$ with $n > N$ and (ii) it contains a relatively high stationary *N*-photon component. The cutoff is useful for applications, e.g., in quantum cryptography [35]. A simultaneous creation of *N* photons is advantageous for medical applications due to a greater penetration depth and better resolution [27,36–40]. On timescales longer than the size of the bundle, Planck's constant is effectively renormalized in the relationship between frequency and energy, $E = N\hbar\omega$. Since in a stationary state an *N*-photon component is always redistributed to states with lower $n < N$ due to cavity losses, the characteristic bundle statistics according to Eq. (1) reflects both important properties.

Cavity losses are both unavoidable and necessary for actual quantum technological applications, because, typically, the photon state created inside the cavity has to be delivered to a recipient outside the cavity structure. Although the target *N*-photon component in the stationary bundle state is lower than subsequent *n*-photon components [cf. Eq. (1) for $n < N$], it still realizes the highest possible relative *N*-photon component that can be achieved in a stationary situation with loss processes. In this sense, the *N*-photon bundle is probably the best compromise between creating a pure *N*-photon Fock state $|N\rangle$ only inside the cavity and delivering a high *N*-photon component in a stationary fashion.

From a detection point of view this means the following: When a Poissonian source emits photons, their arrival times at the detector are distributed randomly; in the case of an *N*-photon bundle emission, the bundles arrive randomly, but the photons contained in each bundle obey the temporal order as sketched in Fig. 1. Therefore there is a Poissonian distribution over bundles. In this sense, *N*-photon bundles can be
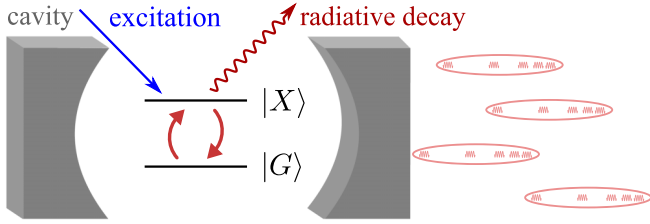
FIG. 1. Sketch of a two-level system (2LS) embedded in a cavity resulting in the coupling to one cavity mode. The 2LS is driven by a continuous external excitation. It can decay radiatively, while the cavity is lossy. For particular sets of parameters, N-photon bundles leave the cavity. They are characterized by the specific temporal spacing between the constituent photons and their specific photon number statistics. Exemplary, four five-photon bundles are depicted.

considered as an alternative to Fock states as building blocks for more complex quantum states of light. In addition to optical applications, even bundle generation using phonons instead of photons has been proposed [41].

In this work, we consider the bundle statistics in Eq. (1) as one of the possible ways to characterize a bundle and study this fingerprint in two different solid-state platforms: (i) semiconductor quantum dots (QDs) in microcavities and (ii) superconducting qubits in microwave resonators.

In QDs, the coupling to longitudinal acoustic phonons is known as the main source of decoherence. Furthermore, phonon emission and absorption can assist off-resonant single-photon processes and, thus, influence the competition between these processes and direct higher-order multi-photon processes [42]. Because the N-photon bundle is associated with an N-photon resonance, phonons can impact the bundle generation. We therefore analyze a QD–cavity system coupled to a phonon environment modeled in a microscopic picture. This full many-body problem is solved in a numerically exact way by employing a path-integral formalism. We compare these results with those found in a model accounting for phonons only via a phenomenological pure dephasing rate. For realistic parameters that are currently achievable, we find that the phonon influence leads to photon number distributions that deviate significantly from the bundle statistics in Eq. (1).

In superconducting qubit–microwave resonator systems, pure dephasing is negligible. For these systems, we propose a set of parameters experimentally well within reach, where the bundle statistics with $N = 2$ is preserved. We show that for this purpose a resonator with a mediocre Q factor is optimal.

II. MODEL AND METHODS

A. cQED model

Both example systems can be described by a strongly driven Jaynes–Cummings model with the Hamiltonian in a frame corotating with the frequency of the external excitation ω_L in the usual dipole and rotating-wave approximations

$$
\begin{aligned}
H_{\text{Sys}} = {} & -\hbar\Delta\omega_{\text{LX}}|X\rangle\langle X| + \hbar\Delta\omega_{\text{CL}}a^\dagger a \\
& + \hbar g(|X\rangle\langle G|a + |G\rangle\langle X|a^\dagger) \\
& + \hbar f(|X\rangle\langle G| + |G\rangle\langle X|).
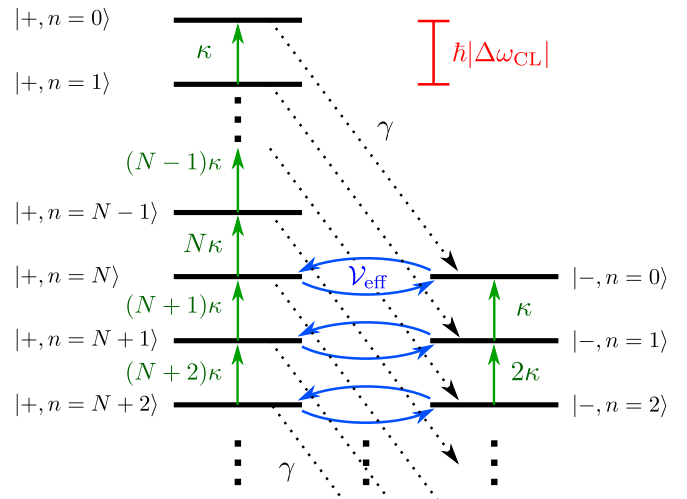\end{aligned}
\tag{2}
$$

FIG. 2. Schematic sketch of the N-bundle mechanism. Black lines indicate the energetic position of systems states $|\pm, n\rangle$ where the driven 2LS is in the upper (lower) laser-dressed state $|+\rangle \approx |X\rangle$ ($|-\rangle \approx |G\rangle$) and $n \in \mathbb{N}_0$ photons are inside the resonator. Note that in the rotating frame the contribution of a resonator photon $\hbar\Delta\omega_{\text{CL}}$ to the total energy is negative in the regime where bundles are found (cf. Fig 3). The states $|-, 0\rangle$ and $|+, N\rangle$ are in resonance and the resonator introduces an effective coupling $\mathcal{V}_{\text{eff}}$ between them (blue arrows). Green (dashed black) arrows indicate the action of the resonator loss (radiative decay) with rate $n\kappa$ (γ) on a system state $|\pm, n\rangle$.

The two-level system (2LS) has an excited state $|X\rangle$ at energy $\hbar\omega_X$ and a ground state $|G\rangle$ at energy zero. a ($a^\dagger$) is the annihilation (creation) operator of a photon in the single resonator mode at energy $\hbar\omega_C$ coupled to the 2LS by g. The detuning between the external excitation with strength f and the upper state $|X\rangle$ is denoted by $\Delta\omega_{\text{LX}} = \omega_L - \omega_X$ and the detuning between resonator and external excitation $\Delta\omega_{\text{CL}} = \omega_C - \omega_L$ is defined analogously. The detuning between resonator and the upper state $|X\rangle$, $\Delta\omega_{\text{CX}} = \omega_C - \omega_X$, is fixed by the growth process of the structure. Hence, we keep it constant in our analysis.

When the 2LS is strongly driven ($f \gg g$) and it is in the dispersive regime ($\Delta\omega_{\text{CX}} \gg g$), a sharp N-photon resonance emerges with N being an integer. It corresponds to a polariton of the type $(|G, 0\rangle \pm |X, N\rangle)/\sqrt{2}$, where $|\chi, n\rangle$ denotes the product state of the 2LS state $|\chi\rangle$ with $\chi \in \{G, X\}$ and the photon number state $|n\rangle$. When dissipative channels are included by introducing the excited state's radiative decay with rate γ and resonator losses with rate κ, this resonance becomes a source of N-photon bundles [27].

This mechanism is sketched in Fig. 2. Because the 2LS is strongly driven ($f \gg g$) and the dispersive regime ($\Delta\omega_{\text{CX}} \gg g$) is considered, the coupling to the resonator represents a small perturbation to the driven 2LS. Thus the system is best discussed using the two eigenstates

$$|+\rangle = \alpha|G\rangle + \beta|X\rangle, \tag{3a}$$

$$|-\rangle = \beta|X\rangle - \alpha|G\rangle \tag{3b}$$

of the system Hamiltonian H_{Sys} without the resonator coupling, i.e., $g = 0$ in Eq. (2), which are typically referred to as the laser-dressed states. In general, the laser-dressed states are admixtures of both bares states, and the mixing coefficients $\alpha, \beta \in \mathbb{R}$ depend on the driving strength f and the detuning $\Delta\omega_{LX}$. In order to create *N*-photon bundles, the resonator mode (in the rotating frame) is adjusted to the *N*-photon resonance between the lower laser-dressed state without photons $|-, 0\rangle$ and the higher laser-dressed state with N photons inside the resonator $|+, N\rangle$. The resonator introduces then an effective (*N*th-order) coupling between these two states [29], which we denote as $\mathcal{V}_{eff}$ in Fig. 2. In the relevant situation here, were the laser is typically strongly detuned from the 2LS, the laser-dressed states are essentially the bare states $|+\rangle \approx |X\rangle$ and $|-\rangle \approx |G\rangle$. Therefore the polariton $(|G, 0\rangle \pm |X, N\rangle)/\sqrt{2}$ is formed which corresponds to *N*-photon Rabi oscillations between the involved states. Dissipative channels lead to further couplings between the states $|\pm, n\rangle$, cf. schematic sketch in Fig. 2. Therefore, after the state $|+, N\rangle$ has been reached due to the effective resonator coupling, the resonator losses with rate $n\kappa$ lead to a cascaded decay. The characteristic *N*-photon bundle statistics is a direct result of the ratio $(n + 1)/n$ between subsequent loss rates $n\kappa$ associated with the state $|+, n\rangle$. In contrast, the radiative decay with rate γ provides a pathway from $|+, n\rangle \approx |X, n\rangle$ to $|-, n\rangle \approx |G, n\rangle$ at the same photon number.

We include both dissipative effects by accounting for the Lindblad superoperators $\mathcal{L}_{|G\rangle\langle X|, \gamma}$ and $\mathcal{L}_{a, \kappa}$ acting on the density matrix ρ as

$$\mathcal{L}_{O, \Gamma}\rho = \Gamma\left(O\rho O^\dagger - \tfrac{1}{2}\{\rho, O^\dagger O\}_+\right), \qquad (4)$$

describing loss processes with rate Γ on a dissipation channel O, where $\{A, B\}_+$ is the anti-commutator of operators A and B.

The time evolution of the density matrix ρ is then governed by the Liouville-von Neumann equation

$$\frac{\partial}{\partial t}\rho = \frac{1}{i\hbar}[H, \rho]_- + \mathcal{L}_{a, \kappa}\rho + \mathcal{L}_{|G\rangle\langle X|, \gamma}\rho, \qquad (5)$$

where $[A, B]_-$ is the commutator of operators A and B. In the following, we introduce two different driven 2LS-resonator systems. Depending on the considered system, the Hamilton operator H may include further contributions in addition to H_{Sys}.

1. QD model

At first, we consider a self-assembled GaAs QD system in a single-mode microcavity. In these systems, additionally the pure-dephasing coupling of the electronic states to an environment of longitudinal acoustic phonons is important [43,44], i.e., $H = H_{Sys} + H_{Ph}$ in Eq. (5). It is described by the Hamiltonian [45–48]

$$H_{Ph} = \hbar \sum_q \omega_q b_q^\dagger b_q$$
$$+ \hbar \sum_q \left(\gamma_q^X b_q^\dagger + \gamma_q^{X*} b_q\right)|X\rangle\langle X|, \qquad (6)$$

where b_q ($b_q^\dagger$) annihilates (creates) a phonon of energy $\hbar\omega_q$ in mode q with the coupling strength γ_q^X. The phonons

are assumed to be initially in thermal equilibrium at temperature T.

This coupling to phonons is the source of many well-known effects in QDs, like the phonon sideband in the QD emission spectrum [45,49], the renormalization of the Rabi frequency [50,51], and the damping of Rabi oscillations [52–54]. It should be noted that because of the QD-phonon interaction resonances are found at different spectral positions due to the polaron shift. Whenever we refer to the excited state energy when phonons are taken into account, we mean the polaron-shifted excited state energy.

To treat this full many-body Hamiltonian in a numerically exact way, we employ an iterative real-time path-integral formalism [55–59] to solve the Liouville–von Neumann equation. Details on the used path-integral algorithm can be found in Appendix A. Within this approach, all effects mentioned above are thus taken into account.

Unless noted otherwise, we take $\hbar g = 0.02$ meV [60], $\gamma = 1$ ns^{-1}, and $\kappa = 8.5$ ns^{-1} [61]. These values, in particular, the cavity loss rate κ are realistically achievable [61]. The record in cavity quality so far is around $\kappa \approx 4$ ns^{-1} to 6 ns^{-1} [60], which means that it should be possible to achieve the value of κ chosen here with current state-of-the-art equipment with reasonable effort. Further, following Ref. [27], we set $\hbar\Delta\omega_{CX} = -60\hbar g = -1.2$ meV and $\hbar f = 32\hbar g = 0.64$ meV. For the phonon coupling, standard GaAs parameters [59,62] are chosen for a QD with a radius of 3 nm.

2. Superconducting qubit model

As a second example, we consider a superconducting qubit in a microwave resonator. Here, pure dephasing is negligible. Therefore no addition to the model in Sec. II A is necessary, i.e., $H = H_{Sys}$ in Eq. (5).

We use the parameter set $\hbar g = 0.079$ µeV, $\gamma = 1.54$ µs^{-1}, $\kappa = 0.29$ µs^{-1}, i.e., $\kappa \ll \gamma$, taken from Ref. [5]. Again, following Ref. [27], we choose $\hbar\Delta\omega_{CX} = -60\hbar g = -4.71$ µeV and $\hbar f = 32\hbar g = 2.51$ µeV.

III. RESULTS: QD-CAVITY SYSTEM

A. Resonance landscape and $N = 2$

The resonance corresponding to an *N*-photon bundle is found at [27,63]

$$\Delta\omega_{LX} = \frac{\sqrt{4(N^2 - 1)f^2 + N^2\Delta\omega_{CX}^2} + \Delta\omega_{CX}}{N^2 - 1}$$
$$+ \Delta\omega_{CX}. \qquad (7)$$

In this work, we focus mostly on the case $N = 2$. For the QD–cavity system, this results in a detuning value of $\hbar\Delta\omega_{LX} = -0.51$ meV. Higher-order bundles with $N > 2$ can be reached by tuning the excitation to the corresponding resonance according to Eq. (7), however for the realistic set of parameters assumed here they are negligible.

To illustrate the appearing resonances, we scan the stationary probability P_n of occupying the photon number states $|n\rangle$ with the laser frequency ω_L. Figure 3 shows the corresponding results for the photon number states $|n\rangle = |1\rangle$, $|2\rangle$, and $|3\rangle$ in the QD–cavity system. Three resonance peaks emerge in
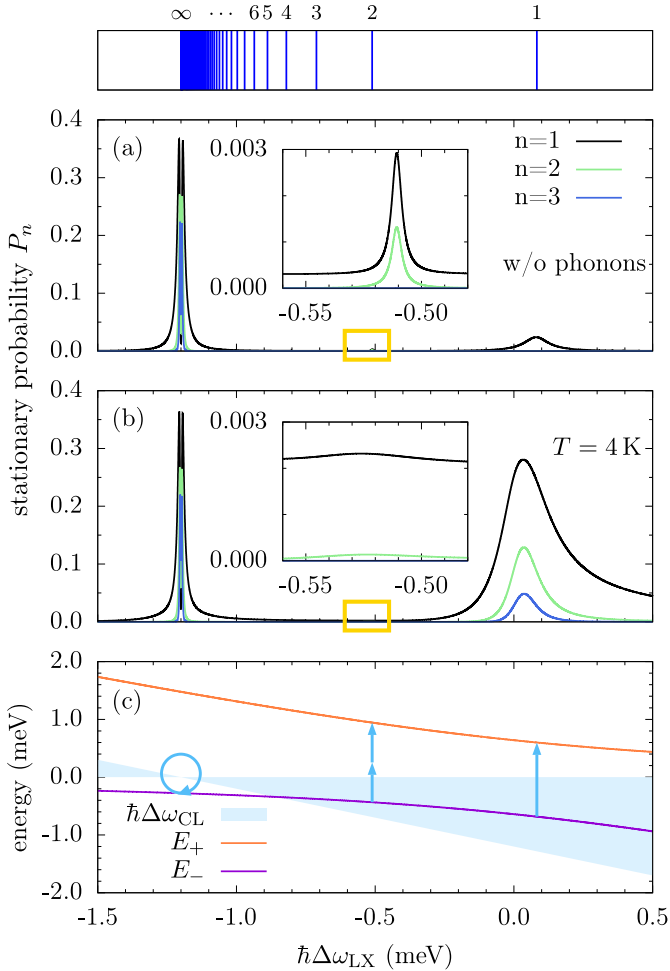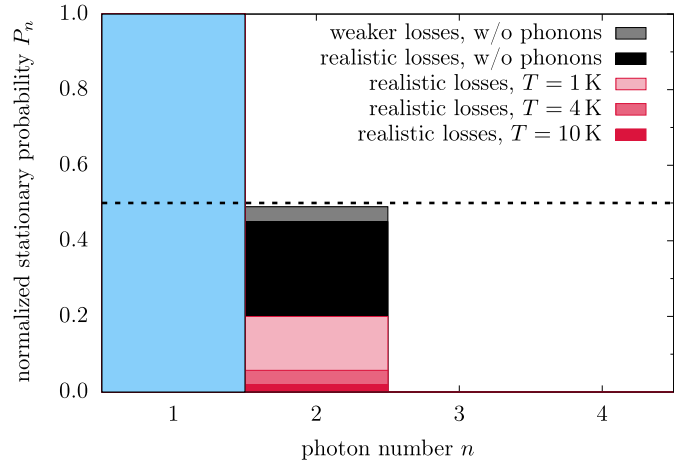
FIG. 4. The stationary probability P_n of occupying the photon number states $|n\rangle$ normalized to its value at $n = 1$ for the QD–cavity system. While the data labeled 'realistic losses' is obtained using the parameters listed in Sec. II A 1, weaker losses of $\gamma = 0.01g$ and $\kappa = 0.1g$ were chosen following Ref. [27] for the calculation shown in gray. Note that in the phonon-free case, the absolute values of the Fock state with $n = 1$ are 0.016 for the weaker losses and 0.003 for the realistic parameter set.

states with $n > 1$ are not occupied due to a photon blockade effect [cf. Fig. 3(a)], which is spoiled once phonons are considered: then, the system can climb up the Jaynes-Cummings ladder [cf. Fig. 3(b)]. The different physical mechanisms giving rise to these two limiting cases and the phonon influence on them is discussed in detail in Appendix B.

We now consider the range of bundle physics for $1 < N < \infty$ and focus on $N = 2$. The characteristic bundle statistics as denoted in Eq. (1) is well visible for the two-photon bundle shown in the inset of Fig. 3(a), in particular, the three-photon occupation probability is zero.

To understand all the resonances, we diagonalize the Hamiltonian of the laser-driven 2LS neglecting the cavity (since $f \gg g$). As a result, we obtain the laser-dressed states $|+\rangle$ and $|-\rangle$. Their energies in the laser-rotating frame are plotted in Fig. 3(c) along with the energy of a cavity photon given by $\hbar\Delta\omega_{\mathrm{CL}}$ in this frame.

The analysis in terms of laser-dressed states confirms the fact that the two-photon bundle resonance at $\hbar\Delta\omega_{\mathrm{LX}} = -0.51$ meV originates from a two-photon process [27], in this case a transition from $|-, 0\rangle$ to $|+, 2\rangle$. The study of the influence of the phonons on this resonance shows that already at 4 K [inset of Fig. 3(b)], it is strongly suppressed. The occupation probability P_1 strongly rises around the resonance peak. While the absolute value of P_1 is only weakly affected when phonons are included, the height of the peak associated with P_2 is reduced by one order of magnitude from 1.3×10^{-3} to 1.3×10^{-4}. In particular, the characteristic $1/n$ fingerprint [cf. Eq. (1)] of the number distribution is violated.

To illustrate this point in more detail, the stationary photon number distribution normalized to its value at $n = 1$ is shown in Fig. 4. First of all, it is interesting to note that the ideal bundle statistics $P_n \propto 1/n$ is only observed for loss parameters weaker than the realistic, state-of-the-art values (cf. gray data in Fig. 4). This parameter set consists of $\gamma = 0.01g =$

FIG. 3. Stationary probability P_n of occupying the photon number states $|n\rangle$ in the QD–cavity system as a function of the laser–exciton detuning $\Delta\omega_{\mathrm{LX}}$ (a) without taking phonon effects into account, (b) including phonons initially at $T = 4$ K (the insets show the region marked by yellow boxes on a larger scale), (c) the corresponding energies of the laser-dressed states $|+\rangle$ and $|-\rangle$. The energy of a photon in the rotating frame is given by the cavity–laser detuning $\hbar\Delta\omega_{\mathrm{CL}}$, which is plotted as a shaded area to illustrate its modulus. Arrows indicate the number of photons involved in the processes leading to the various resonance peaks, while their length corresponds to their energy $\hbar\Delta\omega_{\mathrm{CL}}$. The circular arrow indicates a one-photon process with a photon energy (in the rotating frame) of $\hbar\Delta\omega_{\mathrm{CL}} = 0$. The blue lines above panel (a) mark the energetic positions of the bundle resonances, starting for $N = 1$ and quickly converging to $\hbar\Delta\omega_{\mathrm{CX}}$ for larger N. Since the bundle resonance is derived from the condition that N cavity photons energetically fit between the two dressed states, an equation analogous to Eq. (7) can be found for the trivial case $N = 1$.

the vicinity of the bundle resonance [presented in Fig. 3(a)], which itself is shown on a magnified scale in the inset.

The most prominent peaks are found for the limiting cases $N \to \infty$ and $N = 1$. For $N \to \infty$ a double-peaked structure emerges at $\hbar\Delta\omega_{\mathrm{LX}} = \hbar\Delta\omega_{\mathrm{CX}} = -1.2$ meV (cf. Fig. 8 in Appendix B for a zoom-in). At its center the photon statistics is Poissonian and is hardly influenced by phonons [cf. Figs. 3(a) and 3(b)]. In contrast, the peak at $\hbar\Delta\omega_{\mathrm{LX}} \approx 0.08$ meV corresponds to the resonance for $N = 1$. Here, Fock

0.3 ns^{-1} and $\kappa = 0.1g = 3$ ns^{-1}, following the values chosen in Ref. [27]. Already the slightly higher values chosen in our work in accordance with current experiments (cf. Sec. II A 1) lead to a ratio of the stationary two- to the one-photon occupation probability

$$r := \lim_{t \to \infty} \frac{\langle |2\rangle\langle 2| \rangle(t)}{\langle |1\rangle\langle 1| \rangle(t)} = \lim_{t \to \infty} \frac{P_2(t)}{P_1(t)} \tag{8}$$

equal to 0.45. Thus the ratio deviates from the target of 0.50, which is a necessary indicator for an $N = 2$ bundle. The phonon coupling pushes this value down to $r = 0.20$ already at $T = 1$ K. For higher temperatures up to 10 K, r swiftly approaches zero and the two-photon bundle fingerprint cannot be observed anymore. The N-photon bundle statistics ($1 < N < \infty$) therefore seems to be hard to find in state-of-the-art QD–cavity systems.

The reason for the drastic phonon influence can be understood by revisiting Fig. 2. Besides the effective two-photon process (blue arrows) creating the bundle, the coupling to the cavity also introduces one-photon processes between $|\pm, n\rangle$ and $|\pm, n + 1\rangle$. In the phonon-free situation, these processes are strongly detuned from the cavity mode, and therefore highly unlikely to occur. But when LA phonons are considered, the energetic mismatch can be compensated by a simultaneous phonon emission. Note that phonon emission is possible at any temperature and always dominates over phonon absorption. The phonon-assisted one-photon transitions from $|-, 0\rangle$ to $|-, 1\rangle$ are competing against the two-photon bundle process (blue arrows). This competing second-order process, where one photon and one phonon are emitted simultaneously dominates over the bundle mechanisms. After the state $|-, 1\rangle$ is reached due to the phonon-assisted one-photon transitions, the cavity losses direct the system back to state $|-, 0\rangle$, provided that the cavity loss rate is larger than the phonon-assisted coupling towards further states $|-, n\rangle$ with $n > 1$. Consequently, the system just transitions back and forth between these two states, resulting in a suppressed two-photon occupation probability and a violation of the bundle statistics. With increasing temperature, phonon-assisted processes gain importance, resulting in an even stronger suppression of the bundle.

Our finding that due to the phonon influence the occupation probability P_2 of the $n = 2$ Fock state compared with the $n = 1$ state is much lower than expected for an $N = 2$ bundle does, however, not mean that two-photon emission features are precluded from observation. The latter can still be made prominent, e.g., by spectrally filtering the emission as has been shown in Ref. [29].

B. Comparison with a phenomenological dephasing model

The phonon environment has a drastic influence on the N-photon bundle statistics as shown in the previous section for the case $N = 2$. Already at a low temperature of $T = 1$ K the $1/n$-distribution characteristic for the bundle [cf. Eq. (1)] is not recognizable anymore (cf. Fig. 4). This result was obtained within a microscopic model of the phonon influence. In contrast, in Ref. [27], the dephasing has been analyzed using a phenomenological Lindblad operator $\mathcal{L}_{|X\rangle\langle X|, \gamma_\phi}$.
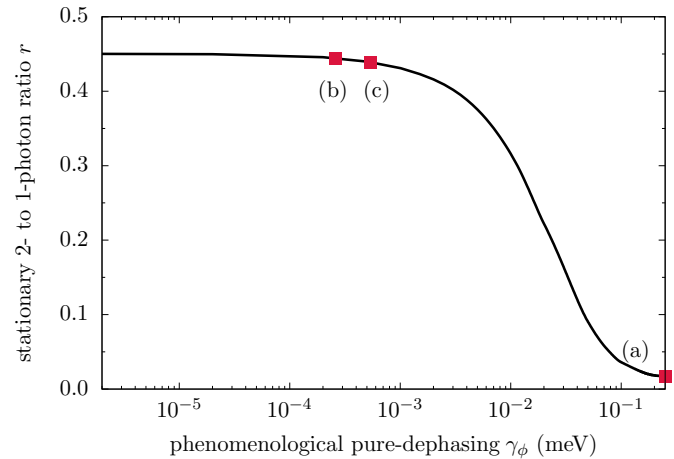

FIG. 5. The stationary ratio between the two- and the one-photon occupation probability in the QD–cavity system with the phonon influence approximated by a Lindblad operator with a phenomenological pure dephasing rate γ_ϕ instead of the microscopic Hamiltonian H_{Ph} in Eq. (6), cf. main text. (a) γ_ϕ corresponding to the full driven Jaynes–Cummings model at $T = 4$ K. (b) γ_ϕ corresponding to a Jaynes–Cummings dynamics with $n = 1$. (c) γ_ϕ corresponding to a Jaynes–Cummings dynamics with $n = 2$.

It is therefore instructive to compare the microscopic model with the phenomenological one to check whether the latter is valid. On first sight, we find a quite different behavior: for the phenomenological model taking values for the corresponding Lindblad rate γ_ϕ from the literature on semiconductor QD-cavity systems, the impact of pure dephasing is almost negligible [27].

To analyze this in more detail, we have plotted results of the phenomenological model in Fig. 5, which shows the stationary ratio r as a function of the phenomenological pure-dephasing rate γ_ϕ which is incorporated into the model by the addition of the Lindblad operator $\mathcal{L}_{|X\rangle\langle X|, \gamma_\phi}$ instead of the microscopic Hamiltonian model H_{Ph}. Indeed, in that approximation a large plateau range is found where the ratio stays essentially at its phonon-free value of $r = 0.45$ (cf. also Fig. 4).

To assess, what γ_ϕ should be chosen in the reduced model to best approximate the full phonon effect, we apply the following procedure: We compare the exciton dynamics resulting from the full calculation (where phonons are included by H_{Ph}) with the phenomenological model (where H_{Ph} is replaced by $\mathcal{L}_{|X\rangle\langle X|, \gamma_\phi}$) and vary γ_ϕ until the envelopes of the two dynamical results essentially match. Note that we set $\kappa = \gamma = 0$ for this procedure to extract the pure phonon influence on the dynamics. Furthermore, this comparison is conducted for the all-resonant case, i.e., $\Delta\omega_{\mathrm{LX}} = \Delta\omega_{\mathrm{CX}} = 0$. We perform this procedure at $T = 4$ K for three different cases and mark the resulting rate γ_ϕ by red squares in Fig. 5. (a) Driven Jaynes-Cummings system with the initial state $|G, 0\rangle$, resembling the closest approximation to the full calculation, (b) Jaynes-Cummings system without driving ($f = 0$) for the initial state $|G, 1\rangle$, and (c) same as (b) but with $|G, 2\rangle$ as the initial state. The three extracted rates (cf. Fig. 5) indicate that a very large pure-dephasing rate of the order of 10^{-1} meV is necessary to reproduce the dynamics of the full microscopic model [cf. red

square labeled with (a)]. With such a large rate, the ratio r is close to zero, meaning that no two-photon bundle statistics is observed in accordance with the results of the full model at $T = 4$ K (cf. Fig. 4).

The reason for such a significant increase in γ_ϕ lies in the impact of the pure dephasing mechanism, which gains in strength for larger Rabi frequencies related to the effective couplings present in the system. While in (b) and (c) the cavity Rabi frequency amounts to $2g\sqrt{n+1}$ with n the number of photons present in the cavity, the driving $f \gg g$ introduces the highest transition frequency in (a). In Fig. 5, it becomes clear that the pure-dephasing rate increases with larger effective coupling, in accordance with earlier observations in the case of a microscopic description of phonons [53,64,65]. The values of γ_ϕ in (b) and (c) are of the order of experimentally found pure-dephasing rates for strong QD-cavity coupling like the one studied here (cf. Sec. II A 1), but without external driving. Choosing such values for the rate indeed results in a marginal influence of pure dephasing, since both points lie well inside the plateau region.

Thus the conclusion in Ref. [27] that dephasing does not significantly affect the N-photon bundle generation can be traced back to the fact that values for dephasing rates have been considered that are no longer applicable in the regime of very strong driving as required for this protocol. The physical reason lies in the fact that an optically driven system is influenced by the phonon Hamiltonian in a profoundly different way than its nondriven counterpart: while phonons cannot induce transitions between the two electronic states in the undriven case, they can lead to transitions between the laser-dressed states, which are the eigenstates of the driven two-level system [66]. In essence, the dephasing rate depends on the driving strength. A quadratic dependence $\gamma_\phi \propto f^2$ can be derived in a weak-coupling limit [67].

In conclusion, a phenomenological pure dephasing model is also able to qualitatively predict that the characteristic statistical fingerprint of N-photon bundles is violated. The challenge is the choice of a proper rate, which has to be calibrated to the full phonon system. Since non-Markovian features are missing in the phenomenological model our results indicate that, in the present case, non-Markovian effetcs are of minor importance and, indeed, phonon-induced tranitions between laser dressed states are the origin of the violation of the bundle statistics.

IV. RESULTS: SUPERCONDUCTING QUBIT-MICROWAVE RESONATOR SYSTEMS

Superconducting qubit–microwave resonator systems have been successfully used to demonstrate the on-demand preparation of various highly nonclassical photon states, such as Fock states [4], superpositions thereof, and Voodoo cat states, i.e., coherent superpositions of three coherent states [5]. In none of these experiments, a significant impact of pure dephasing was reported.

For state-of-the-art superconducting systems [5], the resonator losses are much smaller than the decay of the qubit ($\kappa \ll \gamma$ as in Sec. II A 2). Again, the two-photon bundle resonance is achieved by an external excitation tuned according to Eq. (7). The resulting photon number distribution is shown
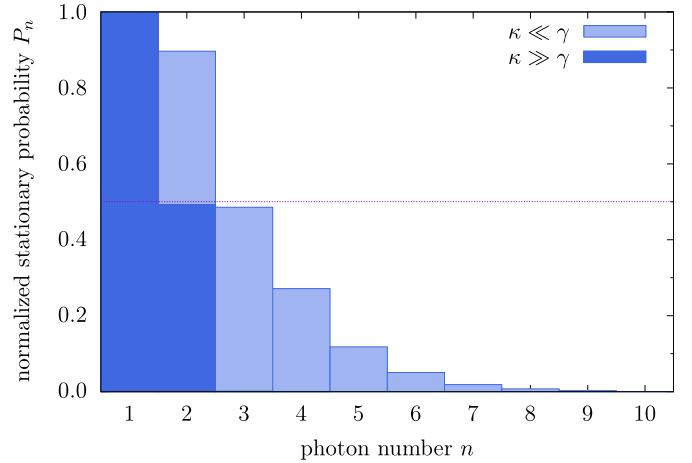

FIG. 6. The stationary probability P_n of occupying the photon number states $|n\rangle$ normalized to its value at $n = 1$ for the superconducting qubit–microwave system. The data labeled $\kappa \ll \gamma$ is obtained using the parameters from Sec. II A 2. In dark blue, the result of a calculation with a cavity loss rate two orders of magnitude larger than in Sec. II A 2 is shown, namely $\kappa = 0.1g = 7.76\gamma$, cf. Fig. 4.

in Fig. 6, normalized to its value at $n = 1$ (light blue bars). No bundle statistics is found, as higher order photon number states can be reached. Consequently, the characteristic cutoff for $n > N = 2$ is not observed.

The reason for this finding lies in the fact that the radiative decay with rate γ can induce transitions from states $|+, n\rangle$ to $|-, n\rangle$, as indicated in Fig. 2. After the state $|+, N\rangle$ is reached due to the N-photon resonance in the bundle-mechanism, these radiative transitions represent a competing channel in addition to the cascaded decay caused by the resonator losses. If at any point in the subsequent cascade, the radiative decay rate γ becomes comparable to the resonator loss rate $n\kappa$ ($n \leqslant N$) associated with the state $|+, n\rangle$, the system can reach the state $|-, n\rangle$. Because the coupling to the resonator does not only induce an effective coupling between the states $|-, 0\rangle$ and $|+, N\rangle$, but between all pairs $|-, n\rangle$ and $|+, n+N\rangle$, cf. Fig. 2, a subsequent emission of N additional resonator photons is possible when the system transitions into the state $|+, n+N\rangle$. Consequently, the characteristic cutoff is lost and higher order Fock states can be reached, violating the bundle-statistics.

This interpretation is supported by Fig. 6. For $n = 5$, the resonator loss rate $n\kappa$ becomes comparable to γ. Thus the last significant two-photon emission occurs due to the transition from $|-, 5\rangle$ to $|+, 7\rangle$. Afterwards the resonator losses dominate and the stationary probabilities P_n essentially vanish for $n > 7$.

Thus the failure of the superconducting qubit to show the statistical fingerprint can be traced back to the lack of resonator losses κ in comparison to radiative decay γ. Indeed, if we consider a resonator loss rate much larger (following Ref. [27], $\kappa = 0.1g$ has been chosen, cf. also Fig. 4 for this specific choice), we can obtain a near-perfect two-photon bundle statistics. The resulting photon number distribution (cf. dark blue bars in Fig. 6) indeed shows a near-perfect two-photon bundle fingerprint, with $r = 0.49$ and no occupation
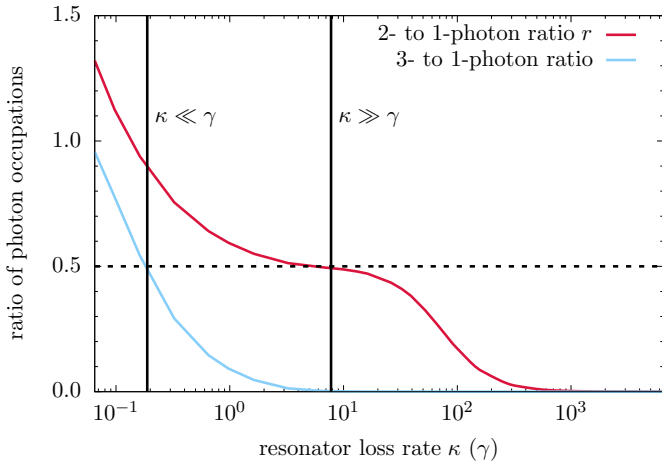
FIG. 7. The stationary ratios of the two- to one-photon occupation probabilities and of the three- to one-photon occupation probabilities as functions of the resonator loss rate κ (in units of γ) for the superconducting qubit–microwave system. The two vertical black lines mark those values of κ, which are used to obtain the corresponding data in Fig. 6. The dotted black line shows the target value of 0.5 for the ratio r.

probability for $n > 2$. This means that though much effort is usually invested into resonators of better quality, here the use of a bad resonator is mandatory.

To analyze the impact of the losses in more detail, we study the bundle statistics as a function of the resonator losses. To this end, the two- to one-photon ratio r is shown as a function of κ in Fig. 7 as well as the three- to one-photon ratio, which should vanish for an ideal two-photon bundle emission due to the cutoff for $n > N = 2$. Indeed, these two quantities confirm that the chosen value of $\kappa = 0.1g = 7.76\gamma$ lies well within a plateau region of $r \approx 0.5$ and a vanishing occupation probability for $n > 2$. While resonator losses too low compared to the decay of the qubit result in the occupation of states with $n > 2$, using very low-quality resonators with $\kappa \gtrsim 20\gamma$ (cf. Fig. 7) leads to a drastic reduction of r and thus a photon statistics, which displays a two-photon component much smaller than the ideal two-photon bundle. While constructing resonators of better quality is always an experimental challenge, creating a resonator of intermediate quality should be a lesser problem. Thus superconducting qubit-microwave resonator systems are indeed suitable candidates for sources of N-photon bundles, in agreement with Ref. [68].

V. CONCLUSION

We have studied the N-photon bundle statistics in two solid-state platforms: semiconductor quantum-dot–cavity systems and superconducting qubit-microwave resonator systems.

In quantum-dot–cavity systems, pure dephasing is induced by longitudinal acoustic phonons. We have found that even at low operating temperatures of a few kelvin, the characteristic bundle statistics [cf. Eq. (1)] cannot prevail for $N = 2$, thereby implying that a corresponding statistics for $N > 2$ is also out of reach with current state-of-the-art samples. The reason is the considered driving regime that is required to address the

bundle resonance, which also favors the phonon activity in the electronic subsystem of the quantum dot.

In contrast, superconducting qubit–microwave resonator systems are suitable candidates for the observation of the N-photon bundle statistics. Here, the pure dephasing does not play a notable role. However, the quality of the resonator has to be in a certain, optimal range. In particular, it should not be too high to facilitate the emission of photon bundles.

ACKNOWLEDGMENTS

APPENDIX A: ITERATIVE REAL-TIME PATH-INTEGRAL ALGORITHM

In this section, a brief description of the iterative real-time path-integral algorithm is given. This formalism is used to obtain the time evolution of the reduced density matrix $\bar{\rho}$ for the system of interest, i.e., the driven QD-cavity system, which is coupled to LA phonons via the pure-dephasing type Hamiltonian H_{Ph}.

The time evolution of the full statistical operator ρ of the system, containing all QD, photonic and phonon degrees of freedom, is governed by the Liouville-von Neumann equation

$$\frac{\partial}{\partial t}\rho = \mathcal{L}_{\mathrm{Sys}}\rho + \mathcal{L}_{\mathrm{Ph}}\rho, \tag{A1a}$$

$$\mathcal{L}_{\mathrm{Sys}}\rho = \frac{1}{i\hbar}[H_{\mathrm{Sys}}, \rho]_- + \mathcal{L}_{a,\kappa}\rho + \mathcal{L}_{|G\rangle\langle X|,\gamma}\rho, \tag{A1b}$$

$$\mathcal{L}_{\mathrm{Ph}}\rho = \frac{1}{i\hbar}[H_{\mathrm{Ph}}, \rho]_-. \tag{A1c}$$

First, a basis of ket states $|\mu\rangle$ and corresponding bra states $\langle\nu|$ for the system of interest is introduced. In the situation studied here, the basis $|\mu\rangle$ comprises the states $|G, n\rangle$, $|X, n\rangle$ with $n \leqslant N_{\mathrm{max}} \in \mathbb{N}_0$, where N_{max} is the maximum number of cavity photons that are considered in our numerical simulations. The reduced density matrix $\bar{\rho} = \mathrm{Tr}_{\mathrm{Ph}}[\rho]$, which is obtained from the statistical operator of the complete system by performing the trace over the phonon degrees of freedom can be expressed in the basis of the driven QD-cavity system as

$$\bar{\rho} = \sum_{\nu,\mu} \bar{\rho}_{\nu\mu} |\nu\rangle\langle\mu|, \tag{A2a}$$

$$\bar{\rho}_{\nu\mu} = \langle\nu|\mathrm{Tr}_{\mathrm{Ph}}[\rho]|\mu\rangle. \tag{A2b}$$

In Ref. [55], it was demonstrated that when the system dynamics is Hamiltonian, $\bar{\rho}_{\nu\mu}$ can be expressed as a sum over paths that can be performed iteratively, without introducing further approximations to the model. Furthermore, it has been shown recently that this still holds when non-Hamiltonian contributions to $\mathcal{L}_{\mathrm{Sys}}$ are taken into account, as provided, e.g., by $\mathcal{L}_{a,\kappa}$ and $\mathcal{L}_{|G\rangle\langle X|,\gamma}$ [58].

The general idea is to rewrite the formal solution of Eq. (A1a) by discretizing the time-evolution operator into small steps and integrating over the phonon degrees of freedom. When an equally spaced time discretization $t_\ell = \Delta t\,\ell$

with time step Δt and $\ell \in \mathbb{N}_0$ as well as a finite memory length $t_m = n_m \Delta t$ is considered, and the states of the driven QD-cavity system at time t_ℓ are labeled by ν_ℓ or μ_ℓ, the reduced density matrix at time t_n is given by

$$\bar{\rho}_{\nu_n \mu_n}(t_n) = \sum_{\substack{\nu_{n-1}...\nu_{n-n_m+1} \\ \mu_{n-1}...\mu_{n-n_m+1}}} \rho_{\nu_n...\nu_{n-n_m+1}}^{\mu_n...\mu_{n-n_m+1}}. \tag{A3}$$

The so called *augmented density matrix* (ADM) [55,56] $\rho_{\nu_n...\nu_{n-n_m+1}}^{\mu_n...\mu_{n-n_m+1}} := \sum_{\substack{\nu_{n-n_m}...\nu_0 \\ \mu_{n-n_m}...\mu_0}} R_{\nu_n...\nu_0}^{\mu_n...\mu_0}$ obeys the recurrence [58]

$$\rho_{\nu_n...\nu_{n-n_m+1}}^{\mu_n...\mu_{n-n_m+1}}$$
$$= \mathcal{M}_{\nu_n \mu_n}^{\nu_{n-1}\mu_{n-1}} \sum_{\substack{\nu_{n-n_m} \\ \mu_{n-n_m}}} \exp\left(\sum_{\ell=n-n_m}^{n} S_{\nu_n \mu_n}^{\nu_\ell \mu_\ell}\right) \rho_{\nu_{n-1}...\nu_{n-n_m}}^{\mu_{n-1}...\mu_{n-n_m}}, \tag{A4}$$

where

$$\mathcal{M}_{\nu_\ell \mu_\ell}^{\nu_{\ell-1}\mu_{\ell-1}} = \langle \nu_\ell | \mathcal{M}_{t_{\ell-1},t_\ell}[|\nu_{\ell-1}\rangle\langle\mu_{\ell-1}|] |\mu_\ell\rangle, \tag{A5a}$$

$$\mathcal{M}_{t,t'}[\cdot] = \mathcal{T} \exp\left(\int_t^{t'} \mathcal{L}_{\text{Sys}} \, dt''\right)[\cdot], \tag{A5b}$$

$$R_{\nu_n...\nu_0}^{\mu_n...\mu_0} := \bar{\rho}_{\nu_0 \mu_0} \prod_{\ell=1}^{n} \mathcal{M}_{\nu_\ell \mu_\ell}^{\nu_{\ell-1}\mu_{\ell-1}} \exp\left(\sum_{\ell=1}^{n} \sum_{\ell'=1}^{\ell} S_{\nu_{\ell'} \mu_{\ell'}}^{\nu_\ell \mu_\ell}\right). \tag{A5c}$$

Here it is assumed that initially the system is in its ground state $|G, 0\rangle$ while the phonons are in a thermal equilibrium at temperature T. The influence of the phonons is captured in the functions $S_{\nu_\ell \mu_\ell}^{\nu_{\ell'} \mu_{\ell'}}$, which introduce a finite memory.

For the pure-dephasing type Hamiltonian H_{Ph} with real couplings γ_q^{X}, the explicit expressions for these functions are [57,59]

$$S_{\nu_\ell \mu_\ell}^{\nu_{\ell'} \mu_{\ell'}} = -K_{\nu_{\ell'} \nu_\ell}(t_\ell - t_{\ell'}) - K_{\mu_\ell \mu_{\ell'}}^*(t_\ell - t_{\ell'}) + K_{\nu_\ell \mu_{\ell'}}^*(t_\ell - t_{\ell'}) + K_{\nu_{\ell'} \mu_\ell}(t_\ell - t_{\ell'}), \tag{A6a}$$

$$K_{\nu_\ell \mu_{\ell'}}(\tau) = 2 \int_0^\infty d\omega \frac{J_{\nu_\ell \mu_{\ell'}}(\omega)}{\omega^2} [1 - \cos(\omega \Delta t)] \left[\coth\left(\frac{\hbar\omega}{2k_B T}\right) \cos(\omega\tau) - i \sin(\omega\tau)\right], \quad \tau > 0 \tag{A6b}$$

$$K_{\nu_\ell \mu_\ell}(0) = \int_0^\infty d\omega \frac{J_{\nu_\ell \mu_\ell}(\omega)}{\omega^2} \left[\coth\left(\frac{\hbar\omega}{2k_B T}\right)(1 - \cos(\omega\Delta t)) + i \sin(\omega\Delta t) - i\omega\Delta t\right], \tag{A6c}$$

$$J_{\nu\mu}(\omega) = \sum_q \gamma_q^\nu \gamma_q^{\mu*} \delta(\omega - \omega_q); \quad \text{with } \gamma_q^\nu = n_\nu \gamma_q^{\text{X}}. \tag{A6d}$$

They display two important properties. (i) In the case of a continuum of phonon modes, the induced memory is finite, i.e., the memory kernel $K_{\nu_\ell \mu_{\ell'}}(t_\ell - t_{\ell'})$, and in turn $S_{\nu_\ell \mu_\ell}^{\nu_{\ell'} \mu_{\ell'}}$, become negligibly small for $t_\ell - t_{\ell'} > t_m = n_m \Delta t$. This property is already exploited in the recurrence Eq. (A4), where it is sufficient to memorize only the past n_m time steps to calculate the next one.

(ii) The function $S_{\nu_\ell \mu_\ell}^{\nu_{\ell'} \mu_{\ell'}}$ depends on the indices $\nu_\ell, \mu_\ell, \nu_{\ell'}, \mu_{\ell'}$ solely via the *phonon spectral density* $J_{\nu\mu}(\omega)$ and its dependence on the corresponding couplings $\gamma_q^\nu = n_\nu \gamma_q^{\text{X}}$, where $n_\nu \in \{0, 1\}$ is the number of excitons present in the QD-cavity state $|\nu\rangle$. This property is exploited

in an advanced algorithm, that was first introduced in the supplement of Ref. [59].

The central idea is to divide the QD-cavity states $|\nu\rangle$ into groups where each member couples identically to the phonon degrees of freedom. In the situation considered here, the coupling to the LA phonons depends solely on the QD state. Thus the states $|\nu\rangle$ can be sorted into two groups $\{|G, n\rangle\}$ and $\{|X, n\rangle\}$. Formally, the states can be re-labeled $|\nu\rangle \to |\lambda, k\rangle$ and $|\mu\rangle \to |\bar{\lambda}, \bar{k}\rangle$, where $\lambda \in \{1, 2\}$ denotes the group and k distinguishes the different members within this group. After defining the *partially summed ADM* (PSADM)

$$\rho_{(\lambda_n, k_n)\lambda_{n-1}...\lambda_{n-n_m+1}}^{(\bar{\lambda}_n, \bar{k}_n)\bar{\lambda}_{n-1}...\bar{\lambda}_{n-n_m+1}} := \sum_{\substack{k_{n-1}...k_{n-n_m+1} \\ \bar{k}_{n-1}...\bar{k}_{n-n_m+1}}} \rho_{(\lambda_n, k_n)(\lambda_{n-1}, k_{n-1})...(\lambda_{n-n_m+1}, k_{n-n_m+1})}^{(\bar{\lambda}_n, \bar{k}_n)(\bar{\lambda}_{n-1}, \bar{k}_{n-1})...(\bar{\lambda}_{n-n_m+1}, \bar{k}_{n-n_m+1})}. \tag{A7}$$

One obtains the recursion relation [59]

$$\rho_{(\lambda_n, k_n)\lambda_{n-1}...\lambda_{n-n_m+1}}^{(\bar{\lambda}_n, \bar{k}_n)\bar{\lambda}_{n-1}...\bar{\lambda}_{n-n_m+1}} = \sum_{\substack{k_{n-1} \\ \bar{k}_{n-1}}} \mathcal{M}_{(\lambda_n, k_n)(\bar{\lambda}_n, \bar{k}_n)}^{(\lambda_{n-1}, k_{n-1})(\bar{\lambda}_{n-1}, \bar{k}_{n-1})} \sum_{\substack{\lambda_{n-n_m} \\ \bar{\lambda}_{n-n_m}}} \exp\left(\sum_{\ell=n-n_m}^{n} S_{\lambda_n \bar{\lambda}_n}^{\lambda_\ell \bar{\lambda}_\ell}\right) \rho_{(\lambda_{n-1}, k_{n-1})\lambda_{n-2}...\lambda_{n-n_m}}^{(\bar{\lambda}_{n-1}, \bar{k}_{n-1})\bar{\lambda}_{n-2}...\bar{\lambda}_{n-n_m}} \tag{A8}$$

for this quantity. Then, the reduced density matrix for the driven QD-cavity system at time t_n is given by

$$\bar{\rho}_{\nu_n \mu_n}(t_n) = \sum_{\substack{\lambda_{n-1}...\lambda_{n-n_m+1} \\ \bar{\lambda}_{n-1}...\bar{\lambda}_{n-n_m+1}}} \rho_{(\lambda_n, k_n)\lambda_{n-1}...\lambda_{n-n_m+1}}^{(\bar{\lambda}_n, \bar{k}_n)\bar{\lambda}_{n-1}...\bar{\lambda}_{n-n_m+1}}. \tag{A9}$$

Equations (A7)–(A9) represent an exact reformulation without any additional approximation to the model. Numerical errors can be caused either by the number of considered photons per QD state N_{max} or by two intrinsic parameters of the path-integral algorithm: (i) The finite time step Δt and (ii)

the truncation of the memory to t_m. Usually, these convergence parameters can be well controlled. A simulation is considered to be *numerically complete* if neither a further reduction of Δt nor a further increase of t_m or $N_{\max}$ changes the numerical results noticeably.

An explicit expression for the phonon spectral density $J_{\nu\mu}(\omega)$ and the material parameters used in the simulations can be found in the supplement of Ref. [59]. Typically, calculations at low temperatures are most demanding, since they require the longest memory length [57]. For the calculations at a temperature of $T = 1$ K performed in the main text, numerically complete simulations were obtained for the parameter set: $\Delta t = 0.65$ ps, $n_m = 9$, and $N_{\max} = 4$. Note that, for this set of parameters, the advanced algorithm based on the PSADM reduces the number of terms to be iterated from $N_{\mathrm{ADM}} = 10^{2n_m} \approx 1.0 \times 10^{18}$ for the full ADM to $N_{\mathrm{PSADM}} = 10^2 \cdot 2^{2(n_m-1)} \approx 6.6 \times 10^6$ [59]. Thus this reduction of the numerical demand by more than 11 orders of magnitude is the reason that a numerically complete investigation of the considered system of interest becomes feasible at all. However, it is indeed the numerically complete treatment of the microscopic model that enables us to make a judgment on the phonon influence on the bundle statistics without prejudice.

APPENDIX B: RESONANCE PEAKS FOR $N \to \infty$ AND $N = 1$

Since the peaks at $\hbar\Delta\omega_{\mathrm{LX}} = -1.2$ meV and 0.08 meV are the most striking features in Fig. 3, we shall discuss them in some detail in this Appendix. This will give additional insights into the physics taking place in this parameter regime in general, although the analysis reveals that these peaks are not related to the bundles which are the main target of our paper. The most prominent peak in Fig. 3 at $\hbar\Delta\omega_{\mathrm{LX}} = \hbar\Delta\omega_{\mathrm{CX}} = -1.2$ meV is obtained in the limit $N \to \infty$ and corresponds to a process where the photon energy in a frame rotating with the laser frequency is $\hbar\Delta\omega_{\mathrm{CL}} = 0$ and the system can climb up the photon ladder from $|-, n\rangle$ to $|-, n+1\rangle$, such that a Poissonian distribution with respect to n emerges. Note that one observes a double-peaked structure at this resonance in Fig. 3. At its center, the order of the photon occupation probabilities is reversed, i.e., the occupation probability of $n = 2$ is higher than that of $n = 1$, consistent with a Poissonian with an average photon number of $\langle n \rangle = 6.6$ and a maximum occupation probability of 0.15 at $n = 6$. A magnification of this peak, where the reversal of the photon order is visible, is replotted in Fig. 8. An analysis of the corresponding Wigner function [5,26] (not shown here) confirms that the corresponding state is a (Glauber) coherent state.

The peak at $\hbar\Delta\omega_{\mathrm{LX}} \approx 0.08$ meV corresponds to a one-photon bundle resonance, i.e., a one-photon Fock state, and also results from a one-photon process. But in contrast to the
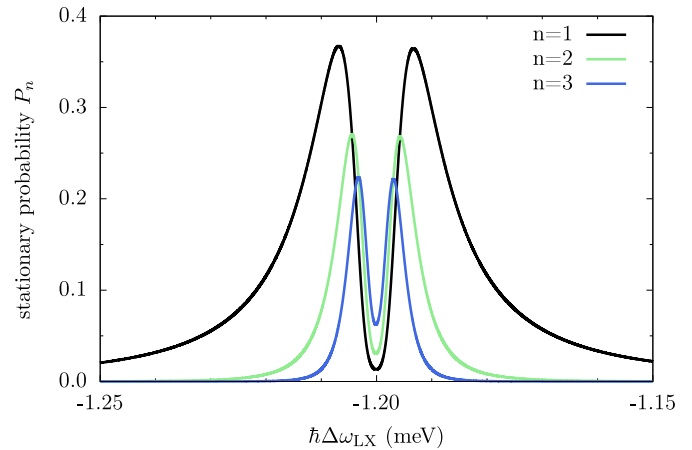

FIG. 8. Stationary probability P_n of occupying the photon number states $|n\rangle$ in the QD–cavity system as a function of the laser-exciton detuning $\Delta\omega_{\mathrm{LX}}$ without taking phonon effects into account. This is a magnification of the resonance peak for $N \to \infty$ in Fig. 3(a). On this scale, the double-peak structure and the reversal of the photon order at its center are well visible.

previously discussed case, the photon is emitted only by the transition from $|-, 0\rangle$ to $|+, 1\rangle$. Due to an energy mismatch between the photon energy and the transition between $|+, 1\rangle$ and $|\pm, 2\rangle$, no further photons are put into the cavity, as can be seen in the stationary probabilities P_n of occupying the photon number states $|n\rangle$ at this peak in Fig. 3(a). This effect is commonly known as the photon blockade [69].

The phonon influence on the stationary probability P_n of occupying the photon number states $|n\rangle$ at $T = 4$ K as shown in Fig. 3(b) could not be more different for these two resonances. The first one for $N \to \infty$ at $\hbar\Delta\omega_{\mathrm{LX}} = -1.2$ meV is hardly influenced by phonons at all. Indeed, the photon number distribution remains Poissonian with a slightly lower average photon number of $\langle n \rangle = 5.6$ and a similar maximum occupation probability of 0.16 at $n = 5$. The reason lies in the fact that the photons are emitted from transitions, where the electronic (laser-dressed) state remains $|-\rangle$ and does not change. Since this is the energetically lower dressed state and at temperatures below a few tens of kelvins phonon absorption is highly unlikely, phonons have only a slight influence on the stationary photon distribution.

On the other hand, the second peak at $\hbar\Delta\omega_{\mathrm{LX}} \approx 0.08$ meV for $N = 1$ experiences strong phonon enhancement, since the photon blockade is spoiled. The energy mismatch between $|+, n\rangle$ and $|-, n\rangle$ is now bridged by phonon emission, which is possible for all temperatures down to absolute zero, and a subsequent resonant transition to $|+, n+1\rangle$ can take place. Therefore the phonon coupling drives the occupation probability of higher-order Fock states beyond $n = 1$ [59,70].

[1] F. W. Cummings and A. K. Rajagopal, Production of number states of the electomagnetic field, Phys. Rev. A **39**, 3414 (1989).

[2] B. T. H. Varcoe, S. Brattke, M. Weidinger, and H. Walther, Preparing pure photon number states of the radiation field, Nature (London) **403**, 743 (2000).

[3] X. Zhou, I. Dotsenko, B. Peaudecerf, T. Rybarczyk, C. Sayrin, S. Gleyzes, J. M. Raimond, M. Brune, and S. Haroche, Field Locked to a Fock State by Quantum Feedback with Single Photon Corrections, Phys. Rev. Lett. **108**, 243602 (2012).

[4] M. Hofheinz, E. M. Weig, M. Ansmann, R. C. Bialczak, E. Lucero, M. Neeley, A. D. O'Connell, H. Wang, J. M. Martinis,

and A. N. Cleland, Generation of Fock states in a superconducting quantum circuit, Nature (London) **454**, 310 (2008).

[5] M. Hofheinz, H. Wang, M. Ansmann, R. C. Bialczak, E. Lucero, M. Neeley, A. D. O'Connell, D. Sank, J. Wenner, J. M. Martinis, and A. N. Cleland, Synthesizing arbitrary quantum states in a superconducting resonator, Nature (London) **459**, 546 (2009).

[6] P. Michler, A. Kiraz, C. Becher, W. V. Schoenfeld, P. M. Petroff, L. Zhang, E. Hu, and A. Imamoglu, A quantum dot single-photon turnstile device, Science **290**, 2282 (2000).

[7] C. Santori, M. Pelton, G. Solomon, Y. Dale, and Y. Yamamoto, Triggered Single Photons from a Quantum Dot, Phys. Rev. Lett. **86**, 1502 (2001).

[8] C. Santori, D. Fattal, J. Vuckovic, G. S. Solomon, and Y. Yamamoto, Indistinguishable photons from a single-photon device, Nature (London) **419**, 594 (2002).

[9] Y.-M. He, Y. He, Y.-J. Wei, D. Wu, M. Atatüre, C. Schneider, S. Höfling, M. Kamp, C.-Y. Lu, and J.-W. Pan, On-demand semiconductor single-photon source with near-unity indistinguishability, Nat. Nanotechnol. **8**, 213 (2013).

[10] Y.-J. Wei, Y.-M. He, M.-C. Chen, Y.-N. Hu, Y. He, D. Wu, C. Schneider, M. Kamp, S. Höfling, C.-Y. Lu, and J.-W. Pan, Deterministic and robust generation of single photons from a single quantum dot with 99.5% indistinguishability using adiabatic rapid passage, Nano Lett. **14**, 6515 (2014).

[11] X. Ding, Y. He, Z.-C. Duan, N. Gregersen, M.-C. Chen, S. Unsleber, S. Maier, C. Schneider, M. Kamp, S. Höfling, C.-Y. Lu, and J.-W. Pan, On-Demand Single Photons with High Extraction Efficiency and Near-Unity Indistinguishability from a Resonantly Driven Quantum Dot in a Micropillar, Phys. Rev. Lett. **116**, 020401 (2016).

[12] N. Somaschi, V. Giesz, L. De Santis, J. C. Loredo, M. P. Almeida, G. Hornecker, S. L. Portalupi, T. Grange, C. Antón, J. Demory, C. Gómez, I. Sagnes, N. D. Lanzillotti-Kimura, A. Lemaître, A. Auffeves, A. G. White, L. Lanco, and P. Senellart, Near-optimal single-photon sources in the solid state, Nat. Photonics **10**, 340 (2016).

[13] L. Schweickert, K. D. Jöns, K. D. Zeuner, S. F. Covre da Silva, H. Huang, T. Lettner, M. Reindl, J. Zichi, R. Trotta, A. Rastelli, and V. Zwiller, On-demand generation of background-free single photons from a solid-state source, Appl. Phys. Lett. **112**, 093106 (2018).

[14] L. Hanschke, K. A. Fischer, S. Appel, D. Lukin, J. Wierzbowski, S. Sun, R. Trivedi, J. Vučković, J. J. Finley, and K. Müller, Quantum dot single-photon sources with ultra-low multi-photon probability, npj Quantum Inf. **4**, 43 (2018).

[15] M. Cosacchi, F. Ungar, M. Cygorek, A. Vagov, and V. M. Axt, Emission-Frequency Separated High Quality Single-Photon Sources Enabled by Phonons, Phys. Rev. Lett. **123**, 017403 (2019).

[16] N. Akopian, N. H. Lindner, E. Poem, Y. Berlatzky, J. Avron, D. Gershoni, B. D. Gerardot, and P. M. Petroff, Entangled Photon Pairs from Semiconductor Quantum Dots, Phys. Rev. Lett. **96**, 130501 (2006).

[17] R. M. Stevenson, R. J. Young, P. Atkinson, K. Cooper, D. A. Ritchie, and A. J. Shields, A semiconductor source of triggered entangled photon pairs, Nature (London) **439**, 179 (2006).

[18] R. Hafenbrak, S. M. Ulrich, P. Michler, L. Wang, A. Rastelli, and O. G. Schmidt, Triggered polarization-entangled photon pairs from a single quantum dot up to 30k, New J. Phys. **9**, 315 (2007).

[19] A. Dousse, J. Suffczynski, A. Beveratos, O. Krebs, A. Lemaître, I. Sagnes, J. Bloch, P. Voisin, and P. Senellart, Ultrabright source of entangled photon pairs, Nature (London) **466**, 217 (2010).

[20] E. del Valle, Distilling one, two and entangled pairs of photons from a quantum dot with cavity QED effects and spectral filtering, New J. Phys. **15**, 025019 (2013).

[21] M. Müller, S. Bounouar, K. D. Jöns, M. Glässl, and P. Michler, On-demand generation of indistinguishable polarization-entangled photon pairs, Nat. Photonics **8**, 224 (2014).

[22] A. Orieux, M. A. M. Versteegh, K. D. Jöns, and S. Ducci, Semiconductor devices for entangled photon pair generation: A review, Rep. Prog. Phys. **80**, 076001 (2017).

[23] T. Seidelmann, F. Ungar, A. M. Barth, A. Vagov, V. M. Axt, M. Cygorek, and T. Kuhn, Phonon-Induced Enhancement of Photon Entanglement in Quantum Dot-Cavity Systems, Phys. Rev. Lett. **123**, 137401 (2019).

[24] M. Cosacchi, J. Wiercinski, T. Seidelmann, M. Cygorek, A. Vagov, D. E. Reiter, and V. M. Axt, On-demand generation of higher-order Fock states in quantum-dot–cavity systems, Phys. Rev. Research **2**, 033489 (2020).

[25] J. Gea-Banacloche, Collapse and Revival of the State Vector in the Jaynes-Cummings Model: An Example of State Preparation by a Quantum Apparatus, Phys. Rev. Lett. **65**, 3385 (1990).

[26] M. Cosacchi, T. Seidelmann, J. Wiercinski, M. Cygorek, A. Vagov, D. E. Reiter, and V. M. Axt, Schrödinger cat states in quantum-dot-cavity systems, Phys. Rev. Research **3**, 023088 (2021).

[27] C. S. Muñoz, E. del Valle, A. G. Tudela, K. Müller, S. Lichtmannecker, M. Kaniber, C. Tejedor, J. J. Finley, and F. P. Laussy, Emitters of n-photon bundles, Nat. Photonics **8**, 550 (2014).

[28] Q. Bin, Y. Wu and X.-Y. Lü, Parity-Symmetry-Protected Multiphoton Bundle Emission, Phys. Rev. Lett. **127**, 073602 (2021).

[29] C. S. Muñoz, F. P. Laussy, E. del Valle, C. Tejedor, and A. González-Tudela, Filtering multiphoton emission from state-of-the-art cavity quantum electrodynamics, Optica **5**, 14 (2018).

[30] G. Diaz-Camacho, E. Zubizarreta Casalengua, J. C. López Carreño, S. Khalid, C. Tejedor, E. del Valle, and F. P. Laussy, Multiphoton emission, arXiv:2109.12049 [quant-ph].

[31] J. C. López Carreño, E. del Valle, and F. P. Laussy, Frequency-resolved monte carlo, Sci. Rep. **8**, 6975 (2018).

[32] M. Schmidt, M. von Helversen, M. López, F. Gericke, E. Schlottmann, T. Heindel, S. Kück, S. Reitzenstein, and J. Beyer, Photon-number-resolving transition-edge sensors for the metrology of quantum light sources, J. Low Temp. Phys. **193**, 1243 (2018).

[33] E. Schlottmann, M. von Helversen, H. A. Leymann, T. Lettau, F. Krüger, M. Schmidt, C. Schneider, M. Kamp, S. Höfling, J. Beyer, J. Wiersig, and S. Reitzenstein, Exploring the Photon-Number Distribution of Bimodal Microlasers with a Transition Edge Sensor, Phys. Rev. Applied **9**, 064030 (2018).

[34] M. Schmidt, I. H. Grothe, S. Neumeier, L. Bremer, M. von Helversen, W. Zent, B. Melcher, J. Beyer, C. Schneider, S. Höfling, J. Wiersig, and S. Reitzenstein, Bimodal behavior of microlasers investigated with a two-channel photon-number-resolving transition-edge sensor system, Phys. Rev. Research **3**, 013263 (2021).

[35] M. Bozzio, M. Vyvlecka, M. Cosacchi, C. Nawrath, T. Seidelmann, J. C. Loredo, S. L. Portalupi, V. M. Axt, P. Michler, and P. Walther, Enhancing quantum cryptography with quantum dot single-photon sources, npj Quantum Information **8**, 104 (2022).

[36] W. Denk, J. H. Strickler, and W. W. Webb, Two-photon laser scanning fluorescence microscopy, Science **248**, 73 (1990).

[37] N. G. Horton, K. Wang, D. Kobat, C. G. Clark, F. W. Wise, C. B. Schaffer, and C. Xu, In vivo three-photon microscopy of subcortical structures within an intact mouse brain, Nat. Photonics **7**, 205 (2013).

[38] C. J. Rowlands, D. Park, O. T. Bruns, K. D. Piatkevich, D. Fukumura, R. K. Jain, M. G. Bawendi, E. S. Boyden, and P. T. So, Wide-field three-photon excitation in biological samples, Light: Science & Applications **6**, e16255 (2017).

[39] D. G. Ouzounov, T. Wang, M. Wang, D. D. Feng, N. G. Horton, J. C. Cruz-Hernández, Y.-T. Cheng, J. Reimer, A. S. Tolias, N. Nishimura, and C. Xu, In vivo three-photon imaging of activity of GCaMP6-labeled neurons deep in intact mouse brain, Nat. Methods **14**, 388 (2017).

[40] A. Escobet-Montalbán, F. M. Gasparoli, J. Nylk, P. Liu, Z. Yang, and K. Dholakia, Three-photon light-sheet fluorescence microscopy, Opt. Lett. **43**, 5484 (2018).

[41] Q. Bin, X.-Y. Lü, F. P. Laussy, F. Nori, and Y. Wu, *n*-Phonon Bundle Emission Via the Stokes Process, Phys. Rev. Lett. **124**, 053601 (2020).

[42] T. Seidelmann, F. Ungar, M. Cygorek, A. Vagov, A. M. Barth, T. Kuhn, and V. M. Axt, From strong to weak temperature dependence of the two-photon entanglement resulting from the biexciton cascade inside a cavity, Phys. Rev. B **99**, 245301 (2019).

[43] D. E. Reiter, T. Kuhn, M. Glässl, and V. M. Axt, The role of phonons for exciton and biexciton generation in an optically driven quantum dot, J. Phys.: Condens. Matter **26**, 423203 (2014).

[44] D. E. Reiter, T. Kuhn, and V. M. Axt, Distinctive characteristics of carrier-phonon interactions in optically driven semiconductor quantum dots, Adv. Phys.: X **4**, 1655478 (2019).

[45] L. Besombes, K. Kheng, L. Marsal, and H. Mariette, Acoustic phonon broadening mechanism in single quantum dot emission, Phys. Rev. B **63**, 155307 (2001).

[46] P. Borri, W. Langbein, S. Schneider, U. Woggon, R. L. Sellin, D. Ouyang, and D. Bimberg, Ultralong Dephasing Time in InGaAs Quantum Dots, Phys. Rev. Lett. **87**, 157401 (2001).

[47] B. Krummheuer, V. M. Axt, and T. Kuhn, Theory of pure dephasing and the resulting absorption line shape in semiconductor quantum dots, Phys. Rev. B **65**, 195313 (2002).

[48] V. M. Axt, T. Kuhn, A. Vagov, and F. M. Peeters, Phonon-induced pure dephasing in exciton-biexciton quantum dot systems driven by ultrafast laser pulse sequences, Phys. Rev. B **72**, 125309 (2005).

[49] D. P. S. McCutcheon, Optical signatures of non-Markovian behavior in open quantum systems, Phys. Rev. A **93**, 022119 (2016).

[50] A. Krügel, V. M. Axt, T. Kuhn, P. Machnikowski, and A. Vagov, The role of acoustic phonons for rabi oscillations in semiconductor quantum dots, Appl. Phys. B **81**, 897 (2005).

[51] A. J. Ramsay, T. M. Godden, S. J. Boyle, E. M. Gauger, A. Nazir, B. W. Lovett, A. M. Fox, and M. S. Skolnick, Phonon-Induced Rabi-Frequency Renormalization of Optically Driven Single InGaAs/GaAs Quantum Dots, Phys. Rev. Lett. **105**, 177402 (2010).

[52] J. Förstner, C. Weber, J. Danckwerts, and A. Knorr, Phonon-Assisted Damping of Rabi Oscillations in Semiconductor Quantum Dots, Phys. Rev. Lett. **91**, 127401 (2003).

[53] P. Machnikowski and L. Jacak, Resonant nature of phonon-induced damping of Rabi oscillations in quantum dots, Phys. Rev. B **69**, 193302 (2004).

[54] A. J. Ramsay, A. V. Gopal, E. M. Gauger, A. Nazir, B. W. Lovett, A. M. Fox, and M. S. Skolnick, Damping of Exciton Rabi Rotations by Acoustic Phonons in Optically Excited InGaAs/GaAs Quantum Dots, Phys. Rev. Lett. **104**, 017402 (2010).

[55] N. Makri and D. E. Makarov, Tensor propagator for iterative quantum time evolution of reduced density matrices. I. Theory, J. Chem. Phys. **102**, 4600 (1995).

[56] N. Makri and D. E. Makarov, Tensor propagator for iterative quantum time evolution of reduced density matrices. II. Numerical methodology, J. Chem. Phys. **102**, 4611 (1995).

[57] A. Vagov, M. D. Croitoru, M. Glässl, V. M. Axt, and T. Kuhn, Real-time path integrals for quantum dots: Quantum dissipative dynamics with superohmic environment coupling, Phys. Rev. B **83**, 094303 (2011).

[58] A. M. Barth, A. Vagov, and V. M. Axt, Path-integral description of combined Hamiltonian and non-Hamiltonian dynamics in quantum dissipative systems, Phys. Rev. B **94**, 125439 (2016).

[59] M. Cygorek, A. M. Barth, F. Ungar, A. Vagov, and V. M. Axt, Nonlinear cavity feeding and unconventional photon statistics in solid-state cavity QED revealed by many-level real-time path-integral calculations, Phys. Rev. B **96**, 201201(R) (2017).

[60] D. Najer, I. Söllner, P. Sekatski, V. Dolique, M. C. Löbl, D. Riedel, R. Schott, S. Starosielec, S. R. Valentin, A. D. Wieck, N. Sangouard, A. Ludwig, and R. J. Warburton, A gated quantum dot strongly coupled to an optical microcavity, Nature (London) **575**, 622 (2019).

[61] C. Schneider, P. Gold, S. Reitzenstein, S. Höfling, and M. Kamp, Quantum dot micropillar cavities with quality factors exceeding 250, 000, Appl. Phys. B **122**, 19 (2016).

[62] B. Krummheuer, V. M. Axt, T. Kuhn, I. D'Amico, and F. Rossi, Pure dephasing and phonon dynamics in GaAs- and GaN-based quantum dot structures: Interplay between material parameters and geometry, Phys. Rev. B **71**, 235329 (2005).

[63] Y.-T. Chough, H.-J. Moon, H. Nha, and K. An, Single-atom laser based on multiphoton resonances at far-off resonance in the jaynes-cummings ladder, Phys. Rev. A **63**, 013804 (2000).

[64] A. Vagov, M. D. Croitoru, V. M. Axt, T. Kuhn, and F. M. Peeters, Nonmonotonic Field Dependence of Damping and Reappearance of Rabi Oscillations in Quantum Dots, Phys. Rev. Lett. **98**, 227403 (2007).

[65] M. Glässl, L. Sörgel, A. Vagov, M. D. Croitoru, T. Kuhn, and V. M. Axt, Interaction of a quantum-dot cavity system with acoustic phonons: Stronger light-matter coupling can reduce the visibility of strong coupling effects, Phys. Rev. B **86**, 035319 (2012).

[66] M. R. Klaßen and D. E. Reiter, Optical signals to monitor the dynamics of phonon-modified rabi oscillations in a quantum dot, Annalen der Physik **533**, 2100086 (2021).

[67] A. Nazir and D. P. S. McCutcheon, Modelling exciton-phonon

interactions in optically driven quantum dots, J. Phys.: Condens. Matter **28**, 103002 (2016).

[68] S.-L. Ma, X.-K. Li, Y.-L. Ren, J.-K. Xie, and F.-L. Li, Antibunched *n*-photon bundles emitted by a josephson photonic device, Phys. Rev. Research **3**, 043020 (2021).

[69] K. M. Birnbaum, A. Boca, R. Miller, A. D. Boozer, T. E. Northup, and H. J. Kimble, Photon blockade in an optical cavity with one trapped atom, Nature (London) **436**, 87 (2005).

[70] M. Cosacchi, T. Seidelmann, F. Ungar, M. Cygorek, A. Vagov, and V. M. Axt, Transiently changing shape of the photon number distribution in a quantum-dot–cavity system driven by chirped laser pulses, Phys. Rev. B **101**, 205304 (2020).

Publication 8

"Deterministic Photon Storage and Readout in a Semimagnetic Quantum Dot-Cavity System Doped with a Single Mn Ion"

M. Cosacchi, **T. Seidelmann**, A. Mielnik-Pyszczorski, M. Neumann, T. K. Bracht, M. Cygorek, A. Vagov, D. E. Reiter, and V. M. Axt.

Adv. Quantum Technol. **5**, 2100131 (2022).

Author contributions

M. Cosacchi has designed the concept of this study, has performed the numerical data generation and analysis, and has implemented the problem-specific C++ code. He has provided interpretations of the results and has written the first draft of the publication. In particular, he has proposed the idea for a feasible protocol to store one photon in an optically dark state. During the publication process, he has moderated all discussions, has organized the submission and revision of the manuscript, and has written the answer to the referees.

The author has participated in the general discussion of the results and their interpretations. Furthermore, he has discussed the results in detail with M. Cosacchi and has provided the analytic approximation resulting in Eq. (19). He has also contributed to revisions of the draft and the answers to the referees.

A. Mielnik-Pyszczorski has participated in the general discussion of the results and their interpretations. Furthermore, he has discussed the results in detail with M. Cosacchi and has provided an extensive literature research for the first draft of the publication. He has also contributed to revisions of the draft and the answers to the referees.

M. Neumann has discussed the background of the proposed scheme, in particular, the preparation of the dark state and suitable AC-Stark pulse parameters, with M. Cosacchi. She has also contributed to revisions of the draft and the answers to the referees.

T. K. Bracht has provided reference calculations with the correlation expansion method for convergence tests as well as details concerning the preparation of the dark state. He has also contributed to revisions of the draft and the answers to the referees.

M. Cygorek, A. Vagov, and D. E. Reiter have co-supervised this work. In particular, they have

participated in the discussion of the results and their interpretations. They have also contributed to the optimization of the presentation, revisions of the draft, and the answers to the referees.

V. M. Axt has advised M. Cosacchi throughout his work as the main supervisor, has obtained the funding for this work, and has provided the practical means. He has participated in the discussion of the results and their interpretations. He has also contributed to the optimization of the presentation, revisions of the draft, and the answers to the referees.

Deterministic Photon Storage and Readout in a Semimagnetic Quantum Dot–Cavity System Doped with a Single Mn Ion

Michael Cosacchi,* Tim Seidelmann, Adam Mielnik-Pyszczorski, Miriam Neumann, Thomas K. Bracht, Moritz Cygorek, Alexei Vagov, Doris E. Reiter, and Vollrath M. Axt

Light trapping is a crucial mechanism for synchronization in optical communication. Especially on the level of single photons, control of the exact emission time is desirable. In this paper, a single-photon buffering device composed of a quantum dot doped with a single Mn atom in a cavity is theoretically proposed. A method to detain a single cavity photon as an excitation of the dot is presented. The storage scheme is based on bright to dark exciton conversion performed with an off-resonant external optical field and mediated via a spin-flip with the magnetic ion. The induced Stark shift brings both exciton states to resonance and results in an excitation transfer to the optically inactive one. The stored photon can be read out on demand in the same manner by repopulating the bright state, which has a short lifetime. The results indicate the possibility to suspend a photon for almost two orders of magnitude longer than the lifetime of the bright exciton.

M. Cosacchi, T. Seidelmann, A. Mielnik-Pyszczorski, A. Vagov, V. M. Axt
Lehrstuhl für Theoretische Physik III
Universität Bayreuth
Universitätsstraße 30, Bayreuth 95447, Germany
E-mail: michael.cosacchi@uni-bayreuth.de

A. Mielnik-Pyszczorski
Department of Theoretical Physics
Wrocław University of Science and Technology
Wrocław 50-370, Poland

M. Neumann, T. K. Bracht, D. E. Reiter
Institut für Festkörpertheorie
Universität Münster
Wilhelm-Klemm-Straße 10, Münster 48149, Germany

M. Cygorek
Institute of Photonics and Quantum Sciences
Heriot-Watt University
Edinburgh EH14 4AS, UK

A. Vagov
ITMO University
Kronverksky Pr. 49, St. Petersburg 197101, Russia

1. Introduction

Self-assembled quantum dots (QDs) are optically active and allow the control of electronic states with light.[1–4] In return, they can serve as photon sources, which makes them attractive for quantum communication devices.[5,6] A QD–cavity system greatly increases light emission efficiency due to the Purcell effect[7] and has a favored direction of emission in contrast to a standalone QD, providing easier in- and outcoupling. While QDs in cavities are a suitable platform for quantum information processing devices,[8] the realization requires the synchronization of signals,[9] for which a photon buffer is desirable.

In all-optical systems, buffers were realized with fibers and waveguides.[9–12] Another proposed realization of an optical memory cell is a three-level Λ system, which gives the possibility to store information in a dark state.[13] Extremely long light storage was achieved in atomic systems, where the slow light effect is commonly based on electromagnetically induced transparency (EIT). Adequate coupling in the Λ system highly reduces the group velocity of light and results in slow propagation of a beam through atoms or even reversible trapping of light in atomic excitations.[13–16] Recent experiments were performed even on the single-photon level,[17–19] raising hopes for use in quantum communication. Atomic systems were also used to store time-entangled solitons in a cavity, representing a step toward multiplexed quantum communication.[20]

In solid-state systems, photons may be absorbed and stored as excitons. However, the typical lifetime of a bright exciton is short (typically a few hundred ps up to one ns). Therefore, a separated electron-hole pair, the indirect exciton, was used in coupled nanostructures to extend the storage time.[21–29] On the other hand, in a single QD–cavity system, the lifetime of an exciton may be increased by the Stark shift, which decouples the exciton from the cavity mode.[30] A more attractive direction for storing excitations in a QD is to use a dark state, which lives for at least an order of magnitude longer than the bright one. For a long time, dark excitons were beyond much interest as they are not optically active and hence not directly accessible.

Recent progress allows for indirectly accessing the dark exciton with light[31,32] or other complexes,[33] but all-optical control

**ADVANCED
SCIENCE NEWS**

www.advancedsciencenews.com

**ADVANCED
QUANTUM
TECHNOLOGIES**

www.advquantumtech.com

of the dark state using an intermediate biexciton state has also been proposed for the use as a long-lived qubit.[31,34–37] Another possibility is the coupling of bright and dark states using micromechanical resonators, making the dark state addressable by light.[38] Still, it is much easier to excite the bright state. Hence, a method to realize the bright-to-dark conversion for excitation storage was already proposed for colloidal systems.[39] Yet, they cannot be easily integrated on-chip. A dark state was also used as a microsecond valley polarization memory in transition metal dichalcogenides.[40] More recently, a controllable occupation transfer between bright and dark excitons in a QD–cavity system was suggested.[41]

Our method facilitates QDs with a single magnetic dopant, which can be deterministically fabricated for several years,[42] with dopand atoms like Manganese (Mn),[43,44] Chromium,[45] Iron,[46] or Cobalt.[47] Interestingly, the spin state of the dopant can be changed via optical control.[48–52] Here, we choose an Mn doped CdTe/ZnTe QD in a microcavity.[53] The exchange coupling between the Mn and the electron spin enables a coupling between bright and dark excitons in the quantum dot under the simultaneous flip of the Mn spin.[48,54] Given a spin state, the states can be interpreted as a Λ-type three-level system, as specified in the next section.

The buffering scheme relies on storing the photon in the dark state. After the photon is converted to the bright exciton state, an AC-Stark pulse is utilized to facilitate the conversion of the bright into a dark exciton. We stress that the Stark pulse is the only external pulse which is used in the buffering scheme. Because the coupling between bright and dark excitons in this system is enabled by the exhange interaction with the Mn dopant, no external magnetic field needs to be applied as in other studies.[41,55,56] This is a significant advantage because it gives a possibility to integrate magnetically doped QDs into compact on-chip devices.

2. Mn-Doped Quantum Dot System

We consider a self-assembled CdTe quantum dot (QD) doped by a single Mn ion inside a ZnTe micropillar cavity. Due to the strong spatial confinement of the carriers in the QD, only the lowest conduction band state and the uppermost valence band state need to be considered, namely electrons in the s-like conduction band and holes in the p-like heavy-hole band.

Excitons form as pairs of conduction band electrons and valence band heavy holes. Having a spin component of $S_z^h = \pm\frac{3}{2}$, heavy holes can form two types of excitons with the spin-$\frac{1}{2}$ electrons: the optically active bright states with a circular polarization of ± 1 and the dipole-dark states with ± 2. For typical fine-structure splittings of a few tens of µeV[57] between the two bright exciton states of opposite circular polarization, only excitons of one polarization need to be considered, if the external driving has a defined circular polarization.[55,58,59]

Doping such a QD system with a single Mn ion, which has a spin of $\frac{5}{2}$, introduces an additional state space, namely the six possible orientations of its spin. The Mn spin interacts with electrons and holes via the exchange interaction[43,48,60–63]

$$H_{ex} = j_e \boldsymbol{M} \cdot \boldsymbol{S}^e + j_h \boldsymbol{M} \cdot \boldsymbol{S}^h \tag{1}$$

Table 1. Parameters used for the simulations.

Electron-Mn coupling	J_e [meV nm^3]	-15	[65]
Hole-Mn coupling	J_h [meV nm^3]	60	[65]
Intrinsic dark-bright splitting	δ_{XD} [meV]	0.95	[66]
Mn g-factor	g_{Mn}	2.0075	[60]
Electron g-factor	g_e	-1.5	[43]
QD–cavity coupling	$\hbar g$ [meV]	0.1	[67]
Cavity loss rate	κ [ns^{-1}]	8.5	[68]
Radiative decay rate of $|X\rangle$	γ_X [ns^{-1}]	2.4	[67]
Residual decay rate of $|D\rangle$	γ_D [ns^{-1}]	0.01	[69]
Electron deformation potential	D_e [eV]	-5	[70]
Hole deformation potential	D_h [eV]	1	[70]
Density	ρ_D [kg m^{-3}]	5510	[70]
Sound velocity	c_s [m s^{-1}]	4000	[70]
Electron-to-hole confinement ratio	a_e/a_h	1.38	[71, 72]
Electron confinement radius	a_e [nm]	3.0	[73–75]

where $\boldsymbol{M}$ denotes the spin of the Mn ion. $\boldsymbol{S}^e$ ($\boldsymbol{S}^h$) is the operator of the electron (hole) spin in the QD. $j_{e/h} = J_{e/h}|\Psi_0^{e/h}(\boldsymbol{r}_{Mn})|^2$ are composed of the coupling constants $J_{e/h}$ between the electon/hole and the Mn spin (cf., **Table 1**) and the carrier ground state wave function Ψ_0 at the position $\boldsymbol{r}_{Mn}$ of the Mn atom. Modelling the QD with a hard wall cubic potential[63,64] with in-plane widths of 6 nm and a height of 2 nm, the coupling strengths $j_{e/h}$ depends on the position of the Mn atom.

For a more intuitive understanding of the exchange Hamiltonian, it can be rewritten as

$$H_{ex} = j_e M_z S_z^e + \frac{j_e}{2}\left(M_+ S_-^e + M_- S_+^e\right)$$

$$+ j_h M_z S_z^h + \frac{j_h}{2}\left(M_+ S_-^h + M_- S_+^h\right) \tag{2}$$

with $M_\pm := M_x \pm iM_y$ and $S_\pm^{e/h} := S_x^{e/h} \pm iS_y^{e/h}$. The Ising terms[76] arising from the z-component of the interaction lead to energy shifts of the exciton states with different spin configuration. These contributions lead to the characteristic splitting of the exciton line into six lines even at zero magnetic field.[42–44,62] The electron flip-flop term[77] on the other hand results in a coupling between the excitonic bright state with total spin ± 1 and the excitonic dark state with ± 2 via simultaneous spin flip. While usually the flip-flop term is much weaker than the energetic splitting, for an applied magnetic field in Faraday configuration, this coupling is seen as anti-crossing in the optical spectrum at a field of several Tesla.[78,79] Note that the flip-flop term regarding the hole[80] can be neglected since the hole spin is pinned in a pure heavy-hole system.[48]

Assuming the Mn spin to be initially prepared in the state $M_z = -\frac{5}{2}$, we can reduce our system to a three-level system. This preparation can be achieved in numerous ways: by thermal occupation at low temperatures since by applying a magnetic field, it becomes the energetically lowest state[48]; or by an all-optical protocol,[81] thus avoiding the necessity of an additional external magnetic field. Then, the three states are: the ground state without an electronic excitation $|G\rangle := |0, -\frac{5}{2}\rangle$, the bright exciton
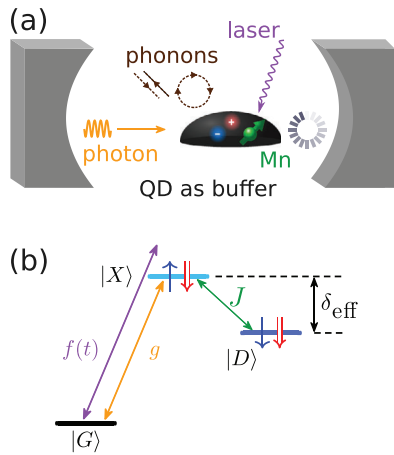
**ADVANCED
SCIENCE NEWS**

www.advancedsciencenews.com

**ADVANCED
QUANTUM
TECHNOLOGIES**

www.advquantumtech.com

Figure 1. a) Sketch of the QD–cavity system. The Mn ion provides the magnetic field necessary to facilitate the storage of a single cavity photon. An off-resonant external laser controls both the storage and the release time and thus the entire buffering procedure deterministically. b) The Λ-type three-level model of the QD. The spin configuration of the two exciton states is symbolized by arrows.

$|X\rangle := |-1, -\frac{5}{2}\rangle$, and the dark exciton $|D\rangle := |-2, -\frac{3}{2}\rangle$. Here, the first entry denotes the projection of the total spin of the electronic excitation and the second one the Mn spin orientation. Note that a circular polarization of the external laser of -1 is assumed, from which the sign of the bright exciton spin follows.

3. Model of the Λ-Type Three-Level System

In the basis of the three states $|G\rangle$, $|X\rangle$, and $|D\rangle$ the Hamiltonian reads as follows:

$$H = H_{QD} + H_{flip} + H_{driv}(t) + H_C + H_{Ph} \tag{3}$$

consisting of the QD part H_{QD} and the flip-flop term H_{flip} as introduced in Equation (2). In addition, we account for the driving of the system with an external laser pulse $H_{driv}(t)$, the coupling to a single-mode cavity H_C, and the coupling to longitudinal acoustic (LA) phonons H_{Ph}. A sketch of the system and its level structure is shown in **Figure 1**.

The QD part is composed of

$$H_{QD} = \hbar\omega_X |X\rangle\langle X| + (\hbar\omega_X - \delta_{eff})|D\rangle\langle D| \tag{4}$$

where the energy of the ground state is set to zero, the bright exciton has the energy $\hbar\omega_X$, and the effective dark-bright splitting is δ_{eff}. Three contributions enter the latter quantity: the intrinsic splitting δ_{XD} due to the electron-hole exchange interaction and the splitting arising from the Ising terms in Equation (2)

$$\delta_{eff} = \delta_{XD} - 2j_e + \frac{3}{2}j_h + (g_{Mn} - g_e)\mu_B B_z \tag{5}$$

The third contribution is a Zeeman splitting due to an external magnetic field in Faraday configuration $\boldsymbol{B} = B_z \boldsymbol{e}_z$. g_{Mn} and g_e in Equation (5) denote the Mn and the electron g-factors (cf., Table 1), respectively, and μ_B is the Bohr magneton.

One arm of our Λ-type system is coupled by the flip-flop term

$$H_{flip} = -\frac{1}{2}J(|X\rangle\langle D| + |D\rangle\langle X|) \tag{6}$$

The interaction strength results from calculating the corresponding matrix elements in the three-level basis as $J = -\sqrt{5}j_e$. We assume the position of the Mn atom to be 30% away from the QD edge in both x and y direction and 13% in z direction. This results in a coupling strength of $J = 0.25$ meV and an effective dark-bright splitting of $\delta_{eff} = 1.85$ meV in the field-free case $B_z = 0$. This value can be interpreted as the Mn spin providing an effective magnetic field for the excitons with a strength of roughly 3 T.

The other arm of the Λ-type system, that is, the ground to bright exciton state transition is driven by an external laser classically described by the function $f(t) = f_{ACS}(t)e^{-i\omega_{ACS}t}$ with the real envelope function $f_{ACS}(t)$ and the off-resonant AC-Stark frequency ω_{ACS} [cf., Figure 1b]. Although the AC-Stark pulse is off-resonant, the parameters are chosen such that the conditions for the usual dipole and rotating wave approximations still hold and the corresponding coupling can be written as[82, 83]:

$$H_{driv}(t) = -\frac{\hbar}{2}(f^*(t)|G\rangle\langle X| + f(t)|X\rangle\langle G|) \tag{7}$$

The coupling to the single-mode cavity with strength g [cf., Figure 1b] is described by a Jaynes–Cummings model

$$H_C = \hbar\omega_C a^\dagger a + \hbar g(a|X\rangle\langle G| + a^\dagger|G\rangle\langle X|) \tag{8}$$

where a ($a^\dagger$) is the annihilation (creation) operator for a photon at the cavity frequency ω_C, which is assumed to be on resonance with the bright state ω_X.

To model the decoherence in the QD, we consider that the QD is coupled to an environment of LA phonons in the bulk material [cf., Figure 1a][70,84–88]

$$H_{Ph} = \hbar \sum_q \omega_q b_q^\dagger b_q + \hbar \sum_q \left(\gamma_q b_q^\dagger + \gamma_q^* b_q\right)(|X\rangle\langle X| + |D\rangle\langle D|) \tag{9}$$

b_q ($b_q^\dagger$) annihilates (creates) a phonon in the mode $\boldsymbol{q}$ with the frequency ω_q. Both exciton states are assumed to couple to the environment with the same strength γ_q. The role of phonons in QD–cavity systems is typically considered to be detrimental to the preparation of photonic quantum states, for example, single photons[89–97] or entangled photon pairs.[98–104] Nonetheless, in specific situations a phonon enhancement of the single-photon purity is found.[105,106] Also, a boost in the entanglement of two photons has been predicted to be a result of the phonon interaction.[107]

Furthermore, we account for cavity losses ($\mathcal{L}_{a,\kappa}$) as well as radiative decay of the bright exciton ($\mathcal{L}_{|G\rangle\langle X|,\gamma_X}$) and losses of the dark exciton ($\mathcal{L}_{|G\rangle\langle D|,\gamma_D}$) using Lindblad superoperators acting on the density matrix ρ as

$$\mathcal{L}_{O,\Gamma}\rho = \Gamma\left(O\rho O^\dagger - \frac{1}{2}\{\rho, O^\dagger O\}_+\right) \tag{10}$$

**ADVANCED
SCIENCE NEWS**

www.advancedsciencenews.com

**ADVANCED
QUANTUM
TECHNOLOGIES**

www.advquantumtech.com

where $\{A, B\}_+$ is the anti-commutator of operators A and B. These superoperators describe phenomenologically loss processes with rate Γ on a dissipation channel O.

We use an interaction picture representation of this Hamiltonian for the numerics as well as the physical discussion, in order to eliminate fast oscillating terms in the dynamics resulting from transition energies in the eV range. The noninteracting Hamiltonian used for this transform is[41]

$$H_0 = -\hbar\Delta\omega_{AX}|G\rangle\langle G| + \hbar\omega_X(|X\rangle\langle X| + |D\rangle\langle D|) + \hbar\omega_{ACS}a^\dagger a \quad (11)$$

Here, the detuning between the laser and bright exciton frequencies $\Delta\omega_{AX} := \omega_{ACS} - \omega_X$ has been introduced. Then, the transformed Hamiltonian is $H_I = U^\dagger(H - H_0)U$ with $U = \exp[-(i/\hbar)H_0 t]$.

We choose parameters from the experimental literature, in order to perform simulations as realistic as possible. The values are given in Table 1 together with corresponding references.

The dynamics is obtained as the solution of the Liouville-von Neumann equation

$$\frac{\partial}{\partial t}\rho = -\frac{i}{\hbar}\{H, \rho\}_- + \mathcal{L}_{a,\kappa}\rho + \mathcal{L}_{|G\rangle\langle X|,\gamma_X}\rho + \mathcal{L}_{|G\rangle\langle D|,\gamma_D}\rho \quad (12)$$

with the commutator $\{A, B\}_-$ of operators A and B. We treat the phonon Hamiltonian in a numerically exact way based on a quasi-adiabatic path-integral (QUAPI) formalism.[73,108–111] By numerically exact we denote a solution that depends only on the time discretization and the memory length as the sole convergence parameters. Beyond these two convergence parameters, no approximations enter the solution for the QD–cavity dynamics.

Physically, the phonon influence is fully captured by the phonon spectral density $J(\omega) = \sum_q |\gamma_q|^2\delta(\omega - \omega_q)$. Assuming harmonic confinement and a linear dispersion $\omega_q = c_s|\mathbf{q}|$ with sound velocity c_s, the spectral density reads

$$J(\omega) = \frac{\omega^3}{4\pi^2\rho_D\hbar c_s^5}\left(D_e e^{-\omega^2 a_e^2/(4c_s^2)} - D_h e^{-\omega^2 a_h^2/(4c_s^2)}\right)^2 \quad (13)$$

where we have considered deformation potential coupling which is usually the dominant coupling mechanism.[85] Here, ρ_D is the density of the material, D_e (D_h) the electron (hole) deformation potential, and a_e (a_h) the electron (hole) confinement radius, listed in Table 1.

4. Buffering Protocol

4.1. General Idea

We propose a protocol to buffer a single cavity photon deterministically using the Λ-type three-level system described in Section 3. Initially, we assume the QD to be in its ground state $|G\rangle$ and one photon to be present in the cavity, that is, the initial state of the QD–cavity dynamics is $|G, 1\rangle$ (cf., **Figure 2**), where we have introduced the notation $|\chi, n\rangle$ for the QD–cavity product space with $\chi \in \{G, X, D\}$ and the photon number n. Due to the QD–cavity coupling, the cavity photon is absorbed into the bright state $|X\rangle$ after half a coherent Rabi oscillation. Then, the dark state $|D\rangle$ is prepared using a recently proposed protocol relying on the optical Stark shift.[41] The transfer of the excitation from the bright to
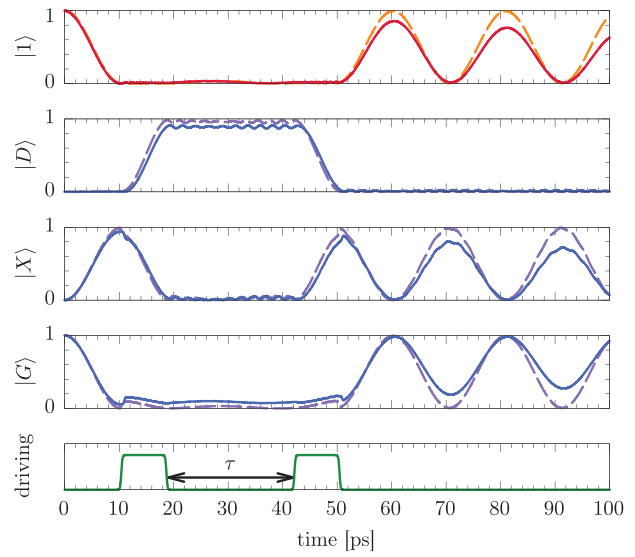
Figure 2. A single cavity photon is stored in the dark exciton state of the QD using a first writing AC-Stark pulse (bottom panel). The occupations of the ground state $|G\rangle$, the bright exciton $|X\rangle$, the dark exciton $|D\rangle$, and the 1-photon Fock state $|1\rangle$ are depicted: ideal case without phonons and losses (dashed lines); including radiative and cavity loss effects (solid lines). A second readout AC-Stark pulse retrieves the single photon. The time between the pulses is the buffer time τ.

the dark state is triggered deterministically using an off-resonant AC-Stark pulse, which shifts the bright state energy such that the bright and dark states are effectively in resonance. The pulse duration is chosen such that exactly half a Rabi oscillation between the two exciton states is possible.

To present a physically clear picture of the processes involved in the buffering scheme, we use rectangular pulses with smoothed edges for the AC-Stark pulse envelopes, following ref. [41]

$$f_{ACS}(t) = \frac{f_0}{(1 + e^{-\alpha(t-t_{on})})(1 + e^{-\alpha(t_{ACS}-(t-t_{on}))})} \quad (14)$$

Here, α determines the rise time of the pulse, which we set to 10 ps^{-1}, t_{on} is the switch-on time, and t_{ACS} the pulse duration. The pulse amplitude f_0 is determined by the effective dark-bright splitting δ_{eff}, which needs to be bridged, and the pulse duration t_{ACS} by the oscillation frequency J.

During the pulse, when the amplitude is essentially f_0, the induced optical Stark shift is

$$\Delta E_{Stark} = \frac{\hbar}{2}\left(\sqrt{\Delta\omega_{AX}^2 + f_0^2} - \Delta\omega_{AX}\right) \quad (15)$$

for $\Delta\omega_{AX} > 0$.[41] By setting $\Delta E_{Stark} = \delta_{eff}$, the pulse amplitude necessary to bridge the dark-bright splitting is determined to be

$$f_0 = \sqrt{\left(2\frac{\delta_{eff}}{\hbar} + \Delta\omega_{AX}\right)^2 - \Delta\omega_{AX}^2} \quad (16)$$

The length t_{ACS} of the pulse has to correspond to half a Rabi oscillation between the two exciton states mediated by the spin-

**ADVANCED
SCIENCE NEWS**

www.advancedsciencenews.com

**ADVANCED
QUANTUM
TECHNOLOGIES**

www.advquantumtech.com

flip coupling[41]

$$t_{\text{ACS}} = \frac{2\pi\hbar}{2\sqrt{J^2 + \left(\delta_{\text{eff}} - \Delta E_{\text{Stark}}\right)^2}} \qquad (17)$$

which simplifies to $t_{\text{ACS}} = \pi\hbar/J$ for $\Delta E_{\text{Stark}} = \delta_{\text{eff}}$.

This leaves only the detuning with respect to the bright exciton frequency $\Delta\omega_{\text{AX}}$ as a free parameter. For a dark-bright splitting in the order of a meV, it has been shown that a detuning of $\Delta\omega_{\text{AX}} = 15$ meV is favorable for the transfer of the excitation from the bright to the dark state.[41]

In an ideal system without losses and decoherence, the excitation is expected to stay in the dark state indefinitely. When including loss effects, it is important to note the different orders of magnitude of the dark and bright exciton decay rates. Since the dark state is not optically active, it is a metastable state. This is reflected in its decay rate γ_D being about two orders of magnitude smaller than the radiative decay rate γ_X of the bright state (cf., Table 1). Therefore, the dark state is a good candidate for storing the photon in a realistic, lossy system. The release of the photon is facilitated by the reverse process with a second AC-Stark pulse.

The time evolution of this protocol in the ideal case (without taking phenomenological losses or phonons into account) is presented in Figure 2 (dashed lines), which shows the occupation of the three states together with the occupation of the 1-photon state and the applied laser pulses as functions of time. The dynamics behaves as predicted by the writing scheme described above. Indeed, the occupation of the dark state after the first writing pulse is close to unity. Small-amplitude oscillations appear due to the residual coupling to the bright state, which depend both on the coupling J and the splitting δ_{eff} between the bright and the dark state.

To release the photon after the buffering time τ (23.5 ps in the example shown in Figure 2), a second readout AC-Stark pulse is required (cf., bottom panel of Figure 2). When the excitation is transferred back to the single-photon state, Rabi oscillations between the cavity mode and the bright exciton are observed. These oscillations are undamped in the ideal case, where no phonon coupling and no phenomenological loss processes are considered (cf., dashed lines in Figure 2). The maximum occupation of the 1-photon state $|1\rangle$ is 99.95 %, implying a close to perfect writing and readout of the buffered single photon in the ideal case.

5. Storage Performance

The key quantity of interest in a buffering scheme is the retrievable percentage of the stored photon after the buffering time τ. Therefore, we here discuss the dependence of this captured 1-photon occupation on the buffering time τ and various system parameters, including the dark-bright coupling J, the splitting δ_{eff}, and the temperature T. An example of the influence of phenomenological losses on the buffering scheme is shown in Figure 2b (solid lines). We find that the scheme is degraded and here we quantify the amount of storage which is still achievable. Since damped Rabi oscillations between the bright exciton and the cavity occur in the protocol proposed in Section 4 after the readout AC-Stark pulse when including phenomenological losses, we take the maximum captured 1-photon occupation (C1PO) after
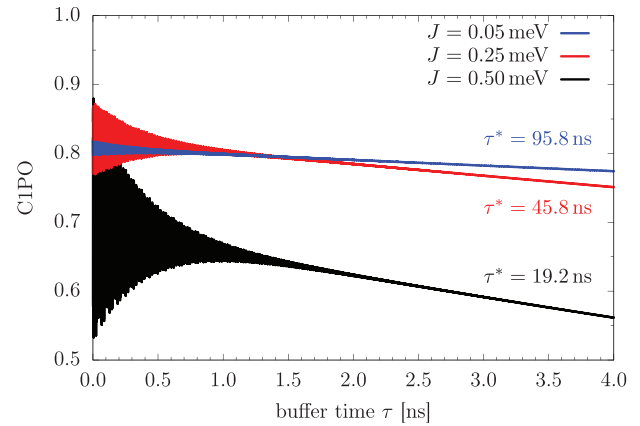
Figure 3. The maximum captured 1-photon occupation (C1PO) after the second AC-Stark pulse as a function of the buffering time τ, that is, the delay time between the two pulses. The dependence is shown for different coupling strengths J between the bright and the dark state. Labels indicate the decay time τ^* extracted from fitting an exponential function to the corresponding curve (cf., main text for detailed explanation).

the readout pulse as a measure of the retrievable percentage of the stored photon.

5.1. Influence of the Dark-Bright Coupling J

Figure 3 shows the dependence of the C1PO on the buffering time τ, that is, the delay time between the two AC-Stark pulses. These calculations are performed considering phenomenological losses, that is, bright and dark exciton decay and cavity losses, but without taking phonons into account. The red line corresponds to the coupling $J = 0.25$ meV. After initial oscillations, the C1PO decreases exponentially. The oscillations are a direct consequence of the dark-bright coupling with strength J, which is off-resonant due to the dark-bright splitting δ_{eff}. This off-resonance leads to low-amplitude high-frequency oscillations of the dark state occupation in between the writing and readout pulses (cf., Figure 2). When the second AC-Stark pulse arrives during a minimum of this oscillation, the corresponding value of the C1PO also becomes minimal.

The damping of these oscillations and the subsequent exponential decay shown in Figure 3 is a result of the decay of the dark state $|D\rangle$. While its intrinsic decay rate γ_D corresponds to a lifetime of 100 ns, the overall effective decay of the dark state depends not only on this decay time, but also on the mixing between the dark and the bright state due to their residual off-resonant coupling. Since the admixture of the bright state decays on the much shorter time scale of $\gamma_X^{-1} = 0.4$ ns, the combined effective decay time of the dark state becomes much faster (cf., analytical discussion in Appendix A).

Fitting an exponential function of the form

$$\text{C1PO}_{\text{fit}}(\tau) = c\, e^{-\tau/\tau^*} \qquad (18)$$

to C1PO(τ) in Figure 3 using the scaling constant c and the decay time τ^* as free parameters, one obtains a decay time of $\tau^* = 45.8$ ns (cf., red line in Figure 3). This value agrees well with the effective decay time of the dark state as derived in the

**ADVANCED
SCIENCE NEWS**

www.advancedsciencenews.com

**ADVANCED
QUANTUM
TECHNOLOGIES**

www.advquantumtech.com

Figure 4. The dependencies of the decay time τ^* and the C1PO at $\tau = 0$ on the effective splitting δ_{eff} between the dark and bright state [panels (a) and (b)] without taking phonons into account and on the temperature T [panels (c) and (d)] including phonon effects. The red soli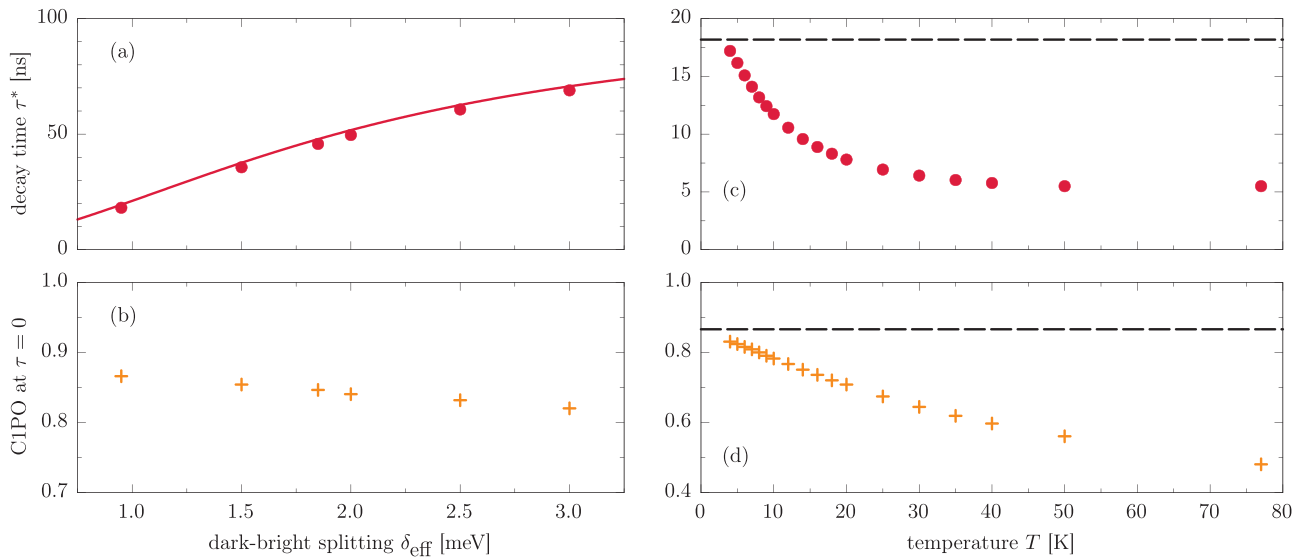d line in panel (a) is the approximate analytical prediction from Equation (19). For the temperature dependent study, the splitting is set to $\delta_{\mathrm{eff}} = \delta_{\mathrm{XD}} = 0.95$ meV.

appendix [cf., also Equation (19)], corroborating the conclusion that the storage performance between writing and readout only depends on the decay of the dark state $|D\rangle$.

Increasing J while keeping all the other parameters fixed, yields a shorter decay time τ^* (cf., black line in Figure 3) and thus a worse performance of the storage protocol. The reason is the increased oscillation amplitude between $|D\rangle$ and $|X\rangle$ stemming from the larger dark-bright coupling. Therefore, the interaction with the faster-decaying bright state is more effective. The higher oscillation amplitude is reflected in the larger initial oscillation amplitude of C1PO. The reverse argument holds for a smaller coupling strength J and indeed for $J = 0.05$ meV (cf., blue line in Figure 3) $\tau^* = 95.8$ ns is already close to the lifetime of 100 ns of the dark exciton without exchange coupling to the bright exciton.

Overall, decay times on the order of a few tens of ns suggest a high storage performance. In comparison, a single photon inside a high-Q cavity with a quality factor of 2.68×10^5,[68] corresponding to our value of κ (cf., Table 1), has a decay time of $\kappa^{-1} = 118$ ps. Therefore, the buffering protocol presented here facilitates a storage time roughly two orders of magnitude longer.

Note that changing the dark-bright coupling J experimentally means that the location of the Mn atom r_{Mn} needs to be changed, thus requiring different QD samples. Changing the Mn position also changes the shifts induced by the carrier-Mn Ising terms. Therefore, an additional magnetic field in Faraday configuration would be necessary to keep δ_{eff} constant (cf., Equation (5)).

5.2. Influence of the Dark-Bright Splitting δ_{eff}

In the previous section, it became clear that the main loss channel during the storage time is the effective decay of the dark state. This in turn depends on the residual coupling to the bright state, which is determined by J and δ_{eff}. In this section, we analyze the influence of the latter by repeating the calculations of C1PO(τ)

by varying δ_{eff} and fitting Equation (18) to the resulting curves, in analogy to Figure 3. We keep the dark-bright coupling fixed at $J = 0.25$ meV.

It is instructive to investigate the dependence of the decay time τ^* on the effective dark-bright splitting δ_{eff} shown in **Figure 4**a. We note that while this analysis is a theoretical parameter study and in principle would require to analyze several QDs, it could also be performed on the same QD by applying an external magnetic field in Faraday configuration with magnitude B_z to control δ_{eff} (cf., Equation (5)).

We vary the splitting around the value of $\delta_{\mathrm{eff}} = 1.85$ meV.[65,66] The corresponding decay time τ^* is the same as the one obtained from the red line in Figure 3. At constant J, a higher splitting means that the residual coupling of the dark to the bright state is weaker. This closes the corresponding radiative loss channel more and more, such that τ^* converges to the intrinsic decay time of the dark state $\gamma_D^{-1} = 100$ ns. The opposite argument holds for smaller splittings. Without any splitting, the two exciton states would perform coherent full-amplitude Rabi oscillations with a frequency corresponding to J, such that the radiative decay channel would diminish the storage performance maximally.

Assuming $g \ll \delta_{\mathrm{eff}}$ and $J \ll \delta_{\mathrm{eff}}$, which holds well for the parameters considered in Figure 4a, an analytical approximation of the following form can be derived (for a detailed derivation, see Appendix A):

$$\tau^*(\delta_{\mathrm{eff}}) = \left[\left(\frac{J}{2\delta_{\mathrm{eff}}} \right)^2 (\gamma_X - \gamma_D) + \gamma_D \right]^{-1} \qquad (19)$$

This function is plotted in **Figure 4**a as a red solid line, reproducing the numerically obtained data well.

To analyze the performance of the writing and reading process separately from the losses during storage, we take the C1PO for $\tau = 0$ as a measure, that is, the writing and readout pulses merge
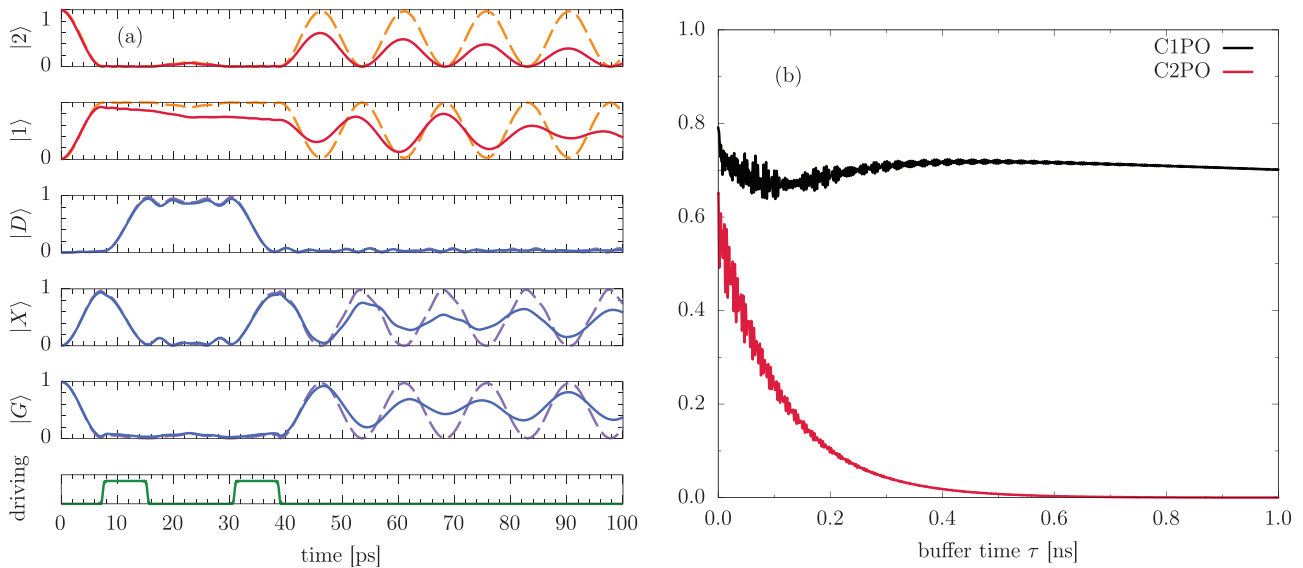
**ADVANCED
SCIENCE NEWS**

www.advancedsciencenews.com

**ADVANCED
QUANTUM
TECHNOLOGIES**

www.advquantumtech.com

Figure 5. a) Same protocol as in Figure 2, but for an initial QD–cavity state of $|G, 2\rangle$. While one of the photons is stored in the dark state, the remaining one can leave the cavity, when cavity losses are taken into account. Ideal case without phonons and losses (dashed lines); including radiative and cavity loss effects (solid lines) b) The maximum captured photon occupation after the second AC-Stark pulse as a function of the buffering time τ. Here, both phenomenological loss effects and the phonon influence at $T = 4$ K are taken into account.

to a single pulse of length $2t_{ACS}$. This value indicates, what percentage of the initially present photon can be retrieved after writing it to the dark state and immediately reading it out again. Note that due to the initial oscillations of C1PO(τ) (cf., data shown in Figure 3), the fit parameter c in Equation (18) does not necessarily correspond to the value of C1PO($\tau = 0$).

The results are shown in Figure 4b. Overall, the losses during writing and readout are restricted to values between 10 % and 20 %, originating from the loss rates γ_X and κ.

5.3. Temperature Dependence

Including the coupling of both the bright and the dark exciton states to LA phonons as described by Equation (9) leads to a faster decay of the initial oscillations of C1PO(τ) and a faster subsequent exponential decay. We perform this analysis for a dark–bright splitting of $\delta_{eff} = \delta_{XD} = 0.95$ meV, that is, for the intrinsic splitting due to the electron-hole exchange, with a coupling of $J = 0.25$ meV.

The resulting decay times τ^* and values of C1PO($\tau = 0$) are shown in Figure 4c and d, respectively. The phonon-free results are marked by dashed black lines. At $T = 4$ K, the decay time is close to its phonon-free counterpart. With rising temperature, though, the decay times become drastically shorter. At $T = 77$ K, it is only roughly a quarter of the phonon-free value. The reason is the asymmetry of phonon absorption and emission at low temperatures that vanishes at higher temperatures. During storage, the state $|D, 0\rangle$ is mostly occupied. The state $|G, 1\rangle$ lies $\delta_{eff} = 0.95$ meV above it and thus cannot be reached by phonon emission, which is predominant at low temperatures. In contrast, at higher temperatures, δ_{eff} can be bridged by phonon absorption. Thus, an additional decay channel of the dark state $|D, 0\rangle$ opens during storage. Reducing the residual coupling during storage

by means of smaller J or a δ_{eff} much larger than the maximum of the phonon spectral density should therefore weaken the phonon influence, too.

The losses due to writing and readout are also hardly influenced at low temperatures, while they become stronger with rising T. This means that the preparation of the dark state during writing is already incomplete. The reason lies in the fact that the phonon interaction dampens the Rabi oscillations between the bright state and the cavity to an extent that already the transfer from the single-photon state to the bright exciton (before the writing pulse) is incomplete.

6. Storage of a Single Photon Out of the State $|n\rangle$ with $n > 1$

We have demonstrated the buffering capacity of our protocol concerning a single-photon state. Now, the question arises how it performs, when higher-order Fock states are present in the cavity. To this end, we consider the state $|G, 2\rangle$ as the initial value of the QD–cavity system and buffer one of the two photons present in the cavity using the presented protocol. The occupation dynamics is shown in **Figure 5**a for a fixed $\tau = 15.5$ ps. The analysis is performed for $J = 0.25$ meV and $\delta_{eff} = \delta_{XD} = 0.95$ meV as before. Dashed lines show the ideal case, while solid lines depict the case including phenomenological losses.

We consider both the C1PO and the captured 2-photon occupation (C2PO) after the buffering time τ in Figure 5b (black and red lines, respectively). All loss processes and the phonon influence at $T = 4$ K are taken into account in these results. The C2PO decays exponentially. The rate corresponds exactly to the cavity loss rate κ. Since one of the two initially present photons is stored in the dark state, the remaining single photon can leave the cavity via the cavity loss channel. Retrieving the other photon from the dark state and recombining it with the remaining one to yield the

**ADVANCED
SCIENCE NEWS**

www.advancedsciencenews.com

**ADVANCED
QUANTUM
TECHNOLOGIES**

www.advquantumtech.com

initial Fock state $|2\rangle$ is only possible, when the remaining one has not left the cavity yet.

Nonetheless, the effective buffering of the 2-photon Fock state outperforms the case, where the state $|2\rangle$ decays without using a storage scheme. The reason is the fact that the Fock state $|n\rangle$ decays with an effective rate of $n\kappa$. Therefore, our single-photon buffering protocol can reduce this effective rate to $(n-1)\kappa$, as shown here for the case $n = 2$. Meanwhile, the dependence of the C1PO on the buffering time corresponds again to the effective lifetime of the dark state of about ~ 20 ns. Interestingly, the dependence of the C1PO on τ is, even when disregarding the high-frequency oscillations in the beginning, nonmonotonous. The reason is the photon that remains in the cavity: the Rabi frequency of the oscillations between the bright state and the cavity depends on the number of photons present in the cavity. Since the frequencies for the different photon numbers are incommensurable, changes in the amplitude and therefore the nonmonotonicity of the C1PO are the consequence.

7. Toward Experimental Realization

To present a clear and well understandable physical picture of the buffering scheme, we used rectangular pulses with smoothed edges as model AC-Stark pulses [cf., Equation (14)]. While such pulses can be generated using fast electro-optical modulators to cut the desired envelopes out of a continuous wave laser,[41] the rise time of $1/\alpha = 0.1$ ps assumed in Section 4.1 in combination with the pulse length necessary for the protocol is out of reach with current state-of-the-art equipment.[41] Experimentally, it is a far lesser challenge to use pulses with Gaussian envelopes.

The AC-Stark pulses are needed for the excitation transfer from the bright to the dark state for the writing and vice versa for the readout procedure. Therefore, we compare the storage capacity of differently shaped pulses by using the maximum occupation of the dark state $|D\rangle$ after the first (writing) pulse (cf., Figure 2) as a target quantity in the following. Note that any losses experienced during writing occur again at readout, thus influencing the C1PO two times. Nonetheless, the pulse shape should not have any influence on the decay time τ^* during storage, since there are no pulses in the time interval between writing and readout.

Using Gaussian pulses of the form

$$f_{\text{ACS}}(t) = \frac{\Theta}{\sqrt{2\pi}\,\sigma} e^{-\frac{(t-t_0)^2}{2\sigma^2}} \tag{20}$$

three parameters have to be determined: the pulse area Θ, the standard deviation σ, which is connected to the full width at half maximum via $\text{FWHM} = 2\sqrt{2\ln 2}\,\sigma$, and the time t_0, where the maximum of the pulse occurs. While the three parameters f_0, t_{ACS}, and t_{on} can be determined from analytical considerations for rectangular pulses from ref. [41], predicting an optimal set of Gaussian pulse parameters is not straightforward. Therefore, we numerically search for the maximum occupation of $|D\rangle$ in the parameter space spanned by Θ, σ, and t_0 by discretizing all three parameters. At $T = 4$ K for example, this optimum is given by $\Theta = 33.77\pi$, $\text{FWHM} = 7.14$ ps, and $t_0 = 15.01$ ps. We perform this optimization for the parameters used in the last two sections, namely $J = 0.25$ meV and $\delta_{\text{eff}} = \delta_{\text{XD}} = 0.95$ meV.
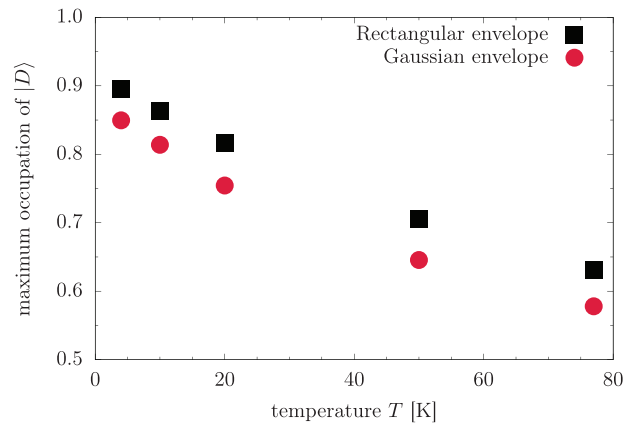
Figure 6. The maximum occupation of the dark exciton $|D\rangle$ after the storage pulse depending on temperature. Pulses with rectangular envelope are compared with Gaussian pulses.

Figure 6 shows the results depending on the temperature T. Although the rectangular pulses consistently outperform the Gaussian ones, the loss in occupation due to the experimentally easier to implement Gaussian shape is only around 5 percentage points for all considered temperatures. Therefore, the presented buffering protocol also works with Gaussian instead of rectangular pulses. This provides a path to an experimental realization in the near future.

Finally, let us comment on the usage of a semimagnetic QD for this protocol. The dark-bright coupling provided by the Mn atom is crucial for the operation of the protocol. The advantage of the Mn doping is that the dark-bright interaction is provided by an intrinsic degree of freedom of the QD, thus pointing the way toward creating compact on-chip devices. Nonetheless, this coupling could also be provided by an additional external magnetic field in Voigt configuration without using the Mn atom as a mediator.[41] Therefore, our proposed storage protocol should in principle also work in nonmagnetic QDs, but the controlled application of a magnetic field only to the buffering device could be obstructive in miniaturized circuits containing several components.

8. Conclusion

We proposed a protocol to deterministically write and read a single photon in a QD–cavity system. Assuming a CdTe QD isoelectrically doped with a single Mn ion yields a Λ-type three-level system consisting of a ground state and two exciton states, one optically active bright state and one that is dipole dark. The storage protocol relies on a coherent transfer of the photon occupation to the bright exciton due to Rabi oscillations. Then, an AC-Stark pulse shifts the bright state to be in resonance with the dark exciton. A coherent excitation transfer during the length of the pulse prepares the dark state, which due to its optical inactivity is a metastable state with long lifetime. The readout procedure is exactly the reverse process.

We analyzed the influence of the dark–bright coupling strength J and the effective dark-bright splitting δ_{eff} on the performance of the protocol as well as its dependence on temperature. During storage in the dark state, its residual coupling

ADVANCED
SCIENCE NEWS
www.advancedsciencenews.com

ADVANCED
QUANTUM
TECHNOLOGIES
www.advquantumtech.com

to the bright state and thus to faster loss channels is controlled by J and δ_{eff}. Reducing this residual coupling by decreasing J or increasing δ_{eff} leads to a better overall performance of the buffering scheme. At rising temperatures, the phonon environment acts on the coupling between the bright state and the cavity. Thus, an additional loss channel during storage has to be considered, which again can be influenced by adjusting the residual coupling of the dark to the bright exciton. Furthermore, phonons have a rather strong influence on the writing and readout procedure. At high enough temperatures, already the transfer of the photon to the bright exciton before writing becomes incomplete.

Nonetheless, for all considered parameter sets the overall storage time as measured by τ^* ranges from a few to tens of ns. Thus, it is two orders of magnitude longer than the lifetime of a photon in a high-Q cavity with a quality factor of $2.68 \cdot 10^5$.[68]

Furthermore, we have shown that the proposed scheme can store a single photon out of a higher-order Fock state $|n\rangle$ with $n > 1$. Thus, the lifetime of the state $|n\rangle$, which is $(n\kappa)^{-1}$ in a cavity with loss rate κ, can be extended to $[(n-1)\kappa]^{-1}$ (for $\gamma_{\text{D}} \ll \kappa$).

Finally, we discussed the possibility of using Gaussian pulses for the buffering protocol instead of rectangular ones, which are experimentally out of reach with current equipment for the pulse characteristics needed for the protocol. For optimal pulse parameters, Gaussian pulses can be used successfully. Pulses of rectangular shape are only ≈ 5 percentage points better concerning the dark state occupation after the writing procedure.

Thus, we expect the proposed scheme to be realizable with state-of-the-art equipment. After QDs have long been discussed as on-demand single-photon sources, this work paves the way for them to also be used as storage components. A main advantage of using magnetically doped QDs is that no external magnetic field is necessary. Such a QD buffering device for single photons could serve as a building block in more complex QD quantum information processing devices.

Appendix A: Derivation of the Effective Decay Rate

Here, we give a brief derivation of the analytic equation given for the effective decay rate in Equation (19). In the basis $\{|D, 0\rangle, |X, 0\rangle, |G, 1\rangle\}$, the Hamiltonian H, describing the coherent part of the system dynamics during the storage time, is given by:

$$H = \begin{pmatrix} -\delta_{\text{eff}} & -\frac{1}{2}J & 0 \\ -\frac{1}{2}J & 0 & \hbar g \\ 0 & \hbar g & 0 \end{pmatrix} \tag{A1}$$

The formal expression for any of the three eigenstates $|\lambda\rangle$ of H is

$$|\lambda\rangle = \mathcal{N}_\lambda \left\{ |D, 0\rangle - \frac{J}{2E_\lambda \left[1 - \left(\frac{\hbar g}{E_\lambda} \right)^2 \right]} \left[|X, 0\rangle + \frac{\hbar g}{E_\lambda} |G, 1\rangle \right] \right\} \tag{A2}$$

where $\mathcal{N}_\lambda$ is a normalization constant and E_λ is the corresponding eigenenergy. In the situation considered here, both coupling constants of the model are much smaller than the effective dark-bright splitting, that is, $J/(2\delta_{\text{eff}}), \hbar g/\delta_{\text{eff}} \ll 1$. Therefore the energetically lowest eigenstate $|d\rangle$ has an energy $E_d \approx -\delta_{\text{eff}}$, which is on the order of the dark-bright splitting, and is thus associated with the dark exciton. Furthermore, the contribution

of the state $|G, 1\rangle$ to $|d\rangle$ is then on the order $J\hbar g/\delta_{\text{eff}}^2$, cf., Equation (A2), and can be neglected. In other words, this means that the coupling to the cavity mode has only a negligible impact on this eigenstate and $|d\rangle$ can in good approximation be written as the energetically lower eigenstate of the upper left 2×2-matrix of H:

$$|d\rangle = c_{\text{D}}|D, 0\rangle + c_{\text{X}}|X, 0\rangle \tag{A3a}$$

$$c_{\text{X}} = \frac{J}{\sqrt{J^2 + \left(\delta_{\text{eff}} + \sqrt{\delta_{\text{eff}}^2 + J^2} \right)^2}}; \qquad c_{\text{D}} = \sqrt{1 - c_{\text{X}}^2} \tag{A3b}$$

$$E_d = -\frac{1}{2} \left(\delta_{\text{eff}} + \sqrt{\delta_{\text{eff}}^2 + J^2} \right) \tag{A3c}$$

Because $|d\rangle$ is strongly associated with the dark exciton state $|D, 0\rangle$ the decay of the excitation during the storage time is determined by the effective decay rate γ_{eff} of this eigenstate. Considering the loss processes via the three Lindblad superoperators $\mathcal{L}_{a,\kappa}$, $\mathcal{L}_{|G\rangle\langle X|, \gamma_X}$, and $\mathcal{L}_{|G\rangle\langle D|, \gamma_{\text{D}}}$ leads to a contribution

$$\frac{\partial}{\partial t} \rho_d = -\left(c_{\text{X}}^2 \gamma_X + c_{\text{D}}^2 \gamma_{\text{D}} \right) \rho_d = -\gamma_{\text{eff}} \, \rho_d \tag{A4}$$

in the dynamical equation for the occupation $\rho_d = \langle d|\rho|d\rangle$ of the state $|d\rangle$. Keeping only terms up to the second order in the small parameter $J/(2\delta_{\text{eff}})$ yields

$$\gamma_{\text{eff}} \approx \left(\frac{J}{2\delta_{\text{eff}}} \right)^2 \gamma_X + \left[1 - \left(\frac{J}{2\delta_{\text{eff}}} \right)^2 \right] \gamma_{\text{D}} \tag{A5}$$

Consequently, the corresponding decay time of the stored excitation is given by $\tau^* = \gamma_{\text{eff}}^{-1}$, which directly leads to the analytic expression given in the main text.

Conflict of Interest

The authors declare no conflict of interest.

Data Availability Statement

The data that support the findings of this study are available from the corresponding author upon reasonable request.

**ADVANCED
SCIENCE NEWS**

www.advancedsciencenews.com

**ADVANCED
QUANTUM
TECHNOLOGIES**

www.advquantumtech.com

[1] A. J. Ramsay, *Semicond. Sci. Technol.* **2010**, *25*, 103001.

[2] A. Greilich, R. Oulton, E. A. Zhukov, I. A. Yugova, D. R. Yakovlev, M. Bayer, A. Shabaev, A. L. Efros, I. A. Merkulov, V. Stavarache, D. Reuter, A. Wieck, *Phys. Rev. Lett.* **2006**, *96*, 227401.

[3] M. Kroner, K. M. Weiss, B. Biedermann, S. Seidl, S. Manus, A. W. Holleitner, A. Badolato, P. M. Petroff, B. D. Gerardot, R. J. Warburton, K. Karrai, *Phys. Rev. Lett.* **2008**, *100*, 156803.

[4] M. V. G. Dutt, J. Cheng, B. Li, X. Xu, X. Li, P. R. Berman, D. G. Steel, A. S. Bracker, D. Gammon, S. E. Economou, R.-B. Liu, L. J. Sham, *Phys. Rev. Lett.* **2005**, *94*, 227403.

[5] K. D. Greve, D. Press, P. L. McMahon, Y. Yamamoto, *Rep. Prog. Phys.* **2013**, *76*, 092501.

[6] W. B. Gao, A. Imamoglu, H. Bernien, R. Hanson, *Nat. Photonics* **2015**, *9*, 363.

[7] E. M. Purcell, H. C. Torrey, R. V. Pound, *Phys. Rev.* **1946**, *69*, 37.

[8] K. Hennessy, A. Badolato, M. Winger, D. Gerace, M. Atatüre, S. Gulde, S. Fält, E. L. Hu, A. Imamoğlu, *Nature* **2007**, *445*, 896.

[9] H. Takesue, N. Matsuda, E. Kuramochi, W. J. Munro, M. Notomi, *Nat. Commun.* **2013**, *4*, 2725.

[10] W. Liu, B. Romeira, M. Li, R. S. Guzzon, E. J. Norberg, J. S. Parker, L. A. Coldren, J. Yao, *J. Lightwave Technol.* **2016**, *34*, 3466.

[11] S. Clemmen, A. Farsi, S. Ramelow, A. L. Gaeta, *Opt. Lett.* **2018**, *43*, 2138.

[12] Y. Lai, M. S. Mohamed, B. Gao, M. Minkov, R. W. Boyd, V. Savona, R. Houdré, A. Badolato, *Sci. Rep.* **2018**, *8*, 14811.

[13] C. Liu, Z. Dutton, C. H. Behroozi, L. V. Hau, *Nature* **2001**, *409*, 490.

[14] L. V. Hau, S. E. Harris, Z. Dutton, C. H. Behroozi, *Nature* **1999**, *397*, 594.

[15] Y. O. Dudin, L. Li, A. Kuzmich, *Phys. Rev. A* **2013**, *87*, 031801.

[16] O. Katz, O. Firstenberg, *Nat. Commun.* **2018**, *9*, 2074.

[17] H. de Riedmatten, M. Afzelius, M. U. Staudt, C. Simon, N. Gisin, *Nature* **2008**, *456*, 773.

[18] M. T. Rakher, R. J. Warburton, P. Treutlein, *Phys. Rev. A* **2013**, *88*, 053834.

[19] E. Saglamyurek, T. Hrushevskyi, L. Cooke, A. Rastogi, L. J. LeBlanc, *Phys. Rev. Res.* **2019**, *1*, 022004.

[20] D. D. M. Welakuh, A. M. Dikandé, *Opt. Commun.* **2017**, *403*, 27.

[21] T. Lundstrom, W. Schoenfeld, H. Lee, P. M. Petroff, *Science* **1999**, *286*, 2312.

[22] B. Song-Bao, T. Yan, L. Gui-Rong, L. Yue-Xia, Y. Fu-Hua, Z. Hou-Zhi, Z. Yi-Ping, *Chin. Phys. Lett.* **2003**, *20*, 1362.

[23] A. G. Winbow, A. T. Hammack, L. V. Butov, A. C. Gossard, *Nano Lett.* **2007**, *7*, 1349.

[24] A. G. Winbow, L. V. Butov, A. C. Gossard, *J. Appl. Phys.* **2008**, *104*, 063515.

[25] A. A. High, E. E. Novitskaya, L. V. Butov, M. Hanson, A. C. Gossard, *Science* **2008**, *321*, 229.

[26] A. M. Fischer, V. L. Campo, M. E. Portnoi, R. A. Römer, *Phys. Rev. Lett.* **2009**, *102*, 096405.

[27] J. Simonin, C. R. Proetto, M. Pacheco, Z. Barticevic, *Phys. Rev. B* **2014**, *89*, 075304.

[28] J. I. Climente, J. Planelles, *Appl. Phys. Lett.* **2014**, *104*, 193101.

[29] F. Tseng, E. Simsek, D. Gunlycke, *J. Phys.: Condens. Matter* **2015**, *28*, 034005.

[30] R. Johne, A. Fiore, *Phys. Rev. A* **2011**, *84*, 053850.

[31] E. Poem, Y. Kodriano, C. Tradonsky, N. H. Lindner, B. D. Gerardot, P. M. Petroff, D. Gershoni, *Nat. Phys.* **2010**, *6*, 993.

[32] M. Zieliński, *Phys. Rev. B* **2020**, *102*, 245423.

[33] J. McFarlane, P. A. Dalgarno, B. D. Gerardot, R. H. Hadfield, R. J. Warburton, K. Karrai, A. Badolato, P. M. Petroff, *Appl. Phys. Lett.* **2009**, *94*, 093113.

[34] I. Schwartz, D. Cogan, E. R. Schmidgall, L. Gantz, Y. Don, M. Zieliński, D. Gershoni, *Phys. Rev. B* **2015**, *92*, 201201.

[35] I. Schwartz, E. R. Schmidgall, L. Gantz, D. Cogan, E. Bordo, Y. Don, M. Zielinski, D. Gershoni, *Phys. Rev. X* **2015**, *5*, 011009.

[36] T. Heindel, A. Thoma, I. Schwartz, E. R. Schmidgall, L. Gantz, D. Cogan, M. Strauß, P. Schnauber, M. Gschrey, J.-H. Schulze, A. Strittmatter, S. Rodt, D. Gershoni, S. Reitzenstein, *APL Photonics* **2017**, *2*, 121303.

[37] E. R. Schmidgall, I. Schwartz, D. Cogan, L. Gantz, Y. Don, D. Gershoni, in *Quantum Dots for Quantum Information Technologies* (Ed: P. Michler), Nano-Optics and Nanophotonics, Springer International Publishing, Cham **2017**, pp. 123–164.

[38] R. Ohta, H. Okamoto, T. Tawara, H. Gotoh, H. Yamaguchi, *Phys. Rev. Lett.* **2018**, *120*, 267401.

[39] R. M. Kraus, P. G. Lagoudakis, A. L. Rogach, D. V. Talapin, H. Weller, J. M. Lupton, J. Feldmann, *Phys. Rev. Lett.* **2007**, *98*, 017401.

[40] C. Jiang, W. Xu, A. Rasmita, Z. Huang, K. Li, Q. Xiong, W.-b. Gao, *Nat. Commun.* **2018**, *9*, 753.

[41] M. Neumann, F. Kappe, T. K. Bracht, M. Cosacchi, T. Seidelmann, V. M. Axt, G. Weihs, D. E. Reiter, *Phys. Rev. B* **2021**, *104*, 075428.

[42] J. Kobak, T. Smoleński, M. Goryca, M. Papaj, K. Gietka, A. Bogucki, M. Koperski, J.-G. Rousset, J. Suffczyński, E. Janik, M. Nawrocki, A. Golnik, P. Kossacki, W. Pacuski, *Nat. Commun.* **2014**, *5*, 3191.

[43] L. Besombes, Y. Léger, L. Maingault, D. Ferrand, H. Mariette, J. Cibert, *Phys. Rev. Lett.* **2004**, *93*, 207403.

[44] M. Goryca, P. Plochocka, T. Kazimierczuk, P. Wojnar, G. Karczewski, J. A. Gaj, P. Potemski, P. Kossacki, *Phys. Rev. B* **2010**, *82*, 165323.

[45] A. Lafuente-Sampietro, H. Utsumi, H. Boukari, S. Kuroda, L. Besombes, *Phys. Rev. B* **2017**, *95*, 035303.

[46] T. Smoleński, T. Kazimierczuk, J. Kobak, M. Goryca, A. Golnik, P. Kossacki, W. Pacuski, *Nat. Commun.* **2016**, *7*, 10484.

[47] J. Kobak, A. Bogucki, T. Smoleński, M. Papaj, M. Koperski, M. Potemski, P. Kossacki, A. Golnik, W. Pacuski, *Phys. Rev. B* **2018**, *97*, 045305.

[48] D. E. Reiter, T. Kuhn, V. M. Axt, *Phys. Rev. Lett.* **2009**, *102*, 177403.

[49] M. Goryca, T. Kazimierczuk, M. Nawrocki, A. Golnik, J. A. Gaj, P. Kossacki, P. Wojnar, G. Karczewski, *Phys. Rev. Lett.* **2009**, *103*, 087401.

[50] C. Le Gall, L. Besombes, H. Boukari, R. Kolodka, J. Cibert, H. Mariette, *Phys. Rev. Lett.* **2009**, *102*, 127402.

[51] D. E. Reiter, V. M. Axt, T. Kuhn, *Phys. Rev. B* **2013**, *87*, 115430.

[52] A. Lafuente-Sampietro, H. Utsumi, H. Boukari, S. Kuroda, L. Besombes, *Appl. Phys. Lett.* **2016**, *109*, 053103.

[53] W. Pacuski, T. Jakubczyk, C. Kruse, J. Kobak, T. Kazimierczuk, M. Goryca, A. Golnik, P. Kossacki, M. Wiater, P. Wojnar, G. Karczewski, T. Wojtowicz, D. Hommel, *Cryst. Growth Des.* **2014**, *14*, 988.

[54] D. E. Reiter, T. Kuhn, V. M. Axt, *Phys. Rev. B* **2012**, *85*, 045308.

[55] S. Lüker, T. Kuhn, D. E. Reiter, *Phys. Rev. B* **2015**, *92*, 201305(R).

[56] S. Lüker, T. Kuhn, D. E. Reiter, *Phys. Rev. B* **2017**, *95*, 195305.

[57] S. Bounouar, C. de la Haye, M. Strauß, P. Schnauber, A. Thoma, M. Gschrey, J.-H. Schulze, A. Strittmatter, S. Rodt, S. Reitzenstein, *Appl. Phys. Lett.* **2018**, *112*, 153107.

[58] S. Lüker, T. Kuhn, D. E. Reiter, *Phys. Rev. B* **2017**, *95*, 195305.

[59] M. Cosacchi, J. Wiercinski, T. Seidelmann, M. Cygorek, A. Vagov, D. E. Reiter, V. M. Axt, *Phys. Rev. Research* **2020**, *2*, 033489.

[60] Y. Léger, L. Besombes, L. Maingault, D. Ferrand, H. Mariette, *Phys. Rev. Lett.* **2005**, *95*, 047403.

[61] Y. Léger, L. Besombes, L. Maingault, H. Mariette, *Phys. Rev. B* **2007**, *76*, 045331.

[62] L. Besombes, Y. Leger, J. Bernos, H. Boukari, H. Mariette, J. P. Poizat, T. Clement, J. Fernández-Rossier, R. Aguado, *Phys. Rev. B* **2008**, *78*, 125324.

[63] D. E. Reiter, V. M. Axt, T. Kuhn, *Phys. Status Solidi B* **2009**, *246*, 779.

[64] J. Fernández-Rossier, *Phys. Rev. B* **2006**, *73*, 045301.

[65] J. K. Furdyna, *J. Appl. Phys.* **1988**, *64*, R29.

[66] L. Besombes, K. Kheng, L. Marsal, H. Mariette, *Phys. Rev. B* **2002**, *65*, 121314.

2100131 (10 of 11)

**ADVANCED
SCIENCE NEWS**

www.advancedsciencenews.com

**ADVANCED
QUANTUM
TECHNOLOGIES**

www.advquantumtech.com

[67] T. Jakubczyk, W. Pacuski, T. Smoleński, A. Golnik, M. Florian, F. Jahnke, C. Kruse, D. Hommel, P. Kossacki, *Appl. Phys. Lett.* **2012**, *101*, 132105.

[68] C. Schneider, P. Gold, S. Reitzenstein, S. Höfling, M. Kamp, *Appl. Phys. B* **2016**, *122*, 19.

[69] J. McFarlane, P. A. Dalgarno, B. D. Gerardot, R. H. Hadfield, R. J. Warburton, K. Karrai, A. Badolato, P. M. Petroff, *Appl. Phys. Lett.* **2009**, *94*, 093113.

[70] L. Besombes, K. Kheng, L. Marsal, H. Mariette, *Phys. Rev. B* **2001**, *63*, 155307.

[71] China Rare Metal Material Co., Ltd., Cadmium Telluride (CdTe), http://www.china-raremetal.com/product/cadmium_telluride_cdte.htm (accessed July **2021**).

[72] S. Lüker, T. Kuhn, D. E. Reiter, *Phys. Rev. B* **2017**, *96*, 245306.

[73] M. Cygorek, A. M. Barth, F. Ungar, A. Vagov, V. M. Axt, *Phys. Rev. B* **2017**, *96*, 201201(R).

[74] J. H. Quilter, A. J. Brash, F. Liu, M. Glässl, A. M. Barth, V. M. Axt, A. J. Ramsay, M. S. Skolnick, A. M. Fox, *Phys. Rev. Lett.* **2015**, *114*, 137401.

[75] S. Bounouar, M. Müller, A. M. Barth, M. Glässl, V. M. Axt, P. Michler, *Phys. Rev. B* **2015**, *91*, 161302.

[76] The terms proportional to M_z in Equation (2)

[77] The terms proportional to $j_e M_\pm$ in Equation (2)

[78] G. Slavcheva, P. Roussignol, (eds.), *Optical Generation and Control of Quantum Coherence in Semiconductor Nanostructures*, Springer, Berlin **2010**.

[79] L. Besombes, Y. Leger, L. Maingault, D. Ferrand, H. Mariette, J. Cibert, *Phys. Rev. B* **2005**, *71*, 161307.

[80] The terms proportional to $j_h M_\pm$ in Equation (2)

[81] C. Le Gall, R. S. Kolodka, C. L. Cao, H. Boukari, H. Mariette, J. Fernández-Rossier, L. Besombes, *Phys. Rev. B* **2010**, *81*, 245315.

[82] E. Jaynes, F. Cummings, *Proc. IEEE* **1963**, *51*, 89.

[83] B. W. Shore, P. L. Knight, *J. Mod. Opt.* **1993**, *40*, 1195.

[84] P. Borri, W. Langbein, S. Schneider, U. Woggon, R. L. Sellin, D. Ouyang, D. Bimberg, *Phys. Rev. Lett.* **2001**, *87*, 157401.

[85] B. Krummheuer, V. M. Axt, T. Kuhn, *Phys. Rev. B* **2002**, *65*, 195313.

[86] V. M. Axt, T. Kuhn, A. Vagov, F. M. Peeters, *Phys. Rev. B* **2005**, *72*, 125309.

[87] D. E. Reiter, T. Kuhn, M. Glässl, V. M. Axt, *J. Phys.: Condens. Matter* **2014**, *26*, 423203.

[88] D. E. Reiter, T. Kuhn, V. M. Axt, *Adv. Phys.: X* **2019**, *4*, 1655478.

[89] P. Michler, A. Kiraz, C. Becher, W. V. Schoenfeld, P. M. Petroff, L. Zhang, E. Hu, A. Imamoglu, *Science* **2000**, *290*, 2282.

[90] C. Santori, M. Pelton, G. Solomon, Y. Dale, Y. Yamamoto, *Phys. Rev. Lett.* **2001**, *86*, 1502.

[91] C. Santori, D. Fattal, J. Vuckovic, G. S. Solomon, Y. Yamamoto, *Nature* **2002**, *419*, 594.

[92] Y.-M. He, Y. He, Y.-J. Wei, D. Wu, M. Atatüre, C. Schneider, S. Höfling, M. Kamp, C.-Y. Lu, J.-W. Pan, *Nat. Nanotechnol.* **2013**, *8*, 213.

[93] Y.-J. Wei, Y.-M. He, M.-C. Chen, Y.-N. Hu, Y. He, D. Wu, C. Schneider, M. Kamp, S. Höfling, C.-Y. Lu, J.-W. Pan, *Nano Lett.* **2014**, *14*, 6515.

[94] X. Ding, Y. He, Z.-C. Duan, N. Gregersen, M.-C. Chen, S. Unsleber, S. Maier, C. Schneider, M. Kamp, S. Höfling, C.-Y. Lu, J.-W. Pan, *Phys. Rev. Lett.* **2016**, *116*, 020401.

[95] N. Somaschi, V. Giesz, L. De Santis, J. C. Loredo, M. P. Almeida, G. Hornecker, S. L. Portalupi, T. Grange, C. Antón, J. Demory, C. Gómez, I. Sagnes, N. D. Lanzillotti-Kimura, A. Lemaître, A. Auffeves, A. G. White, L. Lanco, P. Senellart, *Nat. Photonics* **2016**, *10*, 340.

[96] L. Schweickert, K. D. Jöns, K. D. Zeuner, S. F. Covre da Silva, H. Huang, T. Lettner, M. Reindl, J. Zichi, R. Trotta, A. Rastelli, V. Zwiller, *Appl. Phys. Lett.* **2018**, *112*, 093106.

[97] L. Hanschke, K. A. Fischer, S. Appel, D. Lukin, J. Wierzbowski, S. Sun, R. Trivedi, J. Vučković, J. J. Finley, K. Müller, *npj Quantum Inf.* **2018**, *4*, 1.

[98] N. Akopian, N. H. Lindner, E. Poem, Y. Berlatzky, J. Avron, D. Gershoni, B. D. Gerardot, P. M. Petroff, *Phys. Rev. Lett.* **2006**, *96*, 130501.

[99] R. M. Stevenson, R. J. Young, P. Atkinson, K. Cooper, D. A. Ritchie, A. J. Shields, *Nature* **2006**, *439*, 179.

[100] R. Hafenbrak, S. M. Ulrich, P. Michler, L. Wang, A. Rastelli, O. G. Schmidt, *New J. Phys.* **2007**, *9*, 315.

[101] A. Dousse, J. Suffczynski, A. Beveratos, O. Krebs, A. Lemaître, I. Sagnes, J. Bloch, P. Voisin, P. Senellart, *Nature* **2010**, *466*, 217.

[102] E. del Valle, *New J. Phys* **2013**, *15*, 025019.

[103] M. Müller, S. Bounouar, K. D. Jöns, M. Glässl, P. Michler, *Nat. Photonics* **2014**, *8*, 224.

[104] A. Orieux, M. A. M. Versteegh, K. D. Jöns, S. Ducci, *Rep. Prog. Phys.* **2017**, *80*, 076001.

[105] M. Cosacchi, F. Ungar, M. Cygorek, A. Vagov, V. M. Axt, *Phys. Rev. Lett.* **2019**, *123*, 017403.

[106] S. E. Thomas, M. Billard, N. Coste, S. C. Wein, Priya, H. Ollivier, O. Krebs, L. Tazaïrt, A. Harouri, A. Lemaitre, I. Sagnes, C. Anton, L. Lanco, N. Somaschi, J. C. Loredo, P. Senellart, *Phys. Rev. Lett.* **2021**, *126*, 233601.

[107] T. Seidelmann, F. Ungar, A. M. Barth, A. Vagov, V. M. Axt, M. Cygorek, T. Kuhn, *Phys. Rev. Lett.* **2019**, *123*, 137401.

[108] N. Makri, D. E. Makarov, *J. Chem. Phys.* **1995**, *102*, 4600.

[109] N. Makri, D. E. Makarov, *J. Chem. Phys.* **1995**, *102*, 4611.

[110] A. Vagov, M. D. Croitoru, M. Glässl, V. M. Axt, T. Kuhn, *Phys. Rev. B* **2011**, *83*, 094303.

[111] A. M. Barth, A. Vagov, V. M. Axt, *Phys. Rev. B* **2016**, *94*, 125439.

Publication 9

"Two-Photon Excitation Sets Fundamental Limit to Entangled Photon Pair Generation from Quantum Emitters"

T. Seidelmann, C. Schimpf, T. K. Bracht, M. Cosacchi, A. Vagov, A. Rastelli, D. E. Reiter, and V. M. Axt.

Author contributions

The author has designed the concept of this study, has performed the numerical data generation and analysis, and has implemented the problem-specific C++ code. He has provided interpretations of the results and has written the first draft of the publication. In particular, he has performed analytic calculations that resulted in a concise estimate for the degree of entanglement and enabled a precise picture for the physical mechanism. He has organized the submission and revision of the manuscript and has written the answer to the referees.

C. Schimpf has participated in the discussion of the results and their interpretations. In particular, he has provided experimental insights on state-of-the-art entanglement measurements. He has also contributed to revisions of the draft and the answer to the referees.

T. K. Bracht and M. Cosacchi have participated in the discussion of the results and their interpretations. They have also contributed to revisions of the draft and the answer to the referees.

A. Vagov, A. Rastelli, and D. E. Reiter, have co-supervised this work. In particular, they have participated in the discussion of the results and their interpretations. They have also contributed to the optimization of the presentation, revisions of the draft, and the answer to the referees.

V. M. Axt has advised the author throughout his work as the main supervisor, has obtained the funding for this work, and has provided the practical means. He has participated in the discussion of the results and their interpretations. He has also contributed to the optimization of the presentation,

revisions of the draft, and the answer to the referees.

Two-Photon Excitation Sets Fundamental Limit to Entangled Photon Pair Generation from Quantum Emitters

T. Seidelmann,[1, *] C. Schimpf,[2] T. K. Bracht,[3] M. Cosacchi,[1] A. Vagov,[1] A. Rastelli,[2] D. E. Reiter,[3, †] and V. M. Axt[1]

[1]*Lehrstuhl für Theoretische Physik III, Universität Bayreuth, 95440 Bayreuth, Germany*
[2]*Institute of Semiconductor and Solid State Physics,*
Johannes Kepler University Linz, 4040 Linz, Austria
[3]*Institut für Festkörpertheorie, Universität Münster, 48149 Münster, Germany*

Entangled photon pairs are key to many novel applications in quantum technologies. Semiconductor quantum dots can be used as sources of on-demand, highly entangled photons. The fidelity to a fixed maximally-entangled state is limited by the excitonic fine-structure splitting. This work demonstrates that, even if this splitting is absent, the degree of entanglement cannot reach unity when the excitation pulse in a two-photon resonance scheme has a finite duration. The degradation of the entanglement has its origin in a dynamically induced splitting of the exciton states caused by the laser pulse itself. Hence, in the setting explored here, the excitation process sets a fundamental limit to the achievable concurrence for entangled photons generated in an optically excited four-level quantum emitter.

Entangled quantum states [1–3] inspired the development of applications in the fields of quantum cryptography [4–7], quantum communication [8, 9], or quantum information processing and computing [10–13]. The simplest realization of entangled qubits are entangled photon pairs. These are attractive due to their robustness against environmental decoherence [2]. In the past decades, quantum dots (QDs) have emerged as a versatile platform for the generation of polarization-entangled photon pairs in experiment [14–31] and theory [32–39] as well as for time-bin entangled photon pairs [40–42].

Their generation relies on the biexciton-exciton cascade. After the biexciton is prepared, it decays by one of two paths, cf., Fig. 1 middle panel, ideally emitting either a pair of horizontally (H) or vertically (V) polarized photons. In the ideal case of zero fine-structure splitting, the information of the chosen path (which-path information) is missing, and the resulting two-photon state

$$|\Phi_+\rangle = \frac{1}{\sqrt{2}}\left(|HH\rangle + |VV\rangle\right) \qquad (1)$$

is a maximally entangled Bell state. However, in reality, the generated state deviates from the perfect Bell state. This deviation can be quantified by the fidelity $\mathcal{F}$ [43] or the concurrence C [44], defined such that only $\mathcal{F} = 1$ or $C = 1$ corresponds to a maximally entangled Bell state.

The fine-structure splitting (FSS), i.e., an energy difference between the two exciton levels, is a major obstacle for generating perfectly entangled states. By breaking the symmetry of the system, it introduces a which-path information during the photon generation [45]. Several methods were developed to suppress the FSS [9, 18, 20, 25], resulting in entangled states with higher concurrence. From theory side, it was predicted that an initially prepared biexciton yields a maximally entangled state in the case of vanishing FSS [32, 36], even when cavity and radiative losses as well as phonons are considered.
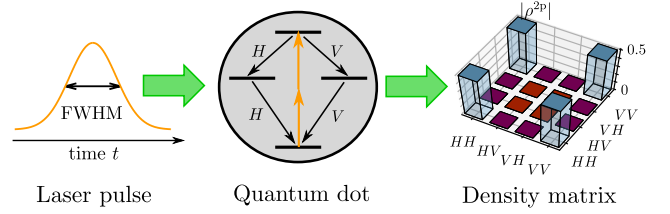
FIG. 1. A Gaussian pulse (left) with finite full-width-at-half-maximum (FWHM) excites a quantum dot. In the two-photon resonant excitation scheme, the central frequency of the laser pulse matches half of the ground state-to-biexciton transition energy. The excited quantum dot decays radiatively, following the diamond-shaped cascade. Ideally, either a pair of horizontally (H) or vertically (V) polarized photons is emitted (center), resulting in a maximally entangled state $|\Phi_+\rangle$ described by the ideal two-photon density matrix $\rho^{2\mathrm{p}}$ (right).

However, the influence of the preparation process is still under debate. Early experimental proof-of-principle studies often employed far off-resonant excitation schemes, where carriers were excited in higher QD states or the wetting layer, which subsequently relaxed into the biexciton state [16–20]. Recent state-of-the-art experiments rely on a coherent two-photon resonant excitation (TPE) scheme with typical pulse durations on the order of 10 picoseconds and light with linear polarization in the QD growth plane, and demonstrate very high degrees of entanglement [6, 24–26, 28, 29, 31, 46], because of the strongly reduced re-excitation probability [47, 48]. Nevertheless, perfectly-entangled photons have not yet been observed, and the question remains whether TPE can still be a source of entanglement degradation.

In this letter, we show that the TPE scheme employed to create the biexciton sets a fundamental limit to the obtainable concurrence. To demonstrate this, we present numerical simulations alongside analytical calculations

TABLE I. Quantum dot parameters used in the calculations.

Parameter		Value
Biexciton binding energy	E_B	4 meV
Exciton-laser detuning	Δ_{XL}	$E_B/2 = 2$ meV
Radiative decay rate exciton	γ_X	0.005 ps^{-1}
Radiative decay rate biexciton	γ_B	$2\gamma_X = 0.010$ ps^{-1}

giving a dependence of the maximally achievable concurrence as a function of the full-width-at-half-maximum (FWHM) of the exciting Gaussian laser pulse. We provide a clear physical picture how the laser introduces a which-path information that significantly reduces the achievable degree of entanglement.

We model the QD as a four-level system, cf., Fig. 1, consisting of the ground state $|G\rangle$, excitons with horizontal and vertical transition dipoles $|X_H\rangle$ and $|X_V\rangle$, and the biexciton $|B\rangle$. The FSS between the two exciton states, which is typically on the order of a few μeV, is denoted as δ and we assume that the energy of $|X_H\rangle$ is always higher than the one of $|X_V\rangle$. E_B is the biexciton binding energy, i.e., the difference between the energy of two uncorrelated excitons and the biexciton. The biexciton (An exciton) decays with a characteristic rate γ_B (γ_X) into an exciton (the ground) state. For the numerical calculations, we use parameters for typical GaAs QDs given in Tab. I.

In experiments, the concurrence is obtained from the two-photon density matrix which is reconstructed employing quantum state tomography [49]. This scheme relies on measuring polarization-resolved two-time correlation functions, where the measurement represents a statistical average over both time arguments - the real time of the first detection event and the delay time until a subsequent second one. In principle, one can restrict the averaging intervals to narrow time windows, which corresponds to selecting different subsets of photon pairs [35]. Such time filtering can be used to alleviate dephasing effects, but at the cost of a reduced photon generation. Here, the two-photon density matrix ρ^{2p} [in the basis $\{|HH\rangle, |HV\rangle, |VH\rangle, |VV\rangle\}$] is calculated based on time-integrated correlation functions, where we average over all possible real and delay times. Details on the theoretical model, the two-photon density matrix, and the concurrence can be found in the Supplemental Material [50].

It is instructive to briefly recapitulate the concurrence predicted for the initial value problem where one assumes an initially prepared biexciton. In the ideal situation of a vanishing FSS, the energy structure is completely symmetric, and the resulting two-photon state is maximally entangled. But, if the FSS is finite, the two emission paths in the biexciton-exciton cascade can be distinguished, and emitted photons with opposite polarization exhibit slightly different energies. Thus, a finite FSS in-

troduces a which-path information into the system. In the two-photon density matrix this which-path information manifests itself in a reduced coherence between the states $|HH\rangle$ and $|VV\rangle$. The corresponding concurrence can be calculated analytically, cf., Supplemental Material [50], yielding

$$C_0(\gamma_X, \delta) = \frac{1}{\sqrt{1 + \left(\frac{\delta}{\hbar\gamma_X}\right)^2}} \quad (2)$$

It depends solely on the ratio between the FSS δ and the decay rate γ_X of the exciton states. We stress that in the case of $\delta = 0$, the concurrence is unity for an initially prepared biexciton, i.e., the maximally entangled Bell state is created. In particular, it was shown that the concurrence in this case is robust against dephasing processes [32, 35, 36].

For a finite FSS, C_0 reflects the integration over a time-dependent phase oscillation of the exciton coherence during the measurement process [45]. Due to this oscillating phase, the two-photon state associated with one possible cascaded decay is

$$|\Phi_\tau\rangle = \frac{1}{\sqrt{2}} \left(|HH\rangle + e^{i\frac{\delta}{\hbar}\tau}|VV\rangle\right) \quad (3)$$

where τ is the delay time between the first (biexciton) and second (exciton) photon emission event. Averaging over all possible realizations with different delay times results in a mixed state with a reduced coherence. Note that the concurrence depends on the averaging window for the delay time in the experiment. Selecting only photon pairs in a small delay-time window results in a higher concurrence [24, 30], but one has to discard the majority of emission events. Furthermore, when the QD is embedded inside a cavity, even in the limit of a vanishing averaging window, the concurrence does not reach unity [35].

Having seen that in the limit of vanishing FSS, an initially prepared biexciton yields unity concurrence, we now consider the impact of the excitation process in the TPE scheme. Here, the biexciton is excited by a laser pulse in resonance with the two-photon biexciton transition. In the simulations, we assume a Gaussian pulse with envelope

$$\Omega(t) = \sqrt{\frac{4\ln(2)}{\pi}} \frac{\Theta}{\text{FWHM}} \exp\left[-4\ln(2)\left(\frac{t}{\text{FWHM}}\right)^2\right] \quad (4)$$

where the FWHM of the laser pulse is the central quantity of interest. Note that the width of the corresponding laser intensity $I(t) \propto \Omega^2(t)$ is characterized by FWHM/$\sqrt{2}$. To achieve a two-photon π-pulse, the pulse area Θ is determined numerically, such that the maximal biexciton occupation is obtained. The optimal value is
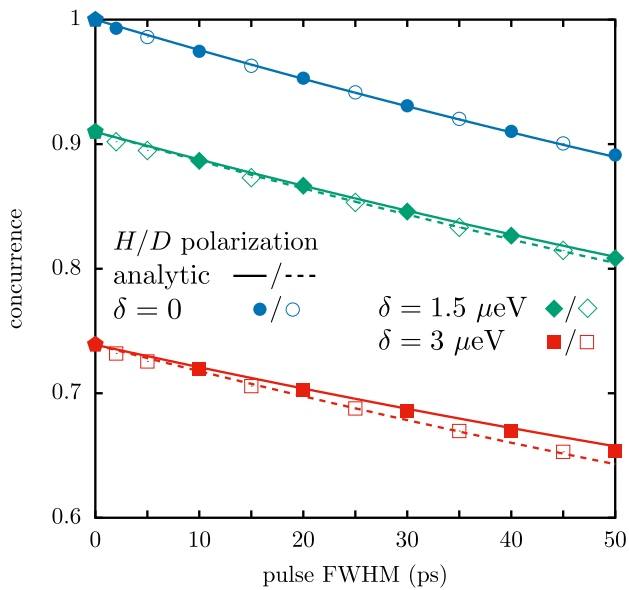
FIG. 2. Concurrence in dependence of the pulse duration, characterized by its FWHM, for two laser polarizations [horizontal (H): filled symbols and diagonal (D): open symbols] and three fine-structure splittings $\delta = 0$ (blue circles), 1.5 μeV (green diamonds), and 3 μeV (red squares). The symbols represent numerical results and lines are the analytic expression Eq. (8) [H/D polarization: solid/dashed line]. For $\delta = 0$, the results for H and D polarization are exactly the same. Data points at FWHM = 0 (pentagons) represent calculations with an initially prepared biexciton without optical excitation.

roughly

$$\Theta \approx \sqrt{\frac{E_{\mathrm{B}}\,\mathrm{FWHM}}{\hbar\sqrt{2\pi\ln(2)}}}\,\pi \tag{5}$$

cf., Supplemental Material [50]. Note that the concurrence is not sensitive to the initial occupation of the biexciton - it can reach unity also for a partially occupied biexciton state.

We start with the case of vanishing FSS, i.e., $\delta = 0$, and consider two different linear laser polarizations: (i) horizontal, i.e., the laser polarization coincides with the polarization H, and (ii) diagonal, i.e., the laser polarization has equal components in H and V. As shown in Fig. 2 (blue symbols), both laser polarizations result in the same concurrence. In contrast to the initial value problem without optical excitation, i.e., data points at FWHM = 0, the concurrence drops significantly with increasing FWHM. For a typical pulse length of 10 ps [6, 26, 29], the concurrence decreases to $C \approx 0.975$. Using a dressed state picture, we can derive (see Supplemental Material [50]) the analytic expression

$$C \approx 1 - 2f(\gamma_{\mathrm{B}}, \mathrm{FWHM}) \tag{6a}$$
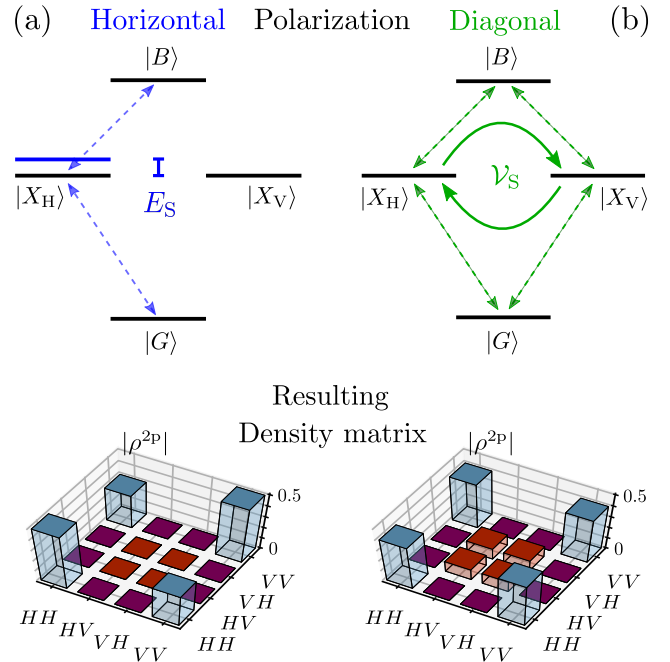
FIG. 3. Top: Sketches of the four-level system with the laser-induced effects for (a) horizontal and (b) diagonal polarization. Black lines are the unperturbed quantum dot states. Optical transitions are indicated by dashed arrows. The laser effect for horizontally polarized excitation can be interpreted as an AC Stark-shift yielding an energetic splitting E_{S}. For a diagonal polarization, the laser-induced interaction can be interpreted as a coupling between the excitons with coupling strength $\mathcal{V}_{\mathrm{S}}$. Bottom: Examples of resulting density matrices for the two polarizations.

$$f(\gamma_{\mathrm{B}}, \mathrm{FWHM}) = \frac{\gamma_{\mathrm{B}}\mathrm{FWHM}}{8}\,\exp\left[-\frac{\gamma_{\mathrm{B}}\mathrm{FWHM}}{4}\right] \tag{6b}$$

which describes the drop of concurrence with increasing FWHM well. The obtained result depends solely on the product of the FWHM and the biexciton decay rate, which can be interpreted as a measure for the number of biexciton photons that are emitted during the pulse. We stress that this drop does not originate from an increasing re-excitation probability, cf., Supplemental Material [50], i.e., the creation of additional photons is negligible.

To understand this drop in concurrence, we start with considering the excitation with horizontal (H) polarization. We recall that a reduced degree of entanglement is associated with which-path information. The only source of the latter in the TPE scheme is the laser pulse, which makes the level configuration (dynamically) asymmetric as illustrated in Fig. 3(a). Only $|X_{\mathrm{H}}\rangle$ interacts with the laser pulse, while $|X_{\mathrm{V}}\rangle$ remains unchanged. The interaction with this laser pulse introduces an AC Stark-shift for $|X_{\mathrm{H}}\rangle$, resulting in a finite energy shift $E_{\mathrm{S}} \propto \Omega^2(t)/E_{\mathrm{B}}$. For the two-photon π-pulse, this energy shift is on the

order of

$$E_S \sim \frac{\hbar\pi}{\text{FWHM}} \qquad (7)$$

cf., Supplemental Material [50]. Hence, during the pulse, the two exciton states are split by E_S. As in the case of a fixed FSS, the dynamic splitting E_S gives rise to phase oscillations of the exciton coherence until the pulse is gone. Thus, on the time-scale of the pulse, a which-path information is introduced by the TPE scheme itself. Note that for a FWHM of 10 ps, $E_S \sim 200$ μeV is one order of magnitude larger than typical FSSs. With increasing pulse length the dynamically induced splitting E_S becomes smaller but persists in a longer time window. Thus, more emitted photon pairs are affected by it, resulting in a monotonic drop of the concurrence with rising FWHM. It is instructive to consider the effect of this which-path information on the two-photon density matrix as shown in Fig. 3(a) bottom row. Similar to what occurs for a finite FSS, we observe a reduced coherence $\rho_{HH,VV}^{2p}$.

Because the reduced concurrence has been traced back to an asymmetry during the pulse, one could naively assume that using a diagonally polarized laser might result in a maximally entangled state. But numerical calculations with a diagonal polarization yield exactly the same degree of entanglement, cf., Fig. 2. Of course, when the FSS is absent, all orthogonal bases, constructed as linear combinations of the horizontally and vertically polarized exciton state, are equivalent. Consequently, all linear laser polarizations yield the same entanglement. Clearly, this applies to the basis states $|X_{D/A}\rangle := (|X_H\rangle \pm |X_V\rangle)/\sqrt{2}$, for which the system becomes identical to the one with the horizontal laser polarization.

It is nevertheless instructive to look at the interpretation of the drop in concurrence for a diagonally polarized excitation. During the laser pulse, the action of the pulse can be described as a full-amplitude (coherent) oscillation between the two different exciton states (cf., Supplemental Material [50]). Thus, if the QD decays into an exciton state via the emission of a biexciton photon already during the pulse duration, the pulse introduces an effective coupling to the other exciton. In Fig. 3(b) this coupling is denoted as $\mathcal{V}_S$. Therefore, during the pulse duration, the exciton state can change and the subsequently emitted exciton photon can have a different polarization than the prior biexciton photon. Consequently, the interaction with the laser enables the creation of two-photon states $|HV\rangle$ and $|VH\rangle$, which represent a deviation from the maximally entangled state $|\Phi_+\rangle$. This interpretation is confirmed by looking at the two-photon density matrix in Fig. 3(b), where the elements $\rho_{HV,HV}^{2p}$ and $\rho_{VH,VH}^{2p}$ become finite, causing a reduced degree of entanglement. Note that for diagonal polarization the occupations $\rho_{HH,HH}^{2p}$ and $\rho_{VV,VV}^{2p}$ have the same value

as the coherence $|\rho_{HH,VV}^{2p}|$ in contrast to the excitation with horizontal polarization where the relative amplitude of this coherence is reduced.

Thus, a diagonal laser polarization corresponds to describing the same effect in a different basis/picture. This is similar to the FSS stemming from the anisotropic exchange interaction, which can also be discussed as an interaction between circularly polarized excitons or an energetic splitting δ between linearly polarized ones. In the TPE scheme, the electromagnetic field plays the role of a tunable exchange interaction.

Finally, we analyze the combined effect of FSS and laser-induced splitting. Figure 2 shows the concurrence obtained for two finite FSSs $\delta = 1.5$ μeV (green) and 3 μeV (red) for a horizontal (H: filled symbols) and diagonal (D: open symbols) laser polarization. We remind that in the limit of a vanishing pulse duration, i.e., FWHM $\rightarrow 0$, the concurrence is given by $C_0(\gamma_X, \delta)$. Starting from this value, the concurrence drops with rising FWHM due to the laser-induced splitting. Depending on the laser polarization, this can be observed either as an additional loss of coherence (horizontal polarization) or an increase of detrimental photon states (diagonal polarization) in the two-photon density matrix, cf., Supplemental Material [50]. Because the effect of the FSS on the TPE scheme is negligible for $\delta \ll E_B$, we find only a marginal difference between the two polarizations.

In this case, the drop in concurrence is well described by the analytic expression

$$C \approx C_0(\gamma_X, \delta) \{1 - f(\gamma_B, \text{FWHM}) [1 + g(\alpha_H)]\}$$
$$- f(\gamma_B, \text{FWHM}) [1 - g(\alpha_H)] \qquad (8a)$$
$$g(\alpha_H) = \left(1 - 2\alpha_H^2\right)^2 \qquad (8b)$$

where C_0 [defined in Eq. (2)] represents the concurrence associated with an initially prepared biexciton, while f [defined in Eq. (6b)] and g capture the influence of the pulse duration and the laser polarization, respectively. The parameter α_H describes the component of the laser polarization in H direction such that the horizontal (diagonal) laser polarization corresponds to $\alpha_H = 1$ ($\alpha_H = 1/\sqrt{2}$). Note that for $\delta = 0$, this expression reduces to Eq. (6) and becomes independent of the laser polarization.

When both, FSS and laser-induced splitting, are present, the laser polarizations have a slightly different impact. The difference between the concurrence obtained for horizontal and diagonal polarization is estimated as

$$\Delta C \approx f(\gamma_B, \text{FWHM}) [1 - C_0(\gamma_X, \delta)] \qquad (9)$$

and increases with pulse duration and FSS. This implies an optimal laser polarization can be found. By analyzing Eq. (8), one finds that the horizontal polarization corresponds to the optimal choice, while diagonal polarization is the most detrimental one.

In conclusion, our analysis shows that the TPE scheme with a pulse of finite duration sets a limitation for the degree of entanglement of photon pairs due to the excitation itself. This result is supported by numerical calculations for a two-photon π-pulse as well as analytical expressions. Its generic nature is explained by an intuitive physical picture of a Stark-induced energy splitting, which introduces a which-path information, and thus, reduces the entanglement. The effect increases for longer pulses, and, in principle, disappears in the limit of instantaneous excitation. However, in this limit the excitation model and the TPE scheme become inadequate. In most practical situations, a pulse shorter than 2-3 ps produces unwanted exciton states in typical InGaAa or GaAs QDs. Consequently, while the FSS in QDs can be reduced to zero, the pulse length cannot, and this sets a fundamental upper limit for the on-demand generation of entangled photon pairs.

Our calculations accounted only for the most basic relaxation mechanisms that are present in all realizations of a four-level emitter, i.e., rates for the cascaded decay. Further influences that might affect the entanglement such as, e.g., phonons were disregarded. Our analysis thus explores an ideal situation highlighting the detrimental effect of the excitation scheme even in the absence of other destructive mechanisms.

Finally, we note that our theoretical prediction of $C \approx 0.975$ is very close to the highest experimentally achieved concurrence of 0.97(1)[26]. This may indicate that the laser-induced which-path information provides a quantitative explanation for the observed deviation from unity.

---

* Corresponding author: tim.seidelmann@uni-bayreuth.de

† Current address: Condensed Matter Theory, Department of Physics, TU Dortmund, 44221 Dortmund, Germany

[1] R. Horodecki, P. Horodecki, M. Horodecki, and K. Horodecki, "Quantum entanglement," Rev. Mod. Phys. 81, 865 (2009).

[2] A. Orieux, M. A. M. Versteegh, K. D. Jöns, and S. Ducci, "Semiconductor devices for entangled photon pair generation: a review," Rep. Prog. Phys. 80, 076001 (2017).

[3] N. Akopian, N. H. Lindner, E. Poem, Y. Berlatzky, J. Avron, D. Gershoni, B. D. Gerardot, and P. M. Petroff, "Entangled Photon Pairs from Semiconductor Quantum Dots," Phys. Rev. Lett. 96, 130501 (2006).

[4] N. Gisin, G. Ribordy, W. Tittel, and H. Zbinden, "Quantum cryptography," Rev. Mod. Phys. 74, 145 (2002).

[5] H.-K. Lo, M. Curty, and K. Tamaki, "Secure quantum key distribution," Nat. Photonics 8, 595 (2014).

[6] C. Schimpf, M. Reindl, D. Huber, B. Lehner, S. F. Covre Da Silva, S. Manna, M. Vyvlecka, P. Walther, and A. Rastelli, "Quantum cryptography with highly entangled photons from semiconductor quantum dots," Sci. Adv. 7, eabe8905 (2021).

[7] F. Basso Basset, M. Valeri, E. Roccia, V. Muredda, D. Poderini, J. Neuwirth, N. Spagnolo, M. B. Rota, G. Carvacho, F. Sciarrino, and R. Trotta, "Quantum key distribution with entangled photons generated on demand by a quantum dot," Sci. Adv. 7, eabe6379 (2021).

[8] L.-M. Duan, M. D. Lukin, J. I. Cirac, and P. Zoller, "Long-distance quantum communication with atomic ensembles and linear optics," Nature 414, 413 (2001).

[9] D. Huber, M. Reindl, J. Aberl, A. Rastelli, and R. Trotta, "Semiconductor quantum dots as an ideal source of polarization-entangled photon pairs on-demand: a review," J. Opt. 20, 073002 (2018).

[10] J.-W. Pan, Z.-B. Chen, C.-Y. Lu, H. Weinfurter, A. Zeilinger, and M. Żukowski, "Multiphoton entanglement and interferometry," Rev. Mod. Phys. 84, 777 (2012).

[11] C. H. Bennett and D. P. DiVincenzo, "Quantum information and computation," Nature 404, 247 (2000).

[12] S. C. Kuhn, A. Knorr, S. Reitzenstein, and M. Richter, "Cavity assisted emission of single, paired and heralded photons from a single quantum dot device," Opt. Express 24, 25446 (2016).

[13] A. Zeilinger, "Light for the quantum. Entangled photons and their applications: a very personal perspective," Phys. Scr. 92, 072501 (2017).

[14] O. Benson, C. Santori, M. Pelton, and Y. Yamamoto, "Regulated and Entangled Photons from a Single Quantum Dot," Phys. Rev. Lett. 84, 2513 (2000).

[15] R. M. Stevenson, R. J. Young, P. Atkinson, K. Cooper, D. A. Ritchie, and A. J. Shields, "A semiconductor source of triggered entangled photon pairs," Nature 439, 179 (2006).

[16] R. J. Young, R. M. Stevenson, P. Atkinson, K. Cooper, D. A. Ritchie, and A. J. Shields, "Improved fidelity of triggered entangled photons from single quantum dots," New J. Phys. 8, 29 (2006).

[17] R. Hafenbrak, S. M. Ulrich, P. Michler, L. Wang, A. Rastelli, and O. G. Schmidt, "Triggered polarization-entangled photon pairs from a single quantum dot up to 30 K," New J. Phys. 9, 315 (2007).

[18] A. Muller, W. Fang, J. Lawall, and G. S. Solomon, "Creating Polarization-Entangled Photon Pairs from a Semiconductor Quantum Dot Using the Optical Stark Effect," Phys. Rev. Lett. 103, 217402 (2009).

[19] A. Dousse, J. Suffczyński, A. Beveratos, O. Krebs, A. Lemaître, I. Sagnes, J. Bloch, P. Voisin, and P. Senellart, "Ultrabright source of entangled photon pairs," Na-

ture **466**, 217 (2010).

[20] A. J. Bennett, M. A. Pooley, R. M. Stevenson, M. B. Ward, R. B. Patel, A. Boyer de la Giroday, N. Sköld, I. Farrer, C. A. Nicoll, D. A. Ritchie, and A. J. Shields, "Electric-field-induced coherent coupling of the exciton states in a single quantum dot," Nat. Phys. **6**, 947 (2010).

[21] R. M. Stevenson, C. L. Salter, J. Nilsson, A. J. Bennett, M. B. Ward, I. Farrer, D. A. Ritchie, and A. J. Shields, "Indistinguishable Entangled Photons Generated by a Light-Emitting Diode," Phys. Rev. Lett. **108**, 040503 (2012).

[22] M. Müller, S. Bounouar, K. D. Jöns, M. Glässl, and P. Michler, "On-demand generation of indistinguishable polarization-entangled photon pairs," Nat. Photonics **8**, 224 (2014).

[23] R. Trotta, J. S. Wildmann, E. Zallo, O. G. Schmidt, and A. Rastelli, "Highly Entangled Photons from Hybrid Piezoelectric-Semiconductor Quantum Dot Devices," Nano Lett. **14**, 3439 (2014).

[24] R. Winik, D. Cogan, Y. Don, I. Schwartz, L. Gantz, E. R. Schmidgall, N. Livneh, R. Rapaport, E. Buks, and D. Gershoni, "On-demand source of maximally entangled photon pairs using the biexciton-exciton radiative cascade," Phys. Rev. B **95**, 235435 (2017).

[25] D. Huber, M. Reindl, Y. Huo, H. Huang, J. S. Wildmann, O. G. Schmidt, A. Rastelli, and R. Trotta, "Highly indistinguishable and strongly entangled photons from symmetric GaAs quantum dots," Nat. Commun. **8**, 15506 (2017).

[26] D. Huber, M. Reindl, S. F. Covre da Silva, C. Schimpf, J. Martín-Sánchez, H. Huang, G. Piredda, J. Edlinger, A. Rastelli, and R. Trotta, "Strain-Tunable GaAs Quantum Dot: A Nearly Dephasing-Free Source of Entangled Photon Pairs on Demand," Phys. Rev. Lett. **121**, 033902 (2018).

[27] S. Bounouar, C. de la Haye, M. Strauß, P. Schnauber, A. Thoma, M. Gschrey, J.-H. Schulze, A. Strittmatter, S. Rodt, and S. Reitzenstein, "Generation of maximally entangled states and coherent control in quantum dot microlenses," Appl. Phys. Lett. **112**, 153107 (2018).

[28] H. Wang, H. Hu, T.-H. Chung, J. Qin, X. Yang, J.-P. Li, R.-Z. Liu, H.-S. Zhong, Y.-M. He, X. Ding, Y.-H. Deng, Q. Dai, Y.-H. Huo, S. Höfling, C.-Y. Lu, and J.-W. Pan, "On-Demand Semiconductor Source of Entangled Photons Which Simultaneously Has High Fidelity, Efficiency, and Indistinguishability," Phys. Rev. Lett. **122**, 113602 (2019).

[29] J. Liu, R. Su, Y. Wei, B. Yao, S. F. Covre da Silva, Y. Yu, J. Iles-Smith, K. Srinivasan, A. Rastelli, J. Li, and X. Wang, "A solid-state source of strongly entangled photon pairs with high brightness and indistinguishability," Nat. Nanotechnol. **14**, 586 (2019).

[30] A. Fognini, A. Ahmadi, M. Zeeshan, J. T. Fokkens, S. J. Gibson, N. Sherlekar, S. J. Daley, D. Dalacu, P. J. Poole, K. D. Jöns, V. Zwiller, and M. E. Reimer, "Dephasing Free Photon Entanglement with a Quantum Dot," ACS Photonics **6**, 1656 (2019).

[31] C. Hopfmann, W. Nie, N. L. Sharma, C. Weigelt, F. Ding, and O. G. Schmidt, "Maximally entangled and gigahertz-clocked on-demand photon pair source," Phys. Rev. B **103**, 075413 (2021).

[32] A. Carmele and A. Knorr, "Analytical solution of the quantum-state tomography of the biexciton cascade in semiconductor quantum dots: Pure dephasing does not affect entanglement," Phys. Rev. B **84**, 075328 (2011).

[33] S. Schumacher, J. Förstner, A. Zrenner, M. Florian, C. Gies, P. Gartner, and F. Jahnke, "Cavity-assisted emission of polarization-entangled photons from biexcitons in quantum dots with fine-structure splitting," Opt. Express **20**, 5335 (2012).

[34] D. Heinze, A. Zrenner, and S. Schumacher, "Polarization-entangled twin photons from two-photon quantum-dot emission," Phys. Rev. B **95**, 245306 (2017).

[35] M. Cygorek, F. Ungar, T. Seidelmann, A. M. Barth, A. Vagov, V. M. Axt, and T. Kuhn, "Comparison of different concurrences characterizing photon pairs generated in the biexciton cascade in quantum dots coupled to microcavities," Phys. Rev. B **98**, 045303 (2018).

[36] T. Seidelmann, F. Ungar, M. Cygorek, A. Vagov, A. M. Barth, T. Kuhn, and V. M. Axt, "From strong to weak temperature dependence of the two-photon entanglement resulting from the biexciton cascade inside a cavity," Phys. Rev. B **99**, 245301 (2019).

[37] T. Seidelmann, F. Ungar, A. M. Barth, A. Vagov, V. M. Axt, M. Cygorek, and T. Kuhn, "Phonon-Induced Enhancement of Photon Entanglement in Quantum Dot-Cavity Systems," Phys. Rev. Lett. **123**, 137401 (2019).

[38] E. del Valle, "Distilling one, two and entangled pairs of photons from a quantum dot with cavity QED effects and spectral filtering," New J. Phys. **15**, 025019 (2013).

[39] F. Troiani, J. I. Perea, and C. Tejedor, "Cavity-assisted generation of entangled photon pairs by a quantum-dot cascade decay," Phys. Rev. B **74**, 235310 (2006).

[40] H. Jayakumar, A. Predojević, T. Kauten, T. Huber, G. S. Solomon, and G. Weihs, "Time-bin entangled photons from a quantum dot," Nat. Commun. **5**, 4251 (2014).

[41] T. Huber, L. Ostermann, M. Prilmüller, G. S. Solomon, H. Ritsch, G. Weihs, and A. Predojević, "Coherence and degree of time-bin entanglement from quantum dots," Phys. Rev. B **93**, 201301 (2016).

[42] L. Ginés, C. Pepe, J. Gonzales, N. Gregersen, S. Höfling, C. Schneider, and A. Predojević, "Time-bin entangled photon pairs from quantum dots embedded in a self-aligned cavity," Opt. Express **29**, 4174 (2021).

[43] R. Jozsa, "Fidelity for Mixed Quantum States," J. Mod. Opt. **41**, 2315 (1994).

[44] W. K. Wootters, "Entanglement of Formation of an Arbitrary State of Two Qubits," Phys. Rev. Lett. **80**, 2245 (1998).

[45] A. J. Hudson, R. M. Stevenson, A. J. Bennett, R. J. Young, C. A. Nicoll, P. Atkinson, K. Cooper, D. A. Ritchie, and A. J. Shields, "Coherence of an Entangled Exciton-Photon State," Phys. Rev. Lett. **99**, 266802 (2007).

[46] C. Schimpf, M. Reindl, F. Basso Basset, K. D. Jöns, R. Trotta, and A. Rastelli, "Quantum dots as potential sources of strongly entangled photons: Perspectives and challenges for applications in quantum networks," Appl. Phys. Lett. **118**, 100502 (2021).

[47] L. Schweickert, K. D. Jöns, K. D. Zeuner, S. F. Covre da Silva, H. Huang, T. Lettner, M. Reindl, J. Zichi, R. Trotta, A. Rastelli, and V. Zwiller, "On-demand generation of background-free single photons from a solid-state source," Appl. Phys. Lett. **112**, 093106 (2018).

[48] L. Hanschke, K. A. Fischer, S. Appel, D. Lukin, J. Wierzbowski, S. Sun, R. Trivedi, J Vucković, J. J. Finley, and K. Müller, "Quantum dot single-photon sources with ultra-low multi-photon probability," npj Quantum

Inf. **4**, 43 (2018).

[49] D. F. V. James, P. G. Kwiat, W. J. Munro, and A. G. White, "Measurement of qubits," Phys. Rev. A **64**, 052312 (2001).

[50] See Supplemental Material at [URL will be inserted by publisher] for details on the theoretical model, the two-photon density matrix, and the concurrence as well as the analytic calculations. Furthermore, the impact of the TPE scheme for horizontal and diagonal laser polarization is discussed in more detail and an extended Fig. 2 is shown. It also includes Refs. [51-55] in addition to references already cited in the Main Text.

[51] G. Lindblad, "On the generators of quantum dynamical semigroups," Commun. Math. Phys. **48**, 119 (1976).

[52] S. Bravyi, D. P. DiVincenzo, and D. Loss, "Schrieffer–Wolff transformation for quantum many-body systems,"

[53] R. Winkler, *Spin-Orbit Coupling Effects in Two-Dimensional Electron and Hole Systems*, Springer Tracts in Modern Physics, Vol. 191 (Springer, Berlin, 2003).

[54] M. Cosacchi, M. Cygorek, F. Ungar, A. M. Barth, A. Vagov, and V. M. Axt, "Path-integral approach for nonequilibrium multitime correlation functions of open quantum systems coupled to Markovian and non-Markovian environments," Phys. Rev. B **98**, 125302 (2018).

[55] T. Seidelmann, M. Cosacchi, M. Cygorek, D. E. Reiter, A. Vagov, and V. M. Axt, "Different Types of Photon Entanglement from a Constantly Driven Quantum Emitter Inside a Cavity," Adv. Quantum Technol. **4**, 2000108 (2021).

Ann. Phys. **326**, 2793 (2011).

Supplement: Two-Photon Excitation Sets Fundamental Limit to Entangled Photon Pair Generation from Quantum Emitters

T. Seidelmann,[1, *] C. Schimpf,[2] T. K. Bracht,[3] M. Cosacchi,[1] A. Vagov,[1] A. Rastelli,[2] D. E. Reiter,[3, †] and V. M. Axt[1]

[1]*Lehrstuhl für Theoretische Physik III, Universität Bayreuth, 95440 Bayreuth, Germany*
[2]*Institute of Semiconductor and Solid State Physics,*
Johannes Kepler University Linz, 4040 Linz, Austria
[3]*Institut für Festkörpertheorie, Universität Münster, 48149 Münster, Germany*

A.   THEORETICAL MODEL, DENSITY MATRIX AND CONCURRENCE

I.   Optically excited quantum dot and system dynamics

In this section, we provide more details on the theoretical model and the determination of the two-photon density matrix and its corresponding degree of entanglement as measured by the concurrence.

In our simulations, we consider the biexciton-exciton cascade of a quantum dot (QD) excited by a two-photon resonant Gaussian laser pulse. In a frame co-rotating with the laser frequency ω_{L}, the Hamiltonian $\hat{H}_{\mathrm{QD\text{-}L}}$, describing the interaction of the QD with the applied laser pulse, is given by

$$\hat{H}_{\mathrm{QD\text{-}L}} = \left(\Delta_{\mathrm{XL}} + \frac{\delta}{2}\right)|X_{\mathrm{H}}\rangle\langle X_{\mathrm{H}}| + \left(\Delta_{\mathrm{XL}} - \frac{\delta}{2}\right)|X_{\mathrm{V}}\rangle\langle X_{\mathrm{V}}| + (2\Delta_{\mathrm{XL}} - E_{\mathrm{B}})|B\rangle\langle B| - \frac{\hbar}{2}\,\Omega(t)\left(\hat{\sigma}_{\mathrm{L}} + \hat{\sigma}_{\mathrm{L}}^{\dagger}\right) \qquad (A1)$$

Here, $\delta = \hbar\,(\omega_{\mathrm{H}} - \omega_{\mathrm{V}})$ denotes the fine-structure splitting between the energies $\hbar\omega_{\mathrm{H}}$ and $\hbar\omega_{\mathrm{V}}$ of the orthogonally polarized exciton states $|X_{\mathrm{H}}\rangle$ and $|X_{\mathrm{V}}\rangle$, which couple to horizontally and vertically polarized light, respectively, and the exciton-laser detuning $\Delta_{\mathrm{XL}} = \hbar\,(\omega_{\mathrm{X}} - \omega_{\mathrm{L}})$ is the energetic difference between the mean exciton energy $\hbar\omega_{\mathrm{X}} = \hbar\,(\omega_{\mathrm{H}} + \omega_{\mathrm{V}})/2$ and the laser. The energy of the ground state $|G\rangle$ is used as the zero of the energy scale and the biexciton binding energy E_{B} lowers the energy of the biexciton state $|B\rangle$ compared to the sum of both exciton energies.

In this article, we assume a Gaussian pulse shape with (real) envelope

$$\Omega(t) = \sqrt{\frac{4\ln(2)}{\pi}}\,\frac{\Theta}{\mathrm{FWHM}}\exp\left[-4\ln(2)\left(\frac{t - t_{\mathrm{L}}}{\mathrm{FWHM}}\right)^{2}\right] \qquad (A2)$$

where Θ is the (one-photon resonant) pulse area and t_{L} is the time of the pulse maximum. The duration in time of this Gaussian pulse is characterized by its full-width-at-half-maximum FWHM. In order to achieve a two-photon resonant excitation of the biexciton state, the laser frequency is set to half of the ground state-to-biexciton transition energy, i.e., $\Delta_{\mathrm{XL}} = E_{\mathrm{B}}/2$ and a linear laser polarization is considered. In the basis spanned by the horizontal (H) and vertical (V) polarization associated with the two orthogonally polarized exciton states, the laser polarization can be described by

$$\hat{\sigma}_{\mathrm{L}} = \alpha_{H}\hat{\sigma}_{H} + \alpha_{V}\hat{\sigma}_{V} \qquad (A3)$$

where the transition operators

$$\hat{\sigma}_{H/V} = |G\rangle\langle X_{\mathrm{H/V}}| + |X_{\mathrm{H/V}}\rangle\langle B| \qquad (A4)$$

describe QD transitions that couple to horizontally/vertically polarized light and the coefficient $\alpha_{H/V} \in \mathbb{R}$ is the component of the laser polarization in H/V direction.

The transitions between QD states accompanied by photon emission are modeled as a radiative decay with rates Γ and incorporated in the model via Lindblad operators [1]

$$\mathcal{L}_{\hat{O},\Gamma}\hat{\rho} = \frac{\Gamma}{2}\left(2\hat{O}\hat{\rho}\hat{O}^{\dagger} - \hat{O}^{\dagger}\hat{O}\hat{\rho} - \hat{\rho}\hat{O}^{\dagger}\hat{O}\right), \qquad (A5)$$

———

* Corresponding author: tim.seidelmann@uni-bayreuth.de
† Current address: Condensed Matter Theory, Department of Physics, TU Dortmund, 44221 Dortmund, Germany

acting on the statistical operator $\hat{\rho}$ of the QD system, where the operator $\hat{O}$ describes the relevant QD transition. Due to the optical selection rules, we consider the four operators $\mathcal{L}_{|G\rangle\langle X_\mathrm{H}|,\gamma_\mathrm{X}}$, $\mathcal{L}_{|G\rangle\langle X_\mathrm{V}|,\gamma_\mathrm{X}}$, $\mathcal{L}_{|X_\mathrm{H}\rangle\langle B|,\frac{\gamma_\mathrm{B}}{2}}$, and $\mathcal{L}_{|X_\mathrm{V}\rangle\langle B|,\frac{\gamma_\mathrm{B}}{2}}$, where γ_B (γ_X) denotes the decay rate of the biexciton (exciton) state.

The dynamics of the statistical operator of the system $\hat{\rho}$ is governed by the Liouville-von Neumann equation

$$\frac{\mathrm{d}}{\mathrm{d}t}\hat{\rho} = \mathcal{L}\hat{\rho} := -\frac{i}{\hbar}\left[\hat{H},\hat{\rho}\right] + \sum_{\ell=H,V}\left\{\mathcal{L}_{|G\rangle\langle X_\ell|,\gamma_\mathrm{X}} + \mathcal{L}_{|X_\ell\rangle\langle B|,\frac{\gamma_\mathrm{B}}{2}}\right\}\hat{\rho}, \tag{A6}$$

where $[\hat{A},\hat{B}]$ denotes the commutator of two operators $\hat{A}$ and $\hat{B}$. This equation is numerically solved using its formal solution

$$\hat{\rho}(t) = \mathcal{P}_{0\to t}\left[\hat{\rho}(0)\right] := \hat{T}\exp\left[\int_0^t \mathrm{d}t'\mathcal{L}(t')\right]\hat{\rho}(0) \tag{A7}$$

where $\mathcal{P}_{0\to t}$ denotes a formal propagator in time, $\hat{T}$ is the time-ordering operator, and we assume the QD to be initially in its ground state.

In order to perform studies using a two-photon resonant π-pulse to excite the biexciton state, the corresponding pulse area Θ of the Gaussian pulse has to be determined. This is done numerically for each individual calculation by optimizing Θ to obtain the maximum biexciton occupation during the real-time dynamics. In the situation considered here where $\Omega(t)/E_\mathrm{B}$ is a small quantity, a first approximation for this value

$$\Theta \approx \sqrt{\frac{E_\mathrm{B}\,\mathrm{FWHM}}{\hbar\sqrt{2\pi\ln 2}}}\,\pi \tag{A8}$$

can be obtained by performing a Schrieffer-Wolff transformation [2, 3] on the QD-laser Hamiltonian $\hat{H}_\mathrm{QD\text{-}L}$. In the actual simulations, the numerically determined optimal value for Θ is typically 5...20% higher, depending on the FWHM.

II. Reconstructed two-photon density matrix

In standard experiments, the emitted photon state is reconstructed using quantum state tomography [4], a well-established scheme that is based on polarization-resolved two-time correlation measurements. The signal obtained in these type of measurements are proportional to two-time correlation functions containing electric field operators at different times. Since electronic transitions in the QD four-level system are the source for the emitted field, the electric field operators are in turn proportional to the QD transition operators $\hat{\sigma}_\mathrm{H/V}$ and the relevant correlation functions can be theoretically calculated by evaluating the correlation functions

$$G^{(2)}_{jk,\ell m}(t,\tau) = \left\langle\hat{\sigma}_j^\dagger(t)\hat{\sigma}_k^\dagger(t+\tau)\hat{\sigma}_m(t+\tau)\hat{\sigma}_\ell(t)\right\rangle, \tag{A9}$$

where $\{j,k,\ell,m\}\in\{H,V\}$. The time t denotes the time of the first detection event and τ is the delay time until a subsequent second one.

In an actual measurement, one always averages over both times, the real time t, as well as the delay time τ. While the integration interval for the real time T_av is extended over the complete decay process, different subsets of photon pairs can be selected by using different integration intervals τ_av for the delay time [5]. For example, simultaneously emitted photon pairs are selected in the limit of a vanishing integration window $\tau_\mathrm{av}\to 0$. But there are always experimental limits to the time resolution down to 20-300 picoseconds, depending on the setup.

Furthermore, in application-oriented experiments, one aims to obtain the maximum photon yield, which corresponds to considering all emission events, i.e., the limit $\tau_\mathrm{av}\to\infty$ is used. Consequently, in our studies, the (normalized) two-photon density matrix ρ^2p is given by

$$\rho^\mathrm{2p}_{jk,\ell m} = \frac{\overline{G}^{(2)}_{jk,\ell m}}{\mathrm{Tr}\left\{\overline{G}^{(2)}\right\}} \tag{A10a}$$

$$\overline{G}^{(2)}_{jk,\ell m} = \lim_{T_\mathrm{av},\tau_\mathrm{av}\to\infty}\int\limits_0^{T_\mathrm{av}}\mathrm{d}t\int\limits_0^{\tau_\mathrm{av}}\mathrm{d}\tau\,G^{(2)}_{jk,\ell m}(t,\tau) \tag{A10b}$$

where, both integration intervals are considered in the limit of infinity. In our numerical calculations, these quantities are evaluated by re-writing Eq. (A9) in the Schrödinger picture [6]

$$G^{(2)}_{jk,\ell m}(t,\tau) = \left\langle \hat{\sigma}^\dagger_k \hat{\sigma}_m \mathcal{P}_{t \to t+\tau} \left[\hat{\sigma}_\ell \mathcal{P}_{0 \to t} \left[\hat{\rho}(0) \right] \hat{\sigma}^\dagger_j \right] \right\rangle \tag{A11}$$

III.   Degree of entanglement

The degree of entanglement associated with a given two-photon density matrix is quantified using the concurrence C, a well-established measure which has a one-to-one correspondence to the entanglement of formation [7]. The concurrence can be obtained directly form the two-photon density matrix $\rho^{2\mathrm{p}}$ by calculating the four (real and positive) eigenvalues λ_j of the matrix

$$M = \rho^{2\mathrm{p}} \, T \, (\rho^{2\mathrm{p}})^* \, T, \tag{A12}$$

where $(\rho^{2\mathrm{p}})^*$ denotes the complex conjugated two-photon density matrix and T is the anti-diagonal matrix with elements $\{-1, 1, 1, -1\}$. After sorting the eigenvalues in decreasing order, $\lambda_{j+1} \leq \lambda_j$, the concurrence is given as [4, 7, 8]:

$$C = \max \left\{ 0, \sqrt{\lambda_1} - \sqrt{\lambda_2} - \sqrt{\lambda_3} - \sqrt{\lambda_4} \right\}, \tag{A13}$$

A quite useful approximation for the concurrence is

$$C \approx 2 \left(|\rho^{2\mathrm{p}}_{HH,VV}| - \rho^{2\mathrm{p}}_{HV,HV} \right). \tag{A14}$$

This expression is exactly fulfilled for a two-photon density matrix, that has the form

$$\rho^{2\mathrm{p}} = \begin{pmatrix} a & 0 & 0 & c \\ 0 & b & d & 0 \\ 0 & d^* & b & 0 \\ c^* & 0 & 0 & a' \end{pmatrix} \tag{A15}$$

in the basis $\{|HH\rangle, |HV\rangle, |VH\rangle, |VV\rangle\}$ where the parameters $a, a', b \in \mathbb{R}^+$, $c, d \in \mathbb{C}$ fulfill $a + a' + 2b = 1$ and $\sqrt{a\, a'} \geq |c| \geq b \geq |d|$. Thus, Eq. (A14) is a good approximation for the concurrence, if a two-photon density matrix is dominated by the elements $\rho^{2\mathrm{p}}_{HH,HH}$, $\rho^{2\mathrm{p}}_{VV,VV}$, and $\rho^{2\mathrm{p}}_{HH,VV}$, the condition $\rho^{2\mathrm{p}}_{HV,HV} = \rho^{2\mathrm{p}}_{VH,VH}$ is approximately fulfilled, and the 8 remaining coherences can be neglected. In our numerical simulations, we obtain density matrices of this kind for the considered parameter regime. Thus we use this approximate formula for the analytic calculations.

B.   INITIAL VALUE CALCULATIONS

In this section a brief derivation for the quantity C_0 is given, which represents the concurrence in the case of an initially prepared biexciton state.

Without an external laser the Hamiltonian describing the system reduces to

$$\hat{H}_0 := \frac{E_\mathrm{B} + \delta}{2} |X_\mathrm{H}\rangle\langle X_\mathrm{H}| + \frac{E_\mathrm{B} - \delta}{2} |X_\mathrm{V}\rangle\langle X_\mathrm{V}| \tag{B1}$$

in a frame rotating with the frequency $\omega_\mathrm{L} = \omega_\mathrm{X} - E_\mathrm{B}/(2\hbar)$. This Hamiltonian is of course diagonal in the basis $\{|G\rangle, |X_\mathrm{H}\rangle, |X_\mathrm{V}\rangle, |B\rangle\}$ and time-independent. Therefore, the formal solution of the Liouville-von Neumann equation

$$\frac{\mathrm{d}}{\mathrm{d}t} \hat{\rho} = \mathcal{L}_0 \hat{\rho} := -\frac{i}{\hbar} \left[\hat{H}_0, \hat{\rho} \right] + \sum_{\ell = H,V} \left\{ \mathcal{L}_{|G\rangle\langle X_\ell|, \gamma_\mathrm{X}} + \mathcal{L}_{|X_\ell\rangle\langle B|, \frac{\gamma_\mathrm{B}}{2}} \right\} \hat{\rho}, \tag{B2}$$

for the statistical operator $\hat{\rho}$ is given by

$$\hat{\rho}(t) = \mathcal{P}^{(0)}_{t_0 \to t} [\hat{\rho}(t_0)] := \exp[\mathcal{L}_0 \, (t - t_0)] \hat{\rho}(t_0). \tag{B3}$$

where $\mathcal{L}_0$ is a time-independent operator in Liouville space and $\mathcal{P}^{(0)}_{t_0 \to t}$ the corresponding formal propagator for the statistical operator. In particular one obtains

$$\langle B | \mathcal{P}^{(0)}_{t_0 \to t} [|B\rangle\langle B|] | B \rangle = e^{-\gamma_{\mathrm{B}}\,(t-t_0)} \tag{B4a}$$

$$\langle X_m | \mathcal{P}^{(0)}_{t_0 \to t} [|X_\ell\rangle\langle X_j|] | X_k \rangle = \delta_{jk}\delta_{\ell m} e^{-[\gamma_{\mathrm{X}} + i(E_\ell - E_j)/\hbar](t-t_0)} \tag{B4b}$$

where $j, k, \ell, m \in \{H, V\}$ and $E_{H/V} = (E_{\mathrm{B}} \pm \delta)/2$. In order to calculate the reconstructed two-photon density matrix, integrated two-time correlation functions have to be evaluated. In the Schrödinger picture Eq. (A10b) can be reformulated as

$$\overline{G}^{(2)}_{jk,\ell m} = \int\limits_0^\infty \mathrm{d}t \int\limits_0^\infty \mathrm{d}\tau\, G^{(2)}_{jk,\ell m}(t,\tau) = \int\limits_0^\infty \mathrm{d}t \int\limits_0^\infty \mathrm{d}\tau\, \mathrm{Tr}\left\{ \hat{\sigma}_k^\dagger \hat{\sigma}_m \mathcal{P}^{(0)}_{t \to t+\tau} \left[\hat{\sigma}_\ell \mathcal{P}^{(0)}_{0 \to t}[\hat{\rho}(0)]\hat{\sigma}_j^\dagger \right] \right\} \tag{B5}$$

Note that in a time evolution governed by the propagator $\mathcal{P}^{(0)}_{t_0 \to t}$ the system can only relax towards its ground state $|G\rangle$ and no excitation is ever transferred to higher excited states, i.e., no excitation is transferred from the ground state $|G\rangle$ (exciton state $|X_j\rangle$) towards an exciton state $|X_j\rangle$ (biexciton state $|B\rangle$). Therefore $\overline{G}^{(2)}_{jk,\ell m}$ is only nonzero if the system is in the biexciton at the time t when the first pair of transition operators is applied. This is a direct consequence of the considered system, where the interaction with the field modes can be modeled as radiative decay. Thus, the re-absorption of emitted photons cannot occur. In other systems, e.g., when the QD is embedded inside a high-quality microcavity, photons inside the cavity are likely to be re-absorbed by the QD, leading to an oscillating biexciton occupation. Furthermore, since the operator $\mathcal{L}_0$ is time-independent, the propagator depends only on a time difference, i.e., $\mathcal{P}^{(0)}_{t_0 \to t} = \mathcal{P}^{(0)}_{0 \to t-t_0}$. Starting with an initially prepared biexciton state, i.e., $\hat{\rho}(0) = |B\rangle\langle B|$, and inserting the formal propagation (B4) one arrives at

$$
\begin{aligned}
\overline{G}^{(2)}_{jk,\ell m} &= \int\limits_0^\infty \mathrm{d}t \int\limits_0^\infty \mathrm{d}\tau\, \mathrm{Tr}\left\{ \hat{\sigma}_k^\dagger \hat{\sigma}_m \mathcal{P}^{(0)}_{t \to t+\tau} \left[|X_\ell\rangle\langle B| \mathcal{P}^{(0)}_{0 \to t} \left[|B\rangle\langle B| \right] |B\rangle\langle X_j| \right] \right\} \\
&= \int\limits_0^\infty \mathrm{d}t \int\limits_0^\infty \mathrm{d}\tau\, \mathrm{Tr}\left\{ \hat{\sigma}_k^\dagger \hat{\sigma}_m \mathcal{P}^{(0)}_{0 \to \tau} \left[e^{-\gamma_{\mathrm{B}} t} |X_\ell\rangle\langle X_j| \right] \right\} = \frac{1}{\gamma_{\mathrm{B}}} \int\limits_0^\infty \mathrm{d}\tau\, \mathrm{Tr}\left\{ \hat{\sigma}_k^\dagger \hat{\sigma}_m \mathcal{P}^{(0)}_{0 \to \tau} \left[|X_\ell\rangle\langle X_j| \right] \right\} \\
&= \frac{1}{\gamma_{\mathrm{B}}} \int\limits_0^\infty \mathrm{d}\tau\, \delta_{jk}\delta_{\ell m} e^{-[\gamma_{\mathrm{X}} + i(E_\ell - E_j)/\hbar]\tau} = \frac{1}{\gamma_{\mathrm{B}}} \delta_{jk}\delta_{\ell m} \frac{1}{\gamma_{\mathrm{X}} + i(E_\ell - E_j)/\hbar}
\end{aligned} \tag{B6}
$$

From these quantities the elements of the two-photon density matrix are obtained according to Eq. (A10a). As expected one finds only four nonzero elements

$$\rho^{2\mathrm{p}}_{HH,HH} = \frac{1}{2} = \rho^{2\mathrm{p}}_{VV,VV} \tag{B7a}$$

$$\rho^{2\mathrm{p}}_{HH,VV} = \frac{1}{2} \frac{1}{1 - i\frac{\delta}{\hbar\gamma_{\mathrm{X}}}} = \left(\rho^{2\mathrm{p}}_{VV,HH} \right)^* \tag{B7b}$$

In this situation, the definition of the concurrence given in Eqs. (A12) and (A13) reduces to

$$C = 2|\rho^{2\mathrm{p}}_{HH,VV}| = \frac{1}{\sqrt{1 + \left(\frac{\delta}{\hbar\gamma_{\mathrm{X}}}\right)^2}} =: C_0(\gamma_{\mathrm{X}}, \delta) \tag{B8}$$

C. CALCULATIONS WITH FINITE FWHM

In this section a brief derivation of the analytic approximation for the concurrence in Eq. (6) in the main text is given, which takes into account the impact of a finite pulse duration in a two-photon resonant excitation scheme. Here, the calculation is performed for an arbitrary linear laser polarization. Special cases and interpretations are discussed in the following Sections D, E and G.

The basic idea for the analytic estimate is inspired by the initial value calculation in the previous section. We consider a short time interval centered around the time of the pulse maximum and assume that the Gaussian pulse only interacts with the QD during this time. Additionally, we replace the time-dependent shape of the pulse by an effective constant driving. Based on these main steps and some further assumptions, in particular that γ_BFWHM/2 and γ_XFWHM are small quantities, we rework the calculations for the concurrence.

I.   Effective model with constant driving

For the effective model, we define a time interval with length F centered around the time of the pulse maximum and assume that the Gaussian pulse only interacts with the QD in this interval $t \in [t_L - F/2, t_L + F/2]$. Additionally, we replace the time-dependent amplitude of the laser pulse $\Omega(t)$ by an effective constant driving strength Ω_{eff}. Furthermore, the fine-structure splitting between the excitons is neglected during the time interval F since a splitting $\delta \ll E_B$ has hardly any impact on the two-photon resonant excitation scheme. Because the two-photon process exciting the QD from the ground state towards the biexciton state is a second order process and scales with $\Omega^2(t)$, it is plausible to assume, that this interval starts at the time FWHM/2 before the pulse maximum, since $\Omega^2(t_L - \text{FWHM}/2) \leq \Omega^2(t_L)/4$. Thus we set $F = \text{FWHM}$ for the moment. An effective constant driving Ω_{eff} should fulfill the relation

$$\int\limits_{t_L-F/2}^{t_L+F/2} \mathrm{d}t\, \Omega(t) = \int\limits_{t_L-F/2}^{t_L+F/2} \mathrm{d}t\, \sqrt{\frac{4\ln(2)}{\pi}} \frac{\Theta}{\text{FWHM}} e^{-4\ln(2)\left(\frac{t-t_L}{\text{FWHM}}\right)^2} = \int\limits_{t_L-F/2}^{t_L+F/2} \mathrm{d}t\, \Omega_{eff} = F\,\Omega_{eff} \tag{C1}$$

With the choice $F = \text{FWHM}$ one obtains

$$\Omega_{eff} \approx 0.81 \sqrt{\frac{4\ln 2}{\pi}} \frac{\Theta}{\text{FWHM}} \tag{C2}$$

Based on these assumptions, the effective Hamiltonian for a laser pulse with an arbitrary linear polarization is given by

$$\hat{H}_{\text{QD-L}}^{\text{eff}} = \begin{cases} \hat{H}_1 & , t \in [t_L - F/2, t_L + F/2] \\ \hat{H}_0 & , \text{otherwise} \end{cases} \tag{C3a}$$

$$\hat{H}_1 = \frac{E_B}{2}\left(|X_H\rangle\langle X_H| + |X_V\rangle\langle X_V|\right) + \frac{\hbar}{2}\Omega_{eff}\left(\hat{\sigma}_L + \hat{\sigma}_L^\dagger\right) \tag{C3b}$$

$$\hat{\sigma}_L = \alpha_H \hat{\sigma}_H + \alpha_V \hat{\sigma}_V \tag{C3c}$$

in the frame co-rotating with the laser frequency ω_L set to the two-photon resonance. The linear polarization of the laser is defined by the (real) coefficients α_H and α_V which fulfill $\alpha_H^2 + \alpha_V^2 = 1$ and represent the component in H and V polarization, respectively. The four energy eigenstates of $\hat{H}_1$ are given by

$$|U\rangle = c\left(|G\rangle + |B\rangle\right) + \sqrt{2}\tilde{c}\left(\alpha_H|X_H\rangle + \alpha_V|X_V\rangle\right) \tag{C4a}$$

$$|M\rangle = \alpha_V|X_H\rangle - \alpha_H|X_V\rangle \tag{C4b}$$

$$|N\rangle = \frac{1}{\sqrt{2}}\left(|G\rangle - |B\rangle\right) \tag{C4c}$$

$$|L\rangle = \tilde{c}\left(|G\rangle + |B\rangle\right) - \sqrt{2}c\left(\alpha_H|X_H\rangle + \alpha_V|X_V\rangle\right) \tag{C4d}$$

with coefficients

$$c = \frac{\hbar\Omega_{eff}}{\sqrt{2(\hbar\Omega_{eff})^2 + 4E_U^2}}; \; \tilde{c} = \sqrt{\frac{1}{2} - c^2} \tag{C5}$$

The corresponding eigenenergies

$$E_U = \frac{1}{4}\left(E_B + \sqrt{E_B^2 + 8(\hbar\Omega_{eff})^2}\right) \tag{C6a}$$

$$E_M = \frac{E_B}{2} \tag{C6b}$$

$$E_N = 0 \tag{C6c}$$

$$E_L = \frac{1}{4}\left(E_B - \sqrt{E_B^2 + 8(\hbar\Omega_{eff})^2}\right) \tag{C6d}$$

are independent of the laser polarization, i.e., independent of $\alpha_{H/V}$.

II. Approximate time dynamics in the effective model

Without radiative decay, the time evolution of the statistical operator for times $t, t_0 \in [t_L - \text{FWHM}/2, t_L + \text{FWHM}/2]$ in the effective model is determined by

$$\hat{\rho}(t) = \mathcal{P}^{(1)}_{t_0 \to t}\hat{\rho}(t_0)] := \exp[\mathcal{L}_1 (t - t_0)]\hat{\rho}(t_0) \tag{C7a}$$

$$\mathcal{L}_1\hat{\rho} := -\frac{i}{\hbar}\left[\hat{H}_1, \hat{\rho}\right] \tag{C7b}$$

Combining the expression (C2) with the estimate for the optimal pulse area in Eq. (A8), we realize that $(\hbar\Omega_{\text{eff}})^2/E_B^2 \ll 1$ for our parameters and, thus, the coefficients c and $\tilde{c}$ fulfill

$$\tilde{c}^2 \approx \frac{1}{2}; \ \left(\frac{c}{\tilde{c}}\right)^2 \ll 1 \tag{C8}$$

Consequently, the two eigenstates $|N\rangle$ and $|L\rangle$ are approximately an equal admixture of ground and biexciton state, i.e., $|N/L\rangle \approx (|G\rangle \mp |B\rangle)/\sqrt{2}$. Therefore, the time evolution after an initially prepared ground state is mainly described by these two eigenstates and the time evolution of the biexciton state can be approximated as

$$\rho_{\text{BB}}(t) = \langle B|\mathcal{P}^{(1)}_{t_0 \to t}[|G\rangle\langle G|]|B\rangle \approx \frac{1}{2}\left[1 - \cos\left(E_L (t - t_0)/\hbar\right)\right] \tag{C9}$$

Taking into account radiative decay described by the Lindblad operators $\mathcal{L}_{|X_H\rangle\langle B|, \frac{\gamma_B}{2}}$ and $\mathcal{L}_{|X_V\rangle\langle B|, \frac{\gamma_B}{2}}$, both eigenstates $|N\rangle$ and $|L\rangle$ should decay with the rate $\gamma_B/2$, since both are close to an equal admixture of $|G\rangle$ and $|B\rangle$. In the situation $(\hbar\Omega_{\text{eff}})^2/E_B^2 \ll 1$, one obtains

$$\frac{E_U - E_M}{\hbar} = \frac{|E_L|}{\hbar} \approx \frac{\hbar\Omega_{\text{eff}}^2}{E_B} = 0.81^2 \frac{2\sqrt{2\pi\ln 2}}{\text{FWHM}} \tag{C10}$$

by inserting Eqs. (A8) and (C2). Furthermore, as stated in Section A I, we observed that in the presence of radiative decay, the optimal pulse area is actually around 10% higher than estimated in Eq. (A8). Taking this factor into account, Eq. (C10) can be (nicely) approximated as

$$\frac{E_U - E_M}{\hbar} = \frac{|E_L|}{\hbar} \approx \frac{\pi}{\text{FWHM}} \tag{C11}$$

This also means that, the energetic splitting between the two upper dressed states E_S (cf., Fig. C1), which is always identical to the energetic splitting between the two lower ones, is approximately

$$E_S = E_U - E_M = E_N - E_L \approx \frac{\hbar\pi}{\text{FWHM}} \tag{C12}$$

Altogether, the biexciton occupation during the effective pulse interval is therefore estimated as

$$\rho_{\text{BB}}(t) = \langle B|\mathcal{P}^{(2)}_{t_0 \to t}[|G\rangle\langle G|]|B\rangle \approx \frac{1}{2}\left[1 - \cos\left(\frac{\pi (t - t_0)}{\text{FWHM}}\right)\right]e^{-\gamma_B(t-t_0)/2} \tag{C13a}$$

$$\mathcal{P}^{(2)}_{t_0 \to t}[\hat{\rho}(t_0)] := \exp[\mathcal{L}_2 (t - t_0)]\hat{\rho}(t_0) \tag{C13b}$$

$$\mathcal{L}_2\hat{\rho} := -\frac{i}{\hbar}\left[\hat{H}_1, \hat{\rho}\right] + \sum_{\ell=H,V}\left\{\mathcal{L}_{|G\rangle\langle X_\ell|, \gamma_X} + \mathcal{L}_{|X_\ell\rangle\langle B|, \frac{\gamma_B}{2}}\right\}\hat{\rho} \tag{C13c}$$

Note that these formulas are independent of the laser polarization. Any linear laser polarization will result in this estimate for the biexciton occupation during the laser pulse.

Figure C2 depicts the comparison of the effective model, where Eq. (C13a) is used to describe the biexciton occupation during the time interval $t \in [t_L - \text{FWHM}/2, t_L + \text{FWHM}/2]$, with the numerical data. For our purposes, the estimated dynamics agrees reasonably well with the numerically obtained dynamics, justifying the choice $F = \text{FWHM}$ and the use of the effective model.
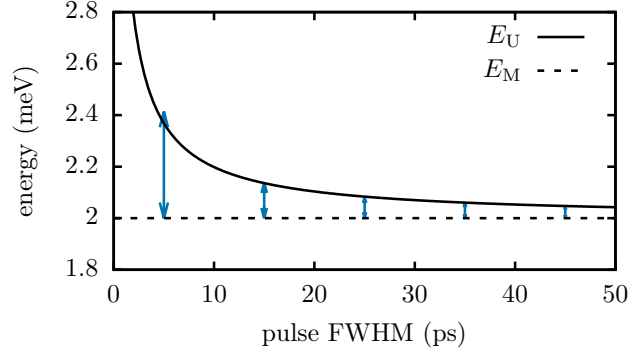
FIG. C1.   Dressed state energies E_U and E_M as function of the FWHM for an effective driving strength Ω_{eff} according to Eq. (C2). In accordance with our numerical observation, the optimal pulse area Θ is set to 1.1 times the value predicted by the Schrieffer-Wolff transformation in Eq. (A8). Blue double-headed arrows indicate the energetic splitting $E_S = \hbar\pi/\text{FWHM}$.
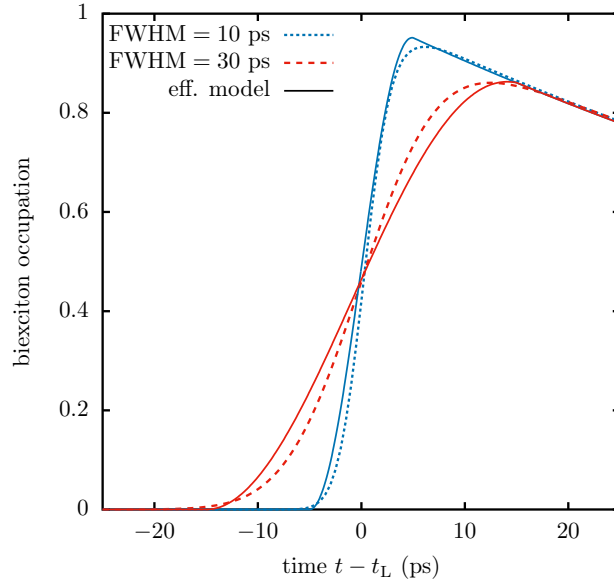
FIG. C2.   Biexciton occupation obtained from the numerical simulations compared to results according to Eq. (C13a) and the effective Hamiltonian.

In the following, we also need an approximation for the propagation of an exciton occupation or coherence during the time window of the laser pulse after the emission of a first biexciton photon. Employing similar approximations, in particular, $|U/M\rangle \approx \alpha_{H/V}|X_H\rangle \pm \alpha_{V/H}|X_V\rangle$ and Eq. (C11), one obtains

$$\langle X_j|\mathcal{P}^{(1)}_{t_0\to t}[|X_j\rangle\langle X_j|]|X_j\rangle \approx 1 + 2\alpha_H^2\alpha_V^2\left[\cos\left(\frac{\pi(t-t_0)}{\text{FWHM}}\right) - 1\right] \tag{C14a}$$

$$\langle X_\ell|\mathcal{P}^{(1)}_{t_0\to t}[|X_j\rangle\langle X_j|]|X_\ell\rangle \approx 2\alpha_H^2\alpha_V^2\left[1 - \cos\left(\frac{\pi(t-t_0)}{\text{FWHM}}\right)\right] \tag{C14b}$$

$$\langle X_V|\mathcal{P}^{(1)}_{t_0\to t}[|X_V\rangle\langle X_H|]|X_H\rangle \approx 2\alpha_H^2\alpha_V^2 + \alpha_H^4 e^{i\pi(t-t_0)/\text{FWHM}} + \alpha_V^4 e^{-i\pi(t-t_0)/\text{FWHM}} \tag{C14c}$$

where $j, \ell \in \{H, V\}$ and $\ell \neq j$. Here the propagator $\mathcal{P}^{(1)}_{t_0\to t}$ is used, i.e., the radiative decay of the exciton state is neglected, cf., Eq. (C7). In the following it will become clear that this corresponds to the approximation that no second photon is emitted during the interval $F = \text{FWHM}$. Note that this assumption in combination with the previous ones results in the feature that the propagation of an exciton occupation or coherence during the interval F can not lead to finite elements outside of the exciton subspace, i.e., $\langle \chi|\mathcal{P}^{(1)}_{t_0\to t}[|X_j\rangle\langle X_{j'}|]|\chi'\rangle = 0$ for $\chi, \chi' \in \{G, B\}$ and $j, j' \in \{H, V\}$.

III. Two-photon density matrix and concurrence

Based on the estimated dynamics of the statistical operator, we now turn to the integrated two-time correlation functions. With the definitions $t_{s/e} := t_{\mathrm{L}} \mp \mathrm{FWHM}/2$ the expression for the integrated two-time correlation function can be re-formulated as

$$\overline{G}^{(2)}_{jk,\ell m} = \int\limits_0^\infty \mathrm{d}t \int\limits_0^\infty \mathrm{d}\tau\, G^{(2)}_{jk,\ell m}(t,\tau) = \int\limits_{t_s}^\infty \mathrm{d}t \int\limits_0^\infty \mathrm{d}\tau\, G^{(2)}_{jk,\ell m}(t,\tau) = \overline{G}^{(I)}_{jk,\ell m} + \overline{G}^{(II)}_{jk,\ell m} + \overline{G}^{(III)}_{jk,\ell m} \tag{C15a}$$

$$\overline{G}^{(I)}_{jk,\ell m} = \int\limits_{t_s}^{t_e} \mathrm{d}t \int\limits_0^{t_e-t} \mathrm{d}\tau\, G^{(2)}_{jk,\ell m}(t,\tau) \tag{C15b}$$

$$\overline{G}^{(II)}_{jk,\ell m} = \int\limits_{t_s}^{t_e} \mathrm{d}t \int\limits_{t_e-t}^\infty \mathrm{d}\tau\, G^{(2)}_{jk,\ell m}(t,\tau) \tag{C15c}$$

$$\overline{G}^{(III)}_{jk,\ell m} = \int\limits_{t_e}^\infty \mathrm{d}t \int\limits_0^\infty \mathrm{d}\tau\, G^{(2)}_{jk,\ell m}(t,\tau) \tag{C15d}$$

Using the effective model, the respective propagators $\mathcal{P}^{(n)}_{t_0 \to t}$ are time-independent, enabling an easier evaluation of $\overline{G}^{(2)}_{jk,\ell m}$. The first contribution can in good approximation be omitted. Due to the very narrow integration intervals for t and τ on the order of the FWHM, it is much smaller than the other two contributions. Note that omitting this term corresponds to the assumption that the probability for emitting two photons during the effective pulse interval is negligible. For the following calculations we use F instead of FWHM in order to shorten the expressions.

We first evaluate the third term. Note that if the real-time argument t is larger than t_e, one only obtains a nonzero contribution when the system is in the biexciton state at this point in time. Starting initially in the ground state, the third term leads to the contribution

$$\begin{aligned}
\overline{G}^{(III)}_{jk,\ell m} &= \int\limits_{t_e}^\infty \mathrm{d}t \int\limits_0^\infty \mathrm{d}\tau\, G^{(2)}_{jk,\ell m}(t,\tau) = \int\limits_{t_e}^\infty \mathrm{d}t \int\limits_0^\infty \mathrm{d}\tau\, \mathrm{Tr}\left\{ \hat{\sigma}_k^\dagger \hat{\sigma}_m \mathcal{P}^{(0)}_{t \to t+\tau} \left[\hat{\sigma}_\ell \hat{\rho}(t) \hat{\sigma}_j^\dagger \right] \right\} \\
&= \int\limits_{t_e}^\infty \mathrm{d}t \int\limits_0^\infty \mathrm{d}\tau\, \mathrm{Tr}\left\{ \hat{\sigma}_k^\dagger \hat{\sigma}_m \mathcal{P}^{(0)}_{0 \to \tau} \left[\hat{\sigma}_\ell \mathcal{P}^{(0)}_{t_e \to t} \left[\langle B | \mathcal{P}^{(2)}_{t_s \to t_e} [|G\rangle\langle G|] | B\rangle\, |B\rangle\langle B| \right] \hat{\sigma}_j^\dagger \right] \right\} \\
&= \int\limits_{t_e}^\infty \mathrm{d}t \int\limits_0^\infty \mathrm{d}\tau\, \mathrm{Tr}\left\{ \hat{\sigma}_k^\dagger \hat{\sigma}_m \mathcal{P}^{(0)}_{0 \to \tau} \left[e^{-\gamma_{\mathrm{B}} F/2} e^{-\gamma_{\mathrm{B}}(t-t_e)} |X_\ell\rangle\langle X_j| \right] \right\} \\
&= e^{-\gamma_{\mathrm{B}} F/2} \frac{1}{\gamma_{\mathrm{B}}} \int\limits_0^\infty \mathrm{d}\tau\, \mathrm{Tr}\left\{ \hat{\sigma}_k^\dagger \hat{\sigma}_m \mathcal{P}^{(0)}_{0 \to \tau} [|X_\ell\rangle\langle X_j|] \right\} = e^{-\gamma_{\mathrm{B}} F/2} \frac{1}{\gamma_{\mathrm{B}}} \delta_{jk} \delta_{\ell m} \frac{1}{\gamma_{\mathrm{X}} + i(E_\ell - E_j)/\hbar}
\end{aligned} \tag{C16}$$

The evaluation of the last integral is known from Eq. (B6).

Next, the second term is evaluated. Because of the insignificant exciton occupation during the effective pulse interval due to the two-photon resonant excitation character, only two photon states are considered, where the first photon is emitted from the biexciton state. These contributions should clearly dominate over ones where the first photon is emitted from an exciton decay. Thus, we set $\hat{\sigma}_\ell = |X_\ell\rangle\langle B|$ and $\hat{\sigma}_j^\dagger = |B\rangle\langle X_j|$. Furthermore, if an exciton occupation or coherence is propagated during the pulse window, the propagator $\mathcal{P}^{(1)}_{t \to t'}$ is used, cf., Eq. (C14). Thus, the radiative decay of the exciton state is neglected in this short interval. This also corresponds to the assumption that no subsequent second photon is emitted during the pulse window and is justified by the numerical observation

that the concurrence hardly depends on γ_{X} as long as $\gamma_{\mathrm{X}}\mathrm{FWHM} \ll 1$.

$$\overline{G}^{(II)}_{jk,\ell m} \approx \int\limits_{t_s}^{t_e} \mathrm{d}t \int\limits_{t_e-t}^{\infty} \mathrm{d}\tau \, \mathrm{Tr}\left\{ \hat{\sigma}_k^\dagger \hat{\sigma}_m \mathcal{P}^{(0)}_{t_e \to t+\tau} \left[\mathcal{P}^{(1)}_{t \to t_e} \left[|X_\ell\rangle\langle B| \, \mathcal{P}^{(2)}_{t_s \to t}[|G\rangle\langle G|] \, |B\rangle\langle X_j| \right] \right] \right\}$$

$$= \int\limits_{t_s}^{t_e} \mathrm{d}t \int\limits_{t_e-t}^{\infty} \mathrm{d}\tau \, \frac{1}{2}\left(1 - \cos[\pi(t-t_s)/F]\right) e^{-\gamma_{\mathrm{B}}(t-t_s)/2} \, \mathrm{Tr}\left\{ \hat{\sigma}_k^\dagger \hat{\sigma}_m \mathcal{P}^{(0)}_{t_e \to t+\tau} \left[\mathcal{P}^{(1)}_{t \to t_e} [|X_\ell\rangle\langle X_j|] \right] \right\} \tag{C17a}$$

$$\overline{G}^{(II)}_{jj,jj} = e^{-\gamma_{\mathrm{B}}F/2} \int\limits_{t_s}^{t_e} \mathrm{d}t \int\limits_{t_e-t}^{\infty} \mathrm{d}\tau \, \frac{1}{2}\left(1 + \cos[\pi(t-t_e)/F]\right) e^{-\gamma_{\mathrm{B}}(t-t_e)/2} \, e^{-\gamma_{\mathrm{X}}(t+\tau-t_e)}$$

$$\times \left\{ 1 + 2\alpha_H^2\alpha_V^2 \left(\cos[\pi(t_e-t)/F] - 1\right) \right\}$$

$$= e^{-\gamma_{\mathrm{B}}F/2} \frac{1}{\gamma_{\mathrm{X}}} \int\limits_{-F}^{0} \mathrm{d}t \, \frac{1}{2}\left(1 + \cos[\pi t/F]\right) e^{-\gamma_{\mathrm{B}}t/2} \left\{ 1 + 2\alpha_H^2\alpha_V^2 \left(\cos[\pi t/F] - 1\right) \right\}$$

$$= e^{-\gamma_{\mathrm{B}}F/2} \frac{1}{\gamma_{\mathrm{X}}} \int\limits_{-F}^{0} \mathrm{d}t \left(\frac{1}{2} - \alpha_H^2\alpha_V^2 \sin^2[\pi t/F] + \frac{1}{2}\cos[\pi t/F] \right) e^{-\gamma_{\mathrm{B}}t/2}$$

$$\approx e^{-\gamma_{\mathrm{B}}F/2} \frac{1}{\gamma_{\mathrm{X}}} \left(\frac{F}{2} - \frac{\alpha_H^2\alpha_V^2 F}{2} \right) e^{\gamma_{\mathrm{B}}F/4} = \frac{F}{2\gamma_{\mathrm{X}}}\left(1 - \alpha_H^2\alpha_V^2\right) e^{-\gamma_{\mathrm{B}}F/4} \tag{C17b}$$

$$\overline{G}^{(II)}_{HH,VV} = e^{-\gamma_{\mathrm{B}}F/2} \int\limits_{t_s}^{t_e} \mathrm{d}t \int\limits_{t_e-t}^{\infty} \mathrm{d}\tau \, \frac{1}{2}\left(1 + \cos[\pi(t-t_e)/F]\right) e^{-\gamma_{\mathrm{B}}(t-t_e)/2} \, e^{-[\gamma_{\mathrm{X}} - i\delta/\hbar](t+\tau-t_e)}$$

$$\times \left\{ 2\alpha_H^2\alpha_V^2 + \alpha_H^4 e^{i\pi(t_e-t)/F} + \alpha_V^4 e^{-i\pi(t_e-t)/F} \right\}$$

$$= e^{-\gamma_{\mathrm{B}}F/2} \frac{1}{\gamma_{\mathrm{X}} - i\delta/\hbar} \int\limits_{-F}^{0} \mathrm{d}t \, \frac{1}{2}\left(1 + \cos[\pi t/F]\right) e^{-\gamma_{\mathrm{B}}t/2} \left\{ 2\alpha_H^2\alpha_V^2 + \alpha_H^4 e^{-i\pi t/F} + \alpha_V^4 e^{i\pi t/F} \right\}$$

$$\approx e^{-\gamma_{\mathrm{B}}F/2} \frac{1}{\gamma_{\mathrm{X}} - i\delta/\hbar} \left(\alpha_H^2\alpha_V^2 F + \frac{\alpha_H^4 F}{4} + \frac{\alpha_V^4 F}{4} \right) e^{\gamma_{\mathrm{B}}F/4} = \frac{F}{2(\gamma_{\mathrm{X}} - i\delta/\hbar)}\left(\frac{1}{2} + \alpha_H^2\alpha_V^2 \right) e^{-\gamma_{\mathrm{B}}F/4} \tag{C17c}$$

$$\overline{G}^{(II)}_{HV,HV} = e^{-\gamma_{\mathrm{B}}F/2} \int\limits_{t_s}^{t_e} \mathrm{d}t \int\limits_{t_e-t}^{\infty} \mathrm{d}\tau \, \frac{1}{2}\left(1 + \cos[\pi(t-t_e)/F]\right) e^{-\gamma_{\mathrm{B}}(t-t_e)/2} \, e^{-\gamma_{\mathrm{X}}(t+\tau-t_e)} \left\{ 2\alpha_H^2\alpha_V^2 \left(1 - \cos[\pi(t_e-t)/F]\right) \right\}$$

$$= e^{-\gamma_{\mathrm{B}}F/2} \frac{1}{\gamma_{\mathrm{X}}} \int\limits_{-F}^{0} \mathrm{d}t \, \alpha_H^2\alpha_V^2 \sin^2[\pi t/F] e^{-\gamma_{\mathrm{B}}t/2} \approx \frac{\alpha_H^2\alpha_V^2 F}{2\gamma_{\mathrm{X}}} e^{-\gamma_{\mathrm{B}}F/4} \tag{C17d}$$

Here, it is assumed that $\gamma_{\mathrm{B}}F/2$ is a small quantity. In this situation one also finds that

$$e^{-\gamma_{\mathrm{B}}F/2} + \frac{\gamma_{\mathrm{B}}F}{2} e^{-\gamma_{\mathrm{B}}F/4} \approx 1 \tag{C18}$$

Note that following the same steps one obtains $\overline{G}^{(II)}_{VH,VH} = \overline{G}^{(II)}_{HV,HV}$. Therefore, one ends up with the total integrated correlation functions

$$\overline{G}^{(2)}_{jj,jj} = \frac{1}{\gamma_{\mathrm{X}}\gamma_{\mathrm{B}}} \left[e^{-\gamma_{\mathrm{B}}F/2} + \frac{\gamma_{\mathrm{B}}F}{2} e^{-\gamma_{\mathrm{B}}F/4}\left(1 - \alpha_H^2\alpha_V^2\right) \right] \approx \frac{1}{\gamma_{\mathrm{X}}\gamma_{\mathrm{B}}}\left(1 - \alpha_H^2\alpha_V^2 \frac{\gamma_{\mathrm{B}}F}{2} e^{-\gamma_{\mathrm{B}}F/4}\right) \tag{C19a}$$

$$\overline{G}^{(2)}_{HH,VV} = \frac{1}{(\gamma_{\mathrm{X}} - i\delta/\hbar)\gamma_{\mathrm{B}}} \left[e^{-\gamma_{\mathrm{B}}F/2} + \frac{\gamma_{\mathrm{B}}F}{2} e^{-\gamma_{\mathrm{B}}F/4}\left(\frac{1}{2} + \alpha_H^2\alpha_V^2 \right) \right]$$

$$\approx \frac{1}{(\gamma_{\mathrm{X}} - i\delta/\hbar)\gamma_{\mathrm{B}}} \left[1 - \frac{\gamma_{\mathrm{B}}F}{4} e^{-\gamma_{\mathrm{B}}F/4}\left(1 - 2\alpha_H^2\alpha_V^2\right) \right] \tag{C19b}$$

$$\overline{G}^{(2)}_{HV,HV} = \frac{1}{\gamma_{\mathrm{X}}\gamma_{\mathrm{B}}} \alpha_H^2\alpha_V^2 \frac{\gamma_{\mathrm{B}}F}{2} e^{-\gamma_{\mathrm{B}}F/4} = \overline{G}^{(2)}_{VH,VH} \tag{C19c}$$

where we employ the approximation given in Eq. (C18). The normalization for the two-photon density matix is thus

$$\text{Tr}\left\{\overline{G}^{(2)}_{jk,\ell m}\right\} = 2\left(\overline{G}^{(2)}_{HH,HH} + \overline{G}^{(2)}_{HV,HV}\right) = \frac{2}{\gamma_\text{X}\gamma_\text{B}} \tag{C20}$$

Finally, the elements of the two-photon density matrix are calculated according to Eq. (A10a):

$$\rho^{\text{2p}}_{HH,HH} = \rho^{\text{2p}}_{VV,VV} = \left(\frac{1}{2} - \alpha_H^2\alpha_V^2\frac{\gamma_\text{B}F}{4}e^{-\gamma_\text{B}F/4}\right) \tag{C21a}$$

$$\rho^{\text{2p}}_{HH,VV} = \frac{1}{1 - i\frac{\delta}{\hbar\gamma_\text{X}}}\left[\frac{1}{2} - \frac{\gamma_\text{B}F}{8}e^{-\gamma_\text{B}F/4}\left(1 - 2\alpha_H^2\alpha_V^2\right)\right] = \left(\rho^{\text{2p}}_{VV,HH}\right)^* \tag{C21b}$$

$$\rho^{\text{2p}}_{HV,HV} = \alpha_H^2\alpha_V^2\frac{\gamma_\text{B}F}{4}e^{-\gamma_\text{B}F/4} = \rho^{\text{2p}}_{VH,VH} \tag{C21c}$$

Using the approximation presented in Eq. (A14) the concurrence can be estimated as

$$C \approx 2\left(|\rho^{\text{2p}}_{HH,VV}| - \rho^{\text{2p}}_{HV,HV}\right) = C_0(\gamma_\text{X},\delta)\left\{1 - f(\gamma_\text{B},F)\left[1 + g(\alpha_H)\right]\right\} - f(\gamma_\text{B},F)\left[1 - g(\alpha_H)\right] \tag{C22a}$$

$$C_0(\gamma_\text{X},\delta) = \frac{1}{\sqrt{1 + \left(\frac{\delta}{\hbar\gamma_\text{X}}\right)^2}} \tag{C22b}$$

$$f(\gamma_\text{B},F) = \frac{\gamma_\text{B}F}{8}\exp\left[-\frac{\gamma_\text{B}F}{4}\right] \tag{C22c}$$

$$g(\alpha_H) = \left(1 - 2\alpha_H^2\right)^2 \tag{C22d}$$

Thus, the analytic approximation for the concurrence presented in Eq. (6) of the main text is obtained.

D. DISCUSSION: HORIZONTAL LASER POLARIZATION

In this section we discuss and interpret the influence of a laser pulse with horizontal polarization. A horizontal laser polarization corresponds to setting $\alpha_H = 1$ and $\alpha_V = 0$. In this situation, the approximate result in Eq. (C22) reduces to

$$C = 2|\rho^{\text{2p}}_{HH,VV}| = C_0(\gamma_\text{X},\delta)\left[1 - 2f(\gamma_\text{B},\text{FWHM})\right] \tag{D1}$$

and the only four non-zero elements of the two-photon density matrix are the occupations $\rho^{\text{2p}}_{HH,HH} = \rho^{\text{2p}}_{VV,VV} = 1/2$ and the coherence $\rho^{\text{2p}}_{HH,VV} = (\rho^{\text{2p}}_{VV,HH})^*$. Thus, the deviation from a maximally entangled states is caused solely by a reduced coherence. The contribution to this effect, that originates from the influence of the laser pulse can be best understood when looking at the dressed states of the effective model and the approximate time evolution of an exciton occupation and coherence during the pulse duration.

For a horizontal laser polarization the four energy eigenstates of $\hat{H}_1$ are, cf., Eq. (C4),

$$|U\rangle = c\left(|G\rangle + |B\rangle\right) + \sqrt{2}\tilde{c}|X_\text{H}\rangle \approx |X_\text{H}\rangle \tag{D2a}$$

$$|M\rangle = |X_\text{V}\rangle \tag{D2b}$$

$$|N\rangle = \frac{1}{\sqrt{2}}\left(|G\rangle - |B\rangle\right) \tag{D2c}$$

$$|L\rangle = \tilde{c}\left(|G\rangle + |B\rangle\right) - \sqrt{2}c|X_\text{H}\rangle \approx \frac{1}{\sqrt{2}}\left(|G\rangle + |B\rangle\right) \tag{D2d}$$

Since the laser pulse couples only to the transitions between $|X_\text{H}\rangle$ and the ground or biexciton state, the interaction of laser and QD leads to the formation of three dressed states $|U\rangle$, $|N\rangle$, and $|L\rangle$ while the remaining state $|X_\text{V}\rangle$ is unaffected. This dressing effect results in an energetic splitting between the vertically polarized exciton state $|X_\text{V}\rangle$ and the dressed state $|U\rangle$, which for our parameters is essentially the horizontally polarized exciton state, cf., discussion in Section C II. Thus the horizontally polarized exciton state experiences a Stark-shift due to the interaction with the laser. According to Eq. (C12), the energetic splitting between the exciton states is approximately

$$E_\text{S} = E_\text{U} - E_\text{M} \approx \frac{\hbar\pi}{\text{FWHM}} \tag{D3}$$

Therefore the laser pulse introduces an effective splitting between the exciton states. After the emission of a first biexciton photon during the pulse window, the QD is in a superposition of the two exciton states. The effective splitting then leads to a phase oscillation of the corresponding exciton coherence. This phase oscillation can be observed in the approximate propagation given in Eq. (C14), which reduces to

$$\mathcal{P}^{(1)}_{t_0 \to t}[|X_j\rangle\langle X_j|] \approx |X_j\rangle\langle X_j| \tag{D4a}$$

$$\mathcal{P}^{(1)}_{t_0 \to t}[|X_\mathrm{V}\rangle\langle X_\mathrm{H}|] \approx e^{i\pi(t-t_0)/\mathrm{FWHM}}|X_\mathrm{V}\rangle\langle X_\mathrm{H}| \tag{D4b}$$

for a horizontal laser polarization. In the measurement process when one integrates correlation functions the integration over this phase oscillation causes a reduced absolute coherence value. In other words, one could also say that the laser introduces a which-path information during its interaction time with the QD, since it causes an effective splitting. Note that for an actual Gaussian pulse, this splitting is a time dependent quantity and scales with $\Omega^2(t)$.

Even in the absence of a fine-structure splitting, i.e. $\delta = 0$, this effect results in a two photon density matrix

$$\rho^{2\mathrm{P}} = \begin{pmatrix} \frac{1}{2} & 0 & 0 & \frac{1}{2}-f \\ 0 & 0 & 0 & 0 \\ 0 & 0 & 0 & 0 \\ \frac{1}{2}-f & 0 & 0 & \frac{1}{2} \end{pmatrix} \tag{D5}$$

in the basis $\{|HH\rangle, |HV\rangle, |VH\rangle, |VV\rangle\}$ with a corresponding concurrence

$$C = 1 - 2f(\gamma_\mathrm{B}, \mathrm{FWHM}) \tag{D6}$$

E. DISCUSSION: DIAGONAL LASER POLARIZATION

In this section we discuss and interpret the influence of a laser pulse with diagonal polarization. The diagonal laser polarization corresponds to setting $\alpha_H = \alpha_V = 1/\sqrt{2}$. Thus, the general approximate result in Eq. (C22) simplifies to

$$C \approx 2\left(|\rho^{2\mathrm{p}}_{HH,VV}| - \rho^{2\mathrm{p}}_{HV,HV}\right) = C_0(\gamma_\mathrm{X}, \delta)\left[1 - f(\gamma_\mathrm{B}, \mathrm{FWHM})\right] - f(\gamma_\mathrm{B}, \mathrm{FWHM}) \tag{E1}$$

and the six most important elements of the two-photon density matrix are the occupations $\rho^{2\mathrm{p}}_{HH,HH} = \rho^{2\mathrm{p}}_{VV,VV}$ and $\rho^{2\mathrm{p}}_{HV,HV} = \rho^{2\mathrm{p}}_{VH,VH}$ as well as the coherence $\rho^{2\mathrm{p}}_{HH,VV} = (\rho^{2\mathrm{p}}_{VV,HH})^*$. In this situation, one obtains the ratio

$$\frac{|\rho^{2\mathrm{p}}_{HH,VV}|}{\rho^{2\mathrm{p}}_{HH,HH}} = C_0 \tag{E2}$$

Thus the ratio of the coherence $\rho^{2\mathrm{p}}_{HH,VV}$ and the occupation $\rho^{2\mathrm{p}}_{HH,HH}$ is precisely the same as for the initial value calculation presented in Section B. Consequently, the impact of the laser pulse as captured by the function f does not equate to an additional effective splitting that reduces the coherence compared to its corresponding occupations. Instead the reduced degree of entanglement originates from finite occupations $\rho^{2\mathrm{p}}_{HV,HV}$ and $\rho^{2\mathrm{p}}_{VH,VH}$, i.e., two-photon states that consist of photons with two different polarizations. Again, the impact of the laser pulse can be analyzed by investigating the dressed states of the effective model and the approximate time evolution of an exciton occupation during the pulse duration.

For a diagonal laser polarization, the four eigenstates of the effective Hamiltonian $\hat{H}_1$, given in Eq. (C4), become

$$|U\rangle = c\left(|G\rangle + |B\rangle\right) + \tilde{c}\left(|X_\mathrm{H}\rangle + |X_\mathrm{V}\rangle\right) \approx \frac{1}{\sqrt{2}}\left(|X_\mathrm{H}\rangle + |X_\mathrm{V}\rangle\right) \tag{E3a}$$

$$|M\rangle = \frac{1}{\sqrt{2}}\left(|X_\mathrm{H}\rangle - |X_\mathrm{V}\rangle\right) \tag{E3b}$$

$$|N\rangle = \frac{1}{\sqrt{2}}\left(|G\rangle - |B\rangle\right) \tag{E3c}$$

$$|L\rangle = \tilde{c}\left(|G\rangle + |B\rangle\right) - c\left(|X_\mathrm{H}\rangle + |X_\mathrm{V}\rangle\right) \approx \frac{1}{\sqrt{2}}\left(|G\rangle + |B\rangle\right) \tag{E3d}$$

In contrast to the horizontal laser polarization, all four states are dressed states, i.e., are a mixture of several bare states. In particular, the two upper dressed states, $|U\rangle$ and $|M\rangle$, are in good approximation equal superpositions of

both exciton states. Just as the lower dressed states $|N\rangle$ and $|L\rangle$ describe the two-photon resonant excitation between the ground and biexciton state (cf., Section C II), the upper ones represent a two-photon resonant process between the two orthogonally polarized exciton states.

This effect is clearly visible in the approximate time dynamics of an exciton state during the pulse interval F. For a diagonal laser polarization, Eq. (C14) yields

$$
\begin{aligned}
\mathcal{P}_{t_0 \to t}^{(1)}[|X_j\rangle\langle X_j|] \approx & \frac{1}{2}\left[1 + \cos\left(\frac{\pi(t-t_0)}{\text{FWHM}}\right)\right]|X_j\rangle\langle X_j| + \frac{i}{2}\sin\left(\frac{\pi(t-t_0)}{\text{FWHM}}\right)(|X_j\rangle\langle X_\ell| - |X_\ell\rangle\langle X_j|) \\
& + \frac{1}{2}\left[1 - \cos\left(\frac{\pi(t-t_0)}{\text{FWHM}}\right)\right]|X_\ell\rangle\langle X_\ell|
\end{aligned}
\tag{E4}
$$

where $j, \ell \in \{H, V\}$ and $\ell \neq j$. This approximate dynamics describes precisely a full-amplitude (coherent) oscillation between the two different exciton states. Thus, if a first biexciton photon is emitted during the pulse duration and the system is in an exciton state, the pulse introduces an effective coupling to the other exciton state. Therefore, the exciton state can change during the pulse duration and the subsequent exciton photon can have a different polarization than the biexciton photon. Consequently, the interaction with the laser, enables the creation of two-photon states $|HV\rangle$ and $|VH\rangle$, which are unwanted and represent a deviation from the maximally entangled state $|\Phi_\pm\rangle$. Hence one obtains a reduced degree of entanglement.

Note that this effective coupling between the exciton states does not include an actual re-excitation back into the biexciton state. Thus no additional photons are created. Still the degree of entanglement drops.

Most importantly, even in the absence of a fine-structure splitting, i.e. $\delta = 0$, the effective coupling results in a two-photon density matrix[9]

$$
\rho^{2\text{P}} = \begin{pmatrix}
\frac{1}{2}(1-f) & 0 & 0 & \frac{1}{2}(1-f) \\
0 & \frac{1}{2}f & \frac{1}{2}f & 0 \\
0 & \frac{1}{2}f & \frac{1}{2}f & 0 \\
\frac{1}{2}(1-f) & 0 & 0 & \frac{1}{2}(1-f)
\end{pmatrix}
\tag{E5}
$$

in the basis $\{|HH\rangle, |HV\rangle, |VH\rangle, |VV\rangle\}$ with a corresponding concurrence

$$
C = 1 - 2f(\gamma_\text{B}, \text{FWHM})
\tag{E6}
$$

The rise of the elements $\rho_{HV,HV}^{2\text{p}}$ and $\rho_{VH,VH}^{2\text{p}}$ by $f/2$ leads to a reduction of the occupations $\rho_{HH,HH}^{2\text{p}}$ and $\rho_{VV,VV}^{2\text{p}}$ and the corresponding coherence $\rho_{HH,VV}^{2\text{p}}$ by the same amount.

Note that the expression for the concurrence is identical to the result for a vanishing fine-structure splitting using a horizontal laser polarization, given in Eq. (D6). From a physical point of view, this must be fulfilled. For a vanishing fine-structure splitting no pair of orthogonal polarized exciton states is distinguished. Therefore, one could simply perform a basis transformation into a new pair of exciton states

$$
|X_\text{D}\rangle = \frac{1}{\sqrt{2}}\left(|X_\text{H}\rangle + |X_\text{V}\rangle\right)
\tag{E7a}
$$

$$
|X_\text{A}\rangle = \frac{1}{\sqrt{2}}\left(|X_\text{H}\rangle - |X_\text{V}\rangle\right)
\tag{E7b}
$$

where only one exciton ($|X_\text{D}\rangle$) couples to the laser polarization and the other is decoupled. Of course after this transformation, the system is identical to the situation of a horizontal laser polarization as discussed in Section D. Consequently the resulting degree of entanglement must also remain the same.

In addition, when one also transforms the measurement basis for the two-photon density matrix accordingly, i.e., from H and V polarization to the diagonal D and anti-diagonal A basis via

$$
|D\rangle = \frac{1}{\sqrt{2}}\left(|H\rangle + |V\rangle\right)
\tag{E8a}
$$

$$
|A\rangle = \frac{1}{\sqrt{2}}\left(|H\rangle - |V\rangle\right)
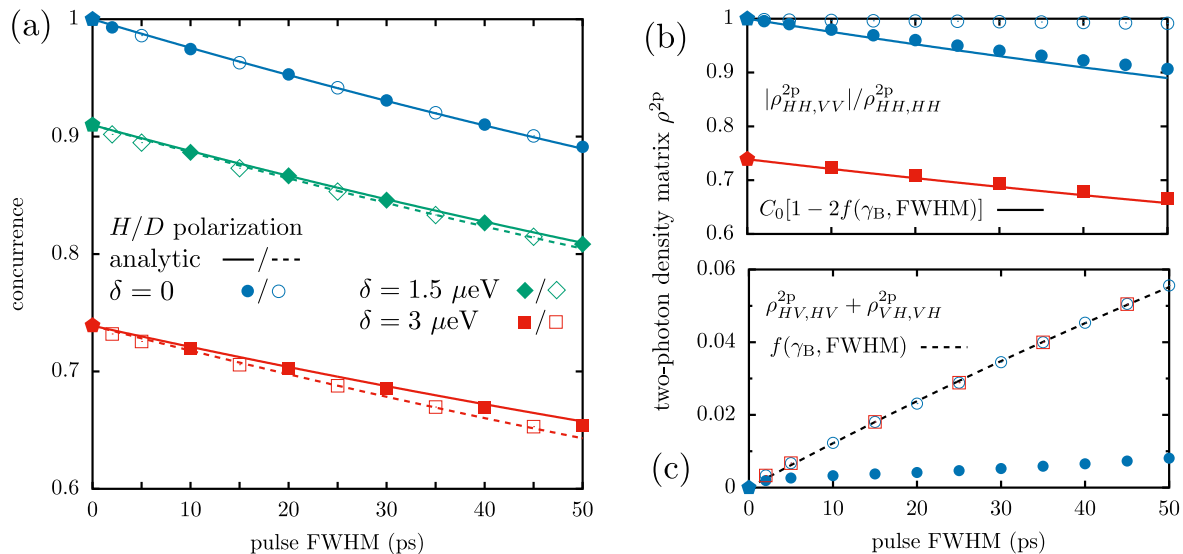\tag{E8b}
$$

FIG. F1. (a) Concurrence in dependence of the pulse duration, characterized by the FWHM. Results are shown for two laser polarizations [horizontal (H): filled symbols and diagonal (D): open symbols] and three fine-structure splittings $\delta = 0$ (blue circles), 1.5 μeV (green diamonds), and 3 μeV (red squares). In addition to numerical results (symbols), the analytic approximation according to Eq. (C22) is included as lines with the same color [H (D) polarization: solid (dashed) line]. For $\delta = 0$, the results for H and D polarization are exactly the same. Data points at FWHM $= 0$ (pentagons) represent calculations with an initially prepared biexciton. (b) Ratio between the density matrix elements $\rho^{2\mathrm{p}}_{HH,VV}$ and $\rho^{2\mathrm{p}}_{HH,HH}$ for $\delta = 0$ (H and D polarization) and $\delta = 3$ μeV (only H polarization) together with the analytic estimate for a horizontal laser polarization. (c) Sum of the elements $\rho^{2\mathrm{p}}_{HV,HV}$ and $\rho^{2\mathrm{p}}_{VH,VH}$ for $\delta = 0$ (H and D polarization) and $\delta = 3$ μeV (only D polarization) together with the analytic estimate for a diagonal laser polarization.

the two-photon density matrix becomes

$$
\rho^{2\mathrm{p}} = \begin{pmatrix} \frac{1}{2} & 0 & 0 & \frac{1}{2} - f \\ 0 & 0 & 0 & 0 \\ 0 & 0 & 0 & 0 \\ \frac{1}{2} - f & 0 & 0 & \frac{1}{2} \end{pmatrix} \tag{E9}
$$

in the basis $\{|DD\rangle, |DA\rangle, |AD\rangle, |AA\rangle\}$. As expected this is precisely the result obtained for a horizontal laser polarization, cf., Eq. (D5). This finding highlights the fact, that for a vanishing fine-structure splitting both laser polarizations are equivalent and that the influence of the laser pulse which introduces an effective splitting in one picture, i.e., horizontal laser polarization, is equivalent to the effective coupling in the other one, i.e., diagonal laser polarization.

Note that we only discussed two limiting cases. For a vanishing fine-structure splitting, any linear laser polarization will result in the same degree of entanglement and the impact of the laser will in general present itself as a combination of both, an effective splitting and an effective coupling, depending on the chosen basis.

F. EXTENDED FIGURE 2 - DENSITY MATRIX ELEMENTS

Figure F1 is an extension to Fig. 2 in the main text which also includes selected elements of the two-photon density matrix. In addition to the concurrence, also the numerical data for the density matrix elements agrees very well with the analytic estimate. Thus, the behavior of the two-photon density matrix supports the physical picture and interpretation.

For a horizontal laser polarization, the decreasing concurrence with rising FWHM is caused by an energetic splitting E_S between the two exciton states $|X_\mathrm{H}\rangle$ and $|X_\mathrm{V}\rangle$, which is introduced by the TPE scheme itself. Thus, the main effect of the laser pulse is an additional loss of coherence, cf., filled symbols in panels (b) and (c). Re-excitation of the system, i.e., the creation of additional photons is negligible. This is evident from the filled blue circles in panel (c). The two-photon density matrix elements $\rho^{2\mathrm{p}}_{HV,HV}$ and $\rho^{2\mathrm{p}}_{VH,VH}$, which in the case of a horizontal laser polarization can only be created after re-excitation, are insignificantly small.

On the other hand, a diagonal laser polarization introduces a direct coupling between the two exciton states $|X_H\rangle$ and $|X_V\rangle$, leading to finite elements with two differently polarized photons $\rho^{2p}_{HV,HV}$ and $\rho^{2p}_{VH,VH}$, cf., open symbols in panels (b) and (c). Note that for a diagonal laser polarization the increase of these matrix elements is caused by the effective coupling which does not include an actual re-excitation into the biexciton state.

A finite fine-structure splitting $\delta \ll E_B$ hardly impacts the TPE scheme. Thus, for typical fine-structure splittings, the impact of the laser is virtually independent of δ. This is evident in Fig. F1(c), where hardly any change can be observed when one compares the results for $\delta = 0$ (open blue circles) and $\delta = 3~\mu eV$ (open red squares).

G. OPTIMAL LASER POLARIZATION

In this section, we discuss the optimal laser polarization. By variation of the coefficient $\alpha_H \in [-1, 1]$ representing the horizontal component of the laser polarization in Eq. (C22), one can determine the optimal laser polarization.

$$\frac{\partial}{\partial \alpha_H} C = f(\gamma_B, \text{FWHM}) \left[1 - C_0(\gamma_X, \delta)\right] \frac{\partial}{\partial \alpha_H} g(\alpha_H) \tag{G1a}$$

$$\frac{\partial}{\partial \alpha_H} g = 8\alpha_H \left(2\alpha_H^2 - 1\right) \tag{G1b}$$

For a vanishing fine-structure splitting $\delta = 0$ the function $C_0(\gamma_X, \delta)$, which represents the concurrence for an initially prepared biexciton state, is unity. Thus, in accordance with the discussion at the end of Section E, all linear laser polarizations are equivalent and result in the same degree of entanglement.

This of course changes when the fine-structure splitting is finite and one pair of orthogonally polarized exciton states is distinct by the system. In the situation considered here, i.e., $\delta \ll E_B/2$, Eq. (G1) has three simple zeros: $\alpha_H \in \{0, \pm 1/\sqrt{2}\}$. Since $g(\alpha_H = \pm 1) = g(\alpha_H = 0)$, the highest degree of entanglement is obtained when the laser polarization coincides with one of the two distinct exciton states. On the other hand, the emitted photon pairs have the lowest possible degree of entanglement if a diagonal polarization is used, which has equal components in H and V polarization, i.e., if $\alpha_H = \pm 1/\sqrt{2}$. The difference between the maximum and minimum degree of entanglement for a given fine-structure splitting and pulse duration is

$$\begin{aligned} \Delta C &= C(\alpha_H = 0) - C(\alpha_H = 1/\sqrt{2}) \\ &= f(\gamma_B, \text{FWHM}) \left[1 - C_0(\gamma_X, \delta)\right] \end{aligned} \tag{G2}$$

[1] G. Lindblad, Commun. Math. Phys. **48**, 119 (1976).
[2] S. Bravyi, D. P. DiVincenzo, and D. Loss, Ann. Phys. **326**, 2793 (2011).
[3] R. Winkler, *Spin-Orbit Coupling Effects in Two-Dimensional Electron and Hole Systems*, Springer Tracts in Modern Physics, Vol. 191 (Springer, Berlin, 2003).
[4] D. F. V. James, P. G. Kwiat, W. J. Munro, and A. G. White, Phys. Rev. A **64**, 052312 (2001).
[5] M. Cygorek, F. Ungar, T. Seidelmann, A. M. Barth, A. Vagov, V. M. Axt, and T. Kuhn, Phys. Rev. B **98**, 045303 (2018).
[6] M. Cosacchi, M. Cygorek, F. Ungar, A. M. Barth, A. Vagov, and V. M. Axt, Phys. Rev. B **98**, 125302 (2018).
[7] W. K. Wootters, Phys. Rev. Lett. **80**, 2245 (1998).
[8] T. Seidelmann, M. Cosacchi, M. Cygorek, D. E. Reiter, A. Vagov, and V. M. Axt, Adv. Quantum Technol. **4**, 2000108 (2021).
[9] Although not all elements are explicitly derived, this expression for the density matrix is the exact result when one uses the effective model and calculation scheme presented in Section C.

Publication 10

"Phonon-induced transition between entangled and nonentangled phases in constantly driven quantum dot-cavity systems"

T. Seidelmann, M. Cosacchi, M. Cygorek, D. E. Reiter, A. Vagov, and V. M. Axt.

Author contributions

The author has designed the concept of this study, has performed the numerical data generation and analysis, and has implemented the problem-specific C++ code. He has provided interpretations of the results and has written the first draft of the publication. In particular, he provided an analytic argument for the form of the two-photon density matrix and constructed a general decomposition into factorizable two-photon states.

M. Cosacchi has participated in the general discussion of the results and their interpretations. Furthermore, he has discussed the results in detail with the author. He has also contributed to revisions of the draft.

M. Cygorek, A. Vagov, and D. E. Reiter have co-supervised this work. In particular, they have participated in the discussion of the results and their interpretations. They have also contributed to the optimization of the presentation and revisions of the draft.

V. M. Axt has advised the author throughout his work as the main supervisor, has obtained the funding for this work, and has provided the practical means. He has participated in the discussion of the results and their interpretations. He has also contributed to the optimization of the presentation and revisions of the draft.

Phonon-induced transition between entangled and nonentangled phases in constantly driven quantum dot-cavity systems

T. Seidelmann,[1, *] M. Cosacchi,[1] M. Cygorek,[2] D. E. Reiter,[3, †] A. Vagov,[1] and V. M. Axt[1]

[1]*Lehrstuhl für Theoretische Physik III, Universität Bayreuth, 95440 Bayreuth, Germany*
[2]*Heriot-Watt University, Edinburgh EH14 4AS, United Kingdom*
[3]*Institut für Festkörpertheorie, Universität Münster, 48149 Münster, Germany*

Entangled photon pairs are essential for many applications in quantum technologies. Recent theoretical studies demonstrated that different types of entangled Bell states can be created in a constantly driven four-level quantum emitter-cavity system. Unlike other candidates for the realization of the four-level emitter, semiconductor quantum dots unavoidably interact with their environment, resulting in carrier-phonon interactions. Surprisingly, phonons change the entanglement of emitted photon pairs in a qualitative way, already at low temperatures on the order of 4 K. While one type of Bell state can still be generated using small driving strengths, the other type is suppressed due to phonon interactions. The degree of entanglement decreases with rising temperature and driving strength until it vanishes at a critical parameter value. Because it remains zero afterwards, we encounter a phonon-induced phase transition between an entangled and nonentangled phase with critical temperatures below 30 K. The concurrence is regarded as the order parameter and, independent of the driving strength, a corresponding critical exponent can be extracted which is found to be 1.

I. INTRODUCTION

The phenomenon of quantum entanglement is one of the most fascinating and unintuitive effects in nature. Being a pure quantum effect, entanglement is interesting not only from a fundamental view, but it also prompted the development of innovative applications in novel research fields, like quantum cryptography [1, 2], quantum communication [3, 4], and quantum information processing and computing [5–8].

An often discussed realization of entangled qubits are polarization entangled photon pairs. Typically, one aims for the generation of one of the four Bell states

$$|\Phi_{\pm}\rangle = \frac{1}{\sqrt{2}} \left(|HH\rangle \pm |VV\rangle\right) \qquad (1a)$$

$$|\Psi_{\pm}\rangle = \frac{1}{\sqrt{2}} \left(|HV\rangle \pm |VH\rangle\right), \qquad (1b)$$

the most prominent maximally entangled states established for linearly polarized photon pairs. Here H and V denote horizontally and vertically polarized photons, respectively, and their order reflects the order of photon detection. One can distinguish between two different types of Bell states (or Bell state entanglement): While in a Φ Bell state (ΦBS) the first and second detected photon possess the same polarization, in a Ψ Bell state (ΨBS) they exhibit the opposite one.

A promising platform for the generation of a maximally entangled Bell state are semiconductor quantum dots (QDs), which realize a four-level quantum emitter [9, 10]. The biexciton-exciton cascade in QDs comprises its ground state, two exciton states, and the biexciton. Due to the optical selection rules, these four electronic levels display a diamond-shaped configuration, cf., Fig. 1. After an initial excitation of the biexciton [11–17], the subsequent photon emission induced by the cascade, should, in an ideal situation, result in the generation of a maximally entangled ΦBS. By embedding the QD inside a microcavity, one can enhance the light-collection efficiency and photon emission rate due to the Purcell effect [18]. Furthermore, the energy of the cavity modes can have a profound impact on the resulting type and degree of entanglement [10, 19–22].

Indeed, various theoretical and experimental studies demonstrated the possibility to obtain ΦBS entanglement in the chosen basis of linearly polarized photons [11, 18, 19, 22–45]. Furthermore, recent theoretical studies [10, 21, 46] showed that a four-level emitter–cavity system, e.g., a QD embedded inside a cavity, can also facilitate the creation of ΨBS entanglement, when a constant laser driving is applied to the emitter. In this setup, four laser-dressed states emerge and their characteristics depend on the applied driving strength. By adjusting the cavity modes to a direct two-photon transition between these dressed states, entangled photon pairs can be created. The resulting type and degree of entanglement depends crucially on the applied driving strength and the energy of the cavity modes [10, 46].

In contrast to other possible realizations of the quantum emitter, e.g., atomic systems, QDs unavoidably interact with their semiconductor environment, which results in carrier-phonon interactions [47–54]. Although phonons are associated with the loss of quantum coherence in the system, their possible impact on the resulting two-photon state and its degree of entanglement cannot be easily predicted. Indeed, various scenarios and de-

pendencies have been found for different QD setups. Although the interaction with phonons often results in a reduced degree of entanglement, their detrimental impact can depend strongly on the chosen cavity arrangement [22]. Furthermore, in highly symmetric situations, phonons may have no impact on entanglement at all [26]. Moreover, even a phonon-induced enhancement of the degree of entanglement has been predicted under special conditions [24]. Therefore, it is not a priori clear in which manner phonons may impact the constantly driven QD-cavity system.

In this article, we investigate the phonon influence on emitted photon pairs in this system. In our theoretical study, we consider the configuration where the highest degrees of ΦBS and ΨBS entanglement have been predicted in the phonon-free analysis of a four-level quantum emitter [10]. Remarkably, the phonon impact on the entanglement is much more severe than in studies employing an initially prepared biexciton without constant driving. Not only does the interaction with phonons strongly reduce the degree of entanglement for small driving strength values already at 4 K, but it results in the absence of entanglement for higher driving strength values and/or temperatures. A qualitative change of the stationary state of a driven dissipative system upon change of a parameter is often referred to as a dissipative phase transition [55, 56]. The observed change of the emitted photon states in the presence of phonon interactions can be understood as a competition between two phases characterized by stationary states being either entangled or not. Thus we encounter a phonon-induced phase transition, where the generated photon pairs transform from an entangled to a nonentangled phase at a critical temperature or driving strength. The concurrence [57], a well established entanglement measure, takes on the role of the order parameter that characterizes this transition.

II. DRIVEN QUANTUM-DOT–CAVITY SYSTEM

We consider the biexciton-exciton cascade of a strongly-confined, self-assembled GaAs semiconductor QD. The QD is embedded inside a microcavity and is continuously driven by an external laser, cf., Fig. 1 for a schematic sketch. Furthermore, the QD interacts with its surrounding semiconductor environment, resulting in a coupling to lattice oscillations, i.e., phonons. In the case of GaAs QDs at low temperatures, the most important interaction is due to the deformation potential coupling to longitudinal acoustic (LA) phonons [58].

The QD comprises the ground state $|G\rangle$, two orthogonally polarized exciton states $|X_{H/V}\rangle$ at energy $\hbar\omega_X$ that couple to horizontally (H) and vertically (V) polarized light, respectively, and the biexciton state $|B\rangle$. In the frame co-rotating with the external laser frequency ω_L,
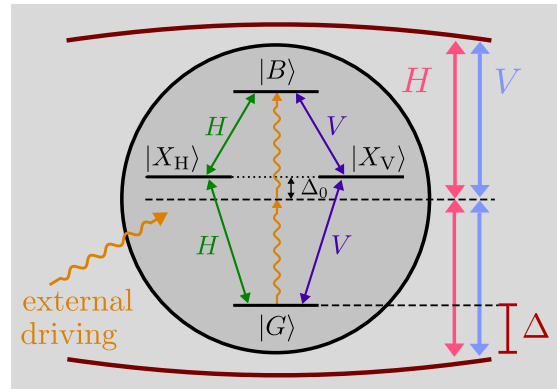

FIG. 1. Schematic sketch of the driven QD-cavity system. The biexciton-exciton cascade comprises the ground state $|G\rangle$, two energetically degenerate exciton states $|X_{H/V}\rangle$ that couple to horizontally or vertically polarized light, respectively (indicated by green and purple arrows), and the biexciton state $|B\rangle$. Curvy orange arrows represent the external laser driving adjusted to the two-photon transition between $|G\rangle$ and $|B\rangle$. The laser is detuned from the exciton energy by the value $\Delta_0 = E_B/2$. The energy of the two degenerate but orthogonally polarized cavity modes (red and blue arrows) is described by the cavity-laser detuning Δ.

the QD-cavity Hamiltonian is given by [10, 21]

$$
\begin{aligned}
\hat{H}_{\text{QD-C}} = {} & \Delta_0 \left(|X_H\rangle\langle X_H| + |X_V\rangle\langle X_V| \right) \\
& + (2\Delta_0 - E_B) |B\rangle\langle B| \\
& + \sum_{\ell=H,V} \Delta \hat{a}_\ell^\dagger \hat{a}_\ell + \sum_{\ell=H,V} g \left(\hat{a}_\ell^\dagger \hat{\sigma}_\ell + \hat{a}_\ell \hat{\sigma}_\ell^\dagger \right),
\end{aligned}
\tag{2}
$$

where the energy of the ground state is used as the zero of the energy scale, $\Delta_0 := \hbar(\omega_X - \omega_L)$ is the energetic detuning between the exciton states and the laser energy, and E_B denotes the biexciton binding energy. The electronic transitions of the QD are described by the operators

$$
\hat{\sigma}_H = |G\rangle\langle X_H| + |X_H\rangle\langle B| \tag{3a}
$$

$$
\hat{\sigma}_V = |G\rangle\langle X_V| + |X_V\rangle\langle B| \tag{3b}
$$

and are coupled to two energetically degenerate, but orthogonally polarized cavity modes with energy $\hbar\omega_C$. The bosonic operator $\hat{a}_{H/V}^\dagger$ creates a cavity photon with the respective polarization, H or V, and the QD-cavity coupling strength g is assumed to be equal for all transitions. The energy of the cavity modes is described by the cavity-laser detuning $\Delta := \hbar(\omega_C - \omega_L)$.

An external laser with driving strength Ω and constant frequency ω_L continuously excites the QD. Following Ref. 10 the frequency is adjusted to the two-photon transition between ground and biexciton state, i.e., $\Delta_0 = E_B/2$, and the polarization is chosen to be diagonal in the basis spanned by H and V. In the rotating

frame, the respective Hamiltonian is given by

$$\hat{H}_{\mathrm{L}} = \Omega \left(\hat{\sigma}_{\mathrm{D}} + \hat{\sigma}_{\mathrm{D}}^{\dagger} \right); \quad \hat{\sigma}_{\mathrm{D}} = \left(\hat{\sigma}_{\mathrm{H}} + \hat{\sigma}_{\mathrm{V}} \right)/\sqrt{2}. \quad (4)$$

The coupling to LA phonons is described by

$$\hat{H}_{\mathrm{Ph}} = \hbar \sum_{\mathbf{q}} \omega_{\mathbf{q}} \hat{b}_{\mathbf{q}}^{\dagger} \hat{b}_{\mathbf{q}} + \hbar \sum_{\chi, \mathbf{q}} n_{\chi} \left(\gamma_{\mathbf{q}}^{X} \hat{b}_{\mathbf{q}}^{\dagger} + \gamma_{\mathbf{q}}^{X*} \hat{b}_{\mathbf{q}} \right) |\chi\rangle\langle\chi|, \quad (5)$$

where the bosonic operator $\hat{b}_{\mathbf{q}}$ destroys a phonon in mode $\mathbf{q}$ with energy $\hbar\omega_{\mathbf{q}}$. $\gamma_{\mathbf{q}}^{X}$ denotes the exciton-phonon coupling strength and $n_{\chi} = \{0, 1, 1, 2\}$ is the number of excitons present in the QD state $|\chi\rangle \in \{|G\rangle, |X_{\mathrm{H}}\rangle, |X_{\mathrm{V}}\rangle, |B\rangle\}$.

Furthermore, important loss channels, namely cavity losses with rate κ and radiative decay with rate γ, are incorporated into the model via Lindblad operators [59]

$$\mathcal{L}_{\hat{O}, \Gamma} \hat{\rho} = \frac{\Gamma}{2} \left(2\hat{O}\hat{\rho}\hat{O}^{\dagger} - \hat{O}^{\dagger}\hat{O}\hat{\rho} - \hat{\rho}\hat{O}^{\dagger}\hat{O} \right), \quad (6)$$

where $\hat{O}$ is the system operator associated with a loss process with rate Γ.

The dynamics of the statistical operator of the system $\hat{\rho}$ is described by the Liouville-von Neumann equation

$$\frac{\mathrm{d}}{\mathrm{d}t}\hat{\rho} = \mathcal{L}\hat{\rho} := -\frac{i}{\hbar} \left[\hat{H}, \hat{\rho} \right] \quad (7)$$
$$+ \sum_{\ell = \mathrm{H, V}} \left\{ \mathcal{L}_{\hat{a}_{\ell}, \kappa} + \mathcal{L}_{|G\rangle\langle X_{\ell}|, \gamma} + \mathcal{L}_{|X_{\ell}\rangle\langle B|, \gamma} \right\} \hat{\rho}$$
$$\hat{H} = \hat{H}_{\mathrm{QD\text{-}C}} + \hat{H}_{\mathrm{L}} + \hat{H}_{\mathrm{Ph}}. \quad (8)$$

where $[\cdot, \cdot]$ denotes the commutator. Employing a real-time path-integral method (consult Refs. 60–64 for details) the time-evolution of the reduced density matrix of the QD-cavity system is evaluated in a numerically exact manner. For our numerical calculations, we assume that the phonons are initially in thermal equilibrium at temperature T and that the QD-cavity system is initially in the ground state $|G\rangle$ without any cavity photons.

Following Refs. 10 and 21 we choose realistic parameters for the QD-cavity system that are summarized in Table I. Furthermore, we consider a spherically symmetric GaAs QD with a harmonic oscillator confinement and an electron (hole) confinement length $a_{\mathrm{e}} = 3$ nm ($a_{\mathrm{h}} = a_{\mathrm{e}}/1.15$). The deformation potential coupling of the QD to LA phonons enters the path-integral calculations via the phonon spectral density $J(\omega) = \sum_{\mathbf{q}} |\gamma_{\mathbf{q}}^{X}|^2 \delta(\omega - \omega_{\mathbf{q}})$. An explicit expression for this quantity, assuming a linear dispersion relation, and the used material parameters can be found in Appendix A.

III. ENTANGLEMENT DETERMINATION

A. Two-photon density matrix

In a typical experimental setup the two-photon density matrix $\rho^{2\mathrm{p}}$ is reconstructed using quantum state

TABLE I. Fixed system parameters used in the calculations.

Parameter		Value
QD-cavity coupling strength	g	0.051 meV
Biexciton binding energy	E_{B}	$20g = 1.02$ meV
Detuning	Δ_0	$E_{\mathrm{B}}/2 = 0.51$ meV
Cavity loss rate	κ	$0.1g/\hbar \approx 7.8$ ns^{-1}
Radiative decay rate	γ	$0.01g/\hbar \approx 0.78$ ns^{-1}

tomography [65]. This reconstruction scheme relies on polarization-resolved two-time correlation measurements. The detected signals in these measurements are proportional to two-time correlation functions

$$G_{jk,\ell m}^{(2)}(t, \tau') = \left\langle \hat{a}_j^{\dagger}(t) \hat{a}_k^{\dagger}(t + \tau') \hat{a}_m(t + \tau') \hat{a}_\ell(t) \right\rangle, \quad (9)$$

where $\{j, k, \ell, m\} \in \{H, V\}$. Here, t is the time when the first photon is detected and τ' the delay time until a subsequent, second photon is detected. Although Eq. (9) describes cavity photons, it can also be used to model correlation functions for photons measured in the free space outside the cavity, when the outcoupling of light from the cavity into the free space is assumed to be a Markovian process [7].

Because in standard experiments the measurement data is typically averaged over finite real and delay time intervals, the reconstructed two-photon density matrix is theoretically calculated as [10, 21]

$$\rho_{jk,\ell m}^{2\mathrm{p}} = \frac{\overline{G}_{jk,\ell m}^{(2)}}{\mathrm{Tr}\left\{ \overline{G}^{(2)} \right\}} \quad (10a)$$

$$\overline{G}_{jk,\ell m}^{(2)} = \frac{1}{\Delta t\, \tau} \int\limits_{t_0}^{t_0 + \Delta t} \mathrm{d}t \int\limits_{0}^{\tau} \mathrm{d}\tau'\, G_{jk,\ell m}^{(2)}(t, \tau') \quad (10b)$$

where t_0 is the starting time of the coincidence measurement and τ (Δt) the used delay time (real time) window. The trace $\mathrm{Tr}\{\cdot\}$ in Eq. (10) is introduced for the purpose of normalization. Note that, in principle, $\rho^{2\mathrm{p}}$ depends on all three measurement parameters: t_0, Δt, and τ [23].

Throughout this article, the two-photon density matrix is determined for the steady state $\hat{\rho}_s$ of the system defined as $\frac{\mathrm{d}}{\mathrm{d}t}\hat{\rho}_s = \mathcal{L}\hat{\rho}_s = 0$. Thus, in the calculation scheme, the time t_0 is chosen such that it occurs after the system has reached a stationary density matrix in the time evolution. Note that in this situation $\overline{G}_{jk,\ell m}^{(2)}$ and therefore also $\rho^{2\mathrm{p}}$ become independent of t_0 and Δt. Thus, the two-photon density matrix does only depend on the delay time window, which we fix to a value of $\tau = 50$ ps [66]. For details on the evaluation of multi-time correlation functions in the path-integral framework, we refer to Ref. 67.

After the two-photon density matrix has been obtained, the type of entanglement can be determined directly from its form. One encounters a ΦBS (ΨBS) when

the corresponding occupations of the two-photon states $|HH\rangle$ and $|VV\rangle$ ($|HV\rangle$ and $|VH\rangle$) dominate.

B. Concurrence

The degree of entanglement associated with a given two-photon density matrix $\rho^{2\mathrm{p}}$ is quantified by the concurrence [57]. The concurrence C has a one-to-one correspondence to the entanglement of formation, which in turn represents the minimal amount of pure-state entanglement that is at least present in a mixed state described by a given two-qubit density matrix [23, 57]. In contrast to the latter, the concurrence can be calculated directly from the two-photon density matrix $\rho^{2\mathrm{p}}$ according to [10, 57, 65]

$$C = \max \left\{ 0, \sqrt{\lambda_1} - \sqrt{\lambda_2} - \sqrt{\lambda_3} - \sqrt{\lambda_4} \right\}, \qquad (11)$$

where $\lambda_j \geq \lambda_{j+1}$ are the (real and positive) eigenvalues of the matrix

$$M = \rho^{2\mathrm{p}} \, T \, (\rho^{2\mathrm{p}})^* \, T. \qquad (12)$$

Here, T is an anti-diagonal 4×4-matrix with elements $\{-1, 1, 1, -1\}$ and $(\rho^{2\mathrm{p}})^*$ denotes the Hermitian conjugated two-photon density matrix. Because $\rho^{2\mathrm{p}}$ depends in principle on the parameters t_0, Δt, and τ, the same applies to the concurrence.

Altogether, the type and degree of entanglement is obtained as follows: (i) The averaged two-photon correlations $\overline{G}^{(2)}_{jk,\ell m}$ are calculated for the steady state employing the path-integral method. (ii) The two-photon density matrix $\rho^{2\mathrm{p}}$ is calculated according to Eq. (10) and the type of entanglement can be identified. (iii) The concurrence is evaluated for the obtained density matrix $\rho^{2\mathrm{p}}$ using Eq. (11).

IV. PHONON-INDUCED PHASE TRANSITION

A. Phonon-free results

Because the parameter space of the considered system is quite large, we restrict our study to the parameters, where the highest degrees of entanglement are obtained in the phonon-free case. In Ref. 10, the phonon-free case was analyzed in detail for a general four-level quantum emitter and it was demonstrated that the resulting type of entanglement and its degree depend on the applied driving strength Ω and the used cavity laser detuning Δ. Furthermore, it was shown that a high degree of either ΦBS or ΨBS entanglement can only be achieved when the cavity modes are close to resonance with a direct two-photon transition between the laser-dressed states of the four-level emitter.

Due to the constant laser excitation, transitions do not take place between the bare states $|G\rangle$, $|X_{\mathrm{H/V}}\rangle$, and $|B\rangle$
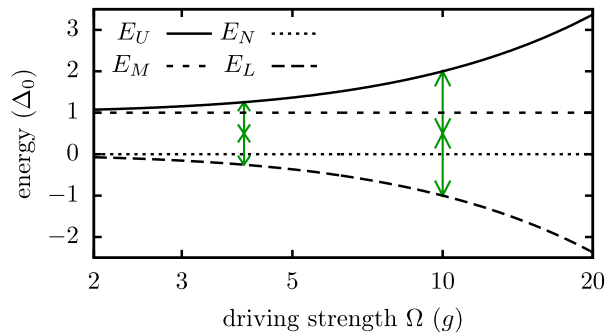

FIG. 2. Energies of the four laser-dressed states $|U\rangle$, $|M\rangle$, $|N\rangle$, and $|L\rangle$ as a function of the driving strength Ω. The cavity modes are always tuned to match the two-photon resonance between $|U\rangle$ and $|L\rangle$. For two exemplary driving strength values, the energy of the cavity modes Δ (in a frame co-rotating with the laser frequency) is indicated as green double-headed arrows.

but rather between eigenstates of the constantly driven QD, i.e., the four laser-dressed states which we denote as $|U\rangle$ ("uppermost"), $|M\rangle$ ("middle"), $|N\rangle$ ("null"), and $|L\rangle$ ("lowest"). The corresponding eigenenergies are given by [10]

$$E_{\mathrm{U}} = \frac{1}{2} \left(\Delta_0 + \sqrt{\Delta_0^2 + 8\Omega^2} \right) \qquad (13\mathrm{a})$$

$$E_{\mathrm{M}} = \Delta_0 \qquad (13\mathrm{b})$$

$$E_{\mathrm{N}} = 0 \qquad (13\mathrm{c})$$

$$E_{\mathrm{L}} = \frac{1}{2} \left(\Delta_0 - \sqrt{\Delta_0^2 + 8\Omega^2} \right) \qquad (13\mathrm{d})$$

and depicted in Fig. 2. Note that these energies, and in turn the transition energies between them, depend on the driving strength.

The transition that yields the highest degree of entanglement was identified to be the two-photon resonance between the uppermost and lowest laser-dressed state. The chosen resonance is selected by adjusting the cavity-laser detuning to [10]

$$\Delta = \frac{\Delta_{\mathrm{UL}}}{2} := \frac{E_{\mathrm{U}} - E_{\mathrm{L}}}{2} = \frac{1}{2}\sqrt{\Delta_0^2 + 8\Omega^2}, \qquad (14)$$

which corresponds to tuning the cavity mode energy to $\hbar\omega_C = \Delta_{\mathrm{UL}}/2 - \Delta_0 + \hbar\omega_X$. Note that the cavity-laser detuning in Eq. (14) depends on the external driving strength Ω. Thus, in the following, this detuning is changed alongside Ω in order to keep the desired two-photon resonance condition, cf., Fig. 2.

Figure 3(a) depicts the concurrence as a function of the driving strength Ω at the two-photon transition between the laser-dressed states $|U\rangle$ and $|L\rangle$. The results in the phonon-free situation (solid line) are in accordance with those presented in Ref. 10. A region of high ΦBS (ΨBS) entanglement, indicated by blue (red) curve segments, is found for low (high) driving strength values. In between
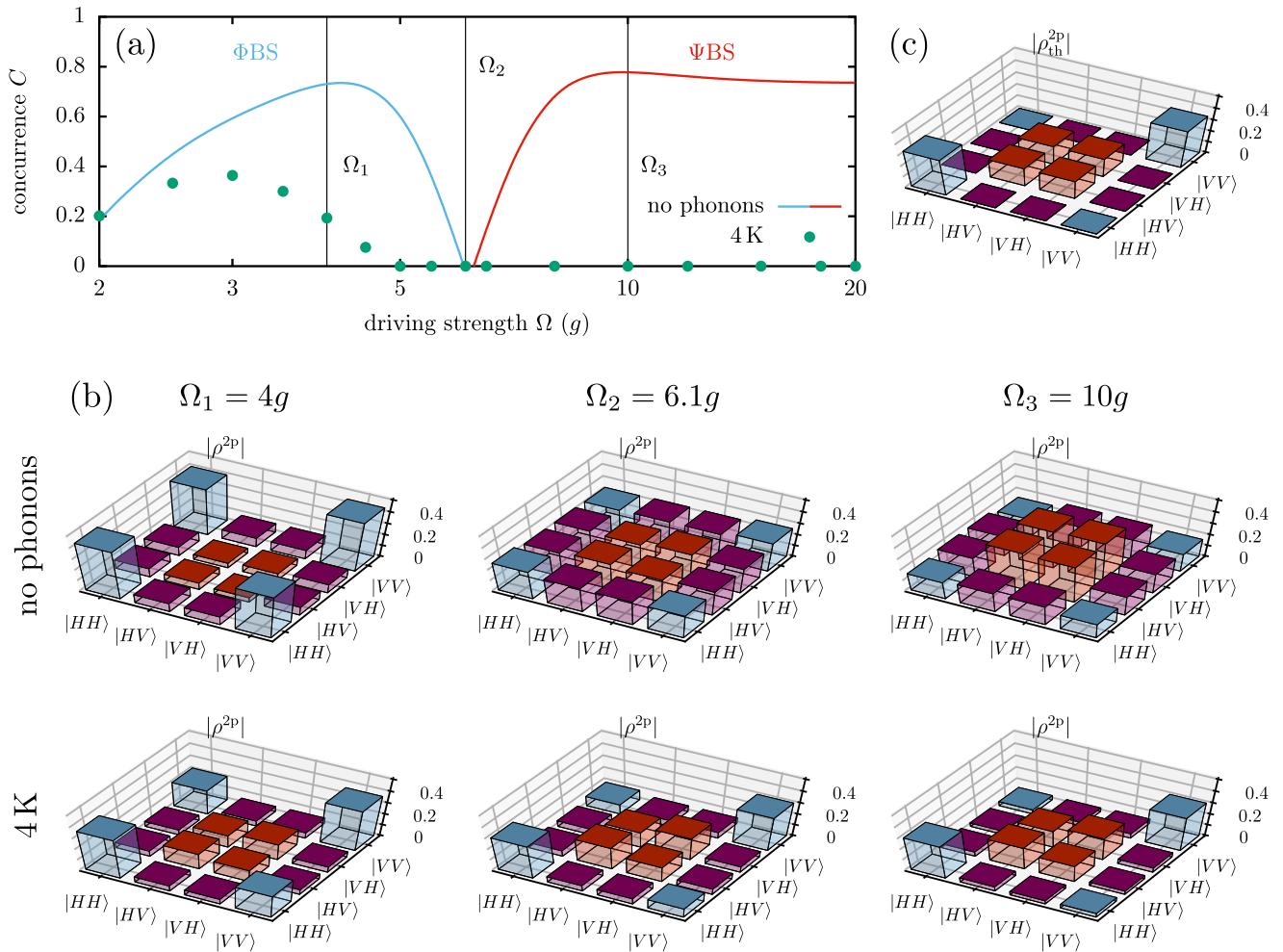
FIG. 3. (a) Concurrence as a function of the driving strength Ω (in units of the coupling strength g) without phonons (solid line) and with phonons at a temperature of 4 K (green dots). The phonon-free curve is color coded: Blue (red) indicates ΦBS (ΨBS) entanglement. Three driving strength values, that are associated with either a high concurrence or a vanishing degree of entanglement in the phonon-free situation, are marked with straight vertical lines. Note that the cavity laser detuning $\Delta = \Delta_{\mathrm{UL}} = \sqrt{\Delta_0^2 + 8\Omega^2}/2$ is changed alongside Ω to keep the desired resonance condition. (b) Corresponding two-photon density matrices (absolute values) for the three driving strengths Ω_j indicated in panel (a). Results are shown for calculations without phonons (upper row) and including phonons at $T = 4$ K (lower row). (c) Two-photon density matrix calculated from the thermally distributed state as described in Eqs. (22) and (23).

the two regions of high entanglement a special point occurs at $\Omega_{\mathrm{sp}} = \sqrt{3/8}\Delta_0 \approx 6.12g$ where the concurrence drops to zero. The corresponding two-photon density matrix, calculated for three selected driving strength values Ω_j and illustrated in the upper row of Fig. 3(b), clearly shows the transition from a state that is close to a maximally entangled ΦBS (cf., Ω_1) to an entangled ΨBS with high concurrence (cf., Ω_3).

The reason for this behavior is analyzed in detail in Ref. 10. With increasing driving strength the composition of the individual laser-dressed states changes, resulting in changing optical selection rules between them. Around the driving strength Ω_1, the system emits predominantly two equally polarized photons when a direct transition between the uppermost dressed state into the

lowest one occurs and, consequently, one finds a ΦBS. With rising driving strength the probability for the simultaneous emission of two photons with opposite polarizations increases. At the driving strength $\Omega_{\mathrm{sp}} = \sqrt{3/8}\Delta_0$ both type of processes have the same probability and the degree of entanglement vanishes. When the driving strength is increased beyond this point, the latter becomes more and more dominant until a direct transition between the dressed states $|U\rangle$ and $|L\rangle$ is almost exclusively accompanied by the emission of two photons with opposite polarization. Thus one obtains a ΨBS in this regime.

B. Results including LA phonons

This well understood behavior changes drastically when the interaction to LA phonons is included in the calculations [green dots in Fig. 3(a)], already at a very low temperature of $T = 4\,$K. Besides a reduced concurrence at small driving strength values and the fact that a maximum concurrence of only $C \approx 0.4$ is reached, the interaction with LA phonons also alters the curve qualitatively.

Although, for small Ω, the concurrence follows the phonon-free result, it starts to decrease already after reaching a maximum around $\Omega \approx 3g$, and drops to zero well before the special point at $\Omega \approx \Omega_2$. In stark contrast to the phonon-free results, the concurrence remains zero for $\Omega > \Omega_2$ and no subsequent region of neither ΦBS nor ΨBS entanglement emerges. It is important to stress that LA phonons do not fully destroy the degree of entanglement in systems without constant laser driving, especially when the fine-structure splitting between the exciton states is zero [22]. In this special situation, theoretical calcualtions of the dynamcis of initially prepared biexciton states even predict a maximally entangled two-photon state, even when phonons are taken into account [22, 26].

In contrast, the constantly driven system demonstrates a behavior similar to a phase transition, where an entangled photon pair is generated only when the driving strength is below a critical value. Above this value the degree of entanglement, as measured by the concurrence, remains strictly zero. Therefore, the concurrence takes on the role of the order parameter, indicating either an entangled or nonentangled photon pair. In the following we provide an explanation for the observed phase transition behavior. To this end, we first examine the two-photon density matrix at $T = 4\,$K and infer the resulting concurrence. In a second step, we consider the role of LA phonons and explain why they lead to the obtained form of the density matrix. Finally, we turn to other properties associated with a phase transition, e.g., its critical temperature and exponent.

C. Concurrence and density matrices at 4 K

The second row of Fig. 3(b) depicts the two-photon density matrix at $T = 4\,$K obtained for three selected driving strength values Ω_j. In the case of the small driving strength $\Omega_1 = 4g$ the characteristics of $\rho^{2\mathrm{p}}$ resemble the two-photon density matrix in the phonon-free case. The occupations of the states $|HH\rangle$ and $|VV\rangle$ and their coherences (blue bars) dominate over the remaining elements. Thus, one detects a finite degree of ΦBS entanglement. A more detailed comparison to the phonon-free result reveals that the coherence associated with the matrix element $|HH\rangle\langle VV|$ is reduced by a factor of 2 due to the phonon interaction, and the occupations and coherences associated with a ΨBS (red bars) are enhanced at the ex-

pense of the blue bars. These two effects combined lead to a finite, but reduced degree of entanglement. When the driving strength is increased at $T = 4\,$K, similar trends can be observed if one compares the subsequent density matrices for Ω_1, Ω_2 and Ω_3. With increasing driving strength, the coherence $|HH\rangle\langle VV|$ is further reduced, while the elements linked to a ΨBS (red bars) increase.

Disregarding other (insignificant) coherences (purple bars), the two-photon density matrices at $T = 4\,$K can all be well represented by matrices with 4 independent entries having the form

$$\rho^{2\mathrm{p}} = \begin{pmatrix} a & 0 & 0 & c \\ 0 & b & d & 0 \\ 0 & d^* & b & 0 \\ c^* & 0 & 0 & a \end{pmatrix}, \qquad (15)$$

where the parameters fulfill the requirements for an arbitrary density matrix

$$a, b \in \mathbb{R}_0^+; \ 2(a+b) = 1; \ c, d \in \mathbb{C}; \ |c| \le a; \ |d| \le b. \ (16)$$

For the case $a > b$, which we encounter here, it can be shown that the concurrence defined in Eq. (11) reduces to

$$C = \begin{cases} 2\left(|c| - b\right), & |c| > b \\ 0, & |c| \le b. \end{cases} \qquad (17)$$

The behavior of the concurrence at $T = 4\,$K shown in Fig. 3(a) is thus directly linked to the difference between two elements in the two-photon density matrix. With increasing driving strength, the elements corresponding to c are reduced, while the occupations b are enhanced. Thus the concurrence decreases with rising driving strength and drops to zero once the condition $|c| = b$ is reached, i.e., when the coherence corresponding to $|HH\rangle\langle VV|$ is reduced to the level of the occupations of $|HV\rangle$ and $|VH\rangle$. Afterwards, the concurrence remains zero as c decreases further. This indicates the existence of a critical driving strength, where the generated photon pair transforms from an entangled phase to a nonentangled one. Note, that in the case without constant laser excitation the situation $|c| \le b$ can never occur. Starting from an initially prepared biexciton, the states $|HV\rangle$ and $|VH\rangle$ cannot be reached in the undriven dynamics, i.e., $b = 0$ in this case. Further note that when examining the two-photon density matrix at Ω_2 [cf., Fig. 3(b) lower row, middle panel], one realizes that at $T = 4\,$K the phase transition occurs before the special point of the phonon-free curve, i.e., before the regime of ΨBS is reached.

At the critical driving strength, the two-photon state transforms from an entangled phase with a finite degree of entanglement to a nonentangled phase. This can be regarded as a phase transition where the concurrence is the corresponding order parameter that is finite below the critical driving strength and strictly zero above it. Because a vanishing concurrence has a well defined physical

meaning, the character of the two-photon state, as described by the density matrix $\rho^{2\mathrm{p}}$, changes qualitatively at the transition point. Due to the one-to-one correspondence between the concurrence and the entanglement of formation, a vanishing concurrence is linked to a distinct physical property of the generated two-photon state.

If the concurrence vanishes, the density matrix $\rho^{2\mathrm{p}}$ can be decomposed into a statistical mixture

$$\rho^{2\mathrm{p}} = \sum_j p_j |\psi_j\rangle\langle\psi_j| \tag{18}$$

where all pure two-photon states $|\psi_j\rangle = |\psi_{j,1}\rangle \otimes |\psi_{j,2}\rangle$ can be factorized into a product of single-photon states which describe only the first and second detected photon, respectively. p_j is the probability to find the system in the corresponding pure state. For the two-photon density matrix of the form in Eq. (15), an explicit expression for a possible decomposition is provided in Appendix B. Therefore, above the critical driving strength, the two-photon state can always be expressed as a statistical mixture of factorizeable states. This property changes when the driving is below its critical value, where no such decomposition is possible. The practical implication of a system being in a factorizable state is that performing a measurement on the first photon has no implication on the outcome of a subsequent measurement on the second photon, in sharp contrast to what is found for an entangled state.

D. Phonon influence on the two-photon density matrix

Because the phase transition and the behavior of the concurrence can be traced back to the form of the two-photon density matrix, the remaining task is to understand the phonon influence on the system and on $\rho^{2\mathrm{p}}$. To this end, we consider the laser-dressed states $\chi \in \{U, M, N, L\}$ accompanied by two-photon states with different combinations for the photon polarizations, i.e., system states $|\chi, 2, 0\rangle$, $|\chi, 1, 1\rangle$ and $|\chi, 0, 2\rangle$. Here a state $|\chi, n_{\mathrm{H}}, n_{\mathrm{V}}\rangle$ denotes a state with n_{H} (n_{V}) horizontally (vertically) polarized photons inside the cavity. The numerical results for the driving strength $\Omega = \Omega_3$ show that two-photon states associated with a fixed laser-dressed state enter the steady state of the system with almost equal occupation probabilities but vanishing coherences between them. This steady state results directly in the obtained two-photon density matrix that can be well described by

$$\rho^{2\mathrm{p}} = \frac{1}{6}\begin{pmatrix} 2 & 0 & 0 & 0 \\ 0 & 1 & 1 & 0 \\ 0 & 1 & 1 & 0 \\ 0 & 0 & 0 & 2 \end{pmatrix} \tag{19}$$

In the following we provide a simplified argument why the interaction with LA phonons leads to this type of steady state and two-photon density matrix. In the absence of further relaxation processes, e.g., cavity losses and radiative decay, phonons lead to a steady state which is close to a thermal distribution over the eigenstates $|\varphi_\nu\rangle$ of the system Hamiltonian without the phonon contribution that can be reached from the initial state. [68–70]. Here, the Hamiltonian describing the driven QD-cavity system without phonons is $\hat{H}_0 := \hat{H}_{\mathrm{QD\text{-}C}} + \hat{H}_{\mathrm{L}}$. The analyses in Ref. 10 suggest that the interaction with the cavity modes introduces a weak coupling between laser-dressed states with different numbers of photons inside the cavity. Hence the eigenstates of the full Hamiltonian $\hat{H}_0$ are best described by

$$|\varphi_\nu\rangle = \sum_{\chi, n_{\mathrm{H}}, n_{\mathrm{V}}} a_\nu(\chi, n_{\mathrm{H}}, n_{\mathrm{V}})|\chi, n_{\mathrm{H}}, n_{\mathrm{V}}\rangle \tag{20}$$

where the mixing coefficients $a_\nu(\chi, n_{\mathrm{H}}, n_{\mathrm{V}})$ depend on the cavity coupling strength g, and the energetic placement of the cavity modes, i.e., the cavity-laser detuning Δ.

The most important two-photon states in a thermalized distribution, which should define the character of the two-photon density matrix $\rho^{2\mathrm{p}}$, are the energetically lowest ones. In the considered system, these are the three two-photon states accompanied by the laser-dressed state $|L\rangle$, i.e., $|L, 2, 0\rangle$, $|L, 1, 1\rangle$ and $|L, 0, 2\rangle$. These three states are precisely the ones distinct by the chosen (two-photon) resonance condition. Using a Schrieffer-Wolff transformation [71, 72] an effective Hamiltonian describing this two-photon resonance can be constructed. The explicit epression for this effective Hamiltonian, in the basis $|U, 0, 0\rangle$, $|L, 1, 1\rangle$, $|L, \Phi_+\rangle = (|L, 2, 0\rangle + |L, 0, 2\rangle)/\sqrt{2}$, and $|L, \Phi_-\rangle = (|L, 2, 0\rangle - |L, 0, 2\rangle)/\sqrt{2}$, is [10]

$$\hat{\tilde{H}}_{\mathrm{UL}}^{(2)} \approx E_{\mathrm{U}}\mathbb{1}_4 + g^2 \begin{pmatrix} \delta^{\mathrm{UL}} & \gamma_1^{\mathrm{UL}} & -\gamma_2^{\mathrm{UL}} & 0 \\ \gamma_1^{\mathrm{UL}} & -\delta_2^{\mathrm{UL}} & \alpha^{\mathrm{UL}} & 0 \\ -\gamma_2^{\mathrm{UL}} & \alpha^{\mathrm{UL}} & -\delta_2^{\mathrm{UL}} & 0 \\ 0 & 0 & 0 & -\delta_2^{\mathrm{UL}} \end{pmatrix} \tag{21}$$

with

$$c = \frac{2\Omega}{\sqrt{8\Omega^2 + \left(\Delta_0 + \sqrt{\Delta_0^2 + 8\Omega^2}\right)^2}}$$

$$\tilde{c} = \sqrt{\frac{1}{2} - c^2}$$

$$\delta^{\mathrm{UL}} = (\tilde{c}^2 - c^2)\left(\frac{2}{\Delta_0} + \frac{4(\tilde{c}^2 - c^2)}{\Delta_{\mathrm{UL}}}\right)$$

$$\delta_2^{\mathrm{UL}} = \delta^{\mathrm{UL}} + \delta_3^{\mathrm{UL}}$$

$$\delta_3^{\mathrm{UL}} = \frac{8(\tilde{c}^2 - c^2)^2}{3\Delta_{\mathrm{UL}}} + \frac{2\tilde{c}^2}{\Delta_{\mathrm{UL}} + \Delta_0/2} + \frac{2c^2}{\Delta_{\mathrm{UL}} - \Delta_0/2}$$

$$\gamma_1^{\mathrm{UL}} = 4c\tilde{c}\frac{1}{\Delta_0} - 16c\tilde{c}(\tilde{c}^2 - c^2)\frac{1}{\Delta_{\mathrm{UL}}}$$

$$\gamma_2^{\mathrm{UL}} = 16c\tilde{c}(\tilde{c}^2 - c^2)\frac{1}{\Delta_{\mathrm{UL}}}$$

$$\alpha^{\mathrm{UL}} = \frac{1}{\Delta_0} - (1 - 16c^2\tilde{c}^2)\frac{1}{\Delta_{\mathrm{UL}}} - \frac{1}{2}\delta_3^{\mathrm{UL}} + \frac{2\tilde{c}^2}{\Delta_{\mathrm{UL}} + \Delta_0/2}.$$

where $\mathbb{1}_4$ is the 4-dimensional identity matrix. All couplings associated with two-photon process (γ's and α's) and energy shifts (δ's) in this effective Hamiltonian are on the order of g^2/Δ_0. Therefore, the energetic splitting between the four eigenstates $|\varphi_\nu^{\mathrm{UL}}\rangle$ of $\hat{\bar{H}}_{\mathrm{UL}}^{(2)}$ is on the same order. For our realistic parameters, the energy $g^2/\Delta_0 = 0.1g \approx 5\,\mu\mathrm{eV}$ is already two orders of magnitude smaller than the thermal energy $k_B T$ at $T = 4\,\mathrm{K}$. Consequently, in a thermalized distribution all four eigenstates $|\varphi_\nu^{\mathrm{UL}}\rangle$ should appear with the same weights.

Note that, if no further loss mechanism are considered, the state $|L, \Phi_-\rangle$ is decoupled from the inital state $|G, 0, 0\rangle$ and cannot occur in a thermalized distribution [70]. But, due to cavity losses and radiative decay, this state can be reached during the system dynamics and, thus, should appear in our situation. In general, the exact steady state of systems with both type of relaxation mechanisms, LA phonon-induced relaxation and further loss processes, is difficult to predict and may differ qualitatively from what is expected in the limiting cases where only one type of relaxation mechanism is considered [63].

However, under the assumption that phonon-induced relaxations dominate over the latter, a steady state should emerge, where the leading two-photon contribution is proportional to a thermal distribution over all four eigenstates $|\varphi_\nu^{\mathrm{UL}}\rangle$:

$$
\begin{aligned}
\hat{\rho}_{\mathrm{th}}^{\mathrm{UL}} &= \frac{1}{Z} \sum_{\nu=1}^{4} \exp\left[-\frac{\epsilon_\nu^{\mathrm{UL}}}{k_B T}\right] |\varphi_\nu^{\mathrm{UL}}\rangle\langle\varphi_\nu^{\mathrm{UL}}| \\
&\approx \frac{1}{4} \sum_{\nu=1}^{4} |\varphi_\nu^{\mathrm{UL}}\rangle\langle\varphi_\nu^{\mathrm{UL}}| \\
&= \frac{1}{4}(|U, 0, 0\rangle\langle U, 0, 0| + |L, 1, 1\rangle\langle L, 1, 1| \\
&\quad + |L, 2, 0\rangle\langle L, 2, 0| + |L, 0, 2\rangle\langle L, 0, 2|)
\end{aligned}
\tag{22}
$$

where $\epsilon_\nu^{\mathrm{UL}}$ are the corresponding energies.

One can calculate a first approximation for the two-photon density matrix due to this contribution

$$
(\rho_{\mathrm{th}}^{2\mathrm{p}})_{jk,\ell m} \approx \mathcal{N}\mathrm{Tr}\left\{\hat{a}_m \hat{a}_\ell \hat{\rho}_{\mathrm{th}}^{\mathrm{UL}} \hat{a}_j^\dagger \hat{a}_k^\dagger\right\} = \frac{1}{6}\begin{pmatrix} 2 & 0 & 0 & 0 \\ 0 & 1 & 1 & 0 \\ 0 & 1 & 1 & 0 \\ 0 & 0 & 0 & 2 \end{pmatrix}
\tag{23}
$$

where $\mathcal{N}$ is a normalization constant and one assumes that the delay time window is small and therefore the limit $\tau \to 0$ is used.

This thermal two-photon density matrix $\rho_{\mathrm{th}}^{2\mathrm{p}}$ is also depicted in Fig. 3(c) for comparison. This density matrix is almost identical to the one obtained for Ω_3 at $T = 4\,\mathrm{K}$. Thus, although the presented argument is only a simplified analysis, it fits quite well to the numerical observations: (i) two-photon states with different combinations of the polarization appear with the same occupation probabilities and vanishing coherences, c.f., Eq. (22).

(ii) The two-photon density matrix $\rho_{\mathrm{th}}^{2\mathrm{p}}$ associated with a phonon-induced thermalization is close to the one encountered in the numerical simulations.

This implies that the role of phonons is a thermalization in laser-driven eigenstates. Furthermore, the two-photon density matrix at Ω_2 is also close to $\rho_{\mathrm{th}}^{2\mathrm{p}}$, the main difference being small, finite coherences. Thus, in this case, the thermalization process is not complete. This points to a competition between different relaxation processes that, each on their own, lead to different steady states in the system dynamics. While the interaction with LA phonons on its own leads to a thermalization and, consequently, to the thermal two-photon density matrix $\rho_{\mathrm{th}}^{2\mathrm{p}}$, the other relaxation processes, i.e., cavity losses and radiative decay, result in the steady state associated with the phonon-free result given in the row above. The imprint of this competition is even more prominent in the two-photon density matrix for the driving strength Ω_1 at $4\,\mathrm{K}$. Here, $\rho^{2\mathrm{p}}$ describes a two-photon state roughly in between the two limiting cases, that are given by the corresponding phonon-free result and $\rho_{\mathrm{th}}^{2\mathrm{p}}$.

Consequently, the two-photon state at $T = 4\,\mathrm{K}$ is a result of two competing relaxation mechanisms, that, each on their own, would result in a different steady state in the system dynamics, but that act on different time scales. While the time scale of the cavity losses and radiative decay is independent of the driving strength Ω, the time scale of the thermalization is reduced with increasing Ω, and thus the two-photon density matrix approaches its thermal limit. The reason for this reduction lies in the phonon spectral density. As the driving strength increases, the transition energies between the laser-dressed states increase as well. Therefore, the main contribution of the phonon spectral density $J(\omega)$ has to be evaluated at a higher frequency. In the parameter range considered in this work, this results in a higher value of J which translates to a stronger average phonon coupling, cf. Appendix A. Consequently the thermalization process should become more dominant with increasing driving strength, pulling the two-photon density matrix closer to $\rho_{\mathrm{th}}^{2\mathrm{p}}$.

The rates leading to thermalization are estimated using Fermi's golden rule for the phonon-induced rates $\Gamma_{\chi\chi'}$ between the laser-dressed states $|\chi\rangle$ and $|\chi'\rangle$ with $\chi, \chi' \in \{U, M, N, L\}$ associated with phonon emission and absorption processes. Based on this estimate, two finite rates Γ_{UN} and Γ_{NL} are extracted, cf. Appendix C, which are shown in Fig. 4 as a function of the driving strength. As expected, in the considered parameter range, both rates increase with Ω, supporting the previous argument on the increasing role of phonons. Interestingly, for $\Omega \approx 5g$, i.e., around the driving strength where the concurrence vanishes, both rates become larger than the cavity loss rate 2κ associated with a two-photon state. Thus, above this point both phonon-related rates exceed the most important cavity or radiate loss rate in the system. According to this estimate, above this point the phonon-induced thermalization dominates the
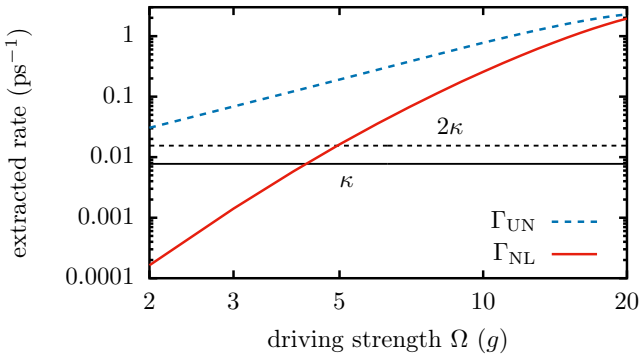
FIG. 4. Phonon-induced transition rate Γ_{UL} (Γ_{NL}) between the laser-dressed states $|U\rangle$ and $|L\rangle$ ($|N\rangle$ and $|L\rangle$) as a function of the driving strength Ω. Additionally, a dashed (solid) horizontal black line indicates the value of the cavity loss rate 2κ (κ) associated with a two-photon (one-photon) state.

system dynamics, leading to a vanishing entanglement.

E. Phase transition - critical temperature

A phase transition, here between an entangled and nonentangled phase of the emitted photon pair, is characterized by its critical temperature. It depends on other parameters, for example the external driving strength Ω. In order to determine the critical temperature, we now analyze the temperature dependence of the concurrence. In Fig. 5(a) the concurrence is shown as a function of the temperature T for different driving strength values between $2.0g$ and $4.5g$. The results further support the idea that a phonon-induced phase transition is taking place. At a given driving strength the concurrence decreases monotonically with rising temperature before vanishing at a certain critical temperature. The concurrence remains zero when the temperature is further increased. Furthermore, as the driving strength increases, the drop becomes more rapid.

Figure 5(b) depicts the critical temperatures calculated for the six driving strength values in panel (a). It is evident that the critical temperature decreases with rising driving strength Ω. As shown in the previous section, a higher driving strength leads to larger phonon-induced rates and faster thermalization. Thus, the critical transition temperature is the lower the higher the applied driving strength. The results imply that even moderate degrees of entanglement in the constantly driven system can be achieved only at temperatures below $30\,\mathrm{K}$. Furthermore at temperatures of $4\,\mathrm{K}$ and above the generation of ΨBS seems to be no longer possible. We find that, for realistic parameters, phonon interactions lead to a vanishing concurrence for driving strengths far below the value needed to switch from ΦBS to ΨBS. Therefore, we observe no ΨBS in simulations accounting for phonons for all parameters considered here.

The average number of phonons in the thermal equilib-

rium and, thus, the phonon influence increases with rising temperature. As a result, the competition between loss processes, i.e., cavity losses and radiative decay, on one hand and the thermalization due to phonons on the other hand, is more and more dominated by the latter. Therefore, the degree of entanglement decreases with rising temperature as the two-photon density matrix is again pulled towards the thermal one. At a certain, critical temperature T_{crit} the phase transition takes place and the order parameter, i.e., the concurrence, drops to zero. At this critical temperature, the coherence between $|HH\rangle$ and $|VV\rangle$ is reduced to the level of the occupations $|HV\rangle$ and $|VH\rangle$, i.e., the two-photon density matrix can be expressed as a statistical sum of factorizable two-photon states. Because the phonon influence only increases at larger temperatures, the concurrence remains zero.

F. Phase transition - critical behavior and exponent

Next, we turn to another aspect associated with a phase transition: the critical behavior near the phase transition and the corresponding critical exponent. In the case of a phase transition, the behavior of the order parameter, i.e., the concurrence, when approaching the critical temperature should be given as a power law

$$C \propto \left(\frac{T}{T_{\mathrm{crit}}} - 1 \right)^{\beta} \tag{24}$$

where the critical exponent β is independent of the driving strength Ω. Indeed, we find that the critical behavior follows this dependence with the same value $\beta = 1$ for all driving strength values considered in Fig. 5. To illustrate this, Fig. 6 depicts the concurrence as a function of the reduced temperature for two selected driving strength values. In both cases, when the temperature approaches the corresponding critical value, the concurrence is described by a power law with the critical exponent $\beta = 1$ and fitted amplitudes A_{Ω}.

We also observe an interesting side aspect: when the temperature is decreased further, the concurrence evaluated for the two driving strengths still exhibits the same behavior. Both curves can be well described by a power law extended by an additional term with a fitted exponent $9/4$ and amplitudes B_{Ω}. This feature holds for all driving strength values considered in Fig. 5 (not shown).

V. CONCLUSION

In conclusion, we have investigated the influence of phonons on entangled photon pairs generated from a constantly driven QD-cavity system. We find a strong reduction and a severe qualitative impact on the degree of entanglement, as measured by the concurrence, already at temperatures as low as $4\,\mathrm{K}$. Unlike in the phonon-free
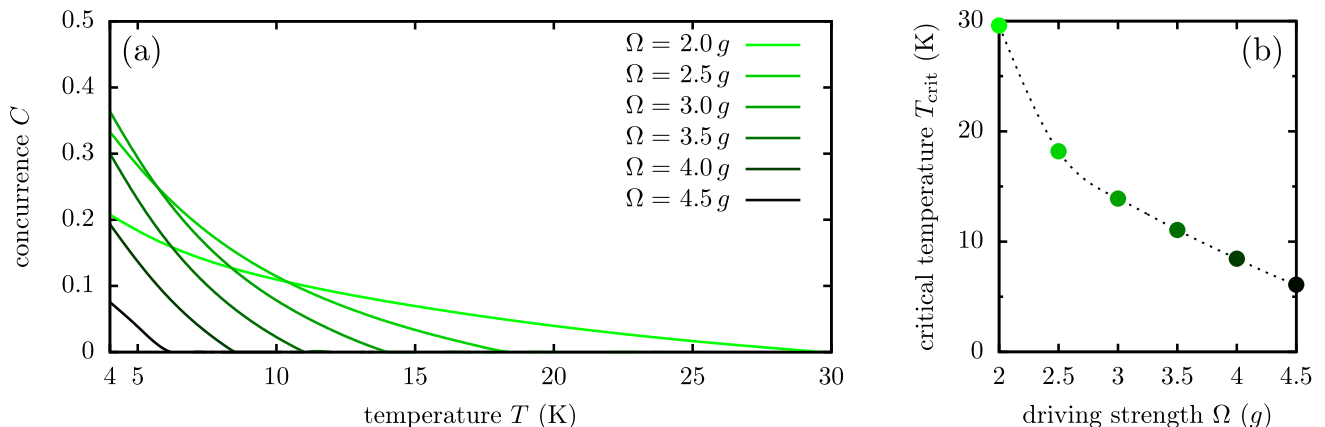
FIG. 5. (a) Concurrence as a function of the temperature (above $4\,\mathrm{K}$) for different driving strength values Ω between $2.0g$ and $4.5g$. (b) Critical temperature T_{crit} of the phonon-induced phase transition for the driving strength values in panel (a). The dashed line is a guide-to-the-eye.
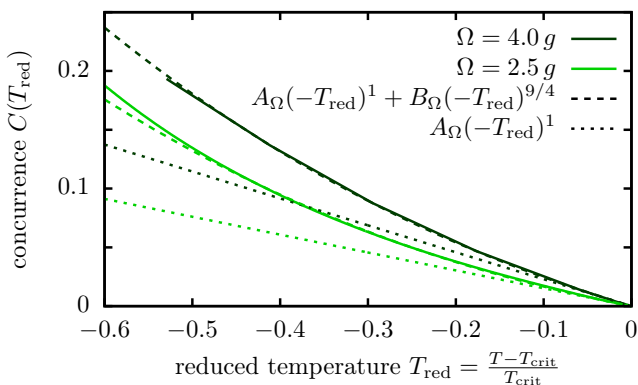

FIG. 6. Critical behavior and exponent. Concurrence as a function of the reduced temperature for two different driving strength values $\Omega = 4.0g$ and $2.5g$ (dark and light green solid lines, respectively). In addition, corresponding fits to power laws containing only the critical exponent $\beta = 1$ (doted lines) and one additional term (dashed lines) are shown with the same color.

situation, the influence of phonons suppresses the generation of $\Psi\mathrm{BS}$ entanglement in the studied parameter range, even at low temperatures. The concurrence decreases with increasing temperature and driving strength until a critical parameter value is reached where it drops to zero and remains so at larger values. This behavior is similar to a phase transition where the concurrence represents the order parameter, indicating either an entangled or nonentangled phase. Consequently, we encounter a phonon-induced phase transition, which cannot take place in a situation without constant laser excitation. The reason behind this phenomenon is a competition between two different mechanisms, a thermalization due to phonons and other loss processes, i.e., radiative decay and cavity losses, that determines the steady state of

the system. A higher temperature or driving strength gives rise to a stronger phonon impact. Eventually, the thermalization dominates, driving the two-photon state towards a thermal state with vanishing degree of entanglement. Thus, the emitted photon pair transforms from an entangled towards a nonentangled phase.

Appendix A: GaAs parameters and phonon spectral density

In this article a spherically symmetric self-assembled GaAs QD with a harmonic oscillator confinement and an electron (hole) confinement length $a_{\mathrm{e}} = 3$ nm ($a_{\mathrm{h}} = a_{\mathrm{e}}/1.15$) is considered. Furthermore a linear dispersion relation is assumed for the LA phonons. In this situation, the explicit expression for the phonon spectral $J(\omega)$ is [63, 69]

$$J(\omega) = \frac{\omega^3}{4\pi^2 \hbar \rho_{\mathrm{D}} c_{\mathrm{S}}^5} \left[D_{\mathrm{e}}\, e^{-\omega^2 a_{\mathrm{e}}^2/(4c_{\mathrm{S}})^2} - D_{\mathrm{h}}\, e^{-\omega^2 a_{\mathrm{h}}^2/(4c_{\mathrm{S}})^2} \right]^2 \tag{A1}$$

The necessary material parameters are taken from literature [73] and listed in Tab. II. For these parameters, the resulting spectral density is shown in Fig. 7. Note that using a spherical QD model provides for the calculation of the reduced density matrix as considered here no loss of generality as shown in Ref. 74.

TABLE II. GaAs material parameters taken from Ref. 73.

Parameter		Value
Mass density (kg/m^3)	ρ_D	5370
Sound velocity (m/s)	c_S	5110
Electron deformation potential (eV)	D_e	7.0
Hole deformation potential (eV)	D_h	-3.5
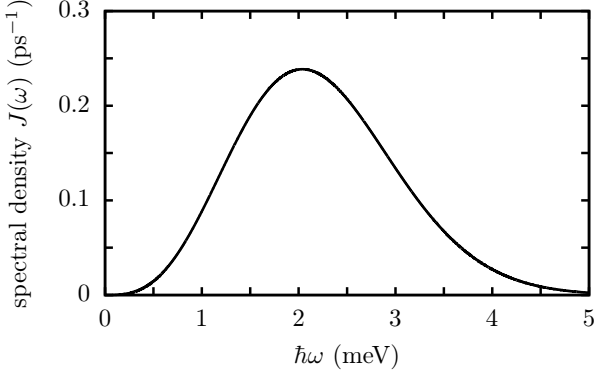
FIG. 7. Phonon spectral density for the considered GaAs QD with electron (hole) confinement length $a_\mathrm{e} = 3$ nm ($a_\mathrm{h} = a_\mathrm{e}/1.15$) and material parameters listed in Tab. II.

Appendix B: Decomposition in factorizable states

Due to the interaction with LA phonons, we encounter two-photon density matrices that can, in good approximation, be described as

$$\rho^{2\mathrm{p}} = \begin{pmatrix} a & 0 & 0 & c \\ 0 & b & d & 0 \\ 0 & d^* & b & 0 \\ c^* & 0 & 0 & a \end{pmatrix}, \tag{B1}$$

in the basis $\{|H_1 H_2\rangle, |H_1 V_2\rangle, |V_1 H_2\rangle, |V_1 V_2\rangle\}$, where the index refers to the first or second detected photon. The parameters fulfill the requirements for an arbitrary density matrix

$$a, b \in \mathbb{R}_0^+; \ 2(a+b) = 1; \ c, d \in \mathbb{C}; \ |c| \leq a; \ |d| \leq b. \tag{B2}$$

In the case $a > b$, the corresponding concurrence is given by

$$C = \begin{cases} 2\left(|c| - b\right), & |c| > b \\ 0, & |c| \leq b. \end{cases} \tag{B3}$$

Because the concurrence has a one-to-one correspondence to the entanglement of formation, obtaining a vanishing concurrence has a well-defined physical meaning: in this situation, there exists at least one decomposition of the density matrix

$$\rho^{2\mathrm{p}} = \sum_j p_j |\psi_j\rangle\langle\psi_j| \tag{B4}$$

where all pure (two-photon) states $|\psi_j\rangle$ factorize into quantum states that describe only the first or second detected photon. p_j is the probability to encounter this pure state in the mixed state described by $\rho^{2\mathrm{p}}$. Since the concurrence vanishes for $|c| \leq b$, such a decomposition must exist in this situation. Here, we give an explicit expression for a possible decomposition.

After introducing the phase φ and θ for the parameter $c = |c|e^{i\varphi}$ and $d = |d|e^{i\theta}$, respectively, we re-write the two-photon density matrix. In the situation $a \geq b \geq |c|$, our decomposition depends on the relation between $|c|$ and $|d|$.

In the case $|d| \geq c$, we obtain the following possible decomposition

$$\rho^{2\mathrm{p}} = 2\left(a - |d|\right)\rho_1^{2\mathrm{p}} + 2\left(b - |d|\right)\rho_2^{2\mathrm{p}} + 4|c|\rho_3^{2\mathrm{p}} \\ + 2\left(|d| - |c|\right)\left(\rho_4^{2\mathrm{p}} + \rho_5^{2\mathrm{p}}\right) \tag{B5}$$

where all contributions $\rho_j^{2\mathrm{p}}$ to the density matrix can be expressed as a mixed state

$$\rho_j^{2\mathrm{p}} = \frac{1}{2}\left(|\psi_j^{(\alpha)}\rangle\langle\psi_j^{(\alpha)}| + |\psi_j^{(\beta)}\rangle\langle\psi_j^{(\beta)}|\right) \tag{B6}$$

containing two factorizable pure states $|\psi_j^{(\alpha/\beta)}\rangle$. The explicit expressions for these quantities are

$$\rho_1^{2\mathrm{p}} = \frac{1}{2}\begin{pmatrix} 1 & 0 & 0 & 0 \\ 0 & 0 & 0 & 0 \\ 0 & 0 & 0 & 0 \\ 0 & 0 & 0 & 1 \end{pmatrix} \tag{B7a}$$

$$|\psi_1^{(\alpha)}\rangle = |H_1\rangle|H_2\rangle; \ |\psi_1^{(\beta)}\rangle = |V_1\rangle|V_2\rangle \tag{B7b}$$

$$\rho_2^{2\mathrm{p}} = \frac{1}{2}\begin{pmatrix} 0 & 0 & 0 & 0 \\ 0 & 1 & 0 & 0 \\ 0 & 0 & 1 & 0 \\ 0 & 0 & 0 & 0 \end{pmatrix} \tag{B7c}$$

$$|\psi_2^{(\alpha)}\rangle = |H_1\rangle|V_2\rangle; \ |\psi_2^{(\beta)}\rangle = |V_1\rangle|H_2\rangle \tag{B7d}$$

$$\rho_3^{2\mathrm{p}} = \frac{1}{4}\begin{pmatrix} 1 & 0 & 0 & e^{i\varphi} \\ 0 & 1 & e^{i\theta} & 0 \\ 0 & e^{-i\theta} & 1 & 0 \\ e^{-i\varphi} & 0 & 0 & 1 \end{pmatrix} \tag{B7e}$$

$$|\psi_3^{(\alpha/\beta)}\rangle = \frac{1}{\sqrt{2}}\left(|H_1\rangle \pm e^{-i(\varphi+\theta)/2}|V_1\rangle\right) \\ \times \frac{1}{\sqrt{2}}\left(|H_2\rangle \pm e^{-i(\varphi-\theta)/2}|V_2\rangle\right) \tag{B7f}$$

$$\rho_{4/5}^{2\mathrm{P}} = \frac{1}{4} \begin{pmatrix} 1 & 0 & 0 & \pm 1 \\ 0 & 1 & e^{i\theta} & 0 \\ 0 & e^{-i\theta} & 1 & 0 \\ \pm 1 & 0 & 0 & 1 \end{pmatrix} \quad \text{(B7g)}$$

The contribution $\rho_4^{2\mathrm{P}}$ ($\rho_5^{2\mathrm{P}}$), exhibiting the positive (negative) coherence $|H_1 H_2\rangle\langle V_1 V_2|$, is a special case of $\rho_3^{2\mathrm{P}}$ with $\varphi = 0$ ($\varphi = \pi$). Thus the corresponding pure states $|\psi_{4/5}^{(\alpha/\beta)}\rangle$ are given as special cases of Eq. (B7f).

In the case $|d| < |c|$, a possible decomposition can be constructed in a slightly different form

$$\rho^{2\mathrm{P}} = 2\left(a - |c|\right)\rho_1^{2\mathrm{P}} + 2\left(b - |c|\right)\rho_2^{2\mathrm{P}} + 4|d|\rho_3^{2\mathrm{P}}$$
$$+ 2\left(|c| - |d|\right)\left(\rho_6^{2\mathrm{P}} + \rho_7^{2\mathrm{P}}\right) \quad \text{(B8)}$$

Again the contributions

$$\rho_{6/7}^{2\mathrm{P}} = \frac{1}{4} \begin{pmatrix} 1 & 0 & 0 & e^{i\varphi} \\ 0 & 1 & \pm 1 & 0 \\ 0 & \pm 1 & 1 & 0 \\ e^{-i\varphi} & 0 & 0 & 1 \end{pmatrix} \quad \text{(B9)}$$

are special cases of $\rho_3^{2\mathrm{P}}$ with $\theta = 0$ and $\theta = \pi$, respectively. Thus they, can be decomposed into a sum over two factorizable pure states $|\psi_{6/7}^{(\alpha/\beta)}\rangle$ which are special cases of $|\psi_3^{(\alpha/\beta)}\rangle$.

Altogether, in the situation $a \geq b \geq |c|$, the two-photon density matrix in Eq. (B1) can be always expressed as a sum over 10 or less factorizable pure (two-photon) states

$$\rho^{2\mathrm{P}} = \sum_j p_j \frac{1}{2}\left(|\psi_j^{(\alpha)}\rangle\langle\psi_j^{(\alpha)}| + |\psi_j^{(\beta)}\rangle\langle\psi_j^{(\beta)}|\right) \quad \text{(B10)}$$

where the probabilities p_j are the corresponding (real and positive) prefactors in the expansion (B5) or (B8), respectively. Because at least one decomposition into factorizable pure states exists, the corresponding entanglement of formation is zero, and in turn the concurrence vanishes.

Appendix C: Phonon-induced transition rates between laser-dressed states

In this section we estimate the phonon-induced rates that lead to a thermalization of the system. To this end,

we consider the four laser-dressed states [10]

$$|U\rangle = c\left(|G\rangle + |B\rangle\right) + \tilde{c}\left(|X_\mathrm{H}\rangle + |X_\mathrm{V}\rangle\right) \quad \text{(C1a)}$$

$$|M\rangle = \frac{1}{\sqrt{2}}\left(|X_\mathrm{H}\rangle - |X_\mathrm{V}\rangle\right) \quad \text{(C1b)}$$

$$|N\rangle = \frac{1}{\sqrt{2}}\left(|G\rangle - |B\rangle\right) \quad \text{(C1c)}$$

$$|L\rangle = \tilde{c}\left(|G\rangle + |B\rangle\right) - c\left(|X_\mathrm{H}\rangle + |X_\mathrm{V}\rangle\right) \quad \text{(C1d)}$$

$$c = \frac{2\Omega}{\sqrt{8\Omega^2 + \left(\Delta_0 + \sqrt{\Delta_0^2 + 8\Omega^2}\right)^2}}; \quad \tilde{c} = \sqrt{\frac{1}{2} - c^2} \quad \text{(C1e)}$$

where Ω is the driving strength and Δ_0 the energetic detuning between exciton states and laser. The corresponding energies E_χ are given in Eq. (13).

According to Fermi's golden rule, the phonon-induced rates $\Gamma_{i \to f}$ between an initial laser-dressed state with zero phonons $|i\rangle$ and a final dressed-state at lower energy with one phonon $|f\rangle$ can be estimated as

$$\Gamma_{i \to f} = \frac{2\pi}{\hbar}|\langle f|\hat{H}_\mathrm{Ph}|i\rangle|^2 g(E_f) \quad \text{(C2)}$$

where $g(E_f)$ is the density of states at the energy of the final state. In our situation, using the phonon spectral density, Eq. (C2) can be re-formulated as

$$\Gamma_{\chi\chi'} = 2\pi\,|\langle\chi|\hat{V}_\mathrm{Ph}|\chi'\rangle|^2\,J(|E_\chi - E_{\chi'}|/\hbar) \quad \text{(C3)}$$

where $\chi, \chi' \in \{U, M, N, L\}$ and the operator $\hat{V}_\mathrm{Ph}$ takes the form

$$\hat{V}_\mathrm{Ph} = \begin{pmatrix} 1 & 0 & \sqrt{2}c & 0 \\ 0 & 1 & 0 & 0 \\ \sqrt{2}c & 0 & 1 & \sqrt{2}\tilde{c} \\ 0 & 0 & \sqrt{2}\tilde{c} & 1 \end{pmatrix} \quad \text{(C4)}$$

in the basis $\{|U\rangle, |M\rangle, |N\rangle, |L\rangle\}$.

Using this estimate, we obtain two finite rates

$$\Gamma_\mathrm{UN} = 4\pi c^2 J([E_\mathrm{U} - E_\mathrm{N}]/\hbar) \quad \text{(C5a)}$$

$$\Gamma_\mathrm{NL} = 4\pi\tilde{c}^2 J([E_\mathrm{N} - E_\mathrm{L}]/\hbar) \quad \text{(C5b)}$$

that are associated with transitions between laser-dressed states $|U\rangle \leftrightarrow |N\rangle$ and $|N\rangle \leftrightarrow |L\rangle$ due to phonon emission or absorption processes. These rates depend on the dressed state energies and the coefficients $c, \tilde{c}$ given by Eq. (C1e) and thus, in particular, on the driving strength Ω.

[1] N. Gisin, G. Ribordy, W. Tittel, and H. Zbinden, Rev. Mod. Phys. **74**, 145 (2002).

[2] H.-K. Lo, M. Curty, and K. Tamaki, Nat. Photonics **8**, 595 (2014).

[3] L.-M. Duan, M. D. Lukin, J. I. Cirac, and P. Zoller, Nature **414**, 413 (2001).

[4] D. Huber, M. Reindl, J. Aberl, A. Rastelli, and R. Trotta, J. Opt. **20**, 073002 (2018).

[5] J.-W. Pan, Z.-B. Chen, C.-Y. Lu, H. Weinfurter, A. Zeilinger, and M. Żukowski, Rev. Mod. Phys. **84**, 777 (2012).

[6] C. H. Bennett and D. P. DiVincenzo, Nature **404**, 247 (2000).

[7] S. C. Kuhn, A. Knorr, S. Reitzenstein, and M. Richter, Opt. Express **24**, 25446 (2016).

[8] A. Zeilinger, Phys. Scr. **92**, 072501 (2017).

[9] A. Orieux, M. A. M. Versteegh, K. D. Jöns, and S. Ducci, Rep. Prog. Phys. **80**, 076001 (2017).

[10] T. Seidelmann, M. Cosacchi, M. Cygorek, D. E. Reiter, A. Vagov, and V. M. Axt, Adv. Quantum Technol. **4**, 2000108 (2021).

[11] M. Müller, S. Bounouar, K. D. Jöns, M. Glässl, and P. Michler, Nat. Photonics **8**, 224 (2014).

[12] P.-L. Ardelt, L. Hanschke, K. A. Fischer, K. Müller, A. Kleinkauf, M. Koller, A. Bechtold, T. Simmet, J. Wierzbowski, H. Riedl, G. Abstreiter, and J. J. Finley, Phys. Rev. B **90**, 241404(R) (2014).

[13] D. E. Reiter, T. Kuhn, M. Glässl, and V. M. Axt, J. Phys.: Condens. Matter **26**, 423203 (2014).

[14] S. Bounouar, M. Müller, A. M. Barth, M. Glässl, V. M. Axt, and P. Michler, Phys. Rev. B **91**, 161302(R) (2015).

[15] L. Hanschke, K. A. Fischer, S. Appel, D. Lukin, J. Wierzbowski, S. Sun, R. Trivedi, J. Vucković, J. J. Finley, and K. Müller, npj Quantum Inf. **4**, 43 (2018).

[16] D. Huber, M. Reindl, Y. Huo, H. Huang, J. S. Wildmann, O. G. Schmidt, A. Rastelli, and R. Trotta, Nat. Commun. **8**, 15506 (2017).

[17] M. Reindl, K. D. Jöns, D. Huber, C. Schimpf, Y. Huo, V. Zwiller, A. Rastelli, and R. Trotta, Nano Lett. **17**, 4090 (2017).

[18] A. Dousse, J. Suffczyński, A. Beveratos, O. Krebs, A. Lemaître, I. Sagnes, J. Bloch, P. Voisin, and P. Senellart, Nature **466**, 217 (2010).

[19] S. Schumacher, J. Förstner, A. Zrenner, M. Florian, C. Gies, P. Gartner, and F. Jahnke, Opt. Express **20**, 5335 (2012).

[20] E. del Valle, A. Gonzalez-Tudela, E. Cancellieri, F. P. Laussy, and C. Tejedor, New J. Phys. **13**, 113014 (2011).

[21] C. Sánchez Muñoz, F. P. Laussy, C. Tejedor, and E. del Valle, New J. Phys. **17**, 123021 (2015).

[22] T. Seidelmann, F. Ungar, M. Cygorek, A. Vagov, A. M. Barth, T. Kuhn, and V. M. Axt, Phys. Rev. B **99**, 245301 (2019).

[23] M. Cygorek, F. Ungar, T. Seidelmann, A. M. Barth, A. Vagov, V. M. Axt, and T. Kuhn, Phys. Rev. B **98**, 045303 (2018).

[24] T. Seidelmann, F. Ungar, A. M. Barth, A. Vagov, V. M. Axt, M. Cygorek, and T. Kuhn, Phys. Rev. Lett. **123**, 137401 (2019).

[25] D. Heinze, A. Zrenner, and S. Schumacher, Phys. Rev. B **95**, 245306 (2017).

[26] A. Carmele and A. Knorr, Phys. Rev. B **84**, 075328 (2011).

[27] R. M. Stevenson, R. J. Young, P. Atkinson, K. Cooper, D. A. Ritchie, and A. J. Shields, Nature **439**, 179 (2006).

[28] R. J. Young, R. M. Stevenson, P. Atkinson, K. Cooper, D. A. Ritchie, and A. J. Shields, New J. Phys. **8**, 29 (2006).

[29] A. Muller, W. Fang, J. Lawall, and G. S. Solomon, Phys. Rev. Lett. **103**, 217402 (2009).

[30] D. Huber, M. Reindl, S. F. Covre da Silva, C. Schimpf, J. Martín-Sánchez, H. Huang, G. Piredda, J. Edlinger, A. Rastelli, and R. Trotta, Phys. Rev. Lett. **121**, 033902 (2018).

[31] H. Wang, H. Hu, T.-H. Chung, J. Qin, X. Yang, J.-P. Li, R.-Z. Liu, H.-S. Zhong, Y.-M. He, X. Ding, Y.-H. Deng, Q. Dai, Y.-H. Huo, S. Höfling, C.-Y. Lu, and J.-W. Pan, Phys. Rev. Lett. **122**, 113602 (2019).

[32] J. Liu, R. Su, Y. Wei, B. Yao, S. F. C. d. Silva, Y. Yu, J. Iles-Smith, K. Srinivasan, A. Rastelli, J. Li, and X. Wang, Nat. Nanotechnol. **14**, 586 (2019).

[33] S. Bounouar, C. de la Haye, M. Strauß, P. Schnauber, A. Thoma, M. Gschrey, J.-H. Schulze, A. Strittmatter, S. Rodt, and S. Reitzenstein, Appl. Phys. Lett. **112**, 153107 (2018).

[34] R. Winik, D. Cogan, Y. Don, I. Schwartz, L. Gantz, E. R. Schmidgall, N. Livneh, R. Rapaport, E. Buks, and D. Gershoni, Phys. Rev. B **95**, 235435 (2017).

[35] A. Fognini, A. Ahmadi, M. Zeeshan, J. T. Fokkens, S. J. Gibson, N. Sherlekar, S. J. Daley, D. Dalacu, P. J. Poole, K. D. Jöns, V. Zwiller, and M. E. Reimer, ACS Photonics **6**, 1656 (2019).

[36] N. Akopian, N. H. Lindner, E. Poem, Y. Berlatzky, J. Avron, D. Gershoni, B. D. Gerardot, and P. M. Petroff, Phys. Rev. Lett. **96**, 130501 (2006).

[37] R. Hafenbrak, S. M. Ulrich, P. Michler, L. Wang, A. Rastelli, and O. G. Schmidt, New J. Phys. **9**, 315 (2007).

[38] A. J. Bennett, M. A. Pooley, R. M. Stevenson, M. B. Ward, R. B. Patel, A. Boyer de la Giroday, N. Sköld, I. Farrer, C. A. Nicoll, D. A. Ritchie, and A. J. Shields, Nat. Phys. **6**, 947 (2010).

[39] E. del Valle, New J. Phys. **15**, 025019 (2013).

[40] F. Troiani, J. I. Perea, and C. Tejedor, Phys. Rev. B **74**, 235310 (2006).

[41] R. M. Stevenson, C. L. Salter, J. Nilsson, A. J. Bennett, M. B. Ward, I. Farrer, D. A. Ritchie, and A. J. Shields, Phys. Rev. Lett. **108**, 040503 (2012).

[42] O. Benson, C. Santori, M. Pelton, and Y. Yamamoto, Phys. Rev. Lett. **84**, 2513 (2000).

[43] F. Basso Basset, M. Valeri, E. Roccia, V. Muredda, D. Poderini, J. Neuwirth, N. Spagnolo, M. B. Rota, G. Carvacho, F. Sciarrino, and R. Trotta, Sci. Adv. **7**, eabe6379 (2021).

[44] C. Schimpf, M. Reindl, D. Huber, B. Lehner, S. F. Covre Da Silva, S. Manna, M. Vyvlecka, P. Walther, and A. Rastelli, Sci. Adv. **7**, eabe8905 (2021).

[45] C. Schimpf, M. Reindl, F. Basso Basset, K. D. Jöns, R. Trotta, and A. Rastelli, Appl. Phys. Lett. **118**, 100502 (2021).

[46] T. Seidelmann, D. E. Reiter, M. Cosacchi, M. Cygorek, A. Vagov, and V. M. Axt, Appl. Phys. Lett. **118**, 164001

(2021).

[47] L. Besombes, K. Kheng, L. Marsal, and H. Mariette, Phys. Rev. B **63**, 155307 (2001).

[48] P. Machnikowski and L. Jacak, Phys. Rev. B **69**, 193302 (2004).

[49] P. Kaer, T. R. Nielsen, P. Lodahl, A.-P. Jauho, and J. Mørk, Phys. Rev. Lett. **104**, 157401 (2010).

[50] K. Roy-Choudhury and S. Hughes, Phys. Rev. B **92**, 205406 (2015).

[51] A. Nazir and D. P. S. McCutcheon, J. Phys.: Condens. Matter **28**, 103002 (2016).

[52] A. Carmele and S. Reitzenstein, Nanophotonics **8**, 655 (2019).

[53] D. P. S. McCutcheon, Phys. Rev. A **93**, 022119 (2016).

[54] D. E. Reiter, T. Kuhn, and V. M. Axt, Adv. Phys.: X **4**, 1655478 (2019).

[55] F. Minganti, I. I. Arkhipov, A. Miranowicz, and F. Nori, New J. Phys. **23**, 122001 (2021).

[56] P. Kirton and J. Keeling, New J. Phys. **20**, 015009 (2018).

[57] W. K. Wootters, Phys. Rev. Lett. **80**, 2245 (1998).

[58] B. Krummheuer, V. M. Axt, and T. Kuhn, Phys. Rev. B **65**, 195313 (2002).

[59] G. Lindblad, Commun. Math. Phys. **48**, 119 (1976).

[60] N. Makri and D. E. Makarov, J. Chem. Phys. **102**, 4600 (1995).

[61] N. Makri and D. E. Makarov, J. Chem. Phys. **102**, 4611 (1995).

[62] A. Vagov, M. D. Croitoru, M. Glässl, V. M. Axt, and T. Kuhn, Phys. Rev. B **83**, 094303 (2011).

[63] A. M. Barth, A. Vagov, and V. M. Axt, Phys. Rev. B **94**, 125439 (2016).

[64] M. Cygorek, A. M. Barth, F. Ungar, A. Vagov, and V. M. Axt, Phys. Rev. B **96**, 201201(R) (2017).

[65] D. F. V. James, P. G. Kwiat, W. J. Munro, and A. G. White, Phys. Rev. A **64**, 052312 (2001).

[66] R. M. Stevenson, A. J. Hudson, A. J. Bennett, R. J. Young, C. A. Nicoll, D. A. Ritchie, and A. J. Shields, Phys. Rev. Lett. **101**, 170501 (2008).

[67] M. Cosacchi, M. Cygorek, F. Ungar, A. M. Barth, A. Vagov, and V. M. Axt, Phys. Rev. B **98**, 125302 (2018).

[68] M. Glässl, A. Vagov, S. Lüker, D. E. Reiter, M. D. Croitoru, P. Machnikowski, V. M. Axt, and T. Kuhn, Phys. Rev. B **84**, 195311 (2011).

[69] A. M. Barth, S. Lüker, A. Vagov, D. E. Reiter, T. Kuhn, and V. M. Axt, Phys. Rev. B **94**, 045306 (2016).

[70] M. Glässl, M. D. Croitoru, A. Vagov, V. M. Axt, and T. Kuhn, Phys. Rev. B **85**, 195306 (2012).

[71] R. Winkler, *Spin-Orbit Coupling Effects in Two-Dimensional Electron and Hole Systems*, Springer Tracts in Modern Physics, Vol. 191 (Springer, Berlin, 2003).

[72] S. Bravyi, D. P. DiVincenzo, and D. Loss, Ann. Phys. **326**, 2793 (2011).

[73] B. Krummheuer, V. M. Axt, T. Kuhn, I. D'Amico, and F. Rossi, Phys. Rev. B **71**, 235329 (2005).

[74] S. Lüker, T. Kuhn, and D. E. Reiter, Phys. Rev. B **96**, 245306 (2017).